

Examples of such loss elements are the resistance of ac generator windings, the resistance of the wire connecting the source and load, the resistance of transformer windings, and the resistance of semiconductor devices and magnetics windings in switching converters. Thus, it is desired to make the rms current as small as possible, while transferring the required amount of energy and average power to the load.

Shunt resistances usually also exist, which cause power loss according to the relation

$$\frac{(\text{rms voltage})^2}{R_{\text{shunt}}} \quad (16.14)$$

Examples include the core losses in transformers and ac generators, and switching converter transistor switching loss. Therefore, it is desired to also make the rms voltage as small as possible while transferring the required average power to the load.

### 16.3 POWER FACTOR

*Power factor* is a figure of merit that measures how effectively energy is transmitted between a source and load network. It is measured at a given surface as in Fig. 16.1, and is defined as

$$\text{power factor} = \frac{(\text{average power})}{(\text{rms voltage})(\text{rms current})} \quad (16.15)$$

The power factor always has a value between zero and one. The ideal case, unity power factor, occurs for a load that obeys Ohm's Law. In this case, the voltage and current waveforms have the same shape, contain the same harmonic spectrum, and are in phase. For a given average power throughput, the rms current and voltage are minimized at maximum (unity) power factor, that is, with a linear resistive load. In the case where the voltage contains no harmonics but the load is nonlinear and contains dynamics, then the power factor can be expressed as a product of two terms, one resulting from the phase shift of the fundamental component of the current, and the other resulting from the current harmonics.

#### 16.3.1 Linear Resistive Load, Nonsinusoidal Voltage

In this case, the current harmonics are in phase with, and proportional to, the voltage harmonics. As a result, all harmonics result in the net transfer of energy to the load. The current harmonic magnitudes and phases are

$$I_n = \frac{V_n}{R} \quad (16.16)$$

$$\theta_n = \phi_n \quad \text{so} \quad \cos(\theta_n - \phi_n) = 1 \quad (16.17)$$

The rms voltage is again

$$(\text{rms voltage}) = \sqrt{V_0^2 + \sum_{n=1}^{\infty} \frac{V_n^2}{2}} \quad (16.18)$$

and the rms current is

$$\begin{aligned}
 (\text{rms current}) &= \sqrt{I_0^2 + \sum_{n=1}^{\infty} \frac{I_n^2}{2}} = \sqrt{\frac{V_0^2}{R^2} + \sum_{n=1}^{\infty} \frac{V_n^2}{2R^2}} \\
 &= \frac{1}{R} (\text{rms voltage})
 \end{aligned} \tag{16.19}$$

By use of Eq. (16.6), the average power is

$$\begin{aligned}
 P_{av} &= V_0 I_0 + \sum_{n=1}^{\infty} \frac{V_n I_n}{2} \cos(\phi_n - \theta_n) \\
 &= \frac{V_0^2}{R} + \sum_{n=1}^{\infty} \frac{V_n^2}{2R} \\
 &= \frac{1}{R} (\text{rms voltage})^2
 \end{aligned} \tag{16.20}$$

Insertion of Eqs. (16.19) and (16.20) into Eq. (16.15) then shows that the power factor is unity. Thus, if the load is linear and purely resistive, then the power factor is unity regardless of the harmonic content of  $v(t)$ . The harmonic content of the load current waveform  $i(t)$  is identical to that of  $v(t)$ , and all harmonics result in the transfer of energy to the load. This raises the possibility that one could construct a power distribution system based on nonsinusoidal waveforms in which the energy is efficiently transferred to the load.

### 16.3.2 Nonlinear Dynamical Load, Sinusoidal Voltage

If the voltage  $v(t)$  contains a fundamental component but no dc component or harmonics, so that  $V_0 = V_2 = V_3 = \dots = 0$ , then harmonics in  $i(t)$  do not result in transmission of net energy to the load. The average power expression, Eq. (16.6), becomes

$$P_{av} = \frac{V_1 I_1}{2} \cos(\phi_1 - \theta_1) \tag{16.21}$$

However, the harmonics in  $i(t)$  do affect the value of the rms current:

$$(\text{rms current}) = \sqrt{I_0^2 + \sum_{n=1}^{\infty} \frac{I_n^2}{2}} \tag{16.22}$$

Hence, as in example 1 (Fig. 16.2), harmonics cause the load to draw more rms current from the source, but not more average power. Increasing the current harmonics does not cause more energy to be transferred to the load, but does cause additional losses in series resistive elements  $R_{series}$ .

Also, the presence of load dynamics and reactive elements, which causes the phase of the fundamental components of the voltage and current to differ ( $\theta_1 - \phi_1$ ), also reduces the power factor. The  $\cos(\phi_1 - \theta_1)$  term in the average power Eq. (16.21) becomes less than unity. However, the rms value of the current, Eq. (16.22), does not depend on the phase. So shifting the phase of  $i(t)$  with respect to  $v(t)$  reduces the average power without changing the rms voltage or current, and hence the power factor is reduced.

By substituting Eqs. (16.21) and (16.22) into (16.15), we can express the power factor for the sinusoidal voltage in the following form:

$$\begin{aligned}
 \text{(power factor)} &= \left( \frac{\frac{I_1}{\sqrt{2}}}{\sqrt{I_0^2 + \sum_{n=1}^{\infty} \frac{I_n^2}{2}}} \right) \left( \cos(\varphi_I - \theta_I) \right) \\
 &= \text{(distortion factor)} \text{ (displacement factor)}
 \end{aligned} \tag{16.23}$$

So when the voltage contains no harmonics, then the power factor can be written as the product of two terms. The first, called the *distortion factor*, is the ratio of the rms fundamental component of the current to the total rms value of the current

$$\text{(distortion factor)} = \left( \frac{\frac{I_1}{\sqrt{2}}}{\sqrt{I_0^2 + \sum_{n=1}^{\infty} \frac{I_n^2}{2}}} \right) = \frac{\text{(rms fundamental current)}}{\text{(rms current)}} \tag{16.24}$$

The second term of Eq. (16.23) is called the *displacement factor*, and is the cosine of the angle between the fundamental components of the voltage and current waveforms.

The *Total Harmonic Distortion* (THD) is defined as the ratio of the rms value of the waveform not including the fundamental, to the rms fundamental magnitude. When no dc is present, this can be written:

$$\text{(THD)} = \frac{\sqrt{\sum_{n=2}^{\infty} I_n^2}}{I_1} \tag{16.25}$$

The total harmonic distortion and the distortion factor are closely related. Comparison of Eqs. (16.24) and (16.25), with  $I_0 = 0$ , leads to

$$\text{(distortion factor)} = \frac{1}{\sqrt{1 + (\text{THD})^2}} \tag{16.26}$$

This equation is plotted in Fig. 16.5. The distortion factor of a waveform with a moderate amount of distortion is quite close to unity. For example, if the waveform contains third harmonic whose magnitude is

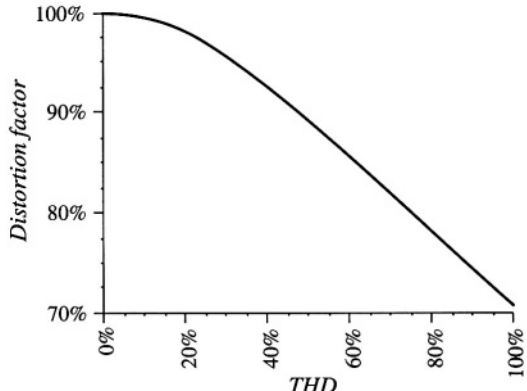


Fig. 16.5 Distortion factor vs. total harmonic distortion.

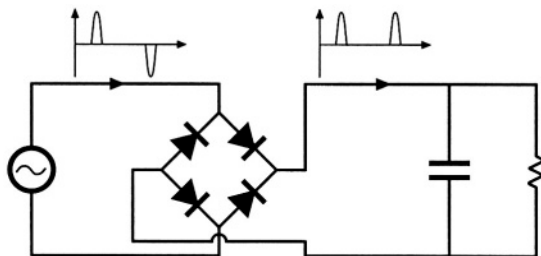


Fig. 16.6 Conventional peak detection rectifier.

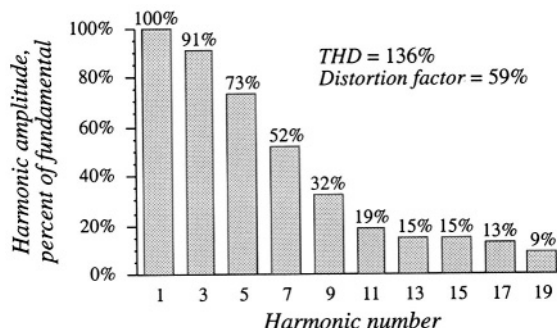


Fig. 16.7 Typical ac line current spectrum of a peak detection rectifier. Harmonics 1 to 19 are shown.

10% of the fundamental, the distortion factor is 99.5%. Increasing the third harmonic to 20% decreases the distortion factor to 98%, and a 33% harmonic magnitude yields a distortion factor of 95%. So the power factor is not significantly degraded by the presence of harmonics unless the harmonics are quite large in magnitude.

An example of a case in which the distortion factor is much less than unity is the conventional peak detection rectifier of Fig. 16.6. In this circuit, the ac line current consists of short-duration current pulses occurring at the peak of the voltage waveform. The fundamental component of the line current is essentially in phase with the voltage, and the displacement factor is close to unity. However, the low-order current harmonics are quite large, close in magnitude to that of the fundamental—a typical current spectrum is given in Fig. 16.7. The distortion factor of peak detection rectifiers is usually in the range 55% to 65%. The resulting power factor is similar in value.

In North America, the standard 120 V power outlet is protected by a 15 A circuit breaker. In consequence, the available load power quite limited. Derating the circuit breaker current by 20%, assuming typical efficiencies for the dc–dc converter and peak detection rectifier, and with a power factor of 55%, one obtains the following estimate for the maximum available dc load power:

$$\begin{aligned}
 & (\text{ac voltage}) (\text{derated breaker current}) (\text{power factor}) (\text{rectifier efficiency}) \\
 & = (120 \text{ V}) \quad (80\% \text{ of } 15 \text{ A}) \quad (0.55) \quad (0.98) \\
 & = 776 \text{ W}
 \end{aligned} \tag{16.27}$$

The less-than-unity efficiency of a dc–dc converter would further reduce the available dc load power. Using a peak detection rectifier to supply a load power greater than this requires that the user install higher amperage and/or higher voltage service, which is inconvenient and costly. The use of a rectifier

circuit having nearly unity power factor would allow a significant increase in available dc load power:

$$\begin{aligned}
 & (\text{ac voltage}) (\text{derated breaker current}) (\text{power factor}) (\text{rectifier efficiency}) \\
 & = (120 \text{ V}) \quad (80\% \text{ of } 15 \text{ A}) \quad (0.99) \quad (0.93) \\
 & = 1325 \text{ W}
 \end{aligned} \tag{16.28}$$

or almost twice the available power of the peak detection rectifier. This alone can be a compelling reason to employ high quality rectifiers in commercial systems.

#### 16.4 POWER PHASORS IN SINUSOIDAL SYSTEMS

The apparent power is defined as the product of the rms voltage and rms current. Apparent power is easily measured—it is simply the product of the readings of a voltmeter and ammeter placed in the circuit at the given surface. Many power system elements, such as transformers, must be rated according to the apparent power that they are able to supply. The unit of apparent power is the volt-ampere, or VA. The power factor, defined in Eq. (16.15), is the ratio of average power to apparent power.

In the case of sinusoidal voltage and current waveforms, we can additionally define the *complex power*  $S$  and the *reactive power*  $Q$ . If the sinusoidal voltage  $v(t)$  and current  $i(t)$  can be represented by the phasors  $V$  and  $I$ , then the complex power is a phasor defined as

$$S = VI^* = P + jQ \tag{16.29}$$

Here,  $I^*$  is the complex conjugate of  $I$ , and  $j$  is the square root of  $-1$ . The magnitude of  $S$ , or  $\|S\|$ , is equal to the apparent power, measured in VA. The real part of  $S$  is the average power  $P$ , having units of watts. The imaginary part of  $S$  is the reactive power  $Q$ , having units of reactive volt-amperes, or VARs.

A phasor diagram illustrating  $S$ ,  $P$ , and  $Q$ , is given in Fig. 16.8. The angle  $(\phi_1 - \theta_1)$  is the angle between the voltage phasor  $V$  and the current phasor  $I$ .  $(\phi_1 - \theta_1)$  is additionally the phase of the complex power  $S$ . The power factor in the purely sinusoidal case is therefore

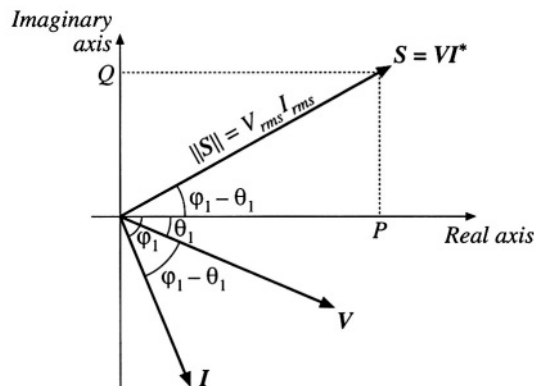


**Fig. 16.8** Power phasor diagram, for a sinusoidal system, illustrating the voltage, current, and complex power phasors.

$$\text{power factor} = \frac{P}{|S|} = \cos(\phi_1 - \theta_1) \quad (16.30)$$

It should be emphasized that this equation is valid only for systems in which the voltage and current are purely sinusoidal. The distortion factor of Eq. (16.24) then becomes unity, and the power factor is equal to the displacement factor as in Eq. (16.30).

The reactive power  $Q$  does not lead to net transmission of energy between the source and load. When reactive power is present, the rms current and apparent power are greater than the minimum amount necessary to transmit the average power  $P$ . In an inductor, the current lags the voltage by  $90^\circ$ , causing the displacement factor to be zero. The alternate storing and releasing of energy in an inductor leads to current flow and nonzero apparent power, but the average power  $P$  is zero. Just as resistors consume real (average) power  $P$ , inductors can be viewed as consumers of reactive power  $Q$ . In a capacitor, the current leads to voltage by  $90^\circ$ , again causing the displacement factor to be zero. Capacitors supply reactive power  $Q$ , and are commonly placed in the utility power distribution system near inductive loads. If the reactive power supplied by the capacitor is equal to the reactive power consumed by the inductor, then the net current (flowing from the source into the capacitor-inductive-load combination) will be in phase with the voltage, leading unity power factor and minimum rms current magnitude.

It will be seen in the next chapter that phase-controlled rectifiers produce a nonsinusoidal current waveform whose fundamental component lags the voltage. This lagging current does not arise from energy storage, but it does nonetheless lead to a reduced displacement factor, and to rms current and apparent power that are greater than the minimum amount necessary to transmit the average power.

## 16.5 HARMONIC CURRENTS IN THREE PHASE SYSTEMS

The presence of harmonic currents can also lead to some special problems in three-phase systems. In a four-wire three-phase system, harmonic currents can lead to large currents in the neutral conductors, which may easily exceed the conductor rms current rating. Power factor correction capacitors may experience significantly increased rms currents, causing them to fail. In this section, these problems are examined, and the properties of harmonic current flow in three-phase systems are derived.

### 16.5.1 Harmonic Currents in Three-Phase Four-Wire Networks

Let us consider the three-phase four-wire network of Fig. 16.9. In general, we can express the Fourier series of the line currents and line-neutral voltages as follows:

$$\begin{aligned} i_a(t) &= I_{a0} + \sum_{k=1}^{\infty} I_{ak} \cos(k\omega t - \theta_{ak}) \\ i_b(t) &= I_{b0} + \sum_{k=1}^{\infty} I_{bk} \cos(k(\omega t - 120^\circ) - \theta_{bk}) \\ i_c(t) &= I_{c0} + \sum_{k=1}^{\infty} I_{ck} \cos(k(\omega t + 120^\circ) - \theta_{ck}) \end{aligned} \quad (16.31)$$

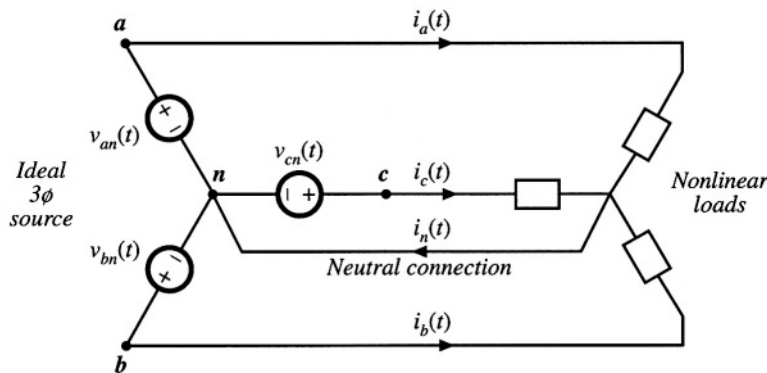


Fig. 16.9 Current flow in a three-phase four-wire network.

$$\begin{aligned} v_{an}(t) &= V_m \cos(\omega t) \\ v_{bn}(t) &= V_m \cos(\omega t - 120^\circ) \\ v_{cn}(t) &= V_m \cos(\omega t + 120^\circ) \end{aligned} \quad (16.32)$$

The neutral current is therefore  $i_n = i_a + i_b + i_c$ , or

$$i_n(t) = I_{a0} + I_{b0} + I_{c0} + \left| \sum_{k=1}^{\infty} \left[ I_{ak} \cos(k\omega t - \theta_{ak}) + I_{bk} \cos(k(\omega t - 120^\circ) - \theta_{bk}) + I_{ck} \cos(k(\omega t + 120^\circ) - \theta_{ck}) \right] \right| \quad (16.33)$$

When the load is unbalanced (even though the voltages are balanced and undistorted), we can say little else about the neutral and line currents. If the load is unbalanced and nonlinear, then the line and neutral currents may contain harmonics of any order, including even and triplen harmonics.

Equation (16.33) is considerably simplified in the case where the loads are balanced. A balanced nonlinear load is one in which  $I_{ak} = I_{bk} = I_{ck} = I_k$  and  $\theta_{ak} = \theta_{bk} = \theta_{ck} = \theta_k$ , for all  $k$ ; that is, the harmonics of the three phases all have equal amplitudes and phase shifts. In this case, Eq. (16.33) reduces to

$$i_n(t) = 3I_0 + \sum_{k=3,6,9,\dots}^{\infty} 3I_k \cos(k\omega t - \theta_k) \quad (16.34)$$

Hence, the fundamental and most of the harmonics cancel out, and do not appear in the neutral conductor. Thus, it is in the interests of the utility to balance their nonlinear loads as well as their harmonics.

But not all of the harmonics cancel out of Eq. (16.34): the dc and *triplen* (triple-n, or 3,6,9,...) harmonics add rather than cancel. The rms neutral current is

$$i_{n,rms} = 3 \sqrt{I_0^2 + \sum_{k=3,6,9,\dots}^{\infty} \frac{I_k^2}{2}} \quad (16.35)$$

#### Example

A balanced nonlinear load produces line currents containing fundamental and 20% third harmonic:  $i_{an}(t) = I_1 \cos(\omega t - \theta_1) + 0.2I_1 \cos(3\omega t - \theta_3)$ . Find the rms neutral current, and compare its amplitude to the rms line current amplitude.

*Solution:*

$$\begin{aligned} i_{n,\text{rms}} &= 3 \sqrt{\frac{(0.2I_1)^2}{2}} = \frac{0.6I_1}{\sqrt{2}} \\ i_{1,\text{rms}} &= \sqrt{\frac{I_1^2 + (0.2I_1)^2}{2}} = \frac{I_1}{\sqrt{2}} \sqrt{1+0.04} \approx \frac{I_1}{\sqrt{2}} \end{aligned} \quad (16.36)$$

So the neutral current magnitude is 60% of the line current magnitude! The triplen harmonics in the three phases add, such that 20% third harmonic leads to 60% third harmonic neutral current. Yet the presence of the third harmonic has very little effect on the rms value of the line current. Significant unexpected neutral current flows.

### 16.5.2 Harmonic Currents in Three-Phase Three-Wire Networks

If there is no neutral connection to the wye-connected load, as in Fig. 16.10, then  $i_n(t)$  must be zero. If the load is balanced, then Eq. (16.34) still applies, and therefore the dc and triplen harmonics of the load currents must be zero. Therefore, the line currents  $i_a$ ,  $i_b$ , and  $i_c$  cannot contain triplen or dc harmonics. What happens is that a voltage is induced at the load neutral point  $n'$ , containing dc and triplen harmonics, which eliminates the triplen and dc load current harmonics.

This result is true only when the load is balanced. With an unbalanced load, all harmonics can appear in the line currents, including triplen and dc. In practice, the load is never exactly balanced, and some small amounts of third harmonic line currents are measured.

With a delta-connected load as in Fig. 16.11, there is also no neutral connection, so the line currents cannot contain triplen or dc components. But the loads are connected line-to-line, and are excited by undistorted sinusoidal voltages. Hence triplen harmonic and dc currents do, in general, flow through the nonlinear loads. Therefore, these currents simply circulate around the delta. If the load is balanced, then again no triplen harmonics appear in the line currents.

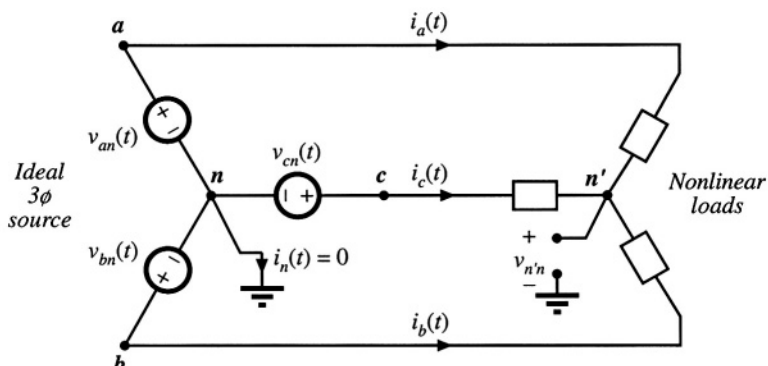
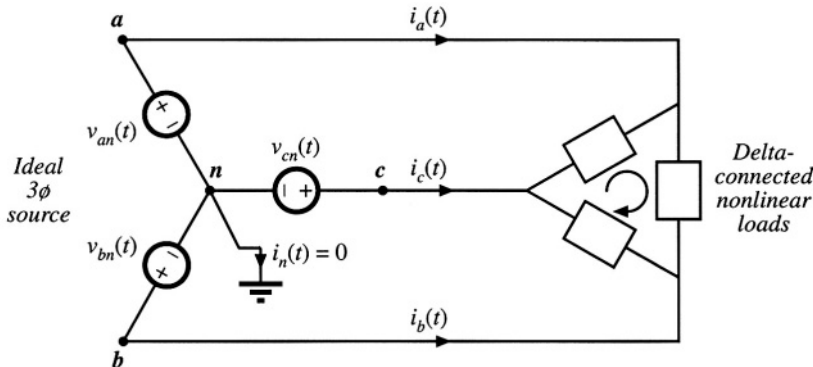


Fig. 16.10 Current flow in a three-phase three-wire wye-connected network.



**Fig. 16.11** A balanced nonlinear delta-connected load may generate triplen current harmonics. These harmonics circulate around the delta, but do not flow through the lines if the load is balanced.

### 16.5.3 Harmonic Current Flow in Power Factor Correction Capacitors

Harmonic currents tend to flow through shunt-connected power factor correction capacitors. To some extent, this is a good thing because the capacitors tend to low-pass filter the power system currents, and prevent nonlinear loads from polluting the entire power system. The flow of harmonic currents is then confined to the nonlinear load and local power factor correction capacitors, and voltage waveform distortion is reduced. High-frequency harmonic currents tend to flow through shunt capacitors because the capacitor impedance decreases with frequency, while the inductive impedance of transmission lines increases with frequency. In this sense, power factor correction capacitors mitigate the effects of harmonic currents arising from nonlinear loads in much the same way that they mitigate the effects of reactive currents that arise from inductive loads.

But the problem is that the power factor correction capacitors may not be rated to handle these harmonic currents, and hence there is a danger that the capacitors may overheat and fail when they are exposed to significant harmonic currents. The loss in capacitors is modeled using an *equivalent series resistance* (esr) as shown in Fig. 16.12. The esr models dielectric loss (hysteresis of the dielectric D-E loop), contact resistance, and foil and lead resistances. Power loss occurs, equal to  $i_{rms}^2 \cdot (esr)$ . Dielectric materials are typically poor conductors of heat, so a moderate amount of power loss can cause a large temperature rise in the center of the capacitor. In consequence, the rms current must be limited to a safe value.

Typical power factor correction capacitors are rated by voltage  $V$ , frequency  $f$ , and reactive power in kVARs. These ratings are computed from the capacitance  $C$  and safe rms current  $I_{rms}$ , assuming undistorted sinusoidal waveforms, as follows:

$$\text{rated rms voltage } V_{rms} = \frac{I_{rms}}{2\pi f C} \quad (16.37)$$

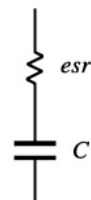


**Fig. 16.12** Capacitor equivalent circuit. Losses are modeled by an equivalent series resistance (esr).

$$\text{rated reactive power} = \frac{I_{\text{rms}}^2}{2\pi f C} \quad (16.38)$$

In an undistorted system, the rms current, and hence also the capacitor esr loss, cannot increase unless the rms voltage is also increased. But high-frequency harmonics can lead to larger rms currents without an increased voltage. Any harmonics that flow result in increased rms current beyond the expected value predicted by Eq. (16.37). If the capacitor is not rated to handle additional power loss, then failure or premature aging can occur.

## 16.6 AC LINE CURRENT HARMONIC STANDARDS

Besides the increased currents and reduced power factors of peak detection rectifiers, the harmonics themselves can be detrimental: if large enough in magnitude, they can pollute the power system. Harmonic currents cause distortion of the voltage waveform via the power system series impedance. These voltage harmonics can interfere with the operation of nearby loads. As noted previously, increased currents in shunt capacitors, and increased losses in distribution transformers and ac machines, can lead to premature aging and failure of these devices. Odd triplen harmonics (triple- $n$ : 3<sup>rd</sup>, 9<sup>th</sup>, 15<sup>th</sup>, etc.) lead to unexpectedly large neutral currents in three-phase systems. Harmonic currents can also excite system resonances some distance from their source, with results that are difficult to predict. For these reasons, a number of organizations have adopted standards that limit the magnitudes of the harmonic currents that a load is allowed to inject into the ac line. The US military was one of the early organizations to recognize these problems; the very strict 3% limit was initially adopted. The standards adopted by the IEC and IEEE are more recent, and are intended for conventional utility systems. A fourth example, not discussed here, is the telephone interference factor, which limits power distribution system harmonics in cases when telephone lines and power lines share the same poles.

### 16.6.1 International Electrotechnical Commission Standard 1000

This international agency adopted a first draft of their IEC 555 standard in 1982. It has since undergone a number of revisions, and has been superceded by IEC 1000 [7]. This standard is now enforced in Europe, making it a de facto standard for commercial equipment intended to be sold worldwide.

The IEC 1000-3-2 standard covers a number of different types of low power equipment, with differing harmonic limits. It specifically limits harmonics for equipment having an input current of up to 16 A, connected to 50 or 60 Hz, 220 V to 240 V single phase circuits (two or three wire), as well as 380 V to 415 V three phase (three or four wire) circuits. In a city environment such as a large building, a large fraction of the total power system load can be nonlinear. For example, a major portion of the electrical load in a building is comprised of fluorescent lights, which present a very nonlinear characteristic to the utility system. A modern office may also contain a large number of personal computers, printers, copiers, etc., each of which may employ peak detection rectifiers. Although each individual load is a negligible fraction of the total local load, these loads can collectively become significant.

The IEC 1000-3-2 standard defines several categories of equipment, each of which is covered by a different set of harmonic limits. As an example, Table 16.1 shows the harmonic limits for *Class A* equipment, which includes low harmonic rectifiers for computer and other office equipment.

The European norm EN 61000-3-2 defines similar limits.

**Table 16.1** IEC 1000-3-2 Harmonic current limits, class A

Odd harmonics		Even harmonics	
Harmonic number	Maximum current	Harmonic number	Maximum current
3	2.30 A	2	1.08 A
5	1.14 A	4	0.43 A
7	0.77 A	6	0.30 A
9	0.40 A	$8 \leq n \leq 40$	$0.23 A \cdot (8/n)$
11	0.33 A		
13	0.21 A		
$15 \leq n \leq 39$	$0.15 A \cdot (15/n)$		

### 16.6.2 IEEE/ANSI Standard 519

In 1993, the IEEE published a revised draft standard limiting the amplitudes of current harmonics, *IEEE Guide for Harmonic Control and Reactive Compensation of Static Power Converters*. The harmonic limits are based on the ratio of the fundamental component of the load current  $I_L$  to the short circuit current at the point of common coupling (PCC) at the utility  $I_{sc}$ . Stricter limits are imposed on large loads than on small loads. The limits are similar in magnitude to IEC 1000, and cover high voltage loads (of much higher power) not addressed by IEC 1000. Enforcement of this standard is presently up to the local utility company.

The odd harmonic limits for general distribution systems at voltages of 120 V to 69 kV are listed in Table 16.2. The limits for even harmonics are 25% of the odd harmonic limits. Limits for general distribution systems at 69.001 kV to 161 kV are 50% of the values listed in Table 16.2. DC current components and half-wave rectifiers are not allowed.

It is the responsibility of the power consumer to meet these current harmonic standards. Standard IEEE-519 also specifies maximum allowable voltage harmonics, listed in Table 16.3. It is the responsibility of the utility, or power supplier, to meet these limits. Both total harmonic distortion and maximum individual harmonic magnitudes are limited.

**Table 16.2** IEEE-519 Maximum odd harmonic current limits for general distribution systems, 120 V to 69 kV

$I_{sc}/I_L$	$n < 11$	$11 \leq n < 17$	$17 \leq n < 23$	$23 \leq n < 35$	$35 \leq n$	THD
< 20	4.0%	2.0%	1.5%	0.6%	0.3%	5.0%
20-50	7.0%	3.5%	2.5%	1.0%	0.5%	8.0%
50-100	10.0%	4.5%	4.0%	1.5%	0.7%	12.0%
100-1000	12.0%	5.5%	5.0%	2.0%	1.0%	15.0%
> 1000	15.0%	7.0%	6.0%	2.5%	1.4%	20.0%

**Table 16.3** IEEE-519 Voltage distortion limits

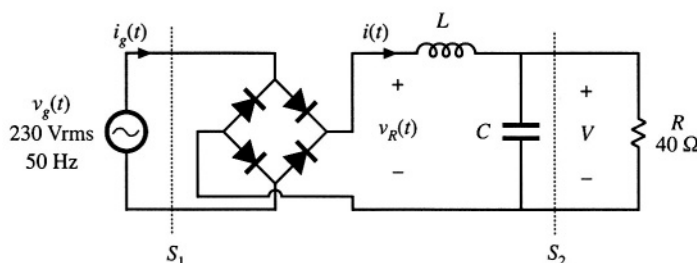
Bus voltage at PCC	Individual harmonics	THD
69 kV and lower	3.0%	5.0%
69.001 kV to 161 kV	1.5%	2.5%
Above 161 kV	1.0%	1.5%

**BIBLIOGRAPHY**

- [1] J. ARRILLAGA, D. BRADLEY, and P. BODGER, *Power System Harmonics*, New York: John Wiley & Sons, 1985.
- [2] R. SMITH and R. STRATFORD, "Power System Harmonics Effects from Adjustable-Speed Drives," *IEEE Transactions on Industry Applications*, Vol. IA-20, No. 4, pp. 973-977, July/August 1984.
- [3] A. EMANUEL, "Powers in Nonsinusoidal Situations—A Review of Definitions and Physical Meaning," *IEEE Transactions on Power Delivery*, Vol. 5, No. 3, pp. 1377-1389, July 1990.
- [4] N. MOHAN, T. UNDELAND, and W. ROBBINS, *Power Electronics: Converters, Applications, and Design*, Second edition, New York: John Wiley & Sons, 1995.
- [5] J. KASSAKIAN, M. SCHLECHT, and G. VERGESE, *Principles of Power Electronics*, Massachusetts: Addison-Wesley, 1991.
- [6] R. GRETSCHE, "Harmonic Distortion of the Mains Voltage by Switched-Mode Power Supplies—Assessment of the Future Development and Possible Mitigation Measures," *European Power Electronics Conference*, 1989 Record, pp. 1255-1260.
- [7] IEC 1000-3-2, First Edition, Commission Electrotechnique Internationale, Geneva, 1995.

**PROBLEMS**

- 16.1** Passive rectifier circuit. In the passive rectifier circuit of Fig. 16.13,  $L$  is very large, such that the inductor current  $i(t)$  is essentially dc. All components are ideal.

**Fig. 16.13** Passive rectifier circuit of Problem 16.1

- (a) Determine the dc output voltage, current, and power.

- (b) Sketch the ac line current waveform  $i_g(t)$  and the rectifier output voltage waveform  $v_R(t)$ .  
 (c) Determine the ac line current rms magnitude, fundamental rms magnitude, and third harmonic rms magnitude. Does this rectifier network conform to the IEC-1000 harmonic current limits?  
 (d) Determine the power factor, measured at surfaces  $S_1$  and  $S_2$ .

**16.2** The three-phase rectifier of Fig. 16.14 is connected to a balanced 60 Hz 3øac 480 V (rms, line-line) sinusoidal source as shown. All elements are ideal. The inductance  $L$  is large, such that the current  $i(t)$  is essentially constant, with negligible 360 Hz ripple.

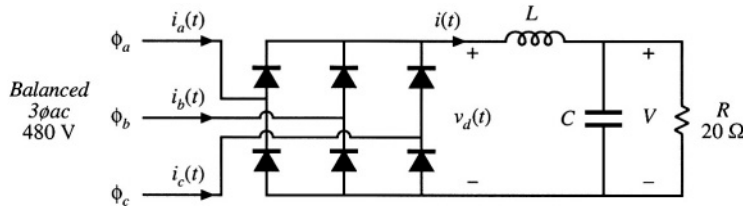


**Fig. 16.14** Three-phase rectifier circuit of Problem 16.2

- (a) Sketch the waveform  $v_d(t)$   
 (b) Determine the dc output voltage  $V$ .  
 (c) Sketch the line current waveforms  $i_a(t)$ ,  $i_b(t)$ , and  $i_c(t)$ .  
 (d) Find the Fourier series of  $i_a(t)$   
 (e) Find the distortion factor, displacement factor, power factor, and line current THD.

**16.3** Harmonic pollution police. In the network of Fig. 16.15, voltage harmonics are observed at the indicated surface. The object of this problem is to decide whether to blame the source or the load for the observed harmonic pollution. Either the source element or the load element contains a nonlinearity that generates harmonics, while the other element is linear.

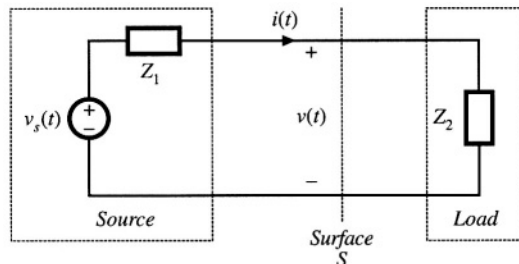


**Fig. 16.15** Single-phase power system of Problems 16.3 to 16.5

- (a) Consider first the case where the load is a passive linear impedance  $Z_2(s)$ , and hence its phase lies in the range  $-90^\circ \leq \angle Z_2(j\omega) \leq +90^\circ$  for all positive  $\omega$ . The source generates harmonics. Express the average power  $P$  in the form

$$P = \sum_{n=0}^{\infty} P_n$$

where  $P_n$  is the average power transmitted to the load by harmonic number  $n$ . What can you say about the polarities of the  $P_n$ s?

- (b) Consider next the case where the load is nonlinear, while the source is linear and can be modeled by a Thevenin-equivalent sinusoidal voltage source and linear impedance  $Z_1(s)$ . Again express the average power  $P$  as a sum of average powers, as in part (a). What can you say about the polarities of the  $P_n$ s in this case?
- (c) The following Fourier series are measured:

Harmonic number	$v(t)$		$i(t)$	
	Magnitude	Phase	Magnitude	Phase
1	230 V	0°	6 A	-20°
3	20 V	180°	4 A	20°
5	8 V	60°	1 A	-110°

Who do you accuse? Explain your reasoning.

- 16.4** For the network and waveforms of Problem 16.3, determine the power factor at the indicated surface, and the average power flowing to the load. Harmonics higher in frequency than the fifth harmonic are negligible in magnitude.

- 16.5** Repeat Problem 16.3(c), using the following Fourier series:

Harmonic number	$v(t)$		$i(t)$	
	Magnitude	Phase	Magnitude	Phase
1	120 V	0°	5 A	25°
3	4 V	60°	0.5 A	40°
5	2 V	-160°	0.2 A	-100°

- 16.6** A balanced three-phase wye-connected load is constructed using a  $20\ \Omega$  resistor in each phase. This load is connected to a balanced three-phase wye-connected voltage source, whose fundamental voltage component is 380 Vrms line-to-line. In addition, each (line-to-neutral) voltage source produces third and fifth harmonics. Each harmonic has amplitude 20 Vrms, and is in phase with the (line-to-neutral) fundamental.

- (a) The source and load neutral points are connected, such that a four-wire system is obtained. Find the Fourier series of the line currents and the neutral current.
- (b) The neutral connection is broken, such that a three-wire system is obtained. Find the Fourier series of the line currents. Also find the Fourier series of the voltage between the source and load neutral points.

---

# 17

## Line-Commutated Rectifiers

---

Conventional diode peak-detection rectifiers are inexpensive, reliable, and in widespread use. Their shortcomings are the high harmonic content of their ac line currents, and their low power factors. In this chapter, the basic operation and ac line current waveforms of several of the most common single-phase and three-phase diode rectifiers are summarized. Also introduced are phase-controlled three-phase rectifiers and inverters, and passive harmonic mitigation techniques. Several of the many references in this area are listed at the end of this chapter [1–15].

Rigorous analytical design of line-commutated rectifier and filter circuits is unfeasible for all but the simplest of circuits. Typical peak-detection rectifiers are numerically ill-conditioned, because small changes in the dc-side ripple voltage lead to large changes in the ac line current waveforms. Therefore, the discussions of this chapter are confined to mostly qualitative arguments, with the objective of giving the reader some insight into the physical operation of rectifier/filter circuits. Waveforms, harmonic magnitudes, and power factors are best determined by measurement or computer simulation.

### 17.1 THE SINGLE-PHASE FULL-WAVE RECTIFIER

A single-phase full-wave rectifier, with uncontrolled diode rectifiers, is shown in Fig. 17.1. The circuit includes a dc-side  $L-C$  filter. There are two conventional uses for this circuit. In the traditional full-wave rectifier, the output capacitor is large in value, and the dc output voltage  $v(t)$  has negligible ripple at the second harmonic of the ac line frequency. Inductor  $L$  is most often small or absent. Additional small inductance may be in series with the ac source  $v_g(t)$ . A second conventional use of this circuit is in the low-harmonic rectifiers discussed in the next chapter. In this case, the resistive load is replaced by a dc-dc converter that is controlled such that its power input port obeys Ohm's law. For the purposes of understanding the rectifier waveforms, the converter can be modeled by an effective resistance  $R$ , as in the cir-

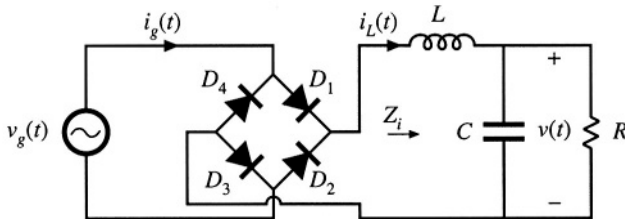


**Fig. 17.1** Conventional single-phase full-wave rectifier, with dc-side  $L$ - $C$  filter

cuit of Fig. 17.1. In this application, the  $L$ - $C$  filter is required to filter the conducted electromagnetic interference (EMI) generated by the converter. The inductor and capacitor element values are typically small in value, and  $v(t)$  is approximately a rectified sinusoid. More generally, there may be several sections of  $L$ - $C$  filter networks, connected to both the dc and ac sides of the diode rectifier, which filter EMI, smooth the dc output voltage, and reduce the ac line current harmonics.

The presence of any filter degrades the ac current waveform of the rectifier. With no reactive elements ( $L = 0$  and  $C = 0$ ), the rectifier presents a purely resistive load to the ac input. The output voltage  $v(t)$  is then a rectified sinusoid, there are no ac line current harmonics, and the power factor is unity. Addition of reactive elements between the rectifier diodes and the load leads in general to ac line current harmonics. Given that such a filter is necessary, one might ask what can be done to keep these harmonics as small as possible. In this section, the dependence of the ac line current total harmonic distortion on the filter parameters is described.

The circuit of Fig. 17.1 generates odd harmonics of the ac line voltage in the ac line current. The dc output voltage contains dc and even harmonics of the ac line voltage. The circuit exhibits several modes of operation, depending on the relative values of  $L$ ,  $C$ , and  $R$ . It is easiest to understand these modes by considering the limiting cases, as follows.

### 17.1.1 Continuous Conduction Mode

When the inductor  $L$  is very large, then the inductor current  $i_L(t)$  is essentially constant. This follows from the inductor definition  $v_L(t) = Ldi_L(t)/dt$ . For a given applied inductor voltage waveform  $v_L(t)$ , the slope  $dv_L(t)/dt$  can be made arbitrarily small by making  $L$  sufficiently large. In the limiting case where  $L$  is infinite, the slope  $dv_L(t)/dt$  becomes zero, and the inductor current is constant dc. To provide a path for the constant inductor to flow, at least two of the rectifier diodes must conduct at any given instant in time. For the circuit of Fig. 17.1, diodes  $D_1$  and  $D_3$  conduct when the ac line voltage  $v_g(t)$  is positive, and  $D_2$  and  $D_4$  conduct when  $v_g(t)$  is negative. The ac line current waveform is therefore a square wave, with  $i_g(t) = i_L(t)$  when  $v_g(t)$  is positive, and  $i_g(t) = -i_L(t)$  when  $v_g(t)$  is negative. The diode conduction angle  $\beta$ , defined as the angle through which one of the diodes conducts, is equal to  $180^\circ$  in CCM.

The rms value of a square wave is equal to its peak value  $I_{pk}$ , in this case the dc load current. The fundamental component of a square wave is equal to  $4I_{pk}/\pi$ . The square-wave contains odd harmonics which vary as  $1/n$ . The distortion factor is therefore

$$\text{distortion factor} = \frac{I_{1,\text{rms}}}{I_{\text{rms}}} = \frac{4}{\pi\sqrt{2}} = 90.0\% \quad (17.1)$$

The total harmonic distortion is

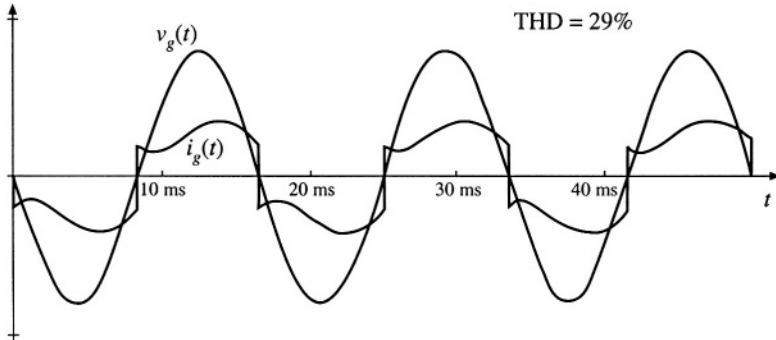


Fig. 17.2 Typical ac line current and voltage waveforms, continuous conduction mode.  $f_0/f_L = 5$ ,  $Q = 0.25$ .

$$\text{THD} = \sqrt{\left(\frac{1}{\text{distortion factor}}\right)^2 - 1} = 48.3\% \quad (17.2)$$

So the limiting case of the large inductor leads to some significant harmonic distortion, although it is not as bad as the peak detection rectifier case. Since the square wave is in phase with the ac input voltage, the displacement factor is unity, and hence the power factor is equal to the distortion factor.

Whenever the inductor is sufficiently large, the rectifier diodes conduct continuously (i.e., there is no time interval in which all four diodes are reverse-biased). This is called the continuous conduction mode (CCM). A typical ac line current waveform is plotted in Fig. 17.2 for a finite but large value of  $L$ . It can be seen that the ac line current is discontinuous at the ac line voltage zero crossing, as in the square-wave limiting case. Some ringing is also present. This waveform contains a total harmonic distortion of approximately 29%.

### 17.1.2 Discontinuous Conduction Mode

The opposite case occurs when the inductor is very small and the capacitor  $C$  is very large. This is the peak detector circuit. In the limit as  $L$  goes to zero and  $C$  goes to infinity, the ac line current approaches a string of delta (impulse) functions that coincide with the peaks of the sinusoidal input voltage waveform. It can be shown that, in this limiting case, the THD becomes infinite while the distortion factor and power factor become zero. Of course, in the practical case the current is not infinite; nonetheless, large THD with low power factor is quite possible. The diodes conduct for less than one-half of the ac line period, and hence  $\beta < 180^\circ$  in DCM.

Whenever the capacitor is large and the inductor is small, the rectifier tends to “peak detect,” and the rectifier operates in the discontinuous conduction mode (DCM). There exist time intervals of nonzero length where all four rectifier diodes are reverse-biased. A typical set of waveforms is plotted in Fig. 17.3, where the capacitor is large but finite, and the inductor is small but nonzero. The ac line voltage and the value of the load resistance are the same as in Fig. 17.2, yet the peak current is substantially larger. The THD for this waveform is 145%, and the distortion factor is 57%.

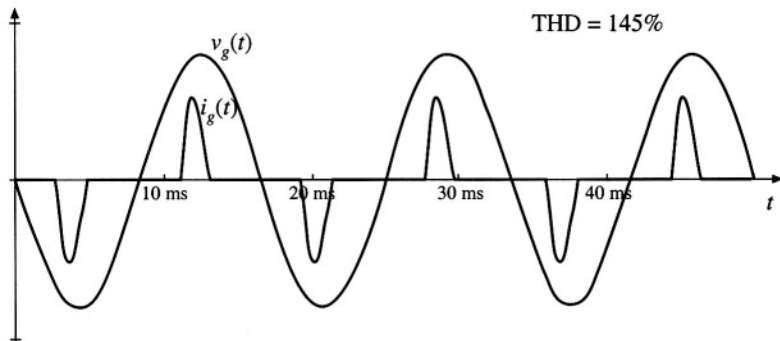


Fig. 17.3 Typical ac line current and voltage waveforms, discontinuous conduction mode.  $f_0/f_L = 8.4$ ,  $Q = 121$ .

### 17.1.3 Behavior When $C$ is Large

A variety of authors have discussed the solution of passive rectifier circuits; several works are listed in the references [8–15]. Analysis of even the simple circuit of Fig. 17.1 is surprisingly complex. For the case when  $C$  is infinite, it was shown in [8] that the rectifier waveshapes can be expressed as a function of a single dimensionless parameter  $K_L$ , defined as

$$K_L = \frac{2L}{RT_L} \quad (17.3)$$

where  $T_L = 1/f_L$  is the ac line period. Equation (17.3) is of the same form as Eq. (5.6), used to define the dimensionless parameter  $K$  which governs the DCM behavior of PWM converters. Figure 17.4 illustrates the behavior of the single-phase rectifier circuit of Fig. 17.1, as a function of  $K_L$  and for infinite  $C$  [8]. When  $K_L$  is greater than approximately 0.1, the rectifier operates in CCM, with waveforms similar to those in Fig. 17.2.

The voltage conversion ratio  $M$  is defined as

$$M = \frac{V}{V_m} \quad (17.4)$$

where  $V_m$  is the peak value of the sinusoidal ac input voltage. In CCM, the output voltage is ideally independent of load, with  $M = 2/\pi$ . Addition of ac-side inductance can cause the output voltage to exhibit a dependence on load current. The total harmonic distortion in CCM is nearly constant and equal to the value given by Eq. (17.2).

Near the boundary between CCM and DCM, the fundamental component of the line current significantly lags the line voltage. The displacement factor reaches a minimum value slightly less than 80%, and power factors between 70% and 80% are observed.

For  $K_L \ll 0.1$ , the rectifier operates heavily in DCM, as a peak-detection rectifier. As  $K_L$  is decreased, the displacement factor approaches unity, while the THD increases rapidly. The power factor is dominated by the distortion factor. The output voltage becomes dependent on the load, and hence the rectifier exhibits a small but nonzero output impedance.

For  $K_L$  less than approximately 0.05, the waveforms are unchanged when some or all of the inductance is shifted to the ac side of the diode bridge. Figure 17.4 therefore applies to rectifiers contain-

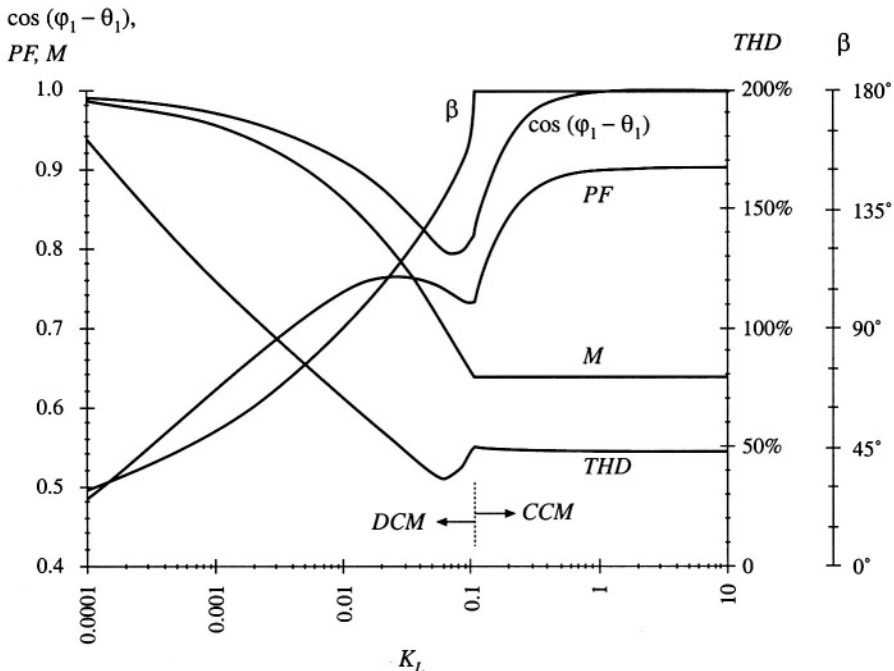


Fig. 17.4 Diode conduction angle  $\beta$ , displacement factor, power factor, conversion ratio, and total harmonic distortion of the rectifier circuit of Fig. 17.1, with infinite capacitance.

ing both ac-side and dc-side inductance, provided that the circuit operates sufficiently deeply in DCM. The parameter  $K_L$  is computed according to Eq. (17.3), with  $L$  taken to be the total ac-side plus dc-side inductance. A common example is the case where the circuit contains no physical discrete inductor; the performance is then determined by parasitic elements such as the capacitor equivalent series inductance, the inductance of the utility distribution wiring, and transformer leakage inductances.

#### 17.1.4 Minimizing THD When $C$ is Small

Let us now consider the performance of the second case, in which the inductor and capacitor are small and are intended solely to prevent load-generated EMI from reaching the ac line. In this case, dc-side filtering of the low-frequency even voltage harmonics of the ac line frequency is not necessary. The filter can be characterized by a corner frequency  $f_0$ , characteristic impedance  $R_0$ , and  $Q$ -factor, where

$$\begin{aligned}
 f_0 &= \frac{1}{2\pi\sqrt{LC}} \\
 R_0 &= \sqrt{\frac{L}{C}} \\
 Q &= \frac{R}{R_0} \\
 f_p &= \frac{1}{2\pi RC} = \frac{f_0}{Q}
 \end{aligned} \tag{17.5}$$

To obtain good filtering of the EMI, the corner frequency  $f_0$  should be selected to be sufficiently low. However, as can be seen from Eq. (17.5), reducing the value of  $f_0$  requires increasing the values of  $L$  and/or  $C$ . As described above, it is undesirable to choose either element value too large, because large distortion results. So  $f_0$  should not be too low, and there is a limit to the amount of filtering that can be obtained without significantly distorting the ac line current waveform.

How low can  $f_0$  be? Once  $f_0$  is chosen, how should  $L$  and  $C$  be chosen such that THD is minimized? We might expect that THD is increased when the phase of the filter input impedance –  $Z_i(j\omega)$ , evaluated at the second harmonic of the line frequency or  $2f_L$ , differs significantly from  $0^\circ$ . When the zero crossings of the voltage and current waveforms do not coincide, then diode switching distorts the current waveform. To a lesser extent, input impedance phase shift at the higher-order even harmonic frequencies of the ac line frequency should also affect the THD. The input impedance  $Z_i(s)$  contains two zeroes at frequency  $f_0$ , and a pole at frequency  $f_p = f_0/Q$ . To obtain small phase shift at low frequency,  $f_0$  must be sufficiently large. In addition,  $Q$  must be neither too small nor too large: small  $Q$  causes the zeroes at  $f_0$  to introduce low-frequency phase shift, while large  $Q$  causes the pole at  $f_p$  to occur at low frequency.

An approximate plot of THD vs. the choice of  $f_0$  and  $Q$  is given in Fig. 17.5. It can be seen that there is an optimum choice for  $Q$ : minimum THD occurs when  $Q$  lies in the range 0.5 to 1. A typical waveform is plotted for the choice  $f_0/f_L = 10$ ,  $Q = 1$ , in Fig. 17.6. The THD for this waveform is 3.6%, and the distortion factor is 99.97%.

Small  $Q$  corresponds to CCM operation, with large  $L$  and small  $C$ . In the extreme case as  $Q \rightarrow 0$ , the ac line current tends to a square wave with THD = 48%. Large  $Q$  corresponds to DCM operation, with small  $L$  and large  $C$ . In the extreme case as  $Q \rightarrow \infty$ , the ac line current tends to a string of delta functions with THD  $\rightarrow \infty$ . The optimum choice of  $Q$  leads to operation near the CCM-DCM boundary, such that the ac line current waveform contains neither step changes nor subintervals of zero current.

In the case when the load resistance  $R$  varies over a wide range of values, it may be difficult to optimize the circuit such that low THD is always obtained. It can be seen that increasing  $f_0/f_L$  leads to low THD for a wider range of load resistance. For example, when  $f_0 = 5f_L$ , THD  $\leq 10\%$  can be obtained only for  $Q$  between approximately 0.6 and 1.5, which is a 2.5:1 range of load resistance variations. If the

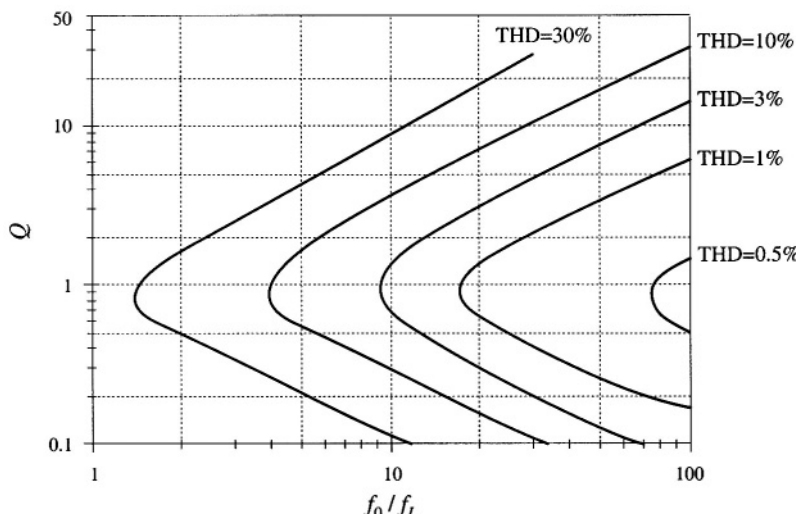
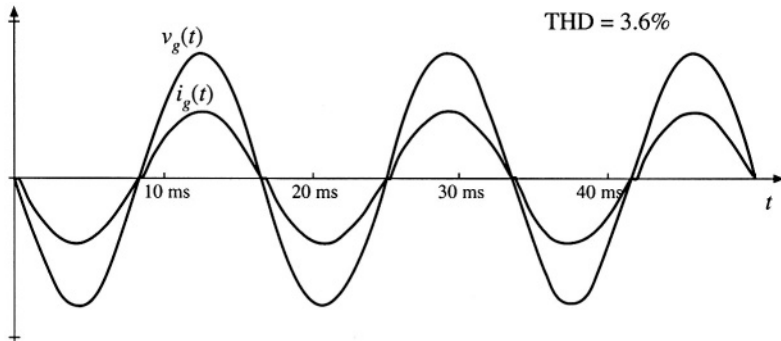


Fig. 17.5 Approximate total harmonic distortion of the single-phase diode rectifier with dc-side  $L-C$  filter.



**Fig. 17.6** Typical ac line current and voltage waveforms, near the boundary between continuous and discontinuous modes and with small dc filter capacitor.  $f_0/f_L = 10$ ,  $Q = 1$ .

filter cutoff frequency  $f_0$  is increased to  $20f_L$ , then  $\text{THD} \leq 10\%$  is obtained for  $Q$  between approximately 0.15 and 7, or nearly a 50:1 range of resistance variations. In most cases, maximum harmonic limits are enforced only at full load, and hence it is possible to design with relatively low values of  $f_0/f_L$  if desired.

## 17.2 THE THREE-PHASE BRIDGE RECTIFIER

A basic full-wave three-phase uncontrolled rectifier with LC output filter is shown in Fig. 17.7. Its behavior is similar to the single-phase case, in that it exhibits both continuous and discontinuous conduction modes, depending on the values of  $L$  and  $C$ . The rectifier generates odd non-triplet harmonics in the ac line current. So the ac line current may contain 1<sup>st</sup>, 5<sup>th</sup>, 7<sup>th</sup>, 11<sup>th</sup>, 13<sup>th</sup>, etc. harmonics. The dc output may contain dc and even triplet harmonics: 0, 6, 12, 18, etc.

In the basic circuit of Fig. 17.7, no more than two of the six diodes can conduct during each interval, and hence the line current waveforms must contain intervals of nonzero length during which the current is zero. Unlike the single-phase case, the ac line current waveform must contain distortion even when the filter elements are removed.

### 17.2.1 Continuous Conduction Mode

In the continuous conduction mode, each ac line current is nonzero for 120 degrees out of each line half-cycle. For the remaining 60 degrees, the current is zero. This mode occurs when the inductance  $L$  is suf-

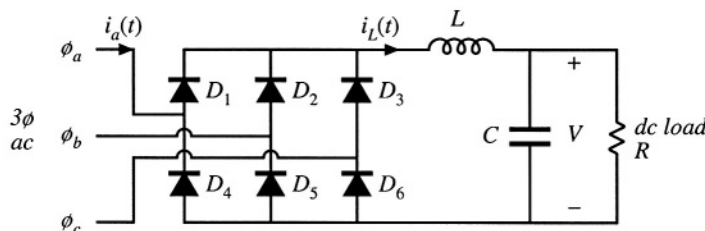


**Fig. 17.7** Basic uncontrolled 3 $\phi$  bridge rectifier circuit, with dc-side  $L-C$  filter.

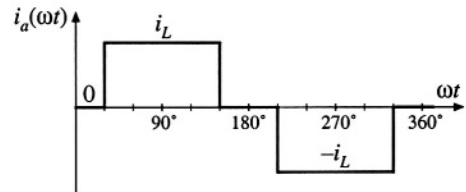


**Fig. 17.8** Ac line current waveform  $i_a(t)$ , for the case when inductor  $L$  is large. The phase is drawn with respect to the zero crossing of the line-to-neutral voltage  $v_{an}(t)$ .

ficiently large, as well as when the filter elements  $L$  and  $C$  are removed entirely.

In the limit, when  $L$  is very large, then the current  $i_L(t)$  is essentially constant. The current in phase  $a$ ,  $i_a(t)$ , is then as shown in Fig. 17.8. It can be shown that the Fourier series for this waveform is

$$i_a(t) = \sum_{n=1,5,7,11,\dots}^{\infty} \frac{4}{n\pi} I_L \sin\left(\frac{n\pi}{2}\right) \sin\left(\frac{n\pi}{3}\right) \sin(n\omega t) \quad (17.6)$$

which is similar to the spectrum of the square wave of the single-phase case, but with the triplen harmonics missing. The THD of this waveform is 31%, and the distortion factor is  $3/\pi = 95.5\%$ . As in the case of the square wave, the amplitude of the odd nontriplet  $n^{\text{th}}$  harmonic is  $(1/n)$  times the fundamental amplitude. So this waveform contains 20% fifth harmonic, 14% seventh harmonic, 9% eleventh harmonic, etc. It is interesting that, in comparison with the square-wave single-phase case, the missing 60° in the three-phase case improves the THD and power factor, by removing the triplen harmonics.

With a less-than-infinite value of inductance, the output ripple causes the ac line currents to be rounded, as in the typical waveform of Fig. 17.9. This waveform has a 31.9% THD, with a distortion factor that is not much different from the waveform of Fig. 17.8.

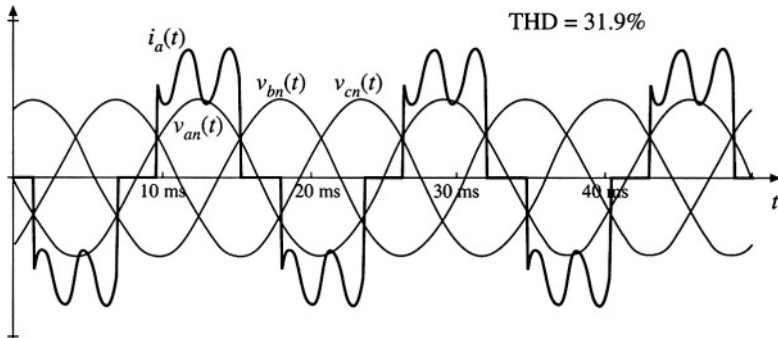


**Fig. 17.9** Continuous conduction mode ac line-neutral voltages and phase  $a$  current, for a moderate value of inductance.

### 17.2.2 Discontinuous Conduction Mode

If the inductance is further reduced, then the three-phase rectifier enters the discontinuous conduction mode. The rectifier then begins to peak-detect, and the current waveforms become narrow pulses of high amplitude, occurring near the peaks of the line-line voltages. The phase  $a$  line current  $i_a(t)$  contains two positive and two negative pulses, at the positive and negative peaks of the line-line voltages  $v_{ab}(t)$  and  $v_{ac}(t)$ . As in the single-phase case, the total harmonic distortion becomes quite large in this case, and the

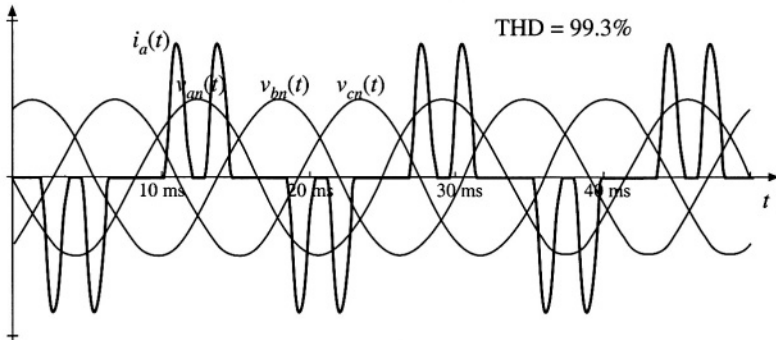


**Fig. 17.10** Discontinuous conduction mode ac line-neutral voltages and phase  $a$  current.

power factor can be significantly degraded.

A typical waveform is given in Fig. 17.10. This waveform has a THD of 99.3%, and a distortion factor of 71%. This would be considered unacceptable in high-power applications, except perhaps at light load.

### 17.3 PHASE CONTROL

There are a wide variety of schemes for controlling the dc output of a  $3\phi$  rectifier using thyristors [1,2]. The most common one is shown in Fig. 17.11, in which the six diodes of Fig. 17.7 are replaced by silicon controlled rectifiers (SCRs). Typical waveforms are given in Fig. 17.12, for large dc-side filter inductance.

If  $Q_1$  were an uncontrolled diode, it would conduct whenever the line-to-line voltage  $v_{ab}$  or  $v_{ac}$  is the largest in magnitude of the six line-line voltages  $v_{ab}$ ,  $v_{bc}$ ,  $v_{ca}$ ,  $v_{ba}$ ,  $v_{cb}$ , and  $v_{ca}$ . This occurs for  $120^\circ$  of each cycle, beginning at the point where  $v_{ab} = v_{cb}$ . In Fig. 17.12, this occurs at  $\omega t = 60^\circ$ . The output voltage of the controlled rectifier is controlled by delaying the firing of  $Q_1$  by an angle  $\alpha$ , such that  $Q_1$  begins conducting at  $\omega t = 60^\circ + \alpha$ . This has the effect of reducing the dc output voltage.

There can be no dc component of voltage across inductor  $L$ . Hence, in steady-state, the dc component of the rectifier output voltage  $v_R(t)$  must equal the dc load voltage  $V$ . But  $v_R(t)$  is periodic, with period equal to six times the ac line period (or  $60^\circ$ ). So the dc component of  $v_R(t)$  can be found by Fourier analysis, and is equal to the average value of  $v_R(t)$ . Over one  $60^\circ$  interval, for example  $(60^\circ + \alpha) \leq \omega t \leq (120^\circ + \alpha)$ ,  $v_R(t)$  follows the line-line voltage  $v_{ab}(t) = 3V_m \sin(\omega t + 30^\circ)$ . The average is therefore

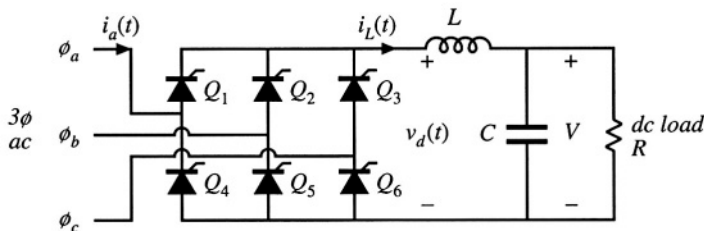


**Fig. 17.11** Basic controlled  $3\phi$  bridge rectifier circuit, with dc-side  $L$ - $C$  filter.

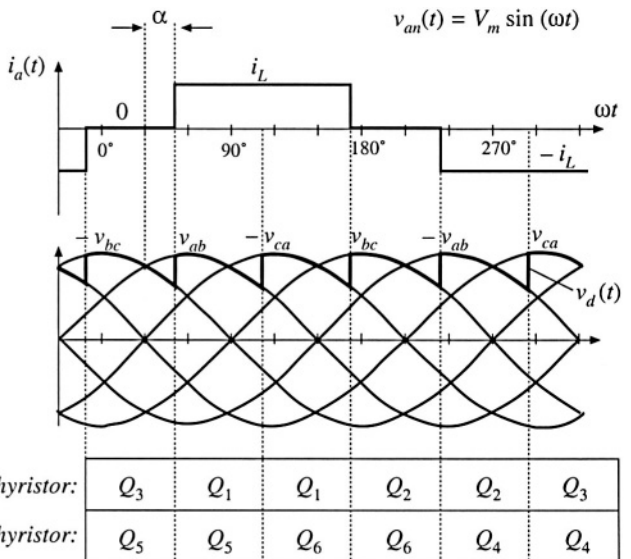


Fig. 17.12 Waveforms for the controlled rectifier of Fig. 17.11, with large dc filter inductance.

$$V = \frac{3}{\pi} \int_{30^\circ + \alpha}^{90^\circ + \alpha} \sqrt{3} V_m \sin(\theta + 30^\circ) d\theta \quad (17.7)$$

$$= \frac{3\sqrt{2}}{\pi} V_{L-L, rms} \cos \alpha$$

where  $V_{L-L, rms}$  is the rms line-to-line voltage. This equation is plotted in Fig. 17.13. It can be seen that, if it is necessary to reduce the dc output voltage to values close to zero, then the delay angle  $\alpha$  must be

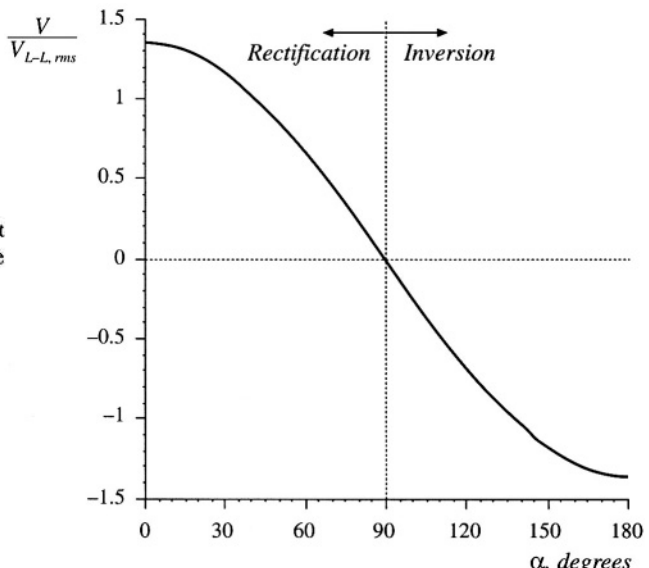


Fig. 17.13 Variation of the dc output voltage  $V$  with delay angle  $\alpha$ , for the phase-controlled circuit of Fig. 17.11.

increased to close to  $90^\circ$ . With a small inductance, the controlled rectifier can also operate in discontinuous conduction mode, with modified output voltage characteristics.

### 17.3.1 Inverter Mode

If the dc load is capable of supplying power, then it is possible for the direction of power flow to reverse. For example, consider the three-phase controlled rectifier circuit of Fig. 17.14. The resistive load is replaced by a voltage source and thevenin-equivalent resistance, capable of either supplying or consuming power. The dc load power is equal to  $VI_L$ , which is positive (rectifier mode) when both  $V$  and  $I_L$  are positive. The thyristor is a unidirectional-current switch, which cannot conduct negative current, and hence  $I_L$  must always be positive. However, it is possible to cause the output voltage  $V$  to be negative, by increasing the delay angle  $\alpha$ . The dc load power  $VI_L$  then becomes a negative quantity (inverter mode), meaning that power flows from the dc load into the  $3\phi$ ac system.

Provided that the dc-side filter inductance  $L$  is sufficiently large, then Eq. (17.7) is valid even when the delay angle  $\alpha$  is greater than  $90^\circ$ . It can be seen in Fig. 17.13 that the dc output voltage  $V$  becomes negative for  $\alpha > 90^\circ$ , and hence the power flow indeed reverses. Delay angles approaching  $180^\circ$  are possible, with the maximum angle limited by commutation of the thyristor devices.

### 17.3.2 Harmonics and Power Factor

Let us next consider the harmonic content and power factor of the phase-controlled rectifier with large inductance. Comparison of the line current waveform of Fig. 17.12 with that of the uncontrolled rectifier (Fig. 17.8) reveals that the waveshapes are identical. The only difference is the phase lag  $\alpha$  present in the phase-controlled rectifier. This has the effect of shifting the fundamental component of current (and the harmonics as well) by angle  $\alpha$ . The Fourier series is therefore

$$i_a(t) = \sum_{n=1,3,5,7,11,\dots}^{\infty} \frac{4}{n\pi} I_L \sin\left(\frac{n\pi}{2}\right) \sin\left(\frac{n\pi}{3}\right) \sin(n\omega t - n\alpha) \quad (17.8)$$

Hence the harmonic amplitudes are the same (the fifth harmonic amplitude is 20% of the fundamental, etc.), the THD is again 31%, and the distortion factor is again 95.5%. But there is phase lag in the fundamental component of current, which leads to a displacement factor of  $\cos(\alpha)$ . The power factor is therefore

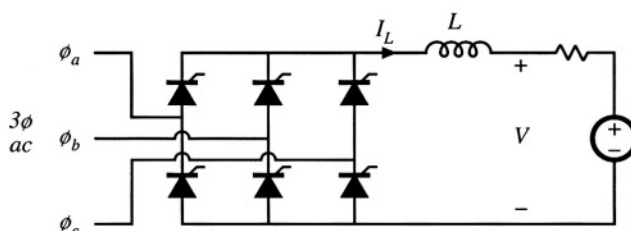


**Fig. 17.14** If the load is capable of supplying power, then the  $3\phi$  bridge circuit functions as an inverter for  $V < 0$  and  $\alpha > 90^\circ$ .

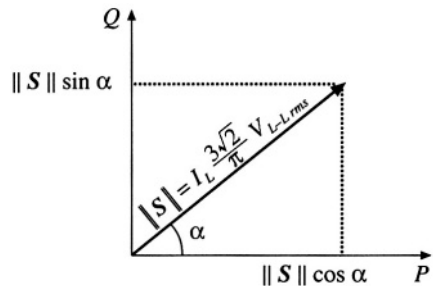


**Fig. 17.15** Fundamental component complex power diagram for the 3ø bridge circuit operating in rectifier mode.

$$\text{power factor} = 0.955 |\cos(\alpha)| \quad (17.9)$$

which can be quite low when the dc output voltage  $V$  is low.

It is at first somewhat puzzling that the introduction of phase control can cause the fundamental current to lag the voltage. Apparently, the rectifier consumes reactive power equal to

$$Q = \sqrt{3} I_{a, rms} V_{L-L, rms} \sin \alpha = I_L \frac{3\sqrt{2}}{\pi} V_{L-L, rms} \sin \alpha \quad (17.10)$$

We normally associate lagging current and the consumption of reactive power with inductive energy storage. But this is not what is happening in the rectifier; indeed, the inductor and capacitor can be removed entirely from the rectifier circuit, and a lagging fundamental current is still obtained by phase control. It is simply the delay of the switching of the rectifiers that causes the current to lag, and no energy storage is involved. So two mechanisms cause the phase-controlled rectifier to operate with low power factor: the lagging fundamental component of current, and the generation of current harmonics.

Equation (17.10) can be further interpreted. Note that the dc output power  $P$  is equal to the dc inductor current  $I_L$  times the dc output voltage  $V$ . By use of Eq. (17.7), this can be written

$$P = I_L \frac{3\sqrt{2}}{\pi} V_{L-L, rms} \cos \alpha \quad (17.11)$$

Comparison of Eqs. (17.10) and (17.11) reveals that the rectifier fundamental volt-amperes can be expressed using the conventional concepts of complex power  $S = P + jQ$ , where  $P$  is the real (average) power consumed and  $Q$  is the fundamental reactive power consumed. The complex power phasor diagram, treating the fundamental components only, is illustrated in Fig. 17.15.

### 17.3.3 Commutation

Let's consider next what happens during the switching transitions. In the phase-controlled rectifier circuit of Fig. 17.16, the dc-side inductor  $L_d$  is large in value, such that its current ripple is negligible. Inductors  $L_a$ ,  $L_b$ , and  $L_c$  are also present in the ac lines; these may be physical inductors of the rectifier circuit, or they may represent the source impedance of the power system, typically the leakage inductances of a nearby transformer. These inductors are relatively small in value.

Consider the switching transition illustrated in Fig. 17.17. Thyristors  $Q_3$  and  $Q_5$  initially conduct. At time  $t_{c1}$ , thyristor  $Q_1$  is gated on, and the dc current  $i_L$  begins to shift from  $Q_3$  to  $Q_1$ . The ac line currents  $i_a(t)$  and  $i_c(t)$  cannot be discontinuous, since inductors  $L_a$  and  $L_c$  are present in the lines. So dur-

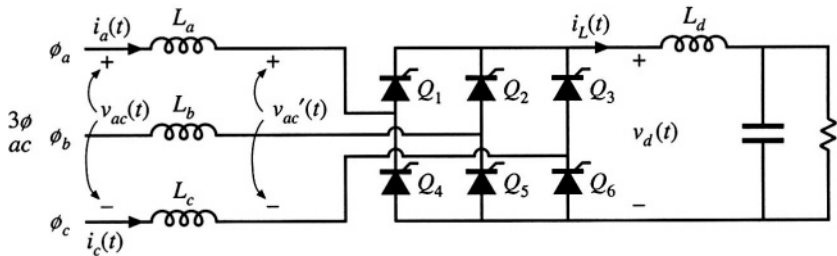


Fig. 17.16 Controlled 3 $\phi$  rectifier circuit, with small ac-side inductances.

ing the interval  $t_{c1} < t < t_{c2}$ , thyristors  $Q_1$  and  $Q_3$  both conduct, and the voltage  $v_{ac}'$  is zero. Voltage is applied across inductors  $L_a$  and  $L_c$ , causing their currents to change; for successful commutation, sufficient volt-seconds must be applied to cause the currents to change from  $i_L$  to zero, and vice versa. Any stored charge that remains in thyristor  $Q_3$  when current  $i_c(t)$  reaches zero must also be removed, and hence  $i_c(t)$  actually continues negative as discussed in Chapter 4. When the reverse recovery process of  $Q_3$  is complete, then  $Q_3$  is finally in the off-state, and the next subinterval begins with the conduction of thyristors  $Q_1$  and  $Q_5$ .

The commutation process described above has several effects on the converter behavior. First, it can be seen that the thyristor bridge dc-side voltage  $v_d(t)$  is reduced in value during the commutation interval. Hence, its average value  $\langle v_d \rangle$  and the dc output voltage  $V$  are reduced. The amount of reduction is dependent on the dc load current: a larger dc load current leads to a longer commutation interval, and hence to a greater reduction in  $\langle v_d \rangle$ . So the rectifier has an effective output resistance. Second, the maximum value of the delay angle  $\alpha$  is limited to some value less than  $180^\circ$ . If  $\alpha$  exceeds this limit, then insufficient volt-seconds are available to change inductor current  $i_c(t)$  from  $i_L$  to zero, leading to *commutation failure*. Third, when the rectifier ac-side inductors are small or zero, so that  $L_a$ ,  $L_b$ , and  $L_c$  represent

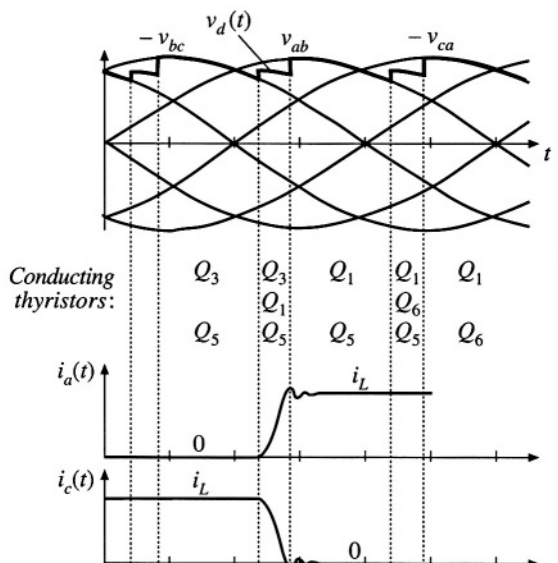
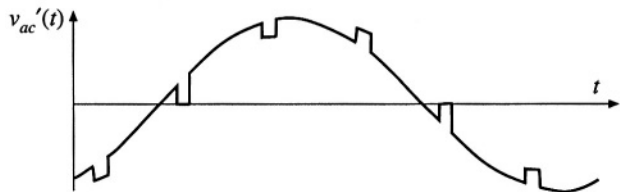


Fig. 17.17 Switching transition waveforms, for the rectifier of Fig. 17.16.



**Fig. 17.18** Notching of the ac line-line voltage waveforms during the commutation intervals.

essentially only the power system source impedance, then commutation causes significant notching of the ac voltage waveforms (Fig. 17.18) at the point of common coupling of the rectifier to the power system. Other elements connected locally to the power system will experience voltage distortion. Limits for the areas of these notches are suggested in IEEE/ANSI standard 519.

#### 17.4 HARMONIC TRAP FILTERS

Passive filters are often employed to reduce the current harmonics generated by rectifiers, such that harmonic limits are met. The filter network is designed to pass the fundamental and to attenuate the significant harmonics such as the fifth, seventh, and perhaps several higher-order odd nontriplet harmonics. Such filters are constructed using resonant tank circuits tuned to the harmonic frequencies. These networks are most commonly employed in balanced three-phase systems. A schematic diagram of one phase of the filter is given in Fig. 17.19.

The ac power system is modeled by the thevenin-equivalent network containing voltage source  $v_s$  and impedance  $Z'_s$ . Impedance  $Z'_s$  is usually inductive in nature, although resonances may occur due to nearby power-factor-correction capacitors. In most filter networks, a series inductor  $L'_s$  is employed; the filter is then called a harmonic trap filter. For purposes of analysis, the series inductor  $L'_s$  can be lumped into  $Z'_s$ , as follows:

$$Z_s(s) = Z'_s(s) + sL'_s \quad (17.12)$$

The rectifier and its current harmonics are modeled by current source  $i_r$ . Shunt impedances  $Z_1, Z_2, \dots$  are

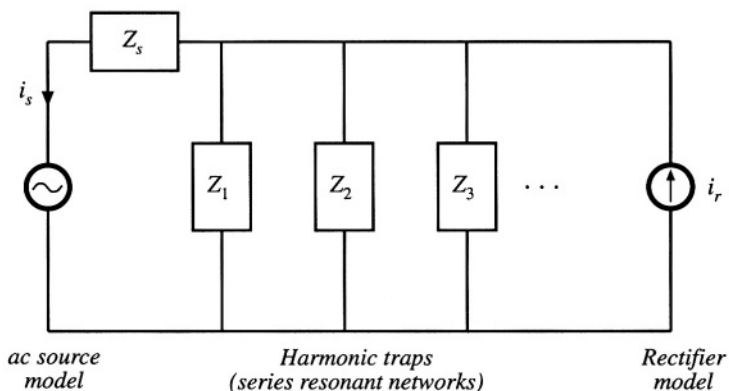


**Fig. 17.19** A harmonic trap filter. One phase is illustrated, on a line-to-neutral basis.

tuned such that they have low impedance at the harmonic frequencies, and hence the harmonic currents tend to flow through the shunt impedances rather than into the ac power system.

The approximate algebra-on-the-graph method described in Chapter 8 is used here to construct the filter transfer function, in terms of impedance  $Z_s$  and the shunt impedances  $Z_1, Z_2, \dots$ . This approach yields a simple intuitive understanding of how the filter operates. Since the harmonic frequencies are close in value, the pole and zero frequencies of the filter are never well separated in value. So the approximate algebra-on-the-graph method is, in general, not sufficiently accurate for the complete design of these filters, and the pole frequencies must be found by numerical methods. A typical design approach might involve estimating element values using the algebra-on-the-graph method, then refining the values using a computer simulation package.

The filter transfer function  $H(s)$  is given by the current divider ratio

$$H(s) = \frac{i_s(s)}{i_r(s)} = \frac{Z_1 \parallel Z_2 \parallel \dots}{Z_s + Z_1 \parallel Z_2 \parallel \dots} \quad (17.13)$$

As discussed in Chapter 8, another way to write this transfer function is

$$H(s) = \frac{i_s(s)}{i_r(s)} = \frac{Z_s \parallel Z_1 \parallel Z_2 \parallel \dots}{Z_s} \quad (17.14)$$

So we can construct  $H(s)$  by first constructing the parallel combination  $Z_s \parallel Z_1 \parallel Z_2 \parallel \dots$ , then dividing by the total line impedance  $Z_s$ . It can be shown that, if  $Z_s(s)$  contains no poles, then the numerator of  $H(s)$  is the product of the zeroes of the shunt impedances  $Z_1, Z_2, \dots$ . So this graphical method yields the exact zeroes of  $H(s)$ , which coincide with the series resonances of the shunt impedances. But the poles of  $H(s)$ , which arise from parallel resonances in the filter, require more work to compute.

Let us first consider the simple case illustrated in Fig. 17.20, where  $Z_1$  consists of a series resonant circuit tuned to eliminate the fifth harmonic, and  $Z_s$  is composed of a single inductor  $L_s$ . Construction of the impedance of a series resonant network is described in Chapter 8. The  $\parallel Z_1 \parallel$  asymptotes follow the capacitor impedance magnitude  $1/\omega C_1$  at low frequency, and the inductor impedance magnitude  $\omega L_1$  at high frequency. At the resonant frequency,  $\parallel Z_1 \parallel$  is equal to  $R_1$ . The asymptotes for  $\parallel Z_1 \parallel$  are constructed in Fig. 17.21 (a).

Figure 17.21 (a) also illustrates the impedance magnitude  $\parallel Z_s \parallel = \omega L_s$ , as well as construction of

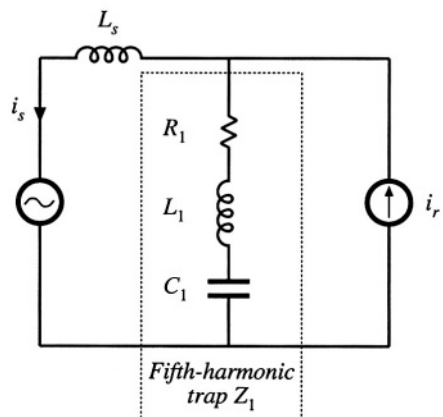


**Fig. 17.20** Simple harmonic trap filter example, containing a series resonant trap tuned to the fifth harmonic, and inductive line impedance.

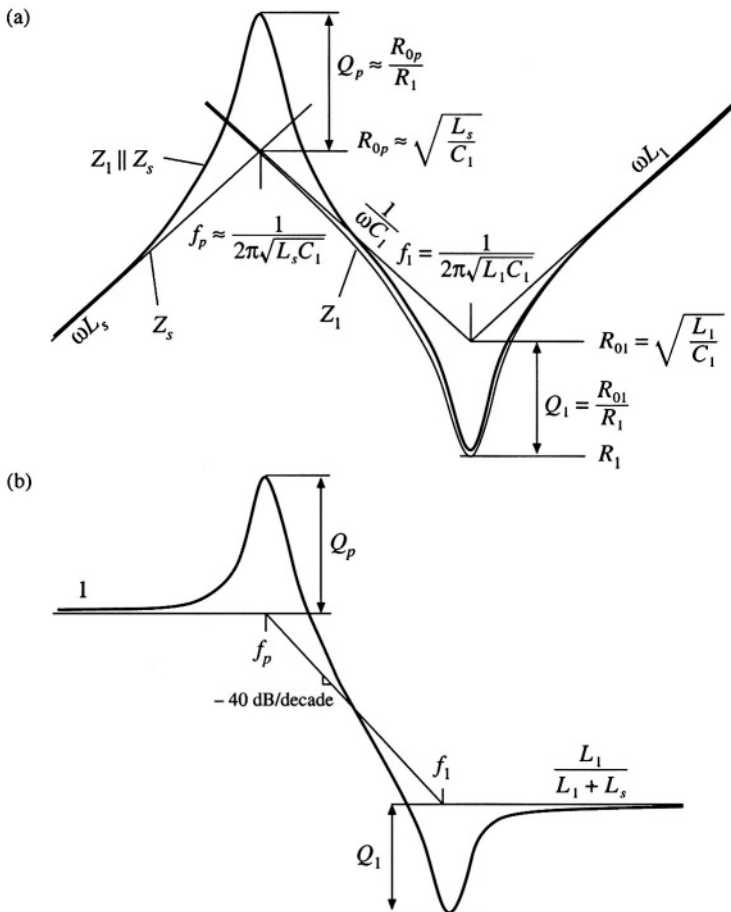
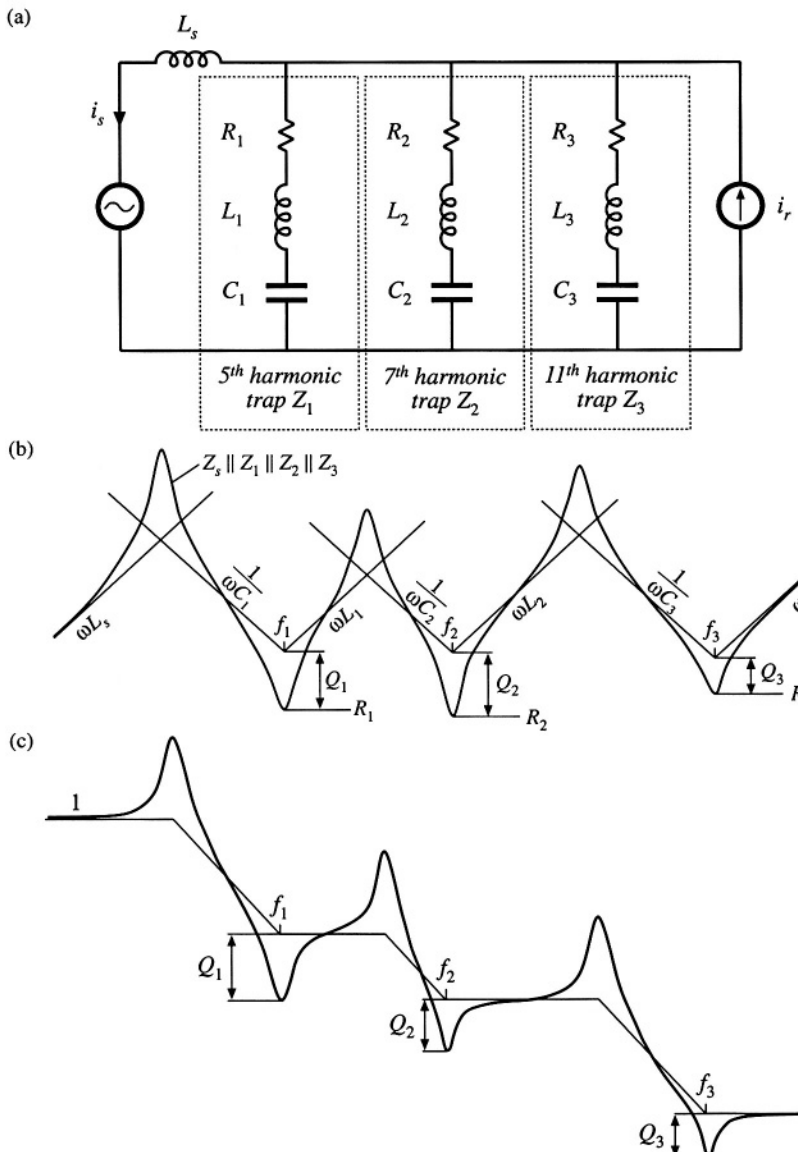


Fig. 17.21 Construction of approximate frequency response using the algebra-on-the-graph method: (a) impedance asymptotes, (b) transfer function asymptotes  $\| H(s) \|$ .

the approximate asymptotes for the parallel combination ( $Z_s \parallel Z_1$ ). Recall that, to construct the approximate asymptotes for the parallel combination, we simply select the smaller of the  $Z_s$  and  $Z_1$  asymptotes. The result is the shaded set of asymptotes shown in the figure: the parallel combination follows  $\omega L_s$  at low frequency, and  $\| Z_1 \|$  at high frequency. Note that, in addition to the intended series resonance at frequency  $f_1$ , a parallel resonance occurs at frequency  $f_p$ .

The filter transfer function  $\| H(s) \|$  is now constructed using Eq. (17.14). As illustrated in Fig. 17.21(b),  $\| H(s) \| = 1$  at low frequencies where both the numerator and the denominator of Eq. (17.14) are equal to  $\omega L_s$ . The parallel resonance at frequency  $f_p$  leads to resonant poles and peaking in  $\| H(s) \|$ . The resonance at frequency  $f_1$  leads to resonant zeroes and attenuation in  $\| H(s) \|$ . At high frequency, the gain is  $L_1/(L_1 + L_s)$ .

So if we want to attenuate fifth harmonic currents, we should choose the element values such that the series resonant frequency  $f_1$  coincides with the fifth harmonic frequency. This frequency is sim-



**Fig. 17.22** Construction of approximate frequency response for a harmonic trap filter that attenuates the fifth, seventh, and eleventh harmonics: (a) impedance asymptotes, (b) transfer function asymptotes.

ply the resonant frequency of the shunt impedance  $Z_1$ , or

$$f_1 = \frac{\omega_1}{2\pi} = \frac{1}{2\pi\sqrt{L_1 C_1}} \quad (17.15)$$

In addition, care must be exercised regarding the parallel resonance. Since no three-phase system is exactly balanced, small amounts of third harmonic currents always occur. These currents usually have negligible effect; however, the parallel resonance of the harmonic trap filter can increase their magnitudes significantly. Even worse, the  $Q$ -factor of the parallel resonance,  $Q_p$ , is greater than the series-resonance  $Q$ -factor  $Q_1$ .

The filter circuit of Fig. 17.20 is simple enough that an exact analysis can be performed easily. The exact transfer function is

$$H(s) = \frac{\left(1 + \frac{s}{\omega_1 Q_1} + \left(\frac{s}{\omega_1}\right)^2\right)}{\left(1 + \frac{s}{\omega_p Q_p} + \left(\frac{s}{\omega_p}\right)^2\right)} \quad (17.16)$$

where

$$f_1 = \frac{\omega_1}{2\pi} = \frac{1}{2\pi\sqrt{L_1 C_1}} \quad f_p = \frac{\omega_p}{2\pi} = \frac{1}{2\pi\sqrt{(L_1 + L_s)C_1}}$$

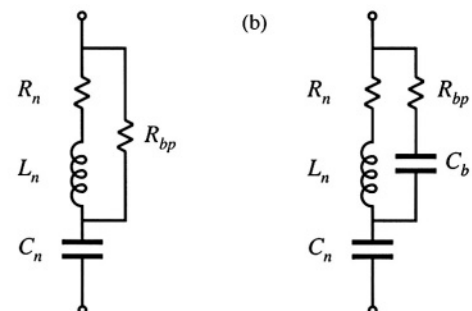
$$Q_1 = \frac{1}{R_1} \sqrt{\frac{L_1}{C_1}} \quad Q_p = \frac{1}{R_1} \sqrt{\frac{(L_1 + L_s)}{C_1}}$$

The resonant zeroes do indeed appear at the series resonant frequency, while the parallel resonance and its associated resonant poles appear at frequency  $f_p$  determined by the series combination of  $L_1$  and  $L_s$ .

To attenuate several harmonics—for example, the fifth, seventh, and eleventh—series resonant networks can be tuned to provide resonant zeroes at each. A circuit is given in Fig. 17.22(a), with the impedance asymptotes of Fig. 17.22(b). The resulting approximate  $\| H(s) \|$  is given in Fig. 17.22(c). It can be seen that, associated with each series resonance is a parallel resonance. Each parallel resonant frequency should be chosen such that it is not significantly excited by harmonics present in the network.

The filter transfer function can be given high-frequency single-pole rolloff by addition of a bypass resistor  $R_{bp}$ , as illustrated in Fig. 17.23(a). Typical impedance and transfer function asymptotes for this network are constructed in Fig. 17.24. The bypass resistor allows some additional attenuation of the higher-order harmonics, without need for series resonant traps tuned to each harmonic. The network of Fig. 17.23(a) is sometimes called a “high pass” network, because it allows high-frequency currents to flow through the shunt branch. But it causes the overall filter transfer function  $H(s)$  to reject high frequencies. A simple harmonic trap filter that contains series resonances that can be tuned to the fifth and

**Fig. 17.23** Addition of bypass resistor  $R_{bp}$  to a series resonant network, to obtain a high-frequency rolloff characteristic: (a) basic circuit, (b) addition of blocking capacitor  $C_b$  to reduce power consumption at the fundamental frequency.



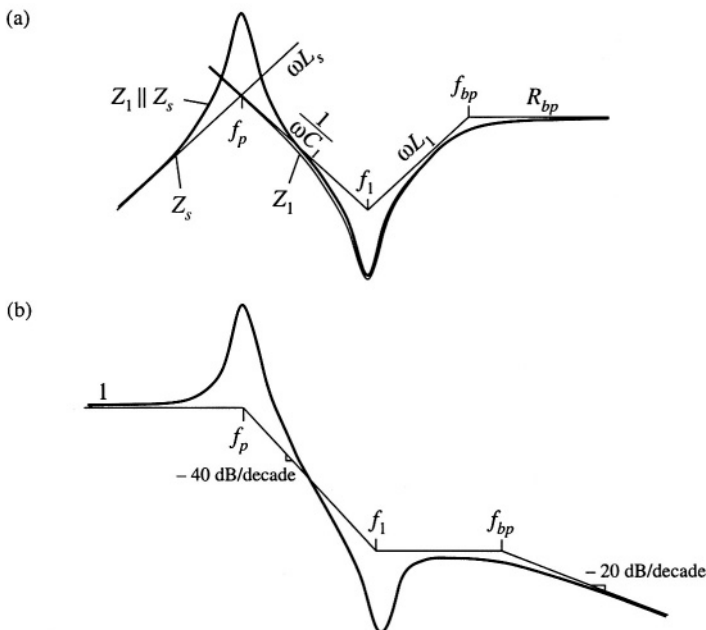


**Fig. 17.24** Construction of approximate frequency response for a harmonic trap filter containing bypass resistor: (a) impedance asymptotes, (b) transfer function asymptotes.

seventh harmonics, with a single-pole rolloff to attenuate higher-order harmonics such as the eleventh and thirteenth, is illustrated in Fig. 17.25.

Power loss in the bypass resistor can be an issue: since  $R_{bp}$  is not part of the resonant network, significant fundamental (50 Hz or 60 Hz) currents can flow through  $R_{bp}$ . The power loss can be reduced by addition of blocking capacitor  $C_b$  as illustrated in Fig. 17.23(b). This capacitor is chosen to increase the impedance of the  $R_{bp}-C_b$  leg at the fundamental frequency, but have negligible effect at the higher-

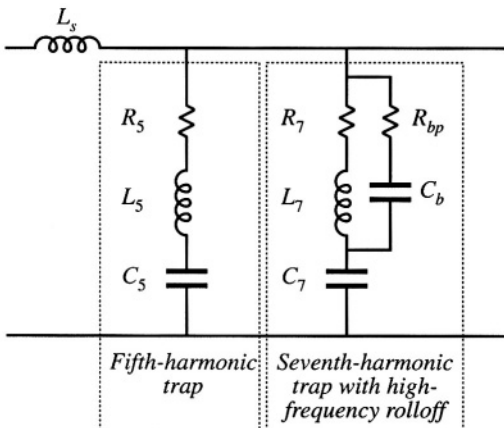


**Fig. 17.25** A harmonic trap filter containing series resonances tuned to the fifth and seventh harmonics, and high-frequency rolloff characteristic.

order harmonic frequencies.

The harmonic trap filter network can also supply significant reactive power to the rectifier and power system. As given by Eq. (17.10), the rectifier fundamental current lags the voltage, and the rectifier consumes reactive power. As seen in Fig. 17.22(a), the impedances of the series resonant tank networks are dominated by their capacitor asymptotes at low frequency. Hence, at the fundamental frequency, the filter impedance reduces to an equivalent capacitor, equal to the parallel combination of the tank capacitors. The current through this capacitance leads the ac line voltage, and hence as mentioned in the previous chapter, the capacitor is a source of reactive power.

## 17.5 TRANSFORMER CONNECTIONS

A final conventional approach to reducing the input harmonics of three-phase rectifiers is the use of phase-shifting transformer circuits. With these schemes, the low-order harmonics, such as the fifth and seventh, can be eliminated. The remaining harmonics are smaller in magnitude, and also are easier to filter.

The rectifier circuit of Fig. 17.7 is known as a *six-pulse* rectifier because the diode output voltage waveform contains six pulses per ac line period. The output voltage ripple has a fundamental frequency that is six times the ac line frequency. As illustrated in Fig. 17.8, the ac line current waveforms contain three steps: at any given instant,  $i_d(t)$  is equal to either  $i_L$ , 0, or  $-i_L$ . The spectrum of the current waveform contains fundamental and odd nontriplet harmonics (1, 5, 7, 11, 13,...), whose amplitudes vary as  $1/n$ .

It is possible to shift the phase of the ac line voltage using three-phase transformer circuits. For example, in the delta-wye transformer circuit of Fig. 17.26, the transformer primary windings are driven by the primary-side line-to-line voltages, while the transformer secondaries supply the secondary-side line-to-neutral voltages. In an ideal transformer, the secondary voltage is equal to the primary voltage multiplied by the turns ratio; hence, the phasor representing the secondary voltage is in phase with the

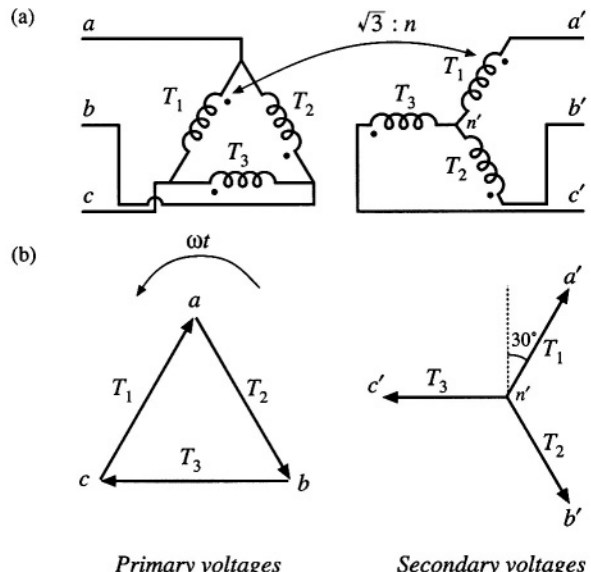


**Fig. 17.26** Three-phase delta-wye transformer connection: (a) circuit, (b) voltage phasor diagram.

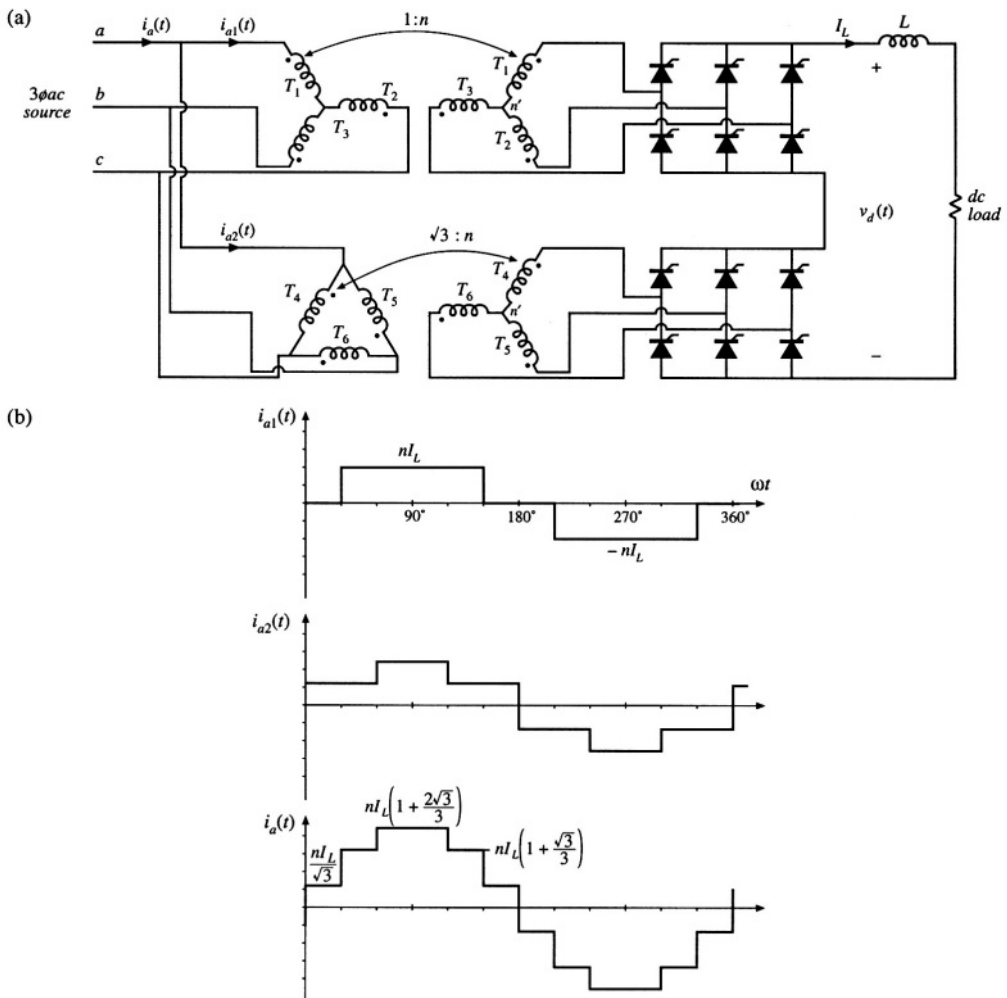


Fig. 17.27 Twelve-pulse rectifier: (a) circuit, (b) input phase  $a$  current waveforms.

primary voltage phasor, and is scaled in magnitude by the turns ratio. So in the delta-wye transformer connection, the secondary line-to-neutral voltages are in phase with the primary line-to-line voltages. In a balanced three-phase system, the line-to-line voltages are shifted in phase by  $30^\circ$  with respect to the line-to-neutral voltages, and are increased in magnitude by a factor of  $\sqrt{3}$ . Hence the secondary line-to-neutral voltages lag the primary line-to-neutral voltages by  $30^\circ$ . The wye-delta connection is also commonly used; this circuit causes the secondary voltages to lead the primary voltages by  $30^\circ$ . Many other more complicated transformer circuits are known, such as the zig-zag, forked-wye, and extended-delta connections, which can lead to phase shifts of any desired amount.

The  $30^\circ$  phase shift of the delta-wye transformer circuit is used to advantage in the twelve-pulse rectifier circuit of Fig. 17.27(a). This circuit consists of two bridge rectifier circuits driven by  $3\phi$  voltages

that differ in phase by  $30^\circ$ . The bridge rectifier outputs are connected in series to the dc filter inductor and load. The total rectifier output voltage  $v_d(t)$  has a fundamental frequency that is twelve times the ac line frequency. The input phase  $a$  ac line current  $i_a(t)$  is the sum of currents in three windings, and has the stepped waveshape illustrated in Fig. 17.27(b). It can be shown that this waveform contains Fourier components at the fundamental frequency and at the 11<sup>th</sup>, 13<sup>th</sup>, 23<sup>rd</sup>, 25<sup>th</sup>,... harmonic frequencies, whose amplitudes vary as  $1/n$ . Doing so is left as a homework problem. Thus, the twelve-pulse rectifier eliminates the 5<sup>th</sup>, 7<sup>th</sup>, 17<sup>th</sup>, 19<sup>th</sup>,... harmonics.

An eighteen-pulse rectifier can be constructed using three six-pulse bridge rectifiers, with transformer circuits that shift the applied voltages by  $0^\circ$ ,  $+ 20^\circ$ , and  $- 20^\circ$ . A twenty-four pulse rectifier requires four six-pulse bridge rectifiers, fed by voltages shifted by  $0^\circ$ ,  $+ 15^\circ$ ,  $- 15^\circ$ , and  $30^\circ$ . If  $p$  is the pulse number, then the rectifier produces line current harmonics of number  $n = pk \pm 1$ , where  $k = 0, 1, 2, 3, \dots$ . If the dc current ripple can be neglected, then the magnitudes of the remaining current harmonics vary as  $1/n$ . The dc-side harmonics are of number  $pk$ .

So by use of polyphase transformer connections and rectifier circuits having high pulse number, quite good ac line current waveforms can be obtained. As the pulse number is increased, the current waveforms approaches a sinusoid, and contains a greater number of steps having smaller amplitude. The low-order harmonics can be eliminated, and the remaining high-frequency harmonics are easily filtered.

## 17.6 SUMMARY

1. With a large dc filter inductor, the single-phase full-wave rectifier produces a square-wave line current waveform, attaining a power factor of 90% and 48% THD. With smaller values of inductance, these figures are degraded. In the discontinuous conduction mode, THD greater than 100%, with power factors of 55% to 65% are typical. When the capacitance is large, the power factor, THD, displacement factor, and conversion ratio can be expressed as a function of only the dimensionless parameter  $K_L$ .
2. In the three-phase case, the bridge rectifier with large dc filter inductor produces a stepped waveform similar to the square wave, but missing the triplen harmonics. This waveform has 31% THD, and leads to a power factor of 95.5%. Reduced dc inductor values again lead to increased THD and reduced power factor, and as  $L$  tends to zero, the THD tends to infinity while the power factor tends to zero. In practice, the minimum effective series inductance is limited by the power system source inductance.
3. With a large dc inductor, phase control does not influence the distortion factor or THD, but does lead to a lagging fundamental current and decreased displacement factor. Phase-controlled rectifiers and inverters are consumers of reactive power.
4. If the load is capable of supplying power, then the phase-controlled rectifier can become an inverter. The delay angle  $\alpha$  is greater than  $90^\circ$ , and the output voltage polarity is reversed with respect to rectifier operation. The maximum delay angle is limited by commutation failure to a value less than  $180^\circ$ .
5. Harmonic trap filters and multipulse-rectifier/polyphase transformer circuits find application in high-power applications where their large size and weight are less of a consideration than their low cost. In the harmonic trap filter, series resonant tank circuits are tuned to the offending harmonic frequencies, and shunt the harmonic currents away from the utility power network. Parallel resonances may cause unwanted peaks in the filter transfer function. Operation of these filters may be understood using the algebra-on-the-graph method, and computer simulations can be used to refine the accuracy of the analysis or design. Rectifiers of higher pulse number can also yield improved current waveforms, whose harmonics are of high frequency and small amplitude, and are easily filtered.

## REFERENCES

- [1] G.K. DUBEY, S.R. DORADLA, A. JOSHI, and R.M.K. SINHA, *Thyristorized Power Controllers*, New Delhi: Wiley Eastern, Ltd., 1986.
- [2] J. VITHAYATHIL, *Power Electronics: Principles and Applications*, New York: McGraw-Hill, 1995.
- [3] N. MOHAN, T. UNDELAND, and W. ROBBINS, *Power Electronics: Converters, Applications, and Design*, Second edition, New York: John Wiley & Sons, 1995.
- [4] J. PHIPPS, "Phase-Shifting Transformers and Passive Harmonic Filters: Interfacing for Power Electronic Motor Drive Controllers," M.S. Thesis, University of Colorado at Denver, 1993.
- [5] J. KASSAKIAN, M. SCHLECHT, and G. VERGESE, *Principles of Power Electronics*, Massachusetts: Addison-Wesley, 1991.
- [6] J. ARRILLAGA, D. BRADLEY, and P. BODGER, *Power System Harmonics*, New York: John Wiley & Sons, 1985.
- [7] A. DOMIJAN and E. EMBRIZ-SANTANDER, "A Summary and Evaluation of Recent Developments on Harmonic Mitigation Techniques Useful to Adjustable-Speed Drives," *IEEE Transactions on Energy Conversion*, Vol. 7, No. 1, pp. 64-71, March 1992.
- [8] S. FREELAND, "I. A Unified Analysis of Converters with Resonant Switches, II. Input-Current Shaping for Single-Phase Ac-dc Power Converters," Ph.D. Thesis, California Institute of Technology, 1988, Chapter 12.
- [9] F. C. SCHWARZ, "A Time-Domain Analysis of the Power Factor for Rectifier Systems with Over- and Sub-critical Inductance," *IEEE Transactions on Industrial Electronics and Control Instrumentation*, Vol. 20, No. 2, May 1973, pp. 61-68.
- [10] S. B. DEWAN, "Optimum Input and Output Filters for Single-Phase Rectifier Power Supply," *IEEE Transactions on Industry Applications*, Vol. 17, No. 3, May/June 1981, pp. 282-288.
- [11] A. KELLEY and W. F. YADUSKY, "Rectifier Design for Minimum Line-Current Harmonics and Maximum Power Factor," *IEEE Transactions on Power Electronics*, Vol. 7, No. 2, April 1992, pp. 332-341.
- [12] A. W. KELLEY and W. F. YADUSKY, "Phase-Controlled Rectifier Line-Current Harmonics and Power Factor as a Function of Firing Angle and Output Filter Inductance," *IEEE Applied Power Electronics Conference*, 1990 Proceedings, March 1990, pp. 588-597.
- [13] P. C. SEN, *Thyristorized DC Drives*, New York: Wiley Interscience, 1981.
- [14] S. DEWAN AND A. STRAUGHEN, *Power Semiconductor Circuits*, New York: John Wiley & Sons, 1975.
- [15] B. PELLY, *Thyristor Phase-Controlled Converters and Cycloconverters: Operation, Control, and Performance*, New York: John Wiley & Sons, 1971.

## PROBLEMS

- 17.1** The half-controlled single-phase rectifier circuit of Fig. 17.28 contains a large inductor  $L$ , whose current  $i_L(t)$  contains negligible ripple. The thyristor delay angle is  $\alpha$ .

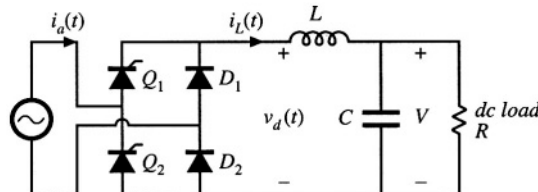


Fig. 17.28 Half-controlled rectifier circuit of Problem 17.1.

- (a) Sketch the waveforms  $v_d(t)$  and  $i_a(t)$ . Label the conduction intervals of each thyristor and diode.
- (b) Derive an expression for the dc output voltage  $V$ , as a function of the rms line-line voltage and the delay angle.
- (c) Derive an expression for the power factor.
- (d) Over what range of  $\alpha$  are your expressions of parts (b) and (c) valid?

- 17.2** The half-controlled rectifier circuit of Fig. 17.29 contains a large inductor  $L$ , whose current  $i_L(t)$  contains negligible ripple. The thyristor delay angle is  $\alpha$ .

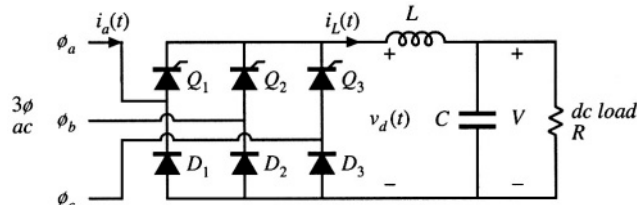


Fig. 17.29 Three-phase half-controlled rectifier circuit of Problem 17.2.

- (a) Sketch the waveforms  $v_d(t)$  and  $i_a(t)$ . Label the conduction intervals of each thyristor and diode.
- (b) Derive an expression for the dc output voltage  $V$ , as a function of the rms line-line voltage and the delay angle.
- (c) Derive an expression for the power factor.
- (d) Over what range of  $\alpha$  are your expressions of parts (b) and (c) valid?

- 17.3** A 3 $\phi$  SCR bridge is connected directly to a resistive load, as illustrated in Fig. 17.30. This circuit operates in the continuous conduction mode for small delay angle  $\alpha$ , and in the discontinuous conduction mode for sufficiently large  $\alpha$ .

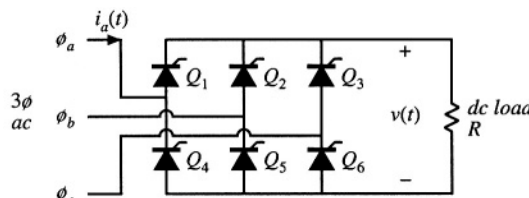


Fig. 17.30 Three-phase controlled rectifier circuit of Problem 17.3.

- (a) Sketch the output voltage waveform  $v(t)$ , for CCM operation and for DCM operation. Clearly label the conduction intervals of each SCR.
- (b) Under what conditions does the rectifier operate in CCM? in DCM?
- (c) Derive an expression for the dc component of the output voltage in CCM.
- (d) Repeat part (c), for DCM operation.

**17.4** A rectifier is connected to the 60 Hz utility system. It is desired to design a harmonic trap filter that has negligible attenuation or amplification of 60 Hz currents, but which attenuates both the fifth- and seventh-harmonic currents by a factor of 10 ( $-20$  dB). The ac line inductance  $L_s$  is  $500 \mu\text{H}$ .

- (a) Select  $L_5$ , the inductance of the fifth harmonic trap, equal to  $500 \mu\text{H}$ , and  $L_7$ , the inductance of the seventh harmonic trap, equal to  $250 \mu\text{H}$ . Compute first-pass values for the resistor and capacitor values of the fifth and seventh harmonic trap circuits, neglecting the effects of parallel resonance.
- (b) Plot the frequency response of your filter. It is suggested that you do this using SPICE or a similar computer program. Does your filter meet the attenuation specifications? Are there significant parallel resonances? What is the gain or attenuation at the third harmonic frequency?
- (c) Modify your element values, to obtain the best design you can. You must choose  $L_s = 500 \mu\text{H}$ , but you may change all other element values. Plot the frequency response of your improved filter. "Best" means that the 20 dB attenuations are obtained at the fifth and seventh harmonic frequencies, that the gain at 60 Hz is essentially 0 dB, and that the  $Q$ -factors of parallel resonances are minimized.

**17.5** A rectifier is connected to the 50 Hz utility system. It is desired to design a harmonic trap filter that has negligible attenuation or amplification of 50 Hz currents, but that attenuates the fifth-, seventh-, and eleventh-harmonic currents by a factor of 5 ( $-14$  dB). In addition, the filter must contain a single-pole response that attenuates the thirteenth and higher harmonics by a factor of  $5n/13$ , where  $n$  is the harmonic number. The ac line inductance  $L_s$  is  $100 \mu\text{H}$ .

Design a harmonic trap filter that meets these specifications. Design the best filter you can, which meets the attenuation specifications, that has nearly unity ( $0 \text{ dB} \pm 1 \text{ dB}$ ) gain at 50 Hz, and that has minimum gains at the third and ninth harmonics. Plot the frequency response of your filter, and specify your circuit element values.

**17.6** A single-phase rectifier operates from a 230 Vrms 50 Hz European single-phase source. The rectifier must supply a 1000 W dc load, and must meet the IEC-1000 class A or class D harmonic current limits. The circuit of Fig. 17.1 is to be used. The dc load voltage may have 100 Hz ripple whose peak-to-peak amplitude is no greater than 5% of the dc voltage component.

- (a) Estimate the minimum value of inductance that will meet these requirements.
- (b) Specify values of  $L$  and  $C$  that meet these requirements, and prove (by simulation) that your design is correct.

**17.7** Figure 17.31 illustrates a twelve-pulse rectifier, containing six controlled (SCR) devices and six uncontrolled (diode) devices. The dc filter inductance  $L$  is large, such that its current ripple is negligible. The SCRs operate with delay angle  $\alpha$ . The SCR bridge is driven by a wye-wye connected three-phase transformer circuit, while the diode bridge is driven by a wye-delta connected three-phase transformer circuit. Since both transformer circuits have wye-connected primaries, they can be combined to realize the circuit with a single wye-connected primary.

- (a) Determine the rms magnitudes and phases of the line-to-line output voltages of the transformer secondaries  $v_{a1'b1'}$  and  $v_{a2'b2'}$ , as a function of the applied line-line primary voltage  $v_{ab}$ .
- (b) Sketch the waveforms of the voltages  $v_{d1}(t)$  and  $v_{d2}(t)$ . Label the conduction intervals of each thyristor and diode.

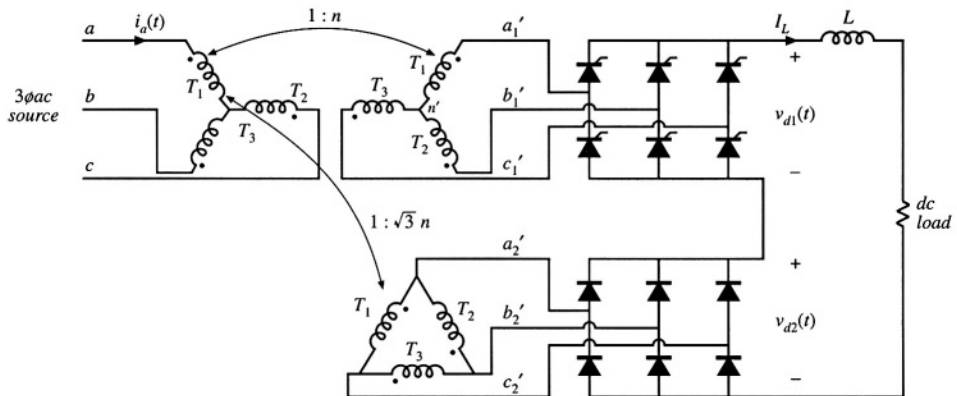


**Fig. 17.31** Twelve-pulse rectifier circuit, with one controlled and one uncontrolled bridge, Problem 17.7.

- (c) Derive an expression for the dc component of the output voltage, as a function of the rms line-line input voltage, the delay angle  $\alpha$ , and the turns ratio  $n$ .
- (d) Over what range of  $\alpha$  is your expression of part (c) valid? What output voltages can be produced by this rectifier?

**17.8**

For the twelve-pulse rectifier circuit of Fig. 17.27(a), determine the Fourier coefficients, for the fundamental through the thirteenth harmonic, of the primary-side currents  $i_{a1}(t)$  and  $i_{a2}(t)$ , as well as for the ac line current  $i_a(t)$ . Express your results in terms of the turns ratio  $n$  and the dc load current  $I_L$ . You may assume that the dc filter inductance  $L$  is large and that the transformers are ideal.

**17.9**

The single-phase controlled-bridge rectifier of Fig. 17.32 operates in the continuous conduction mode. It is desired to regulate the load voltage  $v(t)$  in the presence of slow variations in the amplitude of the sinusoidal input voltage  $v_g(t)$ . Hence, a controller must be designed that varies the delay angle  $\alpha$  such that  $v(t)$  is kept constant, and it is of interest to derive a small-signal ac model for the dc side of the rectifier circuit.

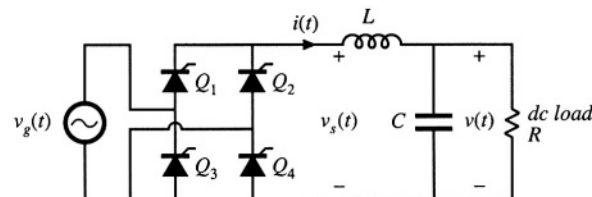


**Fig. 17.32** Single-phase controlled rectifier, Problem 17.9.

- (a) Sketch  $v_s(t)$  and  $v_g(t)$ , and label the delay angle  $\alpha$ .
- (b) Use the circuit averaging method to determine the small-signal transfer functions

$$\frac{\hat{v}_s(s)}{\hat{\alpha}(s)} \quad \text{control-to-output transfer function}$$

and

$$\frac{\hat{v}(s)}{\hat{v}_g(s)} \quad \text{line-to-output transfer function}$$

as well as the steady-state relationship

$$V = f(V_g, A)$$

where

$$\begin{aligned}\alpha(t) &= A + \hat{\alpha}(t) \\ v(t) &= V + \hat{v}(t) \\ v_g(t) &= (V_g + \hat{v}_g(t)) \sin(\omega t)\end{aligned}$$

You may assume that the frequencies of the variations in  $\alpha$ ,  $v$ , and  $v_g$  are much slower than the ac line frequency  $\omega$ , and that the inductor current ripple is small.

---

# 18

## Pulse-Width Modulated Rectifiers

---

To obtain low ac line current THD, the passive techniques described in the previous chapter rely on low-frequency transformers and/or reactive elements. The large size and weight of these elements are objectionable in many applications. This chapter covers active techniques that employ converters having switching frequencies much greater than the ac line frequency. The reactive elements and transformers of these converters are small, because their sizes depend on the converter switching frequency rather than the ac line frequency.

Instead of making do with conventional diode rectifier circuits, and dealing after-the-fact with the resulting low-frequency harmonics, let us consider now how to build a rectifier that behaves as ideally as possible, without generation of line current harmonics. In this chapter, the properties of the *ideal rectifier* are explored, and a model is described. The ideal rectifier presents an effective resistive load to the ac power line; hence, if the supplied ac voltage is sinusoidal, then the current drawn by the rectifier is also sinusoidal and is in phase with the voltage. Converters that approximate the properties of the ideal rectifier are sometimes called *power factor corrected*, because their input power factor is essentially unity [1].

The boost converter, as well as a variety of other converters, can be controlled such that a near-ideal rectifier system is obtained. This is accomplished by control of a high-frequency switching converter, such that the ac line current waveform follows the applied ac line voltage. Both single-phase and three-phase rectifiers can be constructed using PWM techniques. A typical dc power supply system that is powered by the single-phase ac utility contains three major power-processing elements. First, a high-frequency converter with a wide-bandwidth input-current controller functions as a near-ideal rectifier. Second, an energy-storage capacitor smooths the pulsating power at the rectifier output, and a low-bandwidth controller causes the average input power to follow the power drawn by the load. Finally, a dc-dc converter provides a well-regulated dc voltage to the load. In this chapter, single-phase rectifier systems are discussed, expressions for rms currents are derived, and various converter approaches are compared.

The techniques developed in earlier chapters for modeling and analysis of dc-dc converters are extended in this chapter to treat the analysis, modeling, and control of low-harmonic rectifiers. The CCM models of Chapter 3 are used to compute the average losses and efficiency of CCM PWM converters operating as rectifiers. The results yield insight that is useful in power stage design. Several converter control schemes are known, including peak current programming, average current control, critical conduction mode control, and nonlinear carrier control. Ac modeling of the rectifier control system is also covered.

### 18.1 PROPERTIES OF THE IDEAL RECTIFIER

It is desired that the ideal single-phase rectifier present a resistive load to the ac system. The ac line current and voltage will then have the same waveshape and will be in phase. Unity power factor rectification is the result. Thus, the rectifier input current  $i_{ac}(t)$  should be proportional to the applied input voltage  $v_{ac}(t)$ :

$$i_{ac}(t) = \frac{v_{ac}(t)}{R_e} \quad (18.1)$$

where  $R_e$  is the constant of proportionality. An equivalent circuit for the ac port of an ideal rectifier is therefore an effective resistance  $R_e$ , as shown in Fig. 18.1(a).  $R_e$  is also known as the *emulated resistance*. It should be noted that the presence of  $R_e$  does not imply the generation of heat: the power apparently

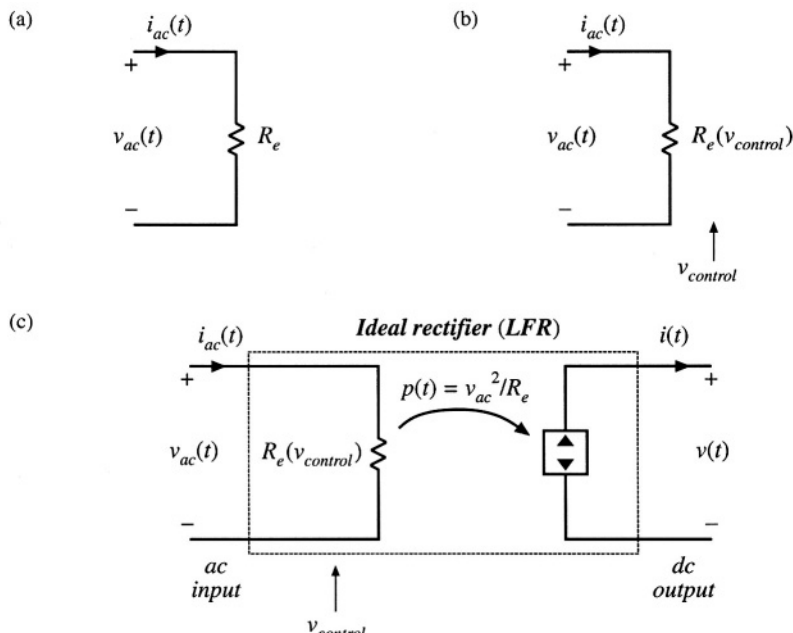


**Fig. 18.1** Development of the ideal rectifier equivalent circuit model: (a) input port resistor emulation; (b) the value of the emulated resistance, and hence the power throughput, is controllable; (c) output port power source characteristic, and complete model.

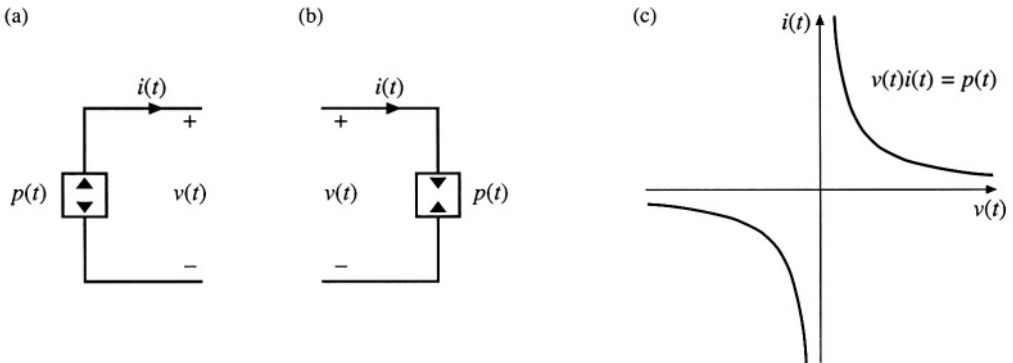


**Fig. 18.2** The dependent power source: (a) power source schematic symbol, (b) power sink schematic symbol, (c)  $i$ - $v$  characteristic.

“consumed” by  $R_e$  is actually transferred to the rectifier dc output port.  $R_e$  simply models how the ideal rectifier loads the ac power system.

Output regulation is accomplished by variation of the effective resistance  $R_e$ , and hence the value of  $R_e$  must depend on a control signal  $v_{control}(t)$  as in Fig. 18.1(b). This allows variation of the rectifier power throughput, since the average power consumed by  $R_e$  is

$$P_{av} = \frac{V_{ac,rms}^2}{R_e(v_{control})} \quad (18.2)$$

Note that changing  $R_e$  results in a time-varying system, with generation of harmonics. To avoid generation of significant amounts of harmonics and degradation of the power factor, variations in  $R_e$  and in the control input must be slow with respect to the ac line frequency.

To the extent that the rectifier is lossless and contains negligible internal energy storage, the instantaneous power flowing into  $R_e$  must appear at the rectifier output port. Note that the instantaneous power throughput

$$p(t) = \frac{v_{ac}^2(t)}{R_e(v_{control}(t))} \quad (18.3)$$

is dependent only on  $v_{ac}(t)$  and the control input  $v_{control}(t)$ , and is independent of the characteristics of the load connected to the output port. Hence, the output port must behave as a source of constant power, obeying the relationship

$$v(t)i(t) = p(t) = \frac{v_{ac}^2(t)}{R_e} \quad (18.4)$$

The *dependent power source* symbol of Fig. 18.2(a) is used to denote such an output characteristic. As illustrated in Fig. 18.1(c), the output port is modeled by a power source that is dependent on the instantaneous power flowing into  $R_e$ .

Thus, a two-port model for the ideal unity-power-factor single-phase rectifier is as shown in Fig. 18.1(c) [2–4]. The two port model is also called a *loss-free resistor* (LFR) because (1) its input port obeys Ohm’s law, and (2) power entering the input port is transferred directly to the output port without loss of

energy. The defining equations of the LFR are:

$$i_{ac}(t) = \frac{v_{ac}(t)}{R_e(v_{control})} \quad (18.5)$$

$$v(t)i(t) = p(t) \quad (18.6)$$

$$p(t) = \frac{v_{ac}^2(t)}{R_e(v_{control}(t))} \quad (18.7)$$

When the LFR output port is connected to a resistive load of value  $R$ , the dc output rms voltages and currents  $V_{rms}$  and  $I_{rms}$  are related to the ac input rms voltages and currents  $V_{ac,rms}$  and  $I_{ac,rms}$  as follows:

$$\frac{V_{rms}}{V_{ac,rms}} = \sqrt{\frac{R}{R_e}} \quad (18.8)$$

$$\frac{I_{ac,rms}}{I_{rms}} = \sqrt{\frac{R}{R_e}} \quad (18.9)$$

The properties of the power source and loss-free resistor network are discussed in Chapter 11. Regardless of the specific converter implementation, any single-phase rectifier having near-ideal properties can be modeled using the LFR two-port model.

## 18.2 REALIZATION OF A NEAR-IDEAL RECTIFIER

Feedback can be employed to cause a converter that exhibits controlled dc transformer characteristics to obey the LFR equations. In the single-phase case, the simplest and least expensive approach employs a full-wave diode rectifier network, cascaded by a dc-dc converter, as in Fig. 18.3. The dc-dc converter is represented by an ideal dc transformer, as discussed in Chapter 3. A control network varies the duty cycle, as necessary to cause the converter input current  $i_g(t)$  to be proportional to the applied input voltage

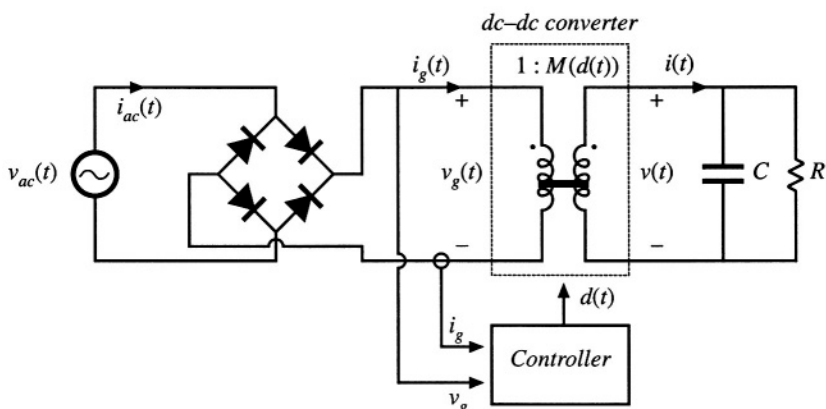


Fig. 18.3 Synthesis of an ideal rectifier by varying the duty cycle of a PWM dc-dc converter.

age  $v_g(t)$  as in Eq. (18.1). The effective turns ratio of the ideal transformer then varies with time. Ideal waveforms are illustrated in Fig. 18.4. If the applied input voltage  $v_{ac}(t)$  is sinusoidal,

$$v_{ac}(t) = V_M \sin(\omega t) \quad (18.10)$$

then the rectified voltage  $v_g(t)$  is

$$v_g(t) = V_M |\sin(\omega t)| \quad (18.11)$$

It is desired that the converter output voltage be a constant dc value  $v(t) = V$ . The converter conversion ratio must therefore be

$$M(d(t)) = \frac{v(t)}{v_g(t)} = \frac{V}{V_M |\sin(\omega t)|} \quad (18.12)$$

This expression neglects the converter dynamics. As can be seen from Fig. 18.4, the controller must cause the conversion ratio to vary between infinity (at the ac line voltage zero crossings) and some minimum value  $M_{min}$  (at the peaks of the ac line voltage waveform).  $M_{min}$  is given by

$$M_{min} = \frac{V}{V_M} \quad (18.13)$$

Any converter topology whose ideal conversion ratio can be varied between these limits can be employed in this application.

To the extent that the dc–dc converter is ideal (i.e., if the losses can be neglected and there is negligible low-frequency energy storage), the instantaneous input and output powers are equal. Hence, the output current  $i(t)$  in Fig. 18.3 is given by

$$i(t) = \frac{v_g(t) i_g(t)}{V} = \frac{v_g^2(t)}{VR_e} \quad (18.14)$$

Substitution of Eq. (18.11) into Eq. (18.14) then leads to

$$\begin{aligned} i(t) &= \frac{V_M^2}{VR_e} \sin^2(\omega t) \\ &= \frac{V_M^2}{2VR_e} (1 - \cos(2\omega t)) \end{aligned} \quad (18.15)$$

Hence, the converter output current contains a dc component and a component at the second harmonic of the ac line frequency. One of the functions of capacitor  $C$  in Fig. 18.3 is to filter out the second harmonic component of  $i(t)$ , so that the load current (flowing through resistor  $R$ ) is essentially equal to the dc component

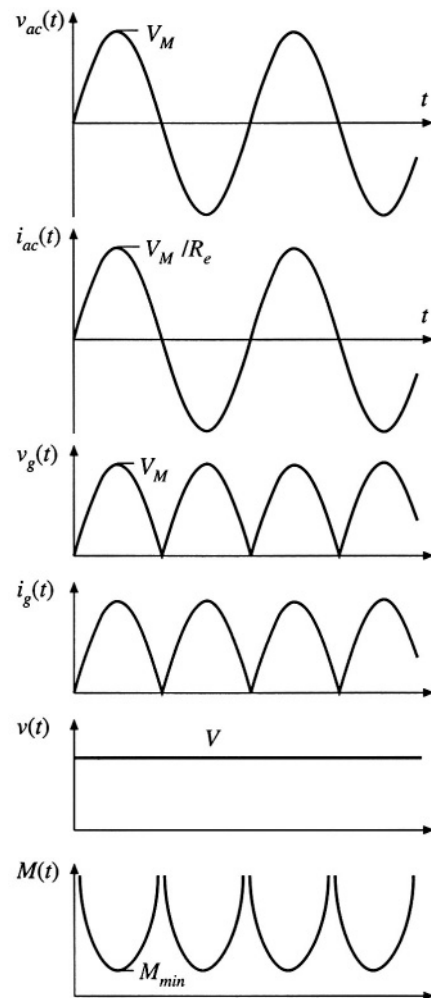


**Fig. 18.4** Waveforms of the rectifier system of Fig. 18.3.

$$I = \langle i(t) \rangle_{T_L} = \frac{V_M^2}{2VR_e} \quad (18.16)$$

where  $T_L$  is the period of the applied ac line voltage.

The average power is

$$P = \frac{V_M^2}{2R_e} \quad (18.17)$$

The above equations are generally valid for PWM converters used as single-phase low-harmonic rectifiers.

### 18.2.1 CCM Boost Converter

A system based on the CCM boost converter is illustrated in Fig. 18.5 [1,5,6]. Ideally, the boost converter can produce any conversion ratio between one and infinity. Hence, the boost converter is capable of producing the  $M(d(t))$  given by Eq. (18.12), provided that  $V \geq V_M$ . Further, the boost converter can produce very low THD, with better transistor utilization than other approaches.

If the boost converter operates in continuous conduction mode, and if the inductor is small enough that its influence on the low-frequency components of the converter waveforms is negligible, then the duty ratio should follow  $M(d(t)) = 1/(1 - d(t))$ . This implies that the duty ratio should follow the function

$$d(t) = 1 - \frac{v_g(t)}{V} \quad (18.18)$$

This expression is true only in the continuous conduction mode. The boost converter operates in the continuous conduction mode provided that the inductor current ripple

$$\Delta i_g(t) = \frac{v_g(t)d(t)T_s}{2L} \quad (18.19)$$

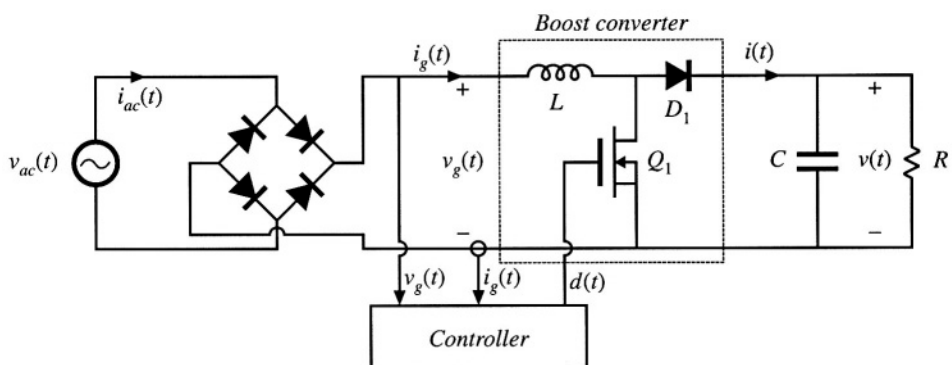


**Fig. 18.5** Rectifier system based on the boost converter.

is greater than the average inductor current, or

$$\langle i_g(t) \rangle_{T_s} = \frac{v_g(t)}{R_e} \quad (18.20)$$

Hence, the converter operates in CCM when

$$\langle i_g(t) \rangle_{T_s} > \Delta i_g(t) \Rightarrow d(t) < \frac{2L}{R_e T_s} \quad (18.21)$$

Substitution of Eq. (18.18) into (18.21) and solution for  $R_e$  leads to

$$R_e < \frac{2L}{T_s \left( 1 - \frac{v_g(t)}{V} \right)} \quad \text{for CCM} \quad (18.22)$$

Since  $v_g(t)$  varies according to Eq. (18.11), Eq. (18.22) may be satisfied at some points on the ac line cycle, and not at others. Since  $0 \leq v_g(t) \leq V_M$ , we can conclude that the converter operates in CCM over the entire ac line cycle when

$$R_e < \frac{2L}{T_s} \quad (18.23)$$

Equations (18.18) and (18.22) then hold for all  $t$ . The converter always operates in DCM when

$$R_e > \frac{2L}{T_s \left( 1 - \frac{V_M}{V} \right)} \quad (18.24)$$

For  $R_e$  between these limits, the converter operates in DCM when  $v_g(t)$  is near zero, and in CCM when  $v_g(t)$  approaches  $V_M$ .

The static input characteristics of the open-loop boost converter are sketched in Fig. 18.6. The input current  $i_g(t)$  is plotted vs. input voltage  $v_g(t)$ , for various duty cycles  $d(t)$ . In CCM, the input characteristics of the boost converter are described by

$$\frac{v_g(t)}{V} = 1 - d(t) \quad \text{in CCM} \quad (18.25)$$

To obtain a general plot, we can normalize the input current and input voltage as follows:

$$m_g(t) = \frac{v_g(t)}{V} \quad (18.26)$$

$$j_g(t) = \frac{2L}{VT_s} i_g(t) \quad (18.27)$$

Equation (18.25) then becomes

$$m_g(t) = 1 - d(t) \quad (18.28)$$

This equation is independent of the input current  $i_g(t)$ , and hence is represented by vertical lines in Fig.

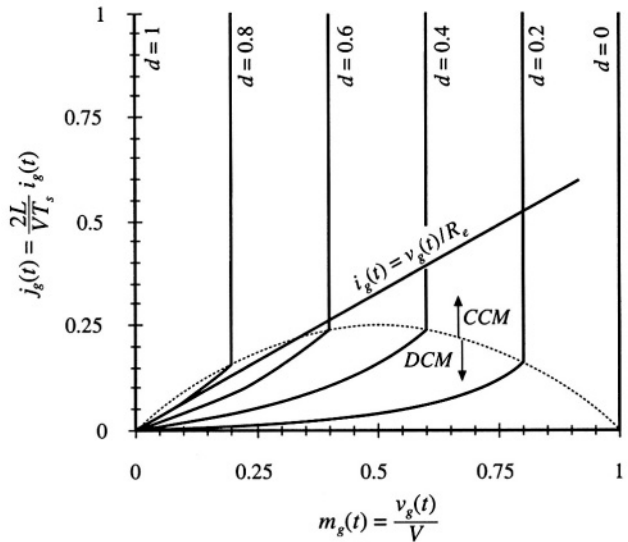


**Fig. 18.6** Static input characteristics of the boost converter. A typical linear resistive input characteristic is superimposed.

### 18.6.

To derive the boost input characteristic for DCM operation, we can solve the steady-state equivalent circuit model of Fig. 11.12(b) (reproduced in Fig. 18.7). *Beware:* the natural DCM effective resistance of Chapter 11,  $R_e = 2L/d^2T_s$ , does not necessarily coincide with the emulated resistance  $R_e = v_g/i_g$  of Eq. (18.1). In this chapter, the quantity  $R_e$  is defined according to Eq. (18.1). Solution of Fig. 18.7 for the input current  $i_g(t)$  leads to:

$$i_g(t) = \frac{v_g(t)}{\left(\frac{2L}{d^2T_s}\right)} + \frac{p(t)}{V - v_g(t)} \quad (18.29)$$

The instantaneous power consumed by the effective resistor in the model of Fig. 18.7 is

$$p(t) = \frac{v_g^2(t)}{\left(\frac{2L}{d^2T_s}\right)} \quad (18.30)$$

Substitution of Eq. (18.30) into Eq. (18.29) and simplification leads to

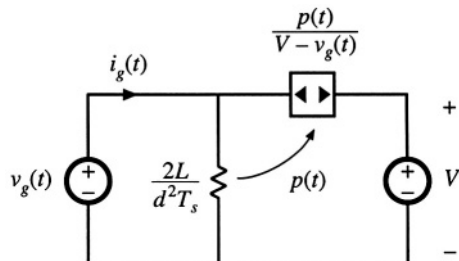


**Fig. 18.7** Averaged equivalent circuit model of the boost converter operating in DCM, derived in Chapter 11.

$$\frac{2L}{VT_s} i_g(t) \left(1 - \frac{v_g(t)}{V}\right) = d^2(t) \frac{v_g(t)}{V} \quad \text{in DCM} \quad (18.31)$$

Normalization of this equation according to Eqs. (18.26) and (18.27) yields

$$j_g(t) \left(1 - m_g(t)\right) = d^2(t) m_g(t) \quad (18.32)$$

This equation describes the curved (DCM) portions of the Fig. 18.6 input characteristics, for low  $i_g(t)$ .

To express the CCM/DCM mode boundary as a function of  $v_g(t)$  and  $i_g(t)$ , Eqs. (18.1) and (18.22) can be combined, leading to

$$\frac{2L}{VT_s} i_g(t) > \left(\frac{v_g(t)}{V}\right) \left(1 - \frac{v_g(t)}{V}\right) \quad \text{for CCM} \quad (18.33)$$

Normalization of this equation, according to Eqs. (18.26) and (18.27), results in

$$j_g(t) > m_g(t) \left(1 - m_g(t)\right) \quad \text{for CCM} \quad (18.34)$$

This equation describes a parabola having roots at  $m_g = 0$  and  $m_g = 1$ , with the maximum value  $j_g = 0.25$  at  $m_g = 0.5$ . The mode boundary equation is plotted as a dashed line in Fig. 18.6

The complete input characteristics for the boost converter were plotted in Fig. 18.6 using Eqs. (18.28), (18.32), and (18.34). Figure 18.6 also illustrates the desired linear resistive input characteristic, Eq. (18.1). For the value of  $R_e$  illustrated, the converter operates in DCM for  $v_g(t)$  near zero, and in CCM for  $v_g(t)$  near  $V_M$ . The intersections of boost input characteristics with the desired linear input characteristic illustrate how the controller must choose the duty cycle at various values of  $v_g(t)$ .

Other converters capable of producing the  $M(d(t))$  of Eq. (18.12) include the buck-boost, SEPIC, and Ćuk converters. The boost, SEPIC, and Ćuk converters share the desirable property of non-pulsating input current, and hence require minimal input EMI filtering. The SEPIC produces a non inverted output voltage. Isolated versions of these converters (see Chapter 6) are also sometimes employed [7–9]. Schemes involving the parallel resonant converter, as well as several types of quasi-resonant converters, are also documented in the literature [10–13].

The open-loop boost converter, when operated in discontinuous conduction mode, is also sometimes used as an approximation of an ideal rectifier. The DCM effective resistance  $2L/d^2(t)T_s$  of Fig. 18.7 is then taken as an approximation of the desired emulated resistance of Eq. (18.1). The model differs from that of the ideal rectifier model of Fig. 18.1(c) in that the power source is connected between the input and output terminals. As a result, harmonics are present in the input current waveform. For example, if  $v_g(t)$  is a rectified sinusoid, then the current through the effective resistance  $2L/d^2(t)T_s$  will also be a rectified sinusoid. However, the input current  $\langle i_g(t) \rangle_{T_s}$  is now equal to the sum of the current through  $R_e$  and the current flowing through the power source element. Since the power source is a nonlinear element,  $\langle i_g(t) \rangle_{T_s}$  contains harmonics. For large  $C$ , the output voltage is essentially constant. The input current waveform is then given by Eq. (18.31). If  $V$  is sufficiently large, then the term  $(1 - v_g(t)/V)$  is approximately equal to one, and the harmonics in  $\langle i_g(t) \rangle_{T_s}$  are small. The zero crossings of  $v_g(t)$ ,  $p(t)$ , and  $\langle i_g(t) \rangle_{T_s}$  coincide. So although the DCM boost converter generates some current harmonics, it is nonetheless possible to construct a low harmonic rectifier that meets harmonic limits. Again, this approach has the disadvantages of the increased peak currents of DCM, and the need for additional filtering of the high-frequency pulsating input currents. Computer simulation of a DCM boost rectifier is described in Appendix B, Section B.2.3.

A similar approach is to operate the boost converter at the boundary between the continuous and discontinuous conduction modes. This approach is known as “critical conduction mode” operation. It eliminates the distortion mechanism described above, but requires variable switching-frequency control. This approach is quite popular at low power levels, and is described further in Section 18.3.3.

Other converters not capable of producing the  $M(d(t))$  of Eq. (18.12), such as the buck converter, are sometimes employed as the dc–dc converter of Fig. 18.3. Distortion of the ac line current waveform must then occur. Nonetheless, at low power levels it may be possible to meet the applicable ac line current harmonic standards using such an approach.

### 18.2.2 DCM Flyback Converter

In Chapter 11, the loss-free resistor network is used to model converters operating in discontinuous conduction mode. This suggests that DCM converters can also be used as near-ideal rectifiers. Indeed, the buck-boost, flyback, SEPIC, and Ćuk converters, when operated in discontinuous conduction mode without additional control, inherently behave as natural loss-free resistors. The DCM effective resistance  $R_e$ , found in Chapter 11 to be equal to  $2L/D^2T_s$ , then coincides with the rectifier emulated resistance of Eq. (18.1). At low power levels, this can be an effective and low-cost approach. Inrush current limiting is also inherent in this approach, and isolation and scaling via a turns ratio are provided by the transformer. Disadvantages are the increased peak currents of DCM, and the need for additional filtering of the high-frequency pulsating input currents.

A simple low-harmonic rectifier system based on the transformer-isolated flyback converter is illustrated in Fig. 18.8 [2]. The ac line voltage is connected through an input EMI filter to a bridge rectifier and a flyback converter. The flyback converter is operated at constant switching frequency  $f_s$  and constant duty cycle  $D$ . The converter is designed such that it operates in the discontinuous conduction mode under all conditions. The input EMI filter smooths the pulsating input current waveform, so that  $i_{ac}(t)$  is approximately sinusoidal.

The flyback converter is replaced by its averaged equivalent circuit in Fig. 18.9. As discussed in Chapter 11, the terminal waveforms of the flyback converter have been averaged over the switching period  $T_s$ , resulting in the loss-free resistor model. This model illustrates how the DCM flyback converter presents a resistive load to the ac input. It also illustrates how the power flow can be controlled, by varia-

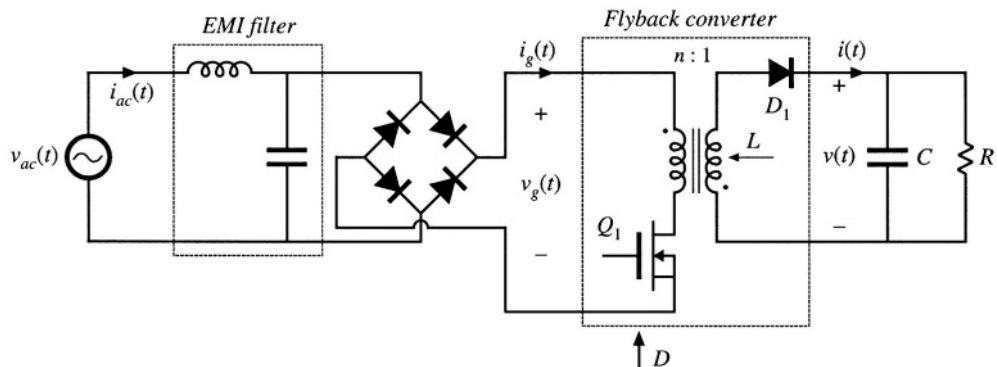


**Fig. 18.8** Low-harmonic rectifier system incorporating a flyback converter that operates in the discontinuous conduction mode.

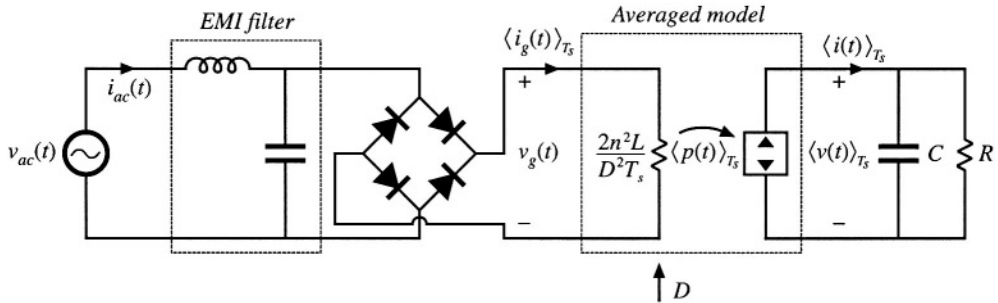


Fig. 18.9 Averaged equivalent circuit that models the system of Fig. 18.8.

tion of  $D$  to control the value of the emulated resistance  $R_e$ .

To design this converter, one must select the value of inductance to be sufficiently small, such that the converter operates in DCM at all points on the ac sine wave, at maximum load. If we denote the lengths of the transistor conduction interval, diode conduction interval, and discontinuous interval as  $DT_s$ ,  $d_2T_s$ , and  $d_3T_s$ , respectively, then the converter operates in DCM provided that  $d_3$  is greater than zero. This implies that

$$d_2(t) < 1 - D \quad (18.35)$$

By volt-second balance on the transformer magnetizing inductance, we can express  $d_2(t)$  as

$$d_2(t) = D \frac{v_g(t)}{nV} \quad (18.36)$$

Substitution of Eq. (18.36) into Eq. (18.35) and solution for  $D$  yields

$$D < \frac{1}{\left(1 + \frac{v_g(t)}{nV}\right)} \quad (18.37)$$

During a given switching period, the converter will operate in DCM provided that the above inequality is satisfied. The worst case occurs when the rectified sinusoid  $v_g(t)$  is equal to its peak value  $V_M$ . The inequality then becomes

$$D < \frac{1}{\left(1 + \frac{V_M}{nV}\right)} \quad (18.38)$$

If Eq. (18.38) is satisfied, then the converter operates in DCM at all points on the ac line sinusoid.

In steady state, the dc output voltage is given by Eq. (18.8). Upon substitution of the expression for  $R_e$  and solution for  $D$ , this equation becomes

$$D = \frac{2nV}{V_M} \sqrt{\frac{L}{RT_s}} \quad (18.39)$$

Insertion of this relationship into Eq. (18.38), and solution for  $L$ , yields

$$L < L_{crit} = \frac{RT_s}{4 \left( 1 + \frac{nV}{V_M} \right)^2} \quad (18.40)$$

For variations in load  $R$  and peak ac input voltage  $V_M$ , the worst case will occur at minimum  $R$  (maximum power) and minimum  $V_M$ . Hence, the designer should choose  $L$  to satisfy

$$L < L_{crit-min} = \frac{R_{min} T_s}{4 \left( 1 + \frac{nV}{V_{M-min}} \right)^2} \quad (18.41)$$

If this equation is violated, then at maximum load power and minimum input voltage amplitude, the convert will operate in CCM near the peak of the ac sinewave. This will lead to an input current waveform having substantial distortion.

### 18.3 CONTROL OF THE CURRENT WAVEFORM

A wide variety of approaches are known for active control of the input current waveform to attain input resistor emulation [14–33]. Average current control [17,18], input voltage feedforward [17], current-programmed control [19–22], hysteretic control and critical conduction mode control [23–27], and nonlinear carrier control [28–30] are briefly surveyed here. Other approaches include sliding-mode control [31], charge control [32], and ASDTIC control [33].

#### 18.3.1 Average Current Control

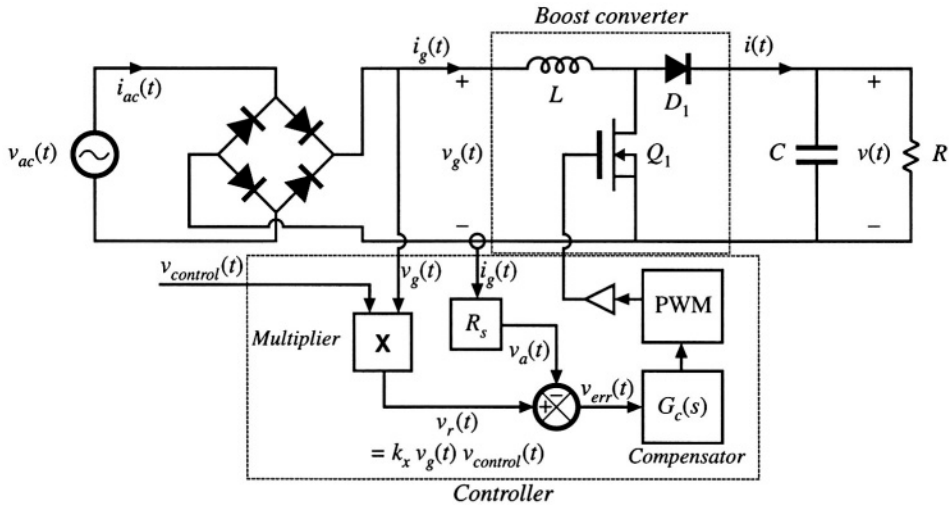
Average current control is a popular method of implementing control of the input current waveform in a low-harmonic rectifier. This approach works in both continuous and discontinuous conduction modes, and can produce high-quality current waveforms over a wide range of input voltages and load powers. The problems of crossover distortion, found in some competing schemes such as current programmed control, are largely avoided. Several popular integrated circuits are available that implement average current control.

Figure 18.10 illustrates average current control of the input current waveform  $\langle i_g(t) \rangle_{T_s}$  in a boost converter. The input current  $i_g(t)$  flows through a shunt resistor. The voltage across this shunt resistor is amplified by an op amp circuit. This op amp circuit contains a low-pass filter characteristic that attenuates the high-frequency switching harmonics. The output voltage  $v_a(t)$  of the op amp circuit is proportional to the low-frequency average value of  $i_g(t)$ :

$$v_a(t) = R_s \langle i_g(t) \rangle_{T_s} \quad (18.42)$$

This signal is compared to the reference voltage  $v_r(t)$ , to produce an error signal that drives the compensator network and pulse-width modulator as illustrated. If the feedback loop is well designed, then the error signal is small:

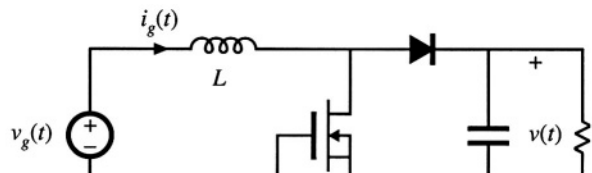
$$v_a(t) \approx v_r(t) \quad (18.43)$$



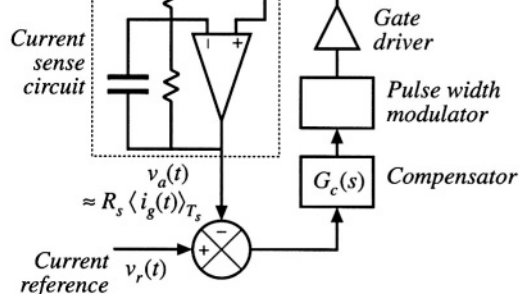
**Fig. 18.11** Average current control of a boost converter, to obtain a low-harmonic rectifier.

The average current controller causes the sensed current  $i_g(t)$  to follow the reference waveform  $v_r(t)$ .

To cause the input current to be proportional to the input voltage, the reference voltage  $v_r(t)$  is derived from the sensed input voltage waveform, as in Fig. 18.11. The current reference signal  $v_r(t)$  is derived from the sensed input voltage  $v_g(t)$ , and hence has a sinusoidal waveshape. Hence, the average current controller causes the average input current  $i_g(t)$  to be proportional to the input voltage  $v_g(t)$ . The multiplier illustrated in Fig. 18.11 allows adjustment of the constant of proportionality, so that the magnitude of the emulated resistance can be controlled via a control signal  $v_{control}(t)$ . Let us assume that the multiplier terminal equations are



**Fig. 18.10** Average current control of the input current in a boost converter.



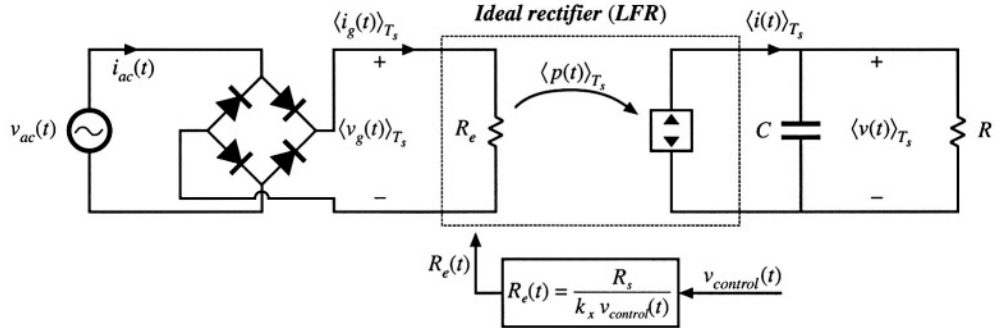


**Fig. 18.12** Model of the system of Fig. 18.5, based on the loss-free resistor model of Fig. 18.1(c), which predicts the low-frequency system waveforms. This model assumes that the feedback loop of Fig. 18.5 operates ideally.

$$v_r(t) = k_x v_g(t) v_{control}(t) \quad (18.44)$$

Then the emulated resistance is

$$R_e = \frac{v_r(t)}{i_g(t)} = \frac{\left( \frac{v_r(t)}{k_x v_{control}(t)} \right)}{\left( \frac{v_g(t)}{R_s} \right)} \quad (18.45)$$

Here, Eqs. (18.44) and (18.42) have been used to eliminate  $v_g$  and  $i_g$ . Substitution of Eq. (18.43) leads to the result

$$R_e(v_{control}(t)) = \frac{R_s}{k_x v_{control}(t)} \quad (18.46)$$

Hence, if the feedback loop is well designed, then the system of Fig. 18.11 can be represented by the LFR model as in Fig. 18.12. The average current controller scheme of Fig. 18.11 and the model of Fig. 18.12 are independent of the dc-dc converter topology, and can be applied to systems containing CCM boost, buck-boost, Ćuk, SEPIC, and other topologies.

Average power flow and the output voltage are regulated by variation of the emulated resistance  $R_e$ , in average current control as well as in most other schemes. This is usually accomplished by use of a multiplier in the input voltage sensing path, as shown in Fig. 18.13. This control loop continually adjusts  $R_e$  to maintain balance of the average rectifier power  $P_{av} = V_{g, rms}^2 / R_e$  and the load power  $P_{load}$ , such that the following relation is obeyed:

$$P_{av} = \frac{V_{g, rms}^2}{R_e} = P_{load} \quad (18.47)$$

Average current control works quite well. Its only disadvantages are the need to sense the average input current, rather than the transistor current, and the need for a multiplier in the controller circuit.

Most average current control implementations include provisions for feedforward of the input voltage amplitude. This allows disturbances in the ac input voltage amplitude to be canceled out by the

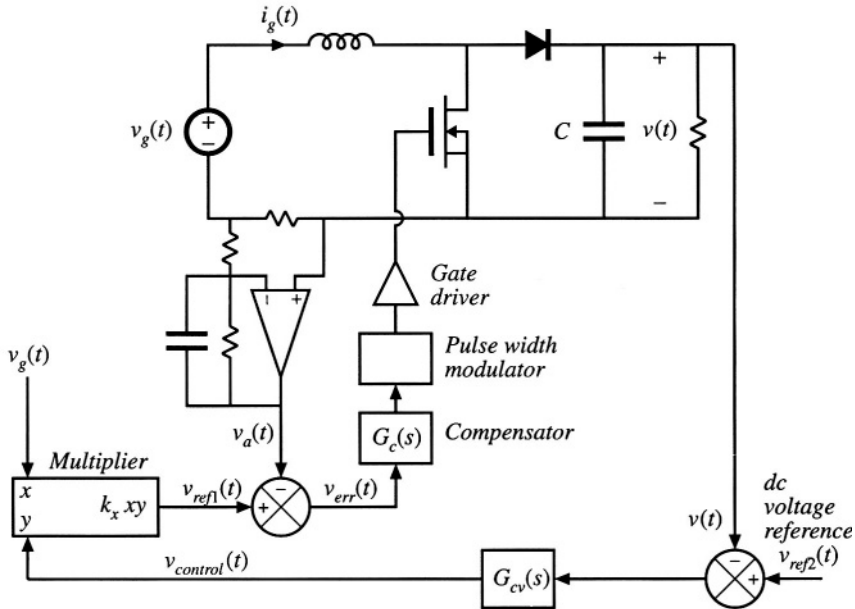


**Fig. 18.13** Average current control incorporating a multiplier for regulation of the output voltage.

controller, such that the dc output voltage is unaffected.

Combination of Eqs. (18.44), (18.46), and (18.47), and solution for  $v_{ref1}(t)$  leads to

$$v_{ref1}(t) = \frac{P_{av}v_g(t)R_s}{V_{g,rms}^2} \quad (18.48)$$

This equation shows how the reference voltage should be varied to maintain a given rectifier average power throughput  $P_{av}$ . Apparently, it is necessary to divide by the square of the rms input voltage amplitude. A controller that implements Eq. (18.48) is illustrated in Fig. 18.14. The multiplier block of Fig. 18.13 has been generalized to perform the function  $k_vxy/z^2$ . It is somewhat complicated to compute the rms value of a general ac waveform; however, the ac input voltage  $v_g(t)$  normally is sinusoidal with negligible harmonics. Hence, the peak value of  $v_g(t)$  is directly proportional to its rms value, and we can use the peak value  $V_M$  in place of  $V_{g,rms}$ . So the controller of Fig. 18.14 produces the reference voltage

$$v_{ref1}(t) = \frac{k_v v_{control}(t) v_g(t)}{V_M^2} \quad (18.49)$$

Comparison of Eqs. (18.48) and (18.49) leads to the conclusion that

$$P_{av} = \frac{k_v v_{control}(t)}{2R_s} \quad (18.50)$$

So the average power throughput is directly controlled by  $v_{control}(t)$ , and is independent of the input voltage  $v_g(t)$ .

Feedforward can cause the rectifier dc output voltage to be less sensitive to variations in the ac

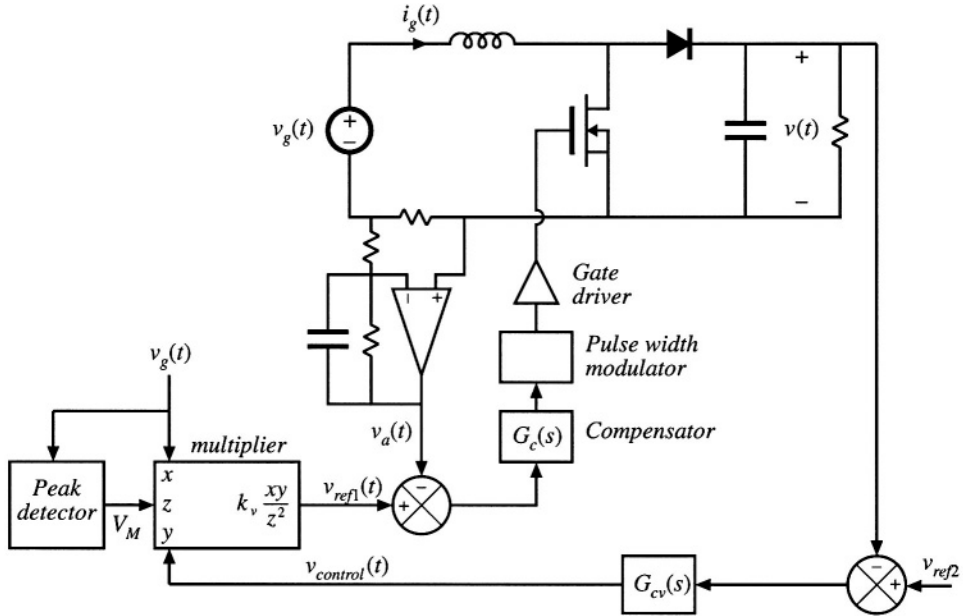


**Fig. 18.14** Average current control incorporating input voltage feedforward.

line voltage. A disadvantage is the ac line current distortion introduced by variations in the voltage produced by the peak detector.

To aid in the design of the inner feedback loop that controls the ac line current waveshape, a converter model is needed that describes how the converter average input current depends on the duty cycle. We would prefer to apply the averaged small-signal modeling techniques of Chapter 7 here. The problem is that the variations in the duty cycle  $d(t)$ , as well as in the ac input voltage  $v_g(t)$  and current  $i_g(t)$ , are not small. As a result, in general the small-signal assumptions are violated, and we are faced with the design of a control system that exhibits significant nonlinear time-varying behavior.

When the rectifier operates near periodic steady state, the output voltage  $v(t)$  of a well-designed system exhibits small variations. So we can write

$$\langle v(t) \rangle_{T_s} = V + \hat{v}(t) \quad (18.51)$$

with

$$|\hat{v}(t)| \ll |V| \quad (18.52)$$

In other words, the small-signal assumption continues to be valid with respect to the rectifier output voltage. In the case of the boost converter, this allows us to linearize the converter input characteristics.

Following the approach of Chapter 7, we can express the average inductor voltage of the boost converter as

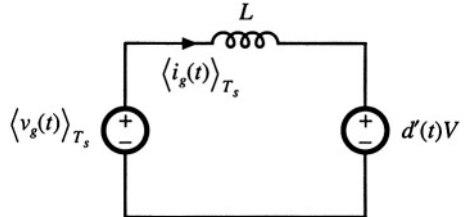


**Fig. 18.15** Linearized model describing the boost converter input characteristics, corresponding to Eq. (18.55)

$$L \frac{d\langle i_g(t) \rangle_{T_s}}{dt} = \langle v_g(t) \rangle_{T_s} - d'(t) \langle v(t) \rangle_{T_s} \quad (18.53)$$

This equation contains the nonlinear term  $d'(t) \langle v(t) \rangle_{T_s}$ . Substitution of Eq. (18.51) into (18.53) yields

$$L \frac{d\langle i_g(t) \rangle_{T_s}}{dt} = \langle v_g(t) \rangle_{T_s} - d''(t)V - d'(t)\hat{v}(t) \quad (18.54)$$

When Eq. (18.52) is satisfied, then the nonlinear term  $-d'(t)\hat{v}(t)$  is much smaller in magnitude than the linear term  $-d'(t)V$ . Therefore, we can discard the nonlinear term to obtain

$$L \frac{d\langle i_g(t) \rangle_{T_s}}{dt} = \langle v_g(t) \rangle_{T_s} - d'(t)V \quad (18.55)$$

This linear differential equation is valid even though  $i_g(t)$ ,  $v_g(t)$ , and  $d(t)$  contain large variations.

An equivalent circuit corresponding to Eq. (18.55) is given in Fig. 18.15. The averaged control-to-input-current transfer function is found by setting the independent inputs other than  $d(t)$  to zero, and then solving for  $i_g$ ; the model predicts that this transfer function is

$$\frac{i_g(s)}{d(s)} = \frac{V}{sL} \quad (18.56)$$

where  $i_g(s)$  is the Laplace transform of  $\langle i_g(t) \rangle_{T_s}$ . So the input characteristics of the boost rectifier can be linearized, even though the ac input variations are not small.

Unfortunately, Eq. (18.52) is not sufficient to linearize the equations describing the input characteristics of the buck-boost, SEPIC, Cuk, and most other single-phase rectifiers. The control system design engineer must then deal with a truly nonlinear time-varying dynamical system.

One approach that is sometimes suggested employs the *quasi-static approximation* [34,35]. It is assumed that the ac line variations are much slower than the rectifier system dynamics, such that the rectifier always operates near equilibrium. The quiescent operating point changes slowly along the input sinusoid; an equilibrium analysis can be performed to find expressions for the slowly-varying “equilibrium” duty ratio and converter voltages and currents. The small-signal dc–dc converter transfer functions derived in Chapters 7 and 8 are evaluated using this time-varying operating point. The converter poles, zeroes, and gains are found to vary along the ac input sinusoid. An average current controller is designed using these time-varying transfer functions, such that the current loop gain has a positive phase margin at all operating points.

We expect that the quasi-static approximation should be valid if the rectifier system dynamics are sufficiently fast, and it is reasonable to anticipate that high-frequency PWM converters have dynam-

ics that are much faster than the ac line frequency. The problem is that no good condition on system parameters, which can justify the approximation, is known for the basic converter topologies. There is room for additional research in this area.

It is well-understood in the field of control systems that, when the rectifier system dynamics are not sufficiently fast, the quasi-static approximation yields neither sufficient nor necessary conditions for stability of the resulting design. Time-varying “loop gains” that always have a positive phase margin may nonetheless be unstable, and a negative phase margin does not always imply instability. Such phenomena are sometimes observed in rectifier systems. Even worse, it is difficult to justify the use of the Laplace transform on rectifiers described by time-varying differential equations, unless the quasi-static approximation can be validated.

### 18.3.2 Current Programmed Control

Another well-known approach to attaining input resistor emulation is the use of current-programmed control. As illustrated in Fig. 18.16, the programmed current  $i_c(t)$  is made proportional to the ac input voltage. This causes the average inductor current, and hence also  $\langle i_g(t) \rangle_{T_s}$ , to approximately follow  $v_g(t)$ . As in average current control, a multiplier is used to adjust the emulated resistance and average power flow; the control signal  $v_{control}(t)$  is typically used to stabilize the dc output voltage magnitude. Several rectifier control ICs are commercially available, which implement current-programmed control.

As discussed in Chapter 12, several mechanisms cause the average inductor current and hence also  $\langle i_g(t) \rangle_{T_s}$  to differ from the programmed  $i_c(t)$ . These mechanisms introduce crossover distortion and line current harmonics. An artificial ramp having sufficiently large slope  $m_a$  is necessary to stabilize the

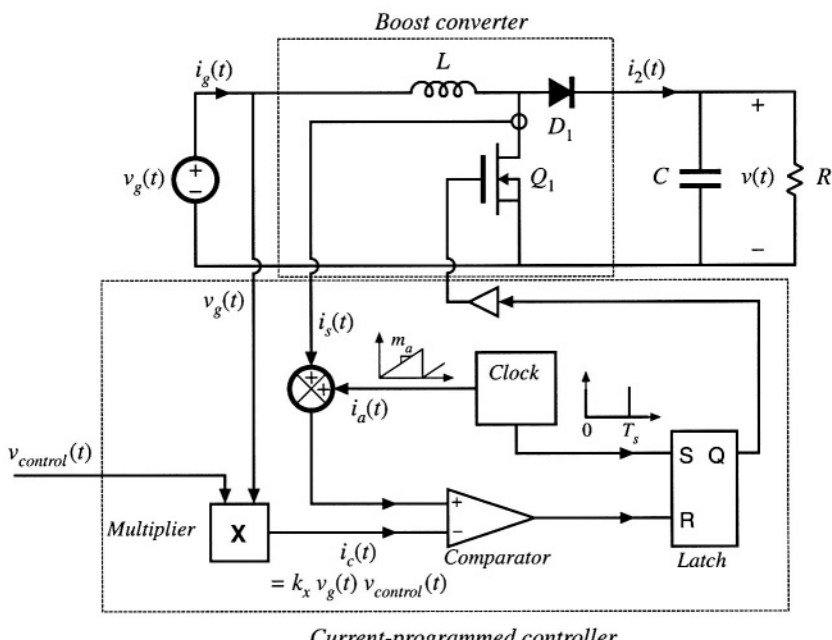


Fig. 18.16 Current-programmed control of a boost rectifier.

current-programmed boost converter when it operates in CCM with  $d(t) > 0.5$ . The addition of this ramp causes  $\langle i_g(t) \rangle_{T_s}$  to differ from  $i_c(t)$ . Additional deviation is introduced by the inductor current ripple. Both mechanisms are most pronounced when the inductor current is small, near the zero-crossings of the ac line waveforms.

The static input characteristics, that is, the average input current vs. the input voltage, of the current-programmed boost converter are given by

$$\langle i_g(t) \rangle_{T_s} = \begin{cases} v_g(t) \frac{Li_c^2(t)f_s V}{2(V - v_g(t)) \left( v_g(t) + m_a L \right)^2} & \text{in DCM} \\ i_c(t) - \left( 1 - \frac{v_g(t)}{V} \right) \left( m_a + \frac{v_g(t)}{2L} \right) T_s & \text{in CCM} \end{cases} \quad (18.57)$$

The converter operates in the continuous conduction mode when

$$\langle i_g(t) \rangle_{T_s} > \frac{T_s V}{2L} \frac{v_g(t)}{V} \left( 1 - \frac{v_g(t)}{V} \right) \quad (18.58)$$

In terms of the control current  $i_c(t)$ , the condition for operation in CCM can be expressed

$$i_c(t) > \frac{T_s V}{L} \left( \frac{m_a L}{V} + \frac{v_g(t)}{V} \right) \left( 1 - \frac{v_g(t)}{V} \right) \quad (18.59)$$

In the conventional current-programmed rectifier control scheme, the control current  $i_c(t)$  is simply proportional to the ac input voltage:

$$i_c(t) = \frac{v_g(t)}{R_e} \quad (18.60)$$

where  $R_e$  is the emulated resistance that would be obtained if the average input current exactly followed the reference current  $i_c(t)$ . The static input characteristics given by Eqs. (18.57) to (18.60) are plotted in Fig. 18.17. The average input current  $\langle i_g(t) \rangle_{T_s}$  is plotted as a function of the applied input voltage  $v_g(t)$ , for several values of emulated resistance  $R_e$ . The region near the CCM–DCM boundary is shown. The curves are plotted for a fixed artificial ramp having slope

$$m_a = \frac{V}{2L} \quad (18.61)$$

This is the minimum value of artificial ramp that stabilizes the boost current-programmed controller at all static operating points. Decreasing  $m_a$  below this value leads to instability at operating points in the continuous conduction mode at low  $v_g(t)/V$ .

To obtain resistor emulation, it is desired that the static input characteristics be linear and pass through the origin. It can be seen from Fig. 18.17 that this is not the case: the curves are reasonably linear in the continuous conduction mode, but exhibit significant curvature as the CCM–DCM boundary is approached. The resulting average current waveforms are summarized in Fig. 18.8.

To minimize the line current THD, it is apparent that the converter should be designed to operate deeply in the continuous conduction mode for most of the ac line cycle. This is accomplished with emulated resistances  $R_e$  that are much smaller than  $R_{base} = 2L/T_s$ . In addition, the artificial ramp slope  $m_a$

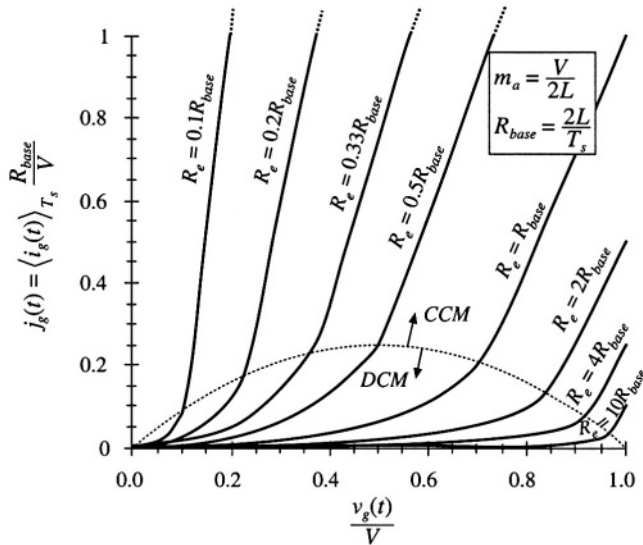


**Fig. 18.17** Static input characteristics of a current-programmed boost converter, with minimum stabilizing artificial ramp of Eq. (18.61).

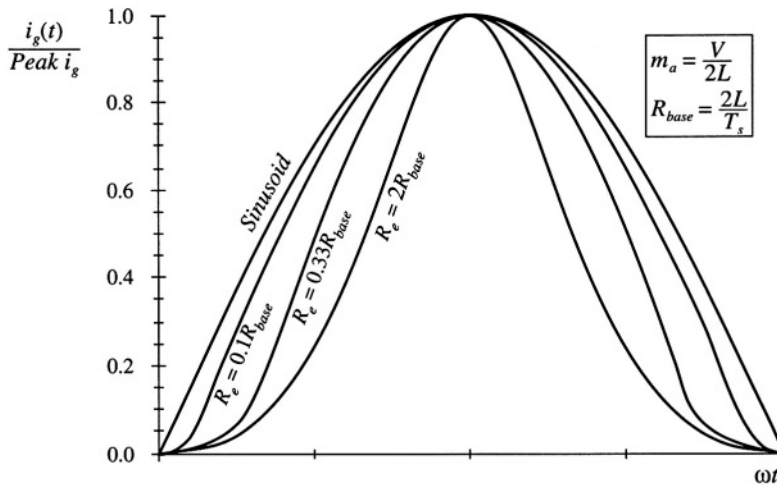


**Fig. 18.18** Input current waveshapes predicted by the static input characteristics of Fig. 18.17, compared with a pure sinusoid. Curves are plotted for the case  $V_M = 0.8V$ , with minimum stabilizing artificial ramp.

should be no greater than otherwise necessary. In practice, THD of 5% to 10% can easily be obtained in rectifiers that function over a narrow range of rms input voltages and load currents. However, low THD cannot be obtained at all operating points in universal-input rectifiers; THD of 20% to 50% may be observed at maximum ac input voltage. This problem can be solved by biasing the current reference waveform. Design of current-programmed rectifiers is discussed in [19–22], and some strategies for solving this problem are addressed in [19].

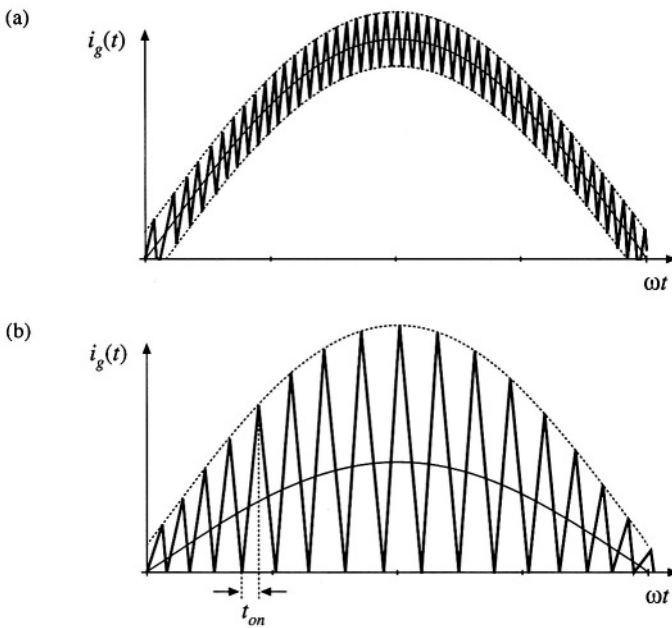


**Fig. 18.19** Input current waveforms of two boost converters with hysteretic control: (a)  $\pm 10\%$  regulation band, (b) critical conduction mode operation ( $\pm 100\%$  regulation band).

### 18.3.3 Critical Conduction Mode and Hysteretic Control

Another control scheme sometimes used in low-harmonic rectifiers, as well as in dc–dc converters and dc–ac inverters, is hysteretic control. Rather than operating at a fixed switching frequency and duty cycle, the hysteretic controller switches the transistor on and off as necessary to maintain a waveform within given limits. A special case of hysteretic control, called *critical conduction mode* control, is implemented in several commercially-available ICs, and is popular for low-harmonic rectifiers rated below several hundred Watts [23–25].

An example is the sinusoid of Fig. 18.19(a), in which the boost converter input current is controlled to follow a sinusoidal reference with a  $\pm 10\%$  tolerance. The inductor current increases when the transistor is on, and decreases when the transistor is off. So this hysteretic controller switches the transistor on whenever the input current falls below 90% of the reference input. The controller switches the transistor off whenever the input current exceeds 110% of the reference. Hysteretic controllers tend to have simple implementations. However, they have the disadvantages of variable switching frequency and reduced noise immunity.

Another example of hysteretic control is the waveform of Fig. 18.19(b). The lower limit is chosen to be zero, while the upper limit is twice the reference input. This controller operates the boost converter at the boundary between the continuous and discontinuous conduction modes. An alternative control scheme that generates the same waveform simply operates the transistor with constant on-time: the transistor is switched on when the inductor current reaches zero, and is switched off after a fixed

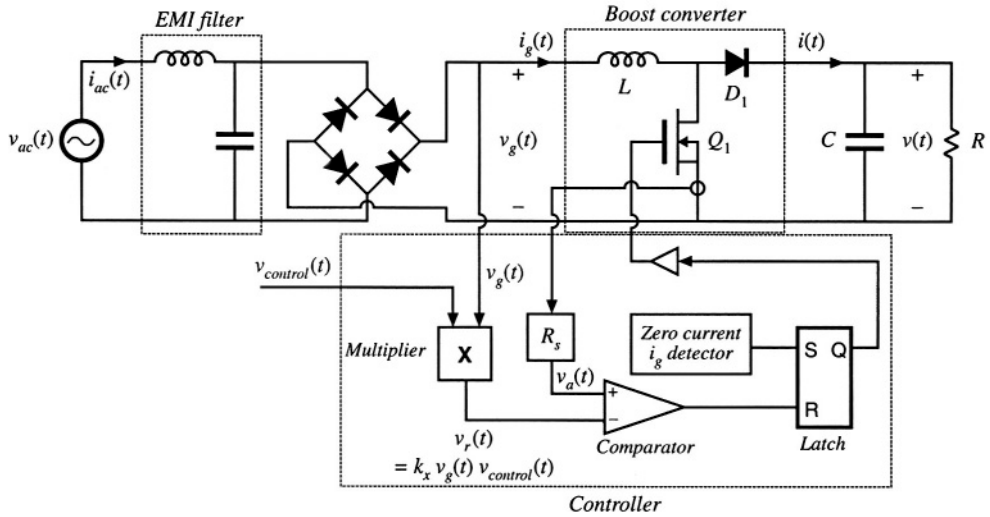


**Fig. 18.20** A typical implementation of critical conduction mode control.

interval of length  $t_{on}$ . The resulting inductor current waveform will have a peak value that depends directly on the applied input voltage, and whose average value is one-half of its peak. With either control approach, the converter naturally exhibits loss-free-resistor or ideal rectifier behavior. The emulated resistance is

$$R_e = \frac{2L}{t_{on}} \quad (18.62)$$

This scheme has the advantage of small inductor size and low-cost control ICs. Disadvantages are increased peak currents, variable switching frequency, and the need for additional input EMI filtering.

A typical critical conduction mode controller is illustrated in Fig. 18.20. A zero-current detector senses when the inductor current is zero; this is typically accomplished by monitoring the voltage across the inductor. The zero-current detector sets a latch, turning on the transistor and initiating the switching period. The transistor current is also monitored, and is compared to a sinusoidal reference  $v_r(t)$  that is proportional to the applied input voltage  $v_g(t)$ . When the sensed current is equal to the reference, the latch is reset and the transistor is turned off.

Since the switching frequency can vary, possibly over a wide range, it is important to carefully design the converter power stage. For a given power  $P$ , the required transistor on-time  $t_{on}$  can be found by combining Eqs. (18.17) and (18.62), and solving for  $t_{on}$ :

$$t_{on} = \frac{4LP}{V_M^2} \quad (18.63)$$

Application of the principle of volt-second balance to inductor  $L$  of Fig. 18.20 leads to the following equation:

$$v_g t_{on} + (v_g - V) t_{off} = 0 \quad (18.64)$$

Hence, the transistor off-time is given by

$$t_{off} = t_{on} \frac{v_g}{(V - v_g)} \quad (18.65)$$

The switching period  $T_s$  is equal to

$$T_s = t_{off} + t_{on} \quad (18.66)$$

Substitution of Eqs. (18.63) and (18.65) into Eq. (18.66) yields

$$T_s = \frac{4LP}{V_M^2} \frac{1}{\left(1 - \frac{v_g(t)}{V}\right)} \quad (18.67)$$

The following expression for switching frequency is found by substitution of Eq. (18.11) into Eq. (18.67):

$$f_s = \frac{1}{T_s} = \frac{V_M^2}{4LP} \left(1 - \frac{V_M}{V} |\sin(\omega t)|\right) \quad (18.68)$$

The maximum switching frequency occurs when  $\sin(\omega t)$  equals zero:

$$\max f_s = \frac{V_M^2}{4LP} \quad (18.69)$$

The minimum switching frequency occurs at the peak of the sine wave:

$$\min f_s = \frac{V_M^2}{4LP} \left(1 - \frac{V_M}{V}\right) \quad (18.70)$$

Equations (18.69) and (18.70) can be used to select the value of the inductance  $L$  and the output voltage  $V$ , so that the switching frequency varies over an acceptable range.

### 18.3.4 Nonlinear Carrier Control

The nonlinear-carrier controller (NLC) is capable of attaining input resistor emulation in boost and other converters that operate in the continuous conduction mode. Implementation of the controller is quite simple, with no need for sensing of the input voltage or input current. There is also no need for a current loop error amplifier. The boost nonlinear-carrier charge controller is inherently stable and is free from the stability problems that require addition of an artificial ramp in current programmed controllers.

A CCM boost rectifier system with nonlinear-carrier charge control is illustrated in Fig. 18.21, and waveforms are given in Fig. 18.22. The reasoning behind this approach is as follows. It is desirable to control the transistor switch current  $i_s(t)$ . This pulsating current is much easier to sense than the continuous converter input current—a simple current transformer can be used, as in Fig. 18.21. Further, it is desirable to control the integral of this current, or the charge, for two reasons: (1) integration of the waveform leads to improved noise immunity, and (2) the integral of the waveform is directly related to its average value,

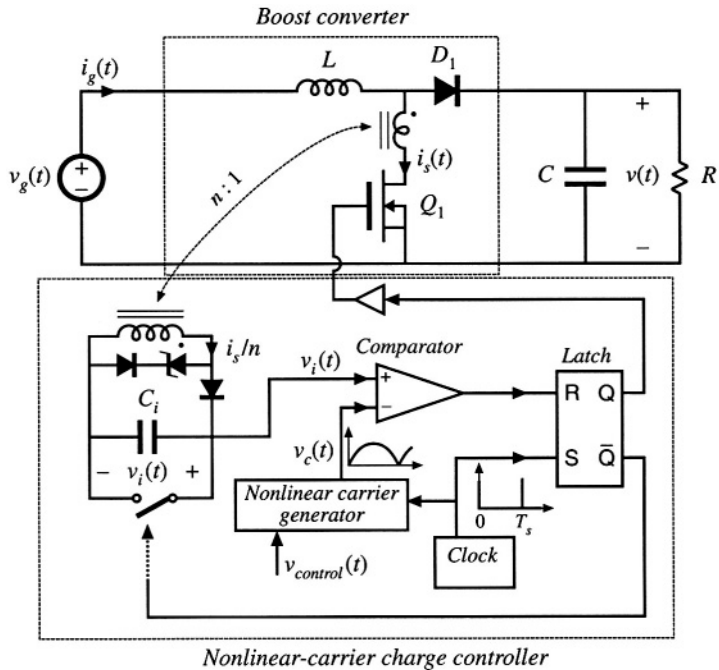


Fig. 18.21 Nonlinear-carrier charge control of a boost converter.

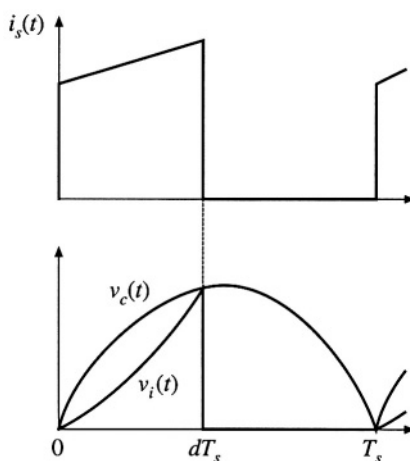


Fig. 18.22 Transistor current  $i_s(t)$ , parabolic carrier voltage  $v_c(t)$ , and integrator voltage  $v_i(t)$  waveforms for the NLC-controlled boost rectifier of Fig. 18.21.

$$\langle i_s(t) \rangle_{T_s} = \frac{1}{T_s} \int_t^{t+T_s} i_s(\tau) d\tau \quad (18.71)$$

In a fixed-frequency system,  $T_s$  is constant, and the integral over one switching period is proportional to the average value. Hence the average switch current can be controlled to be proportional to a reference signal by simply switching the transistor off when the integral of the switch current is equal to the reference. In the controller of Fig. 18.21, the switch current  $i_s(t)$  is scaled by the transformer turns ratio  $n$ , and then integrated by capacitor  $C_i$ , such that

$$v_i(t) = \frac{1}{C_i} \int_0^{dT_s} \frac{i_s(\tau)}{n} d\tau \quad \text{for } 0 < t < dT_s \quad (18.72)$$

The integrator voltage  $v_i(t)$  is reset to zero at the end of each switching period, and the integration process begins anew at the beginning of the next switching period. So at the instant that the transistor is switched off, the voltage  $v_i(dT_s)$  is proportional to the average switch current:

$$v_i(dT_s) = \frac{\langle i_s \rangle_{T_s}}{n C_i f_s} \quad \text{for interval } 0 < t < T_s \quad (18.73)$$

How should the average switch current be controlled? To obtain input resistor emulation, it is desired that

$$\langle i_g(t) \rangle_{T_s} = \frac{\langle v_g(t) \rangle_{T_s}}{R_e(v_{control})} \quad (18.74)$$

It is further desired to avoid sensing either  $i_g(t)$  or  $v_g(t)$ . As with other schemes, we will sense the dc output voltage  $\langle v(t) \rangle_{T_s}$ , to construct a low-bandwidth feedback loop that balances the average input and output powers. So let us determine the relationship between  $\langle i_s(t) \rangle_{T_s}$  and  $\langle v(t) \rangle_{T_s}$  implied by Eq. (18.74). If we assume that the boost converter operates in the continuous conduction mode, then we can write

$$\langle i_s(t) \rangle_{T_s} = d(t) \langle i_g(t) \rangle_{T_s} \quad (18.75)$$

and

$$\langle v_g(t) \rangle_{T_s} = d'(t) \langle v(t) \rangle_{T_s} \quad (18.76)$$

Substitution of Eqs. (18.75) and (18.76) into Eq. (18.74) leads to

$$\langle i_s(t) \rangle_{T_s} = d(t) (1 - d(t)) \frac{\langle v(t) \rangle_{T_s}}{R_e(v_{control})} \quad (18.77)$$

The controller of Fig. 18.21 implements this equation.

The nonlinear carrier generator of Fig. 18.21 produces the parabolic waveform  $v_c(t)$ , given by

$$\begin{aligned} v_c(t) &= v_{control} \left( \frac{t}{T_s} \right) \left( 1 - \frac{t}{T_s} \right) \quad \text{for } 0 \leq t \leq T_s \\ v_c(t + T_s) &= v_c(t) \end{aligned} \quad (18.78)$$

This waveform is illustrated in Fig. 18.22. Note that Eq. (18.78) resembles Eq. (18.77), with  $d(t)$  replaced by  $(t/T_s)$ . The controller switches the transistor off at time  $t = dT_s$  when the integrator voltage  $v_i(t)$  is equal to the carrier waveform  $v_c(t)$ . Hence, it is true that

$$v_i(dT_s) = v_c(dT_s) = v_{control}(t) d(t) (1 - d(t)) \quad (18.79)$$

Substitution of Eq. (18.73) yields

$$\frac{\langle i_s(t) \rangle_{T_s}}{nC_i f_s} = v_{control}(t) d(t) (1 - d(t)) \quad (18.80)$$

This is of the same form as Eq. (18.77). Comparison of Eqs. (18.77) and (18.80) reveals that the emulated resistance  $R_e$  is given by

$$R_e(v_{control}) = d(t) (1 - d(t)) \frac{\langle v(t) \rangle_{T_s}}{\langle i_s(t) \rangle_{T_s}} = \frac{\langle v(t) \rangle_{T_s}}{nC_i f_s v_{control}(t)} \quad (18.81)$$

If the dc output voltage and the control voltage have negligible ac variation, then  $R_e$  is essentially constant, and the ac line current will exhibit low harmonic distortion. So neither the input voltage nor the input current need be sensed, and input resistor emulation can be obtained in CCM boost converters by sensing only the switch current.

A simple way to generate the parabolic carrier waveform uses two integrators, as illustrated in Fig. 18.23. The slowly varying control voltage  $v_{control}(t)$  is integrated, to obtain a ramp waveform  $v_r(t)$  whose peak amplitude is proportional to  $v_{control}(t)$ . The dc component of this waveform is removed, and then integrated again. The output of the second integrator is the parabolic carrier  $v_c(t)$ , illustrated in Fig. 18.22 and given by Eq. (18.78). Both integrators are reset to zero before the end of each switching period.

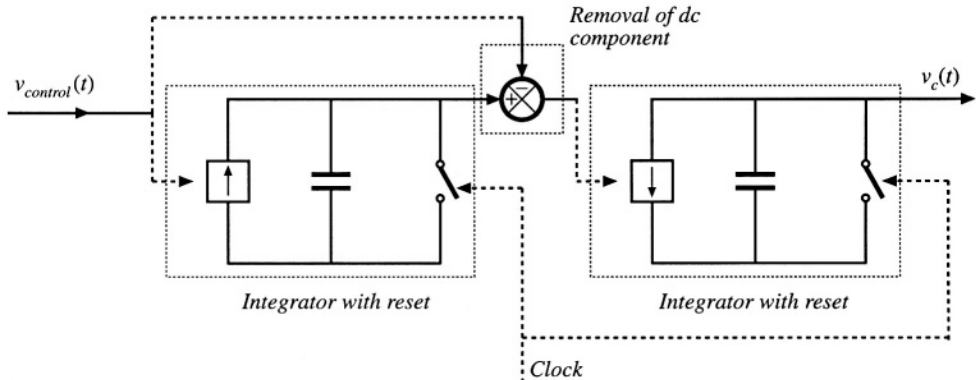


Fig. 18.23 Generation of parabolic carrier waveform by double integration.

by the clock generator. The amplitude of the parabolic carrier, and hence also the emulated resistance, can be controlled by variation of  $v_{control}(t)$ .

Equations (18.75) and (18.76) are valid only when the converter operates in the continuous conduction mode. In consequence, the ac line current waveform is distorted when the converter operates in DCM. Since this occurs near the zero crossings of the ac line voltage, crossover distortion is generated. Nonetheless, the harmonic distortion is less severe than in current-programmed schemes, and it is feasible to construct universal-input rectifiers that employ the NLC control approach. Total harmonic distortion is analyzed and plotted in [28].

Nonlinear carrier control can be applied to current-programmed boost rectifiers, as well as to other rectifiers based on the buck-boost, SEPIC, Ćuk, or other topologies, with either integral charge control or peak-current-programmed control [28,29]. In these cases, a different carrier waveform must be employed. A nonlinear-carrier controller in which the ac input voltage  $v_g(t)$  is sensed, rather than the switch current  $i_s(t)$ , is described in [30].

## 18.4 SINGLE-PHASE CONVERTER SYSTEMS INCORPORATING IDEAL RECTIFIERS

An additional issue that arises in PWM rectifier systems is the control of power drawn from the ac line, the power delivered to the dc load, and the energy stored in a bulk energy storage capacitor.

### 18.4.1 Energy Storage

It is usually desired that the dc output voltage of a converter system be regulated with high accuracy. In practice, this is easily accomplished using a high-gain wide-bandwidth feedback loop. A well-regulated dc output voltage  $v(t) = V$  is then obtained, which has negligible ac variations. For a given constant load characteristic, the load current  $I$  and the instantaneous load power  $p_{load}(t) = P_{load}$ , are also constant:

$$p_{load}(t) = v(t)i(t) = VI \quad (18.82)$$

However, the instantaneous input power  $p_{ac}(t)$  of a single-phase ideal rectifier is not constant:

$$p_{ac}(t) = v_g(t)i_g(t) \quad (18.83)$$

If  $v_g(t)$  is given by Eq. (18.11), and if  $i_g(t)$  follows Eq. (18.1), then the instantaneous input power becomes

$$p_{ac}(t) = \frac{V_M^2}{R_e} \sin^2(\omega t) = \frac{V_M^2}{2R_e} (1 - \cos(2\omega t)) \quad (18.84)$$

which varies with time. The instantaneous input power is zero at the zero crossings of the ac input voltage. Equations (18.82) and (18.84) are illustrated in Fig. 18.24(a). Note that the desired instantaneous load power  $p_{load}(t)$  is not equal to the desired instantaneous rectifier input power  $p_{ac}(t)$ . Some element within the rectifier system must supply or consume the difference between these two instantaneous powers.

Since the ideal rectifier does not consume or generate power, nor does it contain significant internal energy storage, it is necessary to add to the system a low-frequency energy storage element such

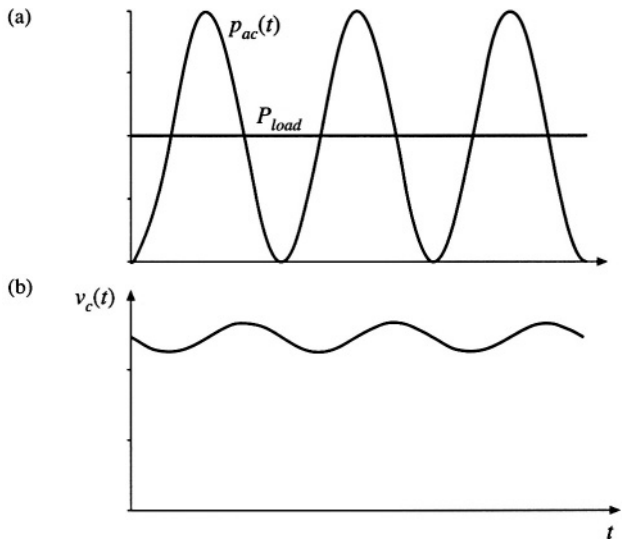


**Fig. 18.24** Waveforms of a single-phase ideal rectifier system: (a) pulsating ac input power  $p_{ac}(t)$ , and constant dc load power  $P_{load}$ ; (b) energy storage capacitor voltage  $v_c(t)$ .

as an electrolytic capacitor. The difference between the instantaneous input and load powers flows through this capacitor.

The waveforms of rectifier systems containing reactive elements can be determined by solution of the rectifier energy equation [36,37]. If the energy storage capacitor  $C$  is the only system element capable of significant low-frequency energy storage, then the power  $p_C(t)$  flowing into the capacitor is equal to the difference between the instantaneous input and output powers:

$$p_C(t) = \frac{dE_C(t)}{dt} = \frac{d\left(\frac{1}{2} Cv_C^2(t)\right)}{dt} = p_{ac}(t) - p_{load}(t) \quad (18.85)$$

where  $C$  is the capacitance,  $v_C(t)$  is the capacitor voltage, and  $E_C(t)$  is the energy stored in the capacitor. Hence as illustrated in Fig. 18.24(b), when  $p_{ac}(t) > p_{load}(t)$  then energy flows into the capacitor, and  $v_C(t)$  increases. Likewise,  $v_C(t)$  decreases when  $p_{ac}(t) < p_{load}(t)$ . So the capacitor voltage  $v_C(t)$  must be allowed to increase and decrease as necessary to store and release the required energy. In steady-state, the average values of  $p_{ac}(t)$  and  $p_{load}(t)$  must be equal, so that over one ac line cycle there is no net change in capacitor stored energy.

Where can the energy storage capacitor be placed? It is necessary to separate the energy storage capacitor from the regulated dc output, so that the capacitor voltage is allowed to independently vary as illustrated in Fig. 18.24(b). A conventional means of accomplishing this is illustrated in Fig. 18.25. A second dc-dc converter is inserted, between the energy storage capacitor and the regulated dc load. A wide-bandwidth feedback loop controls this converter, to attain a well-regulated dc load voltage. The capacitor voltage  $v_C(t)$  is allowed to vary. Thus, this system configuration is capable of (1) wide-bandwidth control of the ac line current waveform, to attain unity power factor, (2) internal low-frequency energy storage, and (3) wide-bandwidth regulation of the dc output voltage. It is also possible to integrate these functions into a single converter, provided that the required low-frequency independence of the input, output, and capacitor voltages is maintained [38].

The energy storage capacitor also allows the system to function in other situations in which the instantaneous input and output powers differ. For example, it is commonly required that the output volt-

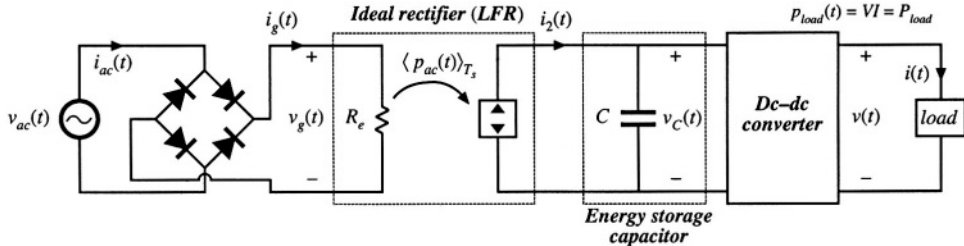


**Fig. 18.25** Elements of a single-phase-ac to dc power supply, in which the ac line current and dc load voltage are independently regulated with high bandwidth. An internal independent energy storage capacitor is required.

age remain regulated during ac line voltage failures of short duration. The *hold-up time* is the duration that the output voltage  $v(t)$  remains regulated after  $v_{ac}(t)$  has become zero. A typical requirement is that the system continue to supply power to the load during one complete missing ac line cycle, that is, for 20 msec in a 50 Hz system. During the hold-up time, the load power is supplied entirely by the energy storage capacitor. The value of capacitance should be chosen such that at the end of the hold-up time, the capacitor voltage  $v_C(t)$  exceeds the minimum value that the dc-dc converter requires to produce the desired load voltage.

The energy storage function could be performed by an element other than a capacitor, such as an inductor. However, use of an inductor is a poor choice, because of its high weight and cost. For example, a  $100 \mu\text{F}$  100 V electrolytic capacitor and a  $100 \mu\text{H}$  100 A inductor can each store 1 Joule of energy. But the capacitor is considerably smaller, lighter, and less expensive.

A problem introduced by the energy storage capacitor is the large *inrush current* observed during the system turn-on transient. The capacitor voltage  $v_C(t)$  is initially zero; substantial amounts of charge and energy are required to raise this voltage to its equilibrium value. The boost converter is not capable of limiting the magnitude of the resulting inrush current: even when  $d(t) = 0$ , a large current flows through the boost converter diode to the capacitor, as long as the converter output voltage is less than the input voltage. Some additional circuitry is required to limit the inrush current of the boost converter. Converters having a buck-boost type conversion ratio are inherently capable of controlling the inrush current. This advantage comes at the cost of additional switch stress.

It is also possible to design the ideal rectifier to operate correctly when connected to utility power systems anywhere in the world. *Universal input* rectifiers can operate with nominal ac rms voltage magnitudes as low as the 100 V encountered in a portion of Japan, or as high as the 260 V found in western Australia, with ac line frequencies of either 50 Hz or 60 Hz. Regardless of the ac input voltage, the universal-input rectifier produces a constant nominal dc output voltage  $V_C$ .

Let us now consider in more detail the low-frequency energy storage process of the system of Fig. 18.25. Let us assume that the dc-dc converter contains a controller having bandwidth much greater than the ac line frequency, such that the load voltage contains negligible low-frequency variations. A low-frequency model of the dc-dc converter is then as illustrated in Fig. 18.26. The dc-dc converter produces constant voltage  $v(t) = V$ , modeled by a voltage source as shown. This causes the load to draw constant current  $i(t) = I$ , leading to load power  $p_{load}(t) = P_{load}$ . To the extent that converter losses can be neglected, the dc-dc converter input port draws power  $P_{load}$ , regardless of the value of  $v_C(t)$ . So the dc-dc converter input port can be modeled as a constant power sink, of value  $P_{load}$ .

The model of Fig. 18.26 implies that the difference between the rectifier power  $p_{ac}(t)$  and the load power  $P_{load}$  flows into the capacitor, as given by Eq. (18.85). The capacitor voltage increases when  $p_{ac}(t)$  exceeds  $P_{load}$ , and decreases when  $p_{ac}(t)$  is less than  $P_{load}$ . In steady state, the average values of  $p_{ac}(t)$  and  $P_{load}$  must be equal. But note that  $p_{ac}(t)$  is determined by the magnitudes of  $v_{ac}(t)$  and  $R_e$ , and

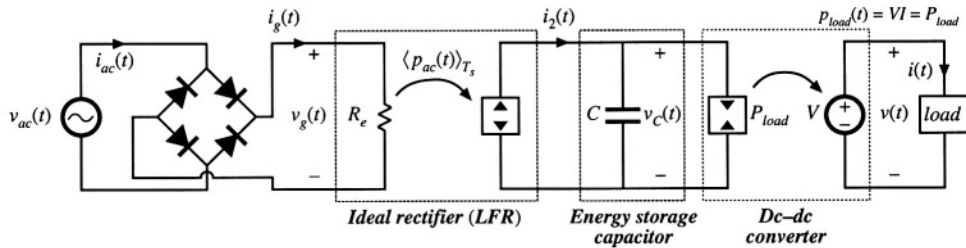


Fig. 18.26 Low-frequency equivalent circuit of the system of Fig. 18.25.

not by the load. The system of Fig. 18.26 contains no mechanism to cause the average rectifier power and load power to be equal. In consequence, it is necessary to add an additional control system that adjusts  $R_e$  as necessary, to cause the average rectifier output power and dc-dc converter input power to balance. The conventional way to accomplish this is simply to regulate the dc component of  $v_C(t)$ .

A complete system containing ideal rectification, energy storage, and wide-bandwidth output voltage regulation is illustrated in Fig. 18.27. This system incorporates the boost converter and controller of Fig. 18.5, as well as a generic dc-dc converter with output voltage feedback. In addition, the system contains a low-bandwidth feedback loop, which regulates the dc component of the energy-storage capacitor voltage to be equal to a reference voltage  $v_{ref2}$ . This is accomplished by slow variations of  $v_{control}(t)$  and  $R_e$ . This controller should have sufficiently small loop gain at the even harmonics of the ac line frequency, so that variations in  $R_e$  are much slower than the ac line frequency.

Increasing the bandwidth of the energy storage capacitor voltage controller can lead to significant ac line current harmonics. When this controller has wide bandwidth and high gain, then it varies  $R_e(t)$  quickly, distorting the ac line current waveform. In the extreme limit of perfect regulation of the

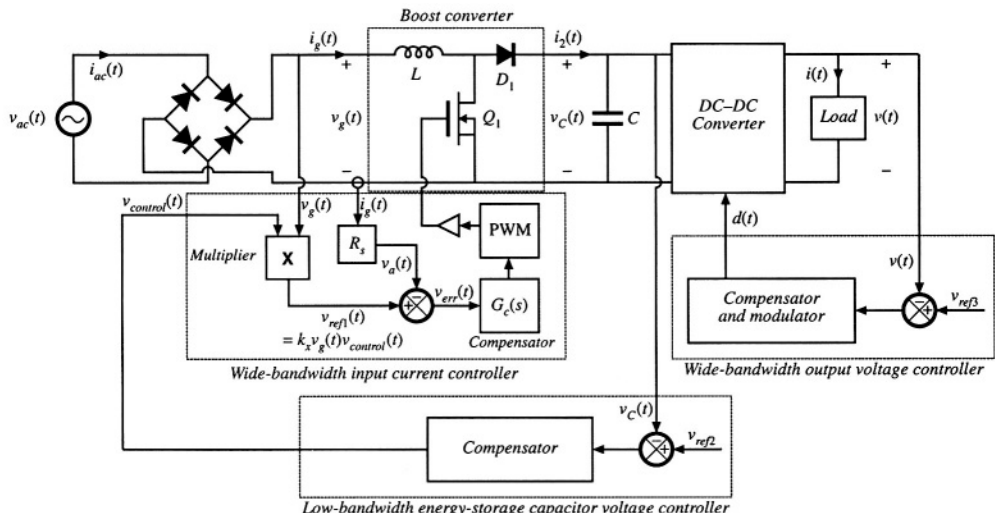
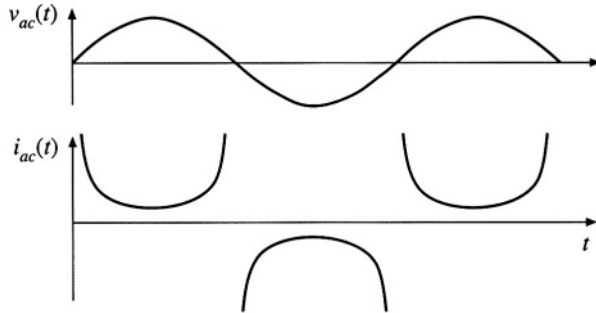


Fig. 18.27 A complete dc power supply system incorporating a near-ideal single-phase boost rectifier system, energy storage capacitor, and dc-dc converter. Wide-bandwidth feedback loops regulate the ac line current waveform and the dc load voltage, and a slow feedback loop regulates the energy storage capacitor voltage.



**Fig. 18.28** Ac line current waveform of the single-phase ideal rectifier with output voltage feedback, when it supplies constant instantaneous power to a dc load. The THD tends to infinity, and the power factor tends to zero.

energy storage capacitor voltage  $v_C(t) = V_C$ , then the capacitor stored energy is constant, and the instantaneous input ac line power  $p_{ac}(t)$  and load power  $p_{load}(t)$  are equal. The controller prevents the energy-storage capacitor from performing its low-frequency energy storage function. The ac line current then becomes

$$i_{ac}(t) = \frac{p_{ac}(t)}{v_{ac}(t)} = \frac{p_{load}(t)}{v_{ac}(t)} = \frac{P_{load}}{V_M \sin(\omega t)} \quad (18.86)$$

This waveform is sketched in Fig. 18.28. In this idealized limiting case, the ac line current tends to infinity at the zero crossings of the ac line voltage waveform, such that the instantaneous input power is constant. It can be shown that the THD of this current waveform is infinite, and its distortion factor and power factor are zero. So the bandwidth of this controller should be limited.

The energy storage capacitor voltage ripple can be found by integration of Eq. (18.85). Under steady-state conditions, where the average value of  $p_{ac}(t) = P_{load}$ , integration of Eq. (18.85) yields

$$E_C(t) = \frac{1}{2} Cv_C^2(t) = E_C(0) + \int_0^t \left( -P_{load} \cos(2\omega t) \right) dt \quad (18.87)$$

where  $\omega$  is the ac line frequency. Evaluation of the integral leads to

$$E_C(t) = E_C(0) - \frac{P_{load} \sin(2\omega t)}{2\omega} \quad (18.88)$$

Therefore, the capacitor voltage waveform is

$$v_C(t) = \sqrt{\frac{2E_C(t)}{C}} = \sqrt{v_C^2(0) - \frac{P_{load}}{\omega C} \sin(2\omega t)} \quad (18.89)$$

It can be verified that the rms value of this waveform is  $V_{C,rms} = v_C(0)$ . Hence, Eq. (18.89) can be written

$$v_C(t) = V_{C,rms} \sqrt{1 - \frac{P_{load}}{\omega C V_{C,rms}^2} \sin(2\omega t)} \quad (18.90)$$

This waveform is sketched in Fig. 18.24(b). The minimum and maximum values of the capacitor voltage occur when  $\sin(2\omega t)$  is equal to 1 and -1, respectively. Therefore, the peak-to-peak capacitor voltage rip-

ple is

$$2\Delta v_C = V_{C,rms} \left[ \sqrt{1 + \frac{P_{load}}{\omega C V_{C,rms}^2}} - \sqrt{1 - \frac{P_{load}}{\omega C V_{C,rms}^2}} \right] = \frac{P_{load}}{\omega C V_{C,rms}} \quad (18.91)$$

The approximation is valid for  $P_{load}/(\omega C V_{C,rms}^2)$  sufficiently less than one, a condition that is satisfied whenever the ac voltage ripple is sufficiently less than  $V_{C,rms}$ .

#### 18.4.2 Modeling the Outer Low-Bandwidth Control System

As discussed above, the outer low-bandwidth controller, which varies the emulated resistance as necessary to balance the average ac input and dc load powers, is common to all near-ideal rectifier systems. For design of this controller, the rectifier can be modeled using the loss-free resistor (LFR) model. Perturbation and linearization of the LFR leads to a small-signal equivalent circuit that predicts the relevant small-signal transfer functions. Such a model is derived in this section [2,39,40].

It is desirable to stabilize the rectifier output voltage against variations in load power, ac line voltage, and component characteristics. Hence, a voltage feedback loop is necessary. As discussed in Section 18.4.1, this loop cannot attempt to remove the capacitor voltage ripple that occurs at the second harmonic of the ac line frequency,  $2\omega$ , since doing so would require that  $R_e(t)$  change significantly at the second harmonic frequency. This would introduce significant distortion, phase shift, and power factor degradation into the ac line current waveform. In consequence this loop must have sufficiently small gain at frequency  $2\omega$ , and hence its bandwidth must be low. Therefore, for the purposes of designing the low-bandwidth outer control loop, it is unnecessary to model the system high-frequency behavior. It can be assumed that any inner wide-bandwidth controller operates ideally at low frequencies, such that the ideal rectifier model of Fig. 18.29(a) adequately represents the low-frequency system behavior.

A small-signal model is derived here that correctly predicts the control-to-output transfer function and output impedance of any rectifier system that can be modeled as a loss-free resistor. The model neglects the complicating effects of high-frequency switching ripple, and is valid for control variations at frequencies sufficiently less than the ac line frequency. Both resistive and dc-dc converter/regulator loads are treated.

The steps in the derivation of the small-signal ac model are summarized in Fig. 18.29. Figure 18.29(a) is the basic ideal rectifier model, in which the converter high frequency switching ripple is removed via averaging over the switching period  $T_s$ , but waveform frequency components slower than the switching frequency are correctly modeled, including the  $2\omega$  second-harmonic and dc components of output voltage. It is difficult to use this model in design of the feedback loop because it is highly nonlinear and time-varying.

If the ac input voltage  $v_g(t)$  is

$$v_g(t) = \sqrt{2} v_{g,rms} \left| \sin(\omega t) \right| \quad (18.92)$$

then the model of Fig. 18.29(a) predicts that the instantaneous output power  $\langle p(t) \rangle_{T_s}$  is

$$\langle p(t) \rangle_{T_s} = \frac{\langle v_g(t) \rangle_{T_s}^2}{R_e(v_{control}(t))} = \frac{v_{g,rms}^2}{R_e(v_{control}(t))} \left( 1 - \cos(2\omega t) \right) \quad (18.93)$$

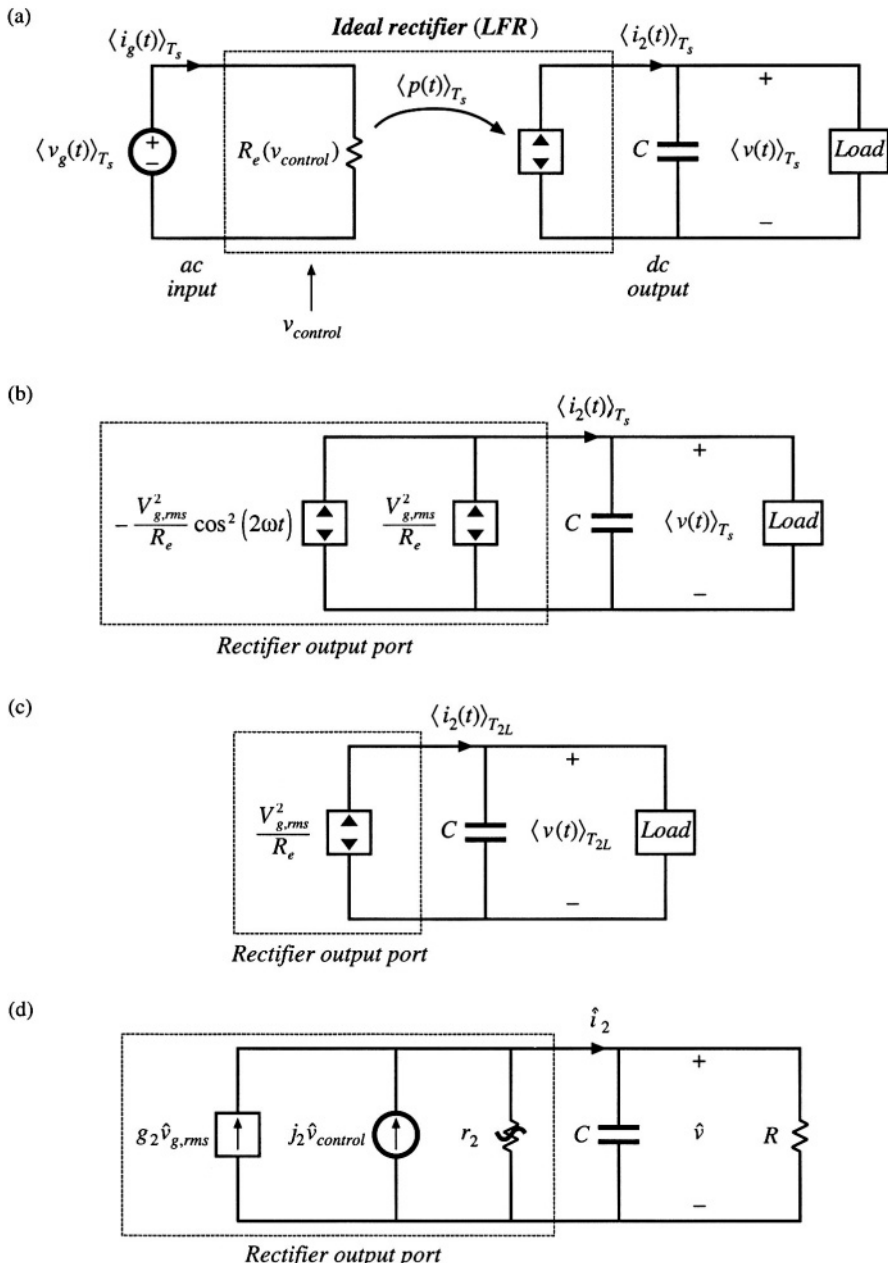


**Fig. 18.29** Steps in the derivation of low-frequency small-signal rectifier model: (a) large-signal LFR model, averaged over one switching period  $T_s$ ; (b) separation of power source into its constant and time-varying components; (c) removal of second-harmonic components by averaging over one-half of the ac line period,  $T_{2L}$ ; (d) small-signal model obtained by perturbation and linearization of Fig. 18.29(c).

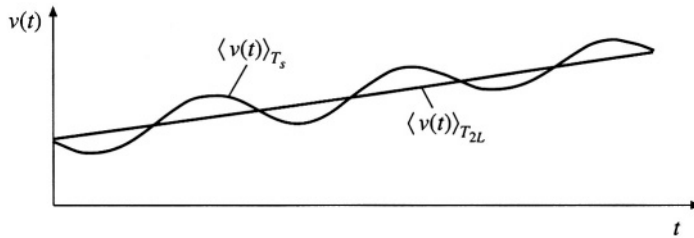


**Fig. 18.30** Removal of components of  $v(t)$  at the harmonics of the ac line frequency, by averaging over one-half of the ac line period,  $T_{2L}$ .

The output power is comprised of a constant term  $v_{g,rms}^2/R_e$ , and a term that varies at the second harmonic of the ac line frequency. These two terms are explicitly identified in Fig. 18.29(b).

The second-harmonic variation in  $\langle p(t) \rangle_{T_s}$  leads to time-varying system equations, and slow variations in  $v_{control}(t)$  lead to an output voltage spectrum containing components not only at the frequencies present in  $v_{control}(t)$ , but also at the even harmonics of the ac line frequency and their sidebands, as well as at the switching frequency and its harmonics and sidebands. It is desired to model only the low-frequency components excited by slow variations in  $v_{control}(t)$ , the load, and the ac line voltage amplitude  $v_{g,rms}$ . The even harmonics of the ac line frequency can be removed by averaging over one-half of the ac line period

$$T_{2L} = \frac{1}{2} \frac{2\pi}{\omega} = \frac{\pi}{\omega} \quad (18.94)$$

Hence, we average over the switching period  $T_s$  to remove the switching harmonics, and then average again over one-half of the ac line period  $T_{2L}$  to remove the even harmonics of the ac line frequency. The resulting model is valid for frequencies sufficiently less than the ac line frequency  $\omega$ . Averaging of the rectifier output voltage is illustrated in Fig. 18.30: averaging over  $T_{2L}$  removes the ac line frequency harmonics, leaving the underlying low-frequency variations. By averaging the model of Fig. 18.29(b) over  $T_{2L}$ , we obtain the model of Fig. 18.29(c). This step removes the second-harmonic variation in the power source.

The equivalent circuit of Fig. 18.29(c) is time-invariant, but nonlinear. We can now perturb and linearize as usual, to construct a small-signal ac model that describes how slow variations in  $v_{control}(t)$ ,  $v_{g,rms}$ , and the load, affect the rectifier output waveforms. Let us assume that the averaged output voltage  $\langle v(t) \rangle_{T_{2L}}$ , rectifier averaged output current  $\langle i_2(t) \rangle_{T_{2L}}$ , rms line voltage amplitude  $v_{g,rms}$ , and control voltage  $v_{control}(t)$ , can be represented as quiescent values plus small slow variations:

$$\begin{aligned} \langle v(t) \rangle_{T_{2L}} &= V + \hat{v}(t) \\ \langle i_2(t) \rangle_{T_{2L}} &= I_2 + \hat{i}_2(t) \\ v_{g,rms} &= V_{g,rms} + \hat{v}_{g,rms}(t) \\ v_{control}(t) &= V_{control} + \hat{v}_{control}(t) \end{aligned} \quad (18.95)$$

with

$$\begin{aligned} V &\gg |\hat{v}(t)| \\ I_2 &\gg |\hat{i}_2(t)| \\ V_{g,rms} &\gg |\hat{v}_{g,rms}(t)| \\ V_{control} &\gg |\hat{v}_{control}(t)| \end{aligned} \quad (18.96)$$

In the averaged model of Fig. 18.29(c),  $\langle i_2(t) \rangle_{T_{2L}}$  is given by

$$\begin{aligned} \langle i_2(t) \rangle_{T_{2L}} &= \frac{\langle p(t) \rangle_{T_{2L}}}{\langle v(t) \rangle_{T_{2L}}} = \frac{V_{g,rms}^2(t)}{R_e(v_{control}(t)) \langle v(t) \rangle_{T_{2L}}} \\ &= f\left(V_{g,rms}(t), \langle v(t) \rangle_{T_{2L}}, v_{control}(t)\right) \end{aligned} \quad (18.97)$$

This equation resembles DCM buck-boost Eq. (11.45), and linearization proceeds in a similar manner. Expansion of Eq. (18.97) in a three-dimensional Taylor series about the quiescent operating point, and elimination of higher-order nonlinear terms, leads to

$$\hat{i}_2(t) = g_2 \hat{v}_{g,rms}(t) + j_2 \hat{v}_{control}(t) - \frac{\hat{v}(t)}{r_2} \quad (18.98)$$

where

$$g_2 = \frac{df\left(V_{g,rms}, V, V_{control}\right)}{dV_{g,rms}} \Bigg|_{V_{g,rms} = V_{g,rms}} = \frac{2}{R_e(V_{control})} \frac{V_{g,rms}}{V} \quad (18.99)$$

$$\left(-\frac{1}{r_2}\right) = \frac{df\left(V_{g,rms}, \langle v \rangle_{T_{2L}}, V_{control}\right)}{d\langle v \rangle_{T_{2L}}} \Bigg|_{\langle v \rangle_{T_{2L}} = V} = -\frac{I_2}{V} \quad (18.100)$$

$$j_2 = \frac{df\left(V_{g,rms}, V, v_{control}\right)}{dv_{control}} \Bigg|_{v_{control} = V_{control}} = -\frac{V_{g,rms}^2}{VR_e^2(V_{control})} \frac{dR_e(v_{control})}{dv_{control}} \Bigg|_{v_{control} = V_{control}} \quad (18.101)$$

A small-signal equivalent circuit based on Eq. (18.98) is given in Fig. 18.29(d). Expressions for the parameters  $g_2$ ,  $j_2$ , and  $r_2$  for several controllers are listed in Table 18.1. This model is valid for the conditions of Eq. (18.96), with the additional assumption that the output voltage ripple is sufficiently small. Figure 18.29(d) is useful only for determining the various ac transfer functions; no information regarding dc conditions can be inferred. The ac resistance  $r_2$  is derived from the slope of the average value of the power source output characteristic, evaluated at the quiescent operating point. The other coefficients,  $j_2$  and  $g_2$ , are also derived from the slopes of the same characteristic, taken with respect to  $v_{control}(t)$  and  $v_{g,rms}$  and evaluated at the quiescent operating point. The resistance  $R$  is the incremental resistance of the load, evaluated at the quiescent operating point. In the boost converter with hysteretic control, the transistor on-time  $t_{on}$  replaces  $v_{control}$  as the control input; likewise, the transistor duty cycle  $d$  is taken as the

**Table 18.1** Small-signal model parameters for several types of rectifier control schemes

Controller type	$g_2$	$j_2$	$r_2$
Average current control with feedforward, Fig. 18.14	0	$\frac{P_{av}}{VV_{control}}$	$\frac{V^2}{P_{av}}$
Current-programmed control, Fig. 18.16	$\frac{2P_{av}}{VV_{g,rms}}$	$\frac{P_{av}}{VV_{control}}$	$\frac{V^2}{P_{av}}$
Nonlinear-carrier charge control of boost rectifier, Fig. 18.21	$\frac{2P_{av}}{VV_{g,rms}}$	$\frac{P_{av}}{VV_{control}}$	$\frac{V^2}{2P_{av}}$
Boost with critical conduction mode control, Fig. 18.20	$\frac{2P_{av}}{VV_{g,rms}}$	$\frac{P_{av}}{VV_{control}}$	$\frac{V^2}{P_{av}}$
DCM buck-boost, flyback, SEPIC, or Ćuk converters	$\frac{2P_{av}}{VV_{g,rms}}$	$\frac{2P_{av}}{VD}$	$\frac{V^2}{P_{av}}$

control input to the DCM buck-boost, flyback, SEPIC, and Ćuk converters. Harmonics are ignored for the current-programmed and NLC controllers; the expressions given in Table 18.1 assume that the converter operates in CCM with negligible harmonics.

The control-to-output transfer function is

$$\frac{\hat{v}(s)}{\hat{v}_{control}(s)} = j_2 R \| r_2 \frac{1}{1 + sC R \| r_2} \quad (18.102)$$

The line-to-output transfer function is

$$\frac{\hat{v}(s)}{\hat{v}_{g,rms}(s)} = g_2 R \| r_2 \frac{1}{1 + sC R \| r_2} \quad (18.103)$$

Thus, the small-signal transfer functions of the high quality rectifier contain a single pole, ascribable to the output filter capacitor operating in conjunction with the incremental load resistance  $R$  and  $r_2$ , the effective output resistance of the power source. Although this model is based on the ideal rectifier, its form is similar to that of the dc-dc DCM buck-boost converter ac model of Chapter 11. This is natural, because the DCM buck-boost converter is itself a natural loss-free resistor. The major difference is that the rms value of the ac input voltage must be used, and that the second harmonic components of  $r_2$ ,  $j_2$ , and  $g_2$  must additionally be removed via averaging. Nonetheless, the equivalent circuit and ac transfer functions are of similar form.

When the rectifier drives a regulated dc-dc converter as in Fig. 18.25, then the dc-dc converter presents a constant power load to the rectifier, as illustrated in Fig. 18.26. In equilibrium, the rectifier and dc-dc converter operate with the same average power  $P_{av}$  and the same dc voltage  $V$ . The incremental resistance  $R$  of the constant power load is negative, and is given by

$$R = -\frac{V^2}{P_{av}} \quad (18.104)$$

which is equal in magnitude but opposite in polarity to the rectifier incremental output resistance  $r_2$ , for all controllers except the NLC controller. The parallel combination  $r_2 \| R$  then tends to an open circuit, and the control-to-output and line-to-output transfer functions become

$$\frac{\hat{v}(s)}{\hat{v}_{control}(s)} = \frac{j_2}{sC} \quad (18.105)$$

and

$$\frac{\hat{v}(s)}{\hat{v}_{R,rms}(s)} = \frac{g_2}{sC} \quad (18.106)$$

In the case of the NLC controller, the parallel combination  $r_2 \parallel R$  becomes equal to  $r_2/2$ , and Eqs. (18.102) and (18.103) continue to apply.

## 18.5 RMS VALUES OF RECTIFIER WAVEFORMS

To correctly specify the power stage elements of a near-ideal rectifier, it is necessary to compute the root-mean-square values of their currents. A typical waveform such as the transistor current of the boost converter (Fig. 18.31) is pulse-width modulated, with both the duty cycle and the peak amplitude varying with the ac input voltage. When the switching frequency is much larger than the ac line frequency, then the rms value can be well-approximated as a double integral. The square of the current is integrated first to find its average over a switching period, and the result is then integrated to find the average over the ac line period.

Computation of the rms and average values of the waveforms of a PWM rectifier can be quite tedious, and this can impede the effective design of the power stage components. In this section, several approximations are developed, which allow relatively simple analytical expressions to be written for the rms and average values of the power stage currents, and which allow comparison of converter approaches [14,41]. The transistor current in the boost rectifier is found to be quite low.

The rms value of the transistor current is defined as

$$I_{Qrms} = \sqrt{\frac{1}{T_{ac}} \int_0^{T_{ac}} i_Q^2(t) dt} \quad (18.107)$$

where  $T_{ac}$  is the period of the ac line waveform. The integral can be expressed as a sum of integrals over all of the switching periods contained in one ac line period:

$$I_{Qrms} = \sqrt{\frac{1}{T_{ac}} T_s \sum_{n=1}^{T_{ac}/T_s} \left( \frac{1}{T_s} \int_{(n-1)T_s}^{nT_s} i_Q^2(t) dt \right)} \quad (18.108)$$

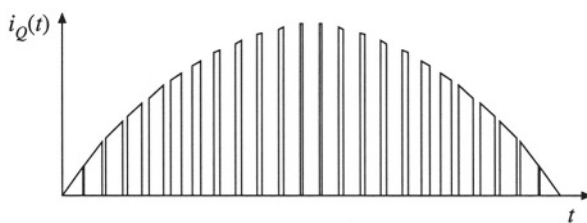


Fig. 18.31 Modulated transistor current waveform, boost rectifier.

where  $T_s$  is the switching period. The quantity inside the parentheses is the value of  $i_Q^2$  averaged over the  $n^{\text{th}}$  switching period. The summation can be approximated by an integral in the case when  $T_s$  is much less than  $T_{ac}$ . This approximation corresponds to taking the limit as  $T_s$  tends to zero, as follows:

$$\begin{aligned} I_{Q\text{rms}} &\approx \sqrt{\frac{1}{T_{ac}} \lim_{T_s \rightarrow 0} \left[ T_s \sum_{n=1}^{T_{ac}/T_s} \left( \frac{1}{T_s} \int_{(n-1)T_s}^{nT_s} i_Q^2(\tau) d\tau \right) \right]} \\ &= \sqrt{\frac{1}{T_{ac}} \int_0^{T_{ac}} \frac{1}{T_s} \int_t^{t+T_s} i_Q^2(\tau) d\tau dt} \\ &= \sqrt{\left\langle \left\langle i_Q^2(t) \right\rangle_{T_s} \right\rangle_{T_{ac}}} \end{aligned} \quad (18.109)$$

So  $i_Q^2(t)$  is first averaged over one switching period. The result is then averaged over the ac line period, and the square root is taken of the result.

### 18.5.1 Boost Rectifier Example

For the boost rectifier, the transistor current  $i_Q(t)$  is equal to the input current when the transistor conducts, and is zero when the transistor is off. Therefore, the average of  $i_Q^2(t)$  over one switching period is

$$\begin{aligned} \left\langle i_Q^2 \right\rangle_{T_s} &= \frac{1}{T_s} \int_t^{t+T_s} i_Q^2(t) dt \\ &= d(t) i_{ac}^2(t) \end{aligned} \quad (18.110)$$

If the input voltage is given by

$$v_{ac}(t) = V_M |\sin \omega t| \quad (18.111)$$

then the input current will be

$$i_{ac}(t) = \frac{V_M}{R_e} |\sin \omega t| \quad (18.112)$$

where  $R_e$  is the emulated resistance. With a constant output voltage  $V$ , the transistor duty cycle must obey the relationship

$$\frac{V}{v_{ac}(t)} = \frac{1}{1 - d(t)} \quad (18.113)$$

This assumes that the converter dynamics are fast compared to the ac line frequency. Substitution of Eq. (18.111) into (18.113) and solution for  $d(t)$  yields

$$d(t) = 1 - \frac{V_M}{V} |\sin \omega t| \quad (18.114)$$

Substitution of Eqs. (18.112) and (18.114) into Eq. (18.110) yields the following expression

$$\langle i_Q^2 \rangle_{T_s} = \frac{V_M^2}{R_e^2} \left( 1 - \frac{V_M}{V} |\sin \omega t| \right) \sin^2(\omega t) \quad (18.115)$$

One can now plug this expression into Eq. (18.109):

$$\begin{aligned} I_{Q\text{rms}} &= \sqrt{\frac{1}{T_{ac}} \int_0^{T_{ac}} \langle i_Q^2 \rangle_{T_s} dt} \\ &= \sqrt{\frac{1}{T_{ac}} \int_0^{T_{ac}} \frac{V_M^2}{R_e^2} \left( 1 - \frac{V_M}{V} |\sin \omega t| \right) \sin^2(\omega t) dt} \end{aligned} \quad (18.116)$$

which can be further simplified to

$$I_{Q\text{rms}} = \sqrt{\frac{2}{T_{ac}} \frac{V_M^2}{R_e^2} \int_0^{T_{ac}/2} \left( \sin^2(\omega t) - \frac{V_M}{V} \sin^3(\omega t) \right) dt} \quad (18.117)$$

This involves integration of powers of  $\sin(\omega t)$  over a complete half-cycle. The integral can be evaluated with the help of the following formula:

$$\frac{1}{\pi} \int_0^\pi \sin^n(\theta) d\theta = \begin{cases} \frac{2}{n} \frac{2 \cdot 4 \cdot 6 \cdots (n-1)}{1 \cdot 3 \cdot 5 \cdots n} & \text{if } n \text{ is odd} \\ \frac{1 \cdot 3 \cdot 5 \cdots (n-1)}{2 \cdot 4 \cdot 6 \cdots n} & \text{if } n \text{ is even} \end{cases} \quad (18.118)$$

This type of integral commonly arises in rms calculations involving PWM rectifiers. The values of the integral for several choices of  $n$  are listed in Table 18.2. Evaluation of the integral in Eq. (18.117) using Eq. (18.118) leads to the following result:

$$I_{Q\text{rms}} = \frac{V_M}{\sqrt{2} R_e} \sqrt{1 - \frac{8}{3\pi} \frac{V_M}{V}} = I_{ac\text{ rms}} \sqrt{1 - \frac{8}{3\pi} \frac{V_M}{V}} \quad (18.119)$$

It can be seen that the rms transistor current is minimized by choosing the output voltage  $V$  to be as small as possible. The best that can be done is to choose  $V = V_M$ , which leads to

$$I_{Q\text{rms}} = 0.39 I_{ac\text{ rms}} \quad (18.120)$$

Larger values of  $V$  lead to a larger rms transistor current.

A similar analysis for the rms diode current leads to the following expression

$$I_{D\text{rms}} = I_{ac\text{ rms}} \sqrt{\frac{8}{3\pi} \frac{V_M}{V}} \quad (18.121)$$

The choice  $V = V_M$  maximizes the rms diode current, with the result

**Table 18.2** Solution of the integral of Eq. (18.118), for several values of  $n$

$n$	$\frac{1}{\pi} \int_0^\pi \sin^n(\theta) d\theta$
1	$\frac{2}{\pi}$
2	$\frac{1}{2}$
3	$\frac{4}{3\pi}$
4	$\frac{3}{8}$
5	$\frac{16}{15\pi}$
6	$\frac{15}{48}$

$$I_{D_{rms}} = 0.92 I_{ac\ rms} \quad (18.122)$$

Larger values of  $V$  lead to smaller rms diode current.

Average currents can be computed in a similar way. The results are

$$\begin{aligned} I_{Qav} &= I_{ac\ rms} \frac{2\sqrt{2}}{\pi} \left( 1 - \frac{\pi}{8} \frac{V_M}{V} \right) \\ I_{Dav} &= I_{ac\ rms} \frac{V_M}{2\sqrt{2} V} \end{aligned} \quad (18.123)$$

Expressions for rms, average, and peak currents of the power stage components of the continuous conduction mode boost converter are summarized in Table 18.3. Expressions are also tabulated for flyback and SEPIC topologies, operating in the continuous conduction mode. In the case of the flyback converter, an  $L_1-C_1$  input filter is also included. In all cases, the effects of switching ripple are neglected.

### 18.5.2 Comparison of Single-Phase Rectifier Topologies

When isolation is not a rectifier requirement, and when it is acceptable that the dc output voltage be marginally larger than the peak ac input voltage, then the boost converter is a very effective approach. For example, consider the design of a 1 kW rectifier operating from the 240 Vrms input line voltage. If the converter efficiency and power factor are both approximately unity, then the rms input current is  $I_{rms} = (1000\text{ W})/(240\text{ V}) = 4.2\text{ A}$ . The dc output voltage is chosen to be 380 V, or slightly larger than the peak ac input voltage. By use of Eq. (18.119), the rms transistor current is found to be 2 A. This is quite a low value—less than half of the rms input current, which demonstrates how effectively the converter utilizes the power switch. The rms diode current is 3.6 A, and the transistor and diode blocking voltages are 380 V. With a 120 V ac input voltage, the transistor and diode rms currents increase to 6.6 A and 5.1 A, respectively.

The only real drawback of the boost converter is its inability to limit inrush currents. When the dc output voltage is less than the instantaneous input voltage, the control circuit of the boost rectifier loses control of the inductor current waveform. A very large inrush current occurs when the dc output capacitor is initially charged. Additional circuitry must be employed to limit the magnitude of this current.

Buck-boost, SEPIC, and Ćuk topologies can be used to solve the inrush current problem. Since these converters have a  $d/(1-d)$  conversion ratio, their waveforms can be controlled when the output voltage is any positive value. But the price paid for this capability is increased component stresses. For the same 1 kW rectifier with 240 Vrms ac input and 380 V output, the transistor rms current and peak voltage of the nonisolated SEPIC are 5.5 A and 719 V. The rms diode current is 4.85 A. The semiconductor voltage stresses can be reduced by reducing the output voltage, at the expense of increased rms currents. With a 120 V ac input voltage, the transistor and diode rms currents increase to 9.8 A and 6.1 A, respectively.

Isolation can also be obtained in the SEPIC and other topologies, as discussed in Chapter 6. The turns ratio of the isolation transformer can also be used to reduce the primary-side currents when the dc output voltage is low. But the transformer winding rms currents are higher than those of a dc-dc converter, because of the pulsating (twice-line-frequency) power flow. For the 1 kW, 240 V ac input SEPIC example, with a 42 V 23.8 A dc load, and a 4:1 transformer turns ratio, the rms transformer currents are 5.5 A (primary) and 36.4 A (secondary). The rms transistor current is 6.9 A. At 120 V ac input voltage,

**Table 18.3** Summary of rectifier current stresses for several converter topologies

	rms	Average	Peak
CCM boost			
Transistor	$I_{ac\ rms} \sqrt{1 - \frac{8}{3\pi} \frac{V_M}{V}}$	$I_{ac\ rms} \frac{2\sqrt{2}}{\pi} \left(1 - \frac{\pi}{8} \frac{V_M}{V}\right)$	$I_{ac\ rms} \sqrt{2}$
Diode	$I_{dc} \sqrt{\frac{16}{3\pi} \frac{nV}{V_M}}$	$I_{dc}$	$2I_{dc} \frac{V}{V_M}$
Inductor	$I_{ac\ rms}$	$I_{ac\ rms} \frac{2\sqrt{2}}{\pi}$	$I_{ac\ rms} \sqrt{2}$
CCM flyback, with $n:1$ isolation transformer and input filter			
Transistor, xfmr primary	$I_{ac\ rms} \sqrt{1 + \frac{8}{3\pi} \frac{V_M}{nV}}$	$I_{ac\ rms} \frac{2\sqrt{2}}{\pi}$	$I_{ac\ rms} \sqrt{2} \left(1 + \frac{V_M}{nV}\right)$
$L_1$	$I_{ac\ rms}$	$I_{ac\ rms} \frac{2\sqrt{2}}{\pi}$	$I_{ac\ rms} \sqrt{2}$
$C_1$	$I_{ac\ rms} \sqrt{\frac{8}{3\pi} \frac{V_M}{nV}}$	0	$I_{ac\ rms} \sqrt{2} \max\left(1, \frac{V_M}{nV}\right)$
Diode, xfmr secondary	$I_{dc} \sqrt{\frac{3}{2} + \frac{16}{3\pi} \frac{nV}{V_M}}$	$I_{dc}$	$2I_{dc} \left(1 + \frac{nV}{V_M}\right)$
CCM SEPIC, nonisolated			
Transistor	$I_{ac\ rms} \sqrt{1 + \frac{8}{3\pi} \frac{V_M}{V}}$	$I_{ac\ rms} \frac{2\sqrt{2}}{\pi}$	$I_{ac\ rms} \sqrt{2} \left(1 + \frac{V_M}{V}\right)$
$L_1$	$I_{ac\ rms}$	$I_{ac\ rms} \frac{2\sqrt{2}}{\pi}$	$I_{ac\ rms} \sqrt{2}$
$C_1$	$I_{ac\ rms} \sqrt{\frac{8}{3\pi} \frac{V_M}{V}}$	0	$I_{ac\ rms} \sqrt{2} \max\left(1, \frac{V_M}{V}\right)$
$L_2$	$I_{ac\ rms} \frac{V_M \sqrt{3}}{V} \frac{1}{2}$	$\frac{I_{ac\ rms}}{\sqrt{2}} \frac{V_M}{V}$	$I_{ac\ rms} \frac{V_M}{V} \sqrt{2}$
Diode	$I_{dc} \sqrt{\frac{3}{2} + \frac{16}{3\pi} \frac{V}{V_M}}$	$I_{dc}$	$2I_{dc} \left(1 + \frac{V}{V_M}\right)$
CCM SEPIC, with $n:1$ isolation transformer			
Transistor	$I_{ac\ rms} \sqrt{1 + \frac{8}{3\pi} \frac{V_M}{nV}}$	$I_{ac\ rms} \frac{2\sqrt{2}}{\pi}$	$I_{ac\ rms} \sqrt{2} \left(1 + \frac{V_M}{nV}\right)$
$L_1$	$I_{ac\ rms}$	$I_{ac\ rms} \frac{2\sqrt{2}}{\pi}$	$I_{ac\ rms} \sqrt{2}$
$C_1$ , xfmr primary	$I_{ac\ rms} \sqrt{\frac{8}{3\pi} \frac{V_M}{nV}}$	0	$I_{ac\ rms} \sqrt{2} \max\left(1, \frac{V_M}{nV}\right)$
Diode, xfmr secondary	$I_{dc} \sqrt{\frac{3}{2} + \frac{16}{3\pi} \frac{nV}{V_M}}$	$I_{dc}$	$2I_{dc} \left(1 + \frac{nV}{V_M}\right)$

with, in all cases,  $\frac{I_{ac\ rms}}{I_{dc}} = \sqrt{2} \frac{V}{V_M}$ , ac input voltage =  $V_M \sin(\omega t)$ , dc output voltage =  $V$ .

these currents increase to 7.7 A, 42.5 A, and 11.4 A, respectively.

## 18.6 MODELING LOSSES AND EFFICIENCY IN CCM HIGH-QUALITY RECTIFIERS

As in the case of dc-dc converters, we would like to model the converter loss elements so that we can correctly specify the power stage components. The equivalent circuit approach used in the dc-dc case can be generalized to include ac-dc low harmonic rectifiers, although the resulting equations are more complicated because of the low-frequency ac modulation of the waveforms.

A dc-dc boost converter and its steady-state equivalent circuit are illustrated in Fig. 18.32. When the converter operates in equilibrium, the model of Fig. 18.32(b) can be solved to determine the converter losses and efficiency. In the ac-dc case, the input voltage  $v_g(t)$  is a rectified sinusoid, and the controller varies the duty cycle  $d(t)$  to cause  $i_g(t)$  to follow  $v_g(t)$  according to

$$i_g(t) = \frac{v_g(t)}{R_e} \quad (18.124)$$

The emulated resistance  $R_e$  is chosen by the controller such that the desired dc output voltage is obtained. Ac variations in  $d(t)$ ,  $v_g(t)$ , and several other system waveforms are not small, and hence the small-signal approximation employed in Chapters 7 to 12 is not justified. We can continue to model the low-frequency components of the converter via averaging, but the resulting equivalent circuits are, in general, time-varying and nonlinear.

For the purposes of determining the rectifier efficiency, it is assumed that (1) the inductor is sufficiently small, such that it has negligible influence on the ac-line-frequency components of the system waveforms, and (2) the capacitor is large, so that the output voltage  $v(t)$  is essentially equal to its equilibrium dc value, with negligible low- or high-frequency ac variations. So in the ac-dc case, the model becomes as shown in Fig. 18.33. Low-frequency components ( $\ll f_s$ ) of the controller waveforms are sketched in Fig. 18.34.

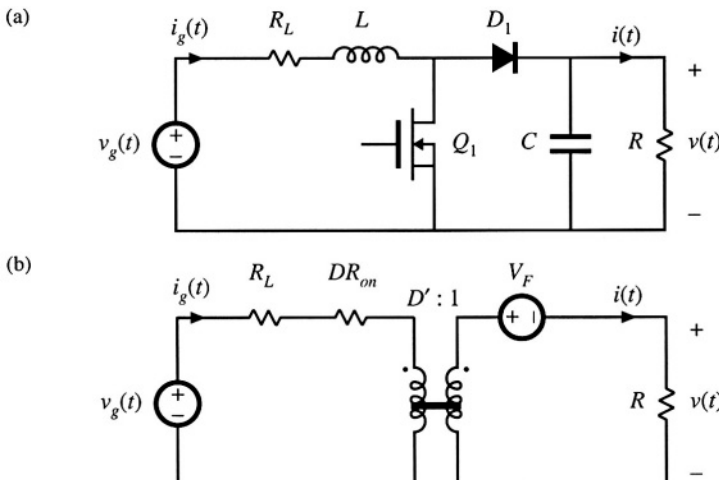


**Fig. 18.32** Dc-dc boost converter, (a), and a steady-state equivalent circuit, (b), which models the inductor resistance  $R_L$ , MOSFET on-resistance  $R_{on}$ , and diode forward voltage drop  $V_F$ .

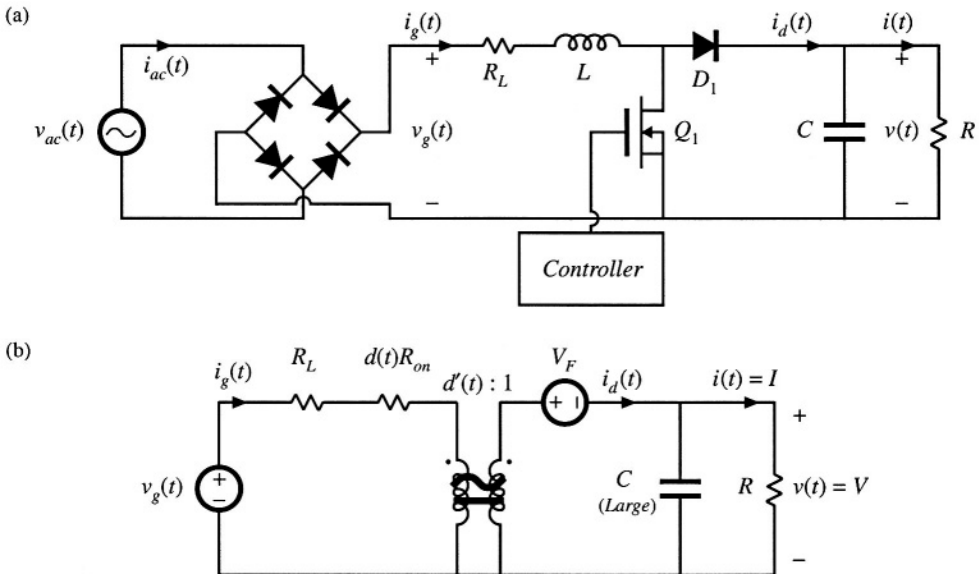


**Fig. 18.33** Ac-dc boost rectifier, (a), and a low-frequency equivalent circuit, (b), that models converter losses and efficiency.

To find the rectifier waveforms, losses, and efficiency, we must solve the circuit of Fig. 18.33(b), under the conditions that the controller varies the duty cycle  $d(t)$  such that Eq. (18.124) is satisfied. This leads to time-varying circuit elements  $d(t)R_{on}$  and the  $d'(t) : 1$  transformer. The solution that follows involves the following steps: (1) solve for the  $d(t)$  waveform; (2) average  $i_d(t)$  to find its dc component, equal to the load current  $I$ ; and (3) find other quantities of interest such as the rectifier efficiency.

The simplified boost converter circuit model of Fig. 18.35, in which only the MOSFET conduction loss is accounted for, is solved here. However, the results can be generalized directly to the circuit of Fig. 18.33(b); doing so is left as a homework problem. A similar procedure can also be followed to derive expressions for the losses and efficiencies of other rectifier topologies.

### 18.6.1 Expression for Controller Duty Cycle $d(t)$

The controller varies the duty cycle  $d(t)$  such that Eq. (18.124) is satisfied. By solving the input-side loop of Fig. 18.35, we obtain

$$i_g(t)d(t)R_{on} = v_g(t) - d'(t)v \quad (18.125)$$

Substitute Eq. (18.124) into (18.125) to eliminate  $i_g(t)$ :

$$\frac{v_g(t)}{R_e} d(t)R_{on} = v_g(t) - d'(t)v \quad (18.126)$$

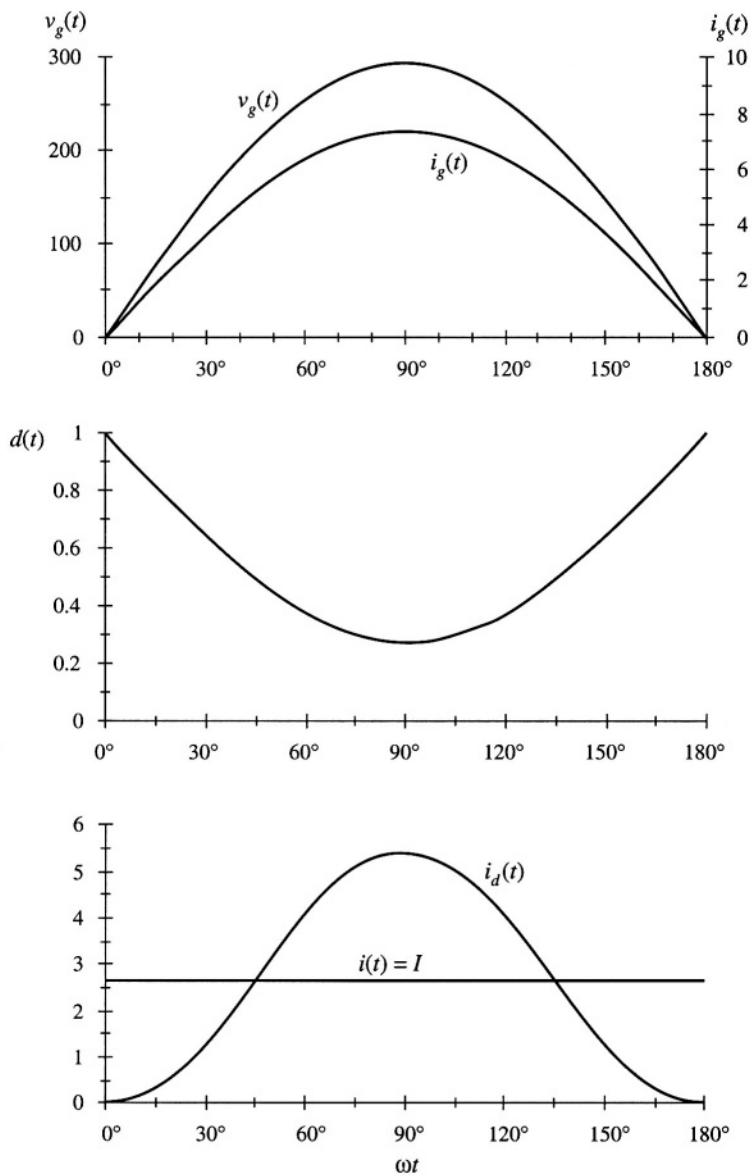


**Fig. 18.34** Typical low-frequency components of the boost rectifier waveforms.

$$\text{with} \quad v_g(t) = V_M |\sin \omega t| \quad (18.127)$$

We can now solve for the duty cycle  $d(t)$ . The result is

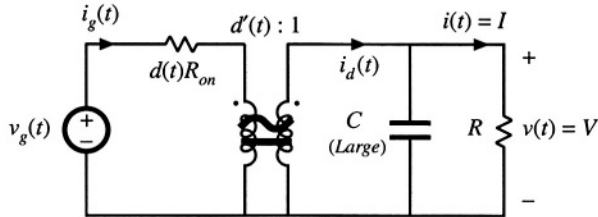


**Fig. 18.35** Simplified boost power stage low-frequency equivalent circuit, in which only the MOSFET on-resistance is modeled.

$$d(t) = \frac{v - v_g(t)}{v - v_g(t) \frac{R_{on}}{R_e}} \quad (18.128)$$

This expression neglects the converter dynamics, an assumption that is justified when these dynamics are sufficiently faster than the ac line voltage variation. The expression also neglects operation in the discontinuous conduction mode near the zero-crossing of the ac line voltage waveform. This is justified when the rectifier operates in the continuous conduction mode for most of the ac line cycle, because the power loss near the zero-crossing is negligible.

### 18.6.2 Expression for the DC Load Current

By charge balance on output capacitor  $C$ , the dc load current  $I$  is equal to the dc component of the diode current  $i_d$ :

$$I = \langle i_d \rangle_{T_{ac}} \quad (18.129)$$

Solution of Fig. 18.35 for  $i_d(t)$  yields

$$i_d(t) = d'(t) i_g(t) = d'(t) \frac{v_g(t)}{R_e} \quad (18.130)$$

From Eq. (18.128),  $d'(t) = 1 - d(t)$  is given by

$$d'(t) = \frac{v_g(t) \left( 1 - \frac{R_{on}}{R_e} \right)}{v - v_g(t) \frac{R_{on}}{R_e}} \quad (18.131)$$

so

$$i_d(t) = \frac{v_g^2(t)}{R_e} \frac{\left( 1 - \frac{R_{on}}{R_e} \right)}{v - v_g(t) \frac{R_{on}}{R_e}} \quad (18.132)$$

Now substitute  $v_g(t) = V_M \sin \omega t$ , and integrate to find  $\langle i_d(t) \rangle_{T_{ac}}$ :

$$I = \langle i_d \rangle_{T_{ac}} = \frac{2}{T_{ac}} \int_0^{T_{ac}/2} \left( \frac{V_M^2}{R_e} \right) \frac{\left( 1 - \frac{R_{on}}{R_e} \right) \sin^2(\omega t)}{\left( v - \frac{V_M R_{on}}{R_e} \sin(\omega t) \right)} dt \quad (18.133)$$

Again,  $T_{ac} = 2\pi/\omega$  is the ac line period. Equation (18.133) can be rewritten as

$$I = \frac{2}{T_{ac}} \frac{V_M^2}{VR_e} \left( 1 - \frac{R_{on}}{R_e} \right) \int_0^{T_{ac}/2} \frac{\sin^2(\omega t)}{1 - a \sin(\omega t)} dt \quad (18.134)$$

$$\text{where } a = \left( \frac{V_M}{V} \right) \left( \frac{R_{on}}{R_e} \right) \quad (18.135)$$

By waveform symmetry, we need only integrate from 0 to  $T_{ac}/4$ . Also, make the substitution  $\theta = \omega t$ :

$$I = \frac{V_M^2}{VR_e} \left( 1 - \frac{R_{on}}{R_e} \right) \frac{2}{\pi} \int_0^{\pi/2} \frac{\sin^2(\theta)}{1 - a \sin(\theta)} d\theta \quad (18.136)$$

Evaluation of this integral is tedious. It arises in not only the boost rectifier, but in a number of other high-quality rectifier topologies as well. The derivation is not given here, but involves the substitution  $z = \tan(\theta/2)$ , performing a partial fraction expansion of the resulting rational function of  $z$ , and integration of the results. The solution is:

$$\frac{4}{\pi} \int_0^{\pi/2} \frac{\sin^2(\theta)}{1 - a \sin(\theta)} d\theta = F(a) = \frac{2}{a^2 \pi} \left( -2a - \pi + \frac{4 \sin^{-1}(a) + 2 \cos^{-1}(a)}{\sqrt{1-a^2}} \right) \quad (18.137)$$

This equation is somewhat complicated, but it is in closed form, and can easily be evaluated by computer spreadsheet. The quantity  $a$ , which is a measure of the loss resistance  $R_{on}$  relative to the emulated resistance  $R_e$ , is typically much smaller than 1.  $F(a)$  is plotted in Fig. 18.36. The function  $F(a)$  can be well-approximated as follows:

$$F(a) \approx 1 + 0.862a + 0.78a^2 \quad (18.138)$$

For  $|a| \leq 0.15$ , the  $F(a)$  predicted by this approximate expression is within 0.1% of the exact value. If the  $a^2$  term is omitted, then the accuracy drops to  $\pm 2\%$  over the same range of  $a$ . The rectifier efficiency  $\eta$  calculated in the next section depends directly on  $F(a)$ , and hence the accuracy of  $F(a)$  coincides with the accuracy of  $\eta$ .

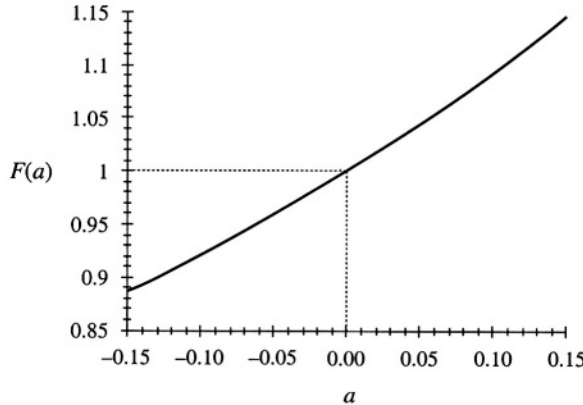


Fig. 18.36 Plot of the integral  $F(a)$  vs.  $a$ .

### 18.6.3 Solution for Converter Efficiency $\eta$

Now that we have found the dc load current, we can calculate the converter efficiency  $\eta$ . The average input power is

$$P_{in} = \left\langle p_{in}(t) \right\rangle_{T_{ac}} = \frac{V_M^2}{2R_e} \quad (18.139)$$

The average load power is

$$P_{out} = VI = \left( V \right) \left( \frac{V_M^2}{VR_e} \left( 1 - \frac{R_{on}}{R_e} \right) \frac{F(a)}{2} \right) \quad (18.140)$$

$$\text{where } a = \left( \frac{V_M}{V} \right) \left( \frac{R_{on}}{R_e} \right) \quad (18.141)$$

Here, we have substituted Eq. (18.136) for  $I$ . The efficiency is therefore

$$\eta = \frac{P_{out}}{P_{in}} = \left( 1 - \frac{R_{on}}{R_e} \right) F(a) \quad (18.142)$$

by substitution of Eqs. (18.139) and (18.140). If desired, the parabolic approximation for  $F(a)$ , Eq. (18.138), can be employed. This leads to

$$\eta \approx \left( 1 - \frac{R_{on}}{R_e} \right) \left( 1 + 0.862 \frac{V_M}{V} \frac{R_{on}}{R_e} + 0.78 \left( \frac{V_M}{V} \frac{R_{on}}{R_e} \right)^2 \right) \quad (18.143)$$

Equations (18.142) and (18.143) show how the efficiency varies with MOSFET on resistance  $R_{on}$  and

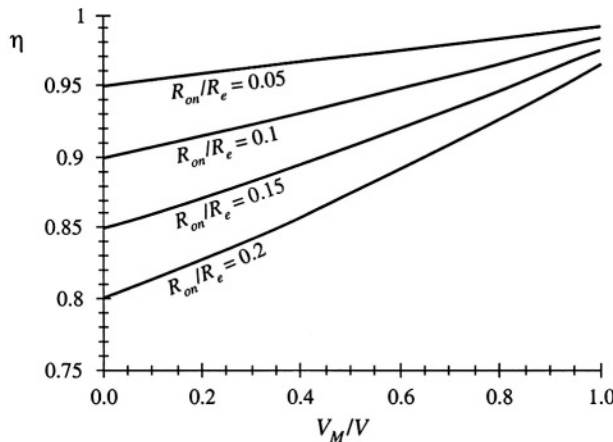


Fig. 18.37 Boost rectifier efficiency, Eq. (18.142), accounting for MOSFET on resistance.

with ac peak voltage  $V_M$ . Equation (18.142) is plotted in Fig. 18.37. It can be seen that high efficiency is obtained when the peak ac line voltage  $V_M$  is close to the dc output voltage  $V$ . Efficiencies in the range 90% to 95% can then be obtained, even with MOSFET on-resistances as high as  $0.2R_e$ . Of course, Fig. 18.37 is optimistic because it neglects sources of loss other than the MOSFET conduction loss.

#### 18.6.4 Design Example

Let us utilize Fig. 18.37 to design for a given efficiency. Consider the following specifications:

Output voltage	390 V
Output power	500 W
rms input voltage	120 V
Efficiency	95%

Assume that losses other than the MOSFET conduction loss are negligible. The average input power is

$$P_{in} = \frac{P_{out}}{\eta} = \frac{500 \text{ W}}{0.95} = 526 \text{ W} \quad (18.144)$$

The emulated resistance is therefore

$$R_e = \frac{V_{g, rms}^2}{P_{in}} = \frac{(120 \text{ V})^2}{526 \text{ W}} = 27.4 \Omega \quad (18.145)$$

Also,

$$\frac{V_M}{V} = \frac{120\sqrt{2} \text{ V}}{390 \text{ V}} = 0.435 \quad (18.146)$$

From Fig. 18.37, or by evaluation of the exact equation (18.142), 95% efficiency with  $V_M/V = 0.435$  occurs with  $R_{on}/R_e \approx 0.077$ . So we require a MOSFET having an on-resistance of

$$R_{on} \leq (0.077) R_e = (0.077) (27.4 \Omega) = 2.11 \Omega \quad (18.147)$$

Of course, other converter losses have not been accounted for, which will reduce the efficiency.

It is instructive to compare this result with that obtained using the expressions for rms current from Section 18.5. The rms transistor current of the ideal CCM boost converter is given by Eq. (18.119). The rms input current will be equal to  $P_{in}/V_{g,rms} = (526 \text{ W})/(120 \text{ V}) = 4.38 \text{ A}$ . Hence, Eq. (18.119) predicts an rms transistor current of

$$\begin{aligned} I_{Qrms} &= I_{ac\ rms} \sqrt{1 - \frac{8}{3\pi} \frac{V_M}{V}} \\ &= (4.38 \text{ A}) \sqrt{1 - \frac{8}{3\pi} \frac{(120 \text{ V}) \sqrt{2}}{(390 \text{ V})}} \\ &= 3.48 \text{ A} \end{aligned} \quad (18.148)$$

Hence, the MOSFET on-resistance should be chosen according to

$$R_{on} \leq \frac{P_{in} - P_{out}}{I_{Qrms}^2} = \frac{(526 \text{ W}) - (500 \text{ W})}{(4.38 \text{ A})^2} = 2.17 \Omega \quad (18.149)$$

This calculation is approximate because Eq. (18.119) was derived using the waveforms of the ideal (lossless) converter. Nonetheless, it gives an answer that is very close to the more exact result of Eq. (18.147). We would expect this approximate approach to exhibit good accuracy in this example, because of the high 95% efficiency.

## 18.7 IDEAL THREE-PHASE RECTIFIERS

The single-phase ideal rectifier concepts of the previous sections can be generalized to cover ideal three-phase rectifiers. Figure 18.38(a) illustrates the properties of an ideal three-phase rectifier, which presents a balanced resistive load to the utility system. A three-phase converter system is controlled such that resistor emulation is obtained in each input phase. The rectifier three-phase input port can then be modeled by per-phase effective resistances  $R_e$ , as illustrated in Fig. 18.38(a). The instantaneous powers apparently consumed by these resistors are transferred to the rectifier dc output port. The rectifier output port can therefore be modeled by power sources equal to the instantaneous powers flowing into the effective resistances  $R_e$ . It is irrelevant whether the three power sources are connected in series or in parallel; in either event, they can be combined into a single source equal to the total three-phase instantaneous input power as illustrated in Fig. 18.38(b).

If the three-phase ac input voltages are

$$\begin{aligned} v_{an}(t) &= V_M \sin(\omega t) \\ v_{bn}(t) &= V_M \sin(\omega t - 120^\circ) \\ v_{cn}(t) &= V_M \sin(\omega t - 240^\circ) \end{aligned} \quad (18.150)$$

then the instantaneous powers flowing into the phase  $a$ ,  $b$ , and  $c$  effective resistances  $R_e$  are

$$\begin{aligned}
 p_a(t) &= \frac{v_{an}^2(t)}{R_e} = \frac{V_M^2}{2R_e} \left( 1 - \cos(2\omega t) \right) \\
 p_b(t) &= \frac{v_{bn}^2(t)}{R_e} = \frac{V_M^2}{2R_e} \left( 1 - \cos(2\omega t - 240^\circ) \right) \\
 p_c(t) &= \frac{v_{cn}^2(t)}{R_e} = \frac{V_M^2}{2R_e} \left( 1 - \cos(2\omega t - 120^\circ) \right)
 \end{aligned} \tag{18.151}$$

Each instantaneous phase power contains a dc term  $V_M^2/(2R_e)$ , and a second-harmonic term. The total instantaneous three-phase power is

$$p_{tot}(t) = p_a(t) + p_b(t) + p_c(t) = \frac{3}{2} \frac{V_M^2}{R_e} \tag{18.152}$$

This is the instantaneous power which flows out of the rectifier dc output port. Note that the second harmonic terms add to zero, such that the rectifier instantaneous output power is constant. This is a consequence of the fact that the instantaneous power flow in any balanced three-phase ac system is constant. So, unlike the single-phase case, the ideal three-phase rectifier can supply constant instantaneous power to a dc load, without the need for internal low-frequency energy storage.

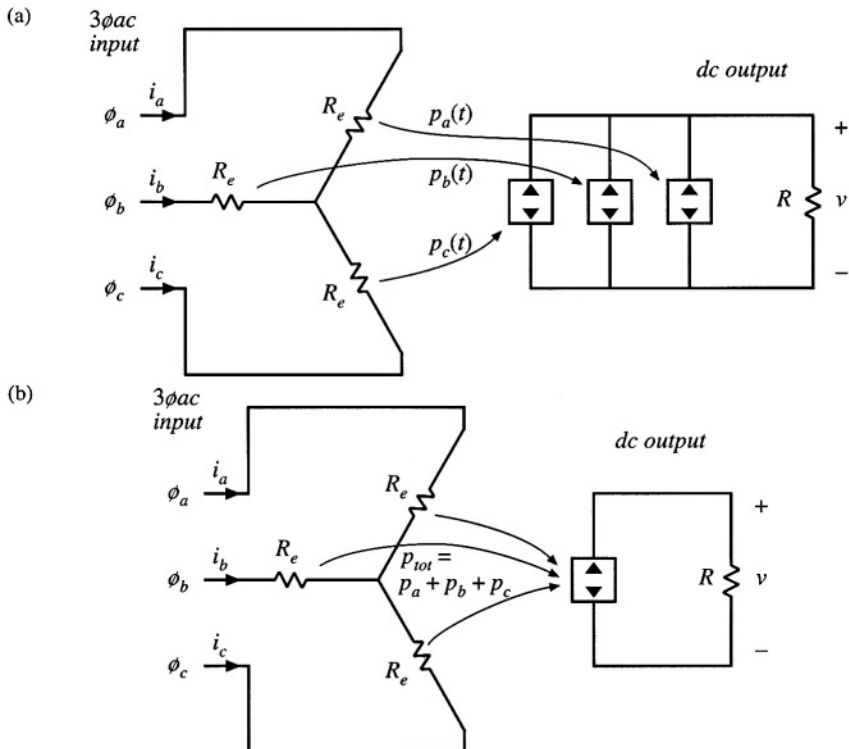


**Fig. 18.38** Development of the ideal three-phase rectifier model: (a) three ideal single-phase rectifiers, (b) combination of the three power sources into an equivalent single power source.

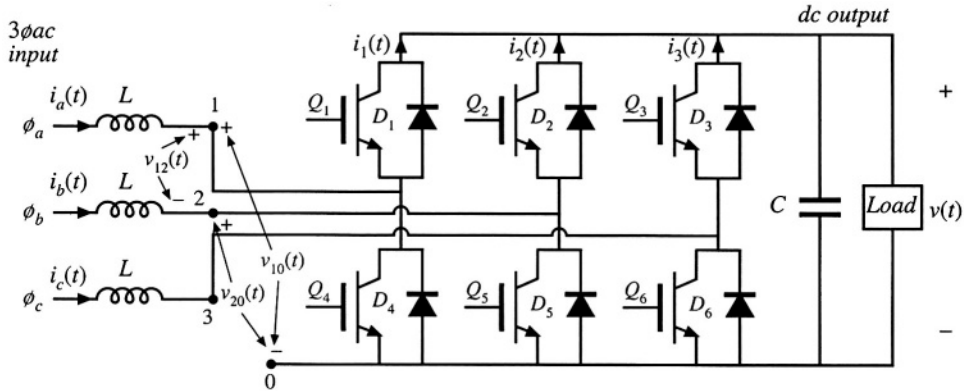
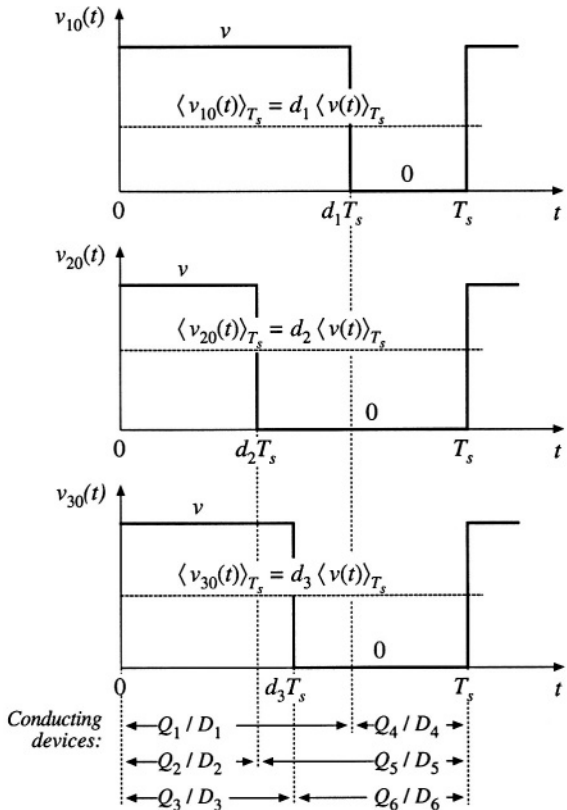


Fig. 18.39 Boost-type 3 $\phi$ ac–dc PWM rectifier.

A variety of 3 $\phi$ ac–dc PWM rectifiers are known; a few of the many references on this subject are listed in the references [42–59]. The most well-known topology is the three-phase ac–dc boost rectifier, illustrated in Fig. 18.39. This converter requires six SPST current-bidirectional two-quadrant switches. The inductors and capacitor filter the high-frequency switching harmonics, and have little influence on the low-frequency ac components of the waveforms. The switches of each phase are controlled to obtain input resistor emulation, either with a multiplying controller scheme similar to Fig. 18.5, or with some other approach. To obtain undistorted line current waveforms, the dc output voltage  $V$  must be greater than or equal to the peak line-to-line ac input voltage  $V_{L,pk}$ . In a typical realization,  $V$  is somewhat greater than  $V_{L,pk}$ . This converter resembles the voltage-source inverter, discussed briefly in Chapter 4, except that the converter is operated as a rectifier, and the converter input currents are controlled via high-frequency pulse-width modulation.

The three-phase boost rectifier of Fig. 18.39 has several attributes that make it the leading candidate for most 3 $\phi$ ac–dc rectifier applications. The ac input currents are nonpulsating, and hence very little additional input EMI filtering is required. As in the case of the single-phase boost rectifier, the rms transistor currents and also the conduction losses of the three-phase boost rectifier are low relative to other 3 $\phi$ ac–dc topologies such as the current-source inverter. The converter is capable of bidirectional power flow. A disadvantage is the requirement for six active devices: when compared with a dc–dc converter of similar ratings, the active semiconductor utilization (discussed in Chapter 6) is low. Also, since the rectifier has a boost characteristic, it is not suitable for direct replacement of traditional buck-type phase-controlled rectifiers.

The literature contains a wide variety of schemes for controlling the switches of a six-switch three-phase bridge network, which are applicable for control of the switches of Fig. 18.39. The basic operation of the converter can be most easily understood by assuming that the switches are controlled via simple sinusoidal pulse-width modulation. Transistor  $Q_1$  is driven with duty cycle  $d_1(t)$ , while transistor  $Q_4$  is driven by the complement of  $d_1(t)$ , or  $d_1'(t) = 1 - d_1(t)$ . Transistors  $Q_2$  and  $Q_5$  are driven with duty cycles  $d_2(t)$  and  $d_2'(t)$ , respectively, and transistors  $Q_3$  and  $Q_6$  are driven with duty cycles  $d_3(t)$  and  $d_3'(t)$ , respectively. The switch voltage waveforms of Fig. 18.40 are obtained. The average switch voltages are



$$\begin{aligned} \langle v_{10}(t) \rangle_{T_s} &= d_1(t) \langle v(t) \rangle_{T_s} \\ \langle v_{20}(t) \rangle_{T_s} &= d_2(t) \langle v(t) \rangle_{T_s} \\ \langle v_{30}(t) \rangle_{T_s} &= d_3(t) \langle v(t) \rangle_{T_s} \end{aligned} \quad (18.153)$$

The averaged line-to-line switch voltages are therefore

$$\begin{aligned} \langle v_{12}(t) \rangle_{T_s} &= \langle v_{10}(t) \rangle_{T_s} - \langle v_{20}(t) \rangle_{T_s} = (d_1(t) - d_2(t)) \langle v(t) \rangle_{T_s} \\ \langle v_{23}(t) \rangle_{T_s} &= \langle v_{20}(t) \rangle_{T_s} - \langle v_{30}(t) \rangle_{T_s} = (d_2(t) - d_3(t)) \langle v(t) \rangle_{T_s} \\ \langle v_{31}(t) \rangle_{T_s} &= \langle v_{30}(t) \rangle_{T_s} - \langle v_{10}(t) \rangle_{T_s} = (d_3(t) - d_1(t)) \langle v(t) \rangle_{T_s} \end{aligned} \quad (18.154)$$

In a similar manner, the average switch currents can be shown to be

$$\begin{aligned}\langle i_1(t) \rangle_{T_s} &= d_1(t) \langle i_a(t) \rangle_{T_s} \\ \langle i_2(t) \rangle_{T_s} &= d_2(t) \langle i_b(t) \rangle_{T_s} \\ \langle i_3(t) \rangle_{T_s} &= d_3(t) \langle i_c(t) \rangle_{T_s}\end{aligned}\quad (18.155)$$

Equations (18.154) and (18.155) lead to the circuit-averaged model of Fig. 18.41.

With sinusoidal PWM, the duty cycles are varied sinusoidally in synchronism with the ac line, as follows:

$$\begin{aligned}d_1(t) &= D_0 + \frac{1}{2} D_m \sin(\omega t - \varphi) \\ d_2(t) &= D_0 + \frac{1}{2} D_m \sin(\omega t - \varphi - 120^\circ) \\ d_3(t) &= D_0 + \frac{1}{2} D_m \sin(\omega t - \varphi - 240^\circ)\end{aligned}\quad (18.156)$$

where  $\omega$  is the ac line frequency. Since each instantaneous duty cycle must lie in the interval [0,1], the dc bias  $D_0$  is required. The factor  $D_m$  is called the *modulation index*; for  $D_0 = 0.5$ ,  $D_m$  must be less than or equal to one. Other choices of  $D_0$  further restrict  $D_m$ . In general, the modulation index can be defined as equal to the peak-to-peak amplitude of the fundamental component of the duty cycle variation.

If the switching frequency is sufficiently large, then filter inductors  $L$  can be small in value, such that they have negligible effect on the low-frequency ac waveforms. The averaged switch voltage  $\langle v_{12}(t) \rangle_{T_s}$  then becomes approximately equal to the ac line-line voltage  $v_{ab}(t)$ :

$$\langle v_{12}(t) \rangle_{T_s} = (d_1(t) - d_2(t)) \langle v(t) \rangle_{T_s} \approx v_{ab}(t) \quad (18.157)$$

Substitution of Eqs. (18.150) and (18.156) leads to

$$\frac{1}{2} D_m \left[ \sin(\omega t - \varphi) - \sin(\omega t - \varphi - 120^\circ) \right] \langle v(t) \rangle_{T_s} = V_M \left[ \sin(\omega t) - \sin(\omega t - 120^\circ) \right] \quad (18.158)$$

For small  $L$ , the angle  $\varphi$  must tend to zero, and hence the sinusoidal terms in Eq. (18.158) cancel out. In steady-state, the dc output voltage is  $\langle v(t) \rangle_{T_s} = V$ . Equation (18.158) then becomes

$$\frac{1}{2} D_m V = V_M \quad (18.159)$$

Solution for the dc output voltage  $V$  leads to

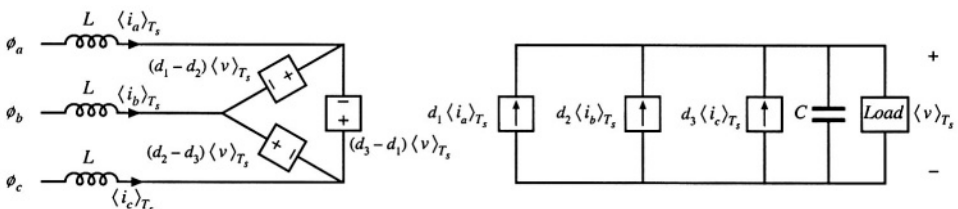


Fig. 18.41 Averaged model of the open-loop 3 $\phi$ ac-dc boost rectifier.

$$V = \frac{2V_M}{D_m} \quad (18.160)$$

Equation (18.160) can be written in terms of the peak line-to-line voltage  $V_{L,pk}$ , as

$$V = \frac{2}{\sqrt{3}} \frac{V_{L,pk}}{D_m} = 1.15 \frac{V_{L,pk}}{D_m} \quad (18.161)$$

With  $D_m \leq 1$ , the dc output voltage  $V$  must be greater than or equal to 1.15 times the peak line-to-line ac input voltage. Thus, the rectifier has a boost characteristic.

The sinusoidal PWM approach of Eq. (18.156) is not the only way to vary the duty cycles to obtain sinusoidal ac voltages and currents. For example, triplen harmonics can be added to the duty cycle expressions of Eq. (18.156). These triplen harmonics cancel out in Eq. (18.154), such that the average inverter input voltages  $\langle v_{12}(t) \rangle_{T_s}$ ,  $\langle v_{23}(t) \rangle_{T_s}$ , and  $\langle v_{31}(t) \rangle_{T_s}$  contain only fundamental. Figure 18.42 illustrates duty cycle variations that lead to a dc output voltage  $V$  equal to  $V_{L,pk}$ . The effective modulation index in this case is 1.15. The ac-side voltages and currents are again undistorted. Further increases in the modulation index can be attained only by introduction of distortion in the ac-side voltages and currents. Of course, in practice the duty cycle modulations are usually generated by the feedback loops that control the input current waveforms to attain resistor emulation.

Three-phase ac-to-dc rectifiers having buck, buck-boost, or other characteristics, are possible, but find much less use than the boost topology. A 3Øac-dc rectifier system can also be constructed simply using three separate single-phase rectifiers [34]; however, each single-phase rectifier must then contain transformer isolation, leading to substantially increased switch stress and loss. Other unconventional approaches to three-phase low-harmonic rectification have also been recently explored, such as the Vienna rectifier [56,59], single-switch approaches [49–55], and other circuits[44,45,46,57,58].

Yet another approach to solving the problem of three-phase rectifier harmonics is the *harmonic correction* scheme illustrated in Fig. 18.43. An active six-switch three-phase bridge removes the harmonics generated by a nonlinear three-phase load such as an uncontrolled rectifier. The harmonic corrector is controlled such that its ac line currents contain harmonics that are equal in magnitude but opposite in phase to the harmonics generated by the nonlinear load. No average power flows into the harmonic corrector. The total kVA rating of the harmonic corrector semiconductor devices depends on the magnitudes of the harmonics produced by the nonlinear load. If the THD generated by the load is not too large, then

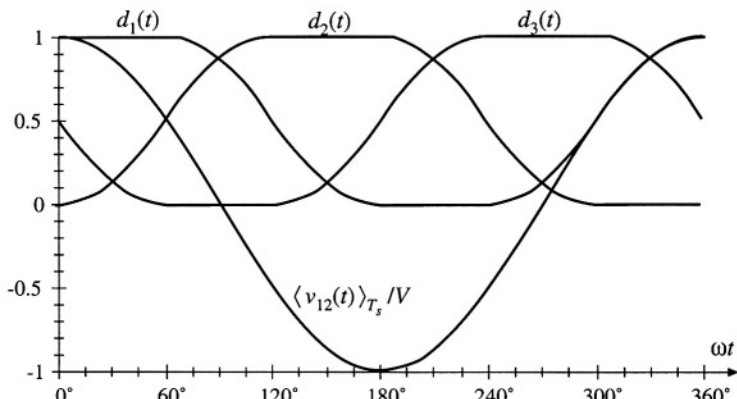


**Fig. 18.42** A modulation strategy that leads to a dc output voltage equal to the peak input line-line voltage.

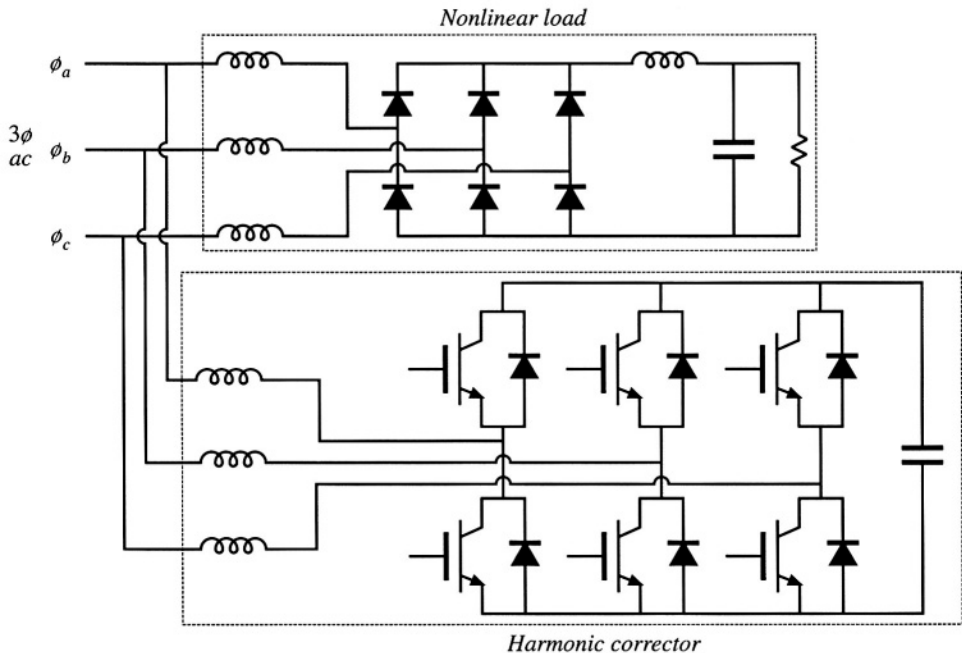


**Fig. 18.43** A harmonic corrector, based on the  $3\phi_{ac}$ -dc CCM boost converter of Fig. 18.39.

the harmonic corrector scheme requires less total active silicon than the CCM boost-type rectifier of Fig. 18.39. But if the uncontrolled rectifier contains small ac line inductances, such that it operates in the discontinuous conduction mode with large THD, then it is probably better to simply replace the uncontrolled rectifier with the CCM boost-type rectifier of Fig. 18.39.

## 18.8 SUMMARY OF KEY POINTS

1. The ideal rectifier presents an effective resistive load, the emulated resistance  $R_e$ , to the ac power system. The power apparently “consumed” by  $R_e$  is transferred to the dc output port. In a three-phase ideal rectifier, input resistor emulation is obtained in each phase. In both the single-phase and three-phase cases, the output port follows a power source characteristic, dependent on the instantaneous ac input power. Ideal rectifiers can perform the function of low-harmonic rectification, without need for low-frequency reactive elements.
2. The dc-dc boost converter, as well as other converters capable of increasing the voltage according to Eq. (18.12), can be adapted to the ideal rectifier application. A control system causes the input current to be proportional to the input voltage. The converter may operate in CCM, DCM, or in both modes. The mode boundary can be expressed as a function of  $R_e$ ,  $2L/T_s$ , and the instantaneous voltage ratio  $v_x(t)/V$ . A well-designed average current controller leads to resistor emulation regardless of the operating mode; however, other schemes may lead to distorted current waveforms when the mode boundary is crossed.
3. In a single-phase system, the instantaneous ac input power is pulsating, while the dc load power is constant. Whenever the instantaneous input and output powers are not equal, the ideal rectifier system must

contain energy storage. A large capacitor is commonly employed; the voltage of this capacitor must be allowed to vary independently, as necessary to store and release energy. A slow feedback loop regulates the dc component of the capacitor voltage, to ensure that the average ac input power and dc load power are balanced.

4. RMS values of rectifiers waveforms can be computed by double integration. In the case of the boost converter, the rms transistor current can be as low as 39% of the rms ac input current, when the dc output voltage  $V$  is close in value to the peak ac input voltage  $V_M$ . Other converter topologies such as the buck-boost, SEPIC, and Ćuk converters exhibit significantly higher rms transistor currents but are capable of limiting the converter inrush current.
5. In the three-phase case, a boost-type rectifier based on the PWM voltage-source inverter also exhibits low rms transistor currents. This approach requires six active switching elements, and its dc output voltage must be greater than the peak input line-to-line voltage. Average current control can be used to obtain input resistor emulation. An equivalent circuit can be derived by averaging the switch waveforms. The converter operation can be understood by assuming that the switch duty cycles vary sinusoidally; expressions for the average converter waveforms can then be derived.
6. Converter losses and efficiency can be modeled using the steady-state equivalent circuit models of Chapter 3, with a time-varying duty cycle. The output current is averaged over one ac line period, to determine its dc component. The converter losses and efficiency can then be computed. This approach is approximate, in that (i) it assumes that the converter dynamics are much faster than the ac line frequency, and (ii) it neglects operation in the discontinuous conduction mode.
7. Average current control involves direct regulation of the low-frequency components of the rectifier input current to follow the input voltage. Feedforward can also be added, to cancel the influence of ac line voltage variations on the dc output voltage.
8. Current programmed control can also be adapted to attain input resistor emulation in rectifiers. The programmed current reference signal  $i_c(t)$  is made proportional to the ac input voltage. The difference between  $i_c(t)$  and the average inductor current leads to distortion, owing to the inductor current ripple and the need for a stabilizing artificial ramp. Several approaches are known for reducing the resulting harmonic distortion of the line current waveform.
9. Hysteretic control, particularly with 100% current ripple, has a simple controller implementation. The disadvantages are variable switching frequency, and increased peak currents.
10. Nonlinear carrier control also leads to a simple controller implementation, and has the advantage of CCM operation with small peak transistor current.
11. The outer low-bandwidth control system, which regulates the dc output voltage to balance the rectifier and load powers, can be modeled by averaging the rectifier waveforms over one-half of the ac line period  $T_{2L}$ . This causes the dc-side system equations to become time-invariant. A small-signal model is then obtained by perturbation and linearization.
12. The inner high-bandwidth control system, which regulates the ac input current waveform to attain resistor emulation, is in general highly nonlinear. However, in the case of the boost rectifier, a valid small-signal model can be derived. This approach is unsuccessful in the case of other converters; one must then resort to other approaches such as the quasi-static approximation or simulation.

## REFERENCES

- [1] D. CHAMBERS and D. WANG, "Dynamic Power Factor Correction in Capacitor Input Off-Line Converters," *Proceedings Sixth National Solid-State Power Conversion Conference* (Powercon 6), pp. B3-1 to B3-6, May 1979.

- [2] R. ERICKSON, M. MADIGAN, and S. SINGER, "Design of a Simple High Power Factor Rectifier Based on the Flyback Converter," *IEEE Applied Power Electronics Conference*, 1990 Record, pp. 792-801.
- [3] S. SINGER and R.W. ERICKSON, "Power Source Element and Its Properties," *IEE Proceedings—Circuits Devices Systems*, Vol. 141, No. 3, pp. 220-226, June 1994.
- [4] S. SINGER, "Realization of Loss-Free Resistive Elements," *IEEE Transactions on Circuits and Systems*, Vol. CAS-36, No. 12, January 1990.
- [5] W. E. RIPPEL, "Optimizing Boost Chopper Charger Design," *Proceedings Sixth National Solid-State Power ConversionConference* (Powercon 6), 1979, pp. D1-1 - D1-20.
- [6] M. F. SCHLECHT and B. A. MIWA, "Active Power Factor Correction for Switching Power Supplies," *IEEE TransactionsonPowerElectronics*, Vol. 2, No. 4, October 1987, pp. 273-281.
- [7] J. SEBASTIAN, J. UCEDA, J. A. COBOS, J. ARAU, and F. ALDANA, "Improving Power Factor Correction in Distributed Power Supply Systems Using PWM and ZCS-QR SEPIC Topologies," *IEEE Power Electronics Specialists Conference*, 1991 Record, pp. 780-791.
- [8] E. YANG, Y. JIANG, G. HUA, and F. C. LEE, "Isolated Boost Circuit for Power Factor Correction," *IEEE Applied Power Electronics Conference*, 1993 Record, pp. 196-203.
- [9] C. A. CANESIN and I BARBI, "A Unity Power Factor Multiple Isolated Outputs Switching Mode Power Supply Using a Single Switch," *IEEE Applied Power Electronics Conference*, 1991 Record, pp. 430-436.
- [10] S. FREELAND, "I. A Unified Analysis of Converters with Resonant Switches, II. Input-Current Shaping for Single-Phase Ac-dc Power Converters," Ph.D. Thesis, California Institute of Technology, 1988.
- [11] M. J. SCHUTTEN, R. L. STEIGERWALD, and M. H. KHERALUWALA, "Characteristics of Load-Resonant Converters Operated in a High Power Factor Mode," *IEEE Applied Power Electronics Conference*, 1991 Record, pp. 5-16.
- [12] J. HONG, E. ISMAIL, R. ERICKSON, and I. KHAN, "Design of the Parallel Resonant Converter as a Low Harmonic Rectifier," *IEEE Applied Power Electronics Conference*, 1993 Record, pp. 833-840.
- [13] I. BARBI and S. A. O. DA SILVA, "Sinusoidal Line Current Rectification at Unity Power Factor with Boost Quasi-Resonant Converters," *IEEE Applied Power Electronics Conference*, 1990 Record, pp. 553-562.
- [14] R. REDL and L. BALOGH, "RMS, DC, Peak, and Harmonic Currents in High-Frequency Power-Factor Correctors with Capacitive Energy Storage," *IEEE Applied Power Electronics Conference*, 1992 Record, pp. 533-540.
- [15] J. SEBASTIAN, J. A. COBOS, P. GIL, and J. UCEDA, "The Determination of the Boundaries Between Continuous and Discontinuous Conduction Modes in PWM Dc-to-Dc Converters Used as Power Factor Preregulators," *IEEE Power Electronics Specialists Conference*, 1992 Record, pp. 1061-1070.
- [16] M. NALBANT, "Design of a 1 kW Power Factor Corrector," *Power Conversion*, October 1989 Proceedings, pp. 121-135.
- [17] R. MAMMANO and R. NEIDORFF, "Improving Input Power Factor—A New Active Controller Simplifies the Task," *Power Conversion*, October 1989 Proceedings, pp. 100-109.

- [18] J. BAZIMET and J. O'CONNOR, "Analysis and Design of a Zero Voltage Transition Power Factor Correction Circuit," *IEEE Applied Power Electronics Conference*, 1994 Record, pp. 591-597.
- [19] R. REDL and B. ERISMAN, "Reducing Distortion in Peak-Current-Controlled Boost Power Factor Correctors," *IEEE Applied Power Electronics Conference*, 1994 Record, pp. 576-583.
- [20] C. ZHOU and M. JOVANOVIC, "Design Tradeoffs in Continuous Current-Mode Controlled Boost Power Factor Correction Circuits," *High Frequency Power Conversion Conference*, 1992 Proceedings, pp. 209-220.
- [21] D. MAKSIMOVIĆ, "Design of the Clamped-Current High-Power-Factor Boost Rectifier," *IEEE Applied Power Electronics Conference*, 1994 Record, pp. 584-590.
- [22] C. CANESIN and I. BARBI, "Analysis and Design of Constant-Frequency Peak-Current-Controlled High-Power-Factor Boost Rectifier with Slope Compensation," *IEEE Applied Power Electronics Conference*, 1996 Record, pp. 807-813.
- [23] J. LAI and D. CHEN, "Design Considerations for Power Factor Correction Boost Converter Operating at the Boundary of Continuous Conduction Mode and Discontinuous Conduction Mode," *IEEE Applied Power Electronics Conference*, 1993 Record, pp. 267-273.
- [24] C. ZHOU, R. RIDLEY, and F. C. LEE, "Design and Analysis of a Hysteretic Boost Power Factor Correction Circuit," *IEEE Power Electronics Specialists Conference*, 1990 Record, pp. 800-807.
- [25] S. AHMED, "Controlled On-Time Power Factor Correction Circuit with Input Filter," M.S. Thesis, Virginia Polytechnic Institute and State University, Blacksburg VA, May 1990.
- [26] M. DAWANDE and G. DUBEY, "Programmable Input Power Factor Correction Method for Switch Mode Rectifiers," *IEEE Applied Power Electronics Conference*, 1993 Record, pp. 274-280.
- [27] J. SPANGLER and A. BEHERA, "A Comparison Between Hysteretic and Fixed Frequency Boost Converters Used for Power Factor Correction," *IEEE Applied Power Electronics Conference*, 1993 Record, pp. 281-286.
- [28] D. MAKSIMOVIĆ, Y. JANG, and R. ERICKSON, "Nonlinear-Carrier Control for High Power Factor Boost Rectifiers," *IEEE Applied Power Electronics Conference*, 1995 Record, pp. 635-641.
- [29] R. ZANE and D. MAKSIMOVIĆ, "Nonlinear Carrier Control for High Power Factor Rectifiers Based on Flyback, Ćuk, or SEPIC Converters," *IEEE Applied Power Electronics Conference*, 1996 Record, pp. 814-820.
- [30] Z. LAI, K. SMEDLEY, and Y. MA, "Time Quantity One-Cycle Control for Power Factor Controllers," *IEEE Applied Power Electronics Conference*, 1996 Record, pp. 821-827.
- [31] L. ROSSETTO, G. SPIAZZI, P. TENTI, B. FABIANO, and C. LICITRA, "Fast-Response High-Quality Rectifier with Sliding-Mode Control," *IEEE Applied Power Electronics Conference*, 1993 Record, pp. 175-181.
- [32] W. TANG, Y. JIANG, G. HUA, F. C. LEE, and I. COHEN, "Power Factor Correction with Flyback Converter Employing Charge Control," *IEEE Applied Power Electronics Conference*, 1993 Record, pp. 293-298.
- [33] F. C. SCHWARZ, "An Improved Method of Resonant Current Pulse Modulation for Power Converters," *IEEE Power Electronics Specialists Conference*, 1975 Record, pp. 194-204.

- [34] M. J. KOCHER and R. L. STEIGERWALD, "An Ac-to-dc Converter with High Quality Input Waveforms," *IEEE Power Electronics Specialists Conference*, 1982 Record, pp. 63-75.
- [35] M. SCHLECHT, "Time-Varying Feedback Gains for Power Circuits with Active Waveshaping," *IEEE Power Electronics Specialists Conference*, 1981 Record, pp. 52-59.
- [36] I. KHAN and R. W. ERICKSON, "Control of Switched-Mode Converter Harmonic-Free Terminal Waveforms Through Internal Energy Storage," *IEEE Power Electronics Specialists Conference*, 1986 Record, pp. 13-26.
- [37] K. MAHABIR, G. VERGESE, J THOTTUVELIL, and A. HEYMAN, "Linear Averaged and Sampled Data Models for Large Signal Control of High Power Factor Ac-dc Converters," *IEEE Power Electronics Specialists Conference*, 1990 Record, pp. 372-381.
- [38] MICHAEL MADIGAN, ROBERT ERICKSON, and ESAM ISMAIL, "Integrated High Quality Rectifier-Regulators," *IEEE Power Electronics Specialists Conference*, 1992 Record, pp. 1043-1051.
- [39] K. MAHABIR, G. VERGESE, J THOTTUVELIL, and A. HEYMAN, "Linear Averaged and Sampled Data Models for Large Signal Control of High Power Factor AC-DC Converters," *IEEE Power Electronics Specialists Conference*, 1990 Record, pp. 372-381.
- [40] R. RIDLEY, "Average Small-Signal Analysis of the Boost Power Factor Correction Circuit," *Proceedings of the Virginia Power Electronics Center Seminar*, Blacksburg, VA, Sept. 1989, pp. 108-120.
- [41] M. MADIGAN, "Single-Phase High-Quality Rectifier-Regulators," Ph.D. Thesis, University of Colorado at Boulder, 1992.
- [42] N. MOHAN, T. UNDELAND and W. ROBBINS, *Power Electronics: Converters, Applications, and Design*, Second edition, New York: John Wiley & Sons, 1995, Chapters 8 and 18.
- [43] H. MAO, D. BOROVACHEVICH, A. RAVINDRA, and F. LEE, "Analysis and Design of a High Frequency Three-Phase Boost Rectifier," *IEEE Applied Power Electronics Conference*, 1996 Record, pp. 538-544.
- [44] B. T. OOI, J. C. SALMON, J. W. DIXON, and A. B. KULKARNI, "A Three-Phase Controlled-Current PWM Converter with Leading Power Factor," *IEEE Transactions on Industry Applications*, Vol. 23, No. 1, pp. 78-84, 1987.
- [45] P. TENTI and L. MALSANI, "Three-Phase AC/DC PWM Converter with Sinusoidal AC Currents and Minimum Filter Requirements," *IEEE Transactions on Industry Applications*, Vol. 23, No. 1, pp. 71-77, 1987.
- [46] A-M. MAJED, T. C. GREEN, and B. W. WILLIAMS, "Dynamic Properties of a Step-Down Sinusoidal Current AC/DC Converter Under State-Feedback Control," *IEEE Applied Power Electronics Conference*, 1993 Record, pp. 161-167.
- [47] M. RASTOGI, N. MOHAN, and C. HENZE, "Three-Phase Sinusoidal Current Rectifier with Zero Current Switching," *IEEE Applied Power Electronics Conference*, 1994 Record, pp. 718-724.
- [48] K. D. T. NGO, S. ĆUK, and R. D. MIDDLEBROOK, "A New Flyback Dc-to-Three-Phase Converter with Sinusoidal Outputs," *IEEE Power Electronics Specialists Conference*, 1983 Record, pp. 377-388.
- [49] A. R. PRASAD, P. D. ZIOGAS, and S. MANIAS, "An Active Power Factor Correction Technique for Three-Phase Diode Rectifiers," *IEEE Power Electronics Specialists Conference*, 1989 Record, pp. 58-66.

- [50] J. KOLAR, H. ERTL, and F. ZACH, "Space Vector Based Analysis of the Input Current Distortion of a Three Phase Discontinuous Conduction Mode Boost Rectifier System," *IEEE Power Electronics Specialists Conference*, 1993 Record, pp. 696-703.
- [51] R. ITOH and K. ISHITAKA, "Three-Phase Flyback Ac-dc Converter with Sinusoidal Supply Currents," *IEE Proceedings*, Vol. 136, Part B, No. 4, pp. 143-151, 1991.
- [52] O. APELDOORN and P. SCHMIDT, "Single Transistor Three-Phase Power Conditioners with High Power Factor and Isolated Output," *IEEE Applied Power Electronics Conference*, 1994 Record, pp. 731-737.
- [53] E. H. ISMAIL and R. W. ERICKSON, "A Single Transistor Three-Phase Resonant Switch for High Quality Rectification," *IEEE Power Electronics Specialists Conference*, 1992 Record, pp. 1341-1351.
- [54] Y. JANG and R. ERICKSON, "New Single-Switch Three-Phase High Power Factor Rectifiers Using Multi-Resonant Zero Current Switching," *IEEE Applied Power Electronics Conference*, 1994 Record, pp. 711-717.
- [55] Y. JANG and R. ERICKSON, "Design and Experimental Results of a 6kW Single-Switch Three-Phase High Power Factor Rectifier Using Multi-Resonant Zero Current Switching," *IEEE Applied Power Electronics Conference*, 1996 Record, pp. 524-530.
- [56] J. KOLAR, H. ERTL, and F. ZACH, "Design and Experimental Investigation of a Three-Phase High Power Density High-Efficiency Unity-Power-Factor PWM (VIENNA) Rectifier Employing a Novel Integrated Power Semiconductor Module," *IEEE Applied Power Electronics Conference*, 1996 Record, pp. 514-523.
- [57] M. RASTOGI, N. MOHAN, and C. HENZE, "Three-Phase Sinusoidal Current Rectifier with Zero Current Switching," *IEEE Applied Power Electronics Conference*, 1994 Record, pp. 718-724.
- [58] S. GATARIĆ, D. BOROVACHEVICH, and F. C. LEE, "Soft-Switched Single-Switch Three-Phase Rectifier with Power Factor Correction," *IEEE Applied Power Electronics Conference*, 1994 Record, pp. 738-744.
- [59] J. KOLAR, U. DROFENIK, AND F. ZACH, "Vienna Rectifier II—A Novel Single-Stage High-Frequency Isolated Three-Phase PWM Rectifier System," *IEEE Applied Power Electronics Conference*, 1998 Record, pp. 23-33.

## PROBLEMS

- 18.1** The boost converter of Fig. 18.5 is replaced by a buck-boost converter. Inductor energy storage has negligible influence on the low-frequency components of the converter waveforms. The average load power is  $P_{load}$ . The dc output voltage is  $V$  and the sinusoidal ac input voltage has peak amplitude  $V_M$ .
- (a) Determine expressions for the duty cycle variations  $d(t)$  and the inductor current variation  $i(t)$ , assuming that the converter operates in the continuous conduction mode.
  - (b) Derive the conditions for operation in the continuous conduction mode. Manipulate your result to show that the converter operates in CCM when  $R_e$  is less than  $R_{e,crit}(L, T_s, v_g(t), V)$ , and determine  $R_{e,crit}$ .
  - (c) For what values of  $R_e$  does the converter always operate in CCM? in DCM?
  - (d) The ac input voltage has rms amplitude in the range 108 V to 132 V. The maximum load power is 100 W, and the minimum load power is 10 W. The dc output voltage is 120 V. The switching frequency is 75 kHz. What value of  $L$  guarantees that the converter always operates in CCM? in DCM?

- 18.2** Derive expressions for the input characteristics of the buck-boost converter, similar to Eqs. (18.25) to (18.33). Sketch the converter input characteristics, and label the CCM–DCM boundary.
- 18.3** Derive expressions for the rms transistor and diode currents of rectifiers based on the single-phase CCM Cuk topology. Express your results in forms similar to those of Table 18.3.
- 18.4** To obtain an isolated dc output, the boost converter in Fig. 18.5 is replaced by the full-bridge transformer-isolated CCM boost converter of Fig. 6.35. Derive an expression for the rms transistor current. Express your result as a function of  $I_{ac\ rms}$ ,  $n$ ,  $V$ , and  $V_M$ .
- 18.5** Comparison of CCM boost and isolated SEPIC topologies as universal-input single-phase rectifiers. You are given that the dc output voltage is  $V = 400$  V, the load power is  $P = 500$  W, and the rms input voltage varies between 90 and 270 V, such that the peak ac input voltage  $V_M$  varies between  $V_{Mmin} = 127$  V and  $V_{Mmax} = 382$  V. Define the transistor stress  $S$  as the product of the worst-case peak transistor voltage and the worst-case rms transistor current. It is desired to minimize  $S$ .
  - (a) Determine  $S$  for the boost converter in this application.
  - (b) Briefly discuss your result of part (a): if universal input operation was not required, and hence  $V_M = 382$  V always, what  $S$  would result?
 In the isolated SEPIC, the transformer turns ratio  $n : 1$  can be chosen to optimize the design.
  - (c) Express  $S$  for the SEPIC as a function of  $n$ ,  $V$ ,  $P$ ,  $V_{Mmin}$ , and  $V_{Mmax}$ .
  - (d) Choose  $n$  for the SEPIC such that  $S$  is minimized in this application. Compare with the results of parts (a) and (b).
- 18.6** In the boost-type dc– $3\phi$ ac rectifier of Fig. 18.39, the ac-side inductances  $L$  are not small: they exhibit line-frequency impedances that should not be ignored. The three-phase ac voltages are given by Eq. (18.150), and the duty cycles are modulated as in Eq. (18.156). The converter operates in the continuous conduction mode.
  - (a) Determine the magnitudes and phases of the line-to-neutral average voltages at the ac inputs to the switch network. Express your result in terms of  $D_m$ ,  $V$ , and  $\phi$ .
  - (b) Determine the real power  $P$  and reactive power  $Q$  drawn from the  $3\phi$ ac source. Express your results as functions of  $V_M$ ,  $V$ ,  $D_m$ ,  $\phi$ , and  $\omega L$ .
  - (c) How must  $\phi$  be chosen to obtain unity power factor?
- 18.7** In the boost-type dc– $3\phi$ ac rectifier of Fig. 18.39, the switch duty ratios are modulated as illustrated in Fig. 18.42. When the inductances  $L$  are sufficiently small, a dc output voltage  $V$  equal to the peak line-to-line ac input voltage can be obtained, with undistorted ac line currents. As illustrated in Fig. 18.42,  $d_1(t)$  is equal to 1 for  $0^\circ \leq \omega t \leq 60^\circ$ , where  $\omega t = 0^\circ$  when  $\langle v_{12}(t) \rangle_{T_s} = V$ .
  - (a) Derive expressions for  $d_2(t)$  and  $d_3(t)$ , over the interval  $0^\circ \leq \omega t \leq 60^\circ$ .
  - (b) State how  $d_1(t)$ ,  $d_2(t)$ , and  $d_3(t)$  should vary over each  $60^\circ$  interval.
- 18.8** The buck-type  $3\phi$ ac–dc rectifier of Fig. 18.44 operates in the continuous conduction mode. Transistors  $Q_1$  to  $Q_6$  operate with duty cycles  $d_1(t)$  to  $d_6(t)$ , respectively.
  - (a) Determine the constraints on switch operation. Which transistors must not conduct simultaneously? Which duty cycles must total unity?
  - (b) Average the  $3\phi$  bridge switch network, to determine expressions for the average ac-side switch currents  $\langle i_a(t) \rangle_{T_s}$ ,  $\langle i_b(t) \rangle_{T_s}$ , and  $\langle i_c(t) \rangle_{T_s}$ .
  - (c) Show that the average de-side switch voltage can be expressed as
 
$$\langle v_d(t) \rangle_{T_s} = (d_1(t) - d_4(t)) \langle v_{an}(t) \rangle_{T_s} + (d_2(t) - d_5(t)) \langle v_{bn}(t) \rangle_{T_s} + (d_3(t) - d_6(t)) \langle v_{cn}(t) \rangle_{T_s}$$
  - (d) The duty cycles are varied as follows:

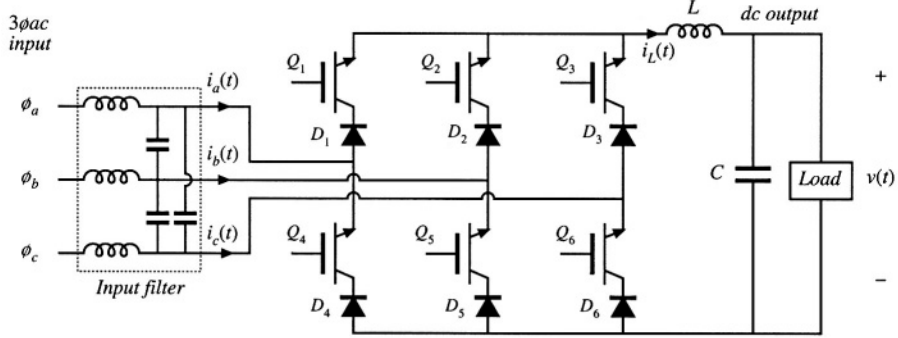


Fig. 18.44 Buck-type 3 $\phi$ ac-dc rectifier, Problem 18.8.

$$\begin{aligned}
 d_1(t) &= \frac{1}{3} + \frac{1}{2} D_m \sin(\omega t - \varphi) \\
 d_2(t) &= \frac{1}{3} + \frac{1}{2} D_m \sin(\omega t - \varphi - 120^\circ) \\
 d_3(t) &= \frac{1}{3} + \frac{1}{2} D_m \sin(\omega t - \varphi - 240^\circ) \\
 d_4(t) &= \frac{1}{3} - \frac{1}{2} D_m \sin(\omega t - \varphi) \\
 d_5(t) &= \frac{1}{3} - \frac{1}{2} D_m \sin(\omega t - \varphi - 120^\circ) \\
 d_6(t) &= \frac{1}{3} - \frac{1}{2} D_m \sin(\omega t - \varphi - 240^\circ)
 \end{aligned}$$

with the ac input voltages given by Eq. (18.150). The input filter has negligible effect of the low-frequency components of the converter waveforms. Determine the steady-state dc output voltage  $V$ , as a function of  $V_M$ ,  $D_m$ , and  $\varphi$ .

- (e) Determine the power factor. You may assume that the input filter completely removes the switching harmonics from the currents  $i_a(t)$ ,  $i_b(t)$ , and  $i_c(t)$ . However, the input filter elements consume or supply negligible line-frequency reactive power.

**18.9** In the three-phase DCM flyback rectifier of Fig. 18.45, the input filter has negligible effect on the low-frequency components of the input ac waveforms. The transistor operates with switching frequency  $f_s$  and duty cycle  $d$ . Flyback transformers  $T_1$ ,  $T_2$ , and  $T_3$  each have magnetizing inductance  $L$  referred to the primary, turns ratio  $n : 1$ , and have negligible leakage inductances.

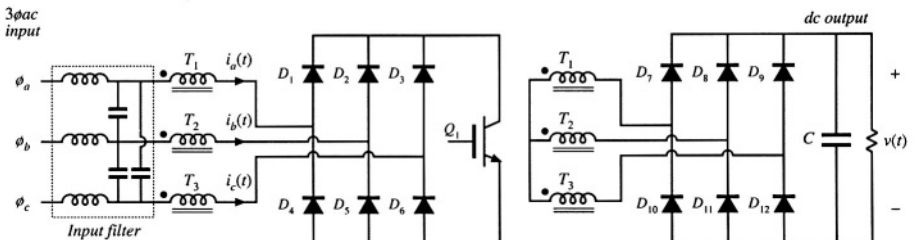


Fig. 18.45 Isolated 3 $\phi$ ac-dc rectifier based on the flyback converter operating in discontinuous conduction mode: Problem 18.9.

- (a) Determine expressions for the low-frequency components of the ac input and dc output currents.  
(b) Derive an averaged equivalent circuit model for the converter, and give expressions for the ele-

ment values.

- (c) Derive the conditions for operation in the discontinuous conduction mode.

18.10

Power stage design of a universal-input boost rectifier. The objective of this problem is to work out the power stage design of a low harmonic rectifier based on the boost converter. This converter is to be designed to operate anywhere in the world, and hence the input voltage may vary over the range 90 to 270 Vrms, 50 to 60 Hz. The converter produces a regulated 385 V dc output, at 1000 W. The switching frequency  $f_s$  is 100 kHz. You may assume that the controller operates perfectly, to produce an undistorted ac line current waveform and a well-regulated dc output voltage.

- (a) Derive an expression for how the duty cycle  $d(t)$  will vary over the ac line cycle. You may neglect converter dynamics and losses. Sketch  $d(t)$  under conditions of maximum and minimum ac line voltage.
- (b) Specify the inductor:
- Specify the value of  $L$  such that, at the peak of the sinusoidal input voltage, and under worst-case conditions, the inductor current ripple  $\Delta i_g$  is 20% of the instantaneous low frequency current  $i_g(t)$ .
  - Specify the worst-case values of the peak and rms inductor current, assuming 100% efficiency.
- (c) Determine the worst-case rms currents of the MOSFET and diode, assuming 100% efficiency.
- (d) Specify the value of  $C$  that leads to a worst-case low-frequency ( $\ll f_s$ ) output voltage peak-peak ripple of 5 V.
- (e) Given the following loss elements

Inductor winding resistance  $0.1 \Omega$

MOSFET on-resistance  $0.4 \Omega$

Diode forward voltage drop  $1.5 \text{ V}$

Switching loss: model as  $i_g^2(t)(0.25 \Omega)$

For a constant 1000 W load, and assuming that the controller operates perfectly as described above, find the rectifier efficiency

- at an ac input voltage of 90 V rms
- at an ac input voltage of 270 V rms

18.11

The flyback converter shown in Fig. 18.46 operates in the continuous conduction mode. The MOSFET

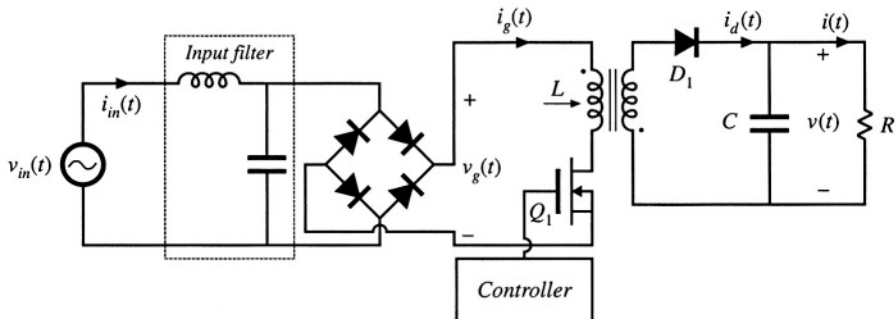


**Fig. 18.46** Low-harmonic rectifier system based on the CCM flyback converter, Problem 18.11.

has on-resistance  $R_{on}$ , and diode  $D_1$  has a constant forward voltage drop  $V_D$ . All other loss elements can

be neglected. The turns ratio of the flyback transformer is 1:1. The controller varies the duty cycle such that  $\langle i_g(t) \rangle_{T_p}$  is equal to  $v_g(t)/R_e$ , where  $R_e$  is the emulated resistance. The input voltage is  $v_{in}(t) = V_M \sin(\omega t)$ . The input filter removes the switching harmonics from the input current  $i_g(t)$ , but has negligible effect on the low-frequency components of the converter waveforms.

- (a) Derive an expression for the rectifier efficiency, in terms of  $V_M$ ,  $V$ ,  $V_D$ ,  $R_{on}$ , and  $R_e$ .
- (b) Given the following values, find the value of MOSFET on-resistance which leads to an efficiency of 96%.

rms input voltage	120 V
DC output voltage	120V
Diode $D_1$ forward voltage drop	1.5V
Load power	200 W

**18.12** Derive an expression for the emulated resistance  $R_e(V_{g,rms}, R_s, k_v, v_{control})$  of the average-current-controlled boost rectifier with ac line voltage feedforward, Fig. 18.14.

**18.13** Derive the CPM boost rectifier static input characteristics, Eq. (18.57).

**18.14** The boost rectifier system of Fig. 18.47 employs average current control with ac line voltage feedforward.

The ac line frequency is 50 Hz. The rectifier drives a constant-power load of 500 W. The pulse-width modulator contains a ramp having a peak-to-peak amplitude of 3 V. There is no compensator in the inner wide-bandwidth average current control feedback loop. The average current sensing circuit has gain

$$\frac{v_a(s)}{i_g(s)} = \frac{R_s}{\left(1 + \frac{s}{\omega_0}\right)}$$

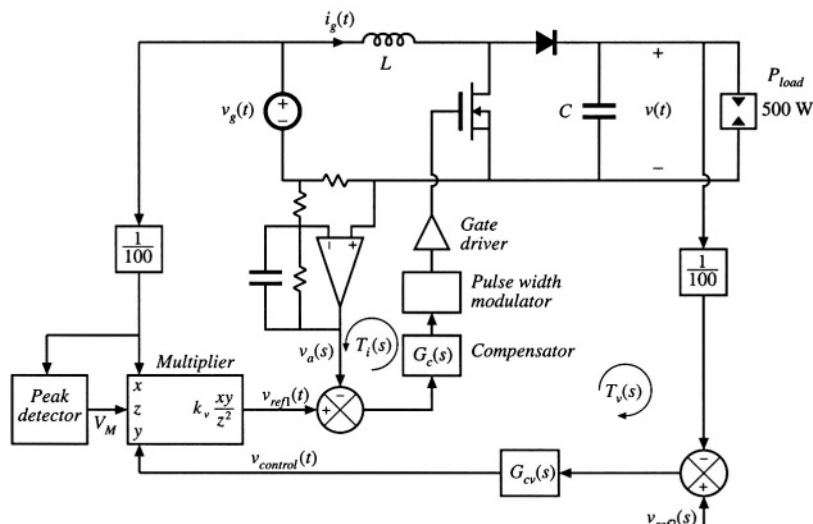


**Fig. 18.47** Average current controlled boost rectifier with input voltage feedforward, Problem 18.14.

Other converter parameter values are

$$f_s = 100 \text{ kHz}$$

$$L = 2.5 \text{ mH}$$

$$f_0 = \frac{\omega_0}{2\pi} = 10 \text{ kHz}$$

$$R_s = 1 \Omega$$

$$V = 385 \text{ V}$$

$$V_{g,rms} = 230 \text{ V}$$

- (a) Construct the magnitude and phase Bode diagrams of the loop gain  $T_i(s)$  of the average-current-control loop. Label important features.
- (b) Determine numerical values of the crossover frequency and phase margin of  $T_i(s)$ .

The outer low-bandwidth feedback loop has loop gain  $T_v(s)$ . The compensator of this loop has constant gain  $G_{cv}(s) = 330$ . The multiplier gain is  $k_v = 2$ . The capacitor value is  $C = 680 \mu\text{F}$ . The reference voltage  $v_{ref2}(t)$  is 3.85 V.

- (c) Determine the peak magnitude of the output 100 Hz voltage ripple.
- (d) Determine the quiescent control voltage  $V_{control}$ .
- (e) Construct the magnitude and phase Bode diagrams of the loop gain  $T_v(s)$  of the outer feedback loop. Label important features.
- (f) Determine numerical values of the crossover frequency and phase margin of  $T_v(s)$ .

**18.15** A critical conduction mode controller causes a boost rectifier to exhibit an ac input current waveform similar to Fig. 18.19(b). The ac input voltage is 120 Vrms at 60 Hz. The rectifier supplies 225 Vdc to a 120 W load. The boost converter inductance is  $L = 600 \mu\text{H}$ .

- (a) Determine the emulated resistance  $R_e$ .
- (b) Write the numerical expression for the converter switching frequency  $f_s$ , as a function of  $t_{on}$  and the applied terminal voltages. Sketch  $f_s$  vs. time.
- (c) What is the maximum switching frequency? What is the minimum switching frequency?
- (d) Derive an analytical expression for the rms transistor current for this control method, as a function of the magnitude of the sinusoidal line current. Compare the rms transistor current of this approach with a CCM boost rectifier having negligible current switching ripple.

# **Part V**

*Resonant Converters*

---

# 19

## Resonant Conversion

---

Part V of this text deals with a class of converters whose operation differs significantly from the PWM converters covered in Parts I to IV. *Resonant power converters* [1–36] contain resonant  $L-C$  networks whose voltage and current waveforms vary sinusoidally during one or more subintervals of each switching period. These sinusoidal variations are large in magnitude, and hence the small ripple approximation introduced in Chapter 2 does not apply.

Dc-to-high-frequency-ac inverters are required in a variety of applications, including electronic ballasts for gas discharge lamps [3,4], induction heating, and electrosurgical generators. These applications typically require generation of a sinusoid of tens or hundreds of kHz, having moderate or low total harmonic distortion. A simple resonant inverter system is illustrated in Fig. 19.1(a). A switch network produces a square wave voltage  $v_s(t)$ . As illustrated in Fig. 19.2, the spectrum of  $v_s(t)$  contains fundamental plus odd harmonics. This voltage is applied to the input terminals of a resonant tank network. The tank network resonant frequency  $f_0$  is tuned to the fundamental component of  $v_s(t)$ , that is, to the switching frequency  $f_s$ , and the tank exhibits negligible response at the harmonics of  $f_s$ . In consequence, the tank current  $i_s(t)$ , as well as the load voltage  $v(t)$  and load current  $i(t)$ , have essentially sinusoidal waveforms of frequency  $f_s$ , with negligible harmonics. By changing the switching frequency  $f_s$  (closer to or further from the resonant frequency  $f_0$ ), the magnitudes of  $i_s(t)$ ,  $v(t)$ , and  $i(t)$  can be controlled. Other schemes for control of the output voltage, such as phase-shift control of the bridge switch network, are also possible. A variety of resonant tank networks can be employed; Fig. 19.1(b) to (d) illustrate the well-known *series*, *parallel*, and *LCC* tank networks. Inverters employing the series resonant tank network are known as the *series resonant*, or *series loaded*, inverter. In the *parallel resonant* or *parallel loaded* inverter, the load voltage is equal to the resonant tank capacitor voltage. The LCC inverter employs tank capacitors both in series and in parallel with the load.

Figure 19.3 illustrates a high-frequency inverter of an electronic ballast for a gas-discharge lamp. A half-bridge configuration of the LCC inverter drives the lamp with an approximately sinusoidal

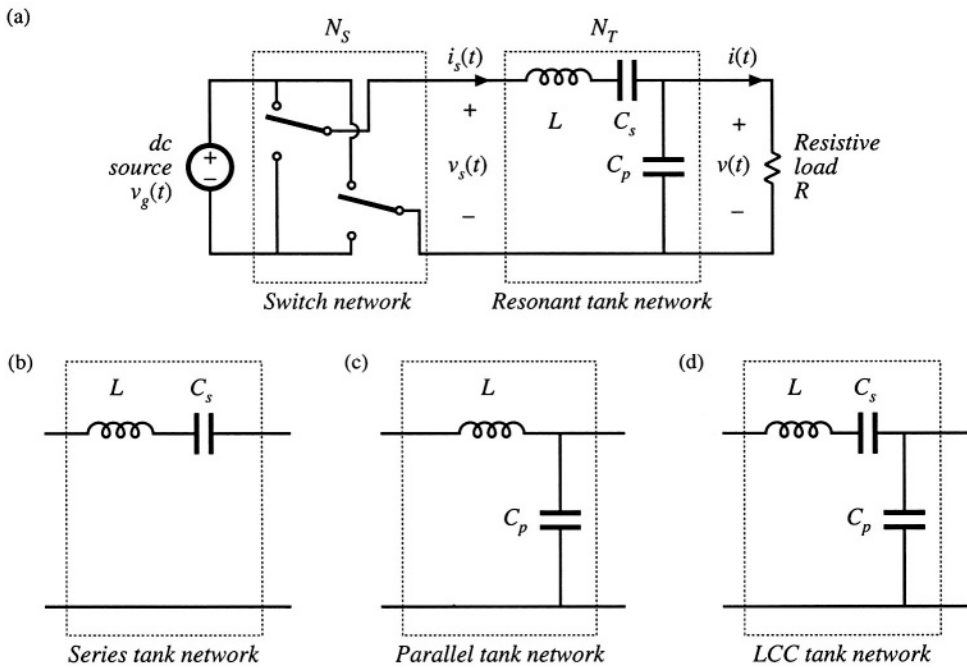


**Fig. 19.1** A basic class of resonant inverters that consist of (a) a switch network  $N_S$  that drives a resonant tank network  $N_T$  near resonance. Several common tank networks: (b) series, (c) parallel, (d) LCC.

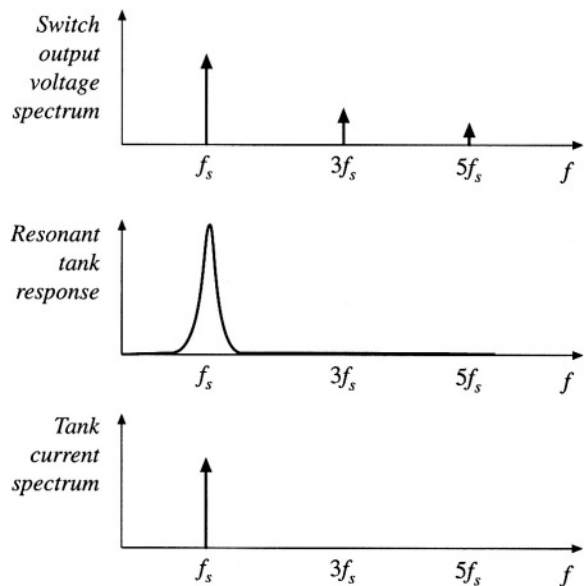


**Fig. 19.2** The tank network responds primarily to the fundamental component of the applied waveforms.

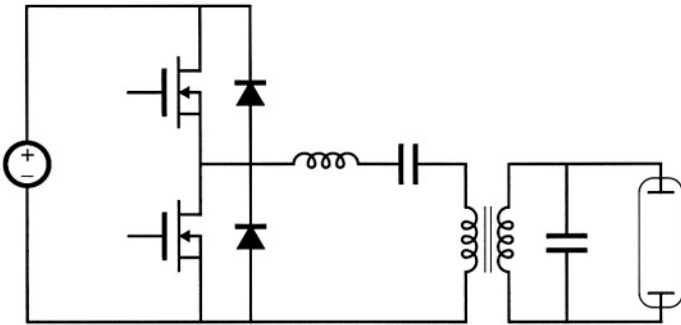


Fig. 19.3 Half-bridge LCC inverter circuit, as an electronic ballast for a gas-discharge lamp.

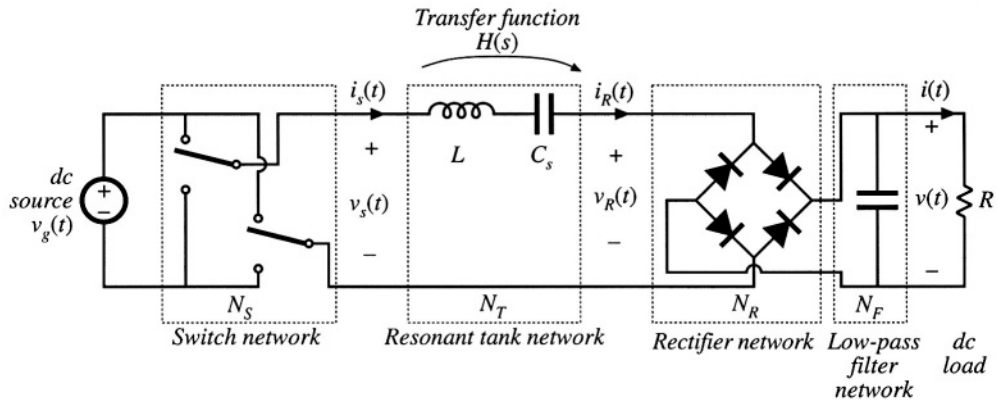
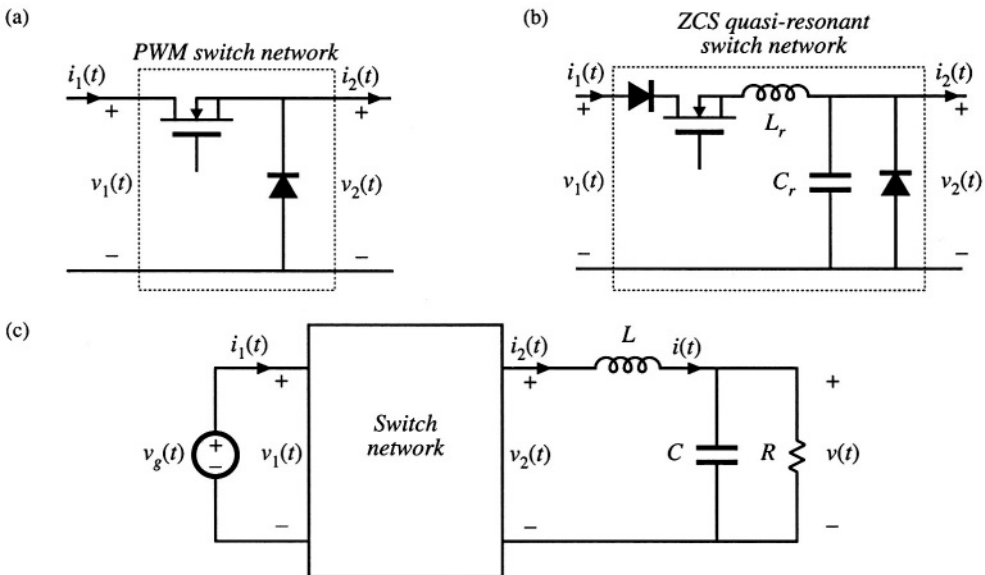


Fig. 19.4 Derivation of a resonant dc-dc converter, by rectification and filtering of the output of a resonant inverter.

high-frequency ac waveform. The converter is controlled to provide a relatively high voltage to start the lamp, and a lower voltage thereafter. When the ballast is powered by the ac utility, a low-harmonic rectifier typically provides the input dc voltage for the inverter.

A resonant dc-dc converter can be constructed by rectifying and filtering the ac output of a resonant inverter. Figure 19.4 illustrates a series-resonant dc-dc converter, in which the approximately sinusoidal resonant tank output current  $i_R(t)$  is rectified by a diode bridge rectifier, and filtered by a large capacitor to supply a dc load having current  $I$  and voltage  $V$ . Again, by variation of the switching frequency  $f_s$  (closer to or further from the resonant frequency  $f_0$ ), the magnitude of the tank current  $i_R(t)$ , and hence also the dc load current  $I$ , can be controlled. Resonant dc-dc converters based on series, parallel, LCC, and other resonant tank networks are well understood. These converters are employed when specialized application requirements justify their use. For example, they are commonly employed in high voltage dc power supplies [5,6], because the substantial leakage inductance and winding capacitance of high-voltage transformers leads unavoidably to a resonant tank network. The same principle can be employed to construct *resonant link* inverters or resonant link cycloconverters [7–9]; controllable switch networks are then employed on both sides of the resonant tank network.

Figure 19.5 illustrates another approach to resonant power conversion, in which resonant ele-



**Fig. 19.5** Derivation of a quasi-resonant converter: (a) conventional PWM switch network, (b) a ZCS quasi-resonant switch network, (c) a quasi-resonant buck converter is obtained by employing a quasi-resonant switch network such as (b) in a buck converter.

ments are inserted into the switch network of an otherwise-PWM converter. A *resonant switch network*, or *quasi-resonant* converter, is then obtained. For example, in Fig. 19.5(b), resonant elements  $L_r$  and  $C_r$  are combined with the switch network transistor and diode. The resonant frequency of these elements is somewhat higher than the switching frequency. This causes the switch network waveforms  $i_1(t)$  and  $v_2(t)$  to become quasi-sinusoidal pulses. The resonant switch network of Fig. 19.5(b) can replace the PWM switch network of Fig. 19.5(a) in nearly any PWM converter. For example, insertion of the resonant switch network of Fig. 19.5(b) into the converter circuit of Fig. 19.5(c) leads to a quasi-resonant buck converter. Numerous resonant switch networks are known, which lead to a large number of resonant switch versions of buck, boost, buck-boost, and other converters. Quasi-resonant converters are described in Chapter 20.

The chief advantage of resonant converters is their reduced switching loss, via mechanisms known as *zero-current switching* (ZCS), and *zero-voltage switching* (ZVS). The turn-on and/or turn-off transitions of the various converter semiconductor elements can occur at zero crossings of the resonant converter quasi-sinusoidal waveforms. This eliminates some of the switching loss mechanisms described in Chapter 4. Hence, switching loss is reduced, and resonant converters can operate at switching frequencies that are higher than in comparable PWM converters. Zero-voltage switching can also eliminate some of the sources of converter-generated electromagnetic interference.

Resonant converters exhibit several disadvantages. Although the resonant element values can be chosen such that good performance with high efficiency is obtained at a single operating point, typically it is difficult to optimize the resonant elements such that good performance is obtained over a wide range of load currents and input voltages. Significant currents may circulate through the tank elements, even when the load is removed, leading to poor efficiency at light load. Also, the quasi-sinusoidal waveforms of resonant converters exhibit greater peak values than those exhibited by the rectangular waveforms of PWM converters, provided that the PWM current spikes due to diode stored charge are ignored. For

these reasons, resonant converters exhibit increased conduction losses, which can offset their reduced switching losses.

In this chapter, the properties of the series, parallel, and other resonant inverters and dc–dc converters are investigated using the *sinusoidal approximation* [3, 10–12]. Harmonics of the switching frequency are neglected, and the tank waveforms are assumed to be purely sinusoidal. This allows simple equivalent circuits to be derived for the bridge inverter, tank, rectifier, and output filter portions of the converter, whose operation can be understood and solved using standard linear ac analysis. This intuitive approach is quite accurate for operation in the continuous conduction mode with a high- $Q$  response, but becomes less accurate when the tank is operated with a low  $Q$ -factor or for operation of dc–dc resonant converters in or near the discontinuous conduction mode.

For dc–dc resonant converters, the important result of this approach is that the dc voltage conversion ratio of a continuous conduction mode resonant converter is given approximately by the ac transfer function of the tank circuit, evaluated at the switching frequency. The tank is loaded by an effective output resistance, having a value nearly equal to the output voltage divided by the output current. It is thus quite easy to determine how the tank components and circuit connections affect the converter behavior. The influence of tank component losses, transformer nonidealities, etc., on the output voltage and converter efficiency can also be found. Several resonant network theorems are presented, which allow the load dependence of conduction loss and of the zero-voltage- or zero-current-switching properties to be explained in a simple and intuitive manner.

It is found that the series resonant converter operates with a step-down voltage conversion ratio. With a 1:1 transformer turns ratio, the dc output voltage is ideally equal to the dc input voltage when the transistor switching frequency is equal to the tank resonant frequency. The output voltage is reduced as the switching frequency is increased or decreased away from resonance. On the other hand, the parallel resonant converter is capable of both step-up and step-down of voltage levels, depending on the switching frequency and the effective tank  $Q$ -factor. The exact steady-state solutions of the ideal series and parallel resonant dc–dc converters are stated in Section 19.5.

Zero-voltage switching and zero-current switching mechanisms of the series resonant converter are described in Section 19.3. In Section 19.4, the dependence of resonant inverter properties on load is examined. A simple frequency-domain approach explains why some resonant converters, over certain ranges of operating points, exhibit large circulating tank currents and low efficiency. The boundaries of zero-voltage switching and zero-current switching are also determined.

It is also possible to modify the PWM converters of the previous chapters, so that zero-current or zero-voltage switching is obtained. A number of diverse approaches are known that lead to *soft switching* in buck, boost, forward, flyback, bridge, and other topologies. Chapter 20 summarizes some of the well-known schemes, including resonant switches, quasi-square wave switches, the full-bridge zero-voltage transition converter, and zero-voltage switching in forward and flyback converters containing active-clamp snubbers. A detailed description of soft-switching mechanisms of diodes, MOSFETs, and IGBTs is also given.

## 19.1 SINUSOIDAL ANALYSIS OF RESONANT CONVERTERS

Consider the class of resonant converters that contain a controlled switch network  $N_s$  that drives a linear resonant tank network  $N_T$ . In a resonant inverter, the tank network drives a resistive load as in Fig. 19.1. The reactive component of the load impedance, if any, can be effectively incorporated into the tank network. In the case of a resonant dc–dc converter, the resonant tank network is connected to an uncontrolled rectifier network  $N_R$ , filter network  $N_F$  and load  $R$ , as illustrated in Fig. 19.4. Many well-known converters can be represented in this form, including the series, parallel, and LCC topologies.

In the most common modes of operation, the controlled switch network produces a square wave voltage output  $v_s(t)$  whose frequency  $f_s$  is close to the tank network resonant frequency  $f_0$ . In response, the tank network rings with approximately sinusoidal waveforms of frequency  $f_s$ . In the case where the resonant tank responds primarily to the fundamental component  $f_s$  of the switch waveform  $v_s(t)$ , and has negligible response at the harmonic frequencies  $n f_s$ ,  $n = 3, 5, 7, \dots$ , then the tank waveforms are well approximated by their fundamental components. As shown in Fig. 19.2, this is indeed the case when the tank network contains a high- $Q$  resonance at or near the switching frequency, and a low-pass characteristic at higher frequencies. Hence, let us neglect harmonics, and compute the relationships between the fundamental components of the tank terminal waveforms  $v_s(t)$ ,  $i_s(t)$ ,  $i_R(t)$ , and  $v_R(t)$ .

### 19.1.1 Controlled Switch Network Model

If the switch network of Fig. 19.6 is controlled to produce a square wave of frequency  $f_s = \omega_s/2\pi$  as in Fig. 19.7, then its output voltage waveform  $v_s(t)$  can be expressed in the Fourier series

$$v_s(t) = \frac{4V_g}{\pi} \sum_{n=1,3,5,\dots} \frac{1}{n} \sin(n\omega_s t) \quad (19.1)$$

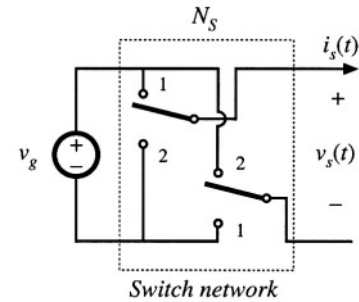
The fundamental component is

$$v_{s1}(t) = \frac{4V_g}{\pi} \sin(\omega_s t) = V_{s1} \sin(\omega_s t) \quad (19.2)$$

which has a peak amplitude of  $(4/\pi)$  times the dc input voltage  $V_g$ , and is in phase with the original square wave  $v_s(t)$ . Hence, the switch network output terminal is modeled as a sinusoidal voltage generator,  $v_{s1}(t)$ .

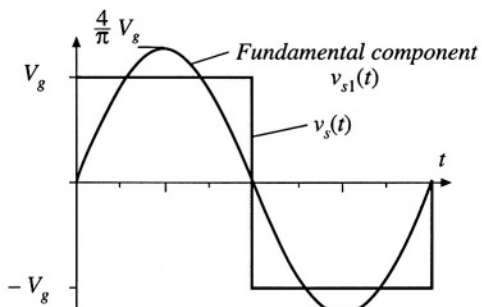
It is also of interest to model the converter dc input port. This requires computation of the dc component  $I_g$  of the switch input current  $i_g(t)$ . The switch input current  $i_g(t)$  is equal to the output current  $i_s(t)$  when the switches are in position 1, and its inverse  $-i_s(t)$  when the switches are in position 2. Under the conditions described above, the tank rings sinusoidally and  $i_s(t)$  is well approximated by a sinusoid of some peak amplitude  $I_{s1}$  and phase  $\varphi_s$ :

$$i_s(t) \approx I_{s1} \sin(\omega_s t - \varphi_s) \quad (19.3)$$



**Fig. 19.6** An ideal switch network.

**Fig. 19.7** Switch network output voltage  $v_s(t)$  and its fundamental component  $v_{s1}(t)$ .



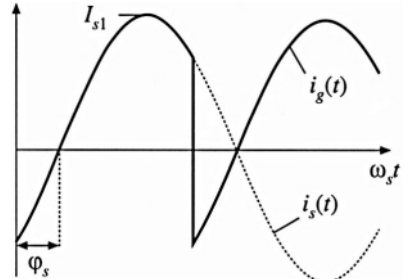


**Fig. 19.8** Switch network waveforms  $i_s(t)$  and  $i_g(t)$ .

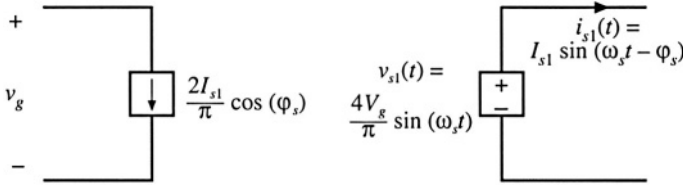


**Fig. 19.9** An equivalent circuit for the switch network, which models the fundamental component of the output voltage waveform and the dc component of the input current waveform.

The input current waveform is shown in Fig. 19.8.

The dc component, or average value, of the input current can be found by averaging  $i_g(t)$  over one half switching period:

$$\begin{aligned}\langle i_g(t) \rangle_{T_s} &= \frac{2}{T_s} \int_0^{T_s/2} i_g(\tau) d\tau \\ &\approx \frac{2}{T_s} \int_0^{T_s/2} I_{s1} \sin(\omega_s \tau - \varphi_s) d\tau \\ &= \frac{2}{\pi} I_{s1} \cos(\varphi_s)\end{aligned}\quad (19.4)$$

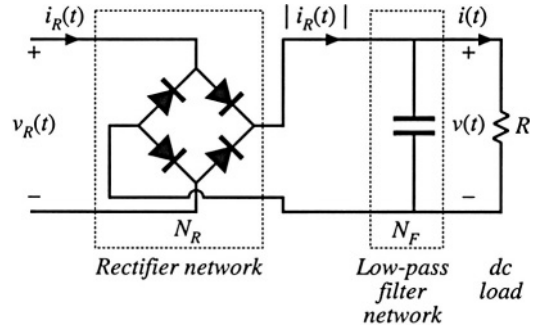
Thus, the dc component of the converter input current depends directly on the peak amplitude of the tank input current  $I_{s1}$  and on the cosine of its phase shift  $\varphi_s$ .

An equivalent circuit for the switch is given in Fig. 19.9. This circuit models the basic energy conversion properties of the switch: the dc power supplied by the voltage source  $V_g$  is converted into ac power at the switch output. Note that the dc power at the source is the product of  $V_g$  and the dc component of  $i_g(t)$ , and the ac power at the switch is the average of  $v_s(t)i_g(t)$ . Furthermore, if the harmonics of  $v_s(t)$  are negligible, then the switch output voltage can be represented by its fundamental component, a sinusoid  $v_{s1}(t)$  of peak amplitude  $4V_g/\pi$ . It can be verified that the switch network dc input power and fundamental average output power, predicted by Fig. 19.9, are equal.

### 19.1.2 Modeling the Rectifier and Capacitive Filter Networks

In the series resonant dc–dc converter, the output rectifier is driven by the nearly sinusoidal tank output current  $i_R(t)$ . A large capacitor  $C_F$  is placed at the dc output, so that the output voltage  $v(t)$  contains negligible harmonics of the switching frequency  $f_s$ , as shown in Fig. 19.10. Hence, we can make the small-rip-

**Fig. 19.10** Uncontrolled rectifier with capacitive filter network, as in the series resonant converter.



ple approximation as usual:  $v(t) \approx V$ ,  $i(t) \approx I$ . The diode rectifiers switch when  $i_R(t)$  passes through zero, as shown in Fig. 19.11. The rectifier input voltage  $v_R(t)$  is essentially a square wave, equal to  $+v(t)$  when  $i_R(t)$  is positive and  $-v(t)$  when  $i_R(t)$  is negative. Note that  $v_R(t)$  is in phase with  $i_R(t)$ .

If the tank output current  $i_R(t)$  is a sinusoid with peak amplitude  $I_{R1}$  and phase shift  $\varphi_R$ :

$$i_R(t) = I_{R1} \sin(\omega_s t - \varphi_R) \quad (19.5)$$

then the rectifier input voltage may be expressed in the Fourier series

$$v_R(t) = \frac{4V}{\pi} \sum_{n=1,3,5,\dots}^{\infty} \frac{1}{n} \sin(n\omega_s t - \varphi_R) \quad (19.6)$$

where  $\varphi_R$  is the phase shift of  $i_R(t)$ , with respect to  $v_s(t)$ . This voltage waveform is impressed on the output port of the resonant tank network. Again, if the tank network responds primarily to the fundamental component ( $f_s$ ) of  $v_R(t)$ , and has negligible response at the harmonic frequencies  $nf_s$ ,  $n = 3, 5, 7, \dots$ , then the harmonics of  $v_R(t)$  can be ignored. The voltage waveform  $v_R(t)$  is then well approximated by its fundamental component  $v_{R1}(t)$ :

$$v_{R1}(t) = \frac{4V}{\pi} \sin(\omega_s t - \varphi_R) = V_{R1} \sin(\omega_s t - \varphi_R) \quad (19.7)$$

The fundamental voltage component  $v_{R1}(t)$  has a peak value of  $(4/\pi)$  times the dc output voltage  $V$ , and is in phase with the current  $i_R(t)$ .

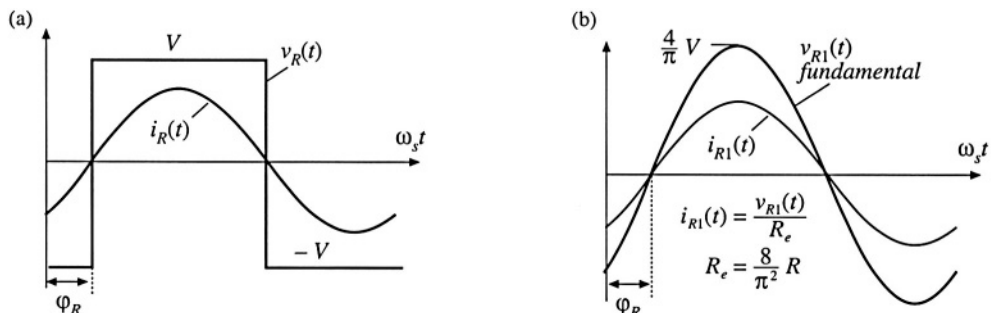


**Fig. 19.11** Rectifier network input terminal waveforms: (a) actual waveforms  $v_R(t)$  and  $i_R(t)$ , (b) fundamental components  $v_{R1}(t)$  and  $i_{R1}(t)$ .

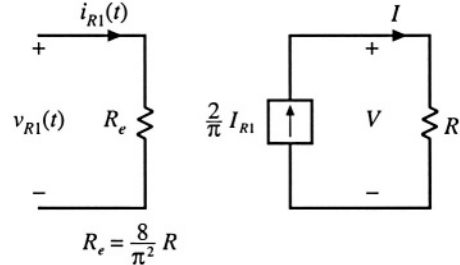


**Fig. 19.12** An equivalent circuit for the rectifier and filter network, which models the fundamental components of the rectifier ac input waveforms and the dc components of the load waveforms. The rectifier presents an effective resistive load  $R_e$  to the tank network.

The rectified tank output current,  $|i_R(t)|$ , is filtered by capacitor  $C_F$ . Since no dc current can pass through  $C_F$ , the dc component of  $|i_R(t)|$  must be equal to the steady-state load current  $I$ . By equating dc components we obtain:

$$\begin{aligned} I &= \frac{2}{T_S} \int_0^{T_S/2} I_{R1} |\sin(\omega_s t - \varphi_R)| dt \\ &= \frac{2}{\pi} I_{R1} \end{aligned} \quad (19.8)$$

Therefore, the load current and the tank output current amplitudes are directly related in steady state.

Since  $v_{R1}(t)$ , the fundamental component of  $v_R(t)$ , is in phase with  $i_R(t)$ , the rectifier presents an effective resistive load  $R_e$  to the tank circuit. The value of  $R_e$  is equal to the ratio of  $v_{R1}(t)$  to  $i_R(t)$ . Division of Eq. (19.7) by Eq. (19.5), and elimination of  $I_{R1}$  using Eq. (19.8) yields

$$R_e = \frac{v_{R1}(t)}{i_R(t)} = \frac{8}{\pi^2} \frac{V}{I} \quad (19.9)$$

With a resistive load  $R$  equal to  $V/I$ , this equation reduces to

$$R_e = \frac{8}{\pi^2} R = 0.8106R \quad (19.10)$$

Thus, the tank network is damped by an effective load resistance  $R_e$  equal to 81% of the actual load resistance  $R$ . An equivalent circuit that models the rectifier network input port fundamental components and output port dc components is given in Fig. 19.12.

### 19.1.3 Resonant Tank Network

We have postulated that the effects of harmonics can be neglected, and we have consequently shown that the bridge can be modeled as a fundamental voltage source  $v_{s1}(t)$ . In the case of a dc-dc converter, the rectifier can be modeled using an effective resistor of value  $R_e$ . We can now solve the resonant tank network by standard linear analysis.

As shown in Fig. 19.13, the tank circuit is a linear network with the following voltage transfer function:

$$\frac{v_{R1}(s)}{v_{s1}(s)} = H(s) \quad (19.11)$$

Hence, the ratio  $V_{R1}/V_{s1}$  of the peak magnitudes of  $v_{R1}(t)$  and  $v_{s1}(t)$  is given by:

$$\frac{V_{R1}}{V_{s1}} = \|H(s)\|_{s=j\omega_s} \quad (19.12)$$

In addition,  $i_R(s)$  is given by:

$$i_R(s) = \frac{v_{R1}(s)}{R_e} = \frac{H(s)}{R_e} v_{s1}(s) \quad (19.13)$$

So the peak magnitude of  $i_R(t)$  is:

$$I_{R1} = \frac{\|H(s)\|_{s=j\omega_s}}{R_e} V_{s1} \quad (19.14)$$

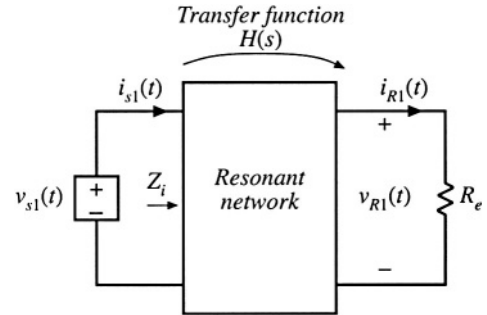


**Fig. 19.13** The linear tank network, excited by an effective sinusoidal input source and driving an effective resistive load.

Thus, the magnitude of the tank transfer function is found, with an effective resistive load.

#### 19.1.4 Solution of Converter Voltage Conversion Ratio $M = V/V_g$

An equivalent circuit of a complete dc–dc resonant converter is depicted in Fig. 19.14. The voltage conversion ratio of the resonant converter can now be found:

$$M = \frac{V}{V_g} = \underbrace{(R)}_{\left(\frac{V}{I}\right)} \underbrace{\left(\frac{2}{\pi}\right)}_{\left(\frac{I}{I_{R1}}\right)} \underbrace{\left(\frac{1}{R_e}\right)}_{\left(\frac{V_{R1}}{V_{s1}}\right)} \underbrace{\left(\|H(s)\|_{s=j\omega_s}\right)}_{\left(\frac{4}{\pi}\right)} \underbrace{\left(\frac{4}{\pi}\right)}_{\left(\frac{V_{s1}}{V_g}\right)} \quad (19.15)$$

Simplification by use of Eq. (19.10) yields:

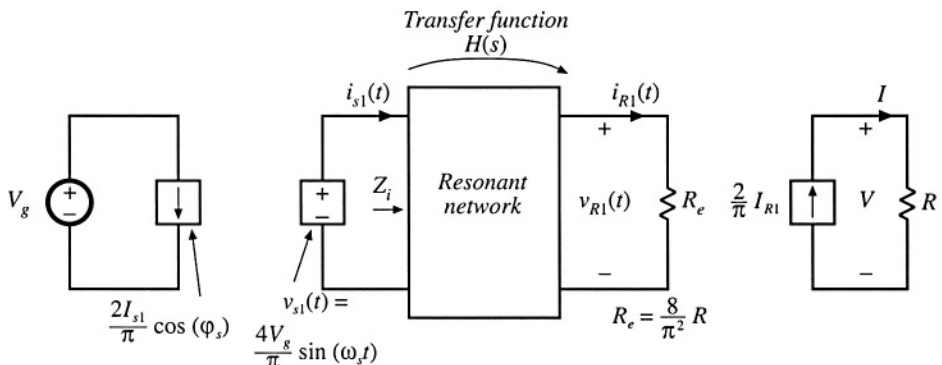


**Fig. 19.14** Steady-state equivalent circuit that models the dc and fundamental components of resonant converter waveforms.

$$\frac{V}{V_g} = |H(s)|_{s=j\omega_s} \quad (19.16)$$

Equation (19.16) is the desired result. It states that the dc conversion ratio of the resonant converter is approximately the same as the ac transfer function of the resonant tank circuit, evaluated at the switching frequency  $f_s$ . This intuitive result can be applied to converters with many different types of tank circuits. However, it should be reemphasized that Eq. (19.16) is valid only if the response of the tank circuit to the harmonics of  $v_s(t)$  is negligible compared to the fundamental response, an assumption that is not always justified. In addition, we have assumed that the switch network is controlled to produce a square wave and that the rectifier network drives a capacitive-type filter network. Finally, the transfer function  $H(s)$  is evaluated using the effective load resistance  $R_e$  given by Eq. (19.9).

## 19.2 EXAMPLES

### 19.2.1 Series Resonant DC–DC Converter Example

The series resonant converter with switching frequency control is shown in Fig. 19.4. Current-bidirectional two-quadrant switches are necessary. For this circuit, the tank network consists of a series  $L$ – $C$  circuit, and Fig. 19.14 can be redrawn as in Fig. 19.15. The transfer function  $H(s)$  is therefore:

$$\begin{aligned} H(s) &= \frac{R_e}{Z_i(s)} = \frac{R_e}{R_e + sL + \frac{1}{sC}} \\ &= \frac{\left(\frac{s}{Q_e \omega_0}\right)}{1 + \left(\frac{s}{Q_e \omega_0}\right) + \left(\frac{s}{\omega_0}\right)^2} \end{aligned} \quad (19.17)$$

where

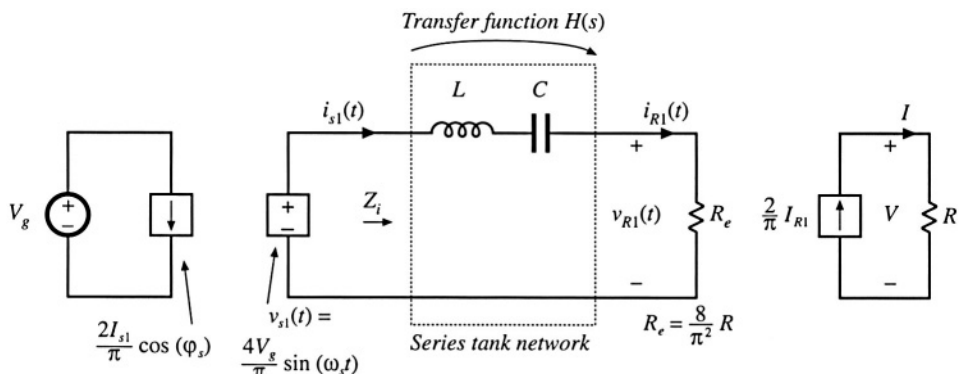


Fig. 19.15 Steady-state equivalent circuit of the series resonant converter.

$$\begin{aligned}\omega_0 &= \frac{1}{\sqrt{LC}} = 2\pi f_0 \\ R_0 &= \sqrt{\frac{L}{C}} \\ Q_e &= \frac{R_0}{R_e}\end{aligned}$$

The magnitude of  $H(j\omega_s)$ , which coincides with the converter dc conversion ratio  $M = V/V_g$ , is

$$M = \|H(j\omega_s)\| = \frac{1}{\sqrt{1 + Q_e^2 \left(\frac{1}{F} - F\right)^2}} \quad (19.18)$$

where

$$F = f_s/f_0 \quad (19.19)$$

The Bode diagrams of  $Z_i(s)$  and  $H(s)$  are constructed in Fig. 19.16, using the graphical construction method of Chapter 8. The series resonant impedance  $Z_i(s)$  is dominated by the capacitor  $C$  at low frequency, and by the inductor  $L$  at high frequency. At the resonant frequency  $f_0$ , the impedances of the inductor and capacitor are equal in magnitude and opposite in phase; hence, they cancel. The series resonant impedance  $Z_i(s)$  is equal to  $R_e$  at  $f = f_0$ .

The transfer function  $\|H(j\omega)\|$  is constructed graphically, by division of  $R_e$  by the  $\|Z_i\|$  asymptotes of Fig. 19.16. At resonance, one obtains  $\|H\| = R_e/R_e = 1$ . At frequencies above or below the resonant frequency,  $\|Z_i\| > R_e$  and hence  $\|H\| < 1$ . So the conversion ratio  $M$  is less than or equal to 1. It can also be seen that a decrease in the load resistance  $R$ , which increases the effective quality factor  $Q_e$ , causes a more peaked response in the vicinity of resonance. Exact characteristics of the series resonant converter are plotted in Fig. 19.45.

Over what range of switching frequencies is Eq. (19.18) accurate? The response of the tank to the fundamental component of  $v_s(t)$  must be sufficiently greater than the response to the harmonics of  $v_s(t)$ . This is certainly true for operation above resonance because  $H(s)$  contains a bandpass characteristic that decreases with a single pole slope for  $f_s > f_0$ . For the same reason, Eq. (19.18) is valid when the switching frequency is below but near resonance.

However, for switching frequencies  $f_s$  much less than the resonant frequency  $f_0$ , the sinusoidal approximation breaks down completely because the tank responds more strongly to the harmonics of

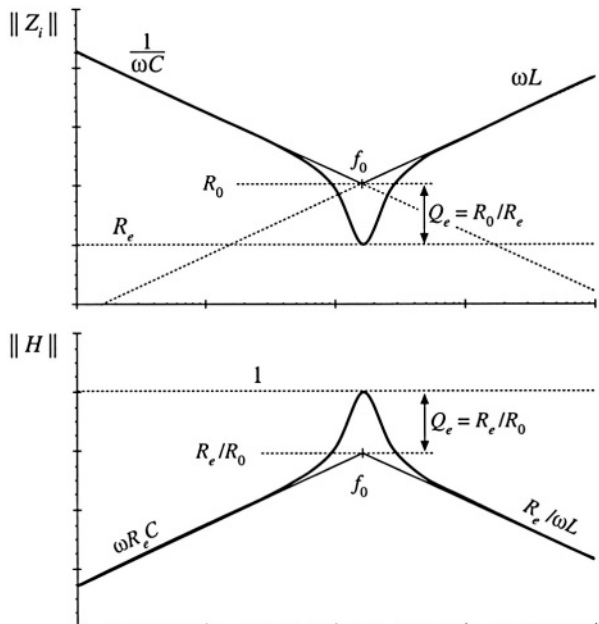


**Fig. 19.16** Construction of the Bode diagrams of  $Z_i(s)$  and  $H(s)$  for the series resonant converter.

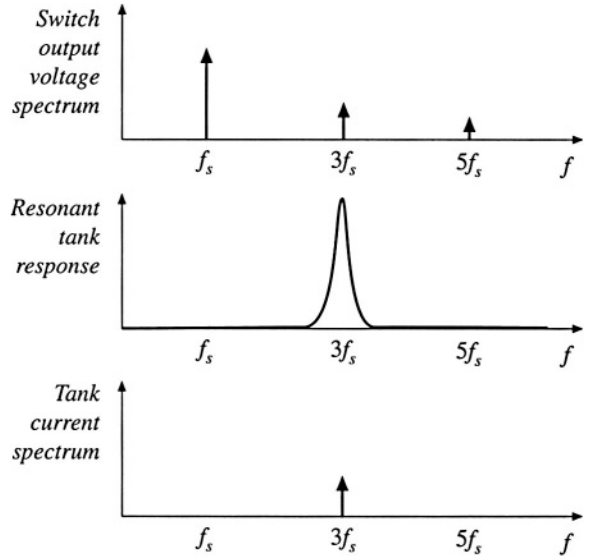


**Fig. 19.17** Excitation of the tank network by the third harmonic of the switching frequency.

$v_s(t)$  than to its fundamental. For example, at  $f_s = f_0/3$ , the third harmonic of  $v_s(t)$  is equal to  $f_0$  and directly excites the tank resonance. Some other type of analysis must be used to understand what happens at these lower frequencies. Also, in the low- $Q$  case, the approximation is less accurate because the filter response is less peaked, and hence does not favor the fundamental component as strongly. As shown in a later section, discontinuous conduction modes may then occur whose waveforms are highly nonsinusoidal.

### 19.2.2 Subharmonic Modes of the Series Resonant Converter

If the  $n^{\text{th}}$  harmonic of the switch output waveform  $v_s(t)$  is close to the resonant tank frequency,  $nf_s \sim f_0$ , and if the tank effective quality factor  $Q_e$  is sufficiently large, then as illustrated in Fig. 19.17, the tank responds primarily to harmonic  $n$ . All other components of the tank waveforms can then be neglected, and it is a good approximation to replace  $v_s(t)$  with its  $n^{\text{th}}$  harmonic component:

$$v_s(t) \approx v_{sn}(t) = \frac{4V_s}{n\pi} \sin(n\omega_s t) \quad (19.20)$$

This expression differs from Eq. (19.2) because the amplitude is reduced by a factor of  $1/n$ , and the fre-

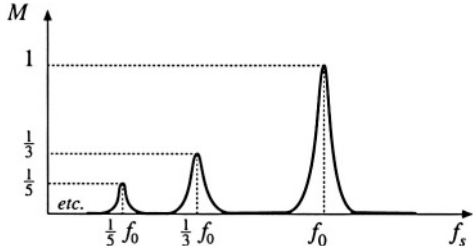


**Fig. 19.18** The subharmonic modes of the series resonant converter. These modes occur when the harmonics of the switching frequency excite the tank resonance.

quency is  $n f_s$  rather than  $f_s$ .

The arguments used to model the tank and rectifier/filter networks are unchanged from Section 19.1. The rectifier presents an effective resistive load to the tank, of value  $R_e = 8R/\pi^2$ . In consequence, the converter dc conversion ratio is given by

$$M = \frac{V}{V_g} = \frac{\|H(jn\omega_s)\|}{n} \quad (19.21)$$

This is a good approximation provided that  $n f_s$  is close to  $f_0$ , and that  $Q_e$  is sufficiently large. Typical characteristics are sketched in Fig. 19.18.

The series resonant converter is not generally designed to operate in a subharmonic mode, since the fundamental modes yield greater output voltage and power, and hence higher efficiency. Nonetheless, the system designer should be aware of their existence, because inadvertent operation in these modes can lead to large signal instabilities.

### 19.2.3 Parallel Resonant DC-DC Converter Example

The parallel resonant dc-dc converter is diagrammed in Fig. 19.19. It differs from the series resonant converter in two ways. First, the tank capacitor appears in parallel with the rectifier network rather than in series: this causes the tank transfer function  $H(s)$  to have a different form. Second, the rectifier drives an inductive-input low-pass filter. In consequence, the value of the effective resistance  $R_e$  differs from that of the rectifier with a capacitive filter. Nonetheless, sinusoidal approximations can be used to understand the operation of the parallel resonant converter.

As in the series resonant converter, the switch network is controlled to produce a square wave  $v_s(t)$ . If the tank network responds primarily to the fundamental component of  $v_s(t)$ , then arguments identical to those of Section 19.1 can be used to model the output fundamental components and input dc components of the switch waveforms. The resulting equivalent circuit is identical to Fig. 19.9.

The uncontrolled rectifier with inductive filter network can be described using the dual of the arguments of Section 19.1.2. In the parallel resonant converter, the output rectifiers are driven by the nearly sinusoidal tank capacitor voltage  $v_R(t)$ , and the diode rectifiers switch when  $v_R(t)$  passes through zero as in Fig. 19.20. If the filter inductor current ripple is small, then in steady-state the filter inductor current is essentially equal to the dc load current  $I$ . The rectifier input current  $i_R(t)$  is therefore a square wave of amplitude  $I$ , and is in phase with the tank capacitor voltage  $v_R(t)$ :

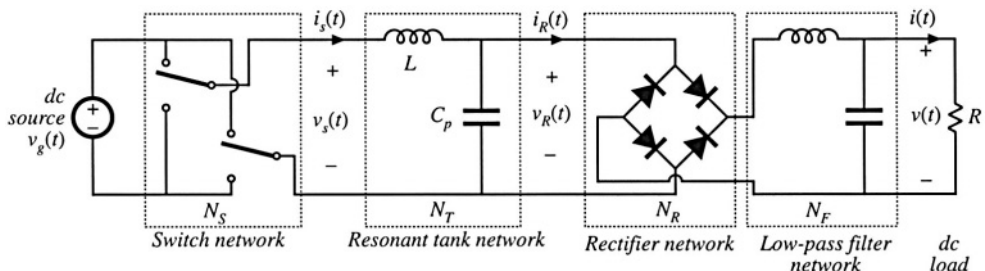
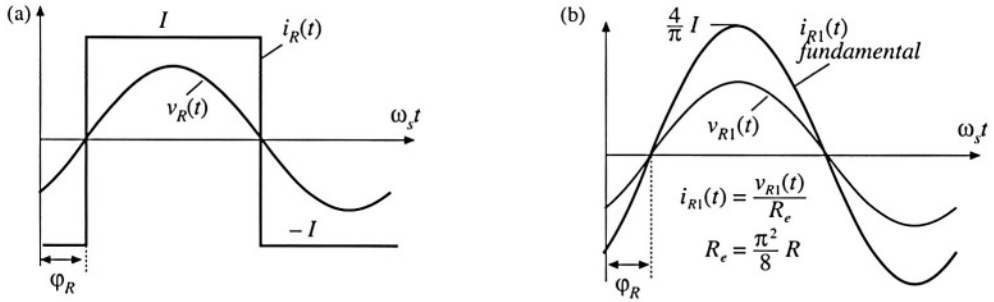


Fig. 19.19 Block diagram of the parallel resonant converter.



**Fig. 19.20** Rectifier network input terminal waveforms, for the parallel resonant converter: (a) actual waveforms  $v_R(t)$  and  $i_R(t)$ , (b) fundamental components  $v_{R1}(t)$  and  $i_{R1}(t)$ .

$$i_R(t) = \frac{4I}{\pi} \sum_{n=1,3,5,\dots}^{\infty} \frac{1}{n} \sin(n\omega_s t - \varphi_R) \quad (19.22)$$

where  $\varphi_R$  is the phase shift of  $v_R(t)$ .

The fundamental component of  $i_R(t)$  is

$$i_{R1}(t) = \frac{4I}{\pi} \sin(\omega_s t - \varphi_R) \quad (19.23)$$

Hence, the rectifier again presents an effective resistive load to the tank circuit, equal to

$$R_e = \frac{v_{R1}(t)}{i_{R1}(t)} = \frac{\pi V_{R1}}{4I} \quad (19.24)$$

The ac components of the rectified tank capacitor voltage  $|v_R(t)|$  are removed by the output low pass filter. In steady state, the output voltage  $V$  is equal to the dc component of  $|v_R(t)|$ :

$$V = \frac{2}{T_S} \int_0^{T_S/2} V_{R1} |\sin(\omega_s t - \varphi_R)| dt = \frac{2}{\pi} V_{R1} \quad (19.25)$$

So the load voltage  $V$  and the tank capacitor voltage amplitude are directly related in steady state. Substitution of Eq. (19.25) and resistive load characteristics  $V = IR$  into Eq. (19.24) yields:

$$R_e = \frac{\pi^2}{8} R = 1.2337R \quad (19.26)$$

An equivalent circuit for the uncontrolled rectifier with inductive filter network is given in Fig. 19.21. This model is similar to the one used for the series resonant converter, Fig. 19.12, except that the roles of the rectifier input voltage  $v_R(t)$  and current  $i_R(t)$  are interchanged, and the effective resistance  $R_e$  has a different value. The model for the complete converter is given in Fig. 19.22.

Solution of Fig. 19.22 yields the converter dc conversion ratio:

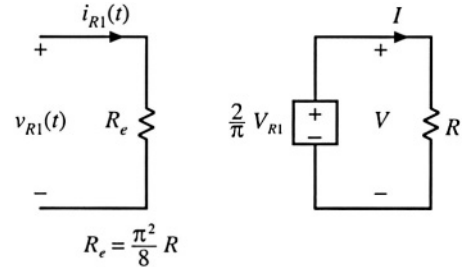


**Fig. 19.21** An equivalent circuit for the rectifier and inductive filter network of the parallel resonant converter, which models the fundamental components of the rectifier ac input waveforms and the dc components of the load waveforms.

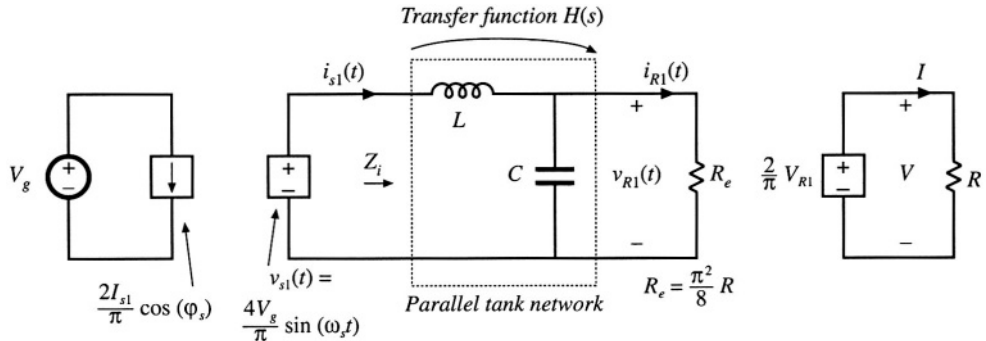


Fig. 19.22 Equivalent circuit for the parallel resonant converter, which models the fundamental components of the tank waveforms, and the dc components of the converter input current and output voltage.

$$M = \frac{V}{V_g} = \frac{8}{\pi^2} |H(s)|_{s=j\omega_s} \quad (19.27)$$

where  $H(s)$  is the tank transfer function

$$H(s) = \frac{Z_o(s)}{sL} \quad (19.28)$$

and

$$Z_o(s) = sL \parallel \frac{1}{sC} \parallel R_e \quad (19.29)$$

The Bode magnitude diagrams of  $H(s)$  and  $Z_o(s)$  are constructed in Fig. 19.23, using the graphical construction method of Chapter 8. The impedance  $Z_o(s)$  is the parallel combination of the impedances of the tank inductor  $L$ , capacitor  $C$ , and effective load  $R_e$ . The magnitude asymptote of the parallel combination of these components, at a given frequency, is equal to the smallest of the individual asymptotes  $\omega L$ ,  $1/\omega C$ , and  $R_e$ . Hence, at low frequency where the inductor impedance dominates the parallel combination,  $\|Z_o(s)\| \approx \omega L$ , while at high frequency the capacitor dominates and  $\|Z_o(s)\| \approx 1/\omega C$ . At resonance, the impedances of the inductor and capacitor are equal in magnitude but opposite in phase, so that their effects cancel. The impedance  $\|Z_o(s)\|$  is then equal to  $R_e$ :

$$\|Z_o(s)\|_{s=j\omega_s} = \frac{1}{\frac{1}{j\omega_0 L} + j\omega_0 C + \frac{1}{R_e}} = R_e \quad (19.30)$$

with

$$\omega_0 L = \frac{1}{\omega_0 C} = R_0$$

The dc conversion ratio is therefore

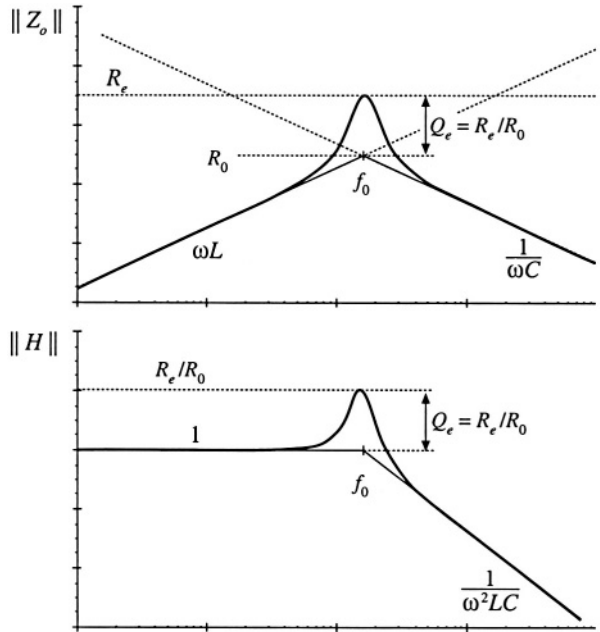


**Fig. 19.23** Construction of Bode diagrams of  $Z_o(s)$  and  $H(s)$  for the parallel resonant converter.

$$\begin{aligned}
 M &= \frac{8}{\pi^2} \left| \frac{Z_o(s)}{sL} \right|_{s=j\omega_s} = \frac{8}{\pi^2} \left| \frac{1}{1 + \frac{s}{Q_e \omega_0} + \left(\frac{s}{\omega_0}\right)^2} \right|_{s=j\omega_s} \\
 &= \frac{8}{\pi^2} \frac{1}{\sqrt{\left(1 - F^2\right)^2 + \left(\frac{F}{Q_e}\right)^2}}
 \end{aligned} \tag{19.31}$$

where  $F = f_s/f_0$ .

At resonance, the conversion ratio is

$$M = \frac{8}{\pi^2} \frac{R_e}{R_0} = \frac{R}{R_0} \tag{19.32}$$

The actual peak value of  $M$  occurs at a switching frequency slightly below the resonant frequency, with peak  $M$  slightly greater than Eq. (19.32). Provided that the load resistance  $R$  is greater than the tank characteristic impedance  $R_e$ , the parallel resonant converter can produce conversion ratios both greater than and less than one. In fact, the ideal parallel resonant converter can produce conversion ratios approaching infinity, provided that the output current is limited to values less than  $V_g/R_0$ . Of course, losses limit the maximum output voltage that can be produced by practical converters.

### 19.3 SOFT SWITCHING

As mentioned previously, the soft-switching phenomena known as zero-current switching (ZCS) and zero-voltage switching (ZVS) can lead to reduced switching loss. When the turn-on and/or turn-off tran-

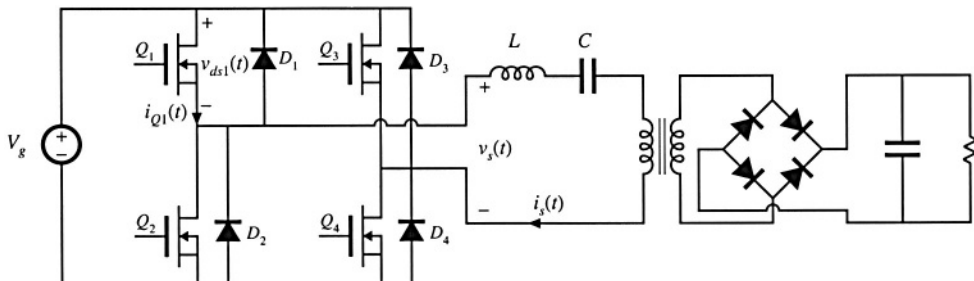


**Fig. 19.24** A series resonant converter incorporating a full-bridge switch network.

sitions of a semiconductor switching device coincide with the zero crossings of the applied waveforms, some of the switching loss mechanisms discussed in Section 4.3 are eliminated. In converters containing MOSFETs and diodes, zero-voltage switching mitigates the switching loss otherwise caused by diode recovered charge and semiconductor output capacitance. Zero-current switching can mitigate the switching loss caused by current tailing in IGBTs and by stray inductances. Zero-current switching can also be used for commutation of SCRs. In the majority of applications, where diode recovered charge and semiconductor output capacitances are the dominant sources of PWM switching loss, zero-voltage switching is preferred.

### 19.3.1 Operation of the Full Bridge Below Resonance: Zero-Current Switching

When the series and parallel resonant inverters and dc-dc converters are operated below resonance, the zero-current switching phenomenon can occur, in which the circuit causes the transistor current to go to zero before the transistor is turned off. Let us consider the operation of the full bridge switch network of the series resonant converter in detail.

A full bridge circuit, realized using power MOSFETs and antiparallel diodes, is shown in Fig. 19.24. The switch output voltage  $v_s(t)$ , and its fundamental component  $v_{s1}(t)$ , as well as the approximately sinusoidal tank current waveform  $i_s(t)$ , are illustrated in Fig. 19.25. At frequencies less than the tank resonant frequency, the input impedance of the series resonant tank network  $Z_i(s)$  is dominated by the tank capacitor impedance [see Fig. 19.16(a)]. Hence, the tank presents an effective capacitive load to the bridge, and switch current  $i_s(t)$  leads the switch voltage fundamental component  $v_{s1}(t)$ , as shown in Fig. 19.25. In consequence, the zero crossing of the current waveform  $i_s(t)$  occurs before the zero crossing of the voltage  $v_s(t)$ .

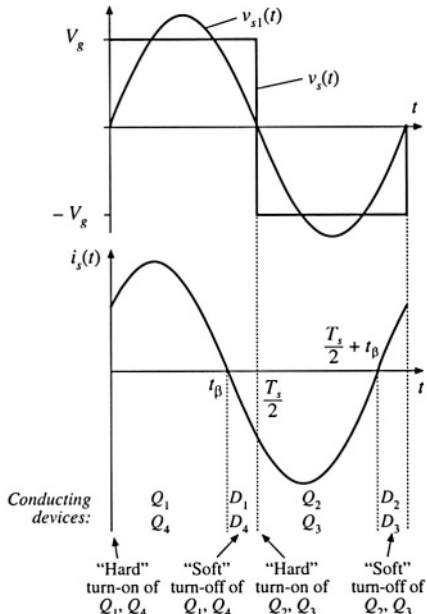


**Fig. 19.25** Switch network output waveforms for the series resonant converter, operated below resonance in the  $k = 1$  CCM. Zero-current switching aids the transistor turn-off process.

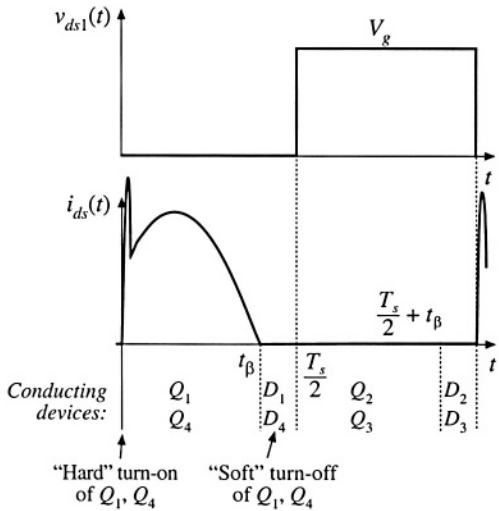


**Fig. 19.26** Transistor  $Q_1$  voltage and current waveforms, for operation of the series resonant converter below resonance in the  $k = 1$  CCM.

For the half cycle  $0 < t < T_s/2$ , the switch voltage  $v_s$  is equal to  $+V_g$ . For  $0 < t < t_\beta$ , the current  $i_s(t)$  is positive and transistors  $Q_1$  and  $Q_4$  conduct. Diodes  $D_1$  and  $D_4$  conduct when  $i_s(t)$  is negative, over the interval  $t_\beta < t < T_s/2$ . The situation during  $T_s/2 < t < T_s$  is symmetrical. Since  $i_{s1}(t)$  leads  $v_{s1}(t)$ , the transistors conduct before their respective antiparallel diodes. Note that, at any given time during the  $D_1$  conduction interval  $t_\beta < t < T_s/2$ , transistor  $Q_1$  can be turned off without incurring switching loss. The circuit naturally causes the transistor turn-off transition to be lossless, and long turn-off switching times can be tolerated.

In general, zero current switching can occur when the resonant tank presents an effective capacitive load to the switches, so that the switch current zero crossings occur before the switch voltage zero crossings. In the bridge configuration, zero current switching is characterized by the half-bridge conduction sequence  $Q_1-D_1-Q_2-D_2$ , such that the transistors are turned off while their respective antiparallel diodes conduct. It is possible, if desired, to replace the transistors with naturally commutated thyristors whenever the zero-current-switching property occurs at the turn-off transition.

The transistor turn-on transition in Fig. 19.26 is similar to that of a PWM switch: it is hard-switched and is not lossless. During the turn-on transition of  $Q_1$ , diode  $D_2$  must turn off. Neither the transistor current nor the transistor voltage is zero,  $Q_1$  passes through a period of high instantaneous power dissipation, and switching loss occurs. As in the PWM case, the reverse recovery current of diode  $D_2$  flows through  $Q_1$ . This current spike can be the largest component of switching loss. In addition, the energy stored in the drain-to-source capacitances of  $Q_1$  and  $Q_2$  and in the depletion layer capacitance of  $D_1$  is lost when  $Q_1$  turns on. These turn-on transition switching loss mechanisms can be a major disadvantage of zero-current-switching schemes. Since zero-current switching does not address the switching loss mechanisms that dominate in MOSFET converters, improvements in efficiency are typically not observed.

### 19.3.2 Operation of the Full Bridge Above Resonance: Zero-Voltage Switching

When the series resonant converter is operated above resonance, the zero-voltage switching phenomenon can occur, in which the circuit causes the transistor voltage to become zero before the controller turns the

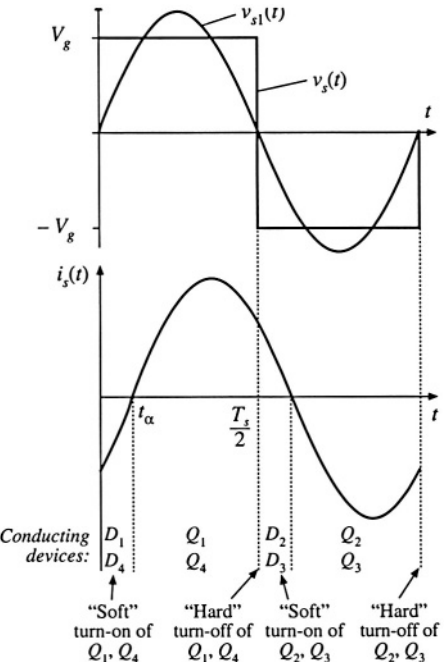


**Fig. 19.27** Switch network output waveforms for the series resonant converter, operated above resonance in the continuous conduction mode. Zero-voltage switching aids the transistor turn-on process.

transistor on. With a minor circuit modification, the transistor turn-off transitions can also be caused to occur at zero voltage. This process can lead to significant reductions in the switching losses of converters based on MOSFETs and diodes.

For the full bridge circuit of Fig. 19.24, the switch output voltage  $v_s(t)$ , and its fundamental component  $v_{s1}(t)$ , as well as the approximately sinusoidal tank current waveform  $i_s(t)$ , are plotted in Fig. 19.27. At frequencies greater than the tank resonant frequency, the input impedance of the tank network  $Z_t(s)$  is dominated by the tank inductor impedance. Hence, the tank presents an effective inductive load to the bridge, and the switch current  $i_s(t)$  lags the switch voltage fundamental component  $v_{s1}(t)$ , as shown in Fig. 19.27. In consequence, the zero crossing of the voltage waveform  $v_s(t)$  occurs before the current waveform  $i_s(t)$ .

For the half cycle  $0 < t < T_s/2$ , the switch voltage  $v_s(t)$  is equal to  $+V_g$ . For  $0 < t < t_\alpha$ , the current  $i_s(t)$  is negative and diodes  $D_1$  and  $D_4$  conduct. Transistors  $Q_1$  and  $Q_4$  conduct when  $i_s(t)$  is positive, over the interval  $t_\alpha < t < T_s/2$ . The waveforms during  $T_s/2 < t < T_s$  are symmetrical. Since the zero crossing of  $v_s(t)$  leads the zero crossing of  $i_s(t)$ , the transistors conduct after their respective antiparallel diodes. Note that, at any given time during the  $D_1$  conduction interval  $0 < t < t_\alpha$ , transistor  $Q_1$  can be turned on without incurring switching loss. The circuit naturally causes the transistor turn-on transition to be lossless, and long turn-on switching times can be tolerated. A particularly significant implication of this is that the switching loss associated with reverse recovery of the antiparallel diodes is avoided. Relatively slow diodes, such as the MOSFET body diodes, can be employed for realization of diodes  $D_1$  to  $D_4$ . In addition, the output capacitances of transistors  $Q_1$  to  $Q_4$  and diodes  $D_1$  to  $D_4$  do not lead to switching loss.

In general, zero-voltage switching can occur when the resonant tank presents an effective inductive load to the switches, and hence the switch voltage zero crossings occur before the switch current zero crossings. In the bridge configuration, zero-voltage switching is characterized by the half-bridge conduction sequence  $D_1-Q_1-D_2-Q_2$ , such that the transistors are turned on while their respective antipar-

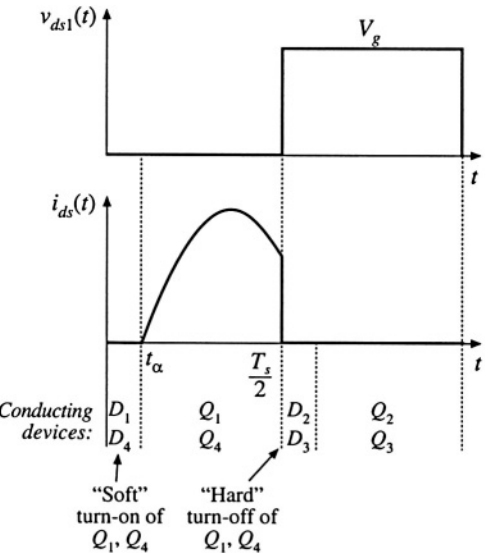


**Fig. 19.28** Transistor  $Q_1$  voltage and current waveforms, for operation of the series resonant converter above resonance in the  $k = 0$  CCM.

allel diodes conduct. Since the transistor voltage is zero during the entire turn on transition, switching loss due to slow turn-on times or due to energy storage in any of the device capacitances does not occur at turn-on.

The transistor turn-off transition in Fig. 19.28 is similar to that of a PWM switch. In converters that employ IGBTs or other minority-carrier devices, significant switching loss may occur at the turn-off transitions. The current tailing phenomenon causes  $Q_1$  to pass through a period of high instantaneous power dissipation, and switching loss occurs.

To assist the transistor turn off process, small capacitors  $C_{leg}$  may be introduced into the legs of the bridge, as demonstrated in Fig. 19.29. In a converter employing MOSFETs, the device output capacitances are sufficient for this purpose, with no need for external discrete capacitors. A delay is also introduced into the gate drive signals, so that there is a short commutation interval when all four transistors are off. During the normal  $Q_1, D_1, Q_2$ , and  $D_2$  conduction intervals, the leg capacitors appear in parallel with the semiconductor switches, and have no effect on the converter operation. However, these capacitors introduce commutation intervals at transistor turn-off. When  $Q_1$  is turned off, the tank current  $i_s(T_s/2)$  flows through the switch capacitances  $C_{leg}$  instead of  $Q_1$ , and the voltage across  $Q_1$  and  $C_{leg}$  increases. Eventually, the voltage across  $Q_1$  reaches  $V_g$ ; diode  $D_2$  then becomes forward-biased. If the MOSFET turn-off time is sufficiently fast, then the MOSFET is switched fully off before the drain voltage rises significantly above zero, and negligible turn-off switching loss is incurred. The energy stored in the device capacitances, that is, in  $C_{leg}$ , is transferred to the tank inductor. The fact that none of the semiconductor device capacitances or stored charges lead to switching loss is the major advantage of zero-voltage switching, and is the most common motivation for its use. MOSFET converters can typically be operated in this manner, using only the internal drain-to-source capacitances. However, other devices such as IGBTs typically require substantial external capacitances to reduce the losses incurred during the IGBT turn-off transitions.

An additional advantage of zero-voltage switching is the reduction of EMI associated with device capacitances. In conventional PWM converters and also, to some extent, in zero-current switching converters, significant high-frequency ringing and current spikes are generated by the rapid charging and discharging of the semiconductor device capacitances during the turn-on and/or turn-off transitions.

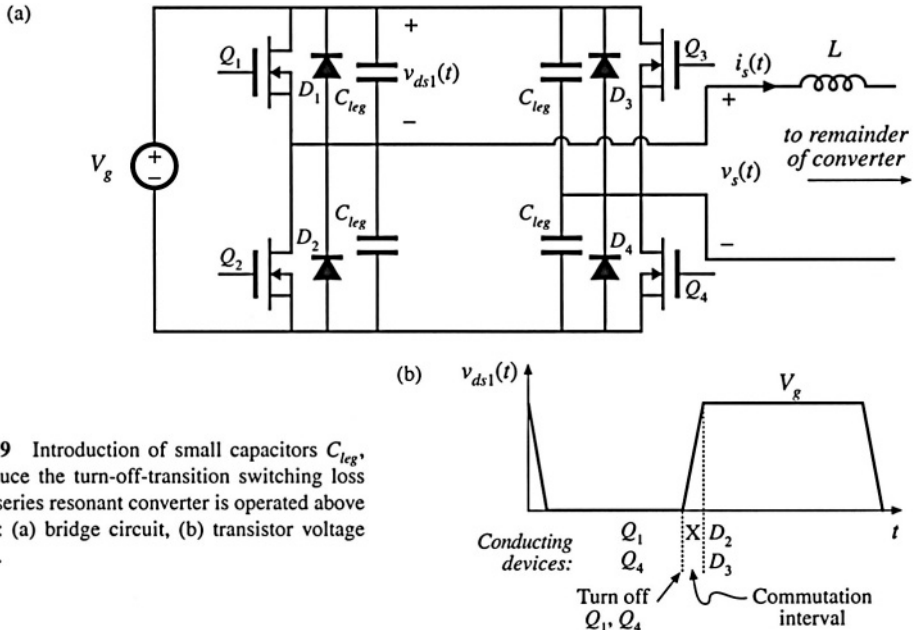


**Fig. 19.29** Introduction of small capacitors  $C_{leg}$ , which reduce the turn-off-transition switching loss when the series resonant converter is operated above resonance: (a) bridge circuit, (b) transistor voltage waveform.

Ringing is conspicuously absent from the waveforms of converters in which all semiconductor devices switch at zero voltage; these converters inherently do not generate this type of EMI.

#### 19.4 LOAD-DEPENDENT PROPERTIES OF RESONANT CONVERTERS

The properties of the CCM PWM converters studied in previous chapters are largely unaffected by the load current. In consequence, these converters exhibit several desirable properties that are often taken for granted. The transistor current is proportional to the load current; hence conduction losses become small at light load, leading to good light-load efficiency. Also, the output impedance is low, and hence the dc output voltage does not significantly depend on the load  $i-v$  characteristic (at least, in CCM). Unfortunately, these good properties are not necessarily shared by resonant converters. Of central importance in design of a resonant converter is the selection of the resonant tank topology and element values, so that the transistor conduction losses at light load are minimized, so that zero-voltage switching is obtained over a wide range of load currents (preferably, for all anticipated loads, but at least at full and intermediate load powers), and so that the converter dynamic range is compatible with the load  $i-v$  characteristic. These design issues are addressed in this section.

The conduction loss caused by circulating tank currents is well-recognized as a problem in resonant converter design. These currents are independent of, or only weakly dependent on, the load current, and lead to poor efficiency at light load. In Fig. 19.30, the switch current  $i_s(s)$  is equal to  $v_s(s)/Z_i(s)$ . If we want the switch current to track the load current, then at the switching frequency  $\| Z_i \|$  should be dominated by, or at least strongly influenced by, the load resistance  $R$ . Unfortunately, this is often not consistent with the requirement for zero-voltage switching, in which  $Z_i$  is dominated by a tank inductor.

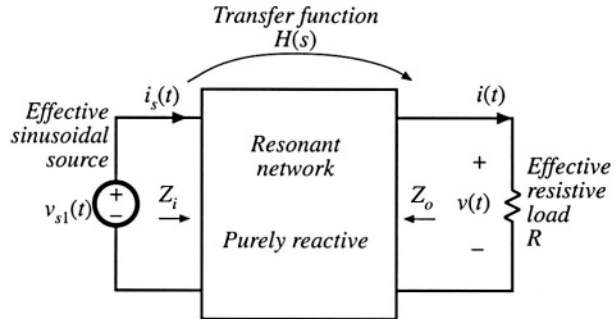


**Fig. 19.30** Resonant inverter model.

To design a resonant converter that exhibits good properties, the engineer must develop physical insight into how the load resistance  $R$  affects the tank input impedance and output voltage.

In this section, the inverter output characteristics, zero-voltage switching boundary, and the dependence of transistor current on load resistance, are related to the properties of the tank network under the extreme conditions of an open-circuited or short-circuited load. The undamped tank network responses are easily plotted, and the insight needed to optimize the tank network design can be gained quickly.

#### 19.4.1 Inverter Output Characteristics

Let us first investigate how the magnitude of the inverter output voltage  $\| v \|$  depends on the load current magnitude  $\| i \|$ . Consider the resonant inverter system of Fig. 19.30. Let  $H_\infty(s)$  be the open-circuit ( $R \rightarrow \infty$ ) transfer function of the tank network:

$$H_\infty(s) = \left. \frac{v(s)}{v_{s1}(s)} \right|_{R \rightarrow \infty} \quad (19.33)$$

and let  $Z_{o0}(s)$  be the output impedance, determined when the source  $v_{s1}(s)$  is short-circuited. Then we can model the output port of the tank network using the Thevenin-equivalent circuit of Fig. 19.31. Solution of this circuit using the voltage divider formula leads to

$$v(s) = H_\infty(s) v_{s1}(s) \frac{R}{R + Z_{o0}(s)} \quad (19.34)$$

At a given angular switching frequency  $\omega_s = 2\pi f_s$ , the phasor representing the magnitude and phase of the ac output voltage is found by letting  $s = j\omega_s$ :

$$v(j\omega_s) = H_\infty(j\omega_s) v_{s1}(j\omega_s) \frac{R}{R + Z_{o0}(j\omega_s)} \quad (19.35)$$

The magnitude can be found by noting that

$$\| v(j\omega_s) \|^2 = v(j\omega_s) v^*(j\omega_s) \quad (19.36)$$

where  $v^*(j\omega_s)$  is the complex conjugate of  $v(j\omega_s)$ . Substitution of Eq. (19.35) into Eq. (19.36) leads to

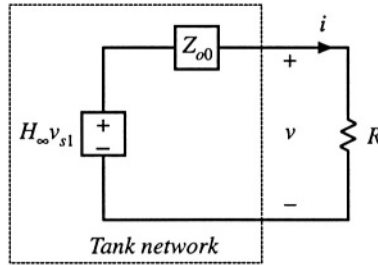


**Fig. 19.31** Thevenin-equivalent circuit that models the output port of the tank network.

$$\begin{aligned}
 \|v(j\omega_s)\|^2 &= \left( H_\infty(j\omega_s) v_{s1}(j\omega_s) \frac{R}{R + Z_{o0}(j\omega_s)} \right) \left( H_\infty(j\omega_s) v_{s1}(j\omega_s) \frac{R}{R + Z_{o0}(j\omega_s)} \right)^* \\
 &= H_\infty(j\omega_s) H_\infty^*(j\omega_s) v_{s1}(j\omega_s) v_{s1}^*(j\omega_s) \frac{R^2}{(R + Z_{o0}(j\omega_s))(R + Z_{o0}^*(j\omega_s))} \\
 &= \|H_\infty(j\omega_s)\|^2 \|v_{s1}(j\omega_s)\|^2 \frac{R^2}{(R + Z_{o0}(j\omega_s))(R + Z_{o0}^*(j\omega_s))}.
 \end{aligned} \tag{19.37}$$

This result can be further simplified with the assumption that the tank network contains only purely reactive elements, i.e., that any losses or other resistive elements within the tank network have negligible effect. Then the output impedance  $Z_{o0}(j\omega_s)$ , as well as all other driving-point impedances of the tank network, are purely imaginary quantities. This implies that the complex conjugate  $Z_{o0}^*(j\omega_s)$  is given by

$$Z_{o0}^*(j\omega_s) = -Z_{o0}(j\omega_s) \tag{19.38}$$

Substitution of Eq. (19.38) into Eq. (19.37) and simplification leads to

$$\|v(j\omega_s)\|^2 = \frac{\|H_\infty(j\omega_s)\|^2 \|v_s(j\omega_s)\|^2}{\left( 1 + \frac{|Z_{o0}(j\omega_s)|^2}{R^2} \right)} \tag{19.39}$$

with

$$R = \frac{|v(j\omega_s)|}{|i(j\omega_s)|} \tag{19.40}$$

Substitution of Eq. (19.40) into Eq. (19.39) and rearrangement of terms yields

$$\|v(j\omega_s)\|^2 + \|i(j\omega_s)\|^2 |Z_{o0}(j\omega_s)|^2 = \|H_\infty(j\omega_s)\|^2 \|v_s(j\omega_s)\|^2 \tag{19.41}$$

Hence, at a given frequency, the inverter output characteristic, that is, the relationship between  $\|v(j\omega_s)\|$  and  $\|i(j\omega_s)\|$ , is elliptical. Equation (19.41) can be further rearranged, into the form

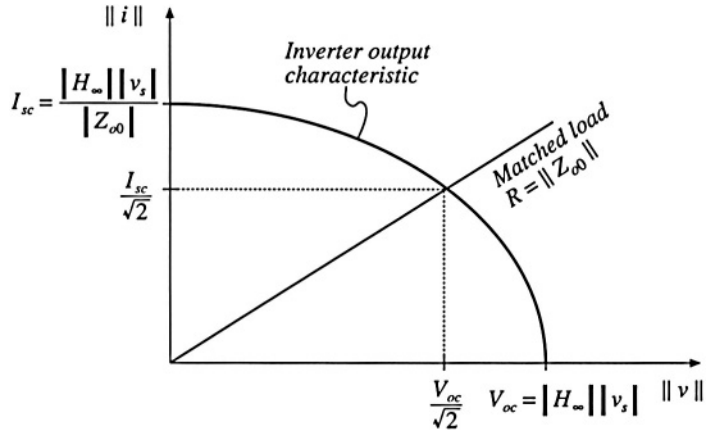


**Fig. 19.32** Elliptical output characteristics of resonant inverters. A resistive matched load is also illustrated.

$$\frac{|v(j\omega_s)|^2}{V_{oc}^2} + \frac{|i(j\omega_s)|^2}{I_{sc}^2} = 1 \quad (19.42)$$

where the open-circuit voltage  $V_{oc}$  and short-circuit current  $I_{sc}$  are given by

$$\begin{aligned} V_{oc} &= |H_\infty(j\omega_s)| |v_s(j\omega_s)| \\ I_{sc} &= \frac{|H_\infty(j\omega_s)| |v_s(j\omega_s)|}{|Z_{o0}(j\omega_s)|} = \frac{V_{oc}}{|Z_{o0}(j\omega_s)|} \end{aligned} \quad (19.43)$$

These inverter output characteristics are constructed in Fig. 19.32. This characteristic describes how, at a given switching frequency, the ac output voltage magnitude varies as the circuit is loaded. The equilibrium output voltage is given by the intersection of this elliptical characteristic with the load  $i$ - $v$  characteristic. For example, Fig. 19.32 also illustrates a superimposed resistive load line having slope  $1/R$ , in the special case where  $R = \|Z_{o0}(j\omega_s)\|$ . This value of  $R$  corresponds to matched load operation, in which the converter output power is maximized. It can be shown that the operating point is then given by

$$\begin{aligned} |v(j\omega_s)|^2 &= \frac{V_{oc}}{\sqrt{2}} \\ |i(j\omega_s)|^2 &= \frac{I_{sc}}{\sqrt{2}} \end{aligned} \quad (19.44)$$

Note that Fig. 19.32 can also be applied to the output  $i$ - $v$  characteristics of resonant dc-dc converters, since the output rectifier then loads the tank with an effective resistive load  $R_e$ .

#### 19.4.2 Dependence of Transistor Current on Load

The transistors must conduct the current appearing at the input port of the tank network,  $i_s(t)$ . This current is determined by the tank network input impedance  $Z_i(j\omega_s)$ :

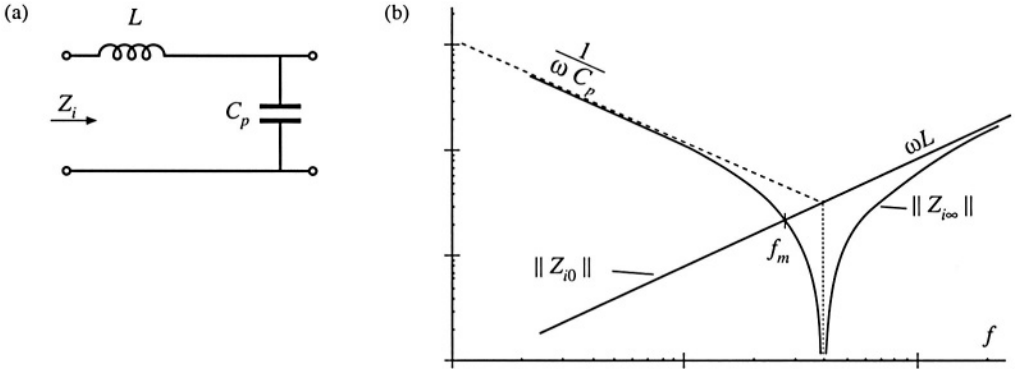


**Fig. 19.33** Tank network, parallel resonant converter example: (a) tank circuit, (b) Bode plot of input impedance magnitude  $\| Z_i \|$  for the limiting cases  $R \rightarrow 0$  and  $R \rightarrow \infty$ .

$$i_{sl}(j\omega_s) = \frac{v_{sl}(j\omega_s)}{Z_i(j\omega_s)} \quad (19.45)$$

As described previously, obtaining good light-load efficiency requires that  $\| Z_i(j\omega_s) \|$  increase as the load resistance  $R$  increases. To understand how  $\| Z_i(j\omega_s) \|$  depends on  $R$ , let us sketch  $\| Z_i(j\omega_s) \|$  in the extreme cases of an open-circuited ( $R \rightarrow \infty$ ) and short-circuited ( $R \rightarrow 0$ ) load:

$$\begin{aligned} Z_{i0}(j\omega_s) &= Z_i(j\omega_s) \Big|_{R \rightarrow 0} \\ Z_{i\infty}(j\omega_s) &= Z_i(j\omega_s) \Big|_{R \rightarrow \infty} \end{aligned} \quad (19.46)$$

For example, consider the parallel resonant converter of Figs. 19.19 to 19.23. The Bode diagrams of the impedances  $\| Z_{i0}(j\omega_s) \|$  and  $\| Z_{i\infty}(j\omega_s) \|$  are constructed in Fig. 19.33.  $Z_{i0}(s)$  is found with the load  $R$  shorted, and is equal to the inductor impedance  $sL$ .  $Z_{i\infty}(s)$ , found with the load  $R$  open-circuited, is given by the series combination  $(sL + 1/sC)$ . It can be seen in Fig. 19.33 that the impedance magnitudes  $\| Z_{i0}(j\omega_s) \|$  and  $\| Z_{i\infty}(j\omega_s) \|$  intersect at frequency  $f_m$ . If the switching frequency is chosen such that  $f_s < f_m$ , then  $\| Z_{i\infty}(j\omega_s) \| > \| Z_{i0}(j\omega_s) \|$ . The converter then exhibits the desirable characteristic that the no-load switch current magnitude  $\| v_s(j\omega_s) \| / \| Z_{i0}(j\omega_s) \|$  is smaller than the switch current under short-circuit conditions,  $\| v_s(j\omega_s) \| / \| Z_{i\infty}(j\omega_s) \|$ . In fact, the short-circuit switch current is limited by the impedance of the tank inductor, while the open-circuit switch current is determined primarily by the impedance of the tank capacitor.

If the switching frequency is chosen such that  $f_s > f_m$ , then  $\| Z_{i\infty}(j\omega_s) \| < \| Z_{i0}(j\omega_s) \|$ . The no-load switch current is then greater in magnitude than the switch current when the load is short-circuited! When the load current is reduced or removed, the transistors will continue to conduct large currents and generate high conduction losses. This causes the efficiency at light load to be poor. It can be concluded that, to obtain good light-load efficiency in the parallel resonant converter, one should choose  $f_s$  sufficiently less than  $f_m$ . Unfortunately, this requires operation below resonance, leading to reduced output voltage dynamic range and a tendency to lose the zero-voltage switching property.

A remaining question is how  $\| Z_i(j\omega_s) \|$  behaves for intermediate values of load between the open-circuit and short-circuit conditions. The answer is given by Theorem 1 below:  $\| Z_i(j\omega_s) \|$  varies monotonically with  $R$ , and therefore is bounded by  $\| Z_{i0}(j\omega_s) \|$  and  $\| Z_{i\infty}(j\omega_s) \|$ . Hence, the Bode plots of

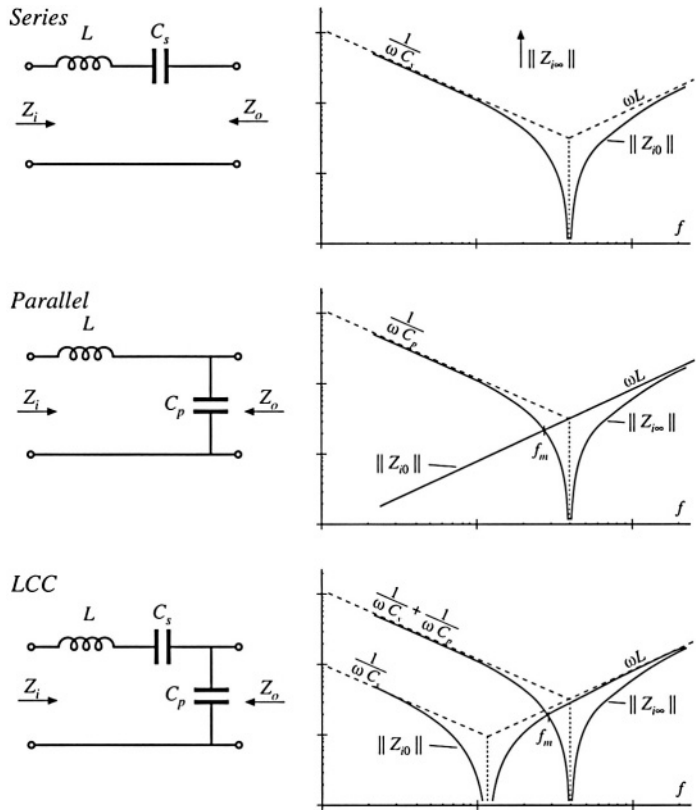


**Fig. 19.34** Series, parallel, and LCC resonant tank networks, and their input impedances  $Z_{i0}$  and  $Z_{ion}$ .

the limiting cases  $\|Z_{i0}(j\omega_s)\|$  and  $\|Z_{ion}(j\omega_s)\|$  provide a correct qualitative understanding of the behavior of  $\|Z_i\|$  for all  $R$ . The theorem is valid for lossless tank networks.

**Theorem 1:** If the tank network is purely reactive, then its input impedance  $\|Z_i\|$  is a monotonic function of the load resistance  $R$ .

This theorem is proven by use of Middlebrook's Extra Element Theorem (see Appendix C). The tank network input impedance  $Z_i(s)$  can be expressed as a function of the load resistance  $R$  and the tank network driving-point impedances, as follows:

$$Z_i(s) = Z_{i0}(s) \frac{\left(1 + \frac{R}{Z_{o0}(s)}\right)}{\left(1 + \frac{R}{Z_{ion}(s)}\right)} = Z_{ion}(s) \frac{\left(1 + \frac{Z_{i0}(s)}{R}\right)}{\left(1 + \frac{Z_{ion}(s)}{R}\right)} \quad (19.47)$$

where  $Z_{i0}$  and  $Z_{ion}$  are the resonant network input impedances, with the load short-circuited or open-circuited, respectively, and  $Z_{o0}$  and  $Z_{ion}$  are the resonant network output impedances, with the source input short-circuited or open-circuited, respectively. These terminal impedances are simple functions of the tank elements, and their Bode diagrams are easily constructed. The input impedances of the series reso-

nant, parallel resonant, and LCC inverters are listed in Fig. 19.34. Since these impedances do not depend on the load, they are purely reactive, ideally have zero real parts [38], and their complex conjugates are given by  $Z_{o0}^* = -Z_{o0}$ ,  $Z_{o\infty}^* = -Z_{o\infty}$ , etc. Again, recall that the magnitude of a complex impedance  $Z(j\omega)$  can be expressed as the square root of  $Z(j\omega)Z^*(j\omega)$ . Hence, the magnitude of  $Z_i(s)$  is given by

$$\begin{aligned} |Z_i|^2 &= Z_i Z_i^* = Z_{i0}(s) Z_{i0}^*(s) \left( \frac{1 + \frac{R}{Z_{o0}(s)}}{1 + \frac{R}{Z_{o\infty}(s)}} \right) \left( \frac{1 + \frac{R}{Z_{o0}^*(s)}}{1 + \frac{R}{Z_{o\infty}^*(s)}} \right) \\ &= |Z_{i0}|^2 \frac{\left( 1 + \frac{R^2}{|Z_{o0}|^2} \right)}{\left( 1 + \frac{R^2}{|Z_{o\infty}|^2} \right)} \end{aligned} \quad (19.48)$$

where  $Z_i^*$  is the complex conjugate of  $Z_i$ .

Next, let us differentiate Eq. (19.48) with respect to  $R$ :

$$\frac{d|Z_i|^2}{dR} = 2R |Z_{i0}|^2 \frac{\left( \frac{1}{|Z_{o0}|^2} - \frac{1}{|Z_{o\infty}|^2} \right)}{\left( 1 + \frac{R^2}{|Z_{o\infty}|^2} \right)^2} \quad (19.49)$$

The derivative has roots at (i)  $R = 0$ , (ii)  $R = \infty$ , and in the special case (iii) where  $|Z_{i0}| = |Z_{i\infty}|$ . Since the derivative is otherwise nonzero, the resonant network input impedance  $|Z_i|$  is a monotonic function of  $R$ , over the range  $0 < R < \infty$ . In special case (iii),  $|Z_i|$  is independent of  $R$ . Therefore, Theorem 1 is proved.

An example is given in Figs. 19.36 and 19.35, for the LCC inverter. Figure 19.35 illustrates the impedance asymptotes of the limiting cases  $|Z_{i0}|$  and  $|Z_{i\infty}|$ . Variation of  $|Z_i|$  between these limits, for finite nonzero  $R$ , is illustrated in Fig. 19.36. The open-circuit resonant frequency  $f_\infty$  and the short-circuit resonant frequency  $f_0$  are given by

$$\begin{aligned} f_0 &= \frac{1}{2\pi\sqrt{LC_s}} \\ f_\infty &= \frac{1}{2\pi\sqrt{L C_s \| C_p }} \end{aligned} \quad (19.50)$$

where  $C_s \| C_p$  denotes inverse addition of  $C_s$  and  $C_p$ :

$$C_s \| C_p = \frac{1}{C_s} + \frac{1}{C_p} \quad (19.51)$$

For the LCC inverter, the impedance magnitudes  $|Z_{i0}|$  and  $|Z_{i\infty}|$  are equal at frequency  $f_m$ , given by

$$f_m = \frac{1}{2\pi\sqrt{L C_s \| 2C_p }} \quad (19.52)$$

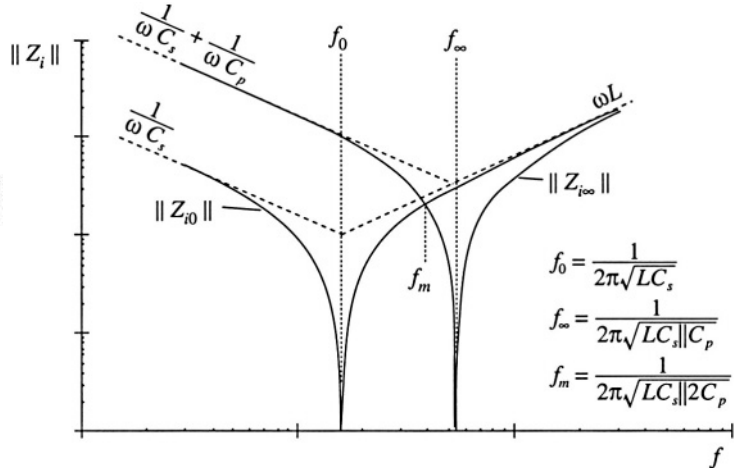


**Fig. 19.35** Construction of the quantities  $\|Z_{i0}\|$  and  $\|Z_{i\infty}\|$ , for the LCC inverter.

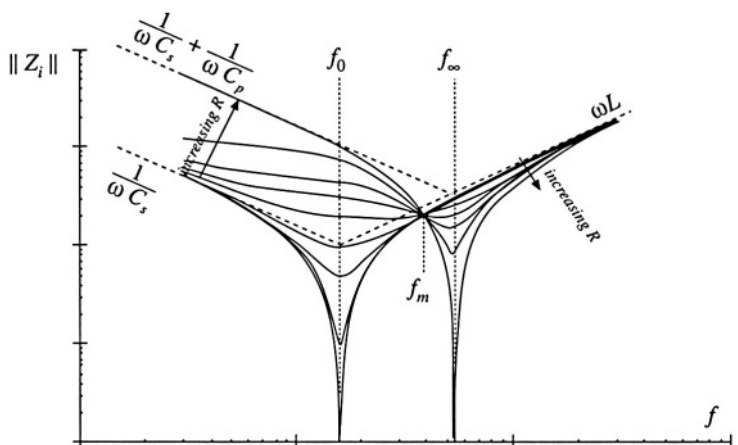


**Fig. 19.36** Variation of tank network input impedance  $\|Z_i\|$  with load resistance  $R$ , LCC inverter. As the load resistance is increased,  $\|Z_i\|$  changes monotonically from  $\|Z_{i0}\|$  to  $\|Z_{i\infty}\|$ .

If the switching frequency is chosen to be greater than  $f_m$ , then  $\|Z_{i\infty}\|$  is less than  $\|Z_{i0}\|$ . This implies that, as the load current is decreased, the transistor current will increase. Such a converter will have poor efficiency at light load, and will exhibit significant circulating currents. If the switching frequency is chosen to be less than  $f_m$ , then the transistor current will increase with decrease with decreasing load current. The short-circuit current is limited by  $\|Z_{i0}\|$ , while the circulating currents under open-circuit conditions are determined by  $\|Z_{i\infty}\|$ . In general, if  $f > f_m$ , then the transistor current is greater than or equal to the short-circuit current for all  $R$ . The inequality is reversed when  $f < f_m$ .

The impedance magnitudes  $\|Z_{i0}\|$  and  $\|Z_{i\infty}\|$  are illustrated in Fig. 19.34 for the series, parallel, and LCC tank networks. In the case of the series tank network,  $\|Z_{i\infty}\| = \infty$ . In consequence, the no-load transistor current is zero, both above resonance and below resonance. Hence, the series resonant inverter exhibits the desirable property that the transistor current is proportional to the load current. In addition, when the load is short-circuited, the current magnitude is limited by the impedance of the series resonant tank. For the parallel and LCC inverters, it is desirable to operate below the frequency  $f_m$ .

Thus, the dependence of the transistor current on load can be easily determined, using an intuitive frequency-domain approach.

### 19.4.3 Dependence of the ZVS/ZCS Boundary on Load Resistance

It is also necessary to determine the critical load resistance  $R = R_{crit}$  at the boundary between ZVS and ZCS. This boundary can also be expressed as a function of the impedances  $Z_{i0}$  and  $Z_{i\infty}$ .

As discussed in Section 19.3, zero-voltage switching occurs when the switch current  $i_s(t)$  lags the switch voltage  $v_s(t)$ . Zero-voltage switching occurs when  $i_s(t)$  leads  $v_s(t)$ . This definition ignores the effects of semiconductor output capacitances, and hence gives an approximate ZVS/ZCS boundary. The phase between the switch current and switch voltage is again determined by the input impedance of the tank network:

$$i_{s1}(j\omega_s) = \frac{v_{s1}(j\omega_s)}{Z_i(j\omega_s)} \quad (19.53)$$

Hence, zero-voltage switching occurs when  $Z_i(j\omega_s)$  is inductive in nature, zero-current switching occurs when  $Z_i(j\omega_s)$  is capacitive in nature, and the ZVS/ZCS boundary occurs where  $Z_i(j\omega_s)$  has zero phase.

It is instructive to again consider the limiting cases of a short-circuited and open-circuited load. The Bode plots of  $Z_{i0}(j\omega_s)$  and  $Z_{i\infty}(j\omega_s)$  for an LCC inverter example are sketched in Fig. 19.37. Since, in these limiting cases, the input impedance  $Z_i$  is composed only of the reactive tank elements,  $Z_{i0}(j\omega_s)$  and  $Z_{i\infty}(j\omega_s)$  are purely imaginary quantities having phase of either  $-90^\circ$  or  $+90^\circ$ . For  $f_s < f_0$ , both  $Z_{i0}(j\omega_s)$  and  $Z_{i\infty}(j\omega_s)$  are dominated by the tank capacitor or capacitors; the phase of  $Z_i(j\omega_s)$  is therefore  $-90^\circ$ . Hence, zero-current switching is obtained under both short-circuit and open-circuit conditions. For  $f_s > f_\infty$ , both  $Z_{i0}(j\omega_s)$  and  $Z_{i\infty}(j\omega_s)$  are dominated by the tank inductor; hence the phase of  $Z_i(j\omega_s)$  is  $+90^\circ$ . Zero-voltage switching is obtained for both a short-circuited and an open-circuited load. For  $f_0 < f_s < f_\infty$ ,  $Z_{i0}(j\omega_s)$  is dominated by the tank inductor while  $Z_{i\infty}(j\omega_s)$  is dominated by the tank capacitors. This implies that zero-voltage switching is obtained under short-circuit conditions, and zero-voltage switching is obtained under open-circuit conditions. For this case, there must be some critical value of load resistance  $R = R_{crit}$  that represents the boundary between ZVS and ZCS, and that causes the phase of  $Z_i(j\omega_s)$  to be equal to  $0^\circ$ .

The behavior of  $Z_i(j\omega_s)$  for nonzero finite  $R$  is easily extrapolated from the limiting cases dis-

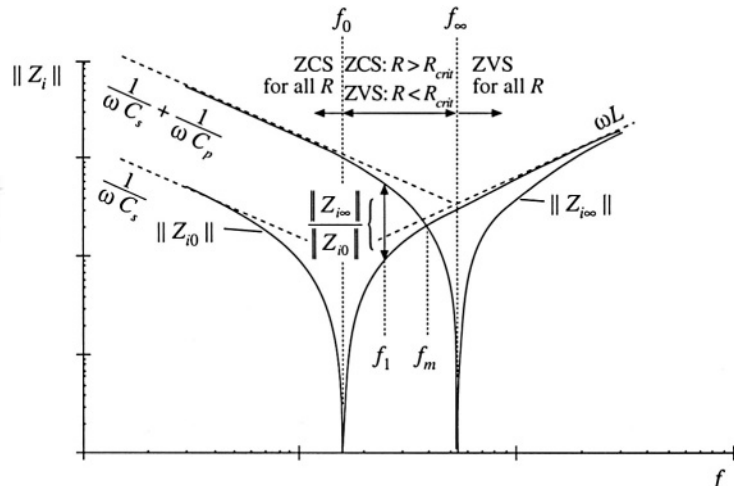


**Fig. 19.37** Use of the input impedance quantities  $Z_{i0}$  and  $Z_{i\infty}$  to determine the ZCS/ZVS boundaries, LCC example.

cussed above. Theorem 2 below shows that:

1. If zero-current switching occurs for both an open-circuited load and a short-circuited load [i.e.,  $Z_{i0}(j\omega_s)$  and  $Z_{i\infty}(j\omega_s)$  both have phase + 90°], then zero-current switching occurs for all loads.
2. If zero-voltage switching occurs for both an open-circuited load and a short-circuited load [i.e.,  $Z_{i0}(j\omega_s)$  and  $Z_{i\infty}(j\omega_s)$  both have phase - 90°], then zero-voltage switching occurs for all loads.
3. If zero-voltage switching occurs for an open-circuited load and zero-current switching occurs for a short-circuited load [i.e.,  $Z_{i0}(j\omega_s)$  has phase - 90° and  $Z_{i\infty}(j\omega_s)$  has phase + 90°], then zero-voltage switching occurs for  $R > R_{crit}$  and zero-current switching occurs for  $R < R_{crit}$  with  $R_{crit}$  given by Eq. (19.54) below.
4. If zero-current switching occurs for an open-circuited load and zero-voltage switching occurs for a short-circuited load [i.e.,  $Z_{i0}(j\omega_s)$  has phase + 90° and  $Z_{i\infty}(j\omega_s)$  has phase - 90°], then zero-current switching occurs for  $R < R_{crit}$  and zero-voltage switching occurs for  $R > R_{crit}$  with  $R_{crit}$  given by Eq. (19.54) below.

For the LCC example, we can therefore conclude that, for  $f_s < f_0$ , zero-current switching occurs for all values of  $R$ . For  $f_s > f_\infty$ , zero-voltage switching occurs for all values of  $R$ . For  $f_0 < f_s < f_\infty$ , the boundary between ZVS and ZCS is given by Eq. (19.54).

**Theorem 2:** If the tank network is purely reactive, then the boundary between zero-current switching and zero-voltage switching occurs when the load resistance  $R$  is equal to the critical value  $R_{crit}$ , given by

$$R_{crit} = \|Z_{o0}\| \sqrt{\frac{-Z_{i\infty}}{Z_{i0}}} \quad (19.54)$$

This theorem relies on the assumption that zero-current switching occurs when the tank input impedance is capacitive in nature, while zero-voltage switching occurs for inductive input impedances. The boundary therefore occurs where the phase of  $Z_i(j\omega)$  is zero. This definition gives a necessary but not sufficient condition for zero-voltage switching when significant semiconductor output capacitance is present.

The result is derived by finding the value of  $R$  which causes the imaginary part of  $Z_i(j\omega)$  in Eq. (19.47) to be zero. Since the tank network is assumed to ideal and lossless, the impedances  $Z_{o\infty}$ ,  $Z_{o0}$ , and  $Z_{i\infty}$  must have zero real parts. Hence,

$$\text{Im}\{Z_i(R_{crit})\} = \text{Im}\{Z_{i\infty}\} \text{Re}\left(\frac{1 + \frac{Z_{o0}}{R_{crit}}}{1 + \frac{Z_{o\infty}}{R_{crit}}}\right) = \text{Im}\{Z_{i\infty}\} \frac{\left(1 - \frac{Z_{o0}Z_{o\infty}}{R_{crit}^2}\right)}{\left(1 + \frac{\|Z_{o\infty}\|^2}{R_{crit}^2}\right)} = 0 \quad (19.55)$$

where  $\text{Im}(Z)$  and  $\text{Re}(Z)$  denote the imaginary and real parts of the complex quantity  $Z$ . The nontrivial solution to Eq. (19.55) is given by

$$1 = \frac{Z_{o0}Z_{o\infty}}{R_{crit}^2} \quad (19.56)$$

hence,

$$R_{crit} = \sqrt{Z_{o0}Z_{o\infty}} \quad (19.57)$$

A useful equivalent form makes use of the reciprocity identities

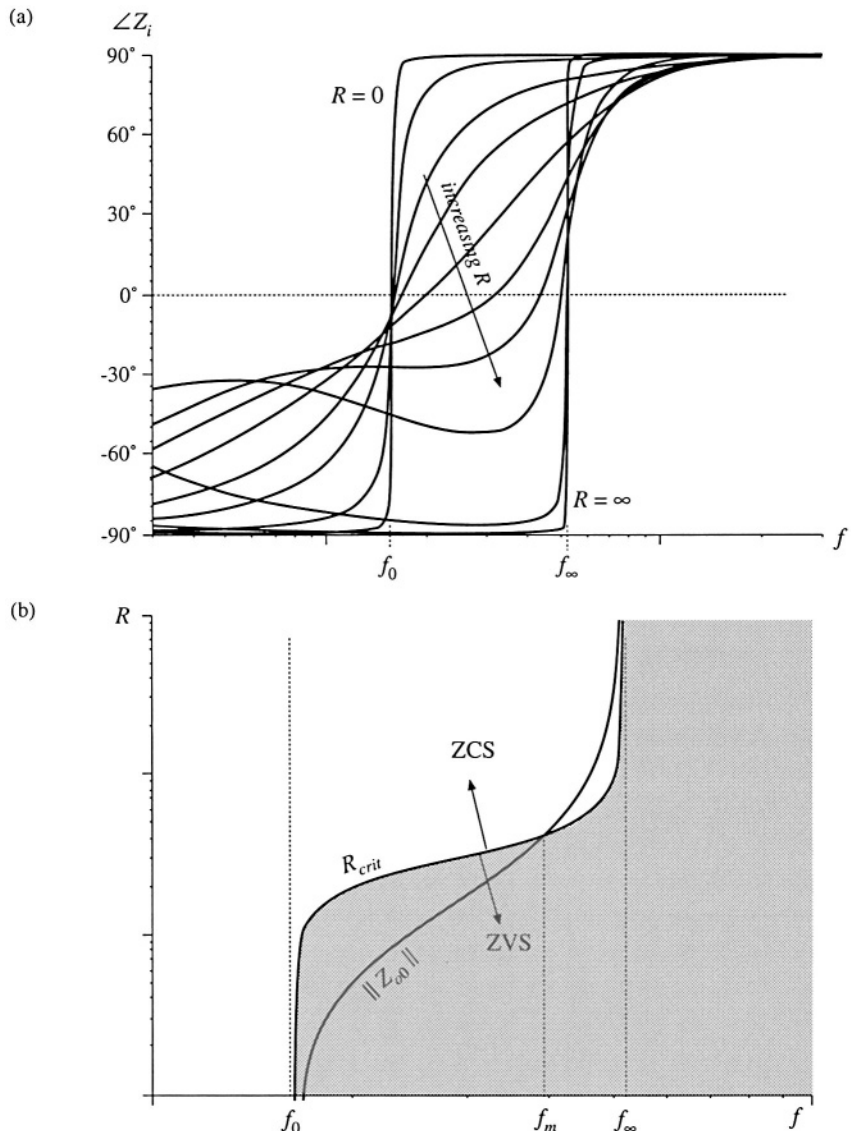


**Fig. 19.38** ZCS/ZVS boundary, LCC inverter example: (a) variation of tank network input impedance phase shift with load resistance, (b) Comparison of  $R_{crit}$  with matched-load impedance  $\|Z_{o0}\|$ .

$$\frac{Z_{o0}}{Z_{o\infty}} = \frac{Z_{i0}}{Z_{i\infty}} \quad (19.58)$$

Use of Eq. (19.58) to eliminate  $Z_{o\infty}$  from Eq. (19.57) leads to

$$R_{crit} = |Z_{o0}| \sqrt{\frac{-Z_{i\infty}}{Z_{i0}}} \quad (19.59)$$

This is the desired result. The quantity  $Z_{o0}$  is the inverter output impedance, and  $R = \|Z_{o0}\|$  corresponds to operation at matched load with maximum output power. The impedances  $Z_{i\infty}$  and  $Z_{i0}$  are purely imaginary, and hence Eq. (19.59) has no real solution unless  $Z_{i\infty}$  and  $Z_{i0}$  are of opposite phase. As illustrated in Fig. 19.37, if at a given frequency  $Z_{i\infty}$  and  $Z_{i0}$  are both inductive, then zero-voltage switching occurs for all loads. Zero-current switching occurs for all loads when  $Z_{i\infty}$  and  $Z_{i0}$  are both capacitive. Therefore, Theorem 2 is proved.

Figure 19.38(a) illustrates the phase response of  $Z_i(j\omega)$  as  $R$  varies from 0 to  $\infty$ , for the LCC inverter. A typical dependence of  $R_{crit}$  and the matched-load impedance  $\|Z_{o0}\|$  on frequency is illustrated in Fig. 19.38(b). Zero-voltage switching occurs for all loads when  $f > f_{\infty}$ , and zero-current switching occurs for all loads when  $f < f_0$ . Over the range  $f_0 < f < f_{\infty}$ ,  $Z_{i0}$  is inductive while  $Z_{i\infty}$  is capacitive; hence, zero-voltage switching occurs for  $R < R_{crit}$  while zero-current switching occurs for  $R > R_{crit}$ . At frequency  $f_m$ ,  $R_{crit} = \|Z_{o0}\|$ , and hence the ZVS/ZCS boundary is encountered exactly at matched load. It is commonly desired to obtain zero-voltage switching at matched load, with low circulating currents and good efficiency at light load. It is apparent that this requires operation in the range  $f_0 < f < f_m$ . Zero-voltage switching will then be obtained under matched-load and short-circuit conditions, but will be lost at light load. The choice of element values such that  $\|Z_{i0}\| \ll \|Z_{i\infty}\|$  is advantageous in that the range of loads leading to zero-voltage switching is maximized.

#### 19.4.4 Another Example

As a final example, let us consider selection of the resonant tank elements to obtain a given output characteristic at a certain switching frequency, and let's evaluate the effect of this choice on  $R_{crit}$ . It is desired to operate a resonant inverter at switching frequency  $f_s = 100$  kHz, with an input voltage of  $V_g = 160$  V. The converter should be capable of producing an open-circuit peak output voltage  $V_{oc} = 400$  V, and should also produce a nominal output of 150 Vrms at 25 W. It is desired to select resonant tank elements that accomplish this.

The specifications imply that the converter should exhibit an open-circuit transfer function of

$$|H_o(j\omega_s)| = \frac{V_{oc}}{V_{sl}} = \frac{(400 \text{ V})}{\left(\frac{4}{\pi} 160 \text{ V}\right)} = 1.96 \quad (19.60)$$

The required short-circuit current is found by solving Eq. (19.42) for  $I_{sc}$ :

$$I_{sc} = \frac{I}{\sqrt{1 - \left(\frac{V}{V_{oc}}\right)^2}} \quad (19.61)$$

The specifications also imply that the peak voltage and current at the nominal operating point are

$$\begin{aligned}
 V &= 150\sqrt{2} = 212 \text{ V} \\
 I &= \frac{P}{V_{rms}}\sqrt{2} = \frac{25 \text{ W}}{150 \text{ V}}\sqrt{2} = 0.236 \text{ A} \\
 R_{nom} &= \frac{V}{I} = 900 \Omega
 \end{aligned} \tag{19.62}$$

Substitution of Eq. (19.62) into Eq. (19.61) yields

$$I_{sc} = \frac{(0.236 \text{ A})}{\sqrt{1 - \left(\frac{212 \text{ V}}{400 \text{ V}}\right)^2}} = 0.278 \text{ A} \tag{19.63}$$

Matched load therefore occurs at the operating point

$$\begin{aligned}
 V_{mat} &= \frac{V_{oc}}{\sqrt{2}} = 283 \text{ V} \\
 I_{mat} &= \frac{I_{sc}}{\sqrt{2}} = 0.278 \text{ A} \\
 |Z_{o0}(j\omega_s)| &= \frac{V_{oc}}{I_{sc}} = 1439 \Omega
 \end{aligned} \tag{19.64}$$

Let us select the values of the tank elements in the LCC tank network illustrated in Fig. 19.39(a). The impedances of the series and parallel branches can be represented using the reactances  $X_s$  and  $X_p$  illustrated in Fig. 19.39(b), with

$$\begin{aligned}
 jX_s &= j\omega_s L + \frac{1}{j\omega_s C_s} = j\left(\omega_s L - \frac{1}{\omega_s C_s}\right) \\
 jX_p &= \frac{1}{j\omega_s C_p} = j\left(-\frac{1}{\omega_s C_p}\right)
 \end{aligned} \tag{19.65}$$

The transfer function  $H_\infty(j\omega_s)$  is given by the voltage divider formula

$$H_\infty(j\omega_s) = \frac{jX_p}{jX_s + jX_p} \tag{19.66}$$

The output impedance  $Z_{o0}(j\omega_s)$  is given by the parallel combination



**Fig. 19.39** Tank network of the LCC inverter example: (a) schematic, (b) representation of series and parallel branches by reactances  $X_s$  and  $X_p$ .

$$Z_{o0}(j\omega_s) = jX_s \parallel jX_p \frac{-X_s X_p}{j(X_s + X_p)} \quad (19.67)$$

Solution of Eqs. (19.66) and (19.67) for  $X_p$  and  $X_s$  leads to

$$\begin{aligned} jX_p &= \frac{Z_{o0}(j\omega_s)}{1 - H_\infty(j\omega_s)} \\ X_s &= X_p \frac{1 - H_\infty(j\omega_s)}{H_\infty(j\omega_s)} \end{aligned} \quad (19.68)$$

Hence, the capacitance  $C_p$  should be chosen equal to

$$\begin{aligned} X_p &= -1493 \Omega \\ C_p &= -\frac{1}{\omega_s X_p} = \frac{H_\infty(j\omega_s) - 1}{\omega_s |Z_{o0}(j\omega_s)|} = \frac{(1.96) - 1}{(2\pi 100 \text{ kHz})(1439 \Omega)} \equiv 1 \text{ nF} \end{aligned} \quad (19.69)$$

and the reactance of the series branch should be chosen according to

$$X_s = X_p \frac{1 - H_\infty(j\omega_s)}{H_\infty(j\omega_s)} = (-1493 \Omega) \frac{1 - (1.96)}{(1.96)} = 733 \Omega \quad (19.70)$$

Since  $X_s$  is comprised of the series combination of the inductor  $L$  and capacitor  $C_s$ , there is a degree of freedom in choosing the values of  $L$  and capacitor  $C_s$  to realize  $X_s$ . For example, we could choose  $C_s$  very large (tending to a short circuit); this effectively would result in a parallel resonant converter with  $L = X_s/\omega_s = 1.17 \text{ mH}$ . For nonzero  $C_s$ ,  $L$  must be chosen according to

$$L = \frac{1}{\omega_s} \left( X_s + \frac{1}{\omega_s C_s} \right) \quad (19.71)$$

For example, the choice  $C_s = C_p = 1.06 \text{ nF}$  leads to  $L = 3.5 \text{ mH}$ . Designs using different  $C_s$  will exhibit exactly the same characteristics at the design frequency; however, the behavior at other switching frequencies will differ.

For the tank network illustrated in Fig. 19.39, the value of  $R_{crit}$  is completely determined by the parameters of the output characteristic ellipse; i.e., by the specification of  $V_g$ ,  $V_{ac}$  and  $I_{sc}$ . Note that  $Z_{o\infty}$ , the tank output impedance with the tank input port open-circuited, is equal to  $jX_p$ . Substitution of expressions for  $Z_{o\infty}$  and  $Z_{o0}$  into Eq. (19.57) leads to the following expression for  $R_{crit}$ :

$$R_{crit} = \sqrt{\frac{Z_{o0}^2(j\omega_s)}{1 - H_\infty(j\omega_s)}} \quad (19.72)$$

Since  $Z_{o0}$  and  $H_\infty$  are determined by the operating point specifications, then  $R_{crit}$  is also. Evaluation of Eq. (19.72) for this example leads to  $R_{crit} = 1466 \Omega$ . Therefore, the inverter will operate with zero-voltage switching for  $R < 1466 \Omega$ , including at the nominal operating point  $R = 900 \Omega$ . Other topologies of tank network, more complex than the circuit illustrated in Fig. 19.39(b), may have additional degrees of freedom that allow  $R_{crit}$  to be independently chosen.

The choice  $C_s = 3C_p = 3.2 \text{ nF}$  leads to  $L = 1.96 \mu\text{H}$ . The following frequencies are obtained:

$$\begin{aligned}f_{\infty} &= 127 \text{ kHz} \\f_m &= 100.6 \text{ kHz} \\f_s &= 100.0 \text{ kHz} \\f_0 &= 64 \text{ kHz}\end{aligned}\tag{19.73}$$

Regardless of how  $C_s$  is chosen, the open-circuit tank input impedance is

$$Z_{ioe} = j(X_s + X_p) = j(733 \Omega + (-1493 \Omega)) = -j760 \Omega\tag{19.74}$$

Therefore, when the load is open-circuited, the transistor peak current has magnitude

$$I_{s1} = \frac{V_{s1}}{\|Z_{ioe}\|} = \frac{\frac{4}{\pi}(160 \text{ V})}{760 \Omega} = 0.268 \text{ A}\tag{19.75}$$

When the load is short-circuited, the transistor peak current has magnitude

$$I_{s1} = \frac{V_{s1}}{\|Z_{lo}\|} = \frac{V_{s1}}{|X_s|} = \frac{\frac{4}{\pi}(160 \text{ V})}{(733 \Omega)} = 0.278 \text{ A}\tag{19.76}$$

which is nearly the same as the result in Eq. (19.75). The somewhat large open-circuit switch current occurs because of the relatively-high specified open-circuit output voltage; lower values of  $V_{oc}$  would reduce the result in Eq. (19.75).

## 19.5 EXACT CHARACTERISTICS OF THE SERIES AND PARALLEL RESONANT CONVERTERS

The exact steady-state behavior of resonant converters can be determined via methods such as state-plane analysis. A detailed analysis of resonant dc–dc converters is beyond the scope of this book. However, the exact steady-state characteristics of ideal series [1, 13–20] and parallel [6, 22–25] resonant dc–dc converters (Fig. 19.40) are summarized in this section. Small-signal ac modeling has also been described in the literature; several relevant papers are [27–30].

### 19.5.1 Series Resonant Converter

At a given switching frequency, the series resonant dc–dc converter can operate in one continuous conduction mode, and possibly in several discontinuous conduction modes. The mode index  $k$  is defined as the integer that satisfies

$$\frac{f_0}{k+1} < f_s < \frac{f_0}{k} \quad \text{or} \quad \frac{1}{k+1} < F < \frac{1}{k}\tag{19.77}$$

where  $F = f_s/f_0$  is the normalized switching frequency. The subharmonic number  $\xi$  is defined as

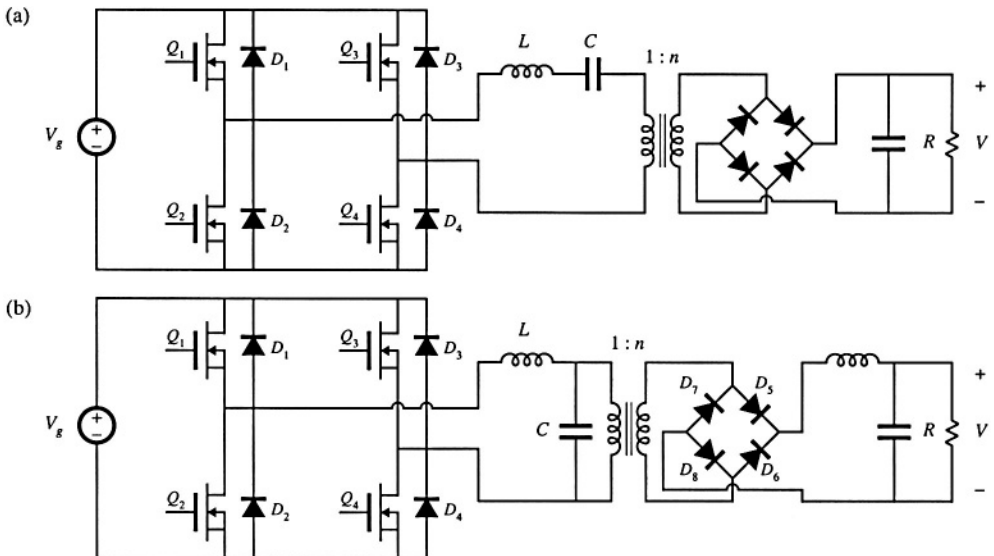


**Fig. 19.40** Transformer-isolated resonant dc-dc converters: (a) series resonant converter, (b) parallel resonant converter.

$$\xi = k + \frac{1 + (-1)^k}{2} \quad (19.78)$$

Values of  $k$  and  $\xi$  as functions of  $f_s$  are summarized in Fig. 19.41 (a). The subharmonic number  $\xi$  denotes the dominant harmonic that excites the tank resonance. When the converter is heavily loaded, it operates in type  $k$  continuous conduction mode. As the load is reduced (i.e., as the load resistance  $R$  is increased), the converter enters the type  $k$  discontinuous conduction mode. Further reducing the load causes the converter to enter the type  $(k - 1)$  DCM, type  $(k - 2)$  DCM, ..., type 1 DCM. There is no type 0 DCM, and hence when the converter operates above resonance, only the type 0 continuous conduction mode is possible.

In the type  $k$  continuous conduction mode, the series resonant converter exhibits elliptical output characteristics, given by

$$M^2 \xi^2 \sin^2 \left( \frac{\gamma}{2} \right) + \frac{1}{\xi^2} \left( \frac{J\gamma}{2} + (-1)^k \right)^2 \cos^2 \left( \frac{\gamma}{2} \right) = 1 \quad (19.79)$$

For the transformer-isolated converters of Fig. 19.40,  $M$  and  $J$  are related to the load voltage  $V$  and load current  $I$  according to

$$M = \frac{V}{nV_g} \quad J = \frac{InR_0}{V_g} \quad (19.80)$$

Again,  $R_0$  is the tank characteristic impedance, referred to the transformer primary side. The quantity  $\gamma$  is the angular length of one-half of the switching period:

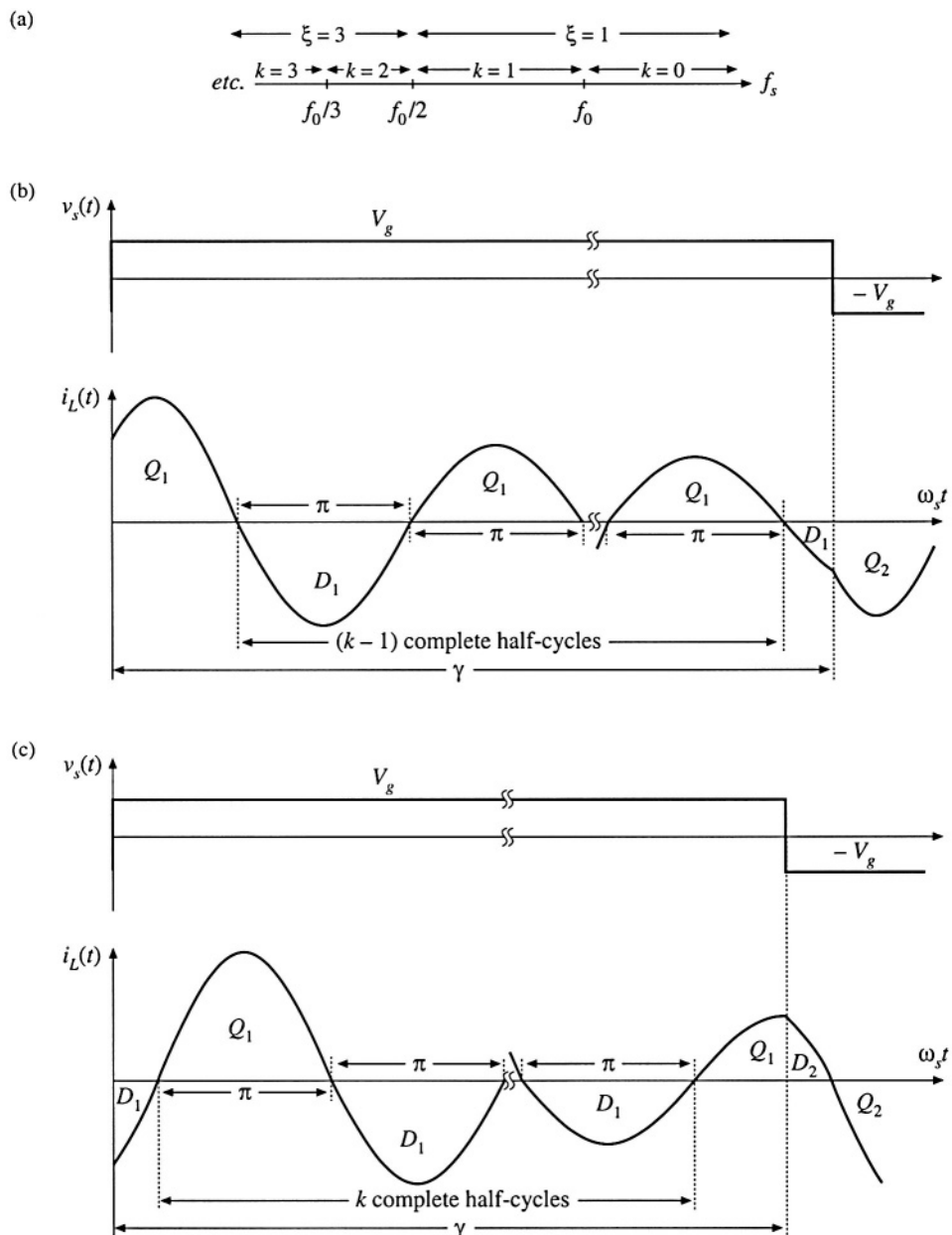


**Fig. 19.41** Continuous conduction modes of the series resonant converter: (a) switching frequency ranges over which various mode indices  $k$  and subharmonic numbers  $\xi$  occur; (b) tank inductor current waveform, type  $k$  CCM, for odd  $k$ ; (c) tank inductor current waveform, type  $k$  CCM, for even  $k$ .

$$\gamma = \frac{\omega_0 T_s}{2} = \frac{\pi}{F} \quad (19.81)$$

Equation (19.79) is valid only for  $k$  satisfying Eq. (19.77). It predicts that the voltage conversion ratio  $M$  is restricted to the range

$$0 \leq M \leq \frac{1}{\xi} \quad (19.82)$$

This is consistent with Eq. (19.21).

Typical CCM tank current waveforms are illustrated in Fig. 19.41. When  $k$  is even, the tank inductor current is initially negative. In consequence, the switch network antiparallel diodes conduct first, for a fraction of a half resonant cycle. If  $k$  is odd, then each half switching period is initiated by conduction of the switch network transistors. In either case, this is followed by  $(\xi - 1)$  complete tank half-cycles of ringing. The half-switching period is then concluded by a subinterval shorter than one complete resonant half-cycle, in which the device that did not initially conduct is on. The next half switching period then begins, and is symmetrical.

The steady-state control-plane characteristic can be found for a resistive load  $R$  obeying  $V = IR$ , by substitution of the normalized relation  $J = MQ$  into Eq. (19.79), where  $Q = n^2 R_0 / R$ . Use of the quadratic formula and some algebraic manipulations allows solution for  $M$ , as a function of load (via  $Q$ ) and switching frequency (via  $\gamma$ ):

$$M = \frac{\left(\frac{Q\gamma}{2}\right)}{\xi^4 \tan^2\left(\frac{\gamma}{2}\right) + \left(\frac{Q\gamma}{2}\right)^2} \left[ (-1)^{k+l} + \sqrt{1 + \frac{\left[\xi^2 - \cos^2\left(\frac{\gamma}{2}\right)\right] \left[\xi^4 \tan^2\left(\frac{\gamma}{2}\right) + \left(\frac{Q\gamma}{2}\right)^2\right]}{\left(\frac{Q\gamma}{2}\right)^2 \cos^2\left(\frac{\gamma}{2}\right)}} \right] \quad (19.83)$$

This is the closed-form relationship between the conversion ratio  $M$  and the switching frequency, for a resistive load. It is valid for any continuous conduction mode  $k$ .

The type  $k$  discontinuous conduction modes, for  $k$  odd, occur over the frequency range

$$f_s < \frac{f_0}{k} \quad (19.84)$$

In these modes, the output voltage is independent of both load current and switching frequency, and is described by

$$M = \frac{1}{k} \quad (19.85)$$

The type  $k$  discontinuous conduction mode, for odd  $k$ , occurs over the range of load currents given by

$$\frac{2(k+1)}{\gamma} > J > \frac{2(k-1)}{\gamma} \quad (19.86)$$

In the odd discontinuous conduction modes, the tank current rings for  $k$  complete resonant half cycles. All four output bridge rectifier diodes then become reverse-biased, and the tank current remains at zero until the next switching half-period begins, as illustrated in Fig. 19.42. Series resonant converters are not

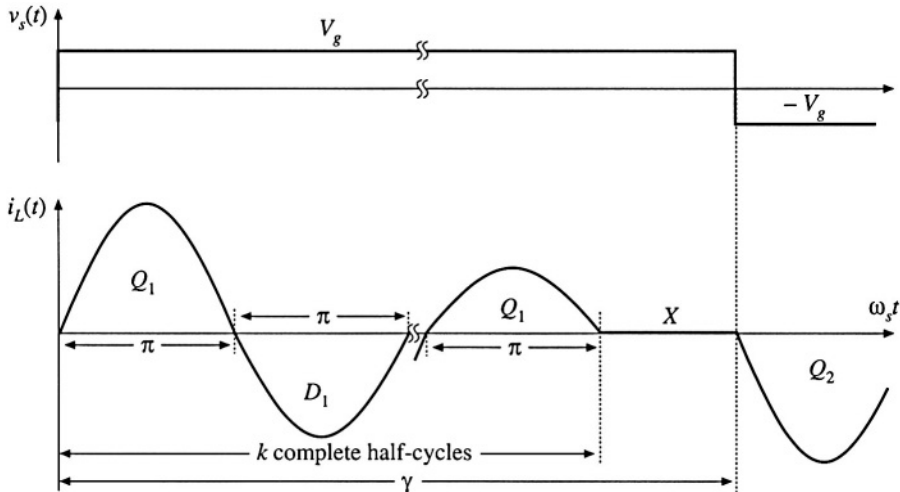


**Fig. 19.42** Tank inductor current waveform, type  $k$  DCM, for odd  $k$ .

normally purposely designed to operate in odd discontinuous conduction modes, because the output voltage is not controllable. Nonetheless, when the load is removed with  $f_s < f_0$ , the series resonant converter operates in  $k = 1$  DCM with  $M = 1$ .

The type  $k$  discontinuous conduction mode, for  $k$  even, also occurs over the frequency range

$$f_s < \frac{f_0}{k} \quad (19.87)$$

Even discontinuous conduction modes exhibit current source characteristics, in which the load current is a function of switching frequency and input voltage, but not of the load voltage. The output relationship is:

$$J = \frac{2k}{\gamma} \quad (19.88)$$

Operation in this mode occurs for

$$\frac{1}{k-1} > M > \frac{1}{k+1} \quad (19.89)$$

In the even discontinuous conduction modes, the tank current rings for  $k$  complete resonant half-cycles during each switching half-period. All four output bridge then become reverse-biased, and the tank current remains at zero until the next switching half-period is initiated. Tank current waveforms are illustrated in Fig. 19.43 for even DCM.

The series resonant converter possesses some unusual properties when operated in an even discontinuous conduction mode. A dc equivalent circuit is given in Fig. 19.44, consisting of a gyrator with gyration conductance  $g = 2k/gn^2R_0$ . The gyrator has the property of transforming circuits into their dual networks; in the typical dc-dc converter application, the input voltage source  $V_g$  is effectively transformed into its dual, an output current source of value  $gV_g$ . Series resonant converters have been purposely designed to operate in the  $k = 2$  DCM, at power levels of several tens of kW.

The complete control plane characteristics can now be plotted using Eqs. (19.77) to (19.89).

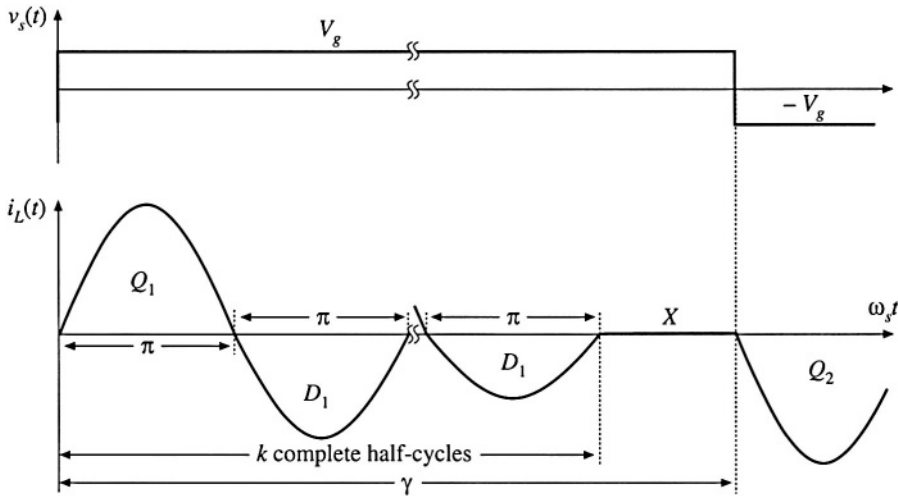


Fig. 19.43 Tank inductor current waveform, type  $k$  DCM, for even  $k$ .

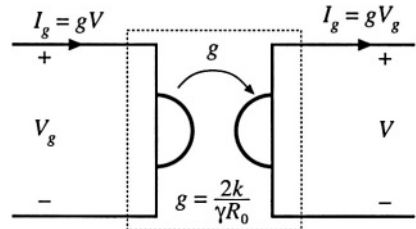


Fig. 19.44 Steady-state equivalent circuit model for an even discontinuous conduction mode: an effective gyrator. The converter exhibits current source characteristics.

The result is shown in Fig. 19.45, and the mode boundaries are explicitly diagrammed in Fig. 19.46. It can be seen that, for operation above resonance, the only possible operating mode is the  $k = 0$  CCM, and that the output voltage decreases monotonically with increasing switching frequency. Reduction in load current (or increase in load resistance, which decreases  $Q$ ) causes the output voltage to increase. A number of successful designs that operate above resonance and utilize zero-voltage switching have been documented in the literature [7,21].

Operation below resonance is complicated by the presence of subharmonic and discontinuous conduction modes. The  $k = 1$  CCM and  $k = 2$  DCM are well behaved, in that the output voltage increases monotonically with increasing switching frequency. Increase of the load current again causes the output voltage to decrease. Successful designs that operate in these modes and employ zero-current switching are numerous. However, operation in the higher-order modes ( $k = 2$  CCM,  $k = 4$  DCM, etc.) is normally avoided.

Given  $F$  and  $Q$ , the operating mode can be evaluated directly, using the following algorithm. First, the continuous conduction mode  $k$  corresponding to operation at frequency  $F$  with heavy loading is found:

$$k = \text{INT}\left(\frac{1}{F}\right) \quad (19.90)$$

where  $\text{INT}(x)$  denotes the integer part of  $x$ . Next, the quantity  $k_1$  is determined:

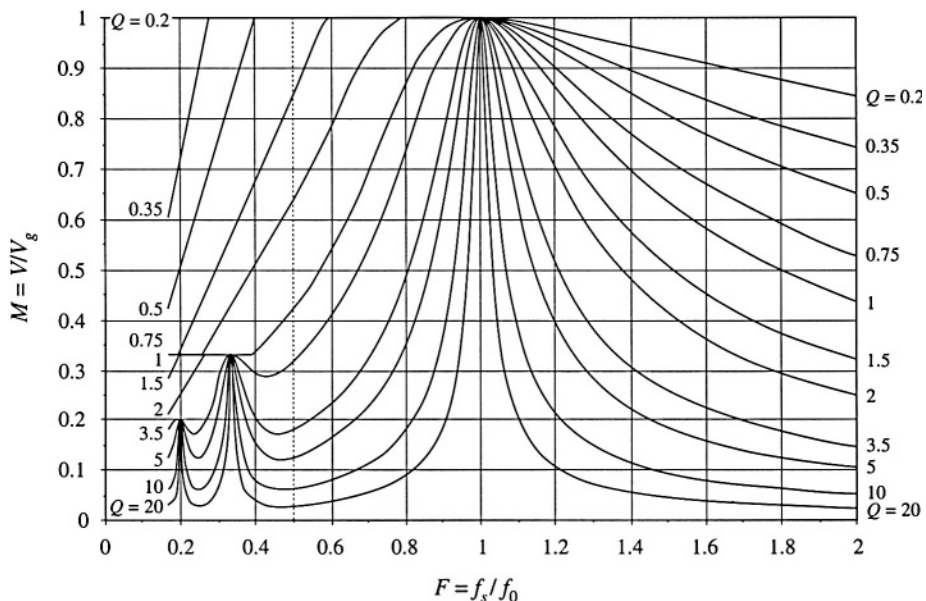


Fig. 19.45 Complete control plane characteristics of the series resonant converter, for the range  $0.2 \leq F \leq 2$ .

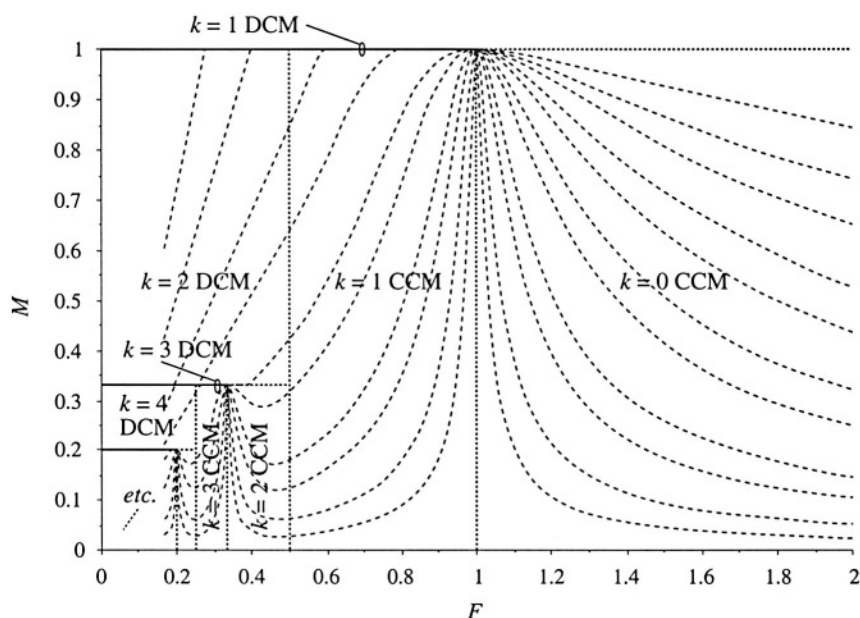


Fig. 19.46 Continuous and discontinuous conduction mode boundaries.

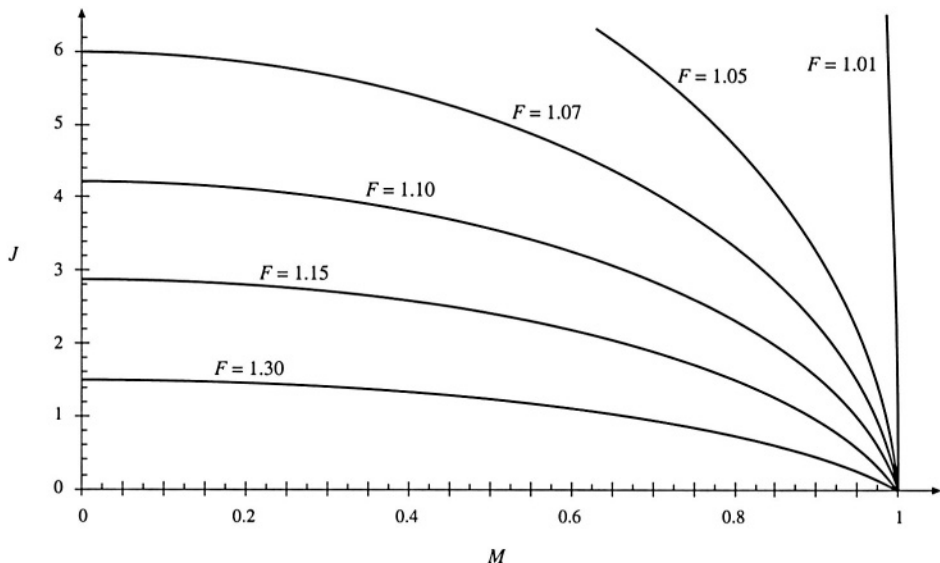


Fig. 19.47 Output characteristics,  $k = 0$  CCM (above resonance).

$$k_1 = \text{INT} \left( \frac{1}{2} + \sqrt{\frac{1}{4} + \frac{Q\pi}{2F}} \right) \quad (19.91)$$

The converter operates in type  $k_1$  CCM provided that:

$$k_1 > k \quad (19.92)$$

Otherwise, the converter operates in type  $k_1$  DCM. A simple algorithm can therefore be defined, in which the conversion ratio  $M$  is computed for a given  $F$  and  $Q$ . First, Eqs. (19.90) to (19.92) are evaluated, to determine the operating mode. Then, the appropriate equation (19.83), (19.85), or (19.88) is evaluated to find  $M$ .

Output  $I$ - $V$  plane characteristics for the  $k = 0$  CCM, plotted using Eq. (19.79), are shown in Fig. 19.47. The constant-frequency curves are elliptical, and all pass through the point  $M = 1, J = 0$ . For a given switching frequency, the operating point is given by the intersection of the elliptical converter output characteristic with the load  $I$ - $V$  characteristic.

Output plane characteristics that combine the  $k = 1$  CCM,  $k = 1$  DCM, and  $k = 2$  DCM are shown in Fig. 19.48. These were plotted using Eqs. (19.79), (19.85), and (19.88). These curves were plotted with the assumption that the transistors are allowed to conduct no longer than one tank half-cycle during each switching half-period; this eliminates subharmonic modes and causes the converter to operate in  $k = 2$  or  $k = 1$  DCM whenever  $f_s < 0.5f_0$ . It can be seen that the constant-frequency curves are elliptical in the continuous conduction mode, vertical (voltage source characteristic) in the  $k = 1$  DCM, and horizontal (current source characteristic) in the  $k = 2$  DCM.

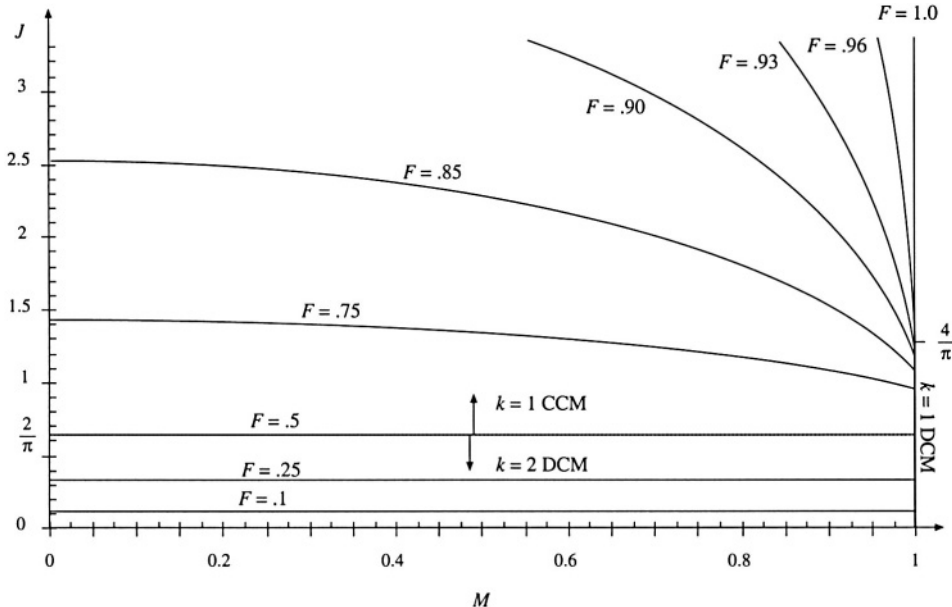


**Fig. 19.48** Output characteristics,  $k = 1$  CCM,  $k = 1$  DCM, and  $k = 2$  DCM (below resonance).

### 19.5.2 Parallel Resonant Converter

For operation in the frequency range  $0.5f_0 < f_s < \infty$ , the parallel resonant dc-dc converter exhibits one continuous conduction mode and one discontinuous conduction mode. Typical CCM switch voltage  $v_s(t)$ , tank inductor current  $i_L(t)$ , and tank capacitor voltage  $v_C(t)$  waveforms are illustrated in Fig. 19.49. The CCM converter output characteristics are given by

$$M = \left( \frac{2}{\gamma} \right) \left( \varphi - \frac{\sin(\varphi)}{\cos\left(\frac{\gamma}{2}\right)} \right) \quad (19.93)$$

$$\varphi = \begin{cases} -\cos^{-1} \left( \cos \left( \frac{\gamma}{2} \right) + J \sin \left( \frac{\gamma}{2} \right) \right) & \text{for } 0 < \gamma < \pi \text{ (above resonance)} \\ +\cos^{-1} \left( \cos \left( \frac{\gamma}{2} \right) + J \sin \left( \frac{\gamma}{2} \right) \right) & \text{for } \pi < \gamma < 2\pi \text{ (below resonance)} \end{cases} \quad (19.94)$$

and where  $M$ ,  $J$ , and  $\gamma$  are again defined as in Eqs. (19.80) and (19.81). Given the normalized load current  $J$  and the half-switching-period-angle  $\gamma$ , one can evaluate Eq. (19.94) to find  $\varphi$ , and then evaluate Eq. (19.93) to find the converter voltage conversion ratio  $M$ . In other words, the output voltage can be found for a given load current and switching frequency, without need for computer iteration.

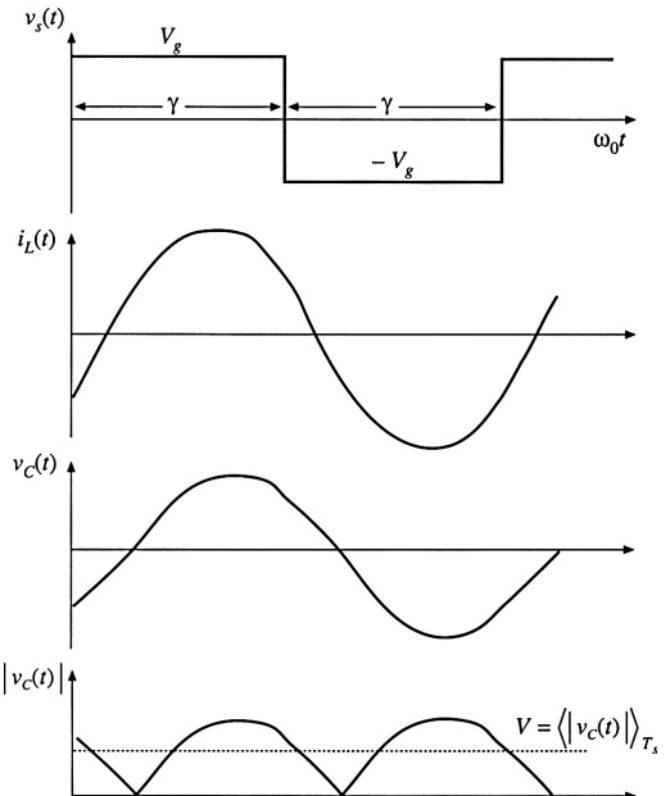


**Fig. 19.49** Typical waveforms of the parallel resonant converter, operating in the continuous conduction mode.

A discontinuous conduction mode mechanism occurs in the parallel resonant converter which is the dual of the discontinuous conduction mode mechanism of the series resonant converter. In this mode, a discontinuous subinterval occurs in which all four output bridge rectifier diodes are forward-biased, and the tank capacitor voltage remains at zero. This mode occurs both above and below resonance when the converter is heavily loaded. Typical DCM tank capacitor voltage and inductor current waveforms are illustrated in Fig. 19.50. The condition for operation in the discontinuous conduction mode is

$$\begin{aligned} J &> J_{cri}(\gamma) && \text{for DCM} \\ J &< J_{cm}(\gamma) && \text{for CCM} \end{aligned} \quad (19.95)$$

where

$$J_{cri}(\gamma) = -\frac{1}{2} \sin(\gamma) + \sqrt{\sin^2\left(\frac{\gamma}{2}\right) + \frac{1}{4} \sin^2(\gamma)} \quad (19.96)$$

The discontinuous conduction mode is described by the following set of equations:

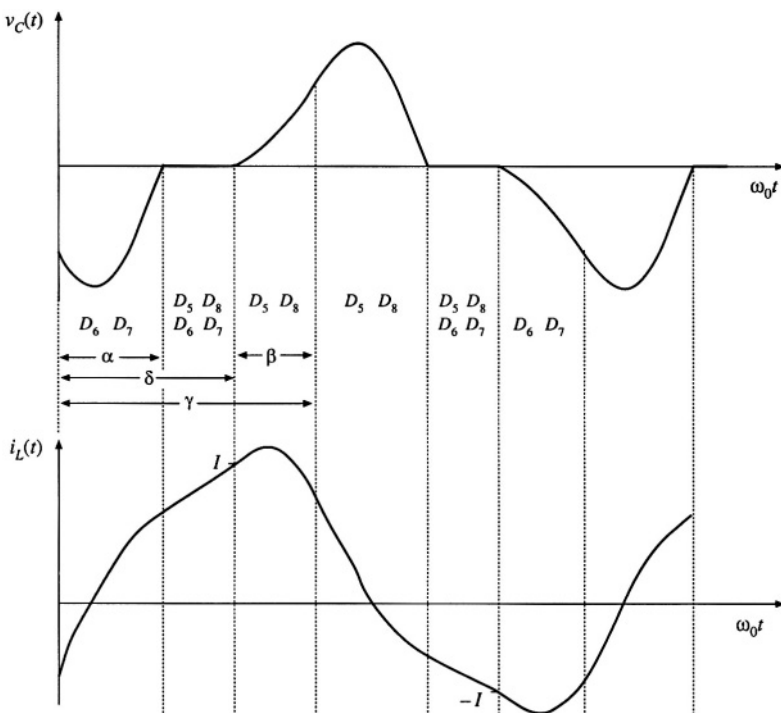


Fig. 19.50 Typical waveforms of the parallel resonant converter, operating in the discontinuous conduction mode.

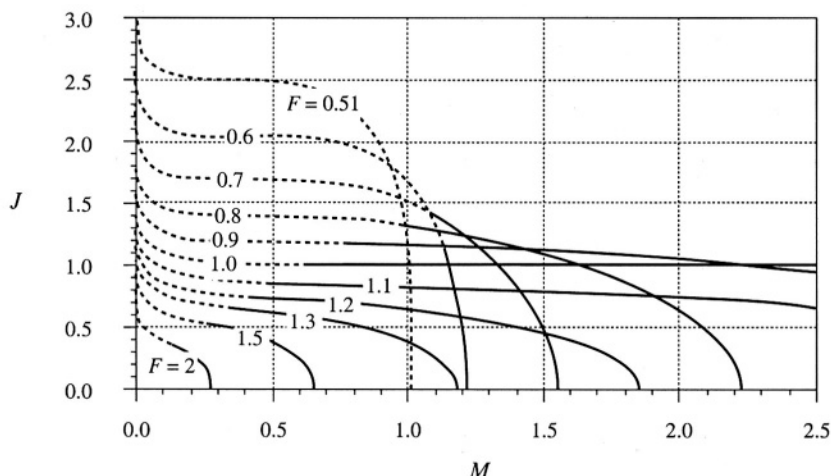
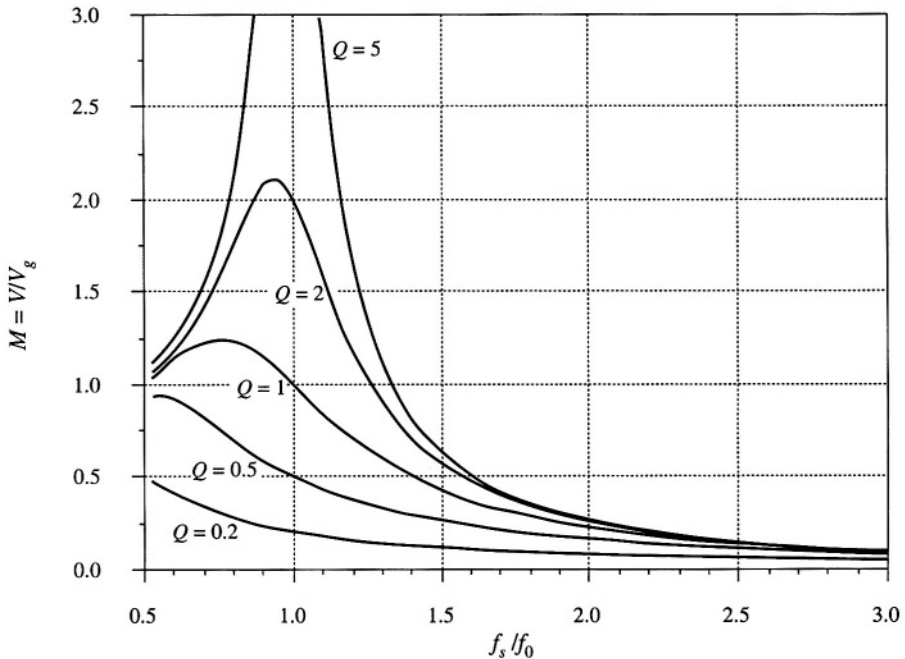


Fig. 19.51 Exact output characteristics of the parallel resonant converter, for  $F > 0.5$ . Solid curves: CCM, dashed curves: DCM.



**Fig. 19.52** Exact control characteristics of the parallel resonant converter, with a resistive load. Both CCM and DCM operation is included, for  $0.5 \leq F \leq 3$ .

$$\begin{aligned}
 M_{C0} &= 1 - \cos(\beta) \\
 J_{L0} &= J + \sin(\beta) \\
 \cos(\alpha + \beta) - 2 \cos(\alpha) &= -1 \\
 -\sin(\alpha + \beta) + 2 \sin(\alpha) + (\delta - \alpha) &= 2J \\
 \beta + \delta &= \gamma \\
 M &= 1 + \left(\frac{2}{\gamma}\right)(J - \delta)
 \end{aligned} \tag{19.97}$$

Unfortunately, the solution to this set of equations is not known in closed form, because of the mixture of linear and trigonometric terms. In consequence, the equations must be solved iteratively. For a given  $\gamma$  and  $J$ , a computer is used to iteratively find the angles  $\alpha$ ,  $\beta$ , and  $\delta$ .  $M$  is then evaluated, and the output plane characteristics can be plotted. The result is given in Fig. 19.51. The dashed lines are the DCM solutions, and the solid lines are the valid CCM solutions. Figure 19.51 describes the complete dc behavior of the ideal parallel resonant converter for all switching frequencies above  $0.5f_0$ . For given values of normalized switching frequency  $F = f_s/f_0 = \pi/\gamma$ , the relationship between the normalized output current  $J$  and the normalized output voltage  $M$  is approximately elliptical. At resonance ( $F = 1$ ), the CCM ellipse degenerates to the horizontal line  $J = 1$ , and the converter exhibits current source characteristics. Above resonance, the converter can both step up the voltage ( $M > 1$ ) and step down the voltage ( $M < 1$ ). The normalized load current is then restricted to  $J < 1$ , corresponding to  $I < V_g/nR_0$ . For a given switching frequency greater than the resonant frequency, the actual limit on maximum load current is even more restrictive than this limit. Below resonance, the converter can also step up and step down the volt-

age. Normalized load currents  $J$  greater than one are also obtainable, depending on  $M$  and  $F$ . However, no solutions occur when  $M$  and  $J$  are simultaneously large.

In Fig. 19.52, the control plane characteristics are plotted for a resistive load. The parameter  $Q$  is defined for the parallel resonant converter as  $Q = R/n^2R_0$ . The normalized load current is then given by  $J = M/Q$ .

## 19.6 SUMMARY OF KEY POINTS

1. The sinusoidal approximation allows a great deal of insight to be gained into the operation of resonant inverters and dc–dc converters. The voltage conversion ratio of dc–dc resonant converters can be directly related to the tank network transfer function. Other important converter properties, such as the output characteristics, dependence (or lack thereof) of transistor current on load current, and zero-voltage- and zero-current-switching transitions, can also be understood using this approximation. The approximation is accurate provided that the effective  $Q$  factor is sufficiently large, and provided that the switching frequency is sufficiently close to resonance.
2. Simple equivalent circuits are derived, which represent the fundamental components of the tank network waveforms, and the dc components of the dc terminal waveforms.
3. Exact solutions of the ideal dc–dc series and parallel resonant converters are listed here as well. These solutions correctly predict the conversion ratios, for operation not only in the fundamental continuous conduction mode, but in discontinuous and subharmonic modes as well.
4. Zero-voltage switching mitigates the switching loss caused by diode recovered charge and semiconductor device output capacitances. When the objective is to minimize switching loss and EMI, it is preferable to operate each MOSFET and diode with zero-voltage switching.
5. Zero-current switching leads to natural commutation of SCRs, and can also mitigate the switching loss due to current tailing in IGBTs.
6. The input impedance magnitude  $\|Z_i\|$ , and hence also the transistor current magnitude, are monotonic functions of the load resistance  $R$ . The dependence of the transistor conduction loss on the load current can be easily understood by simply plotting  $\|Z_i\|$  in the limiting cases as  $R \rightarrow \infty$  and as  $R \rightarrow 0$ , or  $\|Z_{i\infty}\|$  and  $\|Z_{i0}\|$ .
7. The ZVS/ZCS boundary is also a simple function of  $Z_{i\infty}$  and  $Z_{i0}$ . If ZVS occurs at open-circuit and at short-circuit, then ZVS occurs for all loads. If ZVS occurs at short-circuit, and ZCS occurs at open-circuit, then ZVS is obtained at matched load provided that  $\|Z_{i\infty}\| > \|Z_{i0}\|$ .
8. The output characteristics of all resonant inverters considered here are elliptical, and are described completely by the open-circuit transfer function magnitude  $\|H_\infty\|$ , and the output impedance  $\|Z_{o0}\|$ . These quantities can be chosen to match the output characteristics to the application requirements.

## REFERENCES

- [1] F.C. SCHWARZ, “An Improved Method of Resonant Current Pulse Modulation for Power Converters,” *IEEE Power Electronics Specialists Conference*, 1975 Record, pp. 194–204, June 1975.
- [2] R.L. STEIGERWALD, “High Frequency Resonant Transistor Dc–Dc Converters,” *IEEE Transactions on Industrial Electronics*, Vol. 31, No. 2, pp. 181–191, May 1984.
- [3] M. COSBY and R. NELMS, “Designing a Parallel-Loaded Resonant Inverter for an Electronic Ballast Using

- the Fundamental Approximation," *IEEE Applied Power Electronics Conference*, 1993 Record, pp. 413–423.
- [4] M. GULKO and S. BEN-YAAKOV, "Current-Sourcing Push-Pull Parallel-Resonance Inverter (CS-PPRI): Theory and Application as a Fluorescent Lamp Driver," *IEEE Applied Power Electronics Conference*, 1993 Record, pp. 411–417.
- [5] Y. CHERON, H. FOCH, and J. SALESSES, "Study of a Resonant Converter Using Power Transistors in a 25kW X-ray Tube Power Supply," *IEEE Power Electronics Specialists Conference*, Proceedings ESA Sessions, pp. 295–306, June 1985.
- [6] S. D. JOHNSON, A. F. WITULSKI, and R. W. ERICKSON, "A Comparison of Resonant Topologies in High Voltage Applications," *IEEE Transactions on Aerospace and Electronic Systems*, Vol. 24, No. 3, pp. 263–274, July 1988.
- [7] Y. MURAI and T. A. LIPO, "High Frequency Series Resonant Dc Link Power Conversion," *IEEE Industry Applications Society Annual Meeting*, 1988 Record, pp. 648–656.
- [8] F. C. SCHWARZ, "A Doublesided Cyclo-Converter," *IEEE Power Electronics Specialists Conference*, 1979 Record, pp. 437–447.
- [9] D. DIVAN, "The Resonant Dc Link Converter: A New Concept in Static Power Conversion," *IEEE Industry Applications Society Annual Meeting*, 1986 Record, pp. 648–656.
- [10] R.L. STEIGERWALD, "A Comparison of Half-Bridge Resonant Converter Topologies," *IEEE Applied Power Electronics Conference*, 1987 Record, pp. 135–144.
- [11] R. SEVERNS, "Topologies for Three Element Resonant Converters," *IEEE Applied Power Electronics Conference*, 1990 Record, pp. 712–722.
- [12] M. KAZIMIERCZUK, W. SZARANIEC, and S. WANG, "Analysis and Design of Parallel Resonant Converter at High  $Q_L$ ," *IEEE Transactions on Aerospace and Electronic Systems*, Vol. 28, pp. 35–50. January 1992.
- [13] R. KING and T. STUART, "A Normalized Model for the Half Bridge Series Resonant Converter," *IEEE Transactions on Aerospace and Electronic Systems*, March 1981, pp. 180–193.
- [14] V. VORPERIAN and S. ĆUK, "A Complete DC Analysis of the Series Resonant Converter," *IEEE Power Electronics Specialists Conference*, 1982 Record, pp. 85–100, June 1982.
- [15] R. KING and T.A. STUART, "Inherent Overload Protection for the Series Resonant Converter," *IEEE Transactions on Aerospace and Electronic Systems*, Vol. 19, No. 6, pp. 820–830, Nov. 1983.
- [16] A. WITULSKI and R. ERICKSON, "Steady-State Analysis of the Series Resonant Converter," *IEEE Transactions on Aerospace and Electronic Systems*, Vol. 21, No. 6, pp. 791–799, Nov. 1985.
- [17] A. WITULSKI and R. ERICKSON, "Design of the Series Resonant Converter for Minimum Component Stress," *IEEE Transactions on Aerospace and Electronic Systems*, Vol. 22, No. 4, July 1986, pp. 356–363.
- [18] R. ORUGANTI and F.C. LEE, "Resonant Power Processors, Part 1: State Plane Analysis," *IEEE Transactions on Industry Applications*, Vol. 21, Nov./Dec. 1985, pp. 1453–1460.
- [19] C.Q. LEE and K. SIRI, "Analysis and Design of Series Resonant Converter by State Plane Diagram," *IEEE*

*Transactions on Aerospace and Electronic Systems*, Vol. 22, No. 6, pp. 757–763, November 1986.

- [20] S. TRABERT and R. ERICKSON, "Steady-State Analysis of the Duty Cycle Controlled Series Resonant Converter," *IEEE Power Electronics Specialists Conference*, 1987 Record, pp. 545–556.
- [21] K.D.T. NGO, "Analysis of a Series Resonant Converter Pulsewidth-Modulated of Current-Controlled for Low Switching Loss," *IEEE Power Electronics Specialists Conference*, 1987 Record, pp. 527–536, June 1987.
- [22] R. ORUGANTI and F.C. LEE, "State Plane Analysis of the Parallel Resonant Converter," *IEEE Power Electronics Specialists Conference*, 1985 Record, pp. 56–73, June 1985.
- [23] S. JOHNSON, "Steady-State Analysis and Design of the Parallel Resonant Converter," M.S. Thesis, University of Colorado, Boulder, 1986.
- [24] S. JOHNSON and R. ERICKSON, "Steady-State Analysis and Design of the Parallel Resonant Converter," *IEEE Transactions on Power Electronics*, Vol. 3, No. 4, pp. 93–104, Jan. 1988.
- [25] A. BHAT and M. SWAMY, "Analysis and Design of a High-Frequency Parallel Resonant Converter Operating Above Resonance," *IEEE Transactions on Aerospace and Electronic Systems*, Vol. 25, No. 4, July 1989, pp. 449–458.
- [26] F.S. TSAI, P. MATERU, and F.C. LEE, "Constant Frequency, Clamped Mode Resonant Converters," *IEEE Power Electronics Specialists Conference*, 1987 Record, pp. 557–566, June 1987.
- [27] V. VORPERIAN and S. ĆUK, "Small-Signal Analysis of Resonant Converters," *IEEE Power Electronics Specialists Conference*, 1983 Record, pp. 269–282, June 1983.
- [28] V. VORPERIAN, "High- $Q$  Approximation in the Small-Signal Analysis of Resonant Converters," *IEEE Power Electronics Specialists Conference*, 1985 Record, pp. 707–715.
- [29] R. KING and T. STUART, "Small-Signal Model for the Series Resonant Converter," *IEEE Transactions on Aerospace and Electronic Systems*, May 1985, Vol. 21, No. 3, pp. 301–319.
- [30] A. WITULSKI, A. HERNANDEZ, and R. ERICKSON, "Small-Signal Equivalent Circuit Modeling of Resonant Converters," *IEEE Transactions on Power Electronics*, January 1991.
- [31] R. FISHER, K. NGO, and M. KUO, "A 500 kHz, 250 W Dc-dc Converter with Multiple Outputs Controlled by Phase-Shifted PWM and Magnetic Amplifiers," *Proceedings of High Frequency Power Conversion Conference*, pp. 100–110, May 1988.
- [32] L. MWEENE, C. WRIGHT, and M. SCHLECHT, "A 1 kW, 500 kHz Front-End Converter for a Distributed Power Supply System," *IEEE Applied Power Electronics Conference*, 1989 Record, pp. 423–432.
- [33] R. REDL, L. BELOGH, and D. EDWARDS, "Optimum ZVS Full-Bridge DC/DC Converter with PWM Phase-Shift Control: Analysis, Design Considerations, and Experimental Results," *IEEE Applied Power Electronics Conference*, 1994 Record, pp. 159–165.
- [34] J. G. CHO, J. A. SABATE, and F. C. LEE, "Novel Full Bridge Zero-Voltage-Transition PWM DC/DC Converter for High Power Applications," *IEEE Applied Power Electronics Conference*, 1994 Record, pp. 143–149.

- [35] O. D. PATTERSON and D. M. DIVAN, "Pseudo-Resonant Full Bridge DC/DC Converter," *IEEE Power Electronics Specialists Conference*, 1987 Record, pp. 424–430.
- [36] R. FARRINGTON, M. JOVANOVIC, and F. C. LEE, "Analysis of Reactive Power in Resonant Converters," *IEEE Power Electronics Specialists Conference*, 1992 Record, pp. 197–205.
- [37] R. D. MIDDLEBROOK, "Null Double Injection and the Extra Element Theorem," *IEEE Transactions on Education*, Vol. 32, No. 3, pp. 167–180, August 1989.
- [38] D. TUTTLE, *Network Synthesis*, New York: John Wiley & Sons, Vol. 1, Chapter 6, 1958.

## PROBLEMS

- 19.1 Analysis of a half-bridge dc–dc parallel resonant converter, operated above resonance. In Fig. 19.53, the elements  $C_b$ ,  $L_F$ , and  $C_F$  are large in value, and have negligible switching ripple. You may assume that all elements are ideal. You may use the sinusoidal approximation as appropriate.

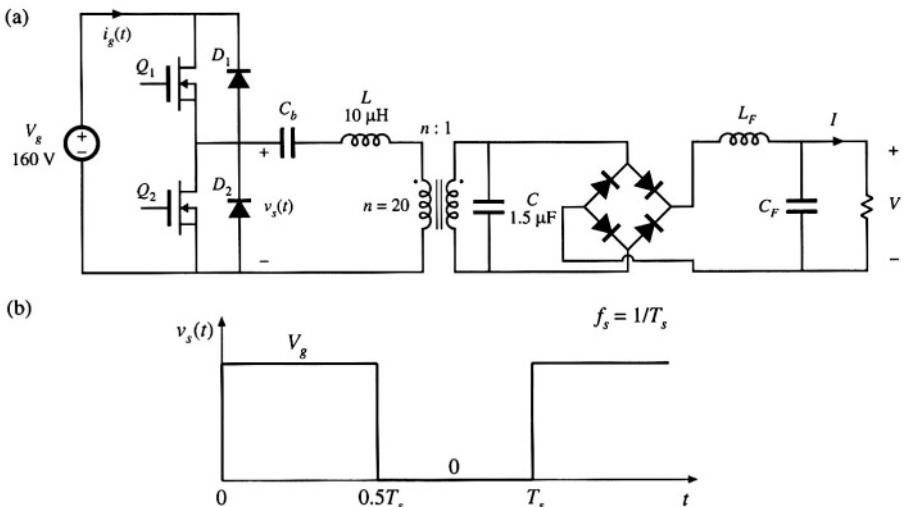


**Fig. 19.53** Half-bridge parallel resonant converter of Problem 19.1: (a) schematic, (b) switch voltage waveform.

- (a) Sketch the waveform of the current  $i_g(t)$ .
- (b) Construct an equivalent circuit for this converter, similar to Fig. 19.22, which models the fundamental components of the tank waveforms and the dc components of the converter input current and output voltage. Clearly label the values and/or give expressions for all elements in your model, as appropriate.
- (c) Solve your model to derive an expression for the conversion ratio  $V/V_g = M(F, Q_r, n)$ .  
At rated (maximum) load, this converter produces  $I = 20$  A at  $V = 3.3$  V.
- (d) What is the converter switching frequency  $f_s$  at rated load?
- (e) What is the magnitude of the peak transistor current at rated load?  
At minimum load, the converter produces  $I = 2$  A at  $V = 3.3$  V.

- (f) What is the converter switching frequency  $f_s$  at minimum load?  
 (g) What is the magnitude of the peak transistor current at minimum load? Compare with your answer from part (e)—what happens to the conduction loss and efficiency at minimum load?

19.2

A dc-dc resonant converter contains an LCC tank network [Fig. 19.1(d)], with an output filter containing a filter inductor as in the parallel resonant dc-dc converter.

- (a) Sketch an equivalent circuit model for this converter, based on the approximate sinusoidal analysis method of Section 19.1. Give expressions for all elements in your model.  
 (b) Solve your model, to derive an expression for the conversion ratio  $M = V/V_g$ . Express  $M$  as a function of  $F = f_s/f_\infty$ ,  $Q_e = R_e/R_0$ , and  $n = C_s/C_p$ , where  $f_\infty$  is defined as in Eq. (19.50) and  $R_0$  is

$$R_0 = \sqrt{\frac{L(C_s + C_p)}{C_s C_p}}$$

- (c) Plot  $M$  vs.  $F$ , for  $n = 1$  and  $Q_e = 1, 2$ , and  $5$ .  
 (d) Plot  $M$  vs.  $F$ , for  $n = 0.25$  and  $Q_e = 1, 2$ , and  $5$ .

19.3

Dual of the series resonant converter. In the converter illustrated in Fig. 19.54,  $L_{F1}$ ,  $L_{F2}$ , and  $C_F$  are large filter elements, whose switching ripples are small.  $L$  and  $C$  are tank elements, whose waveforms  $i_L(t)$  and  $v_C(t)$  are nearly sinusoidal.

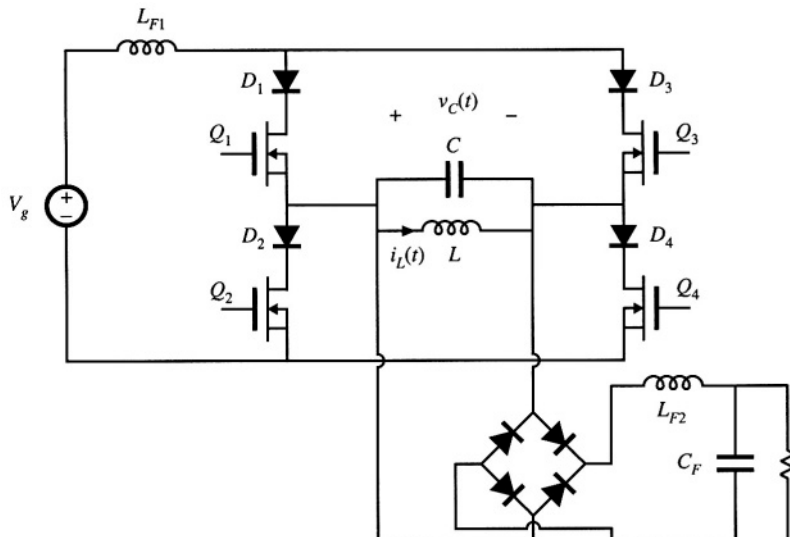


Fig. 19.54 Dual of the series resonant converter, Problem 19.3.

- (a) Using the sinusoidal approximation method, develop equivalent circuit models for the switch network, tank network, and rectifier network.  
 (b) Sketch a Bode diagram of the parallel  $LC$  parallel tank impedance.  
 (c) Solve your model. Find an analytical solution for the converter voltage conversion ratio  $M = V/V_g$ , as a function of the effective  $Q_e$  and the normalized switching frequency  $F = f_s/f_0$ . Sketch  $M$  vs.  $F$ .  
 (d) What can you say about the validity of the sinusoidal approximation for this converter? Which

parts of your  $M$  vs.  $F$  plot of part (c) are valid and accurate?

19.4

The converter of Problem 19.3 operates below resonance.

- (a) Sketch the waveform  $v_C(t)$ . For each subinterval, label: (i) which of the diodes  $D_1$  to  $D_4$  and transistors  $Q_1$  to  $Q_4$  conduct current, and (ii) which devices block voltage.
- (b) Does the reverse recovery process of diodes  $D_1$  to  $D_4$  lead to switching loss? Do the output capacitances of transistors  $Q_1$  to  $Q_4$  lead to switching loss?
- (c) Repeat parts (a) and (b) for operation above resonance.

19.5

A parallel resonant converter operates with a dc input voltage of  $V_g = 270$  V. The converter supplies 5 V to a dc load. The dc load power varies over the range 20 W to 200 W. It is desired to operate the power transistors with zero voltage switching. The tank element values are  $L = 57 \mu\text{H}$ ,  $C_p = 0.9 \text{ nF}$ , referred to the transformer primary. The parallel resonant tank network contains an isolation transformer having a turns ratio of 52:1.

- (a) Define  $F$  as in Eq. (19.19). Derive an expression for  $F$ , as a function of  $M$  and  $Q_e$ .
- (b) Determine the switching frequency, peak transistor current, and peak tank capacitor voltage at the maximum load power operating point.
- (c) Determine the switching frequency, peak transistor current, and peak tank capacitor voltage at the minimum load power operating point.

19.6

In a certain resonant inverter application, the dc input voltage is  $V_g = 320$  V. The inverter must produce an approximately sinusoidal output voltage having a frequency of 200 kHz. Under no load (output open-circuit) conditions, the inverter should produce a peak-to-peak output voltage of 1500 V. The nominal resistive operating point is 200 Vrms applied to  $100 \Omega$ . A nonisolated LCC inverter is employed. It is desired that the inverter operate with zero-voltage switching, at least for load resistances less than  $200 \Omega$ .

- (a) Derive expressions for the output open-circuit voltage  $V_{oc}$  and short-circuit current  $I_{sc}$  of the LCC inverter. Express your results as functions of  $F = f_s/f_\infty$ ,  $V_g$ ,  $R_{\infty} = L/C_s||C_p$  and  $n = C_s/C_p$ . The open-circuit resonant frequency  $f_\infty$  is defined in Eq. (19.50).
- (b) To meet the given specifications, how should the short-circuit current  $I_{sc}$  be chosen?
- (c) Specify tank element values that meet the specifications.
- (d) Under what conditions does your design operate with zero-voltage switching?
- (e) Compute the peak transistor current under no-load and short-circuit conditions.

19.7

A series resonant dc–dc converter operates with a dc input voltage of  $V_g = 550$  V. The converter supplies 30 kV to a load. The dc load power varies over the range 5 kW to 25 kW. It is desired to operate the power transistors with zero-voltage switching. The maximum feasible switching frequency is 50 kHz. An isolation transformer having a  $1:n$  turns ratio is connected in series with the tank network. The peak tank capacitor voltage should be no greater than 2000 V, referred to the primary.

- (a) Derive expressions for the peak tank capacitor voltage and peak tank inductor current.
- (b) Select values for the tank inductance, tank capacitance, and turns ratio, such that the given specifications are met. Attempt to minimize the peak tank inductor current, while maximizing the worst-case minimum switching frequency.

19.8

Figure 19.55 illustrates a full-bridge resonant inverter containing an LLC tank network.

- (a) Sketch the Bode diagrams of the input impedance under short-circuit and open-circuit conditions:  $\|Z_{i0}(j\omega)\|$  and  $\|Z_{i\infty}(j\omega)\|$ . Give analytical expressions for the resonant frequencies and asymptotes.
- (b) Describe the conditions on switching frequency and load resistance that lead to zero-voltage switching.
- (c) Derive an expression for the frequency  $f_m$ , where  $\|Z_{i0}\| = \|Z_{i\infty}\|$ .

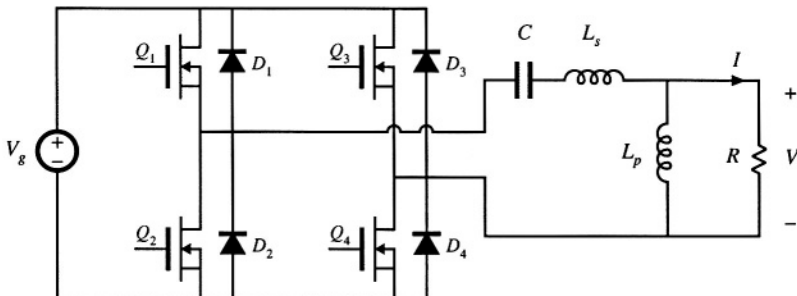


**Fig. 19.55** LLC inverter of Problem 19.8.

- (d) Sketch the Bode plot of  $\| H_\infty(j\omega) \|$ . Label the resonant frequency, and give analytical expressions for the asymptotes.

**19.9** You are given the LLC inverter circuit of Fig. 19.56. Under nominal conditions, this converter operates at switching frequency  $f_s = 100$  kHz. All elements are ideal.

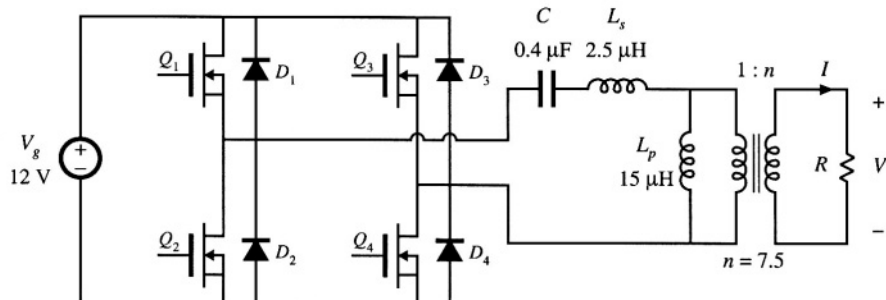


**Fig. 19.56** Transformer-isolated LLC inverter, Problem 19.9.

- (a) Determine the numerical values of the open-circuit peak output voltage  $V_{oc}$  and the short-circuit peak output current  $I_{sc}$ .
- (b) Sketch the elliptical output characteristic. Over what portion of this ellipse does the converter operate with zero-voltage switching? Does it operate with zero-voltage switching at matched load?
- (c) Sketch the Bode plots of  $\| Z_{f_\infty} \|$  and  $\| Z_{i_0} \|$ , and label the numerical values of  $f_0$ ,  $f_\infty$ ,  $f_m$ , and  $f_x$ .
- (d) What is the numerical value of the peak transistor current when  $R = 0$ ? When  $R \rightarrow \infty$ ?
- (e) The inverter operates with load resistances that can vary between  $500 \Omega$  and an open circuit. What is the resulting range of output voltage? Does the inverter always operate with zero-voltage switching?

**19.10** It is desired to obtain a converter with current source characteristics. Hence, a series resonant converter is designed for operation in the  $k = 2$  discontinuous conduction mode. The switching frequency is chosen to be  $f_s = 0.225f_0$ , where  $f_0$  is the tank resonant frequency (consider only open-loop operation). The load  $R$  is a linear resistance which can assume any positive value:  $0 \leq R < \infty$ .

- (a) Plot the output characteristics ( $M$  vs.  $J$ ), for all values of  $R$  in the range  $0 \leq R < \infty$ . Label mode boundaries, evaluate the short-circuit current, and give analytical expressions for the output characteristics.

- (b) Over what range of  $R$  (referred to the tank characteristic impedance  $R_0$ ) does the converter operate as intended, in the  $k = 2$  discontinuous conduction mode?

## 19.11

The parallel resonant converter as a single-phase high-quality rectifier. It is desired to utilize a transformer-isolated parallel resonant dc–dc converter in a single-phase low-harmonic rectifier system. By properly varying the converter switching frequency, a near-ideal rectifier system that can be modeled as in Fig. 18.12 is obtained. You may utilize the results of Section 19.5.2 to answer this problem. The parallel resonant tank network contains an isolation transformer having a  $1:n$  turns ratio. You may use either approximate graphical analysis or computer iteration to answer parts (b) and (c).

- (a) Plot the normalized input characteristics (normalized input voltage  $m_g = nv_g/v$  vs. normalized input current  $j_g = i_g n R_0 / v$ ) of the parallel resonant converter, operated in the continuous conduction mode above resonance. Plot curves for  $F = f_s/f_0 = 1.0, 1.1, 1.2, 1.3, 1.5,$  and  $2.0$ . Compare these characteristics with the desired linear resistive input characteristic  $v_g/i_g = R_{emulated}$ .
- (b) The converter is operated open-loop, with  $F = 1.1$ . The applied normalized input voltage is a rectified sinusoid of unity magnitude:  $m_g(t) = |\sin(\omega t)|$ . Sketch the resulting normalized input current waveform  $j_g(t)$ . Approximately how large is the peak current? The crossover dead time?
- (c) A feedback loop is now added, which regulates the input current to follow the input voltage such that  $i_g(t) = v_g(t)/R_{emulated}$ . You may assume that the feedback loop operates perfectly. For the case  $R_{emulated} = R_0$ , and with the same applied  $m_g(t)$  waveform as in part (b), sketch the switching frequency waveform for one ac line period [i.e., show how the controller must vary  $F$  to regulate  $i_g(t)$ ]. What is the maximum value of  $F$ ? Note: In practice, the converter would be designed to operate with a smaller peak value of  $j_g$ , so that the switching frequency variations would be better behaved.
- (d) Choose element values (tank inductance, tank capacitance, and transformer turns ratio) such that the converter of part (c) meets the following specifications:

Ac input voltage	120 Vrms, 60 Hz
DC output voltage	42 V
Average power	800 W
Maximum switching frequency	200 kHz

Refer the element values to the primary side of the transformer.

---

# 20

## Soft Switching

---

In addition to the resonant circuits introduced in Chapter 19, there has been much interest in reducing the switching loss of the PWM converters of the previous chapters. Several of the more popular approaches to obtaining *soft switching* in buck, boost, and other converters, are discussed in this chapter.

Mechanisms that cause switching loss are discussed in Chapter 4, including diode reverse recovery, semiconductor output capacitances, and IGBT current tailing. Soft switching involves mitigation of one or more of these switching loss mechanisms in a PWM converter. The energy that would otherwise be lost is recovered, and is transferred to the converter source or load. The operation of a semiconductor device, during a given turn-on or turn-off switching transition, can be classified as hard-switched, zero-current switched, or zero-voltage switched. Operation of diodes and transistors with soft switching is examined in Section 20.1. In particular, it is preferable to operate diodes with zero-voltage switching at their turn-off transitions, and to operate MOSFETs with zero-voltage switching during their turn-on transitions. However, zero-voltage switching comes at the expense of increased conduction loss, and so the engineer must consider the effect of soft switching on the overall converter efficiency.

*Resonant switch* converters are a broad class of converters in which the PWM switch network of a conventional buck, boost, or other converter is replaced with a switch cell containing resonant elements. These resonant elements are positioned such that the semiconductor devices operate with zero-current or zero-voltage switching, and such that one or more of the switching loss mechanisms is reduced or eliminated. Other soft-switching approaches may employ resonant switching transitions, but otherwise exhibit the approximately rectangular waveforms of hard-switched converters. In any case, the resulting hybrid converter combines the properties of the resonant switching network and the parent hard-switched PWM converter.

Soft-switching converters can exhibit reduced switching loss, at the expense of increased conduction loss. Obtaining zero-voltage or zero-current switching requires that the resonant elements have large ripple; often, these elements are operated in a manner similar to the discontinuous conduction

modes of the series or parallel resonant converters. As in other resonant schemes, the objectives of designing such a converter are: (1) to obtain smaller transformer and low-pass filter elements via increase of the switching frequency, and/or (2) to reduce the switching loss induced by component nonidealities such as diode stored charge, semiconductor device capacitances, and transformer leakage inductance and winding capacitance.

The resonant switch and soft-switching ideas are quite general, and can be applied to a variety of topologies and applications. A large number of resonant switch networks have been documented in the literature; a few basic approaches are listed here [1–24]. The basic zero-current-switching quasi-resonant switch network is analyzed in detail in Section 20.2. Expressions for the average components of the switch network terminal waveforms are found, leading to determination of the *switch conversion ratio*  $\mu$ . The switch conversion ratio  $\mu$  performs the role of the duty cycle  $d$  of CCM PWM switch networks. For example, the buck converter exhibits conversion ratio  $M$  equal to  $\mu$ . Both half-wave and full-wave ringing of the tank network is considered; these lead to different switch conversion ratio functions  $\mu$ . In general, given a PWM CCM converter having conversion ratio  $M(d)$ , we can replace the PWM switch network with a resonant switch network having switch conversion ratio  $\mu$ . The resulting quasi-resonant converter will then have conversion ratio  $M(\mu)$ . So we can obtain soft-switching versions of all of the basic converters (buck, boost, buck-boost, forward, flyback, etc.), that exhibit zero-voltage or zero-current switching and other desirable properties.

In Section 20.3, the characteristics of several other resonant switch networks are listed: the zero-voltage-switching quasi-resonant switch network, the zero-current-switching and zero-voltage-switching quasi-square-wave networks, and the multiresonant switch network. One can obtain zero-voltage switching in all transistors and diodes using these networks.

Several related soft-switching approaches are now popular, which attain zero-voltage switching of the transistor or transistors in commonly-used converters. The zero-voltage transition approach finds application in full-bridge buck-derived converters. Active-clamp snubbers are often added to forward and flyback converters, to attain zero-voltage switching and to reset the transformer. These circuits lead to zero-voltage switching of the transistors, but (less-than-optimal) zero-current switching of the secondary-side diodes. Nonetheless, high efficiency can be achieved. An auxiliary resonant-commutated pole can achieve zero-voltage switching in voltage-source inverters. These converters are briefly discussed in Section 20.4.

## 20.1    SOFT-SWITCHING MECHANISMS OF SEMICONDUCTOR DEVICES

When loosely used, the terms “zero-current switching” and “zero-voltage switching” normally refer to one or more switching transitions of the transistor in a converter. However, to fully understand how a converter generates switching loss, one must closely examine the switching transitions of every semiconductor device. As described in Section 4.3, there are typically several mechanisms that are sources of significant switching loss. At the turn-off transition of a diode, its reverse-recovery process can induce loss in the transistor or other elements of the converter. The energy stored in the output capacitance of a MOSFET can be lost when the MOSFET turns on. IGBTs can lose significant energy during their turn-off transition, owing to the current-tailing phenomenon. The effects of zero-current switching and zero-voltage switching on each of these devices is discussed in detail below.

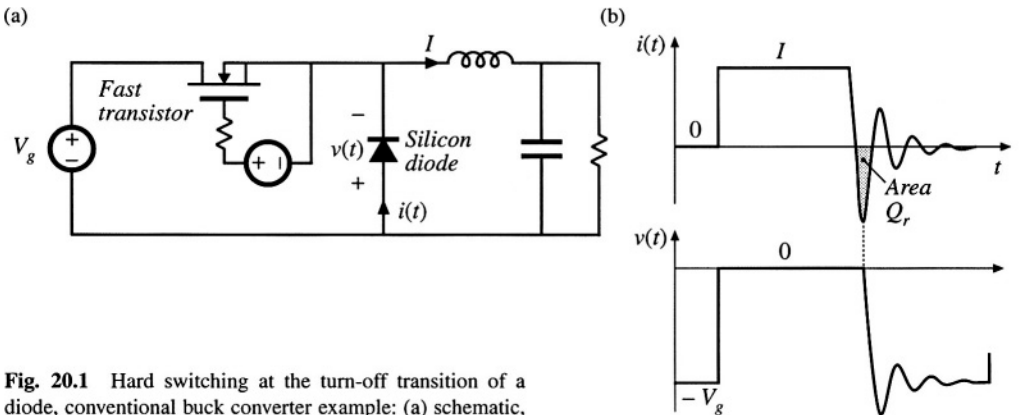


**Fig. 20.1** Hard switching at the turn-off transition of a diode, conventional buck converter example: (a) schematic, (b) diode voltage and current waveforms.

### 20.1.1 Diode Switching

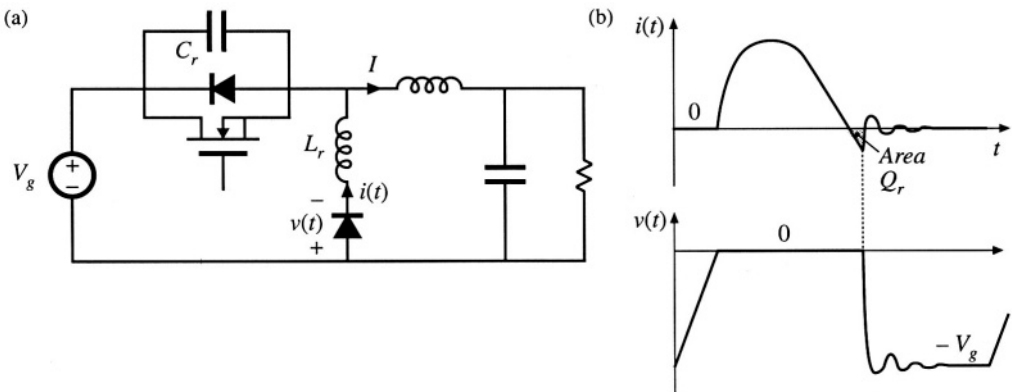
As discussed in Chapter 4, the reverse-recovery process usually leads to significant switching loss associated with the turn-off transition of diodes. This is often the largest single source of loss in a hard-switched converter. Normally, negligible loss is associated with the turn-on transition of power diodes. Three types of diode turn-off transition waveforms are commonly encountered in modern switching converters: hard switching, zero-current switching, and zero-voltage switching.

Figure 20.1 illustrates a conventional hard-switched PWM buck converter. The diode voltage and current waveforms  $v(t)$  and  $i(t)$  are also illustrated, with an exaggerated reverse recovery time. The output inductor current ripple is small. The diode turns off when the transistor is turned on; the reverse recovery process leads to a negative peak current of large amplitude. The diode must immediately support the full reverse voltage  $V_g$ , and hence both  $v(t)$  and  $i(t)$  must change with large slopes during reverse recovery. As described in Section 4.3.2, hard switching of the diode induces energy loss  $W_D$  in the transistor, given approximately by

$$W_D = V_g Q_r + t_r V_g I \quad (20.1)$$

where  $Q_r$  is the diode recovered charge and  $t_r$  is the reverse recovery time, both taken to be positive quantities. The recovered charge is relatively large because the slope  $di/dt$  is large during the turn-off transition. The resonant circuit formed by the diode output capacitance  $C_j$  and the diode package and other wiring inductances leads to ringing at the end of the reverse recovery time.

Figure 20.2 illustrates zero-current switching at the turn-off transition of a diode. The converter example is a quasi-resonant zero-voltage switching buck converter (see Section 20.3.1). The output inductor current ripple is again small. However, tank inductor  $L_r$  is now connected in series with the diode. The resulting diode current waveform  $i(t)$  changes with a limited slope as shown. The diode reverse-recovery process commences when  $i(t)$  passes through zero and becomes negative. The negative  $i(t)$  actively removes stored charge from the diode; during this reverse recovery time, the diode remains forward-biased. When the stored charge is removed, then the diode voltage must rapidly change to  $-V_g$ . As described in Section 4.3.3, energy  $W_D$  is stored in inductor  $L_r$  at the end of the reverse recovery time, given by



**Fig. 20.2** Zero-current switching at the turn-off transition of a diode, ZVS quasi-resonant buck converter example: (a) converter schematic, (b) diode voltage and current waveforms.

$$W_D = V_g Q_r \quad (20.2)$$

The resonant circuit formed by  $L_r$  and the diode output capacitance  $C_j$  then cause this energy to be circulated between  $L_r$  and  $C_j$ . This energy is eventually dissipated by parasitic resistive elements in the circuit, and hence is lost. Since Eqs. (20.1) and (20.2) are similar in form, the switching losses induced by the reverse-recovery processes of diodes operating with hard switching and with zero-current switching are similar in magnitude. Zero-current switching may lead to somewhat lower loss because the reduced  $di/dt$  leads to less recovered charge  $Q_r$ . Zero-current switching of diodes also typically leads to increased peak inverse diode voltage during the ringing of  $L_r$  and  $C_j$ , because of the relatively large value of  $L_r$ .

When a diode operates with hard switching or zero-current switching, and when substantial inductance is present in series with the diode, then significant ringing is observed in the diode voltage waveform. A resonant circuit, comprised of the series inductance and the diode output capacitance, is excited by the diode reverse recovery process, and the resulting ringing voltage can be of large enough magnitude to lead to breakdown and failure of the diode. A common example is the diodes on the secondary side of a hard-switched transformer-isolated converter; the resonant circuit is then formed by the transformer leakage inductance and the diode output capacitance. Other examples are the circuits of Figs. 20.2 and 20.36, in which the series inductance is a discrete tank inductor.

A simple snubber circuit that is often used to protect the diode from excessive reverse voltage is

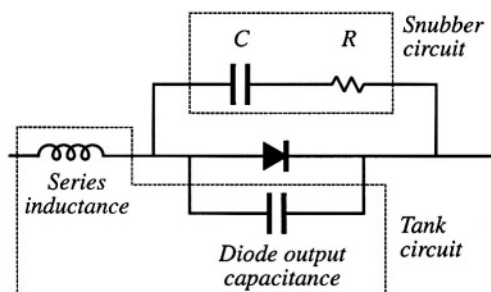


**Fig. 20.3** A dissipative snubber circuit, for protection of a diode from excessive voltage caused by ringing.

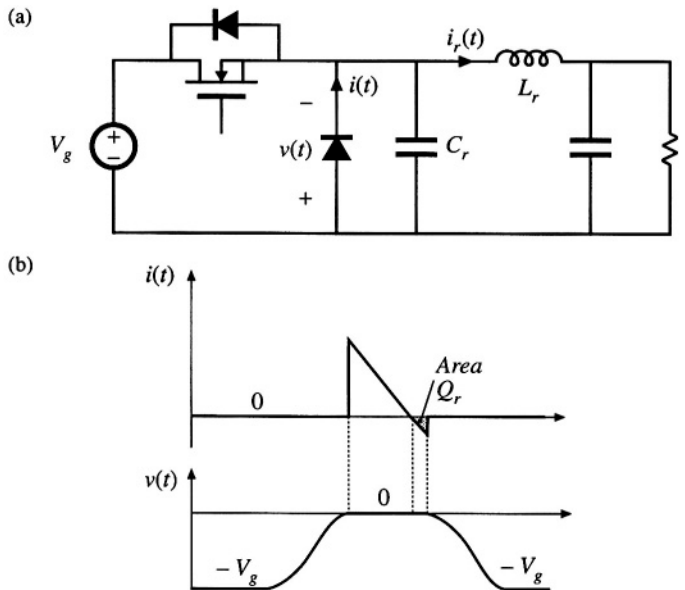


**Fig. 20.4** Zero-voltage switching at the turn-off transition of a diode, (b) ZVS quasi-squarewave buck converter example: (a) converter schematic, (b) diode current and voltage waveforms.

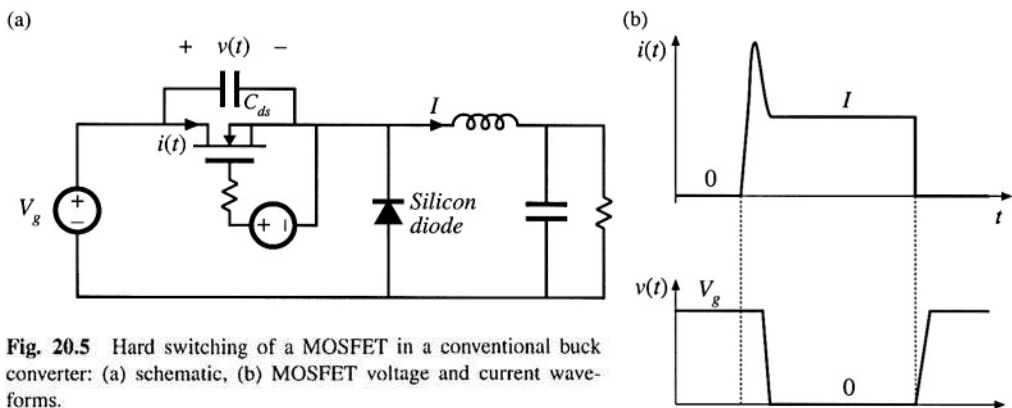
illustrated in Fig. 20.3. Resistor  $R$  damps the ringing of the resonant circuit. Capacitor  $C$  prevents the off-state voltage of the diode from causing excessive power loss in  $R$ . Nonetheless, the energy consumed by  $R$  per switching period is typically greater than Eqs. (20.1) or (20.2).

Figure 20.4 illustrates zero-voltage switching at the turn-off transition of a diode. The figure illustrates the example of a zero-voltage switching quasi-square wave buck converter, discussed in Section 20.3.3. The output inductor  $L_r$  of this converter assumes the role of the tank inductor, and exhibits large current ripple that causes the current  $i_r(t)$  to reverse polarity. While the diode conducts, its current  $i(t)$  is equal to  $i_r(t)$ . When  $i_r(t)$  becomes negative, the diode continues to conduct until its stored charge  $Q_r$  has been removed. The diode then becomes reverse-biased, and  $i_r(t)$  flows through capacitor  $C_r$  and the diode output capacitance  $C_d$ . The diode voltage and current both change with limited slope in this type of switching, and the loss induced by the diode reverse-recovery process is negligible because the waveforms are not significantly damped by parasitic resistances in the circuit, and because the peak currents during reverse recovery are relatively low. The diode stored charge and diode output capacitance both behave as an effective nonlinear capacitor that can be combined with (or replace) tank capacitor  $C_r$ . Snubber circuits such as Fig. 20.3 are not necessary when the diode operates with zero-voltage switching.

Thus, zero-voltage switching at the turn-off transition of a diode is the preferred approach, that leads to minimum switching loss. Zero-current switching at the turn-off transition can be problematic, because of the high peak inverse voltage induced across the diode by ringing.

### 20.1.2 MOSFET Switching

The switching loss mechanisms typically encountered by a MOSFET in a hard-switched converter are discussed in Chapter 4, and typical MOSFET voltage and current waveforms are illustrated in Fig. 20.5. The most significant components of switching loss in the MOSFET of this circuit are: (1) the loss



**Fig. 20.5** Hard switching of a MOSFET in a conventional buck converter: (a) schematic, (b) MOSFET voltage and current waveforms.

induced by the diode reverse recovery process, and (2) the loss of the energy stored in the MOSFET output capacitance  $C_{ds}$ . Both loss mechanisms occur during the MOSFET turn-on process.

In the hard-switched circuit of Fig. 20.5, there is essentially no switching loss incurred during the MOSFET turn-off transition. This occurs because of the substantial output capacitance  $C_{ds}$  of the MOSFET. This capacitance holds the voltage  $v(t)$  close to zero while the MOSFET turns off, so that the turn-off switching loss is very small. After the MOSFET has turned off, the output inductor current  $I$  flows through  $C_{ds}$ . The voltage  $v(t)$  then increases until  $v = V_g$  and the diode becomes forward biased.

However, when the MOSFET turns on, a high peak current flows through the MOSFET channel, induced by the diode reverse recovery and by the output capacitances of the MOSFET and diode. This leads to substantial energy loss during the hard-switched turn-on transition of the MOSFET.

When a MOSFET (or other transistor) operates with hard switching, and when substantial inductance is present in series with the MOSFET, then significant ringing is observed in the MOSFET voltage waveform. A resonant circuit, composed of the MOSFET output capacitance and the series inductance, is excited when the MOSFET turns off, and the resulting ringing voltage can be of large enough magnitude to lead to breakdown and failure of the MOSFET. A common example is the MOS-

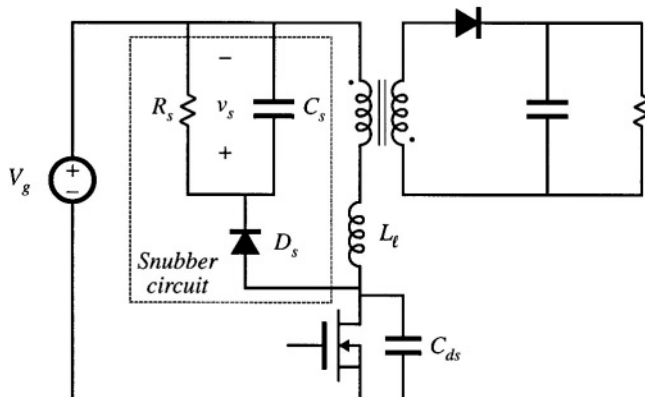


**Fig. 20.6** Insertion of a dissipative voltage-clamped snubber circuit into a flyback converter. The MOSFET voltage is clamped to a peak value of  $(V_g + v_s)$ .

FET of the flyback converter, in which series inductance is introduced by the transformer leakage inductance. An  $R-C$  snubber circuit, similar to that used for the diode in Fig. 20.3, can be used to protect the MOSFET from damage caused by excessive applied voltage. Another common snubber circuit is illustrated in Fig. 20.6. When the MOSFET turns off, the current flowing in the transformer leakage inductance  $L_t$  begins to flow into the MOSFET capacitance  $C_{ds}$ . These parasitic elements then ring, and the peak transistor voltage can significantly exceed the ideal value of  $(D/D')V_g$ .

One simple way to design the snubber circuit of Fig. 20.6 is to choose the capacitance  $C_s$  to be large, so that  $v_s(t) \approx V_s$  contains negligible switching ripple. The resistance  $R_s$  is then chosen so that the power consumption of  $R_s$  at the desired voltage  $V_s$  is equal to the switching loss caused by  $L_t$ :

$$\frac{V_s^2}{R_s} \approx \frac{1}{2} L_t^2 f_s \quad (20.3)$$

The current  $i$  is equal to the current flowing in the transformer primary just before the MOSFET is turned off. This approximate expression is useful for obtaining a first estimate of how to choose  $R_s$  to obtain a given desired  $V_s$ .

Zero-current switching does not affect the switching loss that arises from the MOSFET output capacitance, and it may or may not influence the loss induced by diode reverse recovery. In consequence, zero-current switching is of little or no help in improving the efficiency of converters that employ MOSFETs.

Zero-voltage switching can prevent both diode reverse recovery and semiconductor output capacitances from inducing switching loss in MOSFETs. An example is illustrated in Fig. 20.7. This circuit is again a zero-voltage switching quasi-squarewave example, discussed in Section 20.3.3. The converter circuit naturally discharges the energy stored in  $C_{ds}$ , before the MOSFET is switched on. When the drain-to-source voltage  $v(t)$  passes through zero, the MOSFET body diode becomes forward-biased. The MOSFET can then be turned on at zero voltage, without incurring turn-on switching loss. The MOSFET turn-on transition must be completed before the tank inductor current  $i_r(t)$  becomes positive. The MOSFET turn-off transition is also lossless, and is similar to the hard-switched case discussed above.

Zero-voltage switching of a MOSFET also causes its body diode to operate with zero-voltage switching. This can eliminate the switching loss associated with reverse recovery of the slow body diode, and improve the reliability of circuits that forward-bias this diode.

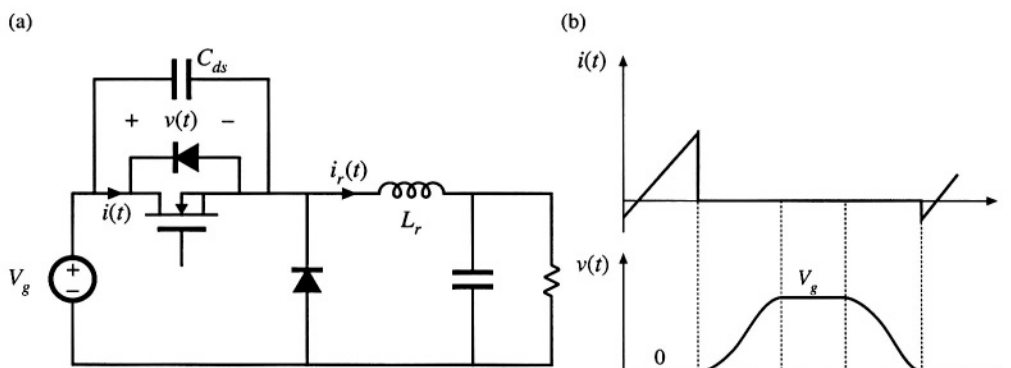


**Fig. 20.7** Zero-voltage switching of a MOSFET, ZVS quasi-squarewave buck converter example. The MOSFET, its body diode, and its output capacitance  $C_{ds}$  are illustrated. (a) converter schematic, (b) MOSFET voltage and current waveforms.

Zero-voltage switching can also eliminate the overvoltage problems associated with transformer leakage inductances, removing the need for voltage-clamped snubber circuits such as in Fig. 20.6. An example is discussed in Section 20.4.2.

### 20.1.3 IGBT Switching

Like the MOSFET, the IGBT typically encounters substantial switching loss during its turn-on transition, induced by the reverse-recovery process of diodes within the converter. In addition, the IGBT exhibits significant switching loss during its turn-off transition, caused by the current tailing phenomenon (*see* Chapter 4).

Zero-voltage switching has been successfully applied to IGBT circuits—an example is the auxiliary resonant commutation circuit discussed in Section 20.4.3. This has the principal advantage of eliminating the switching loss caused by diode reverse recovery. Although zero-voltage switching can reduce the loss incurred during the turn-off transition, it is difficult to eliminate the substantial loss caused by current tailing.

## 20.2 THE ZERO-CURRENT SWITCHING QUASI-RESONANT SWITCH CELL

Figure 20.8(a) illustrates a generic buck converter, consisting of a switch cell cascaded by an  $L-C$  low-pass filter. When the switch cell is realized as in Fig. 20.8(b), then a conventional PWM buck converter is obtained. Figures 20.8(b) and (c) illustrate two other possible realizations of the switch cell: the half-wave and full-wave zero-current-switching quasi-resonant switches [1, 2]. In these switch cells, a resonant tank capacitor  $C_r$  is placed in parallel with diode  $D_2$ , while resonant tank capacitor  $L_r$  is placed in series with the active transistor element.

Both resonant switch cells require a two-quadrant SPST switch. In the half-wave switch cell of Fig. 20.8(c), diode  $D_1$  is added in series with transistor  $Q_1$ . This causes the  $Q_1-D_1$  SPST switch to turn off at the first zero crossing of the tank inductor current  $i_1(t)$ . In the full-wave switch cell of Fig. 20.8(d), antiparallel diode  $D_1$  allows bidirectional flow of the tank inductor current  $i_1(t)$ . With this switch network, the  $Q_1-D_1$  SPST switch is normally turned off at the second zero-crossing of the  $i_1(t)$  waveform. In either switch cell, the  $L_r$  and  $C_r$  elements are relatively small in value, such that their resonant frequency  $f_0$  is greater than the switching frequency  $f_s$ , where

$$f_0 = \frac{1}{2\pi\sqrt{L_r C_r}} = \frac{\omega_0}{2\pi} \quad (20.4)$$

In the analysis which follows, it is assumed that the converter filter element values  $L$  and  $C$  have negligible switching ripple. Hence, the switch cell terminal waveforms  $v_1(t)$  and  $i_2(t)$  are well-approximated by their average values:

$$\begin{aligned} i_2(t) &\approx \langle i_2(t) \rangle_{T_s} \\ v_1(t) &\approx \langle v_1(t) \rangle_{T_s} \end{aligned} \quad (20.5)$$

with the average defined as in Eq. (7.3). In steady-state, we can further approximate  $v_1(t)$  and  $i_2(t)$  by their dc components  $V_1$  and  $I_2$ :

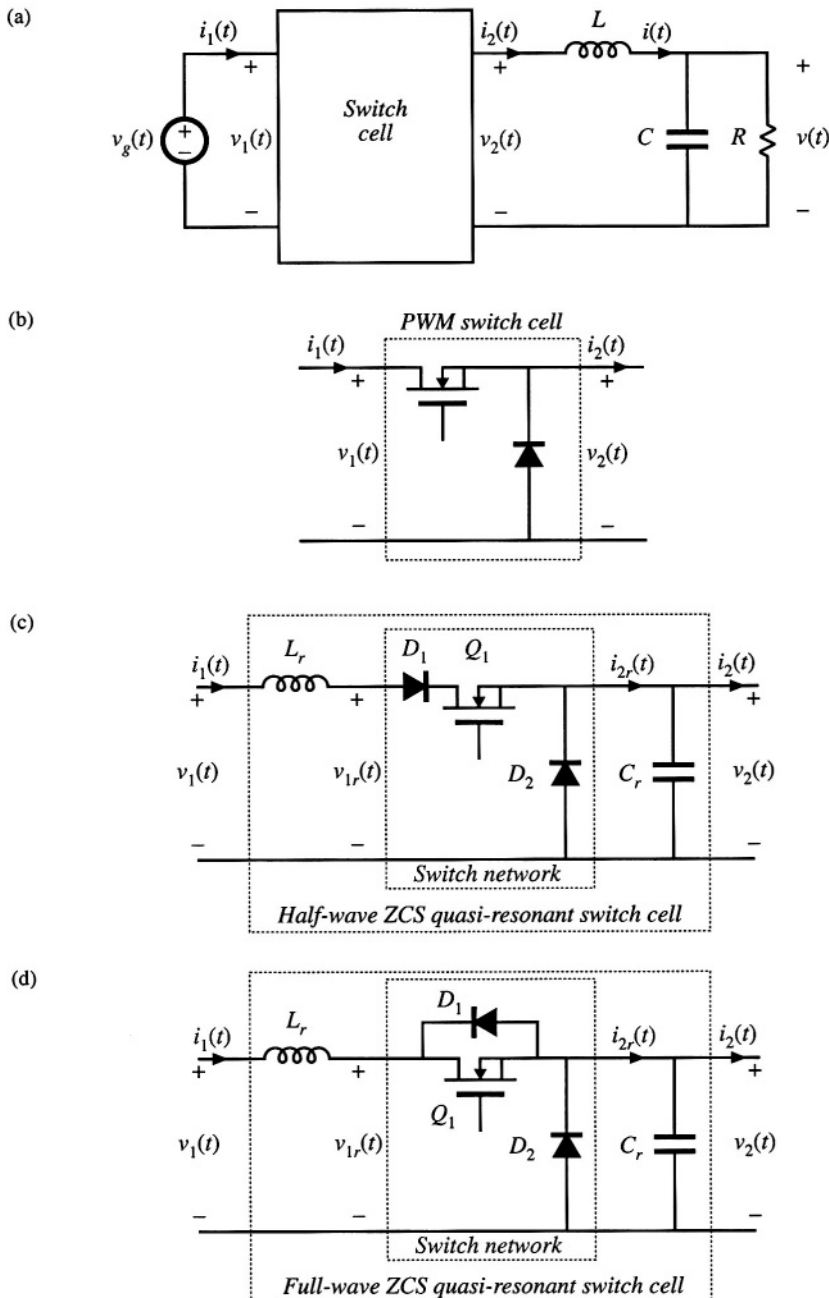


**Fig. 20.8** Implementation of the switch cell in a buck converter: (a) buck converter, with arbitrary switch cell; (b) PWM switch cell; (c) half-wave ZCS quasi-resonant switch cell; (d) full-wave ZCS quasi-resonant switch cell.

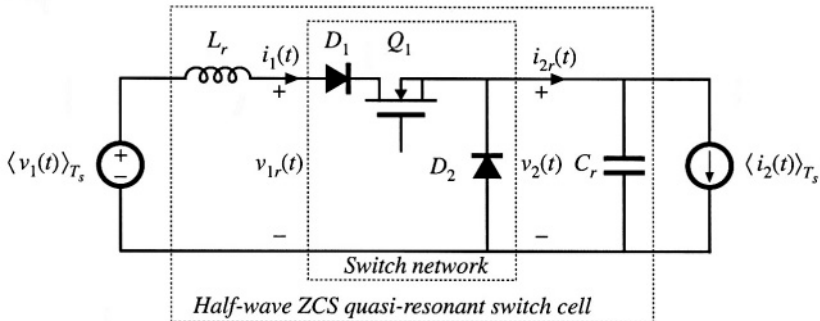


Fig. 20.9 The half-wave ZCS quasi-resonant switch cell, driven by the terminal quantities  $\langle v_1(t) \rangle_{T_s}$  and  $\langle i_2(t) \rangle_{T_s}$ .

$$\begin{aligned} i_2(t) &\approx I_2 \\ v_1(t) &\approx V_1 \end{aligned} \quad (20.6)$$

Thus, the small-ripple approximation is employed for the converter filter elements, as usual.

To understand the operation of the half-wave ZCS quasi-resonant switch cell, we can solve the simplified circuit illustrated in Fig. 20.9. In accordance with the averaged switch modeling approach of Sections 7.4 and 11.1, it is desired to determine the average terminal waveforms  $\langle v_2(t) \rangle_{T_s}$  and  $\langle i_1(t) \rangle_{T_s}$  as functions of the applied quantities  $\langle v_1(t) \rangle_{T_s}$  and  $\langle i_2(t) \rangle_{T_s}$ . The switch conversion ratio  $\mu$  is then given by

$$\mu = \frac{\langle v_2(t) \rangle_{T_s}}{\langle v_{1r}(t) \rangle_{T_s}} = \frac{\langle i_1(t) \rangle_{T_s}}{\langle i_{2r}(t) \rangle_{T_s}} \quad (20.7)$$

In steady state, we can write

$$\mu = \frac{V_2}{V_1} = \frac{I_1}{I_2} \quad (20.8)$$

The steady-state analysis of this section employs Eq. (20.8) to determine  $\mu$ .

### 20.2.1 Waveforms of the Half-Wave ZCS Quasi-Resonant Switch Cell

Typical waveforms of the half-wave cell of Fig. 20.9 are illustrated in Fig. 20.10. Each switching period consists of four subintervals as shown, having angular lengths  $\alpha$ ,  $\beta$ ,  $\delta$ , and  $\xi$ . The switching period begins when the controller turns on transistor  $Q_1$ . The initial values of the tank inductor current  $i_1(t)$  and tank capacitor voltage  $v_2(t)$  are zero. During subinterval 1, all three semiconductor devices conduct. Diode  $D_2$  is forward-biased because  $i_1(t)$  is less than  $I_2$ . In consequence, during subinterval 1 the switch cell reduces to the circuit of Fig. 20.11.

The slope of the inductor current is given by

$$\frac{di_1(t)}{dt} = \frac{V_1}{L_r} \quad (20.9)$$

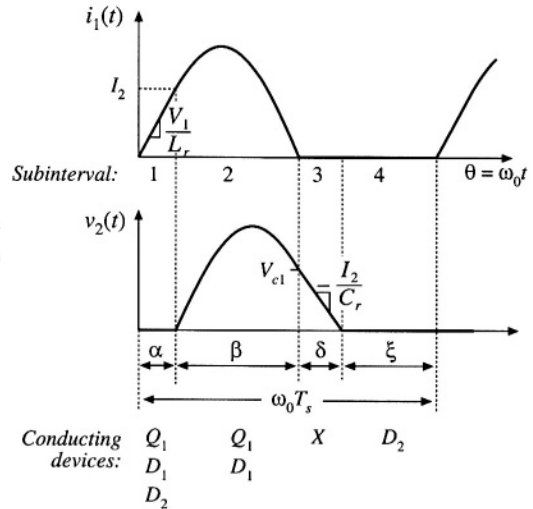


Fig. 20.10 Tank inductor current and capacitor voltage waveforms, for the half-wave ZCS quasi-resonant switch of Fig. 20.9.

with the initial condition  $i_1(0) = 0$ . The solution is

$$i_1(t) = \frac{V_1}{L_r} t = \omega_0 t \frac{V_1}{R_0} \quad (20.10)$$

where the tank characteristic impedance  $R_0$  is defined as

$$R_0 = \sqrt{\frac{L_r}{C_r}} \quad (20.11)$$

It is convenient to express the waveforms in terms of the angle  $\theta = \omega_0 t$ , instead of time  $t$ . At the end of subinterval 1,  $\omega_0 t = \alpha$ . The subinterval ends when diode  $D_2$  becomes reverse-biased. Since the diode  $D_2$  current is equal to  $I_2 - i_1(t)$ , this occurs when  $i_1(t) = I_2$ . Hence, we can write

$$i_1(\alpha) = \alpha \frac{V_1}{R_0} = I_2 \quad (20.12)$$

Solution for  $\alpha$  yields

$$\alpha = \frac{I_2 R_0}{V_1} \quad (20.13)$$

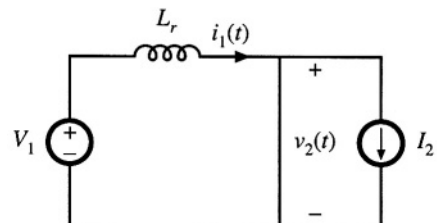
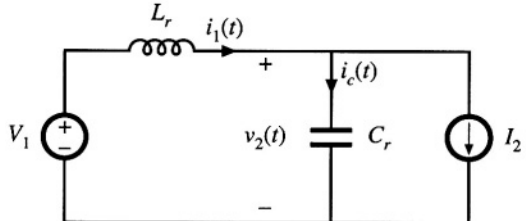


Fig. 20.11 Circuit of the switch network during subinterval 1.



**Fig. 20.12** Circuit of the switch network during subinterval 2.

During subinterval 2, transistor  $Q_1$  and diode  $D_1$  conduct, while diode  $D_2$  is reverse-biased. The switch network then becomes the circuit illustrated in Fig. 20.12. The resonant  $L_r-C_r$  tank network is excited by the constant sources  $V_1$  and  $I_2$ . The network equations are

$$\begin{aligned} L_r \frac{di_1(\omega_0 t)}{dt} &= V_1 - v_2(\omega_0 t) \\ C_r \frac{dv_2(\omega_0 t)}{dt} &= i_1(\omega_0 t) - I_2 \end{aligned} \quad (20.14)$$

with the initial conditions

$$\begin{aligned} v_2(\alpha) &= 0 \\ i_1(\alpha) &= I_2 \end{aligned} \quad (20.15)$$

The solution is

$$\begin{aligned} i_1(\omega_0 t) &= I_2 + \frac{V_1}{R_0} \sin(\omega_0 t - \alpha) \\ v_2(\omega_0 t) &= V_1 \left( 1 - \cos(\omega_0 t - \alpha) \right) \end{aligned} \quad (20.16)$$

The tank inductor current rises to a peak value given by

$$I_{1pk} = I_2 + \frac{V_1}{R_0} \quad (20.17)$$

The subinterval ends at the first zero crossing of  $i_1(t)$ . If we denote the angular length of the subinterval as  $\beta$ , then we can write

$$i_1(\alpha + \beta) = I_2 + \frac{V_1}{R_0} \sin(\beta) = 0 \quad (20.18)$$

Solution for  $\sin(\beta)$  yields

$$\sin(\beta) = -\frac{I_2 R_0}{V_1} \quad (20.19)$$

Care must be employed when solving Eq. (20.19) for the angle  $\beta$ . It can be observed from Fig. 20.10 that the angle  $\beta$  is greater than  $\pi$ . The correct branch of the arcsine function must be selected, as follows:

$$\beta = \pi + \sin^{-1} \left( \frac{I_2 R_0}{V_1} \right) \quad (20.20)$$

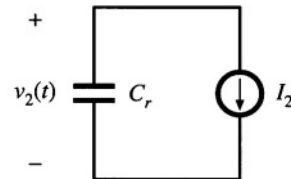


**Fig. 20.13** Circuit of the switch network during subinterval 3.

where

$$-\frac{\pi}{2} < \sin^{-1}(x) \leq \frac{\pi}{2}$$

Note that the inequality

$$I_2 < \frac{V_1}{R_0} \quad (20.21)$$

must be satisfied; otherwise, there is no solution to Eq. (20.19). At excessive load currents, where Eq. (20.21) is not satisfied, the tank inductor current never reaches zero, and the transistor does not switch off at zero current.

The tank capacitor voltage at the end of subinterval 2 is found by evaluation of Eq. (20.16) at  $\omega_0 t = (\alpha + \beta)$ . The  $\cos(\beta)$  term can be expressed as

$$\cos(\beta) = -\sqrt{1 - \sin^2(\beta)} = -\sqrt{1 - \left(\frac{I_2 R_0}{V_1}\right)^2} \quad (20.22)$$

Substitution of Eq. (20.22) into Eq. (20.16) leads to

$$v_2(\alpha + \beta) = V_{cl} = V_1 \left( 1 + \sqrt{1 - \left(\frac{I_2 R_0}{V_1}\right)^2} \right) \quad (20.23)$$

At the end of subinterval 2, diode  $D_1$  becomes reverse-biased. Transistor  $Q_1$  can then be switched off at zero current.

During subinterval 3, all semiconductor devices are off, and the switch cell reduces to the circuit of Fig. 20.13. The tank capacitor  $C_r$  is discharged by the filter inductor current  $I_2$ . Hence, the tank capacitor voltage  $v_2$  decreases linearly to zero. The circuit equations are

$$\begin{aligned} C_r \frac{dv_2(\omega_0 t)}{dt} &= -I_2 \\ v_2(\alpha + \beta) &= V_{cl} \end{aligned} \quad (20.24)$$

The solution is

$$v_2(\omega_0 t) = V_{cl} - I_2 R_0 (\omega_0 t - \alpha - \beta) \quad (20.25)$$

Subinterval 3 ends when the tank capacitor voltage reaches zero. Diode  $D_2$  then becomes forward-biased. Hence, we can write

$$v_2(\alpha + \beta + \delta) = V_{cl} - I_2 R_0 \delta = 0 \quad (20.26)$$

where  $\delta$  is the angular length of subinterval 3. Solution for  $\delta$  yields

$$\delta = \frac{V_{c1}}{I_2 R_0} = \frac{V_1}{I_2 R_0} \left( 1 - \sqrt{1 - \left( \frac{I_2 R_0}{V_1} \right)^2} \right) \quad (20.27)$$

Subinterval 4, of angular length  $\xi$ , is identical to the diode conduction subinterval of the conventional PWM switch network. Diode  $D_2$  conducts the filter inductor current  $I_2$ , and the tank capacitor voltage  $v_2$  is equal to zero. Transistor  $Q_1$  is off, and the input current  $i_1$  is equal to zero.

The angular length of the switching period is

$$\omega_0 T_s = \alpha + \beta + \delta + \xi = \frac{2\pi f_0}{f_s} = \frac{2\pi}{F} \quad (20.28)$$

where

$$F = \frac{f_s}{f_0} \quad (20.29)$$

Quasi-resonant switch networks are usually controlled by variation of the switching frequency  $f_s$  or, in normalized terms, by variation of  $F$ . Note that the interval lengths  $\alpha$ ,  $\beta$ , and  $\delta$  are determined by the response of the tank network. Hence, control of the switching frequency is equivalent to control of the fourth subinterval length  $\xi$ . The subinterval length  $\xi$  must be positive, and hence, the minimum switching period is limited as follows:

Substitution of Eqs. (20.13), (20.20), and (20.27) into Eq. (20.30) yields

$$\frac{2\pi}{F} \geq \frac{I_2 R_0}{V_1} + \pi + \sin^{-1} \left( \frac{I_2 R_0}{V_1} \right) + \frac{V_1}{I_2 R_0} \left( 1 - \sqrt{1 - \left( \frac{I_2 R_0}{V_1} \right)^2} \right) \quad (20.31)$$

This expression limits the maximum switching frequency, or maximum  $F$ , of the half-wave ZCS quasi-resonant switch cell.

### 20.2.2 The Average Terminal Waveforms

It is now desired to solve for the power processing function performed by the switch network. The switch conversion ratio  $\mu$  is a generalization of the duty cycle  $d$ . It expresses how a resonant switch network controls the average voltages and currents of a converter. In our buck converter example, we can define  $\mu$  as the ratio of  $\langle v_2(t) \rangle_{T_s}$  to  $\langle v_1(t) \rangle_{T_s}$ , or equivalently, the ratio of  $\langle i_1(t) \rangle_{T_s}$  to  $\langle i_2(t) \rangle_{T_s}$ . In a hard-switched PWM network, this ratio is equal to the duty cycle  $d$ . Hence, analytical results derived for hard-switched PWM converters can be adapted to quasi-resonant converters, simply by replacing  $d$  with  $\mu$ . In this section, we derive an expression for  $\mu$ , by averaging the terminal waveforms of the switch network.

The switch input current waveform  $i_1(t)$  of Fig. 20.10 is reproduced in Fig. 20.14. The average switch input current is given by

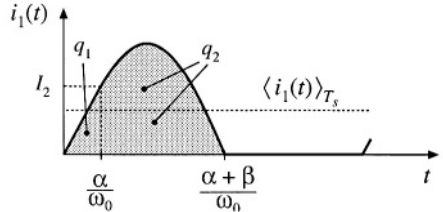


**Fig. 20.14** Input current waveform  $i_1(t)$ , and the areas  $q_1$  and  $q_2$  during subintervals 1 and 2 respectively.

$$\langle i_1(t) \rangle_{T_s} = \frac{1}{T_s} \int_t^{t+T_s} i_1(t) dt = \frac{q_1 + q_2}{T_s} \quad (20.32)$$

The charge quantities  $q_1$  and  $q_2$  are the areas under the  $i_1(t)$  waveform during the first and second subintervals, respectively. The charge  $q_1$  is given by the triangle area formula

$$q_1 = \int_0^{\frac{\alpha}{\omega_0}} i_1(t) dt = \frac{1}{2} \left( \frac{\alpha}{\omega_0} \right) (I_2) \quad (20.33)$$

The time  $\alpha/\omega_0$  is the length of subinterval 1, The charge  $q_2$  is

$$q_2 = \int_{\frac{\alpha}{\omega_0}}^{\frac{\alpha+\beta}{\omega_0}} i_1(t) dt \quad (20.34)$$

According to Fig. 20.12, during subinterval 2 the current  $i_1(t)$  can be related to the tank capacitor current  $i_C(t)$  and the switch output current  $I_2$  by the node equation

$$i_1(t) = i_C(t) + I_2 \quad (20.35)$$

Substitution of Eq. (20.35) into Eq. (20.34) leads to

$$q_2 = \int_{\frac{\alpha}{\omega_0}}^{\frac{\alpha+\beta}{\omega_0}} i_C(t) dt + \int_{\frac{\alpha}{\omega_0}}^{\frac{\alpha+\beta}{\omega_0}} I_2 dt \quad (20.36)$$

Both integrals in Eq. (20.36) can easily be evaluated, as follows. Since the second term involves the integral of the constant current  $I_2$ , this term is

$$\int_{\frac{\alpha}{\omega_0}}^{\frac{\alpha+\beta}{\omega_0}} I_2 dt = I_2 \frac{\beta}{\omega_0} \quad (20.37)$$

The first term in Eq. (20.36) involves the integral of the capacitor current over subinterval 2. Hence, this term is equal to the change in capacitor charge over the second subinterval:

$$\int_{\frac{\alpha}{\omega_0}}^{\frac{\alpha+\beta}{\omega_0}} i_C(t) dt = C \left( v_2 \left( \frac{\alpha+\beta}{\omega_0} \right) - v_2 \left( \frac{\alpha}{\omega_0} \right) \right) \quad (20.38)$$

(recall that  $\Delta q = C\Delta v$  in a capacitor). During the second subinterval, the tank capacitor voltage is initially zero, and has a final value of  $V_{c1}$ . Hence, Eq. (20.38) reduces to

$$\int_{\frac{\alpha}{\omega_0}}^{\frac{\alpha+\beta}{\omega_0}} i_C(t) dt = C(V_{c1} - 0) = CV_{c1} \quad (20.39)$$

Substitution of Eqs. (20.37) and (20.39) into Eq. (20.36) leads to the following expression for  $q_2$ :

$$q_2 = CV_{c1} + I_2 \frac{\beta}{\omega_0} \quad (20.40)$$

Equations (20.33) and (20.40) can now be inserted into Eq. (20.32), to obtain the following expression for the switch input current:

$$\langle i_1(t) \rangle_{T_s} = \frac{\alpha I_2}{2\omega_0 T_s} + \frac{CV_{c1}}{T_s} + \frac{\beta I_2}{\omega_0 T_s} \quad (20.41)$$

Substitution of Eq. (20.41) into (20.8) leads to the following expression for the switch conversion ratio:

$$\mu = \frac{\langle i_1(t) \rangle_{T_s}}{I_2} = \frac{\alpha}{2\omega_0 T_s} + \frac{CV_{c1}}{I_2 T_s} + \frac{\beta}{\omega_0 T_s} \quad (20.42)$$

Finally, the quantities  $\alpha$ ,  $\beta$ , and  $V_{c1}$  can be eliminated, using Eqs. (20.13), (20.20), (20.23). The result is

$$\mu = F \frac{1}{2\pi} \left[ \frac{1}{2} J_s + \pi + \sin^{-1}(J_s) + \frac{1}{J_s} \left( 1 + \sqrt{1 - J_s^2} \right) \right] \quad (20.43)$$

where

$$J_s = \frac{I_2 R_0}{V_1} \quad (20.44)$$

Equation (20.43) is of the form

$$\mu = F P_1(J_s) \quad (20.45)$$

where

$$P_1(J_s) = \frac{1}{2\pi} \left[ \frac{1}{2} J_s + \pi + \sin^{-1}(J_s) + \frac{1}{J_s} \left( 1 + \sqrt{1 - J_s^2} \right) \right] \quad (20.46)$$

Thus, the switch conversion ratio  $\mu$  is directly controllable by variation of the switching frequency, through  $F$ . The switch conversion ratio is also a function of the applied terminal voltage  $V_1$  and current  $I_2$ , via  $J_s$ . The function  $P_1(J_s)$  is sketched in Fig. 20.15. The switch conversion ratio  $\mu$  is sketched in Fig. 20.16, for various values of  $F$  and  $J_s$ . These characteristics are similar in shape to the function  $P(J_s)$ , and are simply scaled by the factor  $F$ . It can be seen that the conversion ratio  $\mu$  is a strong function

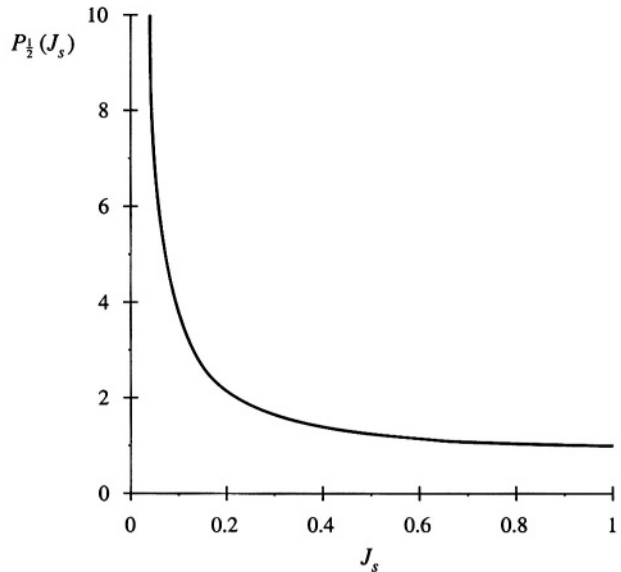


**Fig. 20.15** The function  $P_{1/2}(J_s)$ .

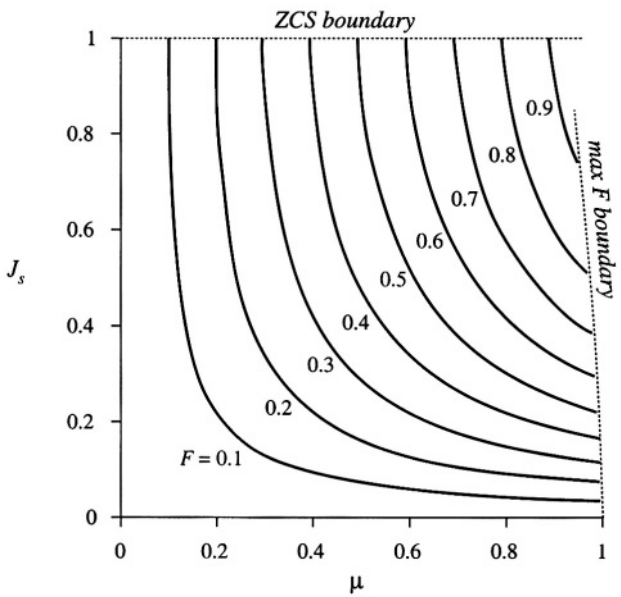


**Fig. 20.16** Characteristics of the half-wave ZCS quasi-resonant switch.

of the current  $I_2$ , via  $J_s$ . The characteristics end at  $J_s = 1$ ; according to Eq. (20.31), the zero current switching property is lost when  $J_s > 1$ . The characteristics also end at the maximum switching frequency limit given by Eq. (20.31). This expression can be simplified by use of Eq. (20.43), to express the limit in terms of  $\mu$  as follows:

$$\mu \leq 1 - \frac{J_s F}{4\pi} \quad (20.47)$$

The switch conversion ratio  $\mu$  is thus limited to a value slightly less than 1.

The averaged waveforms of converters containing half-wave ZCS quasi-resonant switches can now be determined. The results of the analysis of PWM converters operating in the continuous conduction mode can be directly adapted to the related quasi-resonant converters, simply by replacing the duty cycle  $d$  with the switch conversion ratio  $\mu$ . For the buck converter example, the conversion ratio is

$$M = \frac{V}{V_g} = \mu \quad (20.48)$$

This result could also be derived by use of the principle of inductor volt-second balance. The average voltage across the filter inductor is  $(\mu V_g - V)$ . Upon equating this voltage to zero, we obtain Eq. (20.48).

In the buck converter,  $I_2$  is equal to the load current  $I$ , while  $V_1$  is equal to the converter input voltage  $V_g$ . Hence, the quantity  $J_s$  is

$$J_s = \frac{IR_0}{V_g} \quad (20.49)$$

Zero current switching occurs for

$$I \leq \frac{V_g}{R_0} \quad (20.50)$$

The output voltage can vary over the range

$$0 \leq V \leq V_g - \frac{FIR_0}{4\pi} \quad (20.51)$$

which nearly coincides with the PWM output voltage range  $0 \leq V \leq V_g$ .

A boost converter employing a half-wave ZCS quasi-resonant switch is illustrated in Fig. 20.17. The conversion ratio of the boost converter is given by

$$M = \frac{V}{V_g} = \frac{1}{1-\mu} \quad (20.52)$$

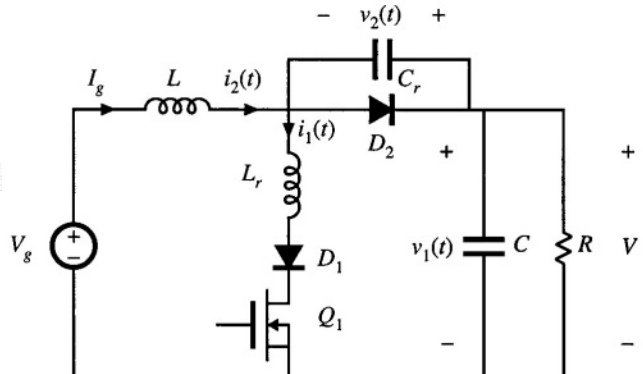


**Fig. 20.17** Boost converter containing a half-wave ZCS quasi-resonant switch.

The half-wave switch conversion ratio  $\mu$  is again given by Eqs. (20.44) to (20.46). For the boost converter, the applied switch voltage  $V_1$  is equal to the output voltage  $V$ , while the applied switch current  $I_2$  is equal to the filter inductor current, or  $I_g$ . Hence, the quantity  $J_s$  is

$$J_s = \frac{I_2 R_0}{V_1} = \frac{I_g R_0}{V} \quad (20.53)$$

Also, the input current  $I_g$  of the boost converter is related to the load current  $I$  according to

$$I_g = \frac{I}{1 - \mu} \quad (20.54)$$

Equations (20.52) to (20.54), in conjunction with Eqs. (20.44) to (20.46), describe the averaged waveforms of the half-wave quasi-resonant ZCS boost converter.

### 20.2.3 The Full-Wave ZCS Quasi-Resonant Switch Cell

The full-wave ZCS quasi-resonant switch cell is illustrated in Fig. 20.8(d). It differs from the half-wave cell in that elements  $D_1$  and  $Q_1$  are connected in antiparallel, to form a current-bidirectional two-quadrant switch. Typical tank inductor current and tank capacitor voltage waveforms are illustrated in Fig. 20.18. These waveforms are similar to those of the half-wave case, except that the  $Q_1/D_1$  switch interrupts the tank inductor current  $i_1(t)$  at its second zero-crossing. While  $i_1(t)$  is negative, diode  $D_1$  conducts, and transistor  $Q_1$  can be turned off at zero current.

The analysis is nearly the same as for the half-wave case, with the exception of subinterval 2. The subinterval 2 angular length  $\beta$  and final voltage  $V_{c1}$  can be shown to be

$$\beta = \begin{cases} \pi + \sin^{-1}(J_s) & (\text{half wave}) \\ 2\pi - \sin^{-1}(J_s) & (\text{full wave}) \end{cases} \quad (20.55)$$

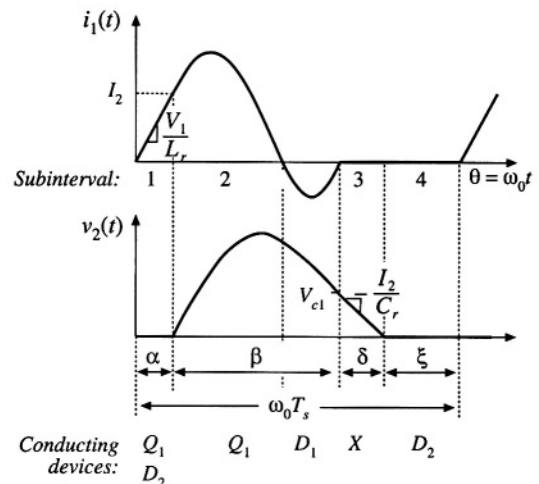


**Fig. 20.18** Tank inductor current and capacitor voltage waveforms, for the full-wave ZCS quasi-resonant switch cell of Fig. 20.8(d).

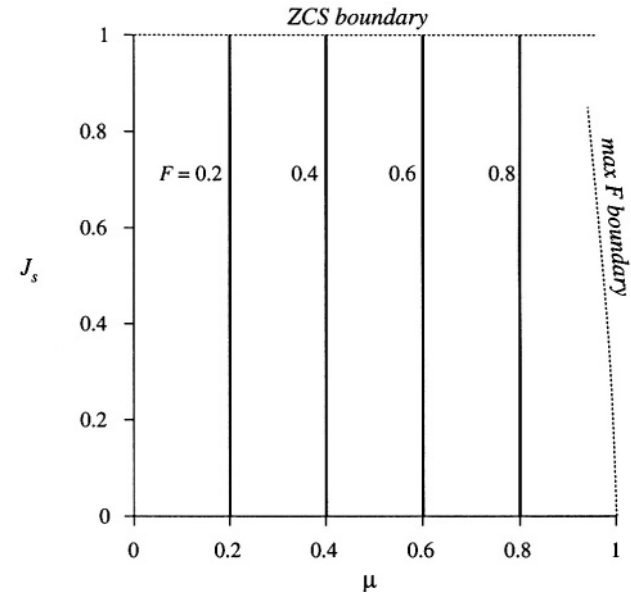


**Fig. 20.19** Characteristics of the full-wave ZCS quasi-resonant switch.

$$V_{cl} = \begin{cases} V_1 \left( 1 + \sqrt{1 - J_s^2} \right) & (\text{half wave}) \\ V_1 \left( 1 - \sqrt{1 - J_s^2} \right) & (\text{full wave}) \end{cases} \quad (20.56)$$

In either case, the switch conversion ratio  $\mu$  is given by Eq. (20.42). For the full-wave switch, one obtains

$$\mu = FP_1(J_s) \quad (20.57)$$

where  $P_1(J_s)$  is given by

$$P_1(J_s) = \frac{1}{2\pi} \left| \frac{1}{2} J_s + 2\pi - \sin^{-1}(J_s) + \frac{1}{J_s} \left( 1 - \sqrt{1 - J_s^2} \right) \right| \quad (20.58)$$

In the full-wave case,  $P_1(J_s)$  is essentially independent of  $J_s$ :

$$P_1(J_s) \approx 1 \quad (20.59)$$

The worst-case deviation of  $P_1(J_s)$  from 1 occurs as  $J_s$  tends to 1, where  $P_1(J_s)$  tends to 0.96. So  $P_1(J_s)$  lies within 4% of unity for  $0 < J_s < 1$ . Hence, for the full-wave case, it is a good approximation to express the switch conversion ratio as

$$\mu \approx F = \frac{f_s}{f_0} \quad (20.60)$$

The full-wave quasi-resonant switch therefore exhibits voltage-source output characteristics, controllable

by  $F$ . Equations describing the average waveforms of CCM PWM converters can be adapted to apply to full-wave ZCS quasi-resonant converters, simply by replacing the duty cycle  $d$  with the normalized switching frequency  $F$ . The conversion ratios of full-wave quasi-resonant converters exhibit negligible dependence on the load current.

The variation of the switch conversion ratio  $\mu$  with  $F$  and  $J_s$  is plotted in Fig. 20.19. For a typical voltage regulator application, the range of switching frequency variations is much smaller in the full-wave mode than in the half-wave mode, because  $\mu$  does not depend on the load current. Variations in the load current do not induce the controller to significantly change the switching frequency.

### 20.3 RESONANT SWITCH TOPOLOGIES

So far, we have considered the zero-current-switching quasi-resonant switch cell, illustrated in Fig. 20.20. The ideal SPST switch is realized using a voltage-bidirectional or current-bidirectional two-quadrant switch, to obtain half-wave or full-wave ZCS quasi-resonant switch networks, respectively.

The resonant elements  $L_r$  and  $C_r$  can be moved to several different positions in the converter, without altering the basic switch properties. For example, Fig. 20.21 illustrates connection of the resonant tank capacitor  $C_r$ , between the cathode of diode  $D_2$ , and the converter output or input terminals. Although this may change the dc component of the tank capacitor voltage, the ac components of the tank capacitor voltage waveform are unchanged. Also, the terminal voltage waveform  $v_2(t)$  is unchanged. The voltages  $v_g(t)$  and  $v(t)$  contain negligible high-frequency ac components, and hence the converter input and output terminal potentials can be considered to be at high-frequency ac ground.

A test to determine the topology of a resonant switch network is to replace all low-frequency filter inductors with open circuits, and to replace all dc sources and low-frequency filter capacitors with short circuits [13]. The elements of the resonant switch cell remain. In the case of the zero-current-switching quasi-resonant switch, the network of Fig. 20.22 is always obtained.

It can be seen from Fig. 20.22 that diode  $D_2$  switches on and off at the zero crossings of the tank capacitor voltage  $v_2(t)$ , while the switch elements  $Q_1$  and  $D_1$  switch at the zero crossings of the tank inductor current  $i_1(t)$ . Zero voltage switching of diode  $D_2$  is highly advantageous, because it essentially eliminates the switching loss caused by the recovered charge and output capacitance of diode  $D_2$ . Zero current switching of  $Q_1$  and  $D_1$  can be used to advantage when  $Q_1$  is realized by an SCR or IGBT. However, in high-frequency converters employing MOSFETs, zero current switching of  $Q_1$  and  $D_1$  is generally a poor choice. Significant switching loss due to the output capacitances of  $Q_1$  and  $D_1$  may be observed. In addition, in the full-wave case, the recovered charge of diode  $D_1$  leads to significant ringing

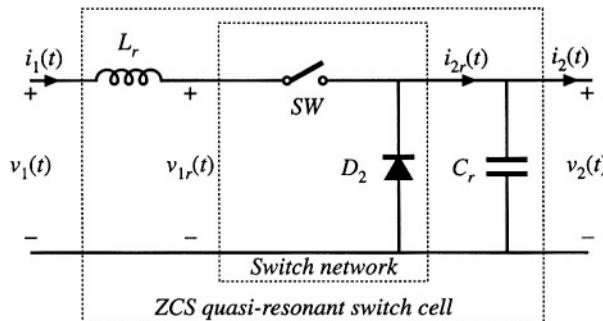
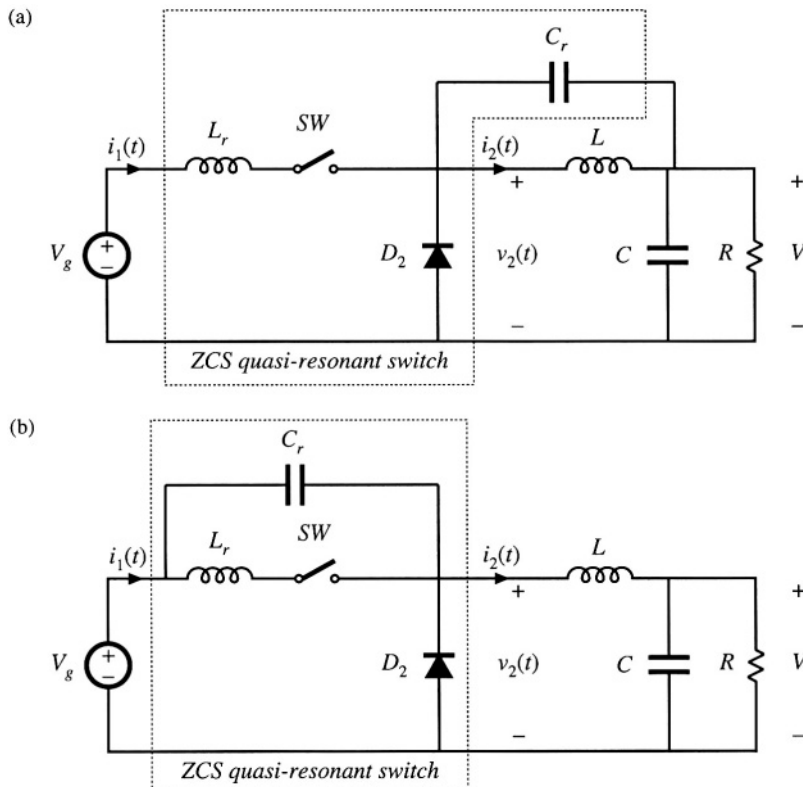
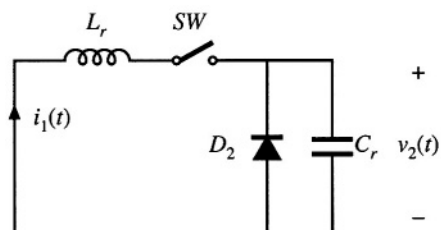


Fig. 20.20 Basic ZCS quasi-resonant switch cell.



**Fig. 20.21** Connection of the tank capacitor of the ZCS quasi-resonant cell to other points at ac ground: (a) connection to the dc output, (b) connection to the dc input. In each case, the ac components of the waveforms are unchanged.



and switching loss at the end of subinterval 2 [3].

The ZCS quasi-resonant switch exhibits increased conduction loss, relative to an equivalent PWM switch, because the peak transistor current is increased. The peak transistor current is given by Eq. (20.17); since  $J_s \leq 1$ , the peak current is  $I_{1pk} \geq 2I_2$ . In addition, the full-wave ZCS switch exhibits poor efficiency at light load, owing to the conduction loss caused by circulating tank currents. The half-wave ZCS switch exhibits additional conduction loss due to the added forward voltage drop of diode  $D_1$ . The peak transistor voltage is  $V_1$ , which is identical to the PWM case.

### 20.3.1 The Zero-Voltage-Switching Quasi-Resonant Switch

The resonant switch network illustrated in Fig. 20.23 is the dual of the network of Fig. 20.22. This network is known as the zero-voltage-switching quasi-resonant switch [4]. Since the tank capacitor  $C_r$  appears in parallel with the SPST switch, the elements  $Q_1$  and  $D_1$  used to realize the SPST switch turn on and off at zero voltage. The tank inductor  $L_r$  is effectively in series with diode  $D_2$ , and hence diode  $D_2$  switches at zero current. Converters containing ZVS quasi-resonant switches can be realized in a number of ways. The only requirement is that, when the low-frequency filter inductors, filter capacitors, and sources are replaced by open- or short-circuits as described above, then the high-frequency switch network of Fig. 20.23 should remain.

For example, a zero-voltage-switching quasi-resonant buck converter is illustrated in Fig. 20.24(a). Typical tank capacitor voltage and tank inductor current waveforms are given in Fig. 20.24(b). A current-bidirectional realization of the two-quadrant SPST switch is shown; this causes the ZVS quasi-resonant switch to operate in the half-wave mode. Use of a voltage-bidirectional two-quadrant SPST switch allows full-wave operation.

By analysis similar to that of Section 20.2, it can be shown that the switch conversion ratio  $\mu$  of the half-wave ZVS quasi-resonant switch is

$$\mu = 1 - FP_{\frac{1}{2}}\left(\frac{1}{J_s}\right) \quad (20.61)$$

The function  $P_{\frac{1}{2}}(J_s)$  is again given by Eq. (20.46), and the quantity  $J_s$  is defined in Eq. (20.44). For the full-wave ZVS quasi-resonant switch, one obtains

$$\mu = 1 - FP_1\left(\frac{1}{J_s}\right) \quad (20.62)$$

where  $P_1(J_s)$  is given by Eq. (20.58). The condition for zero voltage switching is

$$J_s \geq 1 \quad (20.63)$$

Thus, the zero voltage switching property is lost at light load. The peak transistor voltage is given by

$$\text{peak transistor voltage } V_{cr,pk} = (1 + J_s)V_1 \quad (20.64)$$

This equation predicts that load current variations can lead to large voltage stress on transistor  $Q_1$ . For example, if it is desired to obtain zero voltage switching over a 5:1 range of load current variations, then  $J_s$  should vary between 1 and 5. According to Eq. (20.64), the peak transistor voltage then varies between two times and six times the applied voltage  $V_1$ . The maximum transistor current is equal to the applied current  $I_2$ . Although the maximum transistor current in the ZVS quasi-resonant switch is identical to that

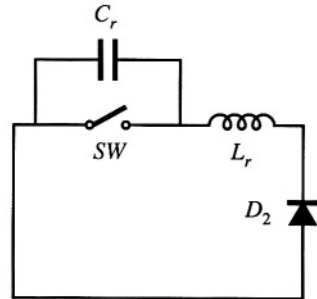


**Fig. 20.23** Elimination of converter low-frequency elements reduces the ZVS quasi-resonant switch cell to this network.

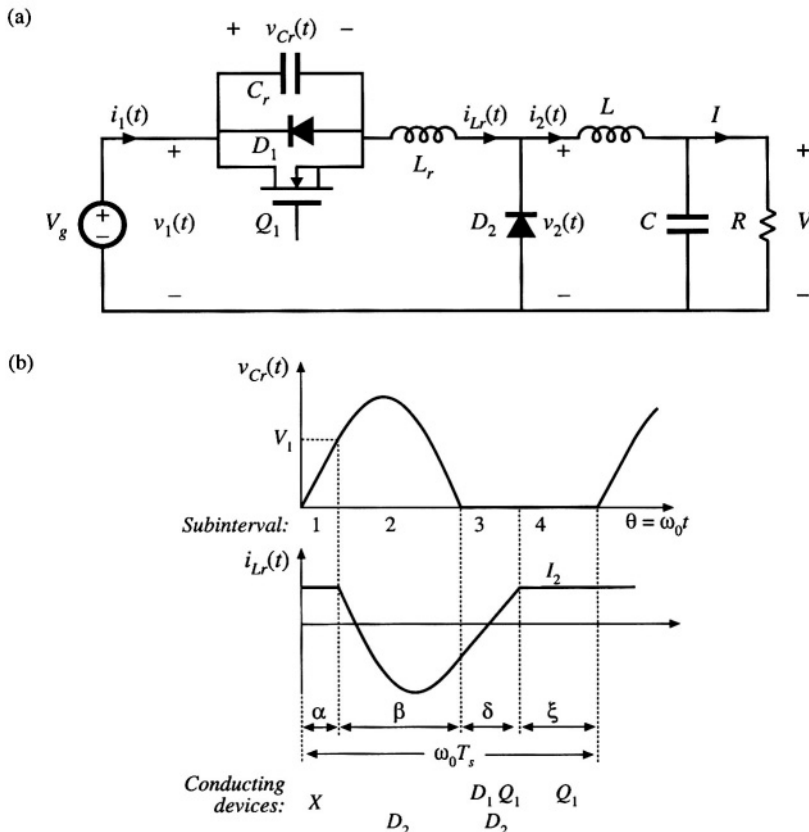


**Fig. 20.24** A ZVS quasi-resonant buck converter: (a) circuit, (b) tank waveforms.

of the PWM switch, the peak transistor blocking voltage is substantially increased. This leads to increased conduction loss, because transistor on-resistance increases rapidly with rated blocking voltage.

### 20.3.2 The Zero-Voltage-Switching Multiresonant Switch

The resonant switch network of Fig. 20.25 contains tank capacitor  $C_d$  in parallel with diode  $D_2$ , as in the ZCS switch network of Fig. 20.22. In addition, it contains tank capacitor  $C_s$  in parallel with the SPST switch, as in the ZVS switch network of Fig. 20.23. In consequence, all semiconductor elements switch at zero voltage. This three-element resonant switch network is known as the zero-voltage-switching multiresonant switch (ZVS MRS). Since no semiconductor output capacitances or diode recovered charges lead to ringing or switching loss, the ZVS MRS exhibits very low switching loss. For the same reason, generation of electromagnetic interference is reduced.

A half-wave ZVS MRS realization of the buck converter is illustrated in Fig. 20.26. In a typical design that must operate over a 5:1 load range and with  $0.4 \leq \mu \leq 0.6$ , the designer might choose a maximum  $F$  of 1.0, a maximum  $J$  of 1.4, and  $C_d/C_s = 3$ , where these quantities are defined as follows:

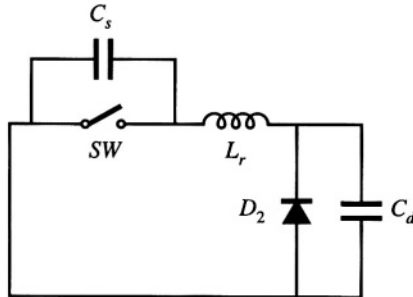


**Fig. 20.25** Elimination of converter low-frequency elements reduces the ZVS multiresonant switch cell to this network.

$$\begin{aligned} f_0 &= \frac{1}{2\pi\sqrt{LC_t}} \quad R_0 = \sqrt{\frac{L}{C_t}} \\ F &= \frac{f_2}{f_0} \quad J = \frac{I_2 R_0}{V_1} \end{aligned} \quad (20.65)$$

As usual, the conversion ratio is defined as  $\mu = V_2/V_1$ . The resulting peak transistor voltage for this typical design is approximately  $2.8V_1$ , while the peak transistor current is  $2I_2$ . Hence, conduction losses are higher than in an equivalent PWM switch. The range of switch conversion ratios  $\mu$  is a function of the capacitor ratio  $C_d/C_s$ ; in a good design, values of  $\mu$  ranging from nearly one to nearly zero can be obtained, with a wide range of dc load currents and while maintaining zero voltage switching.

Analysis and design charts for the ZVS MRS are given in [5–8]. Results for the typical choice  $C_d = 3C_s$  are plotted in Fig. 20.27. These plots illustrate how the switch conversion ratio  $\mu$  varies as a function of load current and switching frequency. Figure 20.27(a) also illustrates the boundary of zero-voltage switching: ZVS is lost for operation outside the dashed lines. Decreasing the ratio of  $C_d$  to  $C_s$  reduces the area of the ZVS region.

Other resonant converters in which all semiconductor devices operate with zero voltage switching are known. Examples include some operating modes of the parallel and LCC resonant converters described in Chapter 19, as well as the class-E converters described in [10–12].

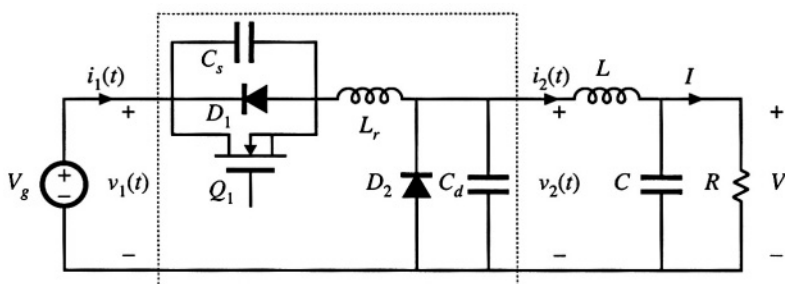


**Fig. 20.26** Half-wave ZVS multiresonant buck converter.

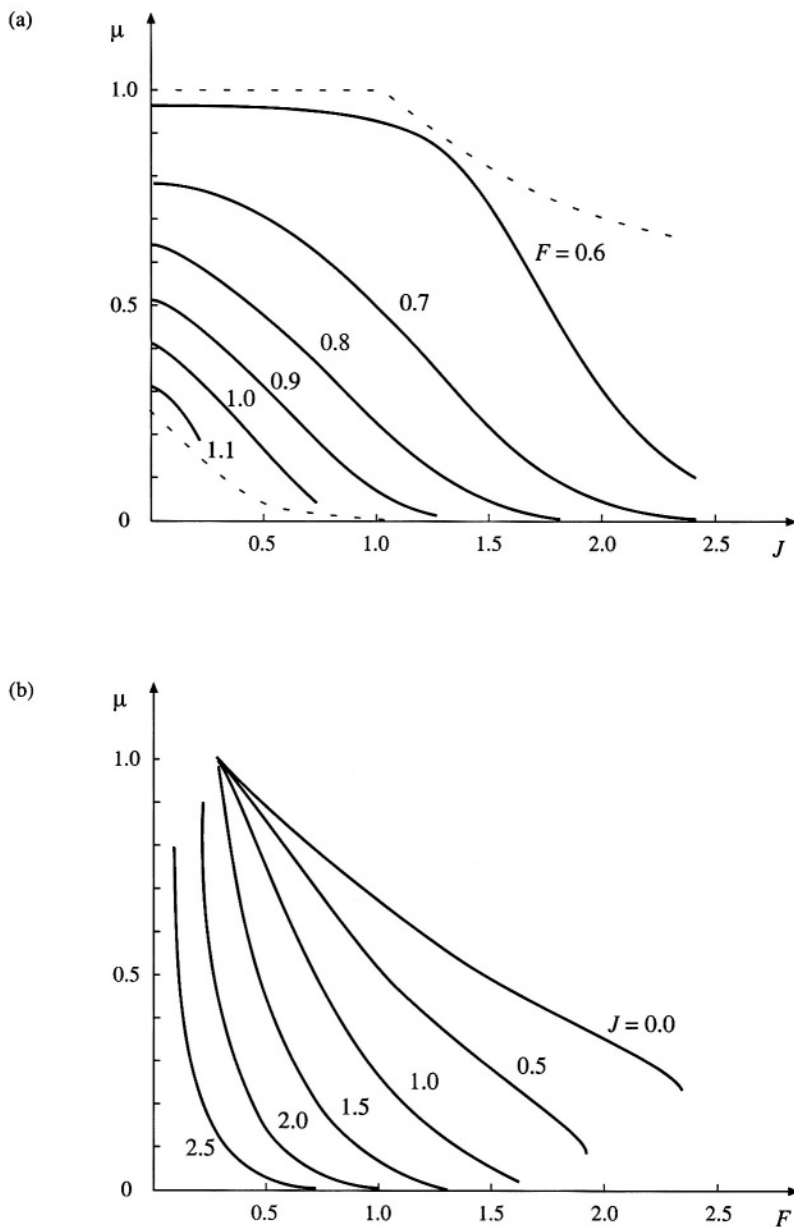


**Fig. 20.27** Conversion ratio  $\mu$  for the multi-resonant switch with  $C_d = 3C_s$ : (a) conversion ratio  $\mu$  vs. normalized current  $J$  (solid lines: conversion ratio; dashed lines: boundaries of zero-voltage switching), (b) conversion ratio  $\mu$  vs. normalized switching frequency  $F$ .

### 20.3.3 Quasi-Square-Wave Resonant Switches

Another basic class of resonant switch networks is the quasi-square wave converters. Both zero-voltage switching and zero-current switching versions are known; the resonant tank networks are illustrated in Fig. 20.28. In the network of Fig. 20.28(a), all semiconductor devices are effectively in series with the tank inductor, and hence operate with zero-current switching. In the network of Fig. 20.28(b), all semiconductor devices are effectively in parallel with the tank capacitor, and hence operate with zero-voltage switching.

Figure 20.29 illustrates implementation of a zero current switching quasi-square wave resonant switch, in a buck converter with input filter. Elements  $L_f$  and  $C_f$  are large in value, and constitute a single-section  $L-C$  input filter. Elements  $L_r$  and  $C_r$  form the series resonant tank; these elements are placed in series with input filter capacitor  $C_f$ . Since  $C_r$  and  $C_f$  are connected in series, they can be combined into a single small-value capacitor. In this zero-current-switching converter, the peak transistor current is identical to the peak transistor current of an equivalent PWM converter. However, the peak transistor blocking voltage is increased. The ZCS QSW resonant switch exhibits a switch conversion ratio  $\mu$  that is restricted to the range  $0 \leq \mu \leq 0.5$ . Analysis of this resonant switch is given in [13–14].

A buck converter, containing a zero-voltage-switching quasi-square wave (ZVS QSW) resonant switch, is illustrated in Fig. 20.30. Typical waveforms are given in Fig. 20.31. Since the tank inductor  $L_r$  and the output filter inductor  $L$  are connected in parallel, these two elements can be combined into a single inductor having a small value nearly equal to  $L_r$ . Analyses of the ZVS QSW resonant switch are given in [14,15,18]. A related full-bridge converter is described in [16]. The ZVS QSW resonant switch is notable because zero voltage switching is obtained in all semiconductor devices, yet the peak transistor voltage is identical to that of an equivalent PWM switch [13]. However, the peak transistor currents are increased.

Characteristics of the zero-voltage-switching quasi-square wave resonant switch are plotted in Fig. 20.32. The switch conversion ratio  $\mu = V_2/V_1$  is plotted as a function of normalized switching fre-

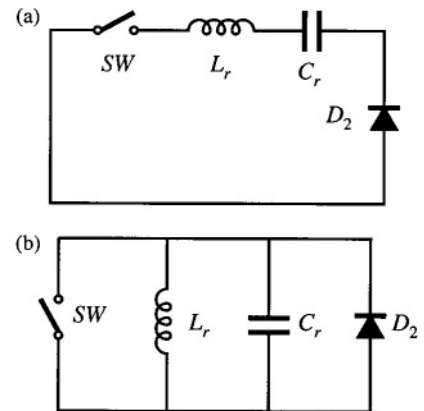


**Fig. 20.28** Elimination of converter low-frequency elements reduces the quasi-square-wave switch cells to these networks:  
 (a) ZCS quasi-square-wave network.  
 (b) ZVS quasi-square-wave network.

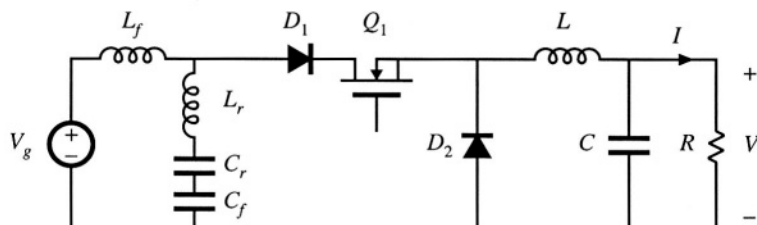


**Fig. 20.29** Incorporation of a ZCS quasi-square-wave resonant switch into a buck converter containing an  $L-C$  input filter.

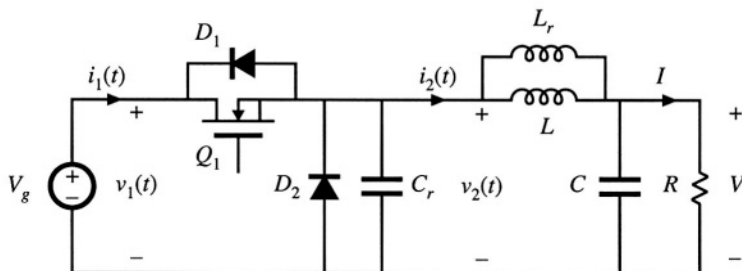


Fig. 20.30 Incorporation of a ZVS quasi-square-wave resonant switch into a buck converter.

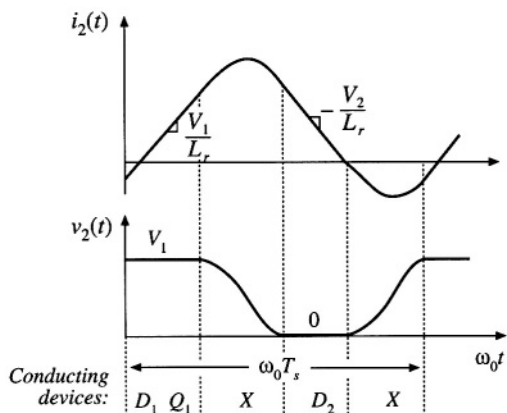


Fig. 20.31 Waveforms of the ZVS quasi-square-wave resonant switch converter of Fig. 20.30.

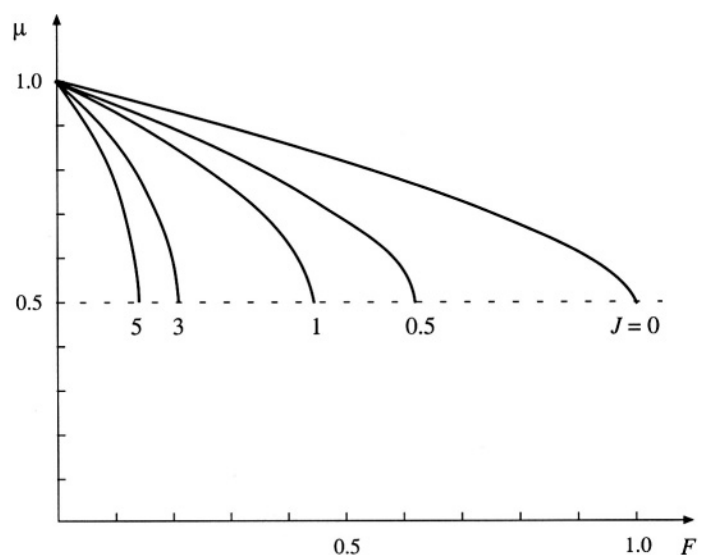
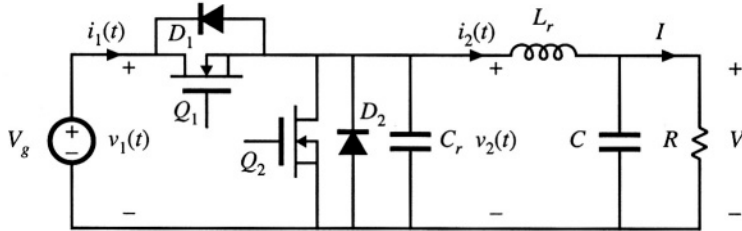


Fig. 20.32 Characteristics of the ZVS quasi-square wave resonant switch network: switch conversion ratio  $\mu$ , as a function of  $F$  and  $J$ . Dashed line: ZVS boundary.



**Fig. 20.33** Quasi-square wave ZVS buck converter containing a synchronous rectifier.

quency  $F$  and normalized output current  $J$ , where these quantities are defined as follows:

$$\begin{aligned} f_0 &= \frac{1}{2\pi\sqrt{L_r C_r}} & R_0 &= \sqrt{\frac{L_r}{C_r}} \\ F &= \frac{f_s}{f_0} & J &= \frac{I_2 R_0}{V_1} \end{aligned} \quad (20.66)$$

In addition, the zero-voltage-switching boundary is plotted. It can be seen that the requirement for zero-voltage switching limits the switch conversion ratio  $\mu$  to the range  $0.5 \leq \mu \leq 1$ . In consequence, the buck converter of Fig. 20.30 cannot produce output voltages less than  $0.5V_g$  without losing the ZVS property. A version which attains  $0 \leq \mu \leq 1$ , at the expense of increased transistor voltage stress, is described in [17]. In addition, the two-switch version of the ZVS-QSW switch can operate with ZVS for  $\mu < 0.5$ .

A useful variant of the converter of Fig. 20.30 involves replacement of the diode with a synchronous rectifier, as illustrated in Fig. 20.33 [8,9]. The second transistor introduces an additional degree of freedom in control of the converter, because this transistor can be allowed to conduct longer than the diode would otherwise conduct. This fact can be used to extend the region of zero-voltage switching to conversion ratios approaching zero, and also to operate the converter with constant switching frequency.

Typical tank element waveforms for the circuit of Fig. 20.33 are illustrated in Fig. 20.34. These waveforms resemble those of the single switch case, Fig. 20.31, except that the tank current is negative while transistor  $Q_2$  conducts. The duty cycle  $D$  is defined with respect to the turn-off transitions

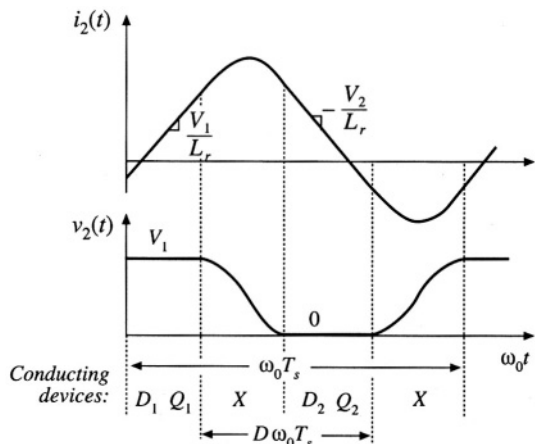


**Fig. 20.34** Waveforms for the two-switch QSW-ZVS converter of Fig. 20.33.

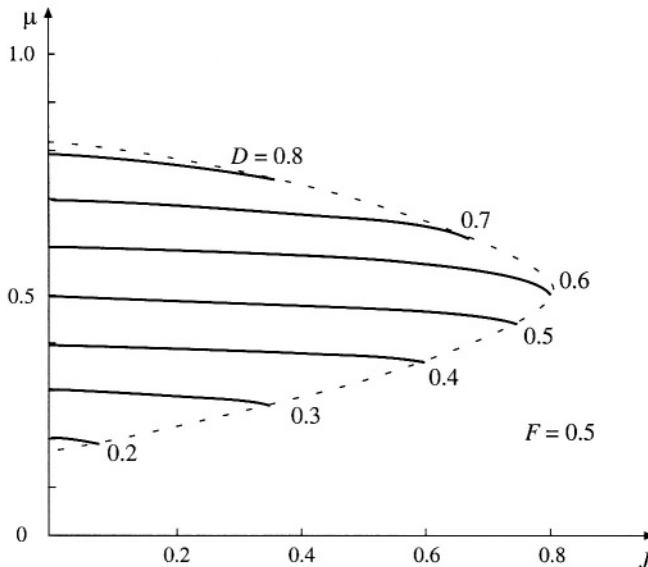


**Fig. 20.35** Conversion ratio  $\mu$ , as a function of duty cycle  $D$  and normalized load current  $J$ , for the two-switch QSW-ZVS switch illustrated in Fig. 20.33. Curves are plotted for constant-frequency control with  $F = 0.5$ . The dashed line is the zero-voltage switching boundary.

of transistors  $Q_1$  and  $Q_2$ , as illustrated.

Characteristics of the two-switch QSW-ZVS switch network are plotted in Fig. 20.35, for the case of constant switching frequency at  $F = 0.5$ . The boundary of zero-voltage switching is also illustrated. Operation at a lower value of  $F$  causes the ZVS boundary to be extended to larger values of  $J$ , and to values of  $\mu$  that more closely approach the extreme values  $\mu = 0$  and  $\mu = 1$ .

To the commutation intervals can be neglected, one would expect that the switch conversion ratio  $\mu$  is simply equal to the duty cycle  $D$ . It can be seen from Fig. 20.35 that this is indeed the case. The characteristics are approximately horizontal lines, nearly independent of load current  $J$ .

Zero-voltage switching quasi-square wave converters exhibit very low switching loss, because all semiconductor elements operate with zero-voltage switching. In the constant-frequency case containing a synchronous rectifier, the converter behavior is nearly the same as for the hard-switched PWM case, since  $\mu \approx D$ . The major disadvantage is the increased conduction loss, caused by the reversal of the inductor current.

## 20.4 SOFT SWITCHING IN PWM CONVERTERS

The quasi-square wave approach of the previous section is notable because it attains zero-voltage switching without increasing the peak voltage applied to the transistor. Several related soft-switching approaches have now become popular, which also attain zero-voltage switching without increasing the transistor peak voltage stress. In this section, popular zero-voltage switching versions of the full bridge, forward, and flyback converters, as well as the voltage-source inverter, are briefly discussed.

### 20.4.1 The Zero-Voltage Transition Full-Bridge Converter

It is possible to obtain soft switching in other types of converters as well. An example is the zero-voltage transition (ZVT) converter based on the full-bridge transformer-isolated buck converter, illustrated in Fig. 20.36 [25–28]. The transistor and diode output capacitances are represented in the figure by capacitances  $C_{leg}$ . Commutating inductor  $L_c$  is placed in series with the transformer; the net inductance  $L_c$  includes both transformer leakage inductance and the inductance of an additional discrete element. This inductor causes the full-bridge switch network to drive an effective inductive load, and results in zero-voltage switching of the primary-side semiconductor devices. Although the waveforms are not sinusoidal, it can nonetheless be said that the switch network output current  $i_c(t)$  lags the voltage  $v_s(t)$ , because the zero crossings of  $i_c(t)$  occur after the ZVS switching transitions are completed.

The output voltage is controlled via phase control. As illustrated in Fig. 20.37, both halves of the bridge switch network operate with a 50% duty cycle, and the phase difference between the half-bridge switch networks is controlled. The idealized waveforms of Fig. 20.37 neglect the switching transitions, and the subinterval numbers correspond to those of the more detailed Fig. 20.38. The phase shift variable  $\phi$  lies in the range  $0 \leq \phi \leq 1$ , and assumes the role of the duty cycle  $d$  in this converter. The quantity  $\phi$  is defined as

$$\phi = \frac{(t_1 - t_0)}{\left(\frac{T_s}{2}\right)} \quad (20.67)$$

By volt-second balance on the secondary-side filter inductor, the conversion ratio  $M(\phi)$  is expressed as

$$M(\phi) = \frac{V}{V_s} = n\phi \quad (20.68)$$

This expression neglects the lengths of the switching transitions.

Although the circuit appears symmetrical, the phase-shift control scheme introduces an asymmetry that causes the two half-bridge switch networks to behave quite differently during the switching transitions. During subintervals 4 and 10, energy is actively transmitted from the source  $V_s$  through the switches and transformer. These subintervals are initiated by the switching of the half-bridge network

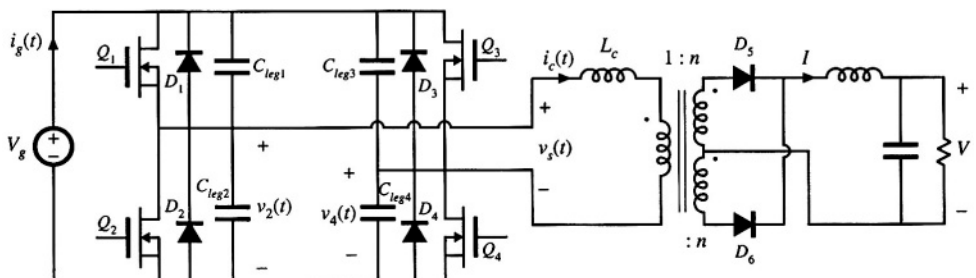


Fig. 20.36 Zero-voltage transition converter, based on the full-bridge isolated buck converter.

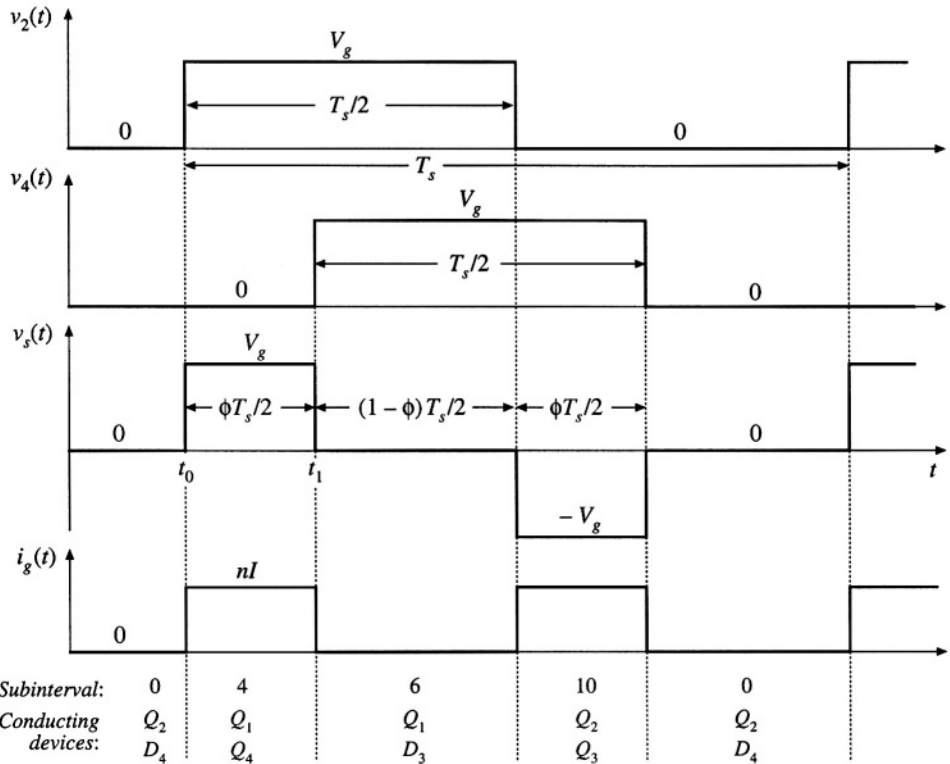
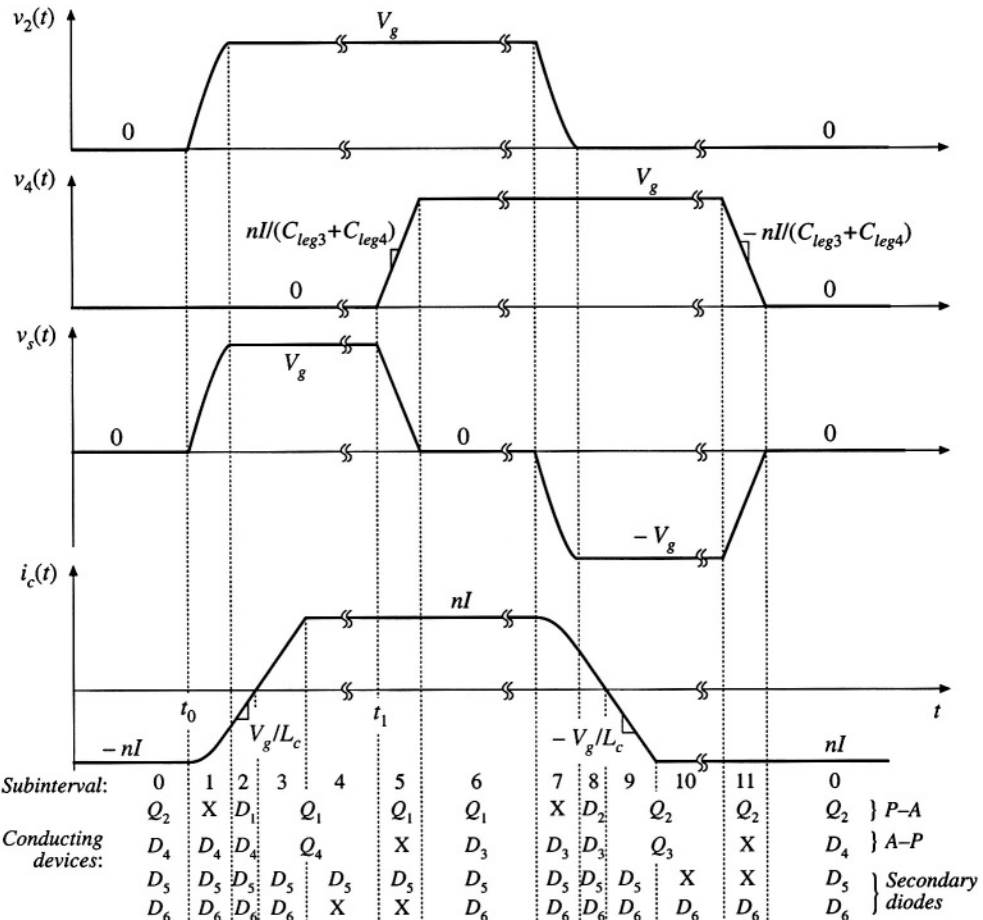


Fig. 20.37 Phase-shift control of the ZVT full-bridge converter. Switching transitions are neglected in this figure, and subinterval numbering follows Fig. 20.38.

composed of the elements  $Q_1$ ,  $D_1$ ,  $Q_2$ , and  $D_2$ , called the “passive-to-active” (P–A) transition [27]. Subintervals 4 and 10 are terminated by the switching of the half-bridge network comprised by the elements  $Q_3$ ,  $D_3$ ,  $Q_4$ , and  $D_4$ , called the “active-to-passive” (A–P) transition.

The turn-on and turn-off switching processes of this converter are similar to the zero-voltage-switching turn-off process described in the previous section. Detailed primary-side waveforms are illustrated in Fig. 20.38. During subinterval 0,  $Q_2$  and  $D_4$  conduct. If the transformer magnetizing current  $i_M$  is negligible, then the commutating inductor current is given by  $i_c(t_0) = -nI$ , where  $I$  is the load current. The passive-to-active transition is initiated when transistor  $Q_2$  is turned off. The negative  $i_c$  then causes capacitors  $C_{leg1}$  and  $C_{leg2}$  to charge, increasing  $v_2(t)$ . During subinterval 1,  $L_c$ ,  $C_{leg1}$ , and  $C_{leg2}$  form a resonant network that rings with approximately sinusoidal waveforms. If sufficient energy was initially stored in  $L_c$ , then  $v_2(t)$  eventually reaches  $V_g$ , terminating subinterval 1. Diode  $D_1$  then clamps  $v_2(t)$  to  $V_g$  during subinterval 2. Transistor  $Q_1$  is turned on at zero voltage during subinterval 2; in practice, this is implemented by insertion of a small delay between the switching transitions of transistors  $Q_2$  and  $Q_1$ .

If  $L_c$  does not initially store sufficient energy to charge the total capacitance ( $C_{leg1} + C_{leg2}$ ) from  $v_2 = 0$  to  $v_2 = V_g$  during subinterval 1, then  $v_2(t)$  will never reach  $V_g$ . Switching loss will then occur when transistor  $Q_1$  is turned on. This situation typically occurs at light load, where  $I$  is small. Sometimes, the design engineer may choose to simply accept this power loss; after all, other losses such as conduction loss are small at light load. An alternative is to modify the circuit to increase the energy stored in  $L_c$  at



**Fig. 20.38** Detailed diagram of primary-side waveforms of the ZVT full-bridge converter, illustrating the zero-voltage switching mechanisms. An ideal transformer is assumed.

$t = t_0$  under light load conditions. One way to accomplish this is to increase the transformer magnetizing current  $i_M(t_0)$  to a significant level; at the beginning of subinterval 1,  $i_c$  is then equal to  $i_c(t_0) = -NI + i_M(t_0)$  with  $i_M(t_0) < 0$ . At light load where  $I$  is small, the magnetizing current maintains the required level of  $i_c$ .

During subintervals 0, 1,2, and 3, secondary-side diodes  $D_5$  and  $D_6$  both conduct; hence, zero voltage appears across all transformer windings. In consequence, voltage  $V_g$  is applied to commutating inductor  $L_c$  during subintervals 2 and 3, causing  $i_c(t)$  to increase with slope  $V_g/L_c$ . Current  $i_c(t)$  reaches zero at the end of subinterval 2, and increases to the positive value  $+nI$  at the end of subinterval 3. The reversal of polarity of  $i_c(t)$  enables zero-voltage switching during the next switching transitions, subinterval 5 and subintervals 7–9.

At the end of subinterval 3, the current in diode  $D_6$  has decreased to zero.  $D_6$  then becomes reverse-biased, with zero-current switching. At this instant, diode  $D_6$  must begin to block voltage  $2nV_e$ .

The output capacitance of  $D_6$  prevents the voltage from changing immediately to  $2nV_g$ ; instead, the resonant circuit formed by  $L_c$  and the  $D_6$  output capacitance begins to ring in a manner similar to Fig. 4.54. Peak  $D_6$  voltages are typically observed that are considerably in excess of  $2nV_g$ , and it is usually necessary to add voltage-clamp snubbers that prevent the secondary-side diode voltages from exceeding a safe value. Several dissipative and non-dissipative approaches are discussed in [26–28].

The active-to-passive switching transition occurs during subinterval 5. This subinterval is initiated when transistor  $Q_4$  is turned off. The positive current  $i_c(t_1)$  is equal to the reflected load current  $nI$ , and charges capacitors  $C_{leg3}$  and  $C_{leg4}$  from  $v_4 = 0$  to  $v_4 = V_g$ . Subinterval 5 ends when  $v_4$  reaches  $V_g$ ; Diode  $D_3$  then becomes forward-biased. Transistor  $Q_3$  is then turned on during subinterval 6, with zero-voltage switching. This is typically implemented by insertion of a small delay between the switching of transistors  $Q_4$  and  $Q_3$ . Because  $i_c$  is constant and equal to  $nI$  during subinterval 5, the active-to-passive transition maintains zero-voltage switching at all load currents.

Circuit behavior during the next half switching period, comprising subintervals 6 to 11, is symmetrical and therefore similar to the behavior observed during subintervals 0 to 5. The switching transitions of transistors  $Q_1$  and  $Q_2$  are passive-to-active transitions, and occur with zero-voltage switching provided that sufficient energy is stored in  $L_c$  as described above. The switching transitions of  $Q_3$  and  $Q_4$  are active-to-passive, and occur with zero-voltage switching at all loads.

The zero-voltage transition converter exhibits low primary-side switching loss and generated EMI. Conduction loss is increased with respect to an ideal PWM full-bridge topology, because of the current  $i_c$  that circulates through the primary-side semiconductors during subintervals 0 and 6. However, this increase in conduction loss can be small if the range of input voltage variations is narrow. This soft-switching approach has now found commercial success.

#### 20.4.2 The Auxiliary Switch Approach

A similar approach can be used in forward, flyback, and other transformer-isolated converters. As illustrated in Fig. 20.39, an “active-clamp snubber” network consisting of a capacitor and auxiliary MOSFET  $Q_2$  is added, that is effectively in parallel with the original power transistor  $Q_1$  [29]. The MOSFET body diodes and output drain-to-source capacitances, as well as the transformer leakage inductance  $L_t$ , participate in the circuit operation. These elements lead to zero-voltage switching, with waveforms similar to those of the ZVT full-bridge converter of Section 20.4.1 or the two-transistor QSW-ZVS switch of Section 20.3.3. The transistors are driven by complementary signals; for example, after turning off  $Q_1$ , the controller waits for a short delay time and then turns on  $Q_2$ .

The active-clamp snubber can be viewed as a voltage-clamp snubber, similar to the dissipative snubber illustrated in Fig. 20.6. However, the snubber contains no resistor; instead, MOSFET  $Q_2$  allows bidirectional power flow, so that the energy stored in capacitor  $C_s$  can flow back into the converter.

The voltage  $v_s$  can be found by volt-second inductance on the transformer magnetizing inductance. If the lengths of the commutation intervals are neglected, and if the voltage ripple in  $v_s(t)$  can be neglected, then one finds that

$$V_s = \frac{D}{D'} V_g \quad (20.69)$$

The voltage  $v_s$  is effectively an unloaded output of the converter. With the two-quadrant switch provided by  $Q_2$ , this output operates in continuous conduction mode with no load, and hence the peak voltage of  $Q_1$  is clamped to the minimum level necessary to balance the volt-seconds applied to the transformer magnetizing inductance.

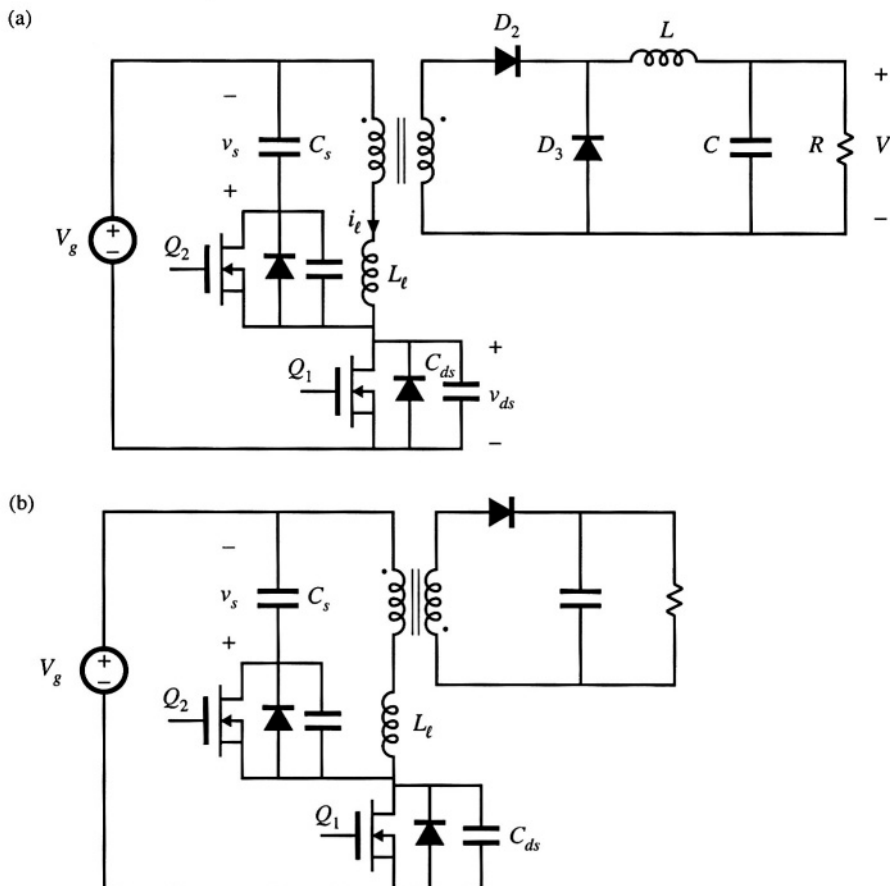


Fig. 20.39 Active-clamp snubber circuits: (a) forward converter, (b) flyback converter.

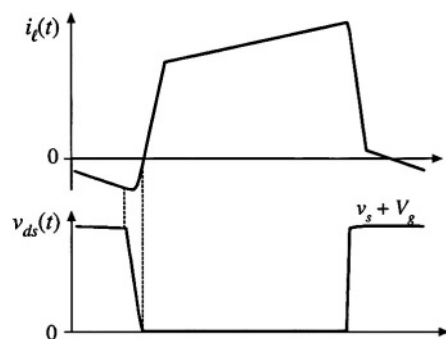


Fig. 20.40 Waveforms of the active-clamp snubber circuit of Fig. 20.39(a).

Typical waveforms for a forward converter incorporating an active-clamp snubber are illustrated in Fig. 20.40. The current  $i_t(t)$  reverses direction while  $Q_2$  conducts. When  $Q_2$  turns off, capacitor  $C_{ds}$  begins to discharge. When  $v_{ds}$  reaches zero, the body diode of  $Q_1$  becomes forward-biased.  $Q_1$  can then be turned on at zero voltage.

An added benefit of the active clamp snubber, when used in a forward converter, is that it resets the transformer. Consequently, the converter can operate at any duty cycle, including duty cycles greater than 50%. When the converter must operate with a wide range of input voltages, this can allow substantial improvements in transistor stresses and efficiency. The MOSFETs in Fig. 20.39 operate with zero-voltage switching, while the secondary-side diodes operate with zero-current switching.

This approach is quite versatile, and similar auxiliary circuits can be added to other converter circuits to obtain zero-voltage switching [30,31].

#### 20.4.3 Auxiliary Resonant Commutated Pole

The auxiliary resonant commutated pole (ARCP) is a related circuit that uses an auxiliary four-quadrant switch (or two equivalent two-quadrant switches) to obtain soft switching in the transistors of a bridge inverter circuit [32–34]. This approach finds application in dc–ac inverter circuits. Figure 20.41 illustrates a half-bridge circuit, or one phase of a three-phase voltage-source inverter, driving an ac load. This circuit can lead to zero-voltage switching that mitigates the switching loss induced by the reverse recovery of diodes  $D_1$  and  $D_2$ . Filter inductor  $L_f$  is relatively large, so that the output current  $i_a(t)$  is essentially constant during the resonant commutation interval. Capacitors  $C_{ds}$  are relatively small, and model the output capacitances of the semiconductor devices. Inductor  $L_r$  is also relatively small, and elements  $L_r$  and  $C_{ds}$  form a resonant circuit that rings during part of the commutation process. Semiconductor switching devices  $Q_3$ ,  $Q_4$ ,  $D_3$ , and  $D_4$  form an auxiliary four-quadrant switch that turns on to initiate the resonant commutation process.

Typical commutation waveforms are illustrated in Fig. 20.42(a), for the case in which the ac load current  $i_a$  is positive. Diode  $D_2$  is initially conducting the output current  $i_a$ . It is desired to turn off  $D_2$  and turn on  $Q_1$ , with zero-voltage switching. This is accomplished with the following sequence:

- Interval 1. Turn on transistor  $Q_3$ . Devices  $D_2$ ,  $Q_3$ , and  $D_4$  conduct.
- Interval 2. When the current in  $D_2$  reaches zero,  $D_2$  turns off. A resonant ringing interval occurs.
- Interval 3. When the voltage  $v_{an}$  reaches  $V_g/2$ , diode  $D_1$  begins to become forward-biased. Transistor  $Q_1$  is then immediately turned on at zero voltage.

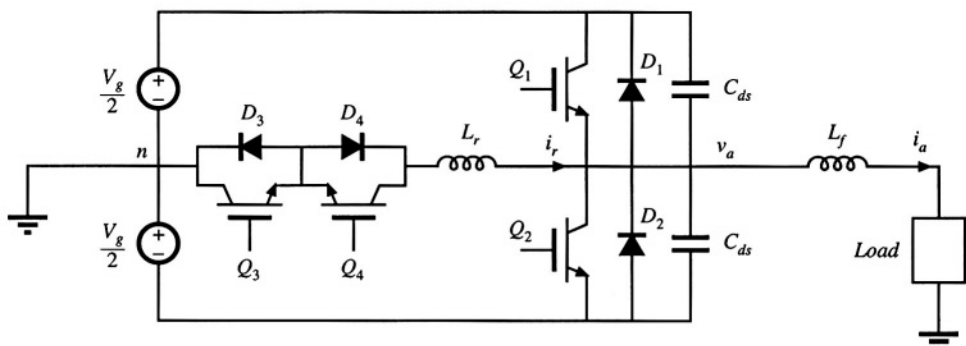


Fig. 20.41 Half-bridge circuit driving an ac load, with ARCP zero-voltage switching.

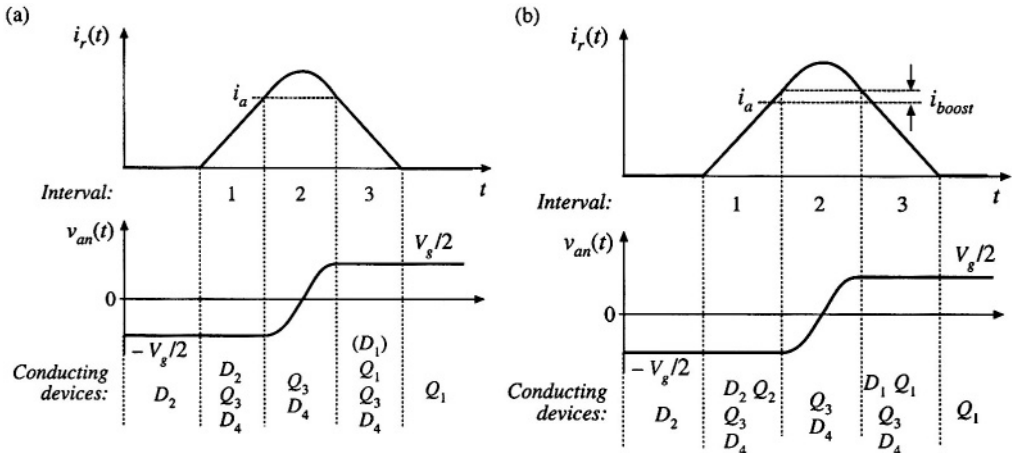


Fig. 20.42 Waveforms of the ARCP circuit of Fig. 20.41: (a) basic waveforms, (b) with current boost.

At the conclusion of interval 3,  $i_r(t)$  reaches zero and diode  $D_3$  turns off. For negative current, the process for commutation of diode  $D_1$  is similar, except that transistor  $Q_4$  and diode  $D_3$  conduct the resonant current  $i_r(t)$ .

One issue related to the waveforms of Fig. 20.42(a) is that the circuit always operates at the boundary of zero-voltage switching. At the end of interval 2, diode  $D_1$  is not actually forward-biased, because its current never actually becomes positive. Instead, transistor  $Q_1$  should be turned on at the beginning of interval 3. If transistor  $Q_1$  is gated on late, then the continued ringing will cause voltage  $v_{an}(t)$  to decrease, and zero-voltage switching will be lost.

To further assist in the zero-voltage switching commutation process, transistor  $Q_2$  can be turned on while  $D_2$  conducts, as illustrated in Fig. 20.42(b). Transistor  $Q_2$  is used to lengthen the duration of interval 1: now, when the current  $i_r(t)$  exceeds current  $i_a$  by an amount  $i_{boost}$ , then the controller turns off  $Q_2$  to end interval 1. This causes diode  $D_1$  to become forward-biased during the beginning of interval 3. Transistor  $Q_1$  is then turned on with zero-voltage switching, while  $D_1$  is conducting.

Regardless of whether the circuit operates with the waveforms of Fig. 20.42(a) or (b), the ARCP approach eliminates the switching loss caused by the reverse recovery of diodes  $D_1$  and  $D_2$ . Unlike the previous circuits of this chapter, the ARCP has no circulating currents that cause conduction loss, because the tank inductor current  $i_r(t)$  is nonzero only in the vicinity of the commutation interval. The approach of Fig. 20.42(a) does not completely eliminate the loss caused by the device output capacitances. This loss is eliminated using the current boost of Fig. 20.42(b), but additional conduction loss is incurred because of the increased peak  $i_r(t)$ . The waveforms of Fig. 20.42(b) may, in fact, lead to reduced efficiency relative to Fig. 20.42(a)!

## 20.5 SUMMARY OF KEY POINTS

1. In a resonant switch converter, the switch network of a PWM converter is replaced by a switch network containing resonant elements. The resulting hybrid converter combines the properties of the resonant switch network and the parent PWM converter.
2. Analysis of a resonant or soft-switching switch cell involves determination of the switch conversion ratio  $\mu$ . The resonant switch waveforms are determined, and are then averaged. The switch conversion ratio  $\mu$  is

a generalization of the PWM CCM duty cycle  $d$ . The results of the averaged analysis of PWM converters operating in CCM can be directly adapted to the related resonant switch converter, simply by replacing  $d$  with  $\mu$ .

3. In the zero-current-switching quasi-resonant switch, diode  $D_2$  operates with zero-voltage switching, while transistor  $Q_1$  and diode  $D_1$  operate with zero-current switching. In the zero-voltage-switching quasi-resonant switch, the transistor  $Q_1$  and diode  $D_1$  operate with zero-voltage switching, while diode  $D_2$  operates with zero-current switching.
4. In the zero-voltage-switching multiresonant switch, all semiconductor devices operate with zero-voltage switching. In consequence, very low switching loss is observed.
5. In the quasi-square-wave zero-voltage-switching resonant switches, all semiconductor devices operate with zero-voltage switching, and with peak voltages equal to those of the parent PWM converter. The switch conversion ratio is restricted to the range  $0.5 \leq \mu \leq 1$ . Versions containing synchronous rectifiers can operate with values of  $\mu$  approaching zero.
6. The zero-voltage transition approach, as well as the active-clamp snubber approach, lead to zero-voltage switching of the transistors and zero-current switching of the diodes. These approaches have been successful in substantially improving the efficiencies of transformer-isolated converters. The auxiliary resonant commutated pole induces zero-voltage switching in bridge circuits such as the voltage-source inverter.

## REFERENCES

- [1] P. VINCIARELLI, "Forward Converter Switching at Zero Current," U.S. Patent 4,415,959, Nov. 1983.
- [2] K. LIU, R. ORUGANTI, and F. C. LEE, "Resonant Switches: Topologies and Characteristics," *IEEE Power Electronics Specialists Conference*, 1985 Record, pp. 106-116.
- [3] M. F. SCHLECHT and L. F. CASEY, "Comparison of the Square-Wave and Quasi-Resonant Topologies," *IEEE Applied Power Electronics Conference*, 1987 Record, pp. 124-134.
- [4] K. LIU and F. C. LEE, "Zero Voltage Switching Technique in Dc-Dc Converters," *IEEE Power Electronics Specialists Conference*, 1986 Record, pp. 58-70.
- [5] W. A. TABISZ and F. C. LEE, "Zero-Voltage-Switching Multi-Resonant Technique—A Novel Approach to Improve Performance of High-Frequency Quasi-Resonant Converters," *IEEE Power Electronics Specialists Conference*, 1988 Record, pp. 9-17.
- [6] W. A. TABISZ, M. M. JOVANOVIC, and F. C. LEE, "High Frequency Multi-Resonant Converter Technology and Its Applications," *IEE International Conference on Power Electronics and Variable Speed Drives*, July 17-19, 1990, p. 1-8.
- [7] R. FARRINGTON, M. JOVANOVIC, and F. C. LEE, "Constant-Frequency Zero-Voltage-Switched Multi-Resonant Converters: Analysis, Design, and Experimental Results," *IEEE Power Electronics Specialists Conference*, 1990 Record, pp. 197-205.
- [8] D. MAKSIMOVIC, "Synthesis of PWM and Quasi-Resonant Dc-to-Dc Power Converters," Ph.D. thesis, California Institute of Technology, January 1989.
- [9] X. ZHOU, X. ZHANG, J. LIU, P. WONG, J. CHEN, H. WU, L. AMOROSO, F. LEE, and D. CHEN, "Investigation of Candidate VRM Topologies for Future Microprocessors," *IEEE Applied Power Electronics Conference*, 1998 Record, pp. 145–150.

- [10] R. REDL, B. MOLNAR, and N. SOKAL, "Class E Resonant Regulated Dc–Dc Power Converters: Analysis of Operation and Experimental Results at 1.5 MHz," *IEEE Transactions on Power Electronics*, 1986, Vol. 1, No. 2, pp. 111-120.
- [11] N. SOKAL and A. SOKAL, "Class-E, A New Class of High Efficiency Tuned Single-Ended Switching Power Amplifiers," *IEEE Journal of Solid State Circuits*, Vol. SC-10, June 1975, pp. 168-176.
- [12] F. H. RAAB, "Idealized Operation of Class-E Tuned Power Amplifier," *IEEE Transactions on Circuits and Systems*, Vol. 24, No. 12, December 1977, pp. 725-735.
- [13] K. D. T. NGO, "Generalization of Resonant Switches and Quasi-Resonant Dc–Dc Converters," *IEEE Power Electronics Specialists Conference*, 1987 Record, pp. 395-403.
- [14] V. VORPERIAN, "Quasi-Square Wave Converters: Topologies and Analysis," *IEEE Transactions on Power Electronics*, Vol. 3, No. 2, April 1988, pp. 183-191.
- [15] D. MAKSIMOVIC, "Design of the Zero-Voltage-Switching Quasi-Square-Wave Resonant Switch," *IEEE Power Electronics Specialists Conference*, 1993 Record, pp. 323-329.
- [16] O. D. PATTERSON and D. M. DIVAN, "Pseudo-Resonant Full-Bridge Dc–Dc Converter," *IEEE Power Electronics Specialists Conference*, 1987 Record, pp. 424-430.
- [17] Y. JANG and R. ERICKSON, "New Quasi-Square Wave and Multi-Resonant Integrated Magnetic Zero Voltage Switching Converters," *IEEE Power Electronics Specialists Conference*, 1993 Record, pp. 721-727.
- [18] V. VORPERIAN, R. TYMERSKI, and F. C. LEE, "Equivalent Circuit Models for Resonant and PWM Switches," *IEEE Transactions on Power Electronics*, Vol. 4, No. 2, April 1989, pp. 205-214.
- [19] S. FREELAND and R. D. MIDDLEBROOK, "A Unified Analysis of Converters with Resonant Switches", *IEEE Power Electronics Specialists Conference*, 1987 Record, pp. 20-30.
- [20] A. WITULSKI and R. ERICKSON, "Extension of State-Space Averaging to Resonant Switches—and Beyond," *IEEE Transactions on Power Electronics*, Vol. 5, No. 1, pp. 98-109, January 1990.
- [21] D. MAKSIMOVIC and S. CUK, "A General Approach to Synthesis and Analysis of Quasi-Resonant Converters," *IEEE Transactions on Power Electronics*, Vol. 6, No. 1, January 1991, pp. 127-140.
- [22] R. ERICKSON, A. HERNANDEZ, A. WITULSKI, and R. XU, "A Nonlinear Resonant Switch," *IEEE Transactions on Power Electronics*, Vol. 4, No. 2, April 1989, pp. 242-252.
- [23] I. BARBI, D. MARTINS, and R. DO PRADO, "Effects of Nonlinear Resonant Inductor on the Behavior of Zero-Voltage Switching Quasi-Resonant Converters," *IEEE Power Electronics Specialists Conference*, 1990 Record, pp. 522-527.
- [24] S. FREELAND, "I. A Unified Analysis of Converters with Resonant Switches, II. Input-Current Shaping for Single-Phase Ac–Dc Power Converters," Ph.D. Thesis, California Institute of Technology, 1988.
- [25] R. FISHER, K. NGO, and M. KUO, "A 500 kHz, 250 W Dc–dc Converter with Multiple Outputs Controlled by Phase-Shifted PWM and Magnetic Amplifiers," *Proceedings of High Frequency Power Conversion Conference*, pp. 100-110, May 1988.
- [26] L. MWEENE, C. WRIGHT, and M. SCHLECHT, "A 1 kW, 500 kHz Front-End Converter for a Distributed

Power Supply System," *IEEE Applied Power Electronics Conference*, 1989 Record, pp. 423–432.

- [27] R. REDL, L. BELOGH, and D. EDWARDS, "Optimum ZVS Full-Bridge DC/DC Converter with PWM Phase-Shift Control: Analysis, Design Considerations, and Experimental Results," *IEEE Applied Power Electronics Conference*, 1994 Record, pp. 159–165.
- [28] J. G. CHO, J. A. SABATE, and F. C. LEE, "Novel Full Bridge Zero-Voltage-Transition PWM DC/DC Converter for High Power Applications," *IEEE Applied Power Electronics Conference*, 1994 Record, pp. 143–149.
- [29] P. VINCIARELLI, "Optimal Resetting of the Transformer's Core in Single-Ended Forward Converters," Reissued U.S. Patent No. Re. 36,098, Feb. 16, 1999.
- [30] C. DUARTE and I. BARBI, "A Family of ZVS-PWM Active-Clamping Dc-to-Dc Converters: Synthesis, Analysis, Design, and Experimentation," *IEEE Transactions on Circuits and Systems—I: Fundamental Theory and Applications*, Vol. 44, No. 8, pp. 698–704, Aug. 1997.
- [31] P. HENG and R. ORUGANTI, "Family of Two-Switch Soft-Switched Asymmetrical PWM Dc/Dc Converters," *IEEE Power Electronics Specialists Conference*, 1994 Record, pp. 85–94.
- [32] R. DEDONCKER and J. LYONS, "The Auxiliary Resonant Commutated Pole Converter," *IEEE Industry Applications Society Annual Meeting*, 1990 Record, pp. 1228–1235.
- [33] R. TEICHMANN and S. BERNET, "Investigation and Comparison of Auxiliary Resonant Commutated Pole Converter Topologies," *IEEE Power Electronics Specialists Conference*, 1998 Record, pp. 15–23, May 1998.
- [34] W. McMURRAY, "Resonant Snubbers with Auxiliary Devices," *IEEE Transactions on Industry Applications*, Vol. 29, No. 2, pp. 355–361, 1993.

## PROBLEMS

- 20.1** In the forward converter of Fig. 20.43,  $L$  and  $C$  are large filter elements while  $L_p$ ,  $L_s$ , and  $C_r$  have relatively small values. The transformer reset mechanism is not shown; for this problem, you may assume that the transformer is ideal.

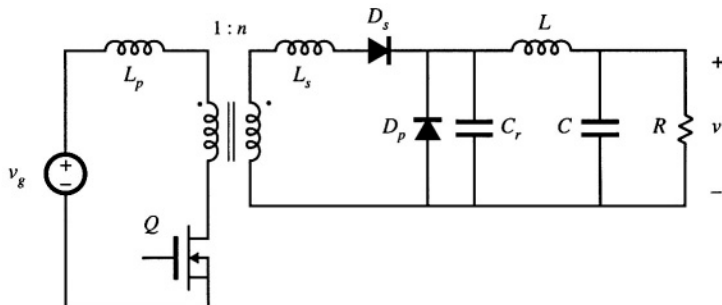


**Fig. 20.43** Forward converter with resonant switch, Problem 20.1.

- (a) Classify the resonant switch.

- (b) Which semiconductor devices operate with zero-voltage switching? With zero-current switching?  
 (c) What is the resonant frequency?

20.2

In the high-voltage converter of Fig. 20.44, capacitor  $C$  is relatively large in value. The transformer model includes an ideal  $1:n$  transformer, in conjunction with magnetizing inductance  $L_{mp}$  (referred to the primary side) and winding capacitance  $C_{ws}$  (referred to the secondary side). Transistor  $Q$  and diode  $D_p$  exhibit total output capacitance  $C_p$ , while the output capacitance of diode  $D_s$  is  $C_s$ . Other nonidealities, such as transformer leakage inductance, can be ignored. The resonant switch is well-designed, such that all elements listed above contribute to ideal operation of the converter and resonant switch.

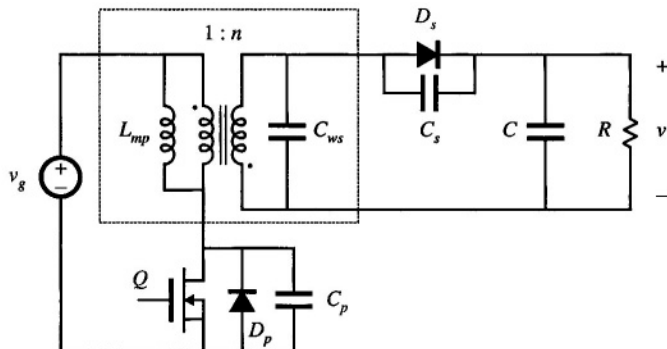


**Fig. 20.44** High-voltage dc-dc converter containing a resonant switch network, Problem 20.2.

- (a) What type of resonant switch is employed? What is the parent PWM converter?  
 (b) Which semiconductor devices operate with zero-voltage switching? With zero-current switching?  
 (c) What is the tank resonant frequency?  
 (d) Sketch the waveforms of the transistor drain-to-source voltage and transformer magnetizing current.

20.3

In the transformer-isolated dc-dc converter of Fig. 20.45, capacitors  $C_1$  and  $C_2$  and inductors  $L_1$  and  $L_M$  are relatively large in value, so that they have small switching ripples. The transformer model includes an ideal  $1:n$  transformer, in conjunction with magnetizing inductance  $L_M$  (referred to the primary side) and leakage inductances  $L_{t1}$  and  $L_{t2}$  as shown. Transistor  $Q_1$  exhibits output capacitances  $C_{ds}$ , while the output capacitance of diode  $D_1$  is  $C_d$ . MOSFET  $Q_1$  contains a body diode (not explicitly shown). Other nonidealities can be ignored. The resonant switch is well-designed, such that all elements listed above contribute to ideal operation of the converter and resonant switch.

- (a) What type of resonant switch is employed? What is the parent PWM converter?  
 (b) Which semiconductor devices operate with zero-voltage switching? With zero-current switching?

20.4

A buck-boost converter is realized using a half-wave ZCS quasi-resonant switch. The load resistance has value  $R$ , the input voltage has value  $V_g$ , and the converter switching frequency is  $f_s$ .

- (a) Sketch the circuit schematic.  
 (b) Write the complete system of equations that can be solved to determine the output voltage  $V$ , in terms of the quantities listed above and the component values. It is not necessary to actually solve your equations. You may also quote results listed in this textbook.

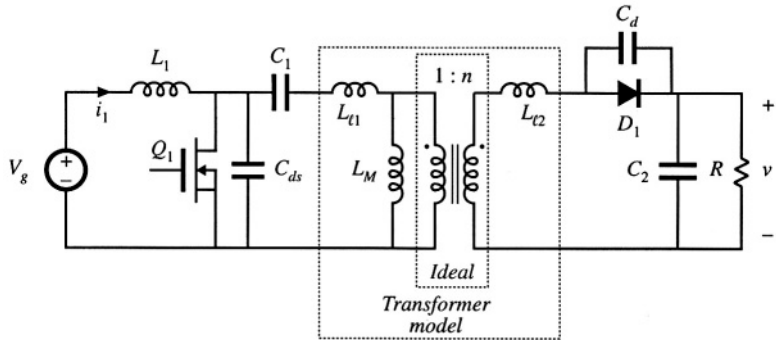


**Fig. 20.45** Transformer-isolated dc-dc converter containing a resonant switch network, Problem 20.3.

### 20.5

It is desired to design a half-wave zero-current-switching quasi-resonant forward converter to operate with the following specifications:  $V_g = 320$  V,  $V_o = 42$  V,  $5 \text{ W} \leq P \leq 100$  W. Design the converter to operate with a maximum switching frequency of 1 MHz and a switch conversion ratio of  $\mu = 0.45$ . Attempt to minimize the peak transistor current, while maintaining zero current switching at all operating points. You may neglect the transformer magnetizing current, and ignore the transformer reset scheme.

- (a) Specify your choices for the turns ratio  $n$ , and the tank elements  $L_r$  and  $C_r$ , referred to the transformer secondary side.
- (b) For your design of part (a), what is the minimum switching frequency?
- (c) What is the worst-case peak transistor current?

### 20.6

Analysis of the ZVS quasi-resonant switch of Fig. 20.24.

- (a) For each subinterval, sketch the resonant switch cell circuit, and derive expressions for the tank inductor current and capacitor voltage waveforms.
- (b) For subinterval 2, in which  $Q_1/D_1$  are off and  $D_2$  conducts, write the loop equation which relates the tank capacitor voltage, tank inductor voltage, and any other network voltages as appropriate. Hence, for subinterval 2 relate the integral of the tank capacitor voltage to the change in tank inductor current.
- (c) Determine the switch-network terminal-waveform average values, and hence derive an expression for the switch conversion ratio  $\mu$ . Verify that your result coincides with Eq. (20.61).

### 20.7

Analysis of the full-bridge zero-voltage transition converter of Section 20.4.1. The converter of Fig. 20.36 operates with the waveforms illustrated in Fig. 20.38. According to Eq. (20.68), the conversion ratio of this converter is given approximately by  $M(\phi) = n\phi$ .

Derive an exact expression for  $M$ , based on the waveforms given in Fig. 20.38. Your result should be a function of the length of subinterval 4, the load current, the switching frequency, and the values of the inductance and capacitances. *Note:* there is a reasonably simple answer to this question.

# **Appendices**

---

# Appendix A

## RMS Values of Commonly Observed Converter Waveforms

---

The waveforms encountered in power electronics converters can be quite complex, containing modulation at the switching frequency and often also at the ac line frequency. During converter design, it is often necessary to compute the rms values of such waveforms. In this appendix, several useful formulas and tables are developed which allow these rms values to be quickly determined.

RMS values of the doubly-modulated waveforms encountered in PWM rectifier circuits are discussed in Section 18.5.

### A.1 SOME COMMON WAVEFORMS

DC, Fig. A.1:

$$rms = I \quad (A.1)$$

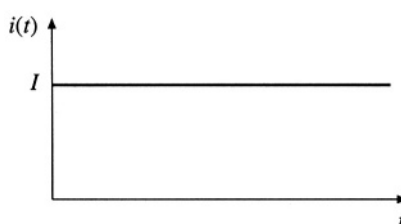


Fig. A.1

DC plus linear ripple, Fig. A.2:

$$rms = I \sqrt{1 + \frac{1}{3} \left( \frac{\Delta i}{I} \right)^2} \quad (A.2)$$

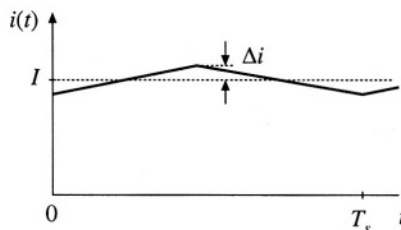


Fig. A.2

Square wave, Fig. A.3:

$$rms = I_{pk} \quad (A.3)$$

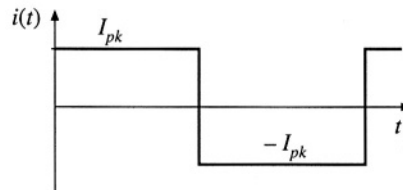


Fig. A.3

Sine wave, Fig. A.4:

$$rms = \frac{I_{pk}}{\sqrt{2}} \quad (A.4)$$

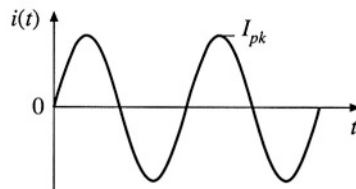


Fig. A.4

Pulsating waveform, Fig. A.5:

$$rms = I_{pk} \sqrt{D} \quad (A.5)$$

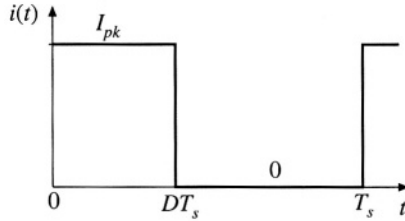


Fig. A.5

Pulsating waveform with linear ripple, Fig. A.6:

$$rms = I \sqrt{D} \sqrt{1 + \frac{1}{3} \left( \frac{\Delta i}{I} \right)^2} \quad (\text{A.6})$$

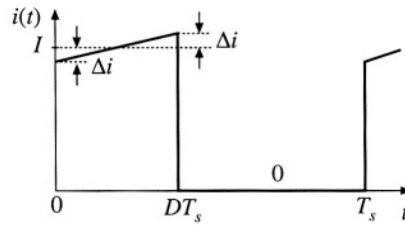


Fig. A.6

Triangular waveform, Fig. A.7:

$$rms = I_{pk} \sqrt{\frac{D_1 + D_2}{3}} \quad (\text{A.7})$$

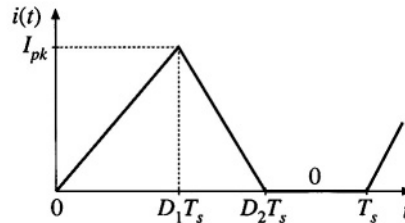


Fig. A.7

Triangular waveform, Fig. A.8:

$$rms = I_{pk} \sqrt{\frac{D_1}{3}} \quad (\text{A.8})$$

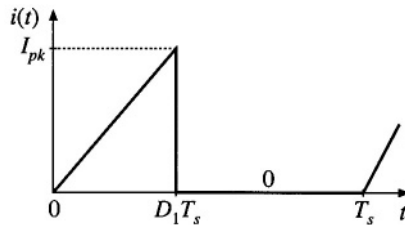


Fig. A.8

Triangular waveform, no dc component, Fig. A.9:

$$rms = \frac{\Delta i}{\sqrt{3}} \quad (\text{A.9})$$

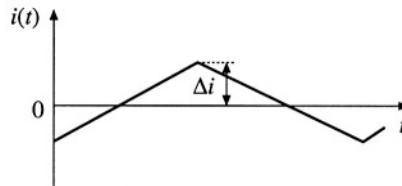


Fig. A.9

Center-tapped bridge winding waveform, Fig. A.10:

$$rms = \frac{1}{2} I_{pk} \sqrt{1+D} \quad (\text{A.10})$$

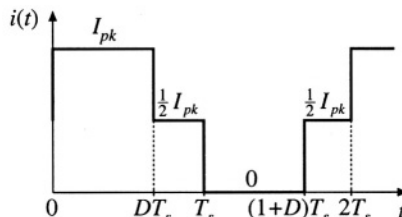


Fig. A.10

General stepped waveform, Fig. A.11:

$$rms = \sqrt{D_1 I_1^2 + D_2 I_2^2 + \dots} \quad (\text{A.11})$$

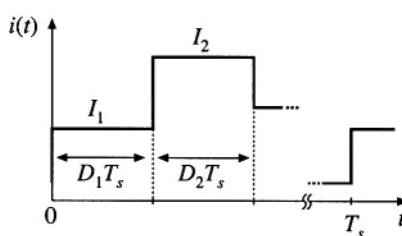
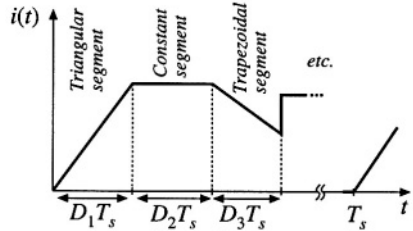


Fig. A.11



**Fig. A.12** General piecewise waveform.

## A.2 GENERAL PIECEWISE WAVEFORM

For a periodic waveform composed of  $n$  piecewise segments as in Fig. A.12, the rms value is

$$rms = \sqrt{\sum_{k=1}^n D_k u_k} \quad (\text{A.12})$$

where  $D_k$  is the duty cycle of segment  $k$ , and  $u_k$  is the contribution of segment  $k$ . The  $u_k$ s depend on the shape of the segments—several common segment shapes are listed below:

Constant segment, Fig. A.13:

$$u_k = I_1^2 \quad (\text{A.13})$$

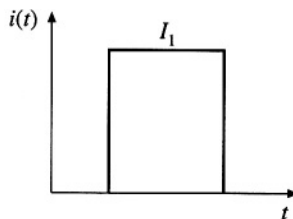


**Fig. A.13**

Triangular segment, Fig. A.14:

$$u_k = \frac{1}{3} I_1^2 \quad (\text{A.14})$$

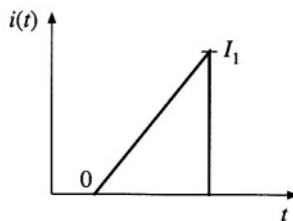


**Fig. A.14**

Trapezoidal segment, Fig. A.15:

$$u_k = \frac{1}{3} (I_1^2 + I_1 I_2 + I_2^2) \quad (\text{A.15})$$

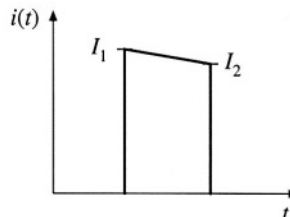


Fig. A.15

Sinusoidal segment, half or full period, Fig. A.16:

$$u_k = \frac{1}{2} I_{pk}^2 \quad (\text{A.16})$$

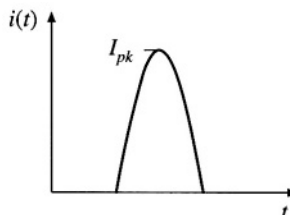


Fig. A.16

Sinusoidal segment, partial period: as in Fig. A.17, a sinusoidal segment of less than one half-period, which begins at angle  $\theta_1$  and ends at angle  $\theta_2$ . The angles  $\theta_1$  and  $\theta_2$  are expressed in radians:

$$u_k = \frac{1}{2} I_{pk}^2 \left( 1 - \frac{\sin(\theta_2 - \theta_1) \cos(\theta_2 + \theta_1)}{(\theta_2 - \theta_1)} \right) \quad (\text{A.17})$$

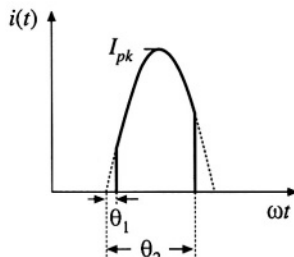
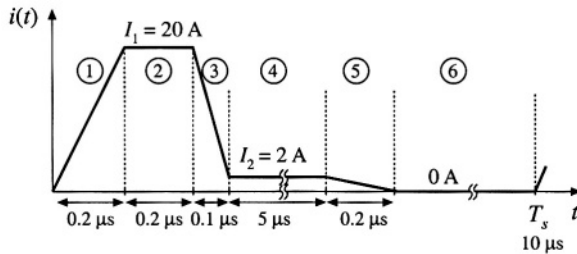


Fig. A.17



**Fig. A.18** Example: an approximate transistor current waveform, including estimated current spike due to diode stored charge.

#### Example

A transistor current waveform contains a current spike due to the stored charge of a freewheeling diode. The observed waveform can be approximated as shown in Fig. A1.18. Estimate the rms current.

The waveform can be divided into six approximately linear segments, as shown. The  $D_k$  and  $u_k$  for each segment are

1. Triangular segment:

$$D_1 = (0.2 \mu s)/(10 \mu s) = 0.02$$

$$u_1 = I_1^2/3 = (20 \text{ A})^2/3 = 133 \text{ A}^2$$

2. Constant segment:

$$D_2 = (0.2 \mu s)/(10 \mu s) = 0.02$$

$$u_2 = I_1^2 = (20 \text{ A})^2 = 400 \text{ A}^2$$

3. Trapezoidal segment:

$$D_3 = (0.1 \mu s)/(10 \mu s) = 0.01$$

$$u_3 = (I_1^2 + I_2^2 + I_3^2)/3 = 148 \text{ A}^2$$

4. Constant segment:

$$D_4 = (5 \mu s)/(10 \mu s) = 0.5$$

$$u_4 = I_2^2 = (2 \text{ A})^2 = 4 \text{ A}^2$$

5. Triangular segment:

$$D_5 = (0.2 \mu s)/(10 \mu s) = 0.02$$

$$u_5 = I_2^2/3 = (2 \text{ A})^2/3 = 1.3 \text{ A}^2$$

6. Zero segment:

$$u_6 = 0$$

The rms value is

$$rms = \sqrt{\sum_{k=1}^6 D_k u_k} = 3.76 \text{ A} \quad (\text{A.18})$$

Even though its duration is very short, the current spike has a significant impact on the rms value of the current—without the current spike, the rms current is approximately 2.0 A.

---

# Appendix B

## Simulation of Converters

---

Computer simulation can be a powerful tool in the engineering design process. Starting from design specifications, an initial design typically includes selection of system and circuit configurations, as well as component types and values. In this process, component and system models are constructed based on vendor-supplied data, and by applications of analysis and modeling techniques. These models, validated by experimental data whenever possible, are the basis upon which the designer can choose parameter values and verify the achieved performance against the design specifications. One must take into account the fact that actual parameter values will not match their nominal values because of inevitable production tolerances, changes in environmental conditions (such as temperature), and aging. In the design verification step, worst-case analysis (or other reliability and production yield analysis) is performed to judge whether the specifications are met under all conditions, i.e., for expected ranges of component parameter values. Computer simulation is very well suited for this task: using reliable models and appropriate simulation setups, the system performance can be tested for various sets of component parameter values. One can then perform design iterations until the worst-case behavior meets specifications, or until the system reliability and production yield are acceptably high.

In the design verification of power electronic systems by simulation, it is often necessary to use component and system models of various levels of complexity:

1. *Detailed, complex models that attempt to accurately represent physical behavior of devices.* Such models are necessary for tasks that involve finding switching times, details of switching transitions and switching loss mechanisms, or instantaneous voltage and current stresses. Component vendors often provide libraries of such device models. To complete a detailed circuit model, one must also carefully examine effects of packaging and board interconnects. With fast-switching power semiconductors, simulation time steps of a few nanoseconds or less may be required, especially during on/off switching transitions. Because of the complexity of detailed device models, and the fine time resolution, the simulation tasks can be very time consuming. In practice, time-domain simulations using detailed device models are usually performed only

on selected parts of the system, and over short time intervals involving a few switching cycles at most. Devices for power converters, and detailed physical device modeling, are areas of active research and development beyond the scope of this book.

2. *Simplified device models.* Since an on/off switching transition usually takes a small fraction of a switching cycle, the basic operation of switching power converters can be explained using simplified, idealized device models. For example, a MOSFET can be modeled as a switch with a small (ideally zero) on-resistance  $R_{on}$  when on, and a very large off-resistance (ideally an open circuit) when off. Such simplified models yield physical insight into the basic operation of switching power converters, and provide the starting point for developments of analytical models described throughout this book. Simplified device models are also useful for time-domain simulations aimed at verifying converter and controller operation, switching ripples, current and voltage stresses, and responses to load or input transients. Since device models are simple, and details of switching transitions are ignored, tasks that require simulations over many switching cycles can be completed efficiently using general-purpose circuit simulators. In addition, specialized tools have been developed to support fast transient simulation of switching power converters based on idealized, piecewise-linear device models [1-7], or a combination of piecewise-linear and nonlinear models [8].
3. *Averaged converter models.* Averaged models that are well suited for prediction of converter steady-state and dynamic responses are discussed throughout this book. These models are essential design tools because they provide physical insight and lead to analytical results that can be used in the design process to select component parameter values for a given set of specifications. In the design verification step, simulations of averaged converter models can be performed to test for losses and efficiency, steady-state voltages and currents, stability, and large-signal transient responses. Since switching transitions and ripples are removed by averaging, simulations over long time intervals and over many sets of parameter values can be completed efficiently. As a result, averaged models are also well suited for simulations of large electronic systems that include switching converters. Furthermore, since large-signal averaged models are nonlinear, but time-invariant, small-signal ac simulations can be used to generate various frequency responses of interest. Selected references on averaged converter modeling for simulation are listed at the end of this chapter [9-18].

Averaged models for computer simulation are covered in this appendix. Based on the material presented in Section 7.4, averaged switch models for computer simulation of converters operating in continuous conduction mode are described in Section B.1. Application examples include finding SEPIC dc conversion ratio and efficiency, and large-signal transient responses of a buck-boost converter. Section B.2 describes an averaged switch model suitable for simulation of converters that may operate either in continuous conduction mode or in discontinuous conduction mode. Application examples include finding SEPIC open-loop frequency responses in CCM and DCM, loop-gain, phase margin and closed-loop responses of a buck voltage regulator, and current harmonics in a DCM boost rectifier. Based on the results from Chapter 12, a simulation model for converters with current programmed control is described in Section B.3, together with a buck converter example that compares control-to-output frequency responses with current programmed control against duty-cycle control.

It is assumed that the reader is familiar with basics of Spice circuit simulations. All simulation models and examples in this appendix are prepared using the PSpice circuit simulator [19]. Netlists are included to help explain details of model implementation and simulation analysis options. Usually, instead of writing netlists, the user would enter circuit diagrams and analysis options from a front-end schematic capture tool. The examples and the library *switch.lib* of subcircuit models described in this appendix are available on-line. Similar models and examples can be constructed for use with other simulation tools.

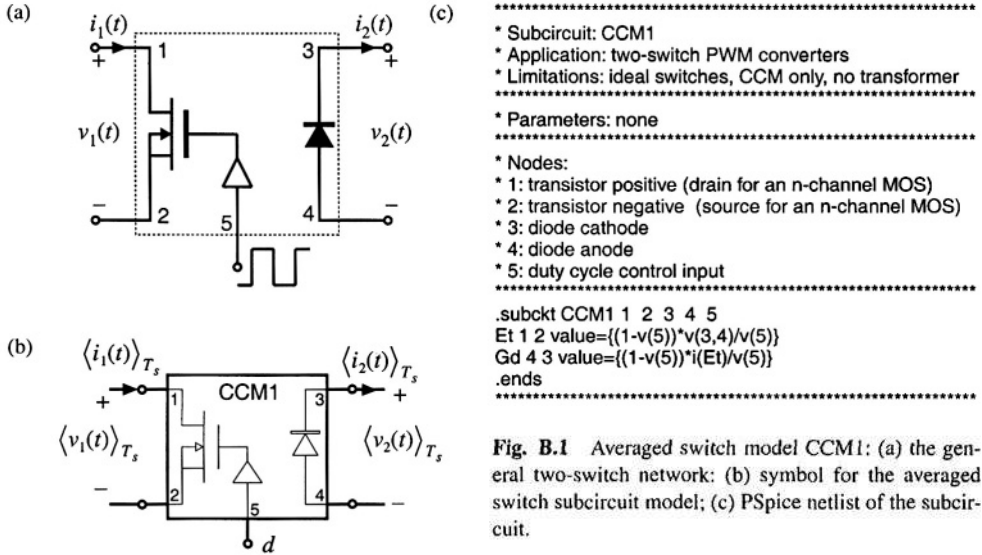


**Fig. B.1** Averaged switch model CCM1: (a) the general two-switch network; (b) symbol for the averaged switch subcircuit model; (c) PSpice netlist of the subcircuit.

## B.1 AVERAGED SWITCH MODELS FOR CONTINUOUS CONDUCTION MODE

The central idea of the *averaged switch modeling* described in Section 7.4 is to identify a switch network in the converter, and then to find an averaged circuit model. The resulting averaged switch model can then be inserted into the converter circuit to obtain a complete model of the converter. An important feature of the averaged switch modeling approach is that the same model can be used in many different converter configurations; it is not necessary to rederive an averaged equivalent circuit for each particular converter. This feature is also very convenient for construction of averaged circuit models for simulation. A general-purpose subcircuit represents a large-signal nonlinear averaged switch model. The converter averaged circuit for simulation is then obtained by replacing the switch network with this subcircuit. Based on the discussion in Section 7.4, subcircuits that represent CCM averaged switch models are described in this section, together with application examples.

### B.1.1 Basic CCM Averaged Switch Model

The large-signal averaged switch model for the general two-switch network of Fig. 7.39(a) is shown in Fig. 7.39(c). A PSpice subcircuit implementation of this model is shown in Fig. B.1. The subcircuit has five nodes. The transistor port of the averaged switch network is connected between the nodes 1 and 2, while the diode port is comprised of nodes 3 and 4. The duty ratio  $d = v(5)$  is the control input to the subcircuit at the node 5. The quantity  $v(5)$  is a voltage that is equal to the duty cycle, and that lies in the range zero to one volt. Figure B.1(c) shows the netlist of the subcircuit. The netlist consists of only four lines of code and several comment lines (the lines starting with \*). The .subckt line defines the name (CCM1) of the subcircuit and the interface nodes. The value of the controlled voltage source  $E_t$ , which

models the transistor port of the averaged switch network, is written according to Eq. (7.136):

$$\langle v_1(t) \rangle_{T_s} = \frac{d'(t)}{d(t)} \langle v_2(t) \rangle_{T_s} \quad (\text{B.1})$$

Note that  $v(3,4)$  in the subcircuit of Fig. B.1 is equal to the switch network independent input  $\langle v_2(t) \rangle_{T_s}$ . Also,  $d(t) = v(5)$ , and  $d'(t) = 1 - d(t) = 1 - v(5)$ . The value of the controlled current source  $G_d$ , which models the diode port, is computed according to Eq. (7.137):

$$\langle i_2(t) \rangle_{T_s} = \frac{d'(t)}{d(t)} \langle i_1(t) \rangle_{T_s} \quad (\text{B.2})$$

The switch network independent input  $\langle i_1(t) \rangle_{T_s}$  equals the current  $i(E_t)$  through the controlled voltage source  $E_t$ . The ends line completes the subcircuit netlist. The subcircuit CCM1 is included in the model library *switch.lib*.

An advantage of the subcircuit CCM1 of Fig. B.1 is that it can be used to construct an averaged circuit model for simulation of any two-switch PWM converter operating in continuous conduction mode, subject to the assumptions that the switches can be considered ideal, and that the converter does not include a step-up or step-down transformer. The subcircuit can be further refined to remove these limitations. In converters with an isolation transformer, the right-hand side of Eqs. (B.1) and (B.2) should be divided by the transformer turns ratio. Inclusion of switch conduction losses is discussed in the next section.

A disadvantage of the model in Fig. B.1 is that Eqs. (B.1) and (B.2) have a discontinuity at duty cycle equal to zero. In applications of the subcircuit, it is necessary to restrict the duty-cycle to the range  $0 < D_{\min} \leq d \leq 1$ .

Following the approach of this section, subcircuits can be constructed for the large-signal averaged models of the buck switch network (see Fig. 7.50(a), and Eqs. (7.150)), and the boost switch network (see Fig. 7.46(a) and Eqs. (7.146)). An advantage of these models is that their defining equations do not have the discontinuity problem at  $d = 0$ .

### B.1.2 CCM Averaged Switch Model that Includes Switch Conduction Losses

Let us modify the model of Fig. B.1 to include switch conduction losses. Figure B.2 shows simple device models that include transistor and diode conduction losses in the general two-switch network of Fig. B.1(a). The transistor is modeled as an ideal switch in series with an on-resistance  $R_{on}$ . The diode is modeled as an ideal diode in series with a forward voltage drop  $V_D$  and resistance  $R_D$ .

Construction of dc equivalent circuits to find dc conversion ratio and efficiency of converters is discussed in Chapter 3. Derivation of an averaged switch model that includes conduction losses arising from  $R_{on}$  and  $V_D$  is described in Section 7.4.5. Following the same averaged switch modeling approach, we can find the following relationships that describe the averaged switch model for the switch network of Fig. B.2:

$$\langle v_1(t) \rangle_{T_s} = \left( \frac{R_{on}}{d(t)} + \frac{d'(t)R_D}{d^2(t)} \right) \langle i_1(t) \rangle_{T_s} + \frac{d'(t)}{d(t)} \left( \langle v_2(t) \rangle_{T_s} + V_D \right) \quad (\text{B.3})$$

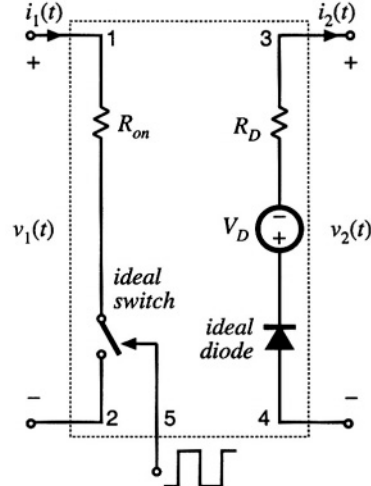


**Fig. B.2** Switch network model that includes conduction loss elements  $R_{on}$ ,  $V_D$  and  $R_D$ .

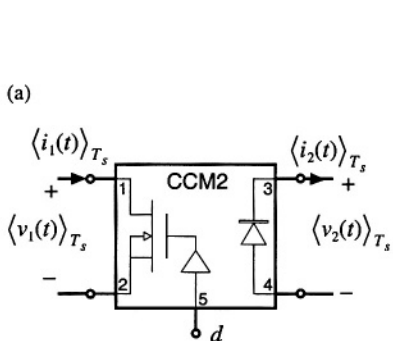


**Fig. B.3** Subcircuit implementation of the CCM averaged switch model that includes conduction losses: (a) circuit symbol; (b) PSpice netlist for the subcircuit.

(b)

```

***** MODEL: CCM2 *****
* Application: two-switch PWM converters, includes
*   conduction losses due to Ron, VD, RD
* Limitations: CCM only, no transformer
*****
* Parameters:
*   Ron = transistor on-resistance
*   VD = diode forward voltage drop
*   RD = diode on-resistance
*****
* Nodes:
*   1: transistor positive (drain for an n-channel MOS)
*   2: transistor negative (source for an n-channel MOS)
*   3: diode cathode
*   4: diode anode
*   5: duty cycle control input
*****
.subckt CCM2 1 2 3 4 5
+params: Ron=0 VD=0 RD=0
Er 1 1x value={i(Et)*(Ron+(1-v(5))*RD/v(5))/v(5)}
Et 1 2x value={(1-v(5))*(V(3,4)+VD)/v(5)}
Gd 4 3 value={(1-v(5))*i(Et)/v(5)}
.ends
*****
```

$$\langle i_2(t) \rangle_{T_s} = \frac{d'(t)}{d(t)} \langle i_1(t) \rangle_{T_s} \quad (\text{B.4})$$

A subcircuit implementation of the averaged switch model described by Eqs. (B.3) and (B.4) is shown in Fig. B.3. The subcircuit terminal nodes are the same as in the CCM1 subcircuit: the transistor port is between the nodes 1 and 2; the diode port is between the nodes 3 and 4; the duty ratio  $d = v(5)$  is the con-

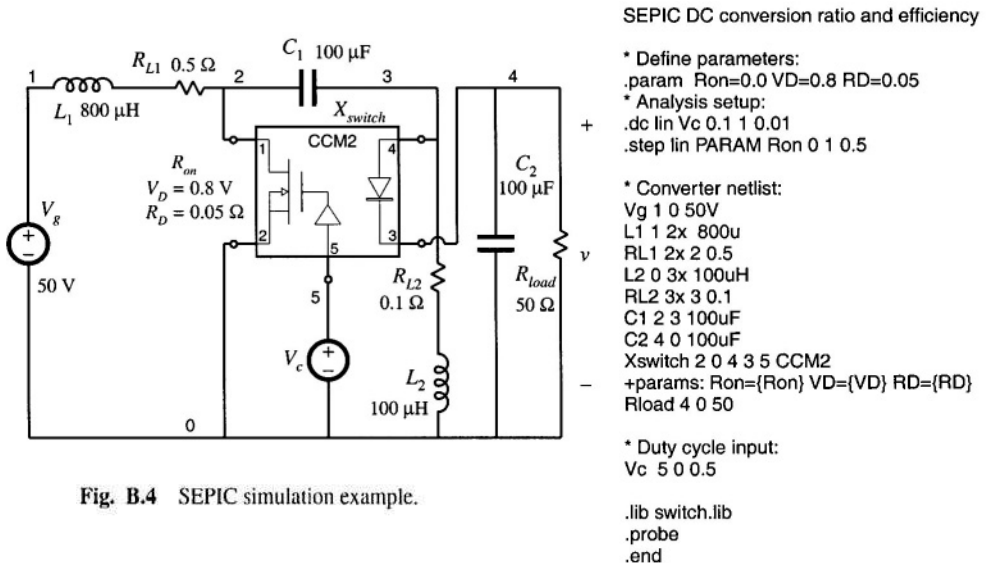


**Fig. B.4** SEPIC simulation example.

trol input to the subcircuit at the node 5. Two controlled voltage sources in series,  $E_r$  and  $E_{r'}$ , are used to generate the port 1 (transistor) averaged voltage according to Eq. (B.3). The controlled voltage source  $E_r$  models the voltage drop across the equivalent resistance  $R_{on}/d(t) + d'(t)R_D/d^2(t)$  in Eq. (B.3). Note that this equivalent resistance is a nonlinear function of the switch duty cycle  $d(t)$ . The controlled voltage source  $E_r$  shows how the port 1 (transistor) averaged voltage depends on the port 2 (diode) averaged voltage. The controlled current source  $G_d$  models the averaged diode current according to Eq. (B.4). The subcircuit CCM2 has three parameters ( $R_{on}$ ,  $V_D$ , and  $R_D$ ) that can be specified when the subcircuit is used in a converter circuit. The default values of the subcircuit parameters,  $R_{on} = 0$ ,  $V_D = 0$ , and  $R_D = 0$ , are defined in the .subckt line. These values correspond to the ideal case of no conduction losses. The subcircuit CCM2 is included in the model library *switch.lib*.

The model of Fig. B.3 is based on the simple device models of Fig. B.2. It is assumed that inductor current ripples are small and that the converter operates in continuous conduction mode. Many practical converters, however, must operate in discontinuous conduction mode at low duty cycles where the diode forward voltage drop is comparable to or larger than the output voltage. In such cases, the model of Fig. B.2, which includes  $V_D$  as a fixed voltage generator, gives incorrect, physically impossible results for polarities of converter voltages and currents, losses and efficiency.

### B.1.3 Example: SEPIC DC Conversion Ratio and Efficiency

Let us consider an example of how the subcircuit CCM2 can be used to generate dc conversion ratio and efficiency curves for a CCM converter. As an example, Figure B.4 shows a SEPIC averaged circuit model. The converter circuit can be found in Fig. 6.38(a), or in Fig. 7.37. To construct the averaged circuit model for simulation, the switch network is replaced by the subcircuit CCM2. In the converter netlist shown in Fig. B.4, the  $X_{switch}$  line shows how the subcircuit is connected to other parts of the converter. The switch duty cycle is set by the voltage source  $V_c$ . All other parts of the converter circuit are simply copied to the averaged circuit model. Inductor winding resistances  $R_{L1} = 0.5 \Omega$  and  $R_{L2} = 0.1 \Omega$  are

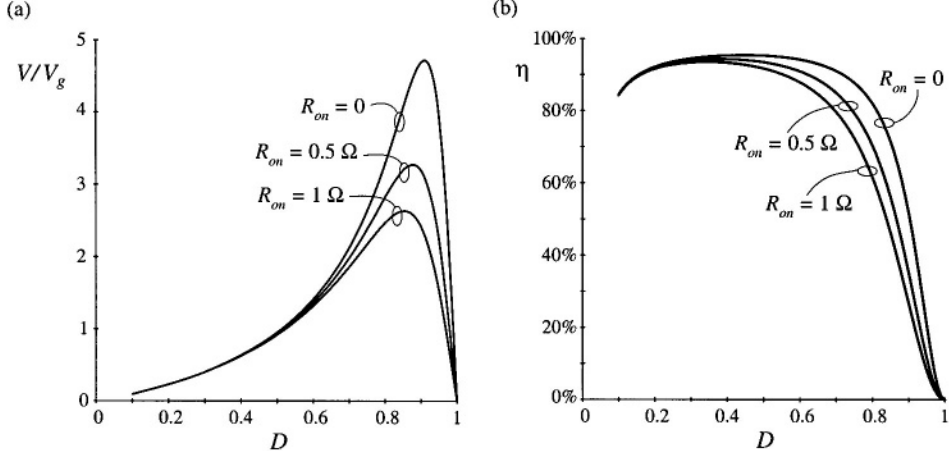


**Fig. B.5** SEPIC simulation example: (a) dc conversion ratio and (b) efficiency.

included to model copper losses of the inductors  $L_1$  and  $L_2$ , respectively. The switch conduction loss parameters are defined by the .param line in the netlist:  $R_{on} = 0$ ,  $V_D = 0.8$  V,  $R_D = 0.05$   $\Omega$ . Notice how these values are passed to the subcircuit CCM2 in the  $X_{switch}$  line. In this example, all other losses in the converter are neglected. A dc sweep analysis (see the .dc line in the netlist) is set to vary the dc voltage source  $V_c$  from 0.1 V to 1 V, in 0.01 V increments, which corresponds to varying the switch duty cycle over the range from  $D = 0.1$  to  $D = 1$ . The range of duty cycles from zero to 0.1 is not covered because of the model discontinuity problem at  $D = 0$  (discussed in Section B.1.1), and because the model predictions for conduction losses at low duty cycles are not valid, as discussed in Section B.1.2. The dc sweep analysis is repeated for values of the switch on-resistance in the range from  $R_{on} = 0 \Omega$  to  $R_{on} = 1 \Omega$  in  $0.5 \Omega$  increments (see the .step line in the netlist). The .lib line refers to the *switch.lib* library, which contains definitions of the subcircuit CCM2 and all other subcircuit models described in this appendix.

Simulation results for the dc output voltage  $V$  and the converter efficiency  $\eta$  are shown in Fig. B.5. Several observations can be made based on the modeling approach and discussions presented in Chapter 3. At low duty cycles, efficiency drops because the diode forward voltage drop is comparable to the output voltage. At higher duty cycles, the converter currents increase, so that the conduction losses increase. Eventually, for duty cycles approaching 1, both the output voltage and the efficiency approach zero. Given a desired dc output voltage and efficiency, the plots in Fig. B.5 can be used to select the transistor with an appropriate value of the on-resistance.

#### B.1.4 Example: Transient Response of a Buck–Boost Converter

In addition to steady-state conversion characteristics, it is often of interest to investigate converter transient responses. For example, in voltage regulator designs, it is necessary to verify whether the output voltage remains within specified limits when the load current takes a step change. As another example, during a start-up transient when the converter is powered up, converter components can be exposed to significantly higher stresses than in steady state. It is of interest to verify that component stresses are

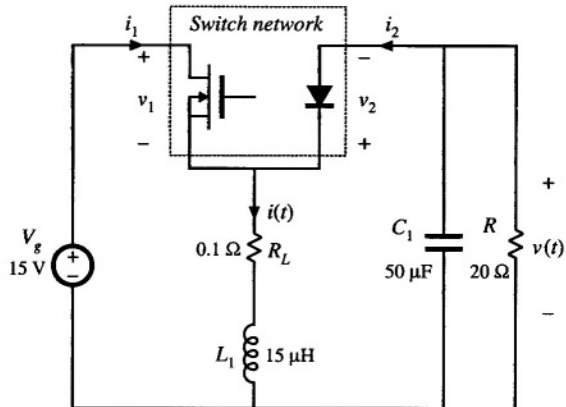


**Fig. B.6** Buck-boost converter example.

within specifications or to make design modifications to reduce the stresses. In these examples, transient simulations can be used to test for converter responses.

Transient simulations can be performed on the converter switching circuit model or on the converter averaged circuit model. As an example, let us apply these two approaches to investigate a start-up transient response of the buck-boost converter shown in Fig. B.6.

Figure B.7 shows a switching circuit model of the buck-boost converter. The inductor winding resistance  $R_L$  is included to model the inductor copper losses. The MOSFET is modeled as a voltage-controlled switch  $S_{q1}$  controlled by a pulsating voltage source  $v_c$ . The switch .model line specifies the switch on-resistance  $R_{on} = 50 \text{ m}\Omega$ , and the switch off-resistance  $R_{off} = 10 \text{ M}\Omega$ . The switch is on when the controlling voltage  $v_c$  is greater than  $V_{on} = 6 \text{ V}$ , and off when the controlling voltage  $v_c$  is less than  $V_{off} = 4 \text{ V}$ . The pulsating source  $v_c$  has the pulse amplitude equal to 10 V. The period is  $T_s = 1/f_s = 10 \mu\text{s}$ , the rise and fall times are  $t_r = t_f = 100 \text{ ns}$ , and the pulse width is  $t_p = 7.9 \mu\text{s}$ . The switch duty cycle is  $D = (t_p + 0.5(t_r + t_f))/T_s = 0.8$ . The built-in nonlinear Spice model is used for the diode. In the diode .model statement, only the parameter  $I_s$  is specified, to set the forward voltage drop across the diode. The switch and the diode models used in this example are very simple. Conduction losses are modeled in a simple manner, and details of complex device behavior during switching transitions are neglected.

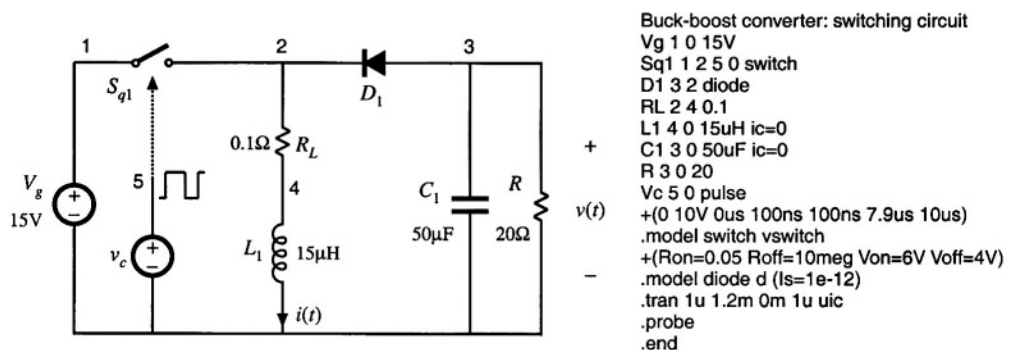


**Fig. B.7** Buck-boost converter simulation example, switching circuit model.

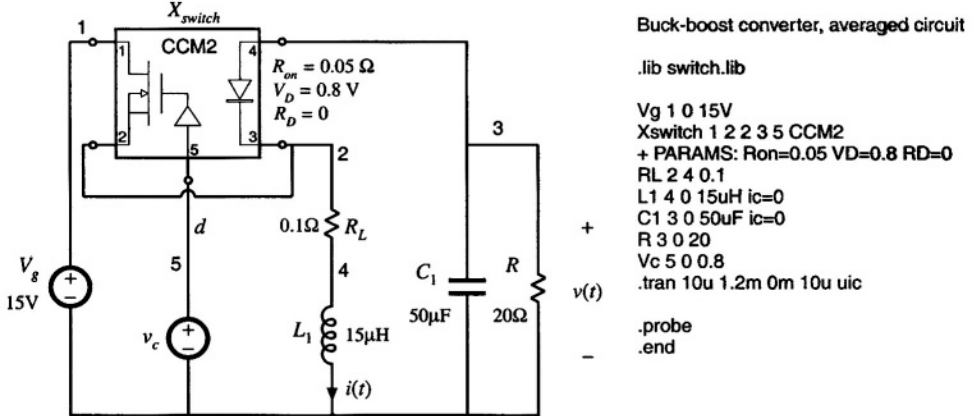


**Fig. B.8** Buck-boost converter simulation example, averaged circuit model.

Therefore, the circuit model of Fig. B.7 cannot be used to examine switching transitions or to predict switching losses in the converter. Nevertheless, basic switching operation is modeled, and a transient simulation can be used to find out how the converter waveforms evolve in time over many switching cycles. Transient simulation parameters are defined by the .tran line: the output time step is 1  $\mu s$ , the final simulation time is 1.2 ms, the output waveforms are generated from the start of simulation at time equal to zero, and the maximum allowed time step is 1  $\mu s$ . The uic (“use initial conditions”) option tells the simulator to start with all capacitor voltages and inductor currents equal to the specified initial values. For example,  $ic=0$  in the  $L_1$  line sets the initial inductor current to zero. In Spice, the default initial conditions are always zero, so that  $ic=0$  statements can be omitted.

An averaged circuit model of the buck-boost converter is shown in Fig. B.8. This circuit model is obtained by replacing the switch network in the converter of Fig. B.6 by the CCM2 subcircuit. Notice that the circuits and the netlists of Figs. B.7 and Fig. B.8 are very similar. The only difference is that the switching devices in the converter circuit of Fig. B.7 are replaced by the CCM2 subcircuit  $X_{switch}$  in Fig. B.8. Also, the pulsating source  $v_c(t)$  in the switching circuit is replaced by a constant voltage source  $v_c$  equal to the switch duty cycle  $D = 0.8$ .

The inductor current and the capacitor voltage waveforms during the start-up transient are shown in Fig. B.9. For comparison, the waveforms obtained by transient simulation of the switching converter circuit shown in Fig. B.7, and by simulation of the averaged circuit model of Fig. B.8 are shown. Switching ripples can be observed in the waveforms obtained by simulation of the switching circuit model. The converter transient response is governed by the converter natural time constants. Since these time constants are much longer than the switching period, the converter start-up transient responses in Fig. B.9 take many switching cycles to reach the steady state. In the results obtained by simulation of the averaged circuit model, the switching ripples are removed, but the low-frequency portions of the converter transient responses, which are governed by the natural time constants of the converter network, match very closely the responses obtained by simulation of the switching circuit.

Based on the results shown in Fig. B.9, we can see that converter components are exposed to significantly higher current stresses during the start-up transient than during steady state operation. The problem of excessive stresses in the start-up transient is quite typical for switching power converters. Practical designs usually include a “soft-start” circuit, where the switch duty cycle is slowly increased

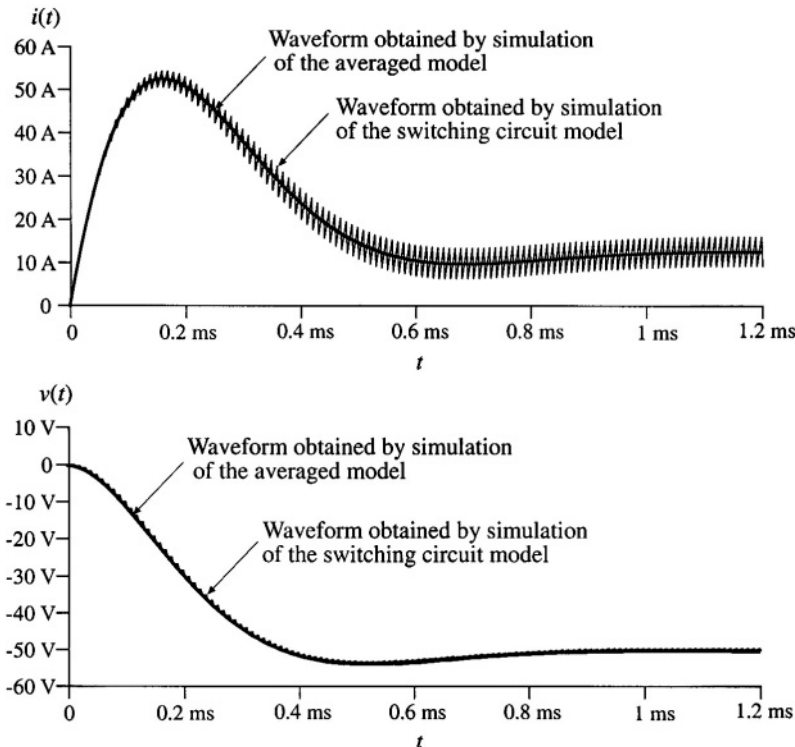


**Fig. B.9** Inductor current and output voltage waveforms obtained by transient simulation of the switching converter circuit shown in Fig. B.7, and by simulation of the averaged circuit model of Fig. B.8

from zero to the steady-state value to reduce start-up transient stresses.

This simulation example illustrates how an averaged circuit model can be used in place of a switching circuit model to investigate converter large-signal transient responses. An advantage of the averaged circuit model is that transient simulations can be completed much more quickly because the averaged model is time invariant, and the simulator does not spend time computing the details of the fast switching transitions. This advantage can be important in simulations of larger electronic systems that include switching power converters. Another important advantage also comes from the fact that the averaged circuit model is nonlinear but time-invariant: ac simulations can be used to linearize the model and generate small-signal frequency responses of interest. This is not possible with switching circuit models. Examples of small-signal ac simulations can be found in Sections B.2 and B.3.

## B.2 COMBINED CCM/DCM AVERAGED SWITCH MODEL

The models and examples of Section B.1 are all based on the assumption that the converters operate in continuous conduction mode (CCM). As discussed in Chapters 5 and 11, all converters containing a diode rectifier operate in discontinuous conduction mode (DCM) if the load current is sufficiently low. In some cases, converters are purposely designed to operate in DCM. It is therefore of interest to develop

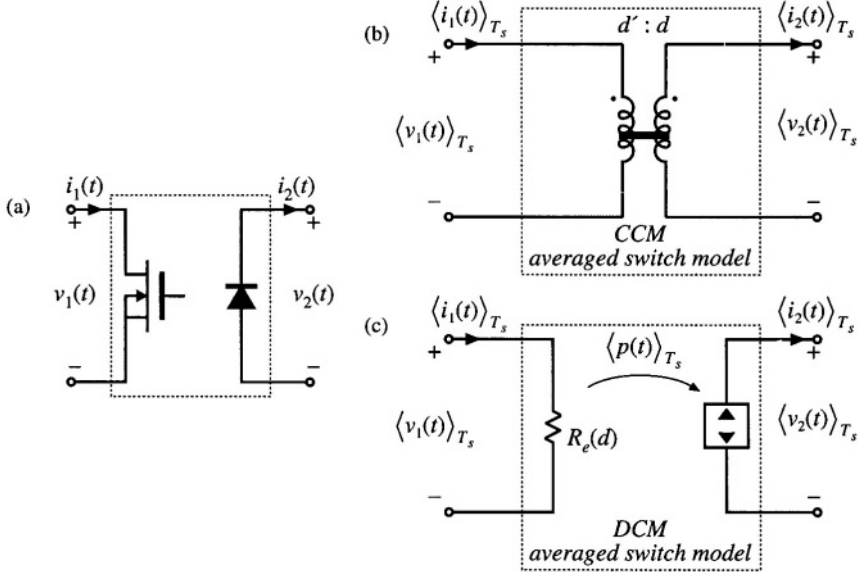


**Fig. B.10** Summary of averaged switch modeling: (a) general two-switch network, (b) averaged switch model in CCM, and (c) averaged switch model in DCM.

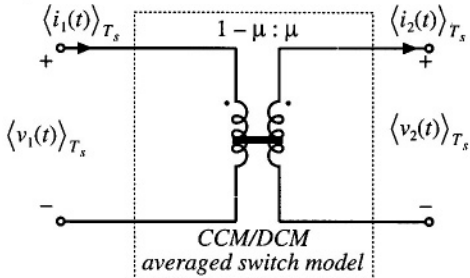


**Fig. B.11** A general averaged switch model using the equivalent switch conversion ratio  $\mu$ .

averaged models suitable for simulation of converters that may operate in either CCM or DCM.

Figure B.10 illustrates the general two-switch network, and the corresponding large-signal averaged models in CCM and DCM. The CCM averaged switch model, which is derived in Section 7.4, is an ideal transformer with  $d' : d$  turns ratio. In DCM, the large-signal averaged switch model is a loss-free resistor, as derived in Section 11.1. Our objective is to construct a combined CCM/DCM averaged switch model that reduces to the model of Fig. B.10(a) or to the model of Fig. B.10(c) depending on the operating mode of the converter. Let us define an effective switch conversion ratio  $\mu(t)$ , so that the averaged switch model in both modes has the same form as in CCM, as shown in Fig. B.11. If the converter operates in CCM, then the switch conversion ratio  $\mu(t)$  is equal to the switch duty cycle  $d(t)$ ,

$$\mu = d \quad (B.5)$$

If the converter operates in DCM, then the effective switch conversion ratio can be computed so that the terminal characteristics of the averaged-switch model of Fig. B.11 match the terminal characteristics of the loss-free resistor model of Fig. B.10(c). Matching the port 1 characteristics gives

$$\langle v_1(t) \rangle_{T_s} = \frac{1-\mu}{\mu} \langle v_2(t) \rangle_{T_s} = R_e \langle i_1(t) \rangle_{T_s} \quad (B.6)$$

which can be solved for the switch conversion ratio  $\mu$ ,

$$\mu = \frac{1}{1 + \frac{R_e \langle i_1(t) \rangle_{T_s}}{\langle v_2(t) \rangle_{T_s}}} \quad (B.7)$$

It can be verified that matching the port 2 characteristics of the models in Figs. B.10(c) and B.11 gives exactly the same result for the effective switch conversion ratio in DCM.

The switch conversion ratio  $\mu(t)$  can be considered a generalization of the duty cycle  $d(t)$  of CCM switch networks. Based on this approach, models and results developed for converters in CCM can be used not only for DCM but also for other operating modes or even for other converter configurations by simply replacing the switch duty cycle  $d(t)$  with the appropriate switch conversion ratio  $\mu(t)$  [21-24]. For example, if  $M(d)$  is the conversion ratio in CCM, then  $M(\mu)$ , with  $\mu$  given by Eq. (B.7), is the conversion ratio in DCM. The switch conversion ratio in DCM depends on the averaged terminal voltage and current, as well as the switch duty cycle  $d$  through the effective resistance  $R_e = 2L/d^2T_s$ . If the converter is completely unloaded, then the average transistor current  $\langle i_1(t) \rangle_{T_s}$  is zero, and the DCM switch conversion ratio becomes  $\mu = 1$ . As a result, the dc output voltage attains the maximum possible value  $V = V_g M(1)$ . This is consistent with the results of the steady-state DCM analyses in Chapter 5 and Section 11.1.

To construct a combined CCM/DCM averaged switch model based on the general averaged switch model of Fig. B.11, it is necessary to specify which of the two expressions for the switch conversion ratio to use: Eq. (B.5), which is valid in CCM, or Eq. (B.7), which is valid in DCM. At the CCM/DCM boundary, these two expressions must give the same result,  $\mu = d$ . If the load current decreases further, the converter operates in DCM, the average switch current  $\langle i_1(t) \rangle_{T_s}$  decreases, and the DCM switch conversion ratio in Eq. (B.7) becomes greater than the switch duty cycle  $d$ . We conclude that the correct value of the switch conversion ratio, which takes into account operation in CCM or DCM, is the larger of the two values computed using Eq. (B.5) and Eq. (B.7).

Figure B.12 shows an implementation of the combined CCM/DCM model as a PSpice subcircuit CCM-DCM1. This subcircuit has the same five interface nodes as the subcircuits CCM1 and CCM2 of Section B.1. The controlled sources  $E_t$  and  $G_d$  model the port 1 (transistor) and port 2 (diode) averaged characteristics, as shown in Fig. B.11. The switch conversion ratio  $\mu$  is equal to the voltage  $v(u)$  at the subcircuit node  $u$ . The controlled voltage source  $E_u$  computes the switch conversion ratio as the greater of the two values obtained from Eqs. (B.5) and (B.7). The controlled current source  $G_a$ , the zero-value voltage source  $V_a$ , and the resistor  $R_a$  form an auxiliary circuit to ensure that the solution found by the simulator has the transistor and the diode currents with correct polarities,  $\langle i_1(t) \rangle_{T_s} > 0$ ,  $\langle i_2(t) \rangle_{T_s} > 0$ . The subcircuit parameters are the inductance  $L$  relevant for CCM/DCM operation, and the switching frequency  $f_s$ . The default values in the subcircuit are arbitrarily set to  $L = 100 \mu\text{H}$  and  $f_s = 100 \text{ kHz}$ .

The PSpice subcircuit CCM-DCM1 of Fig. B.12 can be used for dc, ac, and transient simula-

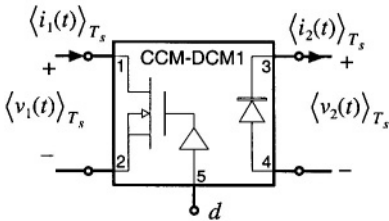


**Fig. B.12** Implementation of the combined CCM/DCM averaged switch model.

```
*****
* MODEL: CCM-DCM1
* Application: two-switch PWM converters, CCM or DCM
* Limitations: ideal switches, no transformer
*****
* Parameters:
*   L = equivalent inductance for DCM
*   fs = switching frequency
*****
* Nodes:
* 1: transistor positive (drain for an n-channel MOS)
* 2: transistor negative (source for an n-channel MOS)
* 3: diode cathode
* 4: diode anode
* 5: duty cycle control input
*****
.subckt CCM-DCM1 1 2 3 4 5
+ params: L=100u fs=1E5
Et 1 2 value={(1-v(u))*v(3,4)/v(u)}
Gd 4 3 value={(1-v(u))*i(Et)/v(u)}
Ga 0 a value=[MAX(i(Et),0)]
Va a b
Ra b 0 1k
Eu u 0 table {MAX(v(5),
+ v(5)*v(5)/(v(5)*v(5)+2*L*fs*i(Va)/v(3,4)))} (0 0) (1 1)
.ends
*****
```

tions of PWM converters containing a transistor switch and a diode switch. This subcircuit is included in the model library *switch.lib*. It can be modified further for use in converters with isolation transformer.

### B.2.1 Example: SEPIC Frequency Responses

As an example, Fig. B.13 shows a SEPIC circuit and the averaged circuit model obtained by replacing the switch network with the CCM-DCM1 subcircuit of Fig. B.12. A part of the circuit netlist is included in Fig. B.13. The connections and the parameters of the CCM-DCM1 subcircuit are defined by the *X<sub>switch</sub>* line. In the SEPIC, the inductance parameter  $L = 83.3 \mu\text{H}$  is equal to the parallel combination of  $L_1$  and  $L_2$ . The voltage source  $v_c$  sets the quiescent value of the duty cycle to  $D = 0.4$ , and the small-signal ac value to  $\hat{d} = 1$ . An ac simulation is performed on a linearized circuit model, so that amplitudes of all small-signal ac waveforms are directly proportional to the amplitude of the ac input, regardless of the input ac amplitude value. For example, the control-to-output transfer function is  $G_{vd} = \hat{v}/\hat{d}$ , where  $\hat{v} = v(4)$  in the circuit of Fig. B.13(b). We can set the input ac amplitude to 1, so that the control-to-output transfer function  $G_{vd}$  can be measured directly as  $v(5)$ . This setup is just for convenience in finding small-signal frequency responses by simulation. For measurements of converter transfer functions in an experimental circuit (see Section 8.5), the actual amplitude of the small-signal ac variation  $\hat{d}$  would be set to a fraction of the quiescent duty cycle  $D$ . Parameters of the ac simulation are set by the .ac line in the netlist: the signal frequency is swept from the minimum frequency of 5 Hz to the maximum frequency of 50 kHz in 201 points per decade.

Figure B.14 shows magnitude and phase responses of the control-to-output transfer function obtained by ac simulations for two different values of the load resistance:  $R = 40 \Omega$ , for which the converter operates in CCM, and  $R = 50 \Omega$ , for which the converter operates in DCM. For these two operating

points, the quiescent (dc) voltages and currents in the circuit are nearly the same. Nevertheless, the frequency responses are qualitatively very different in the two operating modes. In CCM, the converter exhibits a fourth-order response with two pairs of high- $Q$  complex-conjugate poles and a pair of complex-conjugate zeros. Another RHP (right-half plane) zero can be observed at frequencies approaching 50 kHz. In DCM, there is a dominant low-frequency pole followed by a pair of complex-conjugate poles and a pair of complex-conjugate zeros. The frequencies of the complex poles and zeros are very close in value. A high-frequency pole and a RHP zero contribute additional phase lag at higher frequencies.

In the design of a feedback controller around a converter that may operate in CCM or in DCM, one should take into account that the crossover frequency, the phase margin, and the closed-loop responses can be substantially different depending on the operating mode. This point is illustrated by the example of the next section.

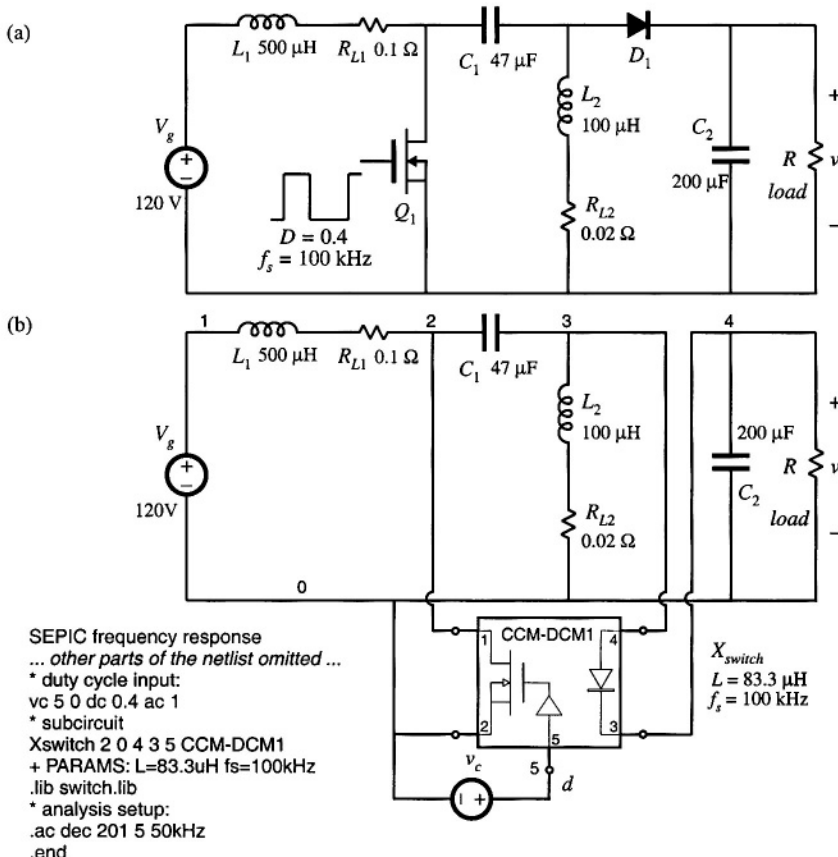
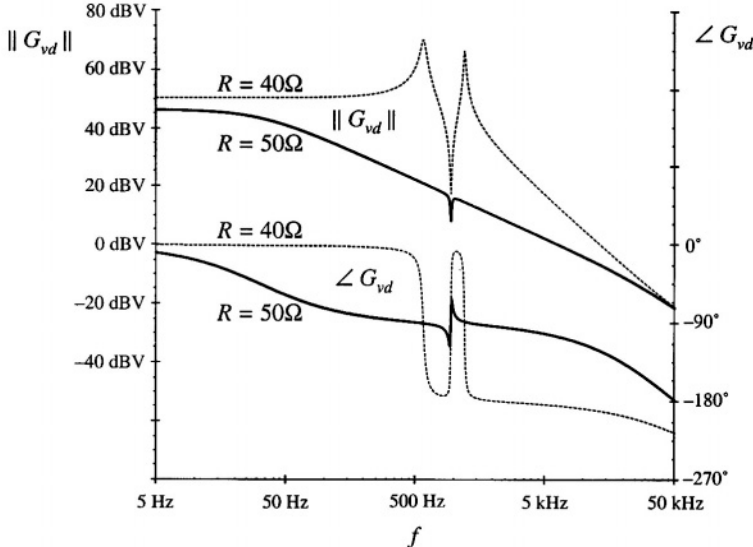


Fig. B.13 SEPIC simulation example: (a) converter circuit, (b) averaged circuit model for simulation.



**Fig. B.14** Magnitude and phase responses of the control-to-output transfer function obtained by simulation of the SEPIC example, for two values of the load resistance. For  $R = 50 \Omega$ , the converter operates in DCM (solid lines), and for  $R = 40 \Omega$ , the converter operates in CCM (dotted lines).

### B.2.2 Example: Loop Gain and Closed-Loop Responses of a Buck Voltage Regulator

A controller design for a buck converter example is discussed in Section 9.5.4. The converter and the block diagram of the controller are shown in Fig. 9.22. This converter system is designed to regulate the dc output voltage at  $V = 15$  V for the load current up to 5 A. Let us test this design by simulation. An averaged circuit model of a practical realization of the buck voltage regulator described in Section 9.5.4 is shown in Fig. B.15. The MOSFET and the diode switch are replaced by the averaged switch model implemented as the CCM-DCM1 subcircuit. The pulse-width modulator with  $V_M = 4$  V is modeled according to the discussion in Section 7.6 as a dependent voltage source  $E_{pwm}$  controlled by the PWM input voltage  $v_x$ . The value of  $E_{pwm}$  is equal to  $1/V_M = 0.25$  times the PWM input voltage  $v_x$ , with a limit for the minimum value set to 0.1 V, and a limit for the maximum value set to 0.9 V. The output of the pulse-width modulator is the control duty-cycle input to the CCM-DCM1 averaged switch subcircuit. Given the specified limits for  $E_{pwm}$ , the switch duty cycle  $d(t)$  can take values in the range:

$$D_{\min} \leq d(t) \leq D_{\max} \quad (\text{B.8})$$

where  $D_{\min} = 0.1$ , and  $D_{\max} = 0.9$ . Practical PWM integrated circuits often have a limit  $D_{\max} < 1$  for the maximum possible duty cycle. The voltage sensor and the compensator are implemented around an op-amp LM324. With very large loop gain in the system, the steady-state error voltage is approximately zero, i.e., the dc voltages at the plus and the minus inputs of the op-amp are almost the same,

$$v(5) = v_{ref} \quad (B.9)$$

As a result, the quiescent (dc) output voltage  $V$  is set by the reference voltage  $v_{ref}$  and the voltage divider comprised of  $R_1$ ,  $R_2$ ,  $R_4$ :

$$V \frac{R_4}{R_1 + R_2 + R_4} = v_{ref} = 5 \text{ V} \quad (B.10)$$

By setting the ac reference voltage  $\hat{v}_{ref}$  to zero, the combined transfer function of the voltage sensor and the compensator can be found as:

$$H(s)G_c(s) = \frac{\hat{v}_y}{\hat{v}} = \frac{R_3 + \frac{1}{sC_3}}{R_1 + R_2 \parallel \frac{1}{sC_2}} \quad (B.11)$$

This transfer function can be written in factored pole-zero form as

$$G_{cm}H \frac{\left(1 + \frac{s}{\omega_i}\right)\left(1 + \frac{\omega_L}{s}\right)}{\left(1 + \frac{s}{\omega_p}\right)} \quad (B.12)$$

where

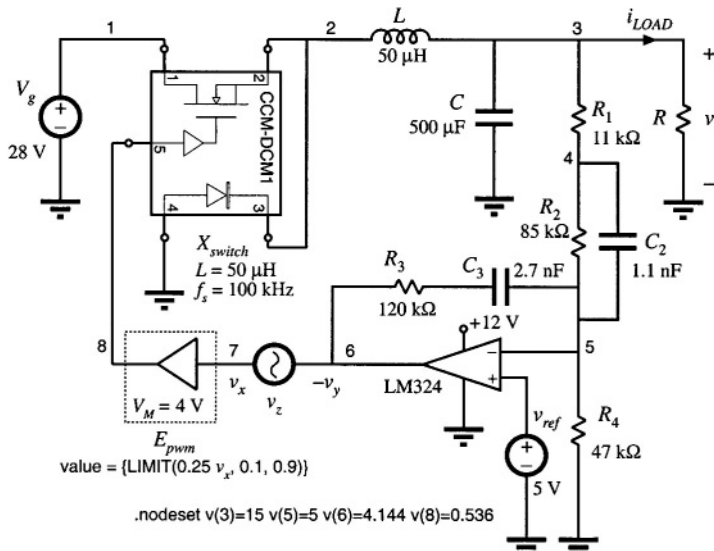


Fig. B.15 Buck voltage regulator example.

$$G_{cm}H = \frac{R_3}{R_1 + R_2} \quad (B.13)$$

$$f_z = \frac{\omega_z}{2\pi} = \frac{1}{2\pi R_2 C_2} \quad (B.14)$$

$$f_L = \frac{\omega_L}{2\pi} = \frac{1}{2\pi R_3 C_3} \quad (B.15)$$

and

$$f_p = \frac{\omega_p}{2\pi} = \frac{1}{2\pi(R_1 \parallel R_2)C_2} \quad (B.16)$$

The design described in Section 9.5.4 resulted in the following values for the gain and the corner frequencies:

$$G_{cm}H = 3.7(1/3) = 1.23, f_z = 1.7 \text{ kHz}, f_L = 500 \text{ Hz}, f_p = 14.5 \text{ kHz} \quad (B.17)$$

Eqs. (B.10) and (B.13) to (B.17) can be used to select the circuit parameter values. Let us (somewhat arbitrarily) choose  $C_2 = 1.1 \text{ nF}$ . Then, from Eq. (B.14), we have  $R_2 = 85 \text{ k}\Omega$ , and Eq. (B.16) yields  $R_1 = 11 \text{ k}\Omega$ . From Eq. (B.13) we obtain  $R_3 = 120 \text{ k}\Omega$ , and Eq. (B.15) gives  $C_3 = 2.7 \text{ }\mu\text{F}$ . Finally,  $R_4 = 47 \text{ k}\Omega$  is found from Eq. (B.10). The voltage regulator design can now be tested by simulations of the circuit in Fig. B.15.

Loop gains can be obtained by simulation using exactly the same techniques described in Section 9.6 for experimental measurement of loop gains [20]. Let us apply the voltage injection technique of Section 9.6.1. An ac voltage source  $v_z$  is injected between the compensator output and the PWM input. This is a good injection point since the output impedance of the compensator built around the op-amp is small, and the PWM input impedance is very large (infinity in the circuit model of Fig. B.15). With the ac source amplitude set (arbitrarily) to 1, and no other ac sources in the circuit, ac simulations are performed to find the loop gain as

$$T(s) = \frac{\hat{v}_y}{\hat{v}_x} = -\frac{v(6)}{v(7)} \quad (B.18)$$

To perform ac analysis, the simulator first solves for the quiescent (dc) operating point. The circuit is then linearized at this operating point, and small-signal frequency responses are computed for the specified range of signal frequencies. Solving for the quiescent operating point involves numerical solution of a system of nonlinear equations. In some cases, the numerical solution does not converge and the simulation is aborted with an error message. In particular, convergence problems often occur in circuits with feedback, especially when the loop gain at dc is very large. This is the case in the circuit of Fig. B.15. To help convergence when the simulator is solving for the quiescent operating point, one can specify approximate or expected values of node voltages using the .nodeset line as shown in Fig. B.15. In this case, we know by design that the quiescent output voltage is close to 15 V ( $v(3) = 15$ ), that the negative input of the op-amp is very close to the reference ( $v(5) = 5$ ), and that the quiescent duty cycle is approximately  $D = V/V_g = 0.536$ , so that  $v(8) = 0.536 \text{ V}$ . Given these approximate node voltages, the numerical solution converges, and the following quiescent operating points are found by the simulator for two values of the load resistance  $R$ :

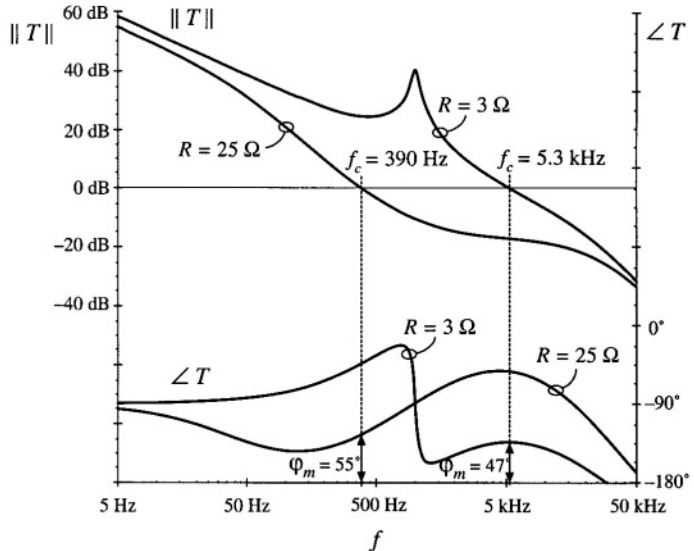


**Fig. B.16** Loop gain in the buck voltage regulator example.

$$R = 3 \Omega, v(3) = 15.2 \text{ V}, v(5) = 5.0 \text{ V}, v(7) = 2.173 \text{ V}, v(8) = 0.543 \text{ V}, D = 0.543 \quad (\text{B.19})$$

$$R = 25 \Omega, v(3) = 15.2 \text{ V}, v(5) = 5.0 \text{ V}, v(7) = 2.033 \text{ V}, v(8) = 0.508 \text{ V}, D = 0.508 \quad (\text{B.20})$$

For the nominal load resistance  $R = 3 \Omega$ , the converter operates in CCM, so that  $D = V/V_g$ . For  $R = 25 \Omega$ , the same dc output voltage is obtained for a lower value of the quiescent duty cycle, which means that the converter operates in DCM.

The magnitude and phase responses of the loop gain found for the operating points given by Eqs. (B.19) and (B.20) are shown in Fig. B.16. For  $R = 3 \Omega$ , the crossover frequency is  $f_c = 5.3 \text{ kHz}$ , and the phase margin is  $\phi_M = 47^\circ$ , very close to the values ( $f_c = 5 \text{ kHz}$ ,  $\phi_M = 52^\circ$ ) that we designed for in Section 9.5.4. At light load, for  $R = 25 \Omega$ , the loop gain responses are considerably different because the converter operates in DCM. The crossover frequency drops to  $f_c = 390 \text{ Hz}$ , while the phase margin is  $\phi_M = 55^\circ$ .

The magnitude responses of the line-to-output transfer function are shown in Fig. B.17, again for two values of the load resistance,  $R = 3 \Omega$  and  $R = 25 \Omega$ . The open-loop responses are obtained by braking the feedback loop at node 8, and setting the dc voltage at this node to the quiescent value  $D$  of the duty cycle. For  $R = 3 \Omega$ , the open-loop and closed-loop responses can be compared to the theoretical plots shown in Fig. 9.32. At 100 Hz, the closed-loop magnitude response is  $0.012 \Rightarrow -38 \text{ dB}$ . A 1 V, 100 Hz variation in  $v_g(t)$  would induce a 12 mV variation in the output voltage  $v(t)$ . For  $R = 25 \Omega$ , the closed loop magnitude response is  $0.02 \Rightarrow -34 \text{ dB}$ , which means that the 1 V, 100 Hz variation in  $v_g(t)$  would induce a 20 mV variation in the output voltage. Notice how the regulator performance in terms of rejecting the input voltage disturbance is significantly worse at light load than at the nominal load.

A test of the transient response to a step change in load is shown in Fig. B.18. The load current is initially equal to 1.5 A, and increases to  $i_{LOAD} = 5 \text{ A}$  at  $t = 0.1 \text{ ms}$ . When the converter is operated in

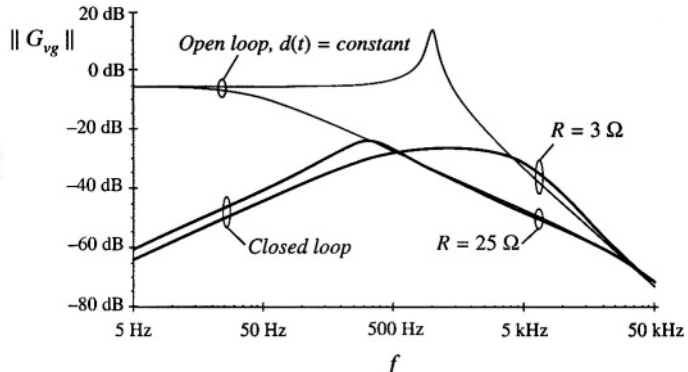


**Fig. B.17** Line to output response of the buck voltage regulator.

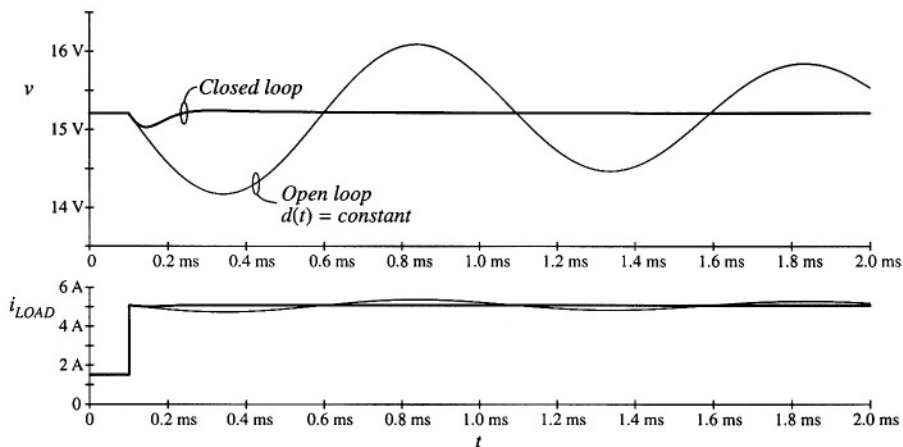


**Fig. B.18** Load transient response of the buck voltage regulator example.

open loop at constant duty cycle, the response is governed by the natural time constants of the converter network. A large undershoot and long lightly-damped oscillations can be observed in the output voltage. With the feedback loop closed, the controller dynamically adjusts the duty cycle  $d(t)$  trying to maintain the output voltage constant. The output voltage drops by about 0.2 V, and it returns to the regulated value after a short, well-damped transient.

The voltage regulator example of Fig. B.15 illustrates how the performance can vary significantly if the regulator is expected to supply a wide range of loads. In practice, further tests would also be performed to account for expected ranges of input voltages, and variations in component parameter values. Design iterations may be necessary to ensure that performance specifications are met under worst case conditions.

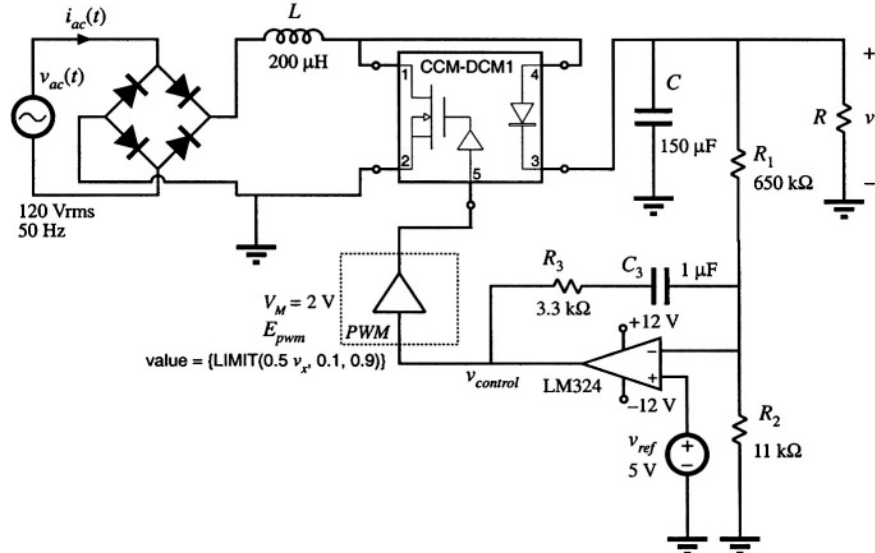


Fig. B.19 DCM boost rectifier example.

### B.2.3 Example: DCM Boost Rectifier

Converters switching at frequencies much above the ac line frequency can be used to construct near-ideal rectifiers where power is taken from the ac line without generation of line current harmonics. Approaches to construction of low-harmonic rectifiers are discussed in Chapter 18. One simple solution is based on the boost converter operating in discontinuous conduction mode, as described in Section 18.2.1. When a boost DCM converter operates at a constant switch duty cycle, the input current approximately follows the input voltage. The DCM effective resistance  $2L/d^2(t)T_s$  is an approximation of the emulated resistance  $R_e$  of the DCM boost rectifier. Ac line current harmonics are not zero, but the rectifier can still be designed to meet harmonic limits. In this section we consider a DCM boost rectifier example and test its performance by simulation.

An averaged circuit model of the boost DCM rectifier is shown in Fig. B.19. Full-wave rectified 120 Vrms, 50 Hz ac line voltage is applied to the input of the boost converter. The converter switches are replaced by the CCM-DCM1 averaged switch subcircuit. It is desired to regulate the dc output voltage at  $V = 300$  V at output power up to  $P_{out} = 120$  W across the load  $R$ . The switching frequency is  $f_s = 100$  kHz. Let us select the inductance  $L$  so that the converter always operates in DCM. From Eq. (18.24), the condition for DCM is:

$$L < \frac{\left(1 - \frac{V_M}{V}\right)R_e}{2f_s} \quad (\text{B.21})$$

where  $R_e$  is the emulated resistance of the rectifier and  $V_M$  is the peak of the ac line voltage. When line

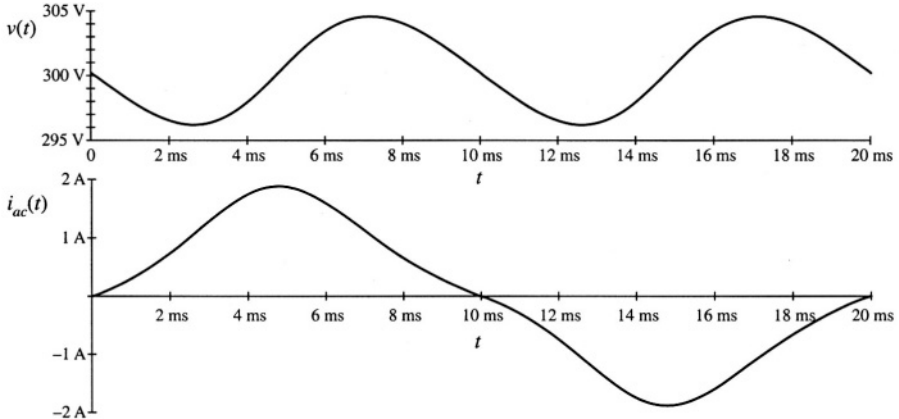


**Fig. B.20** Output voltage and ac line current in the DCM boost rectifier example.

current harmonics and losses are neglected, the rectifier emulated resistance  $R_e$  at the specified load power  $P$  is

$$R_e = \frac{V_M^2}{2P} \quad (\text{B.22})$$

Given  $V_M = 170$  V and  $R_e$  found from Eq. (B.22), Eq. (B.21) gives  $L < 260$   $\mu\text{H}$ . The selected inductance is  $L = 200$   $\mu\text{H}$ . A low-bandwidth voltage feedback loop is closed around the converter to regulate the dc output voltage. The output voltage is sensed and compared to the reference  $v_{ref}$ . A PI compensator is constructed around the LM324 op-amp. The output  $v_{control}$  of the compensator is the input to the pulse-width modulator. By adjusting the switch duty ratio  $d$ ,  $v_{control}$  adjusts the emulated resistance  $R_e = 2L/d^2T_s$  of the rectifier, and thereby controls the power taken from the ac line. In steady state, the input power matches the output power. The dc output voltage  $V$  is regulated at the value set by the reference voltage  $v_{ref}$  and the voltage divider composed of  $R_1$  and  $R_2$ , as follows:

$$V = v_{ref} \frac{R_1 + R_2}{R_1} = 300 \text{ V} \quad (\text{B.23})$$

Modeling of the low-bandwidth voltage regulation loop is discussed in Section 18.4.2.

It is of interest to find ac line current harmonics. First, a long transient simulation is performed to reach steady-state operation. Then, current harmonics are computed using Fourier analysis applied to the ac line current waveform  $i_{ac}(t)$  during one line cycle in steady state. Figure B.20 shows the steady-state ac line current and output voltage obtained for  $R = 900 \Omega$ , i.e., for 100 W of output power. The output voltage has a dc component equal to 300 V, and an ac ripple component at twice the line frequency. The peak-to-peak voltage ripple at twice the line frequency is approximately 8 V, which compares well with the value (7 V) found from Eq. (18.91). The ac line current has noticeable distortion. The spectrum of the ac line current is shown in Fig. B.21. The largest harmonic, the third, has an amplitude of 16.6% of the fundamental, and the total harmonic distortion is 16.7%.

We can also examine what happens if the rectifier is overloaded. The steady-state ac line current waveform for the case when the load resistance is  $R = 500 \Omega$ , and the output power is 180 W, is shown in

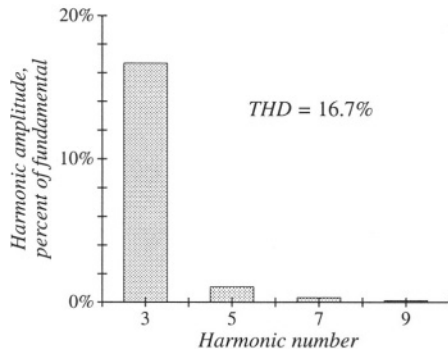


**Fig. B.21** Spectrum of the ac line current in the DCM boost rectifier.

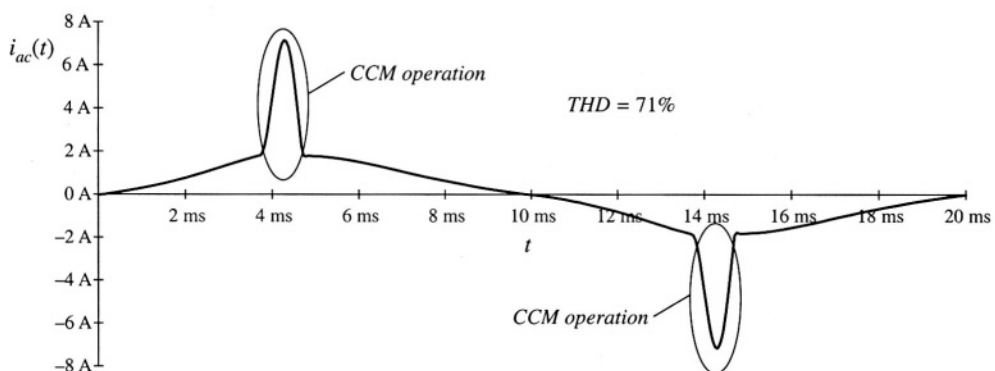


**Fig. B.22** Ac line current of the DCM boost rectifier example, when the output is overloaded.

Fig. B.22. The boost converter operates in CCM near the peak of the ac line voltage; this results in current spikes and significant harmonic distortion.

### B.3 CURRENT PROGRAMMED CONTROL

In the current programmed mode (CPM), which is studied in Chapter 12, the transistor switching is controlled so that the peak transistor current follows a control signal. The transistor duty cycle  $d(t)$  is not directly controlled, but depends on the CPM control input as well as on other converter voltages and currents. In this section, large-signal averaged relationships in CPM are written in a form suitable for implementation as a subcircuit for simulation.

#### B.3.1 Current Programmed Mode Model for Simulation

Typical inductor current and voltage waveforms of CPM converters operating in continuous conduction mode or in discontinuous conduction mode are shown in Fig. B.23. Signal  $i_c(t)$  is the CPM control input. An artificial ramp having slope  $-m_a$  is added to the control input. In the first subinterval,

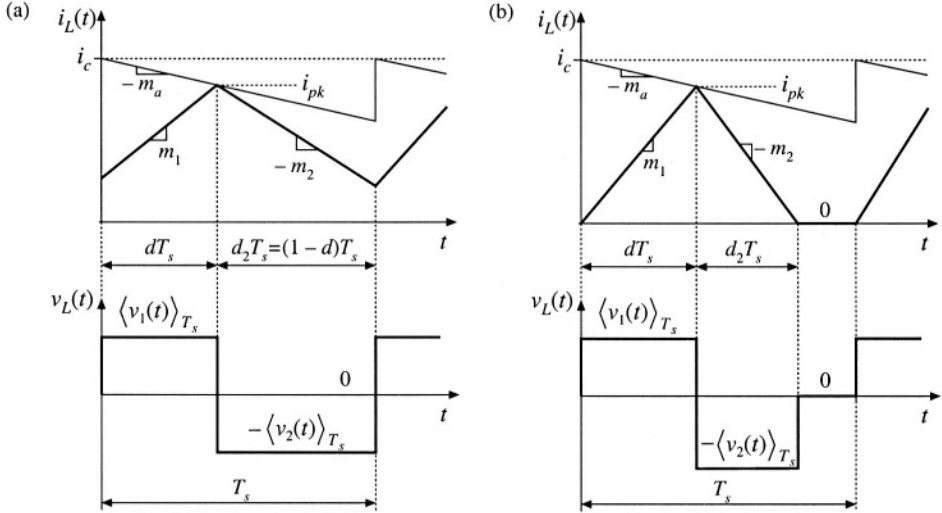


**Fig. B.23** Current programmed mode waveforms: (a) continuous conduction mode; (b) discontinuous conduction mode.

when the transistor is on, the inductor current increases with slope  $m_1$  given by:

$$m_1 = \frac{\langle v_1(t) \rangle_{T_s}}{L} \quad (\text{B.24})$$

It is assumed that voltage ripples are small so that the voltage  $v_1(t)$  across the inductor is approximately equal to the averaged value  $\langle v_1(t) \rangle_{T_s}$ . The length of the first subinterval is  $d(t)T_s$ . The transistor is turned off when the inductor current reaches the peak value  $i_{pk}$  equal to:

$$i_{pk} = i_c - m_a d T_s \quad (\text{B.25})$$

In the second subinterval, when the transistor is off and the diode is on, the inductor current decreases with a negative slope  $-m_2$ . With the assumption the voltage ripples are small, the slope  $m_2$  is given by:

$$m_2 = \frac{\langle v_2(t) \rangle_{T_s}}{L} \quad (\text{B.26})$$

The length of the second subinterval is  $d_2(t)T_s$ . In CCM, the second subinterval lasts until the end of the switching cycle. Therefore:

$$d_2 = 1 - d \quad (\text{B.27})$$

In DCM, the current drops to zero before the end of the switching period. The length of the second subinterval can be computed from:

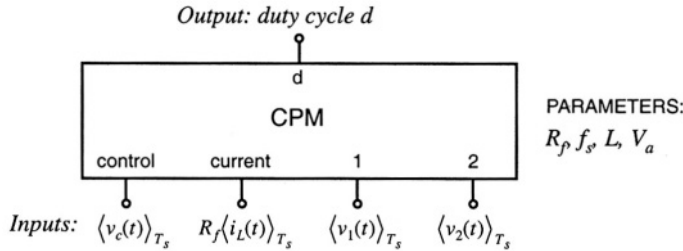


**Fig. B.24** Current programmed mode (CPM) subcircuit.

$$d_2 = \frac{i_{pk}}{m_2 T_s} \quad (B.28)$$

If the converter operates in DCM,  $d_2$  computed from Eq. (B.28) is smaller than  $1 - d$ . If the converter operates in CCM,  $1 - d$  is smaller than  $d_2$  computed from Eq. (B.28). In general, the length of the second subinterval can be found as the smaller of the two values computed using Eqs. (B.27) and (B.28).

The average inductor current can be found by computing the area under the inductor current waveform in Fig. B.23:

$$\langle i_L(t) \rangle_{T_s} = d \left( i_{pk} - \frac{m_1 d T_s}{2} \right) + d_2 \left( i_{pk} - \frac{m_2 d_2 T_s}{2} \right) \quad (B.29)$$

The relationship given by Eq. (B.29) is valid for both CCM and DCM provided that the second subinterval length is computed as the smaller of the values obtained from Eqs. (B.27) and (B.28).

Based on Eqs. (B.24) to (B.29), an averaged CPM subcircuit model is constructed in the form shown in Fig. B.24. The inputs to the CPM subcircuit are the control input  $\langle v_c(t) \rangle_{T_s} = R_f \langle i_c(t) \rangle_{T_s}$ , the measured inductor current  $R_f \langle i_L(t) \rangle_{T_s}$ , and the inductor voltages  $\langle v_1(t) \rangle_{T_s}$  and  $\langle v_2(t) \rangle_{T_s}$  of the two subintervals. The output of the subcircuit is the switch duty cycle  $d$ . The parameters of the CPM subcircuit are the equivalent current-sense resistance  $R_f$ , the inductance  $L$ , the switching frequency  $f_s = 1/T_s$ , and the amplitude  $V_a$  of the artificial ramp:

$$V_a = m_a T_s R_f \quad (B.30)$$

In the subcircuit implementation, the length of the second subinterval is computed as the smaller of the values given by Eqs. (B.27) and (B.28):

$$d_2 = \text{MIN} \left( 1 - d, \frac{i_{pk}}{m_2 T_s} \right) \quad (B.31)$$

Next, the switch duty cycle is found by solving Eq. (B.29). There are many different ways the switch duty cycle can be expressed in terms of other quantities. Although mathematically equivalent to Eq. (B.29), these different forms of solving for  $d$  result in different convergence performance of the numerical solver in the simulator. In the CPM subcircuit available in the *switch.lib* library, the duty cycle is found from:

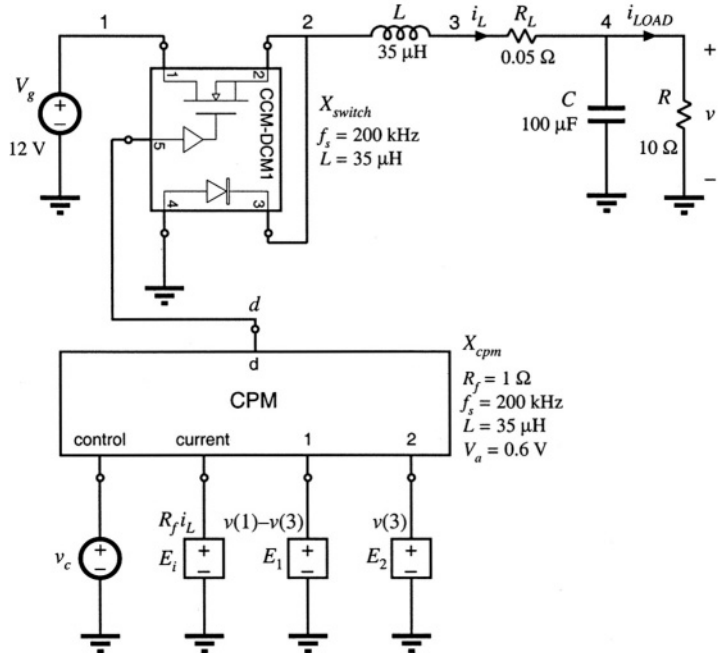


**Fig. B.25** CPM buck converter example.

$$d = \frac{2i_c(d + d_2) - 2\langle i_L(t) \rangle_{T_s} - m_2 d_2^2 T_s}{2m_a(d + d_2)T_s + m_1 d T_s} \quad (\text{B.32})$$

which is obtained by inserting Eq. (B.25) into Eq. (B.29). This implicit expression (notice that  $d$  is on both sides of the equation) is used by the numerical solver in the simulator to compute the switch duty cycle  $d$ .

### B.3.2 Example: Frequency Responses of a Buck Converter with Current Programmed Control

To illustrate an application of the CPM subcircuit, let us consider the example buck converter circuit model of Fig. B.25. To construct this averaged circuit model, the switches are replaced by the CCM-DCM1 averaged switch subcircuit. The control input to the CPM subcircuit is the independent voltage source  $v_c$ . Three dependent voltage sources are used to generate other inputs to the CPM subcircuit. The controlled voltage source  $E_i$  is proportional to the inductor current  $i_L$ . The controlled voltage source  $E_1$  is equal to  $v(1) - v(3)$ , which is equal to the voltage  $\langle v_1(t) \rangle_{T_s}$  applied across the inductor during the first subinterval when the transistor is on and the diode is off. The controlled voltage source  $E_2$  is equal to  $v(3)$ , which is equal to the voltage  $\langle v_2(t) \rangle_{T_s}$  applied across the inductor during the second subinterval when the transistor is off and the diode is on.

Ac simulations are performed at the quiescent operating point obtained for the dc value of the

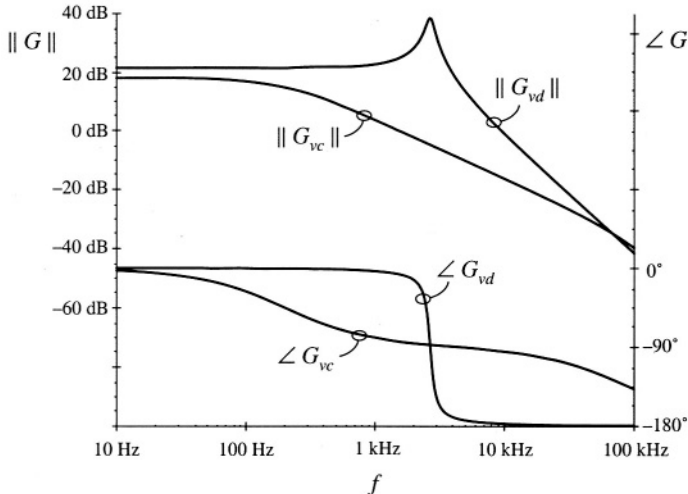


**Fig. B.26** Comparison of CPM control with duty-cycle control, for the control-to-output frequency response of the buck converter example.

control input equal to  $V_c = 1.4$  V. At the quiescent operating point, the switch duty cycle is  $D = 0.676$ , the dc output voltage is  $V = 8.1$  V, and the dc component of the inductor current is  $I_L = 0.81$  A. The converter operates in CCM.

Magnitude and phase responses of the control-to-output transfer functions  $G_{vc}(s) = \hat{v}/\hat{v}_c$  and  $G_{vd}(s) = \hat{v}/d$  are shown in Fig. B.26. The duty-cycle to output voltage transfer function  $G_{vd}(s)$  exhibits the familiar second-order high-Q response. Peaking in the magnitude response and a steep change in phase from  $0^\circ$  to  $-180^\circ$  occur around the center frequency of the pair of complex-conjugate poles. In contrast, the CPM control-to-output response has a dominant low-frequency pole. The phase lag is around  $-90^\circ$  in a wide range of frequencies. A high frequency pole contributes to additional phase lag at higher frequencies. The frequency responses of Fig. B.26 illustrate an advantage of CPM control over duty-cycle control. Because of the control-to-output frequency response dominated by the single low-frequency pole, it can be much easier to close a wide-bandwidth outer voltage feedback loop around the CPM controlled power converter than around a converter where the duty cycle is the control input.

Another advantage of CPM control is in rejection of input voltage disturbances. Line-to-output frequency responses for duty-cycle control and CPM control in the buck example are compared in Fig. B.27. At practically all frequencies of interest, CPM control offers more than 30 dB better attenuation of input voltage disturbances.

It is also interesting to compare the output impedance of the converter with duty-cycle control versus CPM control. The results are shown in Fig. B.28. At low frequencies, duty-cycle controlled converter has very low output impedance determined by switch and inductor resistances. As the frequency goes up, the output impedance increases as the impedance of the inductor increases. At the resonant frequency of the output LC filter, significant peaking in the output impedance of the duty-cycle controlled converter can be observed. At higher frequencies, the output impedance is dominated by the impedance of the filter capacitor, which decreases with frequency. In the CPM controlled converter, the low-frequency impedance is high. It is equal to the parallel combination of the load resistance and the CPM out-

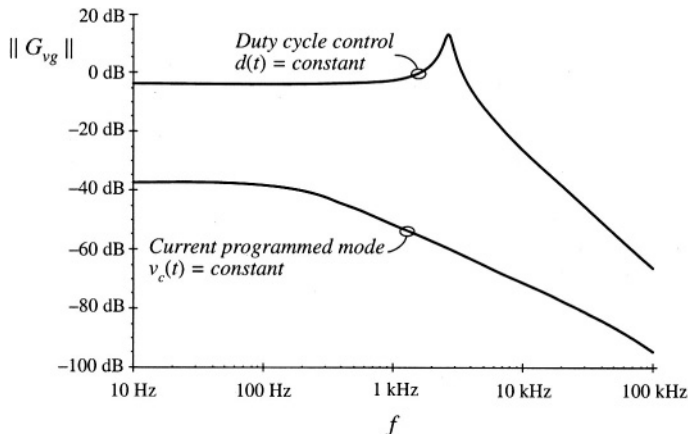


**Fig. B.27** Comparison of CPM control with duty-cycle control, for the line-to-output frequency response of the buck converter example.

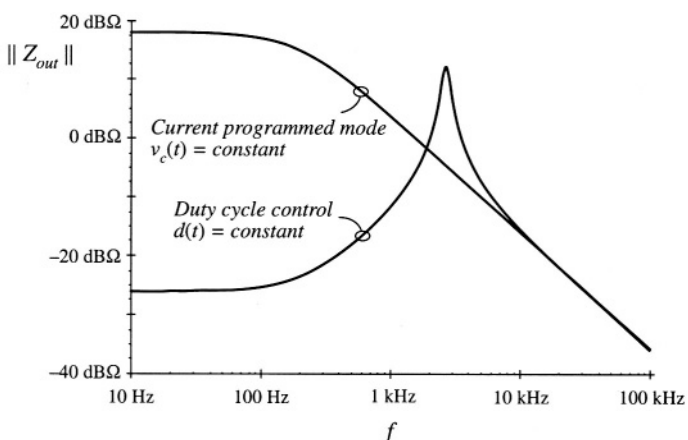


**Fig. B.28** Comparison of CPM control with duty-cycle control, for the output impedance of the buck converter example.

put resistance. Because of the lossless damping introduced by CPM control, the series inductor does not affect the output impedance. As the frequency goes up, the output impedance becomes dominated by the output filter capacitor and it decreases with frequency. At high frequencies the output impedances of the duty-cycle and CPM controlled converters have the same asymptotes.

**REFERENCES**

- [1] R. J. DIRKMAN, "The Simulation of General Circuits Containing Ideal Switches," *IEEE Power Electronics Specialists Conference*, 1987 Record, pp. 185-194.
- [2] C. J. HSIAO, R. B. RIDLEY, H. NAITOH and F. C. LEE, "Circuit-Oriented Discrete-Time Modeling and Simulation of Switching Converters, *IEEE Power Electronics Specialists Conference*, 1987 record, pp. 167-176.
- [3] R. C. WONG, H. A. OWEN, T. G. WILSON, "An Efficient Algorithm for the Time-Domain Simulation of Regulated Energy-Storage DC-to-DC Converters," *IEEE Transactions on Power Electronics*, Vol. 2, No. 2, April 1987, pp. 154-168.
- [4] A. M. LUCIANO and A. G. M. STROLLO, "A Fast Time-Domain Algorithm for Simulation of Switching Power Converters," *IEEE Transactions on Power Electronics*, Vol. 2, No. 3, July 1990, pp. 363-370.
- [5] D. BEDROSIAN and J. VLACH, "Time-Domain Analysis of Networks with Internally Controlled Switches," *IEEE Transactions on Circuits and Systems—I: Fundamental Theory and Applications*, Vol. 39, No.3, March 1992, pp. 199-212.
- [6] P. PEJOVIĆ and D. MAKSIMOVIĆ, "A New Algorithm for Simulation of Power Electronic Systems Using Piecewise-Linear Device Models," *IEEE Transactions on Power Electronics*, Vol. 10, No. 3, May 1995, pp. 340-348.
- [7] PREDRAG PEJOVIĆ, "A Method for Simulation of Power Electronic Systems Using Piecewise-Linear Device Models," Ph.D. thesis, University of Colorado, Boulder, April 1995.
- [8] D. LI, R. TYMERSKI, T. NINOMIYA, "PECS—An Efficacious Solution for Simulating Switched Networks with Nonlinear Elements," *IEEE Power Electronics Specialists Conference*, 2000 Record, pp. 274-279, June 2000.
- [9] V. BELLO, "Computer Aided Analysis of Switching Regulators Using SPICE2," *IEEE Power Electronics Specialists Conference*, 1980 Record, pp. 3-11.
- [10] V. BELLO, "Using the SPICE2 CAD Package for Easy Simulation of Switching Regulators in Both Continuous and Discontinuous Conduction Modes," *Proceedings of the Eighth National Solid-State Power Conversion Conference* (Powercon 8), April 1981.
- [11] V. BELLO, "Using the SPICE2 CAD Package to Simulate and Design the Current Mode Converter," *Proceedings of the Eleventh National Solid-State Power Conversion Conference* (Powercon 11), April 1984.
- [12] D. KIMHI, S. BEN-YAAKOV, "A SPICE Model for Current Mode PWM Converters Operating Under Continuous Inductor Current Conditions," *IEEE Transactions on Power Electronics*, Vol. 6, No. 2, April 1991, pp. 281-286.
- [13] Y. AMRAN, F. HULIEHEL, S. BEN-YAAKOV, "A Unified SPICE Compatible Average Model of PWM Converters," *IEEE Transactions on Power Electronics*, Vol. 6, No. 4, October 1991, pp. 585-594.
- [14] S. BEN-YAAKOV, Z. GAATON, "Generic SPICE Compatible Model of Current Feedback in Switch Mode Converters, *Electronics Letters*, Vol. 28, No. 14, 2nd July 1992.
- [15] S. BEN-YAAKOV, "Average Simulation of PWM Converters by Direct Implementation of Behavioral Rela-

- tionships," *IEEE Applied Power Electronics Conference*, 1993 Record, pp. 510-516, February 1993.
- [16] S. BEN-YAAKOV, D. ADAR, "Average Models as Tools for Studying Dynamics of Switch Mode DC-DC converters," *IEEE Power Electronics Specialists Conference*, 1994 Record, pp. 1369-1376.
- [17] V. M. CANALLI, J. A. COBOS, J. A. OLIVER, J. UCEDA, "Behavioral Large Signal Averaged Model for DC/DC Switching Power Converters," *IEEE Power Electronics Specialists Conference*, 1996 Record, pp. 1675-1681.
- [18] N. JAYARAM, D. MAKSIMOVIĆ, "Power Factor Correctors Based on Coupled-Inductor SEPIC and Ćuk Converters with Nonlinear- Carrier Control," *IEEE Applied Power Electronics Conference*, 1998 Record, pp. 468-474, February 1998.
- [19] J. KEOWN, *OrCAD PSpice and Circuit Analysis*, Fourth Edition, Englewood Cliffs: Prentice Hall, 2000.
- [20] P. W. TUINENGA, *SPICE: A Guide to Circuit Simulation and Analysis Using PSpice*, Third Edition, Englewood Cliffs: Prentice Hall, 1995.
- [21] V. VORPERIAN, "Simplified Analysis of PWM Converters Using the Model of the PWM Switch: Parts I and II," *IEEE Transactions on Aerospace and Electronic Systems*, Vol. AES-26, pp. 490-505, May 1990.
- [22] S. FREELAND and R. D. MIDDLEBROOK, "A Unified Analysis of Converters with Resonant Switches," *IEEE Power Electronics Specialists Conference*, 1987 Record, pp. 20-30.
- [23] ARTHUR WITULSKI and ROBERT ERICKSON, "Extension of State-Space Averaging to Resonant Switches —and Beyond," *IEEE Transactions on Power Electronics*, Vol. 5, No. 1, pp. 98-109, January 1990.
- [24] D. MAKSIMOVIĆ and S. ĆUK, "A Unified Analysis of PWM Converters in Discontinuous Modes," *IEEE Transactions on Power Electronics*, Vol. 6, No. 3, pp. 476-490, July 1991.

---

# Appendix C

## Middlebrook's Extra Element Theorem

---

The *Extra Element Theorem* of R. D. Middlebrook [1–3] shows how a transfer function is changed by the addition of an impedance to the network. The theorem allows one to determine the effects of this extra element on any transfer function of interest, without solving the system all over again. The Extra Element Theorem is a powerful technique of design-oriented analysis. It leads to impedance inequalities which guarantee that an element does not substantially alter a transfer function. The Extra Element Theorem is employed in Chapter 10, where it leads to a relatively simple methodology for designing input filters that do not degrade the loop gains of switching regulators. It is also employed in Section 19.4, to determine how the load resistance affects the properties of a resonant inverter. In this appendix, Middlebrook's Extra Element Theorem is derived, based on the principle of superposition. Its application is illustrated via examples.

### C.1 BASIC RESULT

Consider the linear circuit of Fig. C.1(a). This network contains an input  $v_{in}(s)$  and an output  $v_{out}(s)$ . In addition, it contains a port whose terminals are open-circuited. It is assumed that the transfer function from  $v_{in}(s)$  to  $v_{out}(s)$  is known, and is given by

$$\frac{v_{out}(s)}{v_{in}(s)} = G(s) \Big|_{Z(s) \rightarrow \infty} \quad (\text{C.1})$$

The Extra Element Theorem tells us how the transfer function  $G(s)$  is modified when an impedance  $Z(s)$  is connected between the terminals at the port, as in Fig. C.1(b). The result is

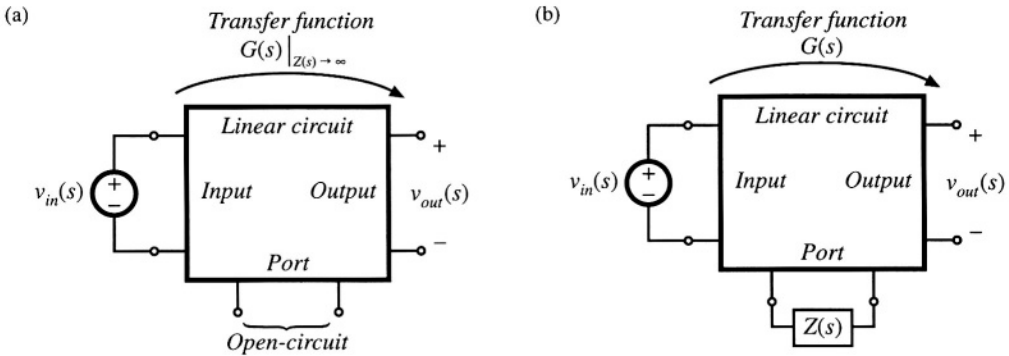


**Fig. C.1** How an added element changes a transfer function  $G(s)$ : (a) original conditions, before addition of the new element; (b) addition of element having impedance  $Z(s)$ .

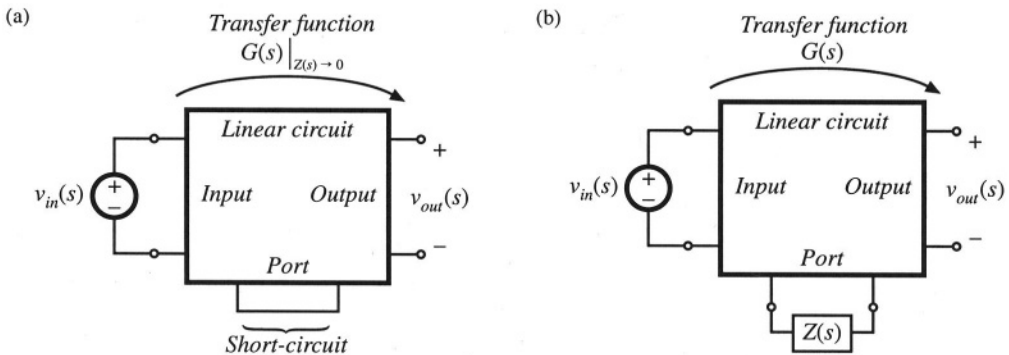


**Fig. C.2** The dual form of the Extra Element Theorem, in which the extra element replaces a short circuit: (a) original conditions, (b) addition of element having impedance  $Z(s)$ .

$$\frac{v_{out}(s)}{v_{in}(s)} = \left( G(s) \Big|_{Z(s) \rightarrow \infty} \right) \left( \frac{1 + \frac{Z_N(s)}{Z(s)}}{1 + \frac{Z_D(s)}{Z(s)}} \right) \quad (\text{C.2})$$

The right-hand side terms involving  $Z(s)$  account for the influence of  $Z(s)$  on  $G(s)$ , and are known as the *correction factor*.

The Extra Element Theorem also applies to the dual form illustrated in Fig. C.2. In this form, the transfer function is initially known under the conditions that the port is short-circuited. In Fig. C.2(b), the short-circuit is replaced by the impedance  $Z(s)$ . In this case, the addition of the impedance  $Z(s)$  causes the transfer function to become

$$\frac{v_{out}(s)}{v_{in}(s)} = \left( G(s) \Big|_{Z(s) \rightarrow 0} \right) \left( \frac{1 + \frac{Z(s)}{Z_N(s)}}{1 + \frac{Z(s)}{Z_D(s)}} \right) \quad (\text{C.3})$$

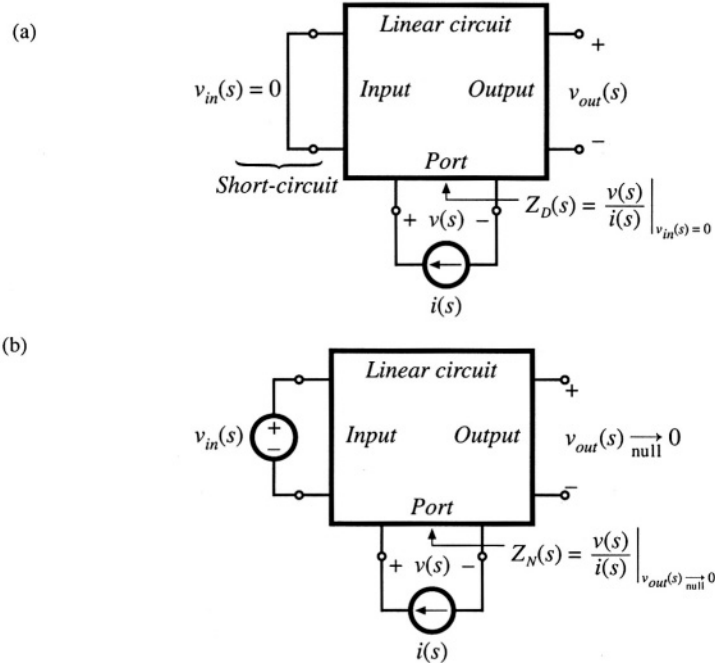


**Fig. C.3** Determination of the quantities  $Z_N(s)$  and  $Z_D(s)$ : (a)  $Z_D(s)$  is the Thevenin-equivalent impedance at the port, and is measured with the input  $v_{in}(s)$  set to zero; (b)  $Z_N(s)$  is the impedance seen at the port under the condition that the output is nulled.

The  $Z_N(s)$  and  $Z_D(s)$  terms in Eqs. (C.2) and (C.3) are identical. By equating the  $G(s)$  expressions of Eqs. (C.2) and (C.3), one can show that

$$\frac{G(s)|_{Z(s) \rightarrow \infty}}{G(s)|_{Z(s) \rightarrow 0}} = \frac{Z_D(s)}{Z_N(s)} \quad (\text{C.4})$$

This is known as the *reciprocity relationship*.

The quantities  $Z_N(s)$  and  $Z_D(s)$  can be found by measuring impedances at the port. The term  $Z_D(s)$  is the Thevenin equivalent impedance seen looking into the port, also known as the driving-point impedance. As illustrated in Fig. C.3(a), this impedance is found by setting the independent source  $v_{in}(s)$  to zero, and then measuring the impedance between the terminals of the port:

$$Z_D(s) = \frac{v(s)}{i(s)} \Big|_{v_{in}(s)=0} \quad (\text{C.5})$$

Thus,  $Z_D(s)$  is the impedance between the port terminals when the input  $v_{in}(s)$  is set to zero.

Determination of the impedance  $Z_N(s)$  is illustrated in Fig. C.3(b). The term  $Z_N(s)$  is found under the conditions that the output  $v_{out}(s)$  is nulled to zero. A current source  $i(s)$  is connected to the terminals of the port. In the presence of the input signal  $v_{in}(s)$ , the current  $i(s)$  is adjusted so that the output  $v_{out}(s)$  is nulled to zero. Under these conditions, the quantity  $Z_N(s)$  is given by

$$Z_N(s) = \left. \frac{v(s)}{i(s)} \right|_{v_{out}(s) \rightarrow 0} \quad (\text{C.6})$$

Note that *nulling* the output is not the same as *shorting* the output. If one simply shorted the output, then a current would flow through the short, which would induce voltage drops and currents in other elements of the network. These voltage drops and currents are not present when the output is nulled. The null condition of Fig. C.3(b) does not employ any connections to the output of the circuit. Rather, the null condition employs the adjustment of the independent sources  $v_{in}(s)$  and  $i(s)$  in a special way that causes the output  $v_{out}(s)$  to be zero. By superposition,  $v_{out}(s)$  can be expressed as a linear combination of  $v_{in}(s)$  and  $i(s)$ ; therefore, for a given  $v_{in}(s)$ , it is always possible to choose an  $i(s)$  that will cause  $v_{out}(s)$  to be zero. Under these null conditions,  $Z_N(s)$  is measured as the ratio of  $v(s)$  to  $i(s)$ . In practice, the circuit analysis to find  $Z_N(s)$  is simpler than analysis of  $Z_D(s)$ , because the null condition causes many of the signals within the circuit to be zero. Several examples are given in Section C.4.

The input and output quantities need not be voltages, but could also be currents or other signals that can be set or nulled to zero. The next section contains a derivation of the Extra Element Theorem with a general input  $u(s)$  and output  $y(s)$ .

## C.2 DERIVATION

Figure C.4(a) illustrates a general linear system having an input  $u(s)$  and an output  $y(s)$ . In addition, the system contains an electrical port having voltage  $v(s)$  and current  $i(s)$ , with the polarities illustrated. Initially, the port is open-circuited:  $i(s) = 0$ . The transfer function of this system, with the port open-circuited, is

$$G_{old}(s) = \left. \frac{y(s)}{u(s)} \right|_{i(s)=0} \quad (\text{C.7})$$

The objective of the extra element theorem is to determine the new transfer function  $G(s)$  that is obtained when an impedance  $Z(s)$  is connected to the port:

$$G(s) = \frac{y(s)}{u(s)} \quad (\text{C.8})$$

The situation is illustrated in Fig. C.4(b). It can be seen that the conditions at the port are now given by

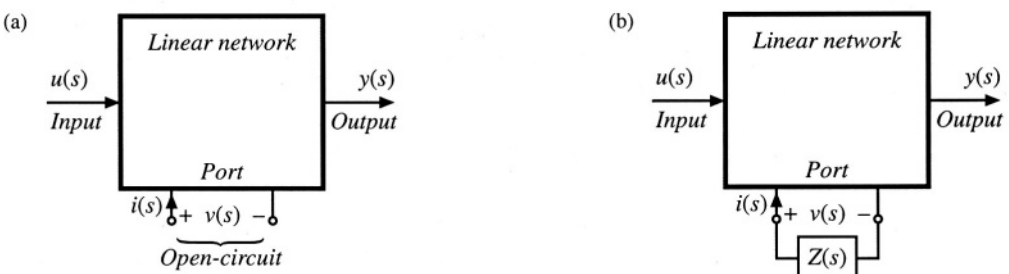


**Fig. C.4** Modification of a linear network by addition of an extra element: (a) original system, (b) modified system, with impedance  $Z(s)$  connected at an electrical port.

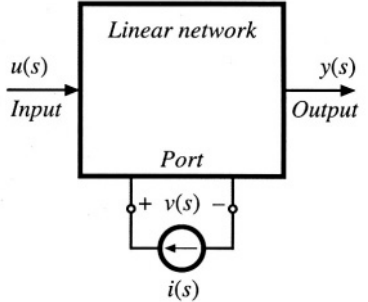


**Fig. C.5** Current injection at the electrical port, by addition of independent current source  $i(s)$ .

$$v(s) = -i(s)Z(s) \quad (\text{C.9})$$

To express the new transfer function  $G(s)$  in Eq. (C.8) in terms of the original transfer function  $G_{old}(s)$  of Eq. (C.7), we use current injection at the port, as illustrated in Fig. C.5. There are now two independent inputs: the input  $u(s)$  and the independent current source  $i(s)$ . The dependent quantities  $y(s)$  and  $v(s)$  can be expressed as functions of these independent inputs using the principle of superposition:

$$y(s) = G_{old}(s)u(s) + G_i(s)i(s) \quad (\text{C.10})$$

$$v(s) = G_v(s)u(s) + Z_D(s)i(s) \quad (\text{C.11})$$

where

$$G_{old}(s) = \frac{y(s)}{u(s)} \Big|_{i(s)=0} \quad (\text{C.12})$$

$$G_i(s) = \frac{y(s)}{i(s)} \Big|_{u(s)=0} \quad (\text{C.13})$$

$$Z_D(s) = \frac{v(s)}{i(s)} \Big|_{u(s)=0} \quad (\text{C.14})$$

$$G_v(s) = \frac{v(s)}{u(s)} \Big|_{i(s)=0} \quad (\text{C.15})$$

are the transfer functions from the independent inputs to the respective dependent quantities  $y(s)$  and  $v(s)$ .

The transfer function  $G(s)$  can be found by elimination of  $v(s)$  and  $i(s)$  from the system of equations (C.9) to (C.11), and solution for  $y(s)$  as a function of  $u(s)$ . The result is

$$G(s) = \frac{y(s)}{u(s)} = G_{old}(s) - \frac{G_v(s)G_i(s)}{Z(s) + Z_D(s)} \quad (\text{C.16})$$

This intermediate result expresses the new transfer function  $G(s)$  as a function of the original transfer function  $G_{old}(s)$  and the extra element  $Z(s)$ , as well as the quantities  $Z_D(s)$ ,  $G_v(s)$ , and  $G_i(s)$ .

Equation (C.14) gives a direct way to find the quantity  $Z_D(s)$ .  $Z_D(s)$  is the driving-point impedance at the port, when the input  $u(s)$  is set to zero. This quantity can be found either by conventional circuit analysis or simulation, or by laboratory measurement.

Although  $G_v(s)$  and  $G_i(s)$  could also be determined from the definitions (C.13) and (C.15), it is preferable to eliminate these quantities, and instead express  $G(s)$  as a function of the impedances at the given port. This can be accomplished via the following thought experiment. In the presence of the input  $u(s)$ , we adjust the independent current source  $i(s)$  in the special way that causes the output  $y(s)$  to be nulled to zero. The impedance  $Z_N(s)$  is defined as the ratio of  $v(s)$  to  $i(s)$  under these null conditions:

$$Z_N(s) = \frac{v(s)}{i(s)} \Big|_{y(s) \xrightarrow{\text{null}} 0} \quad (\text{C.17})$$

The value of  $i(s)$  that achieves the null condition  $y(s) \xrightarrow{\text{null}} 0$  can be found by setting  $y(s) = 0$  in Eq. (C.10), as follows:

$$\left[ G_{old}(s)u(s) + G_i(s)i(s) \right] \xrightarrow{\text{null}} 0 \quad (\text{C.18})$$

Hence, the output  $y(s)$  is nulled when the inputs  $u(s)$  and  $i(s)$  are related as follows:

$$u(s) \Big|_{y(s) \xrightarrow{\text{null}} 0} = -\frac{G_i(s)}{G_{old}(s)} i(s) \Big|_{y(s) \xrightarrow{\text{null}} 0} \quad (\text{C.19})$$

Under this null condition, the voltage  $v(s)$  is given by

$$\begin{aligned} v(s) \Big|_{y(s) \xrightarrow{\text{null}} 0} &= G_v(s) u(s) \Big|_{y(s) \xrightarrow{\text{null}} 0} + Z_D(s) i(s) \Big|_{y(s) \xrightarrow{\text{null}} 0} \\ &= \left( -\frac{G_v(s)G_i(s)}{G_{old}(s)} + Z_D(s) \right) i(s) \Big|_{y(s) \xrightarrow{\text{null}} 0} \end{aligned} \quad (\text{C.20})$$

which follows from Eqs. (C.11) and (C.19). Substitution of Eq. (C.17) into Eq. (C.20) yields

$$v(s) \Big|_{y(s) \xrightarrow{\text{null}} 0} = Z_N(s) i(s) \Big|_{y(s) \xrightarrow{\text{null}} 0} = \left( -\frac{G_v(s)G_i(s)}{G_{old}(s)} + Z_D(s) \right) i(s) \Big|_{y(s) \xrightarrow{\text{null}} 0} \quad (\text{C.21})$$

Hence,

$$Z_N(s) = Z_D(s) - \frac{G_v(s)G_i(s)}{G_{old}(s)} \quad (\text{C.22})$$

Solution for the quantity  $G_v(s)G_i(s)$  yields

$$G_v(s)G_i(s) = (Z_D(s) - Z_N(s))G_{old}(s) \quad (\text{C.23})$$

Thus, the unknown quantities  $G_v(s)$  and  $G_i(s)$  can be related to  $Z_N(s)$  and  $Z_D(s)$ , which are properties of the port at which the new impedance  $Z(s)$  will be connected, and to the original transfer function  $G_{old}(s)$ .

The final step is to substitute Eq. (C.23) into Eq. (C.16), leading to

$$G(s) = G_{old}(s) - \frac{Z_D(s) - Z_N(s)}{Z(s) + Z_D(s)} G_{old}(s) \quad (C.24)$$

This expression can be simplified as follows:

$$G(s) = G_{old}(s) \frac{1 + \frac{Z_N(s)}{Z(s)}}{1 + \frac{Z_D(s)}{Z(s)}} \quad (C.25)$$

or,

$$G(s) = \left( G(s) \Big|_{Z(s) \rightarrow \infty} \right) \left( \frac{1 + \frac{Z_N(s)}{Z(s)}}{1 + \frac{Z_D(s)}{Z(s)}} \right) \quad (C.26)$$

This is the desired result. It states how the transfer function  $G(s)$  is modified by addition of the extra element  $Z(s)$ . The right-most term in Eq. (C.26) is called the *correction factor*; this term gives a quantitative measure of the change in  $G(s)$  arising from the introduction of  $Z(s)$ .

Derivation of the dual result, Eq. (C.3), follows similar steps.

### C.3 DISCUSSION

The general form of the extra element theorem makes it useful for designing a system such that unwanted circuit elements do not degrade the desirable system performance already obtained. For example, suppose that we already know some transfer function or similar quantity  $G(s)$ , under simplified or ideal conditions, and have designed the system such that this quantity meets specifications. We can then use the extra element theorem to answer the following questions:

What is the effect of a parasitic element  $Z(s)$  that was not included in the original analysis?

What happens if we later decide to add some additional components having impedance  $Z(s)$  to the system?

Can we establish some conditions on  $Z(s)$  that ensure that  $G(s)$  is not substantially changed?

A common application of the extra element theorem is the determination of conditions on the extra element that guarantee that the transfer function  $G(s)$  is not significantly altered. According to Eqs. (C.2) and (C.26), this will occur when the correction factor is approximately equal to unity. The conditions are:

$$\begin{cases} |Z(j\omega)| \gg |Z_N(j\omega)| \\ |Z(j\omega)| \gg |Z_D(j\omega)| \end{cases} \quad (C.27)$$

This gives a formal way to show when an impedance can be ignored: one can plot the impedances  $\|Z_N(j\omega)\|$  and  $\|Z_D(j\omega)\|$ , and compare the results with a plot of  $\|Z(j\omega)\|$ . The impedance  $Z(s)$  can be ignored over the range of frequencies where the inequalities (C.27) are satisfied.

For the dual case in which the new impedance is inserted where there was previously a short circuit, Eq. (C.3), the inequalities are reversed:

$$\begin{aligned} \|Z(j\omega)\| &\ll \|Z_N(j\omega)\| \\ \|Z(j\omega)\| &\ll \|Z_D(j\omega)\| \end{aligned} \quad (C.28)$$

This equation shows how to limit the magnitude  $\|Z(j\omega)\|$ , to avoid significantly changing the transfer function  $G(s)$ .

For quantitative design, Eqs. (C.27) and (C.28) raise an additional question: By what factor should  $\|Z(j\omega)\|$  exceed (or be less than)  $\|Z_N(j\omega)\|$  and  $\|Z_D(j\omega)\|$ , in order for the inequalities of Eq. (C.27) or (C.28) to be well satisfied? This question can be answered by plotting the magnitudes and phases of the correction factor terms, as a function of the magnitudes and phases of  $(Z/Z_N)$  and  $(Z/Z_D)$ .

Figure C.6 shows contours of constant  $\|1 + Z/Z_N\|$ , as a function of the magnitude and phase of  $Z/Z_N$ . Figure C.7 shows similar contours of constant  $\angle(1 + Z/Z_N)$ . It can be seen that, when  $\|Z/Z_N\|$  is less than  $-20$  dB, then the maximum deviation caused by the numerator  $(1 + Z/Z_N)$  term is less than  $\pm 1$  dB in magnitude, and less than  $\pm 7^\circ$  in phase. For  $\|Z/Z_N\|$  less than  $-10$  dB, the maximum deviation caused by the numerator  $(1 + Z/Z_N)$  term is less than  $\pm 3.5$  dB in magnitude, and less than  $\pm 20^\circ$  in phase.

Figures C.8 and C.9 contain contours of constant  $\|1/(1 + Z/Z_D)\|$  and  $\angle 1/(1 + Z/Z_D)$ , respectively, as a function of the magnitude and phase of  $Z/Z_D$ . These plots contain minus signs because the terms appear in the denominator of the correction factor; otherwise, they are identical to Figs. C.6 and C.7. Again, for  $\|Z/Z_D\|$  less than  $-20$  dB, the maximum deviation caused by the denominator  $(1 + Z/Z_D)$  term is less than  $\pm 1$  dB in magnitude, and less than  $\pm 7^\circ$  in phase. For  $\|Z/Z_D\|$  less than  $-10$  dB, the maximum deviation caused by the denominator  $(1 + Z/Z_D)$  term is less than  $\pm 3.5$  dB in magnitude, and less than  $\pm 20^\circ$  in phase.

## C.4 EXAMPLES

### C.4.1 A Simple Transfer Function

The first example illustrates how the Extra Element Theorem can be used to find a transfer function essentially by inspection. We are given the circuit illustrated in Fig. C.10. It is desired to solve for the transfer function

$$G(s) = \frac{v_2(s)}{v_1(s)} \quad (C.29)$$

and to express this transfer function in factored pole-zero form. One way to do this is to employ the Extra Element Theorem, treating the capacitor  $C$  as an “extra” element. As illustrated in Fig. C.11, the electrical port is taken to be at the location of the capacitor, and the “original conditions” are taken to be the case when the capacitor impedance is infinite, i.e., an open circuit. Under these original conditions, the transfer function is given by the voltage divider composed of resistors  $R_1, R_3$ , and  $R_4$ . Hence,  $G(s)$  can be expressed as

$$\frac{v_2(s)}{v_1(s)} = G(s) = \left( \frac{R_4}{R_1 + R_3 + R_4} \right) \frac{\left( 1 + \frac{Z_N}{Z} \right)}{\left( 1 + \frac{Z_D}{Z} \right)} \quad (C.30)$$

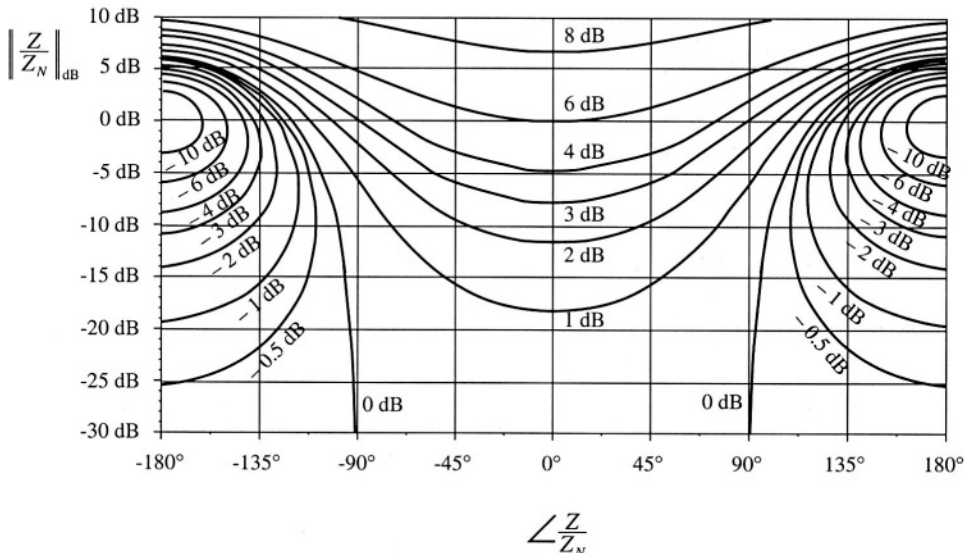


Fig. C.6 Contours of constant  $\|1 + Z/Z_N\|$ , as a function of the magnitude and phase of  $Z/Z_N$ .

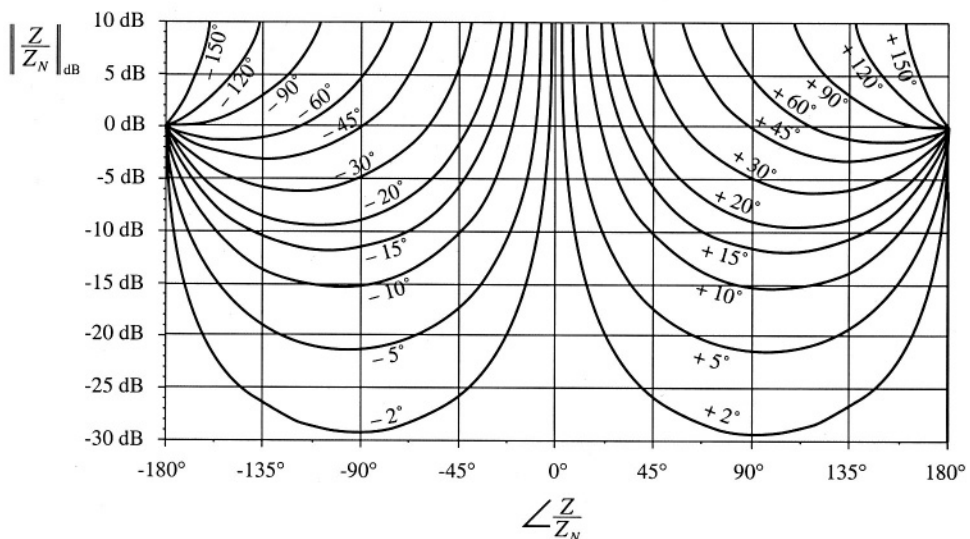
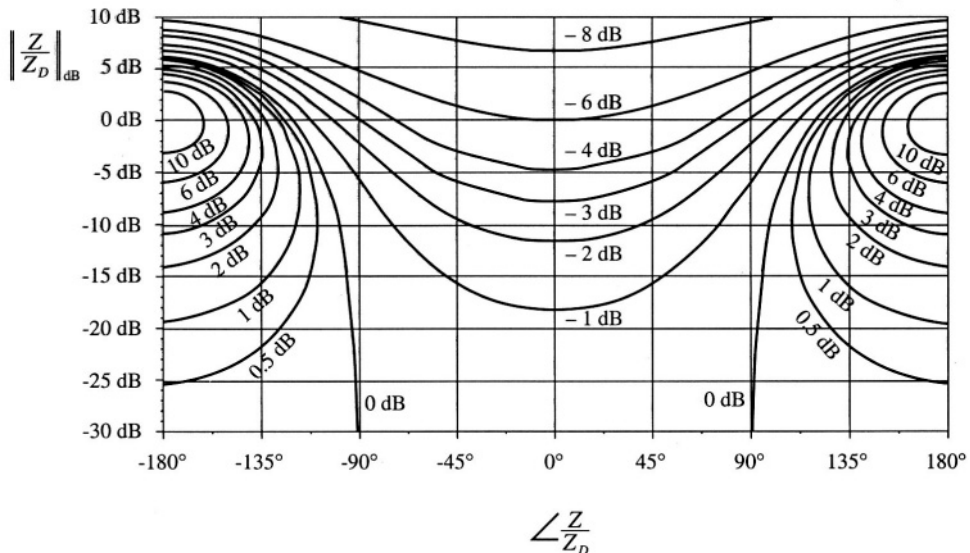
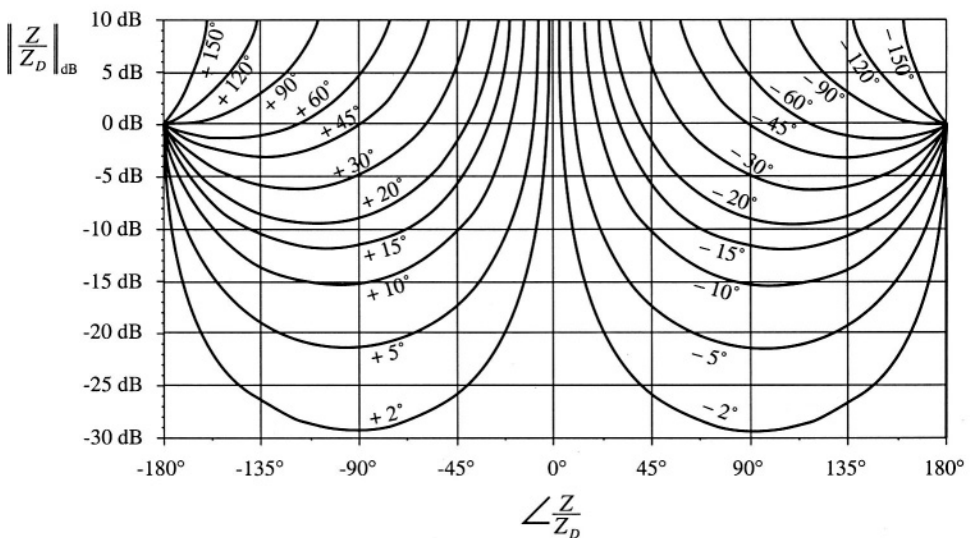


Fig. C.7 Contours of constant  $\angle(1 + Z/Z_N)$ , as a function of the magnitude and phase of  $Z/Z_N$ .



**Fig. C.8** Contours of constant  $\left\| 1/(1 + Z/Z_D) \right\|$ , as a function of the magnitude and phase of  $Z/Z_D$



**Fig. C.9** Contours of constant  $\angle 1/(1 + Z/Z_D)$ , as a function of the magnitude and phase of  $Z/Z_D$ .

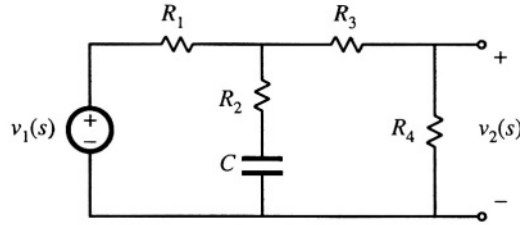


**Fig. C.10** R-C circuit example of Section C.4.1.

where  $Z(s)$  is the capacitor impedance  $1/sC$ .

The impedance  $Z_D(s)$  is the Thevenin equivalent impedance seen at the port where the capacitor is connected. As illustrated in Fig. C.12(a), this impedance is found by setting the independent source  $v_1(s)$  to zero, and then determining the impedance between the port terminals. The result is:

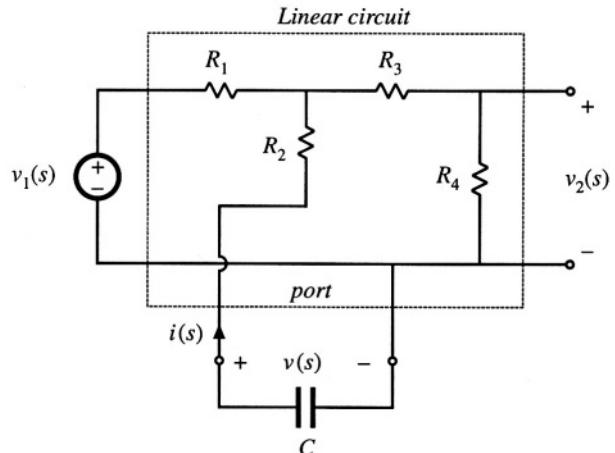
$$Z_D = R_2 + R_1 \parallel (R_3 + R_4) \quad (\text{C.31})$$

Figure C.12(b) illustrates determination of the impedance  $Z_N(s)$ . A current source  $i(s)$  is connected to the port, in place of the capacitor. In the presence of the input  $v_1(s)$ , the current source  $i(s)$  is adjusted so that the output  $v_2(s)$  is nulled. Under these null conditions, the impedance  $Z_N(s)$  is found as the ratio of  $v(s)$  to  $i(s)$ .

It is easiest to find  $Z_N(s)$  by first determining the effect of the null condition on the signals in the circuit. Since  $v_2$  is nulled to zero, there is no current through the resistor  $R_4$ . Since  $R_3$  is connected in series with  $R_4$ , there is also no current through  $R_3$ , and hence no voltage across  $R_3$ . Therefore, the voltage  $v_3$  in Fig. C.12(b) is equal to  $v_2$ , i.e.,

$$v_3 = v_2 \xrightarrow{\text{null}} 0 \quad (\text{C.32})$$

Therefore, the voltage  $v$  is given by  $iR_2$ . The impedance  $Z_N$  is



**Fig. C.11** Manipulation of the circuit of Fig. C.10 into the form of Fig. C.1.

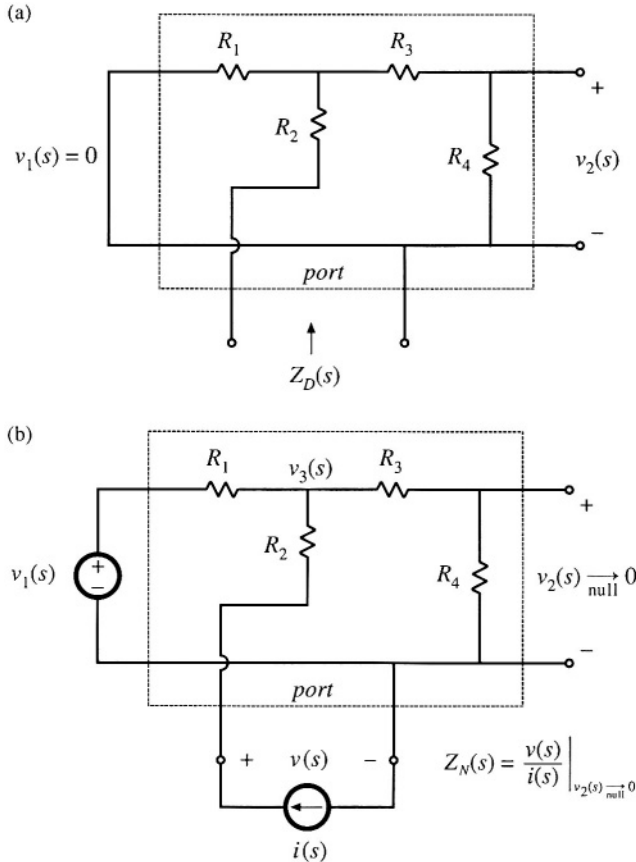


Fig. C.12 Measurement of the quantities  $Z_N(s)$  and  $Z_D(s)$ : (a) determination of  $Z_D(s)$ , (b) determination of  $Z_N(s)$

$$Z_N(s) = \frac{v(s)}{i(s)} \Big|_{v_2(s) \xrightarrow{0}} = R_2 \quad (C.33)$$

Note that, in general, the independent sources  $v_1$  and  $i$  are nonzero during the  $Z_N$  measurement. For this example, the null condition implies that the current  $i(s)$  flows entirely through the path composed of  $R_2$ ,  $R_1$ , and  $v_1$ .

The transfer function  $G(s)$  is found by substitution of Eqs. (C.31) and (C.33) into Eq. (C.30):

$$G(s) = \left( \frac{R_4}{R_1 + R_3 + R_4} \right) \frac{(1 + sCR_2)}{\left( 1 + sC \left[ R_2 + R_1 \parallel (R_3 + R_4) \right] \right)} \quad (C.34)$$

For this example, the result is obtained in standard normalized pole-zero form, because the capacitor is the only dynamic element in the circuit, and because the “original conditions,” in which the capacitor impedance tends to an open circuit, coincide with dc conditions in the circuit. A similar procedure can be

applied to write the transfer function of a circuit, containing an arbitrary number of reactive elements, in normalized form via an extension of the Extra Element Theorem [3].

### C.4.2 An Unmodeled Element

We are told that the transformer-isolated parallel resonant inverter of Fig. C.13 has been designed with the assumption that the transformer is ideal. The approximate sinusoidal analysis techniques of Chapter 19 were employed to model the inverter. It is now desired to specify a transformer; this requires that limits be specified on the minimum allowable transformer magnetizing inductance. One way to approach this problem is to view the transformer magnetizing inductance as an extra element, and to derive conditions that guarantee that the presence of the transformer magnetizing inductance does not significantly change the tank network transfer function  $G(s)$ .

Figure C.14 illustrates the equivalent circuit model of the inverter, derived using the approximate sinusoidal analysis technique of Section 19.1. The switch network output voltage  $v_s(t)$  is modeled by its fundamental component  $v_{s1}(t)$ , a sinusoid. The tank transfer function  $G(s)$  is given by:

$$G(s) = \frac{v_o(s)}{v_{s1}(s)} \quad (\text{C.35})$$

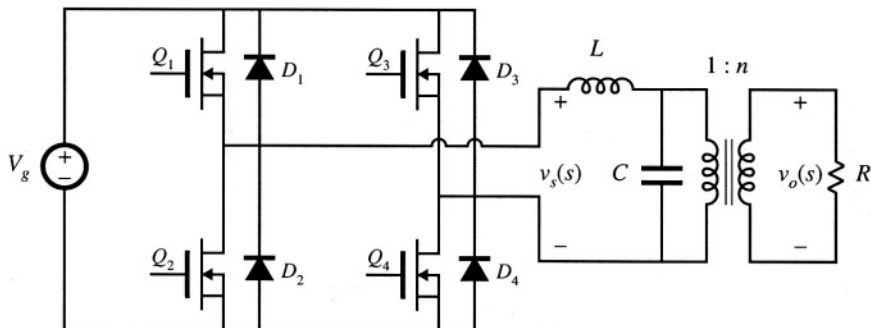


Fig. C.13 Parallel resonant inverter example.

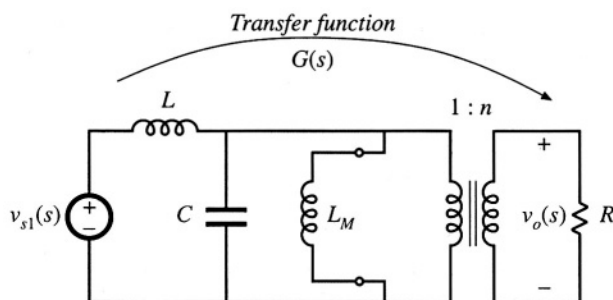
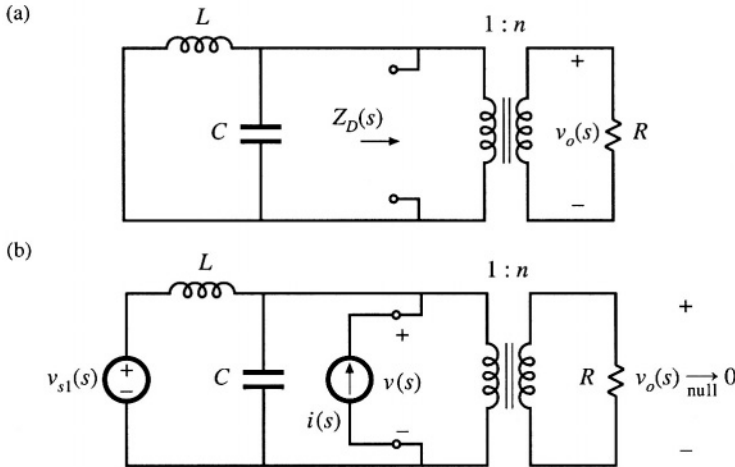


Fig. C.14 Equivalent circuit model of the tank network, based on the approximate sinusoidal analysis technique.



**Fig. C.15** Measurement of  $Z_N(s)$  and  $Z_D(s)$ : (a) determination of  $Z_D(s)$ , (b) determination of  $Z_N(s)$ .

Under the conditions that the transformer is ideal (i.e., the transformer magnetizing inductance  $L_M$  is open circuited), then the transfer function is given by:

$$G(s)|_{L_M \rightarrow \infty} = \frac{n}{1 + s \frac{n^2 L}{R} + s^2 LC} \quad (\text{C.36})$$

We can therefore employ the extra element theorem to determine how finite magnetizing inductance changes  $G(s)$ . With reference to Fig. C.1, the system input is  $v_{s1}(s)$ , the output is the voltage  $v_o(s)$ , and the “port” is the primary winding of the transformer, where the magnetizing inductance is connected. In the presence of the magnetizing inductance, the transfer function becomes

$$G(s) = \left( G(s)|_{L_M \rightarrow \infty} \right) \frac{\left( 1 + \frac{Z_N(s)}{Z(s)} \right)}{\left( 1 + \frac{Z_D(s)}{Z(s)} \right)} \quad (\text{C.37})$$

where  $Z(s)$  is the impedance of the magnetizing inductance referred to the primary winding,  $sL_M$ .

Figure C.15(a) illustrates determination of  $Z_D(s)$ . The input source  $v_{s1}(s)$  is set to zero, and the impedance between the terminals of the port is found. It can be seen that the impedance  $Z_D(s)$  is the parallel combination of the impedances of the tank inductor, tank capacitor, and the reflected load resistance:

$$Z_D(s) = \frac{R}{n^2} \parallel sL \parallel \frac{1}{sC} \quad (\text{C.38})$$

Figure C.15(b) illustrates determination of  $Z_N(s)$ . In the presence of the input source  $v_{s1}(s)$ , a current  $i(s)$  is injected at the port as shown. This current is adjusted such that the output  $v_o(s)$  is nulled. Under these conditions, the quantity  $Z_N(s)$  is given by  $v(s)/i(s)$ . It can be seen that nulling  $v_o(s)$  also nulls the voltage  $v(s)$ . Therefore,

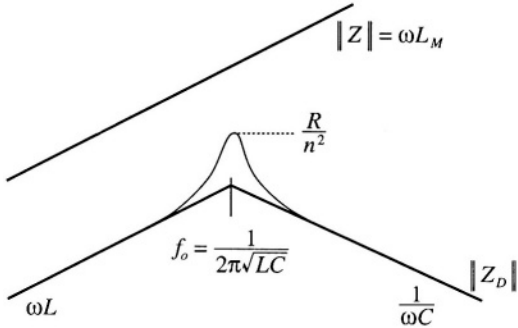


**Fig. C.16** To avoid significantly changing the transfer function  $G(s)$ , the transformer should be designed such that  $\|Z\| \gg \|Z_D\|$ .

$$Z_N(s) = \frac{v(s)}{i(s)} \Big|_{v_o(s) \rightarrow 0} = 0 \quad (\text{C.39})$$

Note that, in general,  $i(s)$  will not be equal to zero during the  $Z_N(s)$  measurement. The null condition is achieved by setting the source  $i(s)$  equal to the value  $-v_{o1}(s)/sL$ . Thus, in the presence of finite magnetizing inductance, the transfer function  $G(s)$  can be expressed as follows:

$$G(s) = \left( G(s) \Big|_{L_M \rightarrow \infty} \right) \frac{\left( 1 + \frac{0}{Z(s)} \right)}{\left( 1 + \frac{Z_D(s)}{Z(s)} \right)} = \frac{\left( G(s) \Big|_{L_M \rightarrow \infty} \right)}{\left( 1 + \frac{Z_D(s)}{Z(s)} \right)} \quad (\text{C.40})$$

We can now plot the impedance inequalities (C.27) that guarantee that the magnetizing inductance does not substantially modify  $G(s)$ . The  $Z_D(s)$  given in Eq. (C.38) is the impedance of a parallel resonant circuit. Construction of the magnitude of this impedance is described in Section 8.3.4, with results illustrated in Fig. C.16. To avoid affecting the transfer function  $G(s)$ , the impedance of the magnetizing inductance must be much greater than  $\|Z_D(j\omega)\|$  over the range of expected operating frequencies. It can be seen that this will indeed be the case provided that the impedance of the magnetizing inductance is greater than the impedances of both the tank inductance and the reflected load impedance:

$$\begin{aligned} L_M &\gg L, \text{ and} \\ \omega_0 L_M &\gg \frac{R}{n^2} \end{aligned} \quad (\text{C.41})$$

where  $\omega_0 = 1/(\sqrt{LC})$ . These conditions can be further reduced to

$$\begin{aligned} L_M &\gg L, \text{ and} \\ L_M &\gg \frac{R}{n^2} \sqrt{LC} \end{aligned} \quad (\text{C.42})$$

### C.4.3 Addition of an Input Filter to a Converter

As discussed in Chapter 10, the addition of an input filter to a switching regulator can significantly alter its loop gain  $T(s)$ . Hence, it is desirable to design the input filter so that it does not substantially change

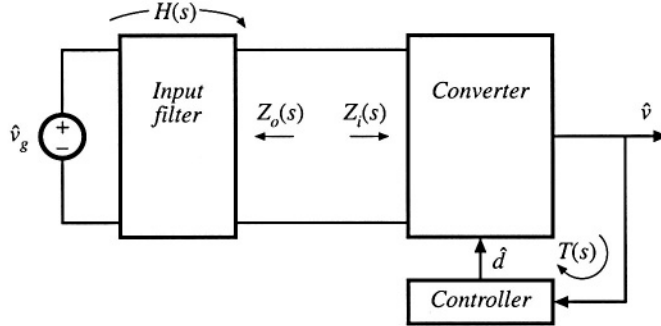


**Fig. C.17** Addition of an input filter to a switching voltage regulator system.

the converter control-to-output transfer function  $G_{vd}(s)$ . The Extra Element Theorem can provide design criteria that show how to design such an input filter.

Figure C.17 illustrates the addition of an input filter to a switching voltage regulator system. The control-to-output transfer function of the converter power stage is given by:

$$G_{vd}(s) = \left. \frac{\hat{v}(s)}{\hat{d}(s)} \right|_{\hat{v}_g(s)=0} \quad (\text{C.43})$$

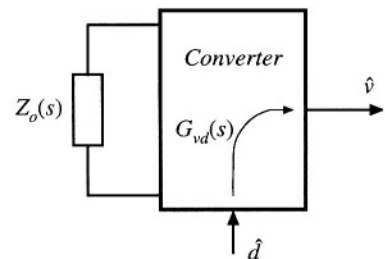
The quantity  $Z_o(s)$  is the Thevenin equivalent output impedance of the input filter. Upon setting  $\hat{v}_g(s)$  to zero in Fig. C.17, the system of Fig. C.18 is obtained. It can be recognized that this system is of the same form as Fig. C.2, in which the "extra element" is the output impedance  $Z_o(s)$  of the added input filter. With no input filter [ $Z_o(s) = 0$ ], the "original" transfer function  $G_{vd}(s)|_{Z_o(s)=0}$  is obtained. In the presence of the input filter,  $G_{vd}(s)$  is expressed according to Eq. (C.3):

$$G_{vd}(s) = \left( G_{vd}(s) \Big|_{Z_o(s) \rightarrow 0} \right) \left( \frac{1 + \frac{Z(s)}{Z_N(s)}}{1 + \frac{Z(s)}{Z_D(s)}} \right) \quad (\text{C.44})$$

where

$$Z_D(s) = Z_i(s) \Big|_{\hat{d}(s)=0} \quad (\text{C.45})$$

**Fig. C.18** Determination of the control-to-output transfer function  $G_{vd}(s)$  for the system of Fig. C.17.



is the impedance seen looking into the power input port of the converter when  $\hat{d}$  is set to zero, and

$$Z_N(s) = Z_i(s) \Big|_{\dot{v}(t) \xrightarrow{\text{null}} 0} \quad (\text{C.46})$$

is the impedance seen looking into the power input port of the converter when the converter output  $\hat{v}$  is nulled. The null condition is achieved by injecting a test current source  $\dot{i}_{test}$  at the converter input port, in the presence of  $\hat{d}$  variations, and adjusting  $\dot{i}_{test}$  such that  $\hat{v}$  is nulled. Derivation of expressions for  $Z_N(s)$  and  $Z_D(s)$  for a buck converter example is described in Section 10.3.1.

According to Eq. (C.28), the input filter does not significantly affect  $G_{vd}(s)$  provided that

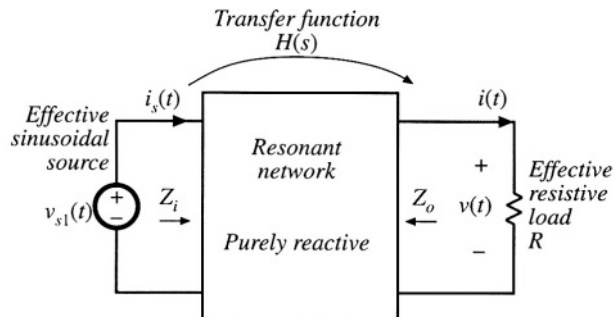
$$\begin{aligned} |Z_o(j\omega)| &\ll |Z_N(j\omega)| \\ |Z_o(j\omega)| &\ll |Z_D(j\omega)| \end{aligned} \quad (\text{C.47})$$

These inequalities can provide an effective set of criteria for designing the input filter. Bode plots of  $\|Z_N(j\omega)\|$  and  $\|Z_D(j\omega)\|$  are constructed, and then the filter element values are chosen to satisfy (C.47). Several examples of this procedure are explained in Chapter 10.

#### C.4.4 Dependence of Transistor Current on Load in a Resonant Inverter

The conduction loss caused by circulating tank currents is a major problem in resonant converter design. These currents are independent of, or only weakly dependent on, the load current, and lead to poor efficiency at light load. The origin of this problem is the weak dependence of the tank network input impedance on the load resistance. For example, Fig. C.19 illustrates the model of the ac portion of a resonant inverter, derived using the sinusoidal approximation of Section 19.1. The resonant network contains the tank inductors and capacitors of the converter, and the load is the resistance  $R$ . The current  $i_s(t)$  flowing in the effective sinusoidal source is equal to the switch current. This model predicts that the switch current  $i_s(s)$  is equal to  $v_{s1}(s)/Z_i(s)$ , where  $Z_i(s)$  is the input impedance of the resonant tank network. If we want the switch current to track the load current, then at the switching frequency  $\|Z_i\|$  should be dominated by, or at least strongly influenced by, the load resistance  $R$ . Unfortunately, this is often not consistent with other requirements, in which  $Z_i$  is dominated by the impedances of the tank elements. To design a resonant converter that exhibits good properties, the engineer must develop physical insight into how the load resistance  $R$  affects the tank input impedance and output voltage.

Fig. C.19 Resonant inverter model.



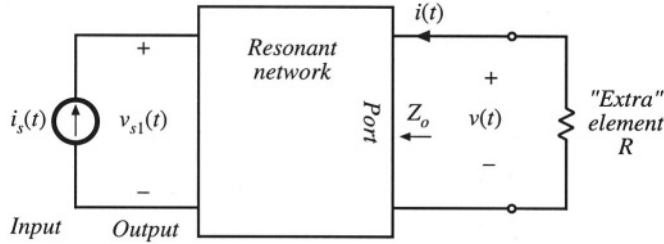


**Fig. C.20** Application of the Extra Element Theorem to the system of Fig. C.19, to expose the dependence of  $Z_i(s)$  on  $R$ .

To expose the dependence of  $Z_i(s)$  on the load resistance  $R$ , we can treat  $R$  as the “extra” element as in Fig. C.20. The input impedance  $Z_i(s)$  is viewed as the transfer function from the current  $i_s$  to the voltage  $v_{s1}$ ; in this sense,  $i_s$  is the “input” and  $v_{s1}$  is the “output.” Equations (C.2) and (C.3) then imply that  $Z_i(s)$  can be expressed as follows:

$$Z_i(s) = \frac{v_{s1}(s)}{i_s(s)} = Z_{i0}(s) \frac{\left(1 + \frac{R}{Z_N(s)}\right)}{\left(1 + \frac{R}{Z_D(s)}\right)} = Z_{i\infty}(s) \frac{\left(1 + \frac{Z_N(s)}{R}\right)}{\left(1 + \frac{Z_D(s)}{R}\right)} \quad (\text{C.48})$$

Here, the impedance  $Z_{i0}(s)$  is

$$Z_{i0}(s) = Z_i(s) \Big|_{R \rightarrow 0} \quad (\text{C.49})$$

i.e., the input impedance  $Z_i(s)$  when the load terminals are shorted. Likewise, the impedance  $Z_{i\infty}(s)$  is

$$Z_{i\infty}(s) = Z_i(s) \Big|_{R \rightarrow \infty} \quad (\text{C.50})$$

which is the input impedance  $Z_i(s)$  when the load is disconnected (open circuited).

Determination of  $Z_N(s)$  and  $Z_D(s)$  is illustrated in Fig. C.21. The quantity  $Z_N(s)$  is found by nulling the “output”  $v_{s1}$  to zero, and then solving for  $v(s)/i(s)$ . The quantity  $Z_N(s)$  coincides with the conventional output impedance  $Z_o(s)$  illustrated in Fig. C.19. In Fig. C.21(a), the act of nulling  $v_{s1}$  is equivalent to shorting the source  $v_{s1}$  of Fig. C.19. In Section 19.4, the quantity  $Z_N(s)$  is denoted  $Z_{o0}(s)$ , because it coincides with the converter output impedance with the switch network shorted.

The quantity  $Z_D(s)$  is found by setting the “input”  $i_s$  to zero, and then solving for  $v(s)/i(s)$ . The quantity  $Z_D(s)$  coincides with the output impedance  $Z_o(s)$  illustrated in Fig. C.19, under the conditions that the source  $v_{s1}$  is open-circuited. In Section 19.4, the quantity  $Z_D(s)$  is denoted  $Z_{o\infty}(s)$ , because it coincides with the converter output impedance with the switch network open-circuited.

The reciprocity relationship, Eq. (C.4), becomes

$$\frac{Z_{i\infty}(s)}{Z_{i0}(s)} = \frac{Z_{o\infty}(s)}{Z_{o0}(s)} \quad (\text{C.51})$$

The above results are used in Section 19.4 to expose how conduction losses and the zero-voltage switching boundary depend on the loading of a resonant converter.

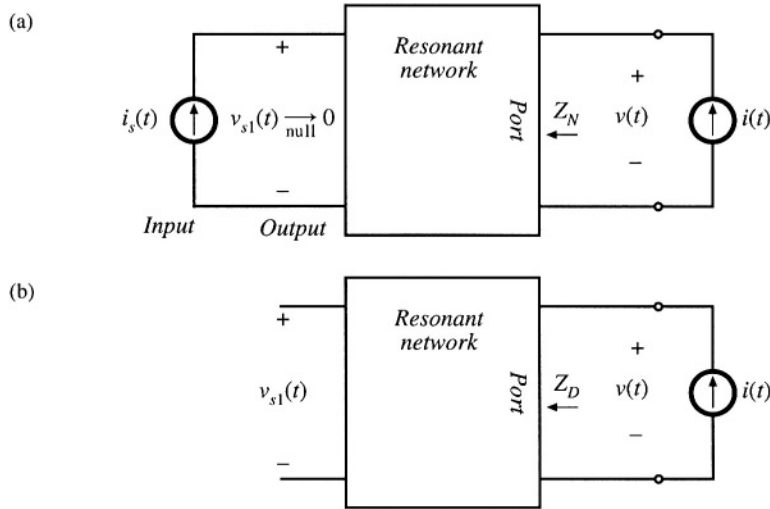


**Fig. C.21** Determination of the quantities  $Z_N(s)$  and  $Z_D(s)$  for the network of Fig. C.20: (a) finding  $Z_N(s)$ , (b) finding  $Z_D(s)$ .

## REFERENCES

- [1] R. D. MIDDLEBROOK, "Null Double Injection and the Extra Element Theorem," *IEEE Transactions on Education*, vol. 32, No. 3, Aug. 1989, pp. 167-180.
- [2] R. D. MIDDLEBROOK, "The Two Extra Element Theorem," *IEEE Frontiers in Education Conference Proceedings*, Sept. 1991, pp. 702-708.
- [3] R. D. MIDDLEBROOK, V. VORPERIAN, AND J. LINDAL, "The N Extra Element Theorem," *IEEE Transactions on Circuits and Systems I: Fundamental Theory and Applications*, Vol. 45, No. 9, Sept. 1998, pp. 919-935.

---

# Appendix D

## Magnetics Design Tables

---

Geometrical data for several standard ferrite core shapes are listed here. The geometrical constant  $K_g$  is a measure of core size, useful for designing inductors and transformers that attain a given copper loss [1]. The  $K_g$  method for inductor design is described in Chapter 14.  $K_g$  is defined as

$$K_g = \frac{A_c^2 W_A}{MLT} \quad (\text{D.1})$$

where  $A_c$  is the core cross-sectional area,  $W_A$  is the window area, and  $MLT$  is the winding mean-length-per-turn. The geometrical constant  $K_{gfe}$  is a similar measure of core size, which is useful for designing ac inductors and transformers when the total copper plus core loss is constrained. The  $K_{gfe}$  method for magnetics design is described in Chapter 15.  $K_{gfe}$  is defined as

$$K_{gfe} = \frac{W_A A_c^{2(1-1/\beta)}}{MLT \ell_m^{2\beta}} u(\beta) \quad (\text{D.2})$$

where  $\ell_m$  is the core mean magnetic path length, and  $\beta$  is the core loss exponent:

$$P_{fe} = K_{fe} B_{max}^\beta \quad (\text{D.3})$$

For modern ferrite materials,  $\beta$  typically lies in the range 2.6 to 2.8. The quantity  $u(\beta)$  is defined as

$$u(\beta) = \left| \left( \frac{\beta}{2} \right)^{-\left( \frac{\beta}{\beta+2} \right)} + \left( \frac{\beta}{2} \right)^{\left( \frac{2}{\beta+2} \right)} \right|^{-\left( \frac{\beta+2}{\beta} \right)} \quad (\text{D.4})$$

$u(\beta)$  is equal to 0.305 for  $\beta = 2.7$ . This quantity varies by roughly 5% over the range  $2.6 \leq \beta \leq 2.8$ . Values of  $K_{gfe}$  are tabulated for  $\beta = 2.7$ ; variation of  $K_{gfe}$  over the range  $2.6 \leq \beta \leq 2.8$  is typically quite small.

Thermal resistances are listed in those cases where published manufacturer's data are available. The thermal resistances listed are the approximate temperature rise from the center leg of the core to ambient, per watt of total power loss. Different temperature rises may be observed under conditions of forced air cooling, unusual power loss distributions, etc. Listed window areas; are the winding areas for conventional single-section bobbins.

An American Wire Gauge table is included at the end of this appendix.

## D.1 POT CORE DATA

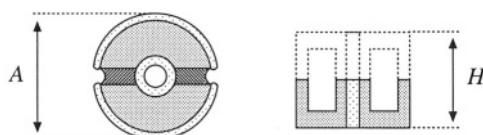
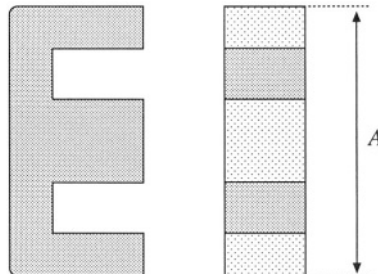


Fig. D.1

Core type (AH) (mm)	Geometrical constant $K_g$ cm <sup>5</sup>	Geometrical constant $K_{gfe}$ cm <sup>x</sup>	Cross-sectional area $A_c$ (cm <sup>2</sup> )	Bobbin winding area $W_A$ (cm <sup>2</sup> )	Mean length per turn $MLT$ (cm)	Magnetic path length $\ell_m$ (cm)	Thermal resistance $R_{th}$ (°C/W)	Core weight (g)
704	$0.738 \cdot 10^{-6}$	$1.61 \cdot 10^{-6}$	0.070	$0.22 \cdot 10^{-3}$	1.46	1.0		0.5
905	$0.183 \cdot 10^{-3}$	$256 \cdot 10^{-6}$	0.101	0.034	1.90	1.26		1.0
1107	$0.667 \cdot 10^{-3}$	$554 \cdot 10^{-6}$	0.167	0.055	2.30	1.55		1.8
1408	$2.107 \cdot 10^{-3}$	$1.1 \cdot 10^{-3}$	0.251	0.097	2.90	2.00	100	3.2
1811	$9.45 \cdot 10^{-3}$	$2.6 \cdot 10^{-3}$	0.433	0.187	3.71	2.60	60	7.3
2213	$27.1 \cdot 10^{-3}$	$4.9 \cdot 10^{-3}$	0.635	0.297	4.42	3.15	38	13
2616	$69.1 \cdot 10^{-3}$	$8.2 \cdot 10^{-3}$	0.948	0.406	5.28	3.75	30	20
3019	0.180	$14.2 \cdot 10^{-3}$	1.38	0.587	6.20	4.50	23	34
3622	0.411	$21.7 \cdot 10^{-3}$	2.02	0.748	7.42	5.30	19	57
4229	1.15	$41.1 \cdot 10^{-3}$	2.66	1.40	8.60	6.81	13.5	104

## D.2 EE CORE DATA



**Fig. D.2**

Core type (A) (mm)	Geometrical constant $K_g$ (cm <sup>5</sup> )	Geometrical constant $K_{gfe}$ (cm <sup>5</sup> )	Cross-sectional area $A_c$ (cm <sup>2</sup> )	Bobbin winding area $W_A$ (cm <sup>2</sup> )	Mean length per turn $MLT$ (cm)	Magnetic path length $\ell_m$ (cm)	Core weight (g)
EE12	$0.731 \cdot 10^{-3}$	$0.458 \cdot 10^{-3}$	0.14	0.085	2.28	2.7	2.34
EE16	$2.02 \cdot 10^{-3}$	$0.842 \cdot 10^{-3}$	0.19	0.190	3.40	3.45	3.29
EE19	$4.07 \cdot 10^{-3}$	$1.3 \cdot 10^{-3}$	0.23	0.284	3.69	3.94	4.83
EE22	$8.26 \cdot 10^{-3}$	$1.8 \cdot 10^{-3}$	0.41	0.196	3.99	3.96	8.81
EE30	$85.7 \cdot 10^{-3}$	$6.7 \cdot 10^{-3}$	1.09	0.476	6.60	5.77	32.4
EE40	0.209	$11.8 \cdot 10^{-3}$	1.27	1.10	8.50	7.70	50.3
EE50	0.909	$28.4 \cdot 10^{-3}$	2.26	1.78	10.0	9.58	116
EE60	1.38	$36.4 \cdot 10^{-3}$	2.47	2.89	12.8	11.0	135
EE70/68/19	5.06	$75.9 \cdot 10^{-3}$	3.24	6.75	14.0	18.0	280

## D.3 EC CORE DATA

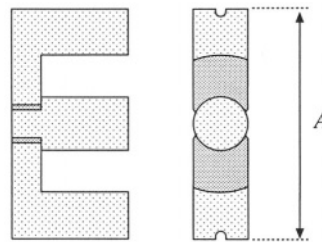


Fig. D.3

Core type	Geometrical constant	Geometrical constant	Cross-sectional area	Bobbin winding area	Mean length per turn	Magnetic path length	Thermal resistance	Core weight
(A) (mm)	$K_g$ (cm <sup>5</sup> )	$K_{gfe}$ (cm <sup>4</sup> )	$A_c$ (cm <sup>2</sup> )	$W_A$ (cm <sup>2</sup> )	MLT (cm)	$\ell_m$ (cm)	$R_{th}$ (°C/W)	(g)
EC35	0.131	$9.9 \cdot 10^{-3}$	0.843	0.975	5.30	7.74	18.5	35.5
EC41	0.374	$19.5 \cdot 10^{-3}$	1.21	1.35	5.30	8.93	16.5	57.0
EC52	0.914	$31.7 \cdot 10^{-3}$	1.80	2.12	7.50	10.5	11.0	111
EC70	2.84	$56.2 \cdot 10^{-3}$	2.79	4.71	12.9	14.4	7.5	256

## D.4 ETD CORE DATA

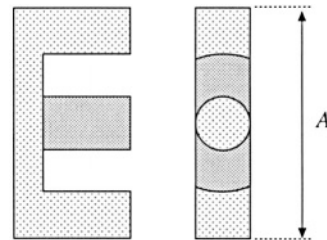
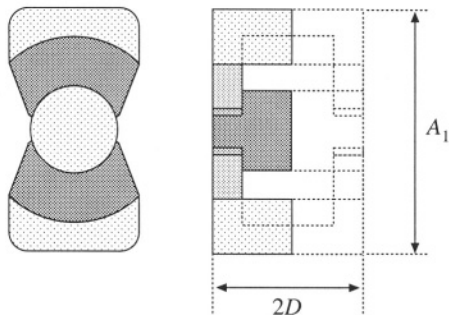


Fig. D.4

Core type	Geometrical constant	Geometrical constant	Cross-sectional area	Bobbin winding area	Mean length per turn	Magnetic path length	Thermal resistance	Core weight
(A) (mm)	$K_g$ (cm <sup>5</sup> )	$K_{gfe}$ (cm <sup>4</sup> )	$A_c$ (cm <sup>2</sup> )	$W_A$ (cm <sup>2</sup> )	MLT (cm)	$\ell_m$ (cm)	$R_{th}$ (°C/W)	(g)
ETD29	0.0978	$8.5 \cdot 10^{-3}$	0.76	0.903	5.33	7.20	30	
ETD34	0.193	$13.1 \cdot 10^{-3}$	0.97	1.23	6.00	7.86	19	40
ETD39	0.397	$19.8 \cdot 10^{-3}$	1.25	1.74	6.86	9.21	15	60
ETD44	0.846	$30.4 \cdot 10^{-3}$	1.74	2.13	7.62	10.3	12	94
ETD49	1.42	$41.0 \cdot 10^{-3}$	2.11	2.71	8.51	11.4	11	124

### D.5 PQ CORE DATA



**Fig. D.5**

Core type	Geometrical constant $(A_1/2D)$ (mm)	Geometrical constant $K_g$ ( $\text{cm}^5$ )	Cross-sectional area $A_c$ ( $\text{cm}^2$ )	Bobbin winding area $W_A$ ( $\text{cm}^2$ )	Mean length per turn $MLT$ (cm)	Magnetic path length $\ell_m$ (cm)	Core weight (g)
PQ 20/16	$22.4 \cdot 10^{-3}$	$3.7 \cdot 10^{-3}$	0.62	0.256	4.4	3.74	13
PQ 20/20	$33.6 \cdot 10^{-3}$	$4.8 \cdot 10^{-3}$	0.62	0.384	4.4	4.54	15
PQ 26/20	$83.9 \cdot 10^{-3}$	$7.2 \cdot 10^{-3}$	1.19	0.333	5.62	4.63	31
PQ 26/25	0.125	$9.4 \cdot 10^{-3}$	1.18	0.503	5.62	5.55	36
PQ 32/20	0.203	$11.7 \cdot 10^{-3}$	1.70	0.471	6.71	5.55	42
PQ 32/30	0.384	$18.6 \cdot 10^{-3}$	1.61	0.995	6.71	7.46	55
PQ 35/35	0.820	$30.4 \cdot 10^{-3}$	1.96	1.61	7.52	8.79	73
PQ 40/40	1.20	$39.1 \cdot 10^{-3}$	2.01	2.50	8.39	10.2	95

**D.6 AMERICAN WIRE GAUGE DATA**

AWG#	Bare area, $10^{-3} \text{ cm}^2$	Resistance, $10^{-6} \Omega/\text{cm}$	Diameter, cm
0000	1072.3	1.608	1.168
000	850.3	2.027	1.040
00	674.2	2.557	0.927
0	534.8	3.224	0.825
1	424.1	4.065	0.735
2	336.3	5.128	0.654
3	266.7	6.463	0.583
4	211.5	8.153	0.519
5	167.7	10.28	0.462
6	133.0	13.0	0.411
7	105.5	16.3	0.366
8	83.67	20.6	0.326
9	66.32	26.0	0.291
10	52.41	32.9	0.267
11	41.60	41.37	0.238
12	33.08	52.09	0.213
13	26.26	69.64	0.190
14	20.02	82.80	0.171
15	16.51	104.3	0.153
16	13.07	131.8	0.137
17	10.39	165.8	0.122
18	8.228	209.5	0.109
19	6.531	263.9	0.0948
20	5.188	332.3	0.0874
21	4.116	418.9	0.0785
22	3.243	531.4	0.0701
23	2.508	666.0	0.0632
24	2.047	842.1	0.0566
25	1.623	1062.0	0.0505
26	1.280	1345.0	0.0452
27	1.021	1687.6	0.0409
28	0.8046	2142.7	0.0366
29	0.6470	2664.3	0.0330

Continued

AWG#	Bare area, $10^{-3} \text{ cm}^2$	Resistance, $10^{-6} \Omega/\text{cm}$	Diameter, cm
30	0.5067	3402.2	0.0294
31	0.4013	4294.6	0.0267
32	0.3242	5314.9	0.0241
33	0.2554	6748.6	0.0236
34	0.2011	8572.8	0.0191
35	0.1589	10849	0.0170
36	0.1266	13608	0.0152
37	0.1026	16801	0.0140
38	0.08107	21266	0.0124
39	0.06207	27775	0.0109
40	0.04869	35400	0.0096
41	0.03972	43405	0.00863
42	0.03166	54429	0.00762
43	0.02452	70308	0.00685
44	0.0202	85072	0.00635

## REFERENCES

- [1] C. W. T. McLYMAN, *Transformer and Inductor Design Handbook*, Second edition, New York: Marcel Dekker, 1988.
- [2] *Ferrite Materials and Components Catalog*, Philips Components.

---

# Index

---

- Air gap  
in coupled inductor, 529, 551, 553  
in flyback transformer, 530, 559  
in inductor, 499-501, 525-526, 539-542, 544  
in transformer, 504
- $A_L$  (mH/1000 turns), 545
- American wire gauge (AWG)  
data, 868-869  
design examples, 557, 560, 575, 580
- Amorphous alloys, 507
- Ampere's law, 493-494
- Amp-second balance (*see* Capacitor charge balance)
- Apparent power, 598
- Artificial ramp  
circuit, 446  
effect on CPM boost low-harmonic rectifier, 654-656  
effect on line-to-output transfer function of CCM buck, 466-469  
effect on small-signal CCM models, 459-466  
effect on small-signal DCM models, 473-480  
effect on stability of CPM controllers, 444-449
- Asymptotes (*see* Bode plots)
- Audiosusceptibility  $G_{\text{yr}}(s)$  (*see* Line-to-output transfer function)
- Average current control  
feedforward, 650-652  
in low-harmonic rectifier systems, 648-654  
modeling of, 652-654
- Averaged switch modeling, 226-247  
of current-programmed CCM converters, 454-459  
of current-programmed DCM converters, 473-480  
in discontinuous conduction mode, 410-431  
equivalent circuit modeling of conduction losses, 242-244, 816-818
- equivalent circuit modeling of switching losses, 244-247
- examples  
nonideal buck converter, 244-247  
nonideal buck-boost converter, 242-244  
CCM SEPIC, 228-235  
of ideal CCM switch networks, 226-241, 815-816, 822-825  
of ideal DCM switch networks, 416, 822-825  
of quasi-resonant converters, 768-790
- Average power  
and Fourier series, 590-593  
modeled by power source element, 414-418, 454-459, 473-480  
in nonsinusoidal systems, 590-603  
predicted by averaged models, 56  
power factor, 594-598  
sinusoidal phasor diagram, 598-599
- Averaging  
approximation, discussion of, 189-190, 194-196  
averaged switch modeling, 226-247  
basic approach, 192-204  
capacitor charge balance, 21-22  
circuit, 226-247  
to find dc component, 5, 14  
flyback ac model, 209-218  
inductor volt-second balance, 20-21  
introduction to, 187-192  
modeling efficiency and loss via, 56  
to model rectifier output, 668-670  
to model 3 $\phi$  converters, 685-690  
of quasi-resonant converters, 768-790  
state-space, 213-226
- Ballast, electronic 705-707

- resonant inverter design, 726-740
- Battery charger, 8, 70
- B-H* loop
  - in an ac inductor, 527-528
  - in a conventional transformer, 148, 528
  - in a coupled inductor, 529-530
  - in a filter inductor, 526-527
  - in a flyback transformer, 530-531
  - modeling of, 494-495
- Bidirectional dc-dc converters, 70
- Bipolar junction transistor (BJT)
  - breakdown mechanisms in, 85-86
  - construction and operation of, 81-86
  - current crowding, 84-85
  - Darlington-connected, 86
  - idealized switch characteristics, 65-66
  - on resistance, 52, 81-82
  - quasi-saturation, 82, 85
  - storage time, 84
  - stored minority charge in, 81-85
  - switching waveforms, 82-84
- Bode plots (*see also* Harmonic trap filters, Sinusoidal approximation)
  - asymptote analytical equations, 281
  - CCM buck-boost example, 294-299
  - combinations, 278-281
  - complex poles, 282-286
  - frequency inversion, 277-278
  - graphical construction of, 302-317
    - addition, 303-307
    - closed-loop transfer functions, 337-340
    - division, 311-313
    - parallel combination, 308-310
    - parallel resonance, 309-310
    - series resonance, 305-307
  - impedance graph paper, 310
  - nonminimum phase zero, 276
  - reactance graph paper, 310
  - real pole, 269-274
  - real zero, 275
  - RHP zero, 276
  - transfer functions of buck, boost, buck-boost, 300
- Body diode (*see* MOSFET)
- Boost converter (*see also* Bridge configuration, Push-pull isolated converters)
  - active switch utilization in, 173, 676
  - averaged switch model, DCM, 419-420
  - circuit-averaged model, 235-239
  - current-programmed
    - averaged switch model, CCM, 455-456
    - averaged switch model, DCM, 477
    - small-signal ac model, CCM, 458-459, 460-463,
  - 469-470
  - small-signal ac model, DCM, 478-480
  - as inverted buck converter, 132-133
  - as low-harmonic rectifier, 642-646, 648-663, 666, 674-685, 832-834
  - nonideal analysis of, 42-49, 52-56
  - quasi-resonant ZCS, 778-779
  - simulation example, 832-834
  - small-signal ac model
    - CCM, 204-205, 252-253
    - DCM, 424-429
  - steady-state analysis of,
    - CCM, 22-27
    - DCM, 117-124
  - transfer functions, CCM, 300
- Bridge configuration (dc-dc converters)
  - boost-derived full bridge, 165-166
  - buck-derived full bridge, 149-152
  - buck-derived half bridge, 152-154
  - full bridge transformer design example, 576-580
  - minimization of transformer copper loss in, 549-550
- Bridge configuration (inverters)
  - single phase, 7-8, 138-141, 143-145
  - three phase, 70, 141-143
- Buck-boost converter (*see also* Flyback converter)
  - averaged switch model, DCM, 410-420
  - as cascaded buck and boost converters, 134-136
  - current-programmed
    - averaged switch model, DCM, 473-477
    - more accurate model, CCM, 461-463
    - simple model, CCM, 450-454
    - small-signal ac model, DCM, 478-480
  - dc-3øac inverter, 71-72
  - DCM characteristics, 112, 124-125, 420
  - as low-harmonic rectifier, 645-646, 650
  - manipulation of ac model into canonical form, 250-252
  - nonideal, state-space averaged model of, 221-226
  - noninverting version, 135, 143-144
  - as rotated three-terminal cell, 137
  - simulation of, 819-822
  - small-signal ac model, CCM, 204-205, 252-253
  - small-signal ac model, DCM, 420-425
  - transfer functions, CCM, 294-300
  - transformer isolation in, 161-165
- Buck converter (*see also* Bridge configuration, Forward converter, Push-pull isolated converters), 5-6, 13-22, 31-33
  - active switch utilization in, 173
  - averaged switch model, 239-241
  - current-programmed
    - averaged switch model, CCM, 454-457

- averaged switch model, DCM, 477-478
- small-signal ac model, CCM, 453, 462, 466-470
- small-signal ac model, DCM, 477-480
- equivalent circuit modeling of,
  - small-signal ac, CCM, 204-205, 253
  - small-signal ac, DCM, 424-426
  - steady-state, CCM, 50-52
  - steady-state, DCM, 420
- as high power factor rectifier, 646
- multi-resonant realization, 784-786
- quasi-square-wave resonant realizations, 787-790
- quasi-resonant realizations
  - zero current switching, 708, 768-782
  - zero voltage switching, 783-784
- simulation examples
  - current programmed control, 837-839
  - voltage regulator, 827-831
- small-signal ac model
  - CCM, 204-205, 253
  - DCM, 424-427
- steady-state analysis of,
  - CCM, 13-22, 31-33, 50-52
  - DCM, 111-117, 418-420
- switching loss in, 93-100, 244-247
- employing synchronous rectifier, 73-74
- transfer functions, CCM, 300
- Buck<sup>2</sup>** converter, 145-146
- Buck 3ø inverter (*see* Voltage source inverter)
  
- Canonical circuit model, 248-253
  - manipulation into canonical form, 250-253
  - parameters for buck, boost, buck-boost, 253
  - physical development of, 248-250
  - transfer functions predicted by, 248-250
- Capacitor amp-second balance (*see* Capacitor charge balance)
- Capacitor charge balance
  - boost converter example, 24-25
  - Ćuk converter example, 29-30
  - definition, 22
  - in discontinuous conduction mode, 115
  - nonideal boost converter examples, 44, 54
- Capacitor voltage ripple
  - boost converter example, 26-27
  - buck converter example, 31-33
  - in converters containing two-pole filters, 31-33
  - Ćuk converter example, 30-31
- Cascade connection of converters, 134-137
- Characteristic value  $\alpha$  (current programmed mode), 445, 448
- Charge balance (*see* Capacitor charge balance)
- Circuit averaging (*see also* Averaged switch modeling),
  - 226-247
  - averaging step, 229-231
  - examples
    - buck, 239-241
    - boost, 235-239
    - SEPIC, 228-234
  - linearization, 232-235
  - obtaining a time-invariant network, 228-229
  - summary of, 226-227
- Commutation
  - failure, 621
  - notching, 622
  - in 3ø phase controlled rectifier, 620-622
- Compensators (*see also* Control system design)
  - design example, 354-362, 827-831
  - lag, 351-353
  - lead, 348-351, 358-359
  - PD, 348-351, 358-359
  - PI, 351-353
  - PID, 353-354, 359-362
- Complex power, 598, 620
- Computer power supply, 7-8
- Computer spreadsheet, design using, 174-176
- Conduction loss (*see* Copper loss, Semiconductor conduction loss)
- Conductivity modulation, 74-76, 78, 82, 83, 87, 89
- Control system design (*see also* Compensators, Negative feedback), 331-376
  - compensation, 348-354
  - construction of closed-loop transfer functions, 334-340
  - design example, 354-362, 827-831
  - for low-harmonic rectifiers
    - approaches, 648-663, 668-673
    - modeling, 652-653, 668-673
  - phase margin
    - test, 341-342
    - vs. closed-loop damping factor, 342-345
  - stability, 340-347
  - voltage regulator
    - block diagram, 332-333, 336, 355-357
    - design specifications, 347-348
- Control-to-output transfer function
  - as predicted by canonical model, 248-250
  - of CCM buck, boost, and buck-boost converters, 300
  - of current programmed converters, 453, 458-459, 464-472, 480
  - of DCM converters, 426-427, 433
  - input filter, effect on, 380-382
- Conversion ratio  $M$  (*see also* Switch conversion ratio  $\mu$ )
  - of boost, 16, 24, 123, 420
  - of buck, 16, 116-117, 420

- of buck-boost, 16, 124, 420
- of Ćuk converter, 29-30, 420
- of loss-free resistor networks, 416-418
- in low-harmonic rectifiers, 641-642
- modeling of, 39-42
- of quasi-resonant converters, 762, 770, 778
- of parallel resonant converter, 719-721, 748-752
- of SEPIC, 146, 420
- of series resonant converter, 716-718, 740-748
- via sinusoidal approximation, 714-715
- Copper loss**
  - allocation of window area to minimize, 545-550, 567-568
  - high frequency effects
    - skin effect, 508-510
    - proximity effect, 510-525
  - inductor design to meet specified, 539-545
  - low frequency, 508
  - modeling in converters, 43-53
  - multiple winding design to meet specified, 545-554
- Core loss, 506-507, 527-529, 560-562, 565-567
- Correction factor (*see also* Extra element theorem), 384, 844, 849
- Coupled inductors, 529-530, 545, 550-554
  - in Ćuk converter, 534-535, 529
  - design of, 545-554
  - in multiple-output buck-derived converters, 529-530, 554-557
- Crossover frequency, 338-346
- Ćuk converter**
  - active switch utilization of, 173
  - as cascaded boost and buck converters, 136-137
  - conversion ratio  $M(D)$ , 30, 420
  - DCM averaged switch model of, 418-420
  - as low-harmonic rectifier, 645-646, 650, 676
  - as rotated three-terminal cell, 136-137
  - steady-state analysis of, 27-31
  - transformer design example, 573-576
  - with transformer isolation, 170-171
- Current-fed bridge, 144-145
- Current injection, 367-368
- Current programmed control, 439-487
  - ac modeling of
    - via averaged switch modeling, CCM, 454-459
    - via averaged switch modeling, DCM, 473-480
    - CCM more accurate model, 459-473
    - CCM simple approximation, 449-459
    - artificial ramp, 445-449
  - controller circuit, 440, 446
  - controller small-signal block diagram, 459-464
  - in full-bridge buck converters, 152
  - in half-bridge buck converters, 154, 441
- in low harmonic rectifiers, 654-656
- oscillation for  $D > 0.5$ , 441-449
- in push-pull buck converters, 160, 441
- Current ripple** (*see* inductor current ripple)
- Current sense circuit, isolated, 181-182
- Current source inverter (CSI), 142-143
- Cycloconverter, 1, 72-73
- Damping** (*see also*  $Q$ -factor, Input filters)
  - factor  $\zeta$ , 283
  - of input filters, 380, 385-392
  - optimal, 392-398
  - vs. overshoot, 346-347
- DC conversion ratio (*see* Conversion ratio  $M$ )
- DC link, 8-9
- DC transformer model**
  - in averaged switch models, 232-235, 237-241, 247
  - in canonical model, 248-253
  - comparison with DCM model, 410
  - derivation of, 40-42
  - equivalence with dependent sources, 40
  - manipulation of circuits containing, 41-42, 47-48
  - in a nonideal boost converter, 47-48, 55
  - in a nonideal buck converter, 51
  - in small-signal ac CCM models, 204-205, 212-213
- Decibel, 267-268
- Delta-wye transformer connection, 628-629
- Dependent power source (*see* Power source element)
- Derating factor, 174
- Design-oriented analysis, techniques of
  - analytical expressions for asymptotes, 281
  - approximate factorization, 289-293
  - doing algebra on the graph, 302-317
  - extra element theorem, 843-861
  - frequency inversion, 277-278
  - graphical construction
    - of Bode plots, 302-317
    - of closed-loop transfer functions, 337-340
  - input filter design inequalities, 381-385, 392, 399
  - load-dependent properties of resonant inverters, 726-740
  - low  $Q$  approximation, 287-289
  - philosophy of, 267, 302-303
- Differential connection of load
  - polyphase inverter, 141-143
  - single-phase inverter, 138-141
- Diode**
  - antiparallel, 67
  - characteristics of, 77
  - fast recovery, 77
  - forward voltage drop (*see also* Semiconductor conduction losses), 52-55, 77

- freewheeling, 67
- parallel operation of, 77
- recovered charge  $Q_r$ , 76-77, 96-98, 722, 763-764, 781
- recovery mechanisms, 76-77, 96-98
- Schottky, 74, 77, 99
- soft recovery, 97-98
- snubbing of, 97, 99, 764-765
- switching loss, 96-100, 763-765
- switching waveforms, 76-77, 97, 100, 763-765
- zero current switching of, 764, 783
- zero voltage switching of, 722-724, 781, 784-785, 787
- Discontinuous conduction mode (DCM)
  - $B-H$  loop, effect on, 530-531
  - boost converter example, 117-124
  - buck converter example, 108-117
  - buck-boost converter example, 410-418
  - in current programmed converters, 473-480
  - equivalent circuit modeling of, 409-420, 473-477
  - in forward converter, 158
  - in line-commutated rectifiers, 611-614, 616-617
  - in low-harmonic rectifiers
    - boost rectifier, 643-646, 832-834
    - flyback rectifier, 646-648
  - mode boundary
    - in boost rectifier, 643-646
    - vs.  $K$ , 110-112, 118-119, 123-124
    - vs. load current and  $R_e$ , 418
    - origin of, 108-112
  - in parallel resonant converter, 749-752
  - in PWM converters, 107-130, 409-437, 473-480
  - in series resonant converter, 741-748
  - small-signal ac modeling of, 420-433
- Displacement factor, 596, 599
- Distortion factor (*see also* Total harmonic distortion), 596-597
  - of single-phase rectifier, 596, 610-613
- Distributed power system, 7
- Doing algebra on the graph (*see* Graphical construction of Bode plots)
- Duty ratio
  - complement of, 14
  - definition of, 14
- EC core data, 866
- Eddy currents
  - in magnetic cores, 506
  - in winding conductors, 508-511
- EE core data, 865
- Effective resistance  $R_e$ 
  - in DCM averaged switch model, 413-420
  - in loss-free resistor model, 413-420
  - in resonant converter models
    - with capacitive filter network, 711-713
    - with inductive filter network, 718-720
- Emulated resistance  $R_e$ , 638-640
- Efficiency, 2
  - averaged switch modeling, predicted by, 247
  - of boost converter
    - as low-harmonic rectifier, 683-685
    - nonideal dc-dc, 48-49, 55
  - calculation via averaged model, 48-49, 55
  - vs. switching frequency, 100-101
- Equivalent circuit modeling
  - by canonical circuit model, 247-253
  - of CCM converters operating in steady-state, 39-61
  - of converters having pulsating input currents, 50-52
  - of current programmed switch networks
    - CCM, 454-459
    - DCM, 473-480
      - small-signal models, 452-453, 457-459, 478-480
      - of flyback converter, CCM, 165, 212-213
      - of ideal rectifiers, 638-640, 658-686
      - of ideal dc-dc converters, 39-41
      - of inductor copper loss, 42-52
      - small-signal models, construction of
        - CCM, 201-203, 211-213, 225-226
        - DCM, 420-433
          - current programmed, 452-453, 457-459, 478-480
        - of switching loss, 246-247
      - of switch networks
        - CCM, 235-241
        - DCM, 410-420
      - of systems containing ideal rectifiers, 666
    - Equilibrium (*see* Steady state)
    - Equivalent series resistance (*esr*) of capacitor, 602-603
    - ETD core data, 866
    - Evaluation and design of converters, 171-176
    - Experimental techniques
      - measurement of impedances, 318-321
      - measurement of loop gains
        - by current injection, 367-368
        - by voltage injection, 364-367
        - of an unstable system, 368
      - measurement of small-signal transfer functions, 317-318
    - Extra element theorem, 843-861
      - applications of
        - input filter design, 381-392, 398-399, 857-859
        - transfer function, solving for, 850-855
        - unmodeled element, effects of, 855-857
        - resonant inverter, load dependence of, 731, 859-
      - 861

- basic result, 843-846
- correction factor, 384, 844, 849
  - deviation caused by, 850-852
- derivation, 846-849
- impedance inequalities, 849-850
- nulling, 845-846
- reciprocity relationship, 736, 845
- $Z_D$  driving-point impedance, 845
- $Z_N$  impedance, 845-846
- Factorization, approximate
  - approximate roots of arbitrary-degree polynomial, 289-293
  - graphical construction of Bode diagrams, 302-317
  - low- $Q$  approximation, 287-289
- Faraday's law, 492-493
- Feedback (*see* Control system design, Negative feedback)
- Ferrite
  - applications of, 528, 556, 557, 574, 577
  - core loss, 506-507, 527-529, 566
  - core tables, 863-867
  - saturation flux density, 495, 503, 507, 527
- Fill factor (*see*  $K_u$ )
- Filter design (*see* Input filter design)
- Filter inductor
  - $B-H$  loop of, 527
  - design of
    - derivation of procedure, 539-544
    - step-by-step procedure, 544-545
- Flux  $\Phi$ , 492
- Flux density  $B$ 
  - definition, 492
  - saturation value  $B_{sat}$ , 495
- Flux-linkage balance (*see* Inductor volt-second balance)
- Flyback converter (*see also* Buck-boost converter)
  - active switch utilization, 171-174
  - derivation of, 161-162
  - nonideal, ac modeling of, 204-213
  - rectifier, 646-648
  - spreadsheet design example, 174-176
  - steady-state analysis of, 161-165
  - two transistor version, 180
  - utilization of flyback transformer, 165
- Flyback transformer, 522, 530-531, 552
  - design example, 557-562
- Forced commutation of SCRs, 89-90
- Forward converter (*see also* Buck converter), 154-159
  - active switch utilization, 173
  - spreadsheet design example, 174-176
  - steady-state analysis of, 154-159
- transformer reset mechanisms, 157-158
- transformer utilization in, 159
- two transistor version, 158-159
- Four-quadrant switches (*see* Switch)
- Freewheeling diode, 67
- Gate turn-off thyristor (GTO), 90
- Geometrical constant (*see*  $K_g$ ,  $K_{gfe}$ )
- Graphical construction of Bode plots (*see also* Bode plots, Design-oriented analysis)
  - of converter transfer functions, 313-317
  - division, 311-313
  - of harmonic trap filters, 622-628
  - parallel combinations, 308-310
  - parallel resonance, 309-310
  - of parallel resonant converter, 720-721
  - series combinations, 303-307
  - series resonance, 305-307
  - of series resonant converter, 715-717
- Grounding problems, 319-321
- Gyrator, 744-745
- Harmonic correction, 690-691
- Harmonic loss factor  $F_H$ , 523-525
- Harmonics in power systems
  - average power vs. Fourier series, 590-593
  - distortion factor, 596
  - harmonic standards, 603-605
  - neutral currents, 599-600
  - power factor, 594-598
  - root-mean-square value of waveform, 593-596
  - rectifier harmonics, 597-598
  - in three-phase systems, 599-603
  - total harmonic distortion, 596
- Harmonic trap filters, 622-628
  - bypass resistor, 626-628
  - parallel resonance in, 624-626
  - reactive power in, 628
- H-bridge, 7, 139-141, 143-145
- Hold-up time, 665
- Hot spot formation, 77, 88
- Hysteresis loss  $P_H$ , 506
- Hysteretic control, 657-659
- Ideal rectifier (*see also* Low harmonic rectifiers)
  - in converter systems, 663-673
  - properties of, 638-640
  - realization of
    - single phase, 640-648
    - three phase, 687-691
  - rms values of waveforms in, 673-677
  - single phase, 638-642

- three phase, 685-687
- IEC 1000, 603-604
- IEEE/ANSI standard 519, 604
- Impedance graph paper, 310
- Inductor copper loss (*see* Copper loss)
- Inductor current ripple
  - in ac inductor, 527-528
  - boost example, 25-26
  - buck example, 19
  - calculation of, 19
  - in converters containing two-pole filters, 31-33
  - Cuk** converter example, 30-31
  - in filter inductor, 525-526
  - magnitude vs DCM, 108-110
- Inductor design
  - ac inductor design
    - derivation, 580-581
    - step-by-step procedure, 582-583
  - filter inductor design
    - derivation, 539-544
    - step-by-step procedure, 544-545
- Inductor volt-second balance
  - boost example, 24
  - buck example, 21
  - Cuk** converter example, 28-29
  - definition, 20
  - in discontinuous conduction mode, 112
- Input filters, 377-408, 857-859
  - cascaded filter sections, 398-404
    - noninteraction, impedance inequalities for, 398-399
    - two-section design example, 400-404
  - conducted EMI, attenuation of, 377-378
  - conducted susceptibility, 378
  - damping of, 391-404
    - $R_f-C_b$  parallel damping, 394, 395-396
    - $R_f-L_b$  parallel damping, 394, 396-397
    - $R_f-L_b$  series damping, 394, 398
  - effect on control-to-output transfer function
    - buck example, 380, 389-392
    - general result, 381-382
    - negative resistance oscillations, 382-384
    - results for basic converters, 382
    - right half-plane zeroes, 390
  - impedance inequalities for design
    - construction of, buck example, 385-389
    - control-to-output transfer function, to avoid changing, 384
    - output impedance, to avoid changing, 385
- Input port, converter
  - ac modeling of, 197
  - boost static characteristics, 643-644, 655-656
- modeling of, via state-space averaging, 222, 225-226
  - steady-state modeling of, 50-52
- Inrush current, 646, 665, 676
- Insulated-gate bipolar transistor (IGBT)
  - construction and operation of, 86-88
  - current tailing in, 87-88, 95-96
  - equivalent circuit, 87
  - forward voltage drop, modeling of, 88
  - idealized switch characteristics, 65-66
  - parallel operation of, 88
  - switching loss in, 95-96, 768
- Inversion of source and load, 132-133
- Inverters, 1
  - high frequency, 705-709, 727-729, 732-739
  - line commutated, 619
  - single phase, 7, 68-69, 138-141
  - sinusoidal analysis of resonant converters, 709-715, 726-740
  - three phase, 69-72, 141-143
- Iron laminations, 495, 507
- $K$ , dimensionless parameter
  - critical value  $K_{crit}(D)$ , 110-112, 116-117, 124
  - and DCM boundary, 110-112, 116-117, 124
  - in line-commutated rectifier analysis, 612-613
  - in steady-state DCM analysis, 117, 123-124
- $K_g$ , core geometrical constant
  - definition of, 543-544, 863
  - ferrite core tables of, 864-869
  - filter inductor design procedure using, 544-545
  - multiple winding magnetics design using, 545, 552-554
- $K_{kfe}$ , ac core geometrical constant
  - ac inductor design procedure using, 580-583
  - definition of, 569-570, 863
  - ferrite core tables of, 864-869
  - transformer design using,
    - derivation, 565-570
    - examples, 573-580
    - step-by-step procedure, 570-573
- $K_L$ , rectifier dimensionless parameter, 612-613
- $K_u$ , window utilization factor, 542
- LCC** resonant converter
  - dependence of transistor current on load, 732-733
  - design example, 737-740
  - introduction to, 705-707
  - ZVS/ZCS boundary, 734-737
- Lenz's law, 493, 506, 508, 510
- Linear ripple approximation (*see* Small ripple approximation)

- Line-to-output transfer function  $G_{vg}(s)$   
 of the buck, boost, and buck-boost converters in  
 CCM, 300  
 canonical model, as predicted by, 248  
 closed-loop, 334-335, 339-340  
 control system design of, 347-348, 361-362  
 of current-programmed converters, 454, 464-466,  
     469-471, 480  
 of DCM converters, 427  
 Litz wire, 522  
 Loop gain (*see also* Control system design, Negative feedback)  
     definition, 335  
     measurement of, 362-368  
 Loss-free resistor model  
     averaged switch model of discontinuous conduction mode, 413-420  
     ideal rectifier model  
         single phase, 638-640  
         three phase, 685-686  
 Low harmonic rectifiers (*see also* Ideal rectifiers)  
     controller schemes  
         average current control, 648-654  
         current programmed control, 654-656  
         critical conduction mode, 657-659  
         feedforward, 650-652  
         hysteretic control, 657-659  
         nonlinear carrier control, 659-663  
     modeling of  
         efficiency and losses, 678-685  
         low-bandwidth control loop, 668-673  
         wide-bandwidth average current control loop,  
             652-654  
     rms calculations in, 673-678  
 Low  $Q$  approximation, 287-289
- Magnetic circuits, 498-501  
 Magnetic field  $H$ , 491-492  
 Magnetic path length  $\ell_m$   
     definition, 497  
     ferrite core tables, 864-867  
 Magnetics, 489-586  
     ac inductor design, 580-583  
     basic relationships, 491-498  
     copper loss, 42-45, 508, 510-525  
     core loss, 42, 506-508, 561-562  
     coupled inductor design, 550-557  
     ferrite core tables, 864-867  
     flyback transformer design, 557-562  
     inductor design, 539-562  
     inductor design, multiple winding, 550-562  
     magnetic circuits, 498-501  
     magnetic devices, types of, 525-531  
     optimizing  $\Delta B$  to minimize total loss, 569-570  
     optimizing window allocation to minimize copper loss, 545-550  
     proximity effect, 508-525  
     transformer basics, 146-149, 501-505  
     transformer design, 565-583  
 Magnetizing current, 147-148, 502-504  
 Magnetomotive force (MMF)  
     definition, 491-492  
     magnetic circuit, in, 498-499  
     MMF diagrams, 512-514  
 Majority carrier devices (*see also* MOSFET, Schottky diode), 74-75  
 Matrix converter, 72-73  
 Mean length per turn (MLT)  
     definition, 543  
     ferrite core tables, 864-867  
 Measurement of transfer functions and loop gains (*see also* Experimental techniques)  
 Middlebrook's extra element theorem (*see* Extra element theorem)  
 Minority carrier devices (*see also* Bipolar junction transistor, Diode, Gate turn-off thyristor, Insulated-gate bipolar transistor, MOS-controlled thyristor, Silicon controlled rectifier), 74-75  
 Modulation index, 689-690  
 MOS-controlled thyristor (MCT), 91-92  
 MOSFET  
     body diode, 67-68, 78-79  
     conduction loss, modeling of, 52-56, 204-213, 816-819  
     construction and operation of, 78-81  
     on resistance, 52-56, 78-81  
     switching loss owing to  $C_{ds}$ , 98-99, 765-768  
     as synchronous rectifier, 73-74  
     terminal capacitances, 80-81  
     typical characteristics, 80-81  
     zero-voltage and zero-current switching of, 721-726, 765-768  
 Motor drive system, 8-9  
 Multiplying controller (*see also* Average current control, Current programmed control), 648-659  
 Multi-resonant switch, 784-786
- Negative feedback (*see also* Control system design)  
     effects of, on network transfer functions, 334-337  
     objectives of, 187, 331-334  
     reduction of disturbances by, 335-337  
     reduction of sensitivity to variations in forward gain by, 337  
 Nonlinear carrier control, 659-663

- Nonminimum-phase zero (*see* Right half-plane zero)
- Output characteristics
  - of the parallel resonant converter, 750
  - of resonant inverters, 727-729
  - of the series resonant converter, 747-748
- Overshoot, 346-347, 348
- Parallel resonant converter
  - analysis via sinusoidal approximation, 718-721
  - dependence of transistor current on load, 730-731
  - exact characteristics
    - continuous conduction mode, 748-751
    - control plane, 751
    - discontinuous conduction mode, 749-751
    - output plane, 750
  - introduction to, 705-706
- Permeability  $\mu$ 
  - definition, 494-495
  - of free space,  $\mu_0$ , 494
  - relative,  $\mu_r$ , 495
- Phase asymptotes
  - of complex poles, 284-285
  - inverted forms, 278
  - of real pole, 272-274
  - of real zero, 275
  - of RHP zero, 276
- Phase control
  - of resonant converters, 705
  - of three-phase rectifiers, 617-622
  - of zero-voltage transition dc-dc converter, 791-794
- Phase margin
  - vs. closed-loop damping factor, 342-346
  - input filter, undamped, effect on, 390-391
  - stability test, 341-342
- Poles
  - complex, Bode plots of, 282-286
  - the low  $Q$  approximation, 287-289
  - real, Bode plots of, 269-274
- Pot core data, 864
- Powdered iron, 495, 507
- Power factor (*see also* Total harmonic distortion, Displacement factor, Distortion factor)
  - definition of, 594-598
  - of bridge rectifier, single phase, 597, 610-613
  - of peak detection rectifier, 597
  - of phase-controlled rectifier, three phase, 616, 619-620
- Power sink element (*see* Power source element)
- Power source element
  - in averaged switch models
    - current programmed mode, CCM, 454-457
  - current programmed mode, DCM, 475-477
  - discontinuous conduction mode, 414-420
  - definition of, 415-416
  - in ideal rectifier model, 638-640, 646-647, 650, 666, 668-670, 686
  - linearization of, 383-384, 423-424, 457, 668-671
  - in loss-free resistor model, 416-417, 639-640
  - properties of, 415-416
  - in switched-mode regulators, 383-384, 455, 665-666
- PQ core data, 867
- Proximity effect
  - conductor spacing factor  $\eta$ , 515
  - interleaving, effect on, 520-522
  - layer copper loss, 515-517
  - Litz wire, effect of, 522
  - MMF diagrams, 512-514
  - PWM waveform harmonics, 522-525
  - simple explanation, 508-512
  - transformer design procedure, accounting for, 572
  - winding loss, total, 518-520
- PSpice (*see* Simulation)
- Pulse width modulation (PWM), 4-6
  - modulator ac model, 253-255
  - operation of modulator, 253-255
  - spectrum of PWM waveform, 188-189
- Push-pull isolated converters
  - based on boost converter, 167-168
  - based on buck converter, 159-160, 441
  - Watkins-Johnson converter, 167-168
- $Q$  factor, 283-286
  - canonical model, predicted by, 300
  - closed-loop, vs. phase margin, 342-346
  - of the CCM buck, boost, and buck-boost converters, 300
  - graphical determination of, 307, 310, 312, 314
  - the low  $Q$  approximation, 287-289
  - vs. overshoot, 346-347
  - of parallel resonant circuit, 309-310
  - of series resonant circuit, 305-307
- Quasi-resonant converters (*see also* Multi-resonant switch, Quasi-square-wave switch)
  - zero-current switching dc-dc
    - full wave, 779-781
    - half wave, 768-779
  - zero-voltage switching dc-dc, 783-784
- Quasi-square-wave converters, 787-790
- Quasi-static approximation, 653-654
- Quiescent operating point, 190-191, 198, 2205
- Reactance graph paper (*see* Impedance graph paper)
- Reactive power

- definition, 598-599  
 in harmonic trap filters, 628  
 in phase-controlled rectifiers, 619-620
- Reciprocity relationship** (*see also* Extra element theorem), 736, 845
- Rectifiers** (*see also* Ideal rectifiers, Low harmonic rectifiers), 1  
 energy storage in single-phase, 663-668  
 high quality, 589  
 ideal, 637-640  
 line-commutated  
   phase control of, 617-622  
   single-phase, 597, 609-615  
   three-phase, 615-617  
   three-phase transformer connections in, 628-630  
   twelve pulse, 628-630  
 in resonant dc-dc converter, 711-713, 718-719
- Regulator system** (*see also* Control system design), 187-188, 331-334, 665-666
- Reluctance**, 498
- Resonance**  
 Bode plots of complex poles, 282-286  
 damping of, 391-398  
 graphical construction examples, 305-313  
 harmonic traps, 622-628  
 the low-*Q* approximation, 287-289  
 parallel resonant network, 309-310  
 series resonant network, 305-307
- Resonant converters** (*see also* Quasi-resonant converters, Multi-resonant converters, Quasi-square-wave converters, Zero voltage transition converter), 705-752  
 analysis of, via sinusoidal approximation, 709-713  
*LCC*, 705-706, 731-733, 737-740  
 parallel, 705-706, 718-722, 731, 733  
 resonant link, 707  
 series, 705-707, 709-718, 722-726, 733, 741-748
- Resonant inverters**, design of, 726-740  
*LCC* design example, 737-740  
 output characteristics, 727-729  
 transistor current, dependence on load, 729-733  
 ZVS boundary, dependence on load, 734-737
- Resonant link converters**, 707
- Resonant switches** (*see* Quasi-resonant converters, Multi-resonant switch, Quasi-square-wave converters)
- Right half-plane zero**  
 Bode plot of, 276  
 caused by input filter, 390  
 physical origins of, 300-302
- Ripple**, switching, 15-19, 108-110, 188-190
- Root mean square value**
- of commonly-observed converter waveforms, 805-812  
 vs. Fourier series, 593-594
- of near-ideal rectifier currents, table of, 677
- of near-ideal rectifier waveforms, 673-678
- Rotation of three-terminal cell**, 137
- Saturation**  
 of inductors, 497-498, 501  
 of magnetic materials, 494-495  
 of transformers, 152, 503-504
- Schottky diode**, 74, 77
- Semiconductor conduction loss**  
 boost converter example, 52-56  
 inclusion in ac model, 204-213, 221-226, 242-244, 816-822  
 with synchronous rectifier, 73-74
- Semiconductor cost**, 173-174
- Semiconductor power devices** (*see also* Bipolar junction transistor, Diode, Gate turn-off thyristor, Insulated-gate bipolar transistor, MOS-controlled thyristor, Schottky diode, Silicon controlled rectifier), 63-102  
 charge control of, 74, 76, 81-84, 94-95, 99  
 conductivity modulation, 74  
 majority vs. minority carriers, 74  
 realization of switches using, 63-74
- SEPIC** (*see* Single-ended primary inductance converter)
- Series pass regulator**, 4
- Series resonant converter**  
 analysis via sinusoidal approximation, 709-718  
 dependence of transistor current on load, 733  
 exact characteristics  
   continuous conduction mode, 741-743  
   control plane, 746  
   even discontinuous conduction mode, 744-745  
   odd discontinuous conduction mode, 743-744  
   output plane, 747-748  
 introduction to, 705-707  
 subharmonic modes in, 717-718  
 zero-current switching in, 722-723  
 zero-voltage switching in, 723-726
- Silicon area** (*see* Switch stress)
- Silicon controlled rectifier (SCR)**  
 construction and characteristics of, 88-92  
 equivalent circuit, 89  
 inverter grade, 90
- Silicon steel**, 495, 507
- Simulation**, 813-842  
 ac, 825-827, 829-831, 837-839  
 averaged switch models

- basic CCM, 815-816
- CCM with conduction losses, 816-818
- combined CCM/DCM, 822-825
- current programmed control model, 834-837
- dc, 818-819
- examples
  - boost rectifier, 832-834
  - buck-boost transient response, 819-822
  - buck current programmed control, 837-839
  - buck voltage regulator, 827-831
  - SEPIC dc conversion ratio and efficiency, 818-819
  - SEPIC frequency responses, 825-827
  - transient, 819-822, 830-831, 833-834
- Single-ended primary inductance converter (SEPIC), 35-36, 145-146
  - averaged switch model of
    - continuous conduction mode, 228-233, 825-827
    - discontinuous conduction mode, 418-420, 825-877
  - conversion ratio  $M(D)$ , 145-146, 420
  - inverse of, 145-146, 168-171
  - as low-harmonic rectifier, 645, 676-677
  - simulation of, 818-819, 825-827
  - transformer isolation in, 168-171
- Single quadrant switch
  - definitions, 63-64
  - implementation, 65-67
  - origins of DCM, 107-112
- Sinusoidal approximation, 709-713
- Sinusoidal PWM, 689-690
- Skin effect (*see also* Proximity effect), 508-510
- Slope compensation (*see* Artificial ramp)
- Small ripple approximation (*see also* Averaging)
  - in ac modeling approach, 192-193, 218-219
  - and average power loss, prediction of, 55-56
  - boost example, 22-27
  - buck example, 17-18
  - Cuk** converter example, 27-31
  - definition, 15-17
  - in discontinuous conduction mode, 112-114
  - failure of, in two-pole filters, 31-33
- Small-signal ac modeling
  - via averaged switch modeling, 226-247, 410-433, 454-459
  - via circuit averaging, 226-235
  - of CCM converters, 187-264
  - of current programmed converters, 449-480
  - of DCM converters, 420-433
  - of low harmonic rectifiers, 668-673
  - via state-space averaging, 213-226
- Snubber networks, 85, 92, 97, 764-765, 767
- Soft switching (*see also* Zero current switching, Zero voltage switching), 761-802
- Spacecraft power system, 8
- Spice (*see* Simulation)
- Spreadsheet design of converters, 174-176
- State equations of a network, 213-216
- State-space averaging, 213-226
  - discussion, 217-221
  - example: nonideal buck-boost converter, 221-226
  - summary of result, 216-217
- Steady state
  - inductor current waveform, 18-22
  - operating point, 190-191, 198, 217
- Subharmonic
  - modes of series resonant converter, 717-718
  - number  $\xi$ , 740-741
- Switch
  - averaged modeling of, 226-247, 410-431, 454-459
  - current-bidirectional two-quadrant, 67-70
  - four-quadrant, 72-73
  - ideal SPDT in converters, 4-7, 13-14, 16, 22, 27
  - ideal SPST, 63-64
  - passive vs. active, 65, 90
  - power dissipated by ideal, 5, 14
  - quasi-resonant, 781-790
  - realization of, using semiconductor devices, 63-74
  - single-quadrant, 65-67
  - synchronous rectifier, 73-74
  - voltage-bidirectional two-quadrant, 71-72
- Switch conversion ratio  $\mu$ 
  - boost converter example, 778-779
  - combined CCM/DCM model, 822-824
  - definition, 770, 823-824
  - of multi-resonant switch, 784-786
  - of quasi-resonant switches
    - full-wave ZCS, 780-781
    - full-wave ZVS, 783
    - half-wave ZCS, 776-779
    - half-wave ZVS, 783
  - of quasi-square-wave switches, 787-790
- Switch network, 227, 235-241
  - boost, 235-239, 241, 424-425, 816
  - buck, 239-241, 424-425, 454-455, 816
  - general two-switch, 228, 230, 233-235, 241, 410-411, 416, 473-474, 815
- Switched mode, 3-7
- Switching frequency
  - converter efficiency vs., 100-101
  - definition of, 14
  - transformer size vs., 576
- Switching harmonics (*see also* Ripple, switching), 5-6
  - removal of via averaging, 188-190

- Switching loss (*see also* Soft switching, Zero current switching, Zero voltage switching)  
 averaged switch modeling of, 244-248  
 with clamped inductive load, 93-96  
 and current tailing, 94-96, 768  
 and device capacitances, 98-100, 766  
 and diode recovered charge, 96-97, 99-100, 763-765  
 effect on converter efficiency, 100-101  
 and ringing waveforms, 98-100, 763-767  
 and stray inductances, 98-100, 764, 766-767
- Switch stress  $S$ , 171-174
- Switch utilization  $U$ , 171-174
- Synchronous rectifier, 73-74
- Temperature rise  
 in a converter, 2-3  
 in magnetics, 864
- Thyristor (*see also* Gate turn-off thyristor, MOS-controlled thyristor, Silicon controlled rectifier)
- Topologies of converters (*see also* Boost, Bridge configuration, Buck, Buck-boost, Ćuk converter, Forward converter, Transformer-isolated converters, etc.)  
 Cascade connections, 134-137  
 Converter synthesis, 143-146  
 Differential connection of load, 138-143  
 Evaluation and comparison, 171-176, 676-678  
 Inversion of source and load, 132-133  
 Low-harmonic single-phase rectifiers, 640-648  
 Resonant converters, 659-664  
 Resonant switch converters, 781-790  
 Rotation of three-terminal cell, 137  
 Transformer isolation, 146-171
- Total harmonic distortion (THD)  
 of current-programmed rectifiers, 655-656  
 definition, 596  
 vs. distortion factor, 596-597  
 IEEE-519 limits, 604-605  
 of peak detection rectifier, 597-598  
 of single-phase bridge rectifiers, 597-598, 610-615  
 of three-phase bridge rectifiers, 615-617, 619
- Transfer functions (*see also* Bode plots)  
 of the buck, boost, and buck-boost converters, 300  
 of current programmed converters, 453-454, 470-473, 837-839  
 of DCM converters, 427-433, 830  
 graphical construction of, 302-317  
 input filter, effect on, 379-392  
 of low-harmonic rectifiers, 668-673,  
 measurement of, 317-318  
 predicted by canonical model, 248-250, 300  
 simulation of, 825-831, 837-839
- Transformer connections in three-phase rectifiers, 628-630
- Transformer-isolated converters, 146-171  
 boost-derived topologies, 165-168  
 Ćuk converter, 170-171  
 evaluation and comparison of, 171-176  
 flyback, 161-165  
 forward, 154-159  
 full bridge buck-derived, 149-152  
 half-bridge buck-derived, 152-154  
 multiple outputs and cross regulation, 147  
 push-pull buck-derived, 159-160  
 SEPIC, 168-169  
 transformer model, 147-149, 501-505  
 use of volt-second balance in, 148-149, 151-152
- Transformers  
*B-H* loop in, 148, 503, 528  
 design of,  
   derivation of procedure, 565-570  
   examples, 573-580  
   step-by-step procedure, 570-573  
   winding area optimization, 545-550  
 flyback transformer, 161-165  
 leakage inductance, 149, 504-505  
 magnetizing inductance, 147-149, 502-504  
 modeling of, 147-149, 501-505  
 SEPIC transformer, 168-169  
 volt-second balance in, 148-149, 151-152
- Triplen harmonics  
 in three-phase four-wire networks, 600-601  
 in three-phase inverter modulation schemes, 690  
 in three-phase rectifier circuits, 615-616  
 in three-phase three-wire networks, 601
- Twelve-pulse rectifier, 629-630
- Two-quadrant switches (*see* Switch)
- Universal-input rectifiers, 665
- Variable-speed ac drive, 8-9
- Voltage conversion ratio (*see* Conversion ratio  $M$ )
- Voltage injection, 364-367
- Voltage-source inverter, 70, 142-143
- Volt-second balance (*see* Inductor volt-second balance)
- Watkins-Johnson converter, 145, 167-168  
 inverse of, 145  
 isolated push-pull, 167-168
- Window area  $W_A$   
 allocation of, to minimize total copper loss, 545-550  
 definition, 542  
 ferrite core tables, 863-867
- Window utilization factor  $K_u$ , 542

Wire area  $A_w$   
 inductor design, 542, 545

American wire gauge (AWG) table, 868-869

Zero-current switching (ZCS), 708

in quasi-resonant converters, 777-778

in quasi-square-wave converters, 787

in series resonant converter, 722-723

ZCS/ZVS boundary, 734-737

Zero-voltage switching (ZVS), 708

in active clamp snubber, 794-796

in auxiliary resonant commutated pole, 796-797

design of *LCC* resonant converter to attain, 739

of diodes, 763-765

of IGBTs, 768

in *LCC* resonant converter, 734-737

of MOSFETs, 765-768

in multi-resonant converters, 784-786

in quasi-resonant converters, 783

in quasi-square-wave converters, 787-790

in series resonant converter, 723-726

in zero-voltage transition converter, 791-794

ZVS/ZCS boundary, 734-737

Zero-voltage transition buck-derived converter, 791-794